E. Beaurepaire H. Bulou F. Scheurer J.P. Kappler *Editors*

SPRINGER PROCEEDINGS IN PHYSICS 133

Magnetism and Synchrotron Radiation

New Trends



SPRINGER PROCEEDINGS IN PHYSICS

Please view available titles in *Springer Proceedings in Physics* on series homepage http://www.springer.com/series/361/

Eric Beaurepaire Hervé Bulou Fabrice Scheurer Jean-Paul Kappler

Editors

Magnetism and Synchrotron Radiation

New Trends

With 208 Figures



Editors

Eric Beaurepaire
Hervé Bulou
Fabrice Scheurer
Jean-Paul Kappler
Université Strasbourg, CNRS, IPCMS
23, rue du Loess BP 43
67034 Strasbourg Cedex 2, France
E-mail: eric.beaurepaire@ipcms.u-strasbg.fr
herve.bulou@ipcms.u-strasbg.fr
Fabrice.Scheurer@ipcms.u-strasbg.fr

 Springer Proceedings in Physics
 ISSN 0930-8989

 ISBN 978-3-642-04497-7
 e-ISBN 978-3-642-04498-4

 DOI 10.1007/978-3-642-04498-4
 Springer Heidelberg Dordrecht London New York

Library of Congress Control Number: 2009938948

© Springer-Verlag Berlin Heidelberg 2010

This work is subject to copyright. All rights are reserved, whether the whole or part of the material is concerned, specifically the rights of translation, reprinting, reuse of illustrations, recitation, broadcasting, reproduction on microfilm or in any other way, and storage in data banks. Duplication of this publication or parts thereof is permitted only under the provisions of the German Copyright Law of September 9, 1965, in its current version, and permission for use must always be obtained from Springer-Verlag. Violations are liable to prosecution under the German Copyright Law.

The use of general descriptive names, registered names, trademarks, etc. in this publication does not imply, even in the absence of a specific statement, that such names are exempt from the relevant protective laws and regulations and therefore free for general use.

Cover design: SPi Publisher Services

Printed on acid-free paper

Springer is a part of Springer Science+Business Media (www.springer.com)

Foreword

Current research in magnetism is driven by the interesting physics of rather complex materials and by technology relevance, as is indicated, for example, by the rapidly increasing demands of the information-storage and -processing industry. The discovery of the Giant Magneto-resistance 20 years ago, honoured by the Nobel Prize in 2007, laid the foundation to the entirely new research field of Spintronics, which attempts to exploit the electron spin as the basic carrier for the functionality and information transfer in electronic devices. The fifth School on Magnetism and Synchrotron Radiation held at Mittelwihr in October 2008 focussed on current and likely future research trends in the area of magnetism and magnetic materials and posed the question about the special tools needed. Advances in the synthesis of new materials and complex structures, often with nanometerscale dimensions, require increasingly sophisticated experimental techniques that can probe the electronic states, the atomic magnetic moments and the magnetic microstructures responsible for the properties of these materials. Tools are needed to explore the microscopic interactions between a spin-polarized current and the magnetization. Processes like spin-transfer torque and spin transfer at interfaces are in the focus of interest.

In the last two decades, experimental techniques based on synchrotron radiation have provided unique capabilities for the study of magnetic phenomena. One reason is that X-ray techniques have the unique advantage of coupling directly to the spin-resolved electronic states of interest. *X-ray Magnetic Circular or Linear Dichroism (XMCD or XMLD) spectroscopy* is a unique tool for measuring element-specific 3*d*, 4 *f* and 5*d* magnetic moments, frequently separated into spin and orbital components. *Inelastic X-ray scattering*, in resonant and non-resonant mode, is a powerful emerging spectroscopic probe that, due to the advent of new instrumentation, provides a wealth of information on electronic states in strongly correlated materials or in materials under high pressure and in strong magnetic fields. Such experiments need the high brightness of a third-generation synchrotron source, like the ESRF or SOLEIL and others.

An important aspect in magnetism research is *dimensionality*. Many modern magnetic materials like thin films, multi-layers and clusters, self-organized or laterally patterned structures show spatial extensions with at least one dimension on the nanometer scale. These novel materials, often heterogeneous or multi-component,

vi Foreword

exhibit structural, electronic and magnetic properties different from those of bulk materials. The ability to control spatial dimensions of magnetic features at the nanometer level opens the possibility to study the fundamental magnetic interactions on this scale.

Synchrotron radiation sources of the third generation have made it possible to perform *magnetic imaging* using X-ray techniques on a sub-micrometer level. This technique combines X-ray microscopy or X-ray photoelectron microscopy with spectroscopy and permits imaging of magnetic domain structures with a lateral spatial resolution of a few 10 nm. A new development is lens-less imaging by Fourier transform X-ray holography, where the diffraction pattern of a coherently illuminated sample is recorded in Fourier space. These methods provide a key technique for research on small structures important in microelectronics, which are often heterogeneous and composed of several elements. Together with the temporal structure of the synchrotron radiation, they permit element-sensitive *time-domain studies*, which are of prime importance for magnetic recording. Examples are the dynamics of domain-wall displacements and transformation or dynamics of the magnetization of mesoscopic magnetic structures. The underlying processes occur at times in the nano- to femto-second range. Understanding is limited due to the lack of a microscopic theory.

A class of materials of particular scientific interest are the *actinide metals* and their compounds. Their physical properties, deriving from the $5\,f$ electron states, show many similarities with the lanthanides, such as electron correlations, superconductivity, or ordered magnetism. But compared to the $4\,f$ metals, their properties and their magnetic structure, in particular, remain poorly understood. This is due to experimental complications and the exotic behavior of the $5\,f$ states that appear to be delocalized for the light actinide metals, but become localized in the latter part of the series. Considerable insight into the electronic ground state can be obtained from core-level X-ray absorption spectroscopy and electron energy loss spectroscopy, together with recent theoretical results.

Current interest in magnetic materials includes *molecular magnets*. They bridge the gap between the atomic and the mesoscopic length scale. A special case is the Single Molecule Magnets, which are coordination compounds of paramagnetic metal ions held together by suitable ligands. Interest in this material is focussed on the understanding of their magnetic hysteresis that occurs at low temperature and presumably is of pure molecular origin.

This Mittelwihr School on the interrelation of magnetism and synchrotron radiation was meant, like the preceding ones, to introducing into the basics of the topic. Hence the first lectures were devoted to the major fundamental phenomena and aspects in magnetism, to the modern theoretical concepts for the description of the interaction of an electromagnetic wave with matter, focussing on core-level X-ray spectroscopies, and to the fundamentals of synchrotron sources and devices. A new spectroscopic tool was presented, X-ray detected magnetic resonance, which uses XMCD to probe the resonant precession of local magnetization spin and orbital components in a microwave pump field. A lecture important for future developments was devoted to report on the progress in the realization of free-electron laser

Foreword vii

sources in the UV and X-ray range. These sources will produce spatially coherent, ultra-short (\sim 100 fs) pulses with very high brilliance and mark the transition from third- to fourth-generation light sources.

In the above lines, I have only addressed what appeared to me as the strong points of the school. The reader interested in the fascinating actual aspects of magnetism as studied by synchrotron radiation will find an excellent presentation in these Lecture Notes.

Göttingen, May 2009 Wolfgang Felsch

Preface

This volume contains the lecture notes of the fifth school on Magnetism and Synchrotron Radiation held in *Mittelwihr*, France, from 19 to 24 October 2008.

We thank the teachers, whose job was very much appreciated, and the members of the scientific committee for their help in establishing the school program. The success of this school is also due to the hard work of our colleagues from the local organization committee, J.-L. Bubendorff (LPSE, Mulhouse), W. Wernher and R.-M. Weller (IPCMS). It is a great pleasure to acknowledge the kind hospitality of the *Centre de Mittelwihr* and the *Communauté des Communes de Ribeauvillé*, which have been welcoming us since 1989.

The present edition benefitted from the expert help of Ch. Brouder, M.-E. Couprie, J.-F. Dayen, U. Flechsig, J.-L. Gallani, C. Hague, L. Joly, J.-M. Mariot, P. Panissod, Ph. Sainctavit, J. Vogel. Many thanks also to W. Felsch, a faithful participant of this school, for writing the Foreword of this volume.

This school would not have been possible without financial support by the following organizations, which we gratefully acknowledge:

- Formation Permanente du CNRS
- European Community Research Infrastructure Action under the FP6 "Structuring the European Research Area" Programme through the Integrated Infrastructure Initiative "Integrating Activity on Synchrotron and Free Electron Laser Science" Contract no.: RII3-CT-2004-506008, and through the Integrated Research Activity NoE MAGMANet "Molecular approach to nanomagnets and multifunctional materials" Contract no.: NMP3-CT-2005-515767
- Université de Haute Alsace
- Université Louis Pasteur (now Université de Strasbourg)
- Institut de Physique et Chimie des Matériaux de Strasbourg
- Conseil Général du Haut-Rhin
- Région Alsace

We also acknowledge kind support from OMICRON Nanotechnology, THERMO FISHER Scientific, TOYAMA Ltd., VAT S.A.R.L., DTA Air Liquide.

Strasbourg, May 2009 E. Beaurepaire H. Bulou F. Scheurer J.-P. Kappler

Scientific Committee

M. Altarelli (European XFEL, Hamburg, Germany)

A. Barla (ALBA - CELLS, Barcelona)

S. Blundell (University of Oxford)

S. Dhesi (DIAMOND Light Source, United Kingdom)

K. Dumesnil (Laboratoire de Physique des Matériaux, Nancy, France)

H. Dürr (BESSY, Berlin, Germany)
A. Fontaine (Institut Néel, Grenoble, France)

F. Gautier (Institut de Physique et Chimie des Matériaux de Strasbourg,

France)

P. Krüger (Université de Bourgogne, France)

J.-M. Mariot (Laboratoire de Chimie Physique - Matière et Rayonnement,

Paris)

F. Nolting (Swiss Light Source, Villigen)

P. Morin (Synchrotron SOLEIL, Gif-sur-Yvette, France)

G. Panaccione (ELETTRA, Trieste, Italy)

F. Petroff (CNRS-THALES, Palaiseau, France)

C. Pirri (Laboratoire de Physique et Spectroscopie Electronique, Mul-

house, France)

A. Rogalev (ESRF, Grenoble, France)

P. Sainctavit (Institut de Minéralogie et de Physique des Milieux Condensés,

Paris, France)

Contents

1			o Magnetism	1
	W. We	eber		1
	1.1	Introduction		
		1.1.1	Definition of the Magnetic Moment	1
		1.1.2	Energy of the Moment in an External	
			Magnetic Field	
		1.1.3	Further Definitions	3
	1.2	Magne	tism of Free Atoms and Electrons	
		1.2.1	Diamagnetism of Free Atoms	
		1.2.2	Paramagnetism of Free Atoms	5
		1.2.3	Pauli Paramagnetism of Free Electrons	
			(in Metals)	9
	1.3	Ferrom	nagnetism	10
		1.3.1	Molecular Field	11
		1.3.2	Exchange Interaction as Origin	
			of the Molecular Field	12
		1.3.3	Mean Field Approximation (MFA)	14
		1.3.4	Spin Waves	18
		1.3.5	Itinerant Ferromagnetism	21
	1.4	Magne	tization Curves $M(H)$	22
		1.4.1	Magnetostatic Energy or Shape Anisotropy	23
		1.4.2	Magneto-Crystalline Anisotropy	24
		1.4.3	Magnetization Curves in the "Uniform	
			Rotation" Model	26
		1.4.4	Domains and Domain Walls	28
	1.5	Thin Fi	ilm Magnetism	35
		1.5.1	Surface Anisotropy	35
		1.5.2	Indirect Exchange Coupling in Multilayers	
		1.5.3	Giant Magnetoresistance	
	Refere	ences		4.0

xii Contents

Spin	tronics: C	onceptual Building Blocks	
JPh	. Anserme	t	
2.1	Spin Pr	recession	
2.2		elaxation	
2.3	Spin-de	ependent Transport: The Collinear Case	
	2.3.1	Collisions	
	2.3.2	Calculation of the Currents	
	2.3.3	Diffusion Equation and the Spin	
		Accumulation	
2.4	Spin Re	elaxation of Conduction Electrons	
	2.4.1	Spin-Lattice Relaxation Time	
		for Conduction Electrons	
	2.4.2	The Bottleneck Regime	
	2.4.3	Spin-Orbit Scattering	
	2.4.4	Electron–Magnon Scattering	
	2.4.5	Spin Mixing by Collisions with Magnons	
2.5	Spin-de	ependent Transport: The Non-collinear Case	
	2.5.1	Toward a Semi-classical Description	
		of Spin Dynamics in Transport	
	2.5.2	Constitutive Equations	
	2.5.3	Spin Diffusion in Non-collinear Configurations	
	2.5.4	Domain Walls	
Inter Y. Jo		Polarized Light with Matter	
3.1	•		
3.2		etion	
3.2		mental Observations of Y Pay Interaction	
	Experi	mental Observations of X-Ray Interaction	
	Experiment	mental Observations of X-Ray Interaction atter	
	Experiment Experiment With M 3.2.1	mental Observations of X-Ray Interaction atter Absorption	
	Experiment with M 3.2.1 3.2.2	mental Observations of X-Ray Interaction atter Absorption Dependence on Energy	
	Experiment With M 3.2.1 3.2.2 3.2.3	mental Observations of X-Ray Interaction atter Absorption Dependence on Energy Dependence on the Atomic Environment	
	Experiment with M 3.2.1 3.2.2 3.2.3 3.2.4	mental Observations of X-Ray Interaction atter Absorption Dependence on Energy Dependence on the Atomic Environment Dependence on the Light Polarization	
2.2	Experir with M 3.2.1 3.2.2 3.2.3 3.2.4 3.2.5	mental Observations of X-Ray Interaction atter Absorption Dependence on Energy Dependence on the Atomic Environment Dependence on the Light Polarization Diffraction Around Edges	
3.3	Experiment with M 3.2.1 3.2.2 3.2.3 3.2.4 3.2.5 The Lig	mental Observations of X-Ray Interaction atter Absorption Dependence on Energy Dependence on the Atomic Environment Dependence on the Light Polarization Diffraction Around Edges	
3.3	Experiment with M 3.2.1 3.2.2 3.2.3 3.2.4 3.2.5 The Lig 3.3.1	mental Observations of X-Ray Interaction atter Absorption Dependence on Energy Dependence on the Atomic Environment Dependence on the Light Polarization Diffraction Around Edges ght Definitions and Notations	
3.3	Experiment with M 3.2.1 3.2.2 3.2.3 3.2.4 3.2.5 The Lig 3.3.1 3.3.2	mental Observations of X-Ray Interaction atter Absorption Dependence on Energy Dependence on the Atomic Environment Dependence on the Light Polarization Diffraction Around Edges ght Definitions and Notations Stokes Parameters	
	Experiment with M 3.2.1 3.2.2 3.2.3 3.2.4 3.2.5 The Lig 3.3.1 3.3.2 3.3.3	mental Observations of X-Ray Interaction atter Absorption Dependence on Energy Dependence on the Atomic Environment Dependence on the Light Polarization Diffraction Around Edges ght Definitions and Notations Stokes Parameters Quantization of the Electromagnetic Field	
3.3	Experiment with M 3.2.1 3.2.2 3.2.3 3.2.4 3.2.5 The Lig 3.3.1 3.3.2 3.3.3 Interact	mental Observations of X-Ray Interaction atter Absorption Dependence on Energy Dependence on the Atomic Environment Dependence on the Light Polarization Diffraction Around Edges ght Definitions and Notations Stokes Parameters Quantization of the Electromagnetic Field tion of Light with an Electron in an Atom	
	Experiment with M 3.2.1 3.2.2 3.2.3 3.2.4 3.2.5 The Lig 3.3.1 3.3.2 3.3.3 Interact 3.4.1	mental Observations of X-Ray Interaction atter Absorption Dependence on Energy Dependence on the Atomic Environment Dependence on the Light Polarization Diffraction Around Edges ght Definitions and Notations Stokes Parameters Quantization of the Electromagnetic Field Linear and Nonlinear Interactions	
	Experiment with M 3.2.1 3.2.2 3.2.3 3.2.4 3.2.5 The Lig 3.3.1 3.3.2 3.3.3 Interact 3.4.1 3.4.2	mental Observations of X-Ray Interaction atter Absorption Dependence on Energy Dependence on the Atomic Environment Dependence on the Light Polarization Diffraction Around Edges ght Definitions and Notations Stokes Parameters Quantization of the Electromagnetic Field tion of Light with an Electron in an Atom Linear and Nonlinear Interactions Interaction Hamiltonian	
	Experiment with M 3.2.1 3.2.2 3.2.3 3.2.4 3.2.5 The Lig 3.3.1 3.3.2 3.3.3 Interact 3.4.1 3.4.2 3.4.3	mental Observations of X-Ray Interaction atter Absorption Dependence on Energy Dependence on the Atomic Environment Dependence on the Light Polarization Diffraction Around Edges ght Definitions and Notations Stokes Parameters Quantization of the Electromagnetic Field tion of Light with an Electron in an Atom Linear and Nonlinear Interactions Interaction Hamiltonian Absorption and Emission	
	Experiment with M 3.2.1 3.2.2 3.2.3 3.2.4 3.2.5 The Lig 3.3.1 3.3.2 3.3.3 Interact 3.4.1 3.4.2 3.4.3 3.4.4	mental Observations of X-Ray Interaction atter Absorption Dependence on Energy Dependence on the Atomic Environment Dependence on the Light Polarization Diffraction Around Edges ght Definitions and Notations Stokes Parameters Quantization of the Electromagnetic Field tion of Light with an Electron in an Atom Linear and Nonlinear Interactions Interaction Hamiltonian Absorption and Emission Scattering	
	Experiment with M 3.2.1 3.2.2 3.2.3 3.2.4 3.2.5 The Lig 3.3.1 3.3.2 3.3.3 Interact 3.4.1 3.4.2 3.4.3	mental Observations of X-Ray Interaction atter Absorption Dependence on Energy Dependence on the Atomic Environment Dependence on the Light Polarization Diffraction Around Edges ght Definitions and Notations Stokes Parameters Quantization of the Electromagnetic Field tion of Light with an Electron in an Atom Linear and Nonlinear Interactions Interaction Hamiltonian Absorption and Emission	

Contents xiii

	3.5	Dielect	ric Function or Macroscopic Point of View	98		
		3.5.1	Complex Permittivity	99		
		3.5.2	Complex Refractive Index	101		
	3.6	X-Ray	Spectroscopies	102		
		3.6.1	Characteristic Times	103		
		3.6.2	The Different Spectroscopies	104		
		3.6.3	Fluorescence and Auger Spectroscopies	106		
		3.6.4	XANES and RXS Formula	107		
		3.6.5	Multipole Analysis	112		
		3.6.6	X-Ray Magnetic Circular Dichroism	118		
	3.7	Monoe	lectronic Simulations	120		
		3.7.1	The Potential	120		
		3.7.2	The Multiple Scattering Theory	121		
		3.7.3	Available Codes			
	3.8	Conclu	sion	123		
	Refer	ences		124		
4	Synch	rotron R	Radiation Sources and Optical Devices	127		
	D. Co	cco and N	M. Zangrando			
	4.1	Optics	for UV and X-Ray	127		
	4.2					
		for Soft	t X-Ray	133		
		4.2.1	SR Sources and Prefocusing or Heat Load			
			Section	133		
		4.2.2	Soft X-Ray Monochromators and			
			Diffraction Gratings	138		
		4.2.3	Refocusing Optics	142		
	Refer	ences				
5	X-Ra	y Magnet	tic Dichroism	145		
	H. We	ende and (C. Antoniak			
	5.1	Introdu	ection	145		
	5.2	X-Ray	Absorption Spectroscopy	146		
		5.2.1	X-Ray Absorption Near-Edge Structure			
		5.2.2	Dichroism in X-Ray Absorption			
			Spectroscopy	148		
	5.3	X-Ray	Magnetic Circular Dichroism			
			Determination of Orbital and Spin			
			Magnetic Moments: Sum Rules			
	5.4	Experi	mental Setup			
	5.5		nalysis			
		5.5.1	Self-absorption and Saturation Effects			
			in Electron Yield	152		
		5.5.2	Standard Analysis			

xiv Contents

	5.6	Examples of Recent Research		
		5.6.1	Failure of Sum Rule-based Analysis	
			for Light 3d Elements	156
		5.6.2	Spin-dependence of Matrix Elements	
			in Rare Earths	159
		5.6.3	Paramagnetic Biomolecules	
			on Ferromagnetic Surfaces	162
	5.7	Conclu	sions and Outlook	
	Refer			
6	X-Ra	y Detecte	ed Optical Activity	169
	A. Ro	galev, J. (Goulon, F. Wilhelm, and A. Bosak	
	6.1	Introdu	ction	169
	6.2	X-Ray	Detected OA Tensor Formalism	171
	6.3	Instrun	nentation and Experimental Considerations	173
	6.4		Optical Activity Detected with X-Rays	
		6.4.1	X-Ray Natural Circular Dichroism	
		6.4.2	Vector Part of X-Ray-detected OA	180
	6.5	Nonrec	riprocal X-Ray-detected OA	182
		6.5.1	Nonreciprocal X-Ray Linear Dichroism	
		6.5.2	X-Ray Magnetochiral Dichroism: XM χD	184
	6.6	Effectiv	ve Operators for X-Ray Detected OA	186
	Refer	ences		188
7	X-Ra	y Detecto	ed Magnetic Resonance:	
	A Ne	w Spectro	oscopic Tool	191
	J. Go		logalev, F. Wilhelm, and G. Goujon	
	7.1	Introdu	ction	191
	7.2	Precess	sion Dynamics Probed with X-Rays	193
		7.2.1	Phenomenological Equation of Motion	193
		7.2.2	Precession Dynamics of Orbital and Spin	
			Magnetization Components	195
		7.2.3	Precession Under High Pumping Power	196
		7.2.4	Nonuniform Eigen Modes of Precession	199
		7.2.5	Longitudinal and Transverse Relaxation	
			Times	202
	7.3	Experii	mental Results	203
		7.3.1	Ferrimagnetic Iron Garnets	
		7.3.2	Modular XDMR Spectrometer	205
		7.3.3	XDMR in Longitudinal Geometry	
		7.3.4	XDMR in Transverse Geometry	
	7.4	Facing	New Challenges	220
	Refer	_		

Contents xv

8	Resor	nant X-R	ay Scattering and Absorption	223	
			d A. Bombardi		
	8.1	Absorp	otion and Scattering: The Optical Theorem	223	
	8.2		etry and X-Ray Absorption		
	8.3	X-Ray	Scattering and Multipole Matrix Elements	226	
	8.4	Cartesi	an Tensors, Magnetism and Anisotropy	228	
	8.5	Neuma	nn's Principle and Symmetry-restricted		
		Tensor	s	231	
	8.6	Scatter	ing Matrix and Stokes Parameters	232	
	8.7	Diffrac	tion Intensity and the Unit-Cell Structure		
		Factor		234	
	8.8		tic Symmetry, Propagation Vector,		
		and the	Magnetic Structure Factor	235	
	8.9	Crystal	Coordinates and Azimuthal Rotations	238	
	8.10		cal and Cartesian Tensors		
	8.11		le: HoFe ₂		
	8.12	Examp	le: ZnO	248	
	8.13	Examp	le: Ca ₃ Co ₂ O ₆	253	
	8.14	Conclu	sions	261	
	Refere	ences		261	
9	An Introduction to Inelastic X-Ray Scattering				
	JP. R				
	9.1		action		
	9.2		tical Concepts		
		9.2.1	Overview of the IXS Process		
		9.2.2	Interaction Hamiltonian		
		9.2.3	IXS Cross Sections and Fermi Golden Rule		
		9.2.4	Nonresonant IXS		
		9.2.5	RIXS		
	9.3		ations of IXS		
		9.3.1	Extreme Conditions		
		9.3.2	Strongly Correlated Materials		
	9.4 Conclusion				
	Refere	ences		277	
	~		OT		
10			CD of Single Molecule Magnets		
	R. Sessoli, M. Mannini, F. Pineider, A. Cornia, and Ph. Sainctavit				
	10.1				
	10.2		Molecule Magnets		
		10.2.1	Building Up a Large Spin	281	
		10.2.2	Magnetic Anisotropy in Single Molecule		
		40 -	Magnets		
		10.2.3	The Dynamics of the Magnetization	287	

xvi Contents

	10.3 10.4	Deposition of Single Molecule Magnets on Surfaces XAS and XMCD of SMMs	
	10.4	10.4.1 XAS and XMCD to Investigate the	293
		Electronic Structure of Mn ₁₂ Clusters	206
		10.4.2 XAS and XMCD of Monolayers of Mn ₁₂	290
		SMMs	208
		10.4.3 XMCD and Magnetic Anisotropy	
		10.4.4 XMCD and the Dynamics of the Magnetization .	
	10.5	Conclusions	
		ences	
	Refere	illes	
11		etic Structure of Actinide Metals	313
	G. van	der Laan and K.T. Moore	
	11.1	Introduction	
	11.2	Volume Change Across the Actinide Series	
		11.2.1 Photoemission Spectroscopy's Two Cents	
	11.3	The Six Crystal Allotropes of Pu Metal	317
		11.3.1 Lowering the Electronic Energy Through	
		a Peierls-like Distortion	
		11.3.2 Comparison with Cerium	
		11.3.3 Stabilized δ-Plutonium	
	11.4	Revised View of the Periodic Table	
	11.5	Actinide Magnetism	323
		11.5.1 Experimental Absence of Magnetic	
		Moments in Plutonium	
		11.5.2 Looking to Other Elements for Clues	
	11.6	Experimental Complications of Plutonium	325
	11.7	One Man's Electron Energy Loss is Another's	
		X-Ray Absorption	
	11.8	Theory	
		11.8.1 Atomic Interactions	
		11.8.2 LS - and jj -Coupling Schemes	
		11.8.3 Intermediate Coupling	
		11.8.4 Moments for f^2	
	11.9	Spectral Calculations	
	11.10	Spin-Orbit Interaction and Sum Rule Analysis	
	11.11	Validity of the Sum Rule	
	11.12	Experimental Results for the $N_{4,5}$ Edges	
		11.12.1 What Our Results Mean for Pu Theory	341
	11.13	Conclusions	342
	Defere	nces	342

Contents xvii

12	_	_	ging with X-rays	345
	F. Nol	_		
	12.1		ction	
	12.2	_	ts of Magnetic Imaging Contrast	
		12.2.1	XMCD Image	
		12.2.2	XMLD Images	
		12.2.3	Polarization Control	
		12.2.4	Local Spectra	355
		12.2.5	Spatial Resolution	356
	12.3	Realiza	tion of the Magnetic Contrast	
		with Di	fferent Microscopes	358
		12.3.1	Photoemission Electron Microscope	358
		12.3.2	STXM/TXM	359
		12.3.3	"Lensless" Imaging	361
		12.3.4	Combining Scanning Probes with X-Rays	
	12.4	Summa	ry	
	Refere			
13	Domo	in Wall S	Spin Structures and Dynamics Probed	
13			n Techniques	367
	M. Kl	äui		
	13.1	Introdu	ction	367
	13.2		jues	
	13.3		Wall Types and Wall Phase Diagrams	
		13.3.1	Theory of Head-to-Head Domain	
		10.011	Wall Spin Structures	369
		13.3.2	Experimental Determination	
		13.3.2	of Head-to-Head Domain Wall	
			Spin Structures	371
		13.3.3	Further Head-to-Head Domain Wall Types	
	13.4		rutilier read-to-ricad Bolham Wall Types	
	13.4	13.4.1	•	
			Field-induced Domain Wall Propagation	
		13.4.2	Current-induced Domain Wall Propagation	377
		13.4.3	Field- and Current-induced Domain Wall	200
		_	Excitations	
	13.5		ıry	
	Refere	ences		382
14	Dyna	mics of M	Iesoscopic Magnetic Objects	385
	C. Qu	itmann, J.	Raabe, A. Puzic, K. Kuepper, and S. Wintz	
	14.1		ction	385
	14.2		copic vs. Mesoscopic Magnetic Objects	
		14.2.1	Magnetic Interactions and Domains	
		14.2.2	Magnetic Time Scales	
		14.2.3	Magnetic Length Scales	

xviii Contents

		14.2.4	Landau-Lifshitz-Gilbert Equation	389
		14.2.5	Experimental Techniques	
	14.3	Dynami	ics in Simple Squares	
		14.3.1	Static Mesoscopic Structures	
		14.3.2	Pulsed Field Excitations	
	14.4	Vortex 1	Dynamics and Switching	
		14.4.1	Current Induced Resonant Vortex Core	
		11	Motion	399
		14.4.2	Bistable Configurations by Pinning	
			the Vortex Core	401
		14.4.3	Resonant Burst Switching	
	14.5		resonant Burst 8 witching	
15	From	Third- to	o Fourth-Generation Light Sources:	
		Lasers in the UV and X-ray Range	407	
	M. Al			
	15.1	tarcin		
	15.1		ction	407
	15.1 15.2	Introdu	ction	407
	10.1	Introduc The SA	SE Process and Short-wavelength	
	10.1	Introduce The SA Free-Ele		
	15.2	Introduc The SA Free-El- First Re	SE Process and Short-wavelength ectron Lasers	409
	15.2	Introduc The SA Free-El- First Re for X-R	SE Process and Short-wavelength ectron Lasers	409
	15.2 15.3 15.4	Introduc The SA Free-El- First Re for X-R The Qu	SE Process and Short-wavelength ectron Lasers	409
	15.2 15.3 15.4 15.5	Introduction The SA Free-Electric First Refor X-R The Quesceded	SE Process and Short-wavelength ectron Lasers esults at FLASH and the Science Case tay FELs est for Hard X-Ray FELs Free-Electron Lasers	409 411 414
	15.2 15.3 15.4 15.5	Introduction The SA Free-Electric First Refor X-R The Quesceded	SE Process and Short-wavelength ectron Lasers	409 411 414
Co	15.2 15.3 15.4 15.5 Refere	Introduc The SA Free-El- First Re for X-R The Qu Seeded ences	SE Process and Short-wavelength ectron Lasers esults at FLASH and the Science Case tay FELs est for Hard X-Ray FELs Free-Electron Lasers	409 411 414 417 418

List of Contributors

- **M. Altarelli** European XFEL, 22607 Hamburg, Germany, massimo.altarelli@xfel. eu
- **J.-Ph. Ansermet** Insitut de Physique des Nanostructures, Ecole Polytechnique Fédérale de Lausanne, Station 3, 1015 Lausanne-EPFL, Switzerland, jean-philippe.ansermet@epfl.ch
- **C. Antoniak** Fachbereich Physik and Center for Nanointegration Duisburg-Essen (CeNIDE), Universität Duisburg-Essen, Lotharstraße 1, 47048 Duisburg, Germany, carolin, antoniak@uni-due.de
- **A. Bombardi** Diamond Light Source Ltd., Diamond House, Harwell Science and Innovation Campus, Didcot, Oxfordshire, OX11 0DE, UK, alessandro.bombardi@diamond.ac.uk
- **A. Bosak** European Synchrotron Radiation Facility (ESRF), B.P.-220, 38043 Grenoble Cedex, France
- **D. Cocco** Sincrotrone Trieste ScpA, SS14 Km 163.5 in Area Science Park, 34012 Trieste, Italy, daniele.cocco@elettra.trieste.it
- **S.P. Collins** Diamond Light Source Ltd, Diamond House, Harwell Science and Innovation Campus, Didcot, Oxfordshire OX11 0DE, UK, steve.collins@diamond.ac.uk
- **A. Cornia** Department of Chemistry and INSTM RU, University of Modena and Reggio Emilia, 41100 Modena, Italy
- **G. Goujan** European Synchrotron Radiation Facility, B.P. 220, 38043, Grenoble, France
- **J. Goulan** European Synchrotron Radiation Facility, B.P. 220, 38043 Grenoble Cedex, France, goulon@esrf.fr
- **Y. Joly** Institut Néel, CNRS and Université Joseph Fourier, BP 166, 38042 Grenoble Cedex 9, France, yves.joly@grenoble.cnrs.fr
- **M. Kläui** Fachbereich Physik and Zukunftskolleg, Universität Konstanz, 78457 Konstanz, Germany, Mathias.Klaeui@uni-konstanz.de

xx List of Contributors

K. Kuepper Forschungszentrum Dresden-Rossendorf, PO Box 51 01 19, 01314 Dresden, Germany

- M. Mannini Laboratory for Molecular Magnetism, Department of Chemistry and INSTM RU, University of Florence, 50019 Sesto Fiorentino, Italy and ISTM-CNR, URT Firenze, 50019 Sesto Fiorentino, Italy, matteo.mannini@unifi.it
- **K.T. Moore** Lawrence Livermore National Laboratory, Livermore, CA 94550, USA
- **F. Nolting** Swiss Light Source, Paul Scherrer Institut, 5232 Villigen PSI, Switzerland, nolting@psi.ch,frithjof.nolting@psi.ch
- **F. Pineider** Laboratory for Molecular Magnetism, Department of Chemistry and INSTM RU, University of Florence, 50019 Sesto Fiorentino, Italy, francesco.pineider@unifi.it
- **A. Puzic** Swiss Light Source, Paul Scherrer Institut, 5232 Villigen PSI, Switzerland
- **C. Quitmann** Swiss Light Source, Paul Scherrer Institut, 5232 Villigen PSI, Switzerland, christoph.quitmann@psi.ch
- **J. Raabe** Swiss Light Source, Paul Scherrer Institut, 5232 Villigen PSI, Switzerland
- **A. Rogalev** European Synchrotron Radiation Facility, B.P. 220, 38043, Grenoble Cedex, France, rogalev@esrf.fr
- **J.-P. Rueff** Synchrotron SOLEIL, L'Orme des Merisiers, BP 48 Saint-Aubin, 91192 Gif sur Yvette, France, jean-pascal.rueff@synchrotron-soleil.fr
- **Ph. Sainctavit** Institut de Minéralogie et de Physique des Milieux Condensés CNRS UMR 7590, Université Pierre et Marie Curie, 75252 Paris Cedex 5, France, Philippe.Sainctavit@impmc.upmc.fr
- **R. Sessoli** Laboratory for Molecular Magnetism, Department of Chemistry and INSTM RU, University of Florence, 50019 Sesto Fiorentino, Italy, roberta.sessoli@unifi.it
- **G. van der Laan** Diamond Light Source, Chilton, Didcot, Oxfordshire OX11 0DE, UK, gerrit.vanderlaan@diamond.ac.uk
- **W. Weber** Institut de Physique et Chimie des Matériaux de Strasbourg, UMR 7504, UdS CNRS, 23 rue du Loess, BP 43, 67034 Strasbourg Cedex 2, France, wolfgang.weber@ipcms.u-strasbg.fr
- **H. Wende** Fachbereich Physik and Center for Nanointegration Duisburg-Essen (CeNIDE), Universität Duisburg-Essen, Lotharstraße 1, 47048 Duisburg, Germany, heiko.wende@uni-due

List of Contributors xxi

F. Wilhelm European Synchrotron Radiation Facility (ESRF), B.P.-220, 38043 Grenoble Cedex, France

- **S. Wintz** Forschungszentrum Dresden-Rossendorf, PO Box 51 01 19, 01314 Dresden, Germany
- **M. Zangrando** Sincrotrone Trieste ScpA, SS14 Km 163.5 in Area Science Park, 34012 Trieste, Italy

Chapter 1 Introduction to Magnetism

W. Weber

Abstract This lecture gives an overview of the main phenomena that determine the magnetism of matter and the properties of magnetic materials. After an introduction, the second section presents the following topics: orbital and spin magnetic moment, dia- and paramagnetism of free atoms, and Pauli-paramagnetism of free electrons. The third section deals with ferromagnetism. The Heisenberg-exchange interaction and its consequences for the magnetization as a function of the applied magnetic field and the temperature are discussed in the molecular field approximation. In particular, the ferromagnetic phase transition and spin waves are described before we finish this section by discussing briefly itinerant ferromagnetism. The fourth section introduces the important concepts of magnetic anisotropy (shape and magneto-crystalline anisotropy) and magnetic domains. Then, we discuss magnetization reversal by the application of a magnetic field, and how it is influenced by the nucleation of domains and domain wall motion. In a last subsection of this section, we discuss the magnetic behavior of small particles. The fifth section deals with the magnetism of thin films and multilayers. We mostly concentrate on two important phenomena observed in multilayers: indirect exchange coupling (RKKY interaction) and giant magnetoresistance.

1.1 Introduction

1.1.1 Definition of the Magnetic Moment

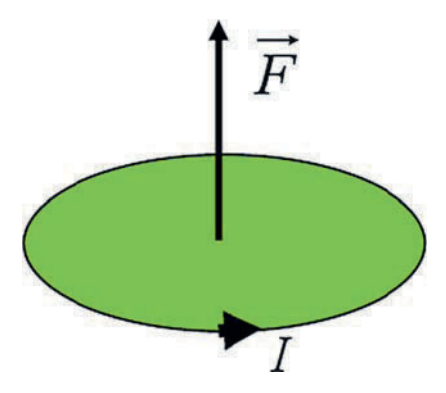
It is not possible to define a magnetic moment in analogy to the electric dipole moment: $\mathbf{p} = Q\mathbf{l}$, with \mathbf{l} the displacement vector between the charges +Q and -Q. It is therefore not possible to write $\mathbf{m} = Q_{\mathbf{M}}\mathbf{l}$, with $Q_{\mathbf{M}}$ the magnetic charge,

Institut de Physique et Chimie des Matériaux de Strasbourg, UMR 7504, UdS - CNRS, 23 rue du Loess, BP 43, F-67034 Strasbourg Cedex 2, France e-mail: wolfgang.weber@ipcms.u-strasbg.fr

1

W. Weber

Fig. 1.1 Magnetic moment due to an eddy current



a so-called magnetic monopole. Up to now, magnetic monopoles have not been discovered, which is expressed by one of Maxwell's equations: $\nabla \mathbf{B} = 0$, that is, there is no source of a magnetic field.

To give a definition of the magnetic dipole moment, we exploit the fact that a bar magnet and a small coil through which a current is driven have similar properties. Both produce, if viewed from a point sufficiently far away from them, a magnetic field of similar shape. Thus, let us define the magnetic dipole moment \mathbf{m} by considering an eddy current (Ampere's definition): $\mathbf{m} = I \cdot \mathbf{F}$, where the direction of the vector \mathbf{F} indicates the sense of the current I and its absolute value the area that is encircled by the current (Fig. 1.1). The unit of the magnetic moment is A \mathbf{m}^2 .

1.1.2 Energy of the Moment in an External Magnetic Field

We emphasize that the magnetic field \mathbf{H} (unit is A m⁻¹) derives from a vector potential and is therefore an axial vector, while the vector of the electric field \mathbf{E} for instance derives from a scalar potential and is thus a polar vector. Their transformations under a mirror symmetry operation are different, as such an operation lets invariant the normal component of \mathbf{H} while the parallel component is reversed. The electric field \mathbf{E} , however, behaves inversely.

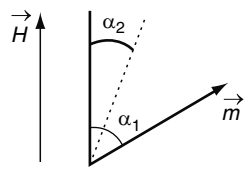
The magnetic field **H** exercises a torque **T** on the magnetic moment **m**:

$$\mathbf{T} = \mu_0 \mathbf{m} \times \mathbf{H},\tag{1.1}$$

with μ_0 the vacuum permeability (= $4\pi \times 10^{-7}$ m kg A⁻² s⁻²). The energy E that is needed to rotate **m** from a position with an angle α_1 between the moment and the magnetic field to the one with an angle α_2 (see Fig. 1.2) is thus given by

$$E = \int_{\alpha_1}^{\alpha_2} \mathbf{T} \, d\boldsymbol{\alpha} = \mu_0 \int_{\alpha_1}^{\alpha_2} mH \sin(\alpha) \, d\alpha = -\mu_0 mH [\cos(\alpha_2) - \cos(\alpha_1)]. \quad (1.2)$$

Fig. 1.2 A magnetic moment **m** in a magnetic field **H**



We have the freedom to set our zero point of energy at $\alpha = 90^{\circ}$, so that we get

$$E = -\mu_0 \mathbf{m} \cdot \mathbf{H}. \tag{1.3}$$

If we allow for an inhomogeneous magnetic field, we have, beside the torque, also a translational force $\mathbf{F} = -\nabla E$. With both the magnetic moment and the magnetic field along the *x*-direction and a field gradient along the *z*-direction, we obtain for the force along the *z*-direction

$$F_z = \mu_0 m_x \frac{\partial H_x}{\partial z}. (1.4)$$

This equation is the basis for the measurement of the magnetic moment by the Faraday balance and the alternating gradient force magnetometer.

1.1.3 Further Definitions

- Magnetization:

$$\mathbf{M} = \frac{1}{V} \sum_{i} \mathbf{m}_{i},\tag{1.5}$$

with V the volume of the system; the unit is A m⁻¹.

- Magnetic induction:

$$\mathbf{B} = \mu_0(\mathbf{H} + \mathbf{M}). \tag{1.6}$$

- Magnetic susceptibility γ:

$$\mathbf{M} = \chi \mathbf{H}.\tag{1.7}$$

For negative χ , we have diamagnetic behavior, that is, the material is repelled by a magnetic field, while for positive χ , the material behaves paramagnetic, that is, it is attracted by a magnetic field. We note that χ is in general a (3×3) tensor.

1.2 Magnetism of Free Atoms and Electrons

1.2.1 Diamagnetism of Free Atoms [1]

In the following we deduce the diamagnetic susceptibility of free atoms in a semiclassical way. We note that all magnetic effects, be it dia- or paramagnetism, cannot be explained in terms of a purely classical theory. This is the content of the Bohrvan Leeuwen theorem, which states that at any finite temperature, and in all finite applied electric or magnetic fields, the net magnetization of a collection of nonrelativistic classical electrons in thermal equilibrium vanishes identically. Thus, it is necessary to introduce some quantum-mechanical assumption to obtain magnetic effects. In the present case, we assume that an electron orbits around the nucleus on a fixed orbit with the angular velocity ω_0 . In this case, the centripetal force is equal to the Coulomb force, and the angular velocity is given by

$$\omega_0 = \sqrt{\frac{Ze^2}{4\pi\varepsilon_0 m_{\rm e}r^3}},\tag{1.8}$$

with r the radius of the orbit and Z the atomic number.

Switching on a magnetic field **H** will result in a Lorentz force $\mathbf{F}_L = -\mu_0 |e|(\mathbf{v} \times \mathbf{H})$, with **v** the velocity of the electron. The condition for equilibrium in the plane perpendicular to the magnetic field results in a new angular velocity:

$$\omega = \omega_0 \sqrt{1 + \left(\frac{\mu_0 e H}{2m_e \omega_0}\right)^2} \pm \frac{\mu_0 |e|}{2m_e} H, \tag{1.9}$$

with the sign in front of the second term depending on the sense of the current. We note that even for the largest laboratory fields one has always $\frac{\mu_0|e|H}{2m_c} << \omega_0$. In fact, typical values of the angular velocity and the magnetic field are $\omega_0(Z=1, r=10^{-10} \, \mathrm{m}) \approx 10^{16} \, \mathrm{s}^{-1}$ and $H=10^7 \, \mathrm{A} \, \mathrm{m}^{-1}$, respectively, so that the ratio $\frac{\mu_0|e|H}{2m_c}$ is of the order of $10^{12} \, \mathrm{s}^{-1}$ and one can write

$$\omega = \omega_0 \pm \frac{\mu_0 |e| H}{2m_e} H = \omega_0 \pm \omega_L, \tag{1.10}$$

with ω_L the Larmor frequency. To obtain the above equation, one has to assume that the radius of the electron orbit is not significantly modified by the presence of the magnetic field. This is the content of the Larmor theorem [2]. The only effect (in first order) of the magnetic field is to impose on the electron a precession motion about the direction of the magnetic field with an angular velocity ω_L .

¹ This theorem was independently discovered by N. Bohr (PhD thesis, 1911) and H.J. van Leeuwen (PhD thesis, 1919).

As the radius and thus the area F that is encircled by the electron orbit is not changed by the magnetic field, one finds for the change of the magnetic moment Δm due to the magnetic field

$$\Delta m = \frac{-|e|\omega_{\rm L}}{2\pi} F. \tag{1.11}$$

If the magnetic field is applied along the z-direction, then F is the circular area that is orbited by the electron in the xy-plane: $F = \pi (x^2 + y^2) = \pi r^2$. Assuming a spherical symmetry of the charge distribution (averaged over time) and averaging over similar electron orbits (<>), one has $\langle x^2 \rangle = \langle y^2 \rangle = \langle z^2 \rangle$ and $\langle r^2 \rangle = \langle x^2 \rangle + \langle y^2 \rangle$, with r the radius of the orbit. On the other hand, the radius R of the sphere fulfills $\langle R^2 \rangle = \langle x^2 \rangle + \langle y^2 \rangle + \langle z^2 \rangle$, so that $\langle r^2 \rangle = \frac{2}{3} \langle R^2 \rangle$. Thus, we find for the total magnetic moment per atom (with Z electrons and a radius R_i for each of them) $\Delta m =$ $-rac{e^2\mu_0}{6m_e}H\sum_{i=1}^Z\langle R_i^2\rangle$. For the magnetic susceptibility $\chi=M/H$, one finds finally the following expres-

sion:

$$\chi = -\frac{N}{V} \frac{e^2 \mu_0}{6m_e} \sum_{i=1}^{Z} \langle R_i^2 \rangle, \tag{1.12}$$

with N the number of atoms in the volume V. One notes that the susceptibility is always negative and one is thus dealing with diamagnetism. The effect of a magnetic field on the electronic motion in an atom is equivalent to an additional current induced on the atom that produces a moment oriented in a direction opposite to that of the applied magnetic field (Lenz' law).

Examples of diamagnetic materials, in which the atoms possess either in the atomic state or in a compound a closed shell electronic structure, are rare gases like He, Ne, and Ar, some of the polyatomic gases like H₂ and N₂, ionic solids like NaCl, and substances formed by covalent bonding like graphite and Bi. We note that the latter two have the strongest diamagnetism among the elements.

Paramagnetism of Free Atoms [3]

In this chapter, one takes into account the quantization of the angular momentum, both of the orbital contribution with the orbital magnetic quantum number m_l = $0, \pm 1, \pm 2, ..., \pm l$ (the eigenvalue of the L_z operator) and of the spin contribution with the spin magnetic quantum number $m_s = -S, -S + 1, ..., +S$ (the eigenvalue of the S_z operator). We note that for not too heavy atoms or ions (transition metals and even rare earth elements) in which the spin-orbit coupling is small compared with spin-spin and orbit-orbit coupling, L and S can still be considered as good quantum numbers.

The permanent magnetic moment of an atom or an ion is determined by the total angular momentum $\mathbf{J} = \mathbf{L} + \mathbf{S}$:

$$\mathbf{m} = -g\mu_{\rm B}\mathbf{J},\tag{1.13}$$

with $\mu_{\rm B}=\frac{|e|\hbar}{2m_e}$ the Bohr magneton and g the Landé-factor:

$$g = 1 + \frac{J(J+1) + S(S+1) - L(L+1)}{2J(J+1)}. (1.14)$$

For a pure orbital angular momentum one obtains g = 1, while a pure spin angular momentum gives g = 2.

Assuming $\mathbf{H} = (0, 0, H)$, the energy of the magnetic moment in the magnetic field is

$$E = -\mu_0 \mathbf{m} \cdot \mathbf{H} = g\mu_0 \mu_B H m_i, \tag{1.15}$$

with $m_j = -J, -J + 1, ..., +J$ the magnetic quantum number of the total angular momentum. For the sake of simplicity, we consider in the following the case $J = S = \frac{1}{2}$ (i.e., g = 2), which gives

$$E = 2\mu_0 \mu_{\rm B} H \left(\pm \frac{1}{2} \right) = \pm \mu_0 \mu_{\rm B} H,$$
 (1.16)

and results in a two-level system (see Fig. 1.3) with $N=N_1+N_2$ the total number of electrons.

According to the Boltzmann distribution, one obtains

$$\frac{N_1}{N} = \frac{e^{-E_1/k_B T}}{e^{-E_1/k_B T} + e^{-E_2/k_B T}},$$
(1.17)

$$\frac{N_2}{N} = \frac{e^{-E_2/k_B T}}{e^{-E_1/k_B T} + e^{-E_2/k_B T}}.$$
(1.18)

As the magnetization is proportional to the difference between N_1 and N_2 , one finds

$$M = \frac{1}{V} (N_1 - N_2) \mu_{\rm B} = \frac{N}{V} \mu_{\rm B} \frac{e^{\alpha} - e^{-\alpha}}{e^{\alpha} + e^{-\alpha}} = \frac{N}{V} \mu_{\rm B} \tanh(\alpha), \tag{1.19}$$

with $\alpha = \frac{\mu_0 \mu_B H}{k_B T}$.

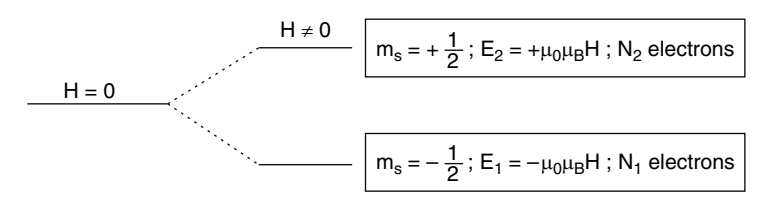


Fig. 1.3 Effect of a magnetic field on the energy levels of the two electron states with $m_s = +1/2$ and $m_s = -1/2$

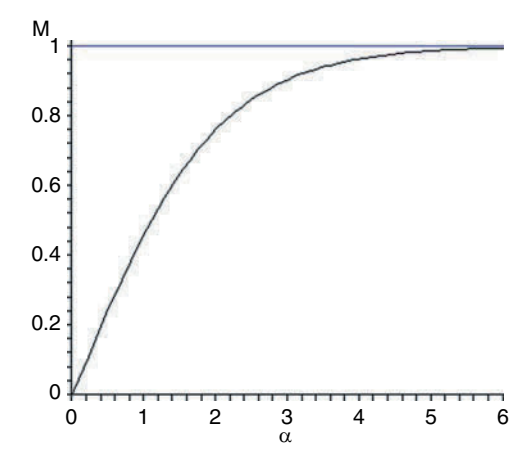


Fig. 1.4 The Brillouin function $B_J(\alpha)$ as a function of $\alpha = g\mu_0\mu_B JH/k_B T$

For $\alpha << 1$, that is, $\mu_0 \mu_B H << k_B T$, one has $\tanh(\alpha) \approx \alpha$ so that one obtains the so-called Curie law [4]

$$\chi = \frac{M}{H} \approx \frac{N\mu_0 \mu_{\rm B}^2}{Vk_{\rm B}T} = \frac{C}{T}.$$
 (1.20)

For $\alpha >> 1$, that is, $\mu_0 \mu_{\rm B} H >> k_{\rm B} T$, one has $\tanh(\alpha) \approx 1$, a situation in which all magnetic moments are aligned and one obtains the saturation value of the magnetization: $M \approx \frac{N}{V} \mu_{\rm B}$.

The above result for the magnetization can be generalized to an arbitrary value of the total angular momentum J:

$$M = \frac{N}{V}g\mu_{\rm B}JB_J(\alpha),\tag{1.21}$$

with $\alpha = \frac{g\mu_0\mu_BJH}{k_BT}$ and the Brillouin-function (see Fig. 1.4)

$$B_J(\alpha) = \frac{2J+1}{2J} \coth\left(\frac{(2J+1)\alpha}{2J}\right) - \frac{1}{2J} \coth\left(\frac{\alpha}{2J}\right). \tag{1.22}$$

For $\alpha \ll 1$, one obtains again the Curie-law

$$\chi = \frac{Np^2\mu_0\mu_{\rm B}^2}{3Vk_{\rm B}T},\tag{1.23}$$

with $p = g\sqrt{J(J+1)}$, the so-called paramagnetic moment.

How can one determine the susceptibility of a substance? For this we need to know the effective number of Bohr magnetons p, that is, we need to know the value of the total angular momentum J. The J of the ground state can be determined by using the empirical Hund's rules [5]:

- (1) The spin angular momentum S is as large as possible (by taking into account Pauli's principle [6]).
 - The larger the spin, the more asymmetric is the spatial part of the wave function, that is, the electrons are farther from each other. This saves Coulomb energy.
- (2) The orbital angular momentum L is as large as possible (taking into account rule (1) and the Pauli principle).
 The larger L, the farther apart are the electrons, which saves again Coulomb
- (3) The total angular momentum J is maximum or minimum. For a shell that is less than half-filled or half-filled, one has J = |L S|. Spin and orbital angular momentum are antiparallel. For a shell that is more than half-filled, one has J = L + S. Spin and orbital angular momentum are parallel.

energy.

Let us compare theoretical and experimental values of the effective number of Bohr magnetons [7]. As a first example, we take ions of the rare-earth elements, in which the 4f-shell is successively filled. With the exception of Sm^{3+} ($4f^5$) and Eu^{3+} ($4f^6$), one has good correspondence (see Fig. 1.5). Because of the screening of the 4f electrons by the $5s^26p^65d^{0,1}6s^2$ electrons – all being at larger radii than the 4f electrons – the atomic case is also realized in the solid state. The deviations in the case of Sm^{3+} and Eu^{3+} are due to the fact that excited states with $J' \neq J$ are close to the ground state J. Their population at a given temperature has therefore to be taken into account.

As second example we consider ions of the iron transition group, in which the 3d-shell is successively filled [7]. There is no correspondence between experimental values and the theoretical values, which have been calculated according to $p_{\rm eff} = g \sqrt{J(J+1)}$ (see Fig. 1.6). However, good correspondence is found with

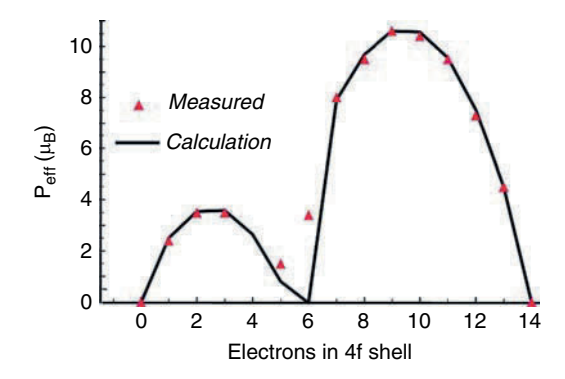


Fig. 1.5 Measured and calculated values (based on Hund's rules) of the effective paramagnetic moment for ions of the rare-earth elements

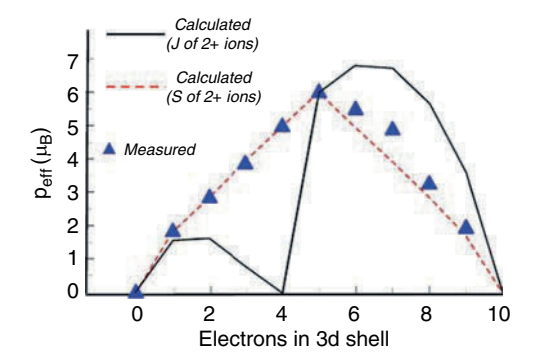


Fig. 1.6 Measured and calculated values (based on Hund's rules) of the effective paramagnetic moment for ions of the iron transition group

 $p_{\rm eff}=g\sqrt{S(S+1)}$, that is, when we assume that J is given only by the spin angular momentum. This is explained by a complete or partial quenching of the orbital angular momentum in the solid. In the free atom, the 3d electrons "feel" a central field, so that both L_z and L^2 are integrals of the motion. In an ionic environment, however, the 3d electrons are subject to a crystal field. In such a noncentral field, L_z is no longer an integral of the motion and an average may lead to a cancelation of the orbital angular momentum.

1.2.3 Pauli Paramagnetism of Free Electrons (in Metals) [10]

Considering a free electron as a particle with a total angular momentum J=S=1/2, one might – according to the theory of the paramagnetism of free atoms (see Sect. 1.2.2) – expect at high temperatures a Curie-law:

$$\chi = \frac{N}{V} \frac{\mu_0 \mu_{\rm B}^2}{k_{\rm B} T}.$$
 (1.24)

However, in metals one observes a magnetic susceptibility that is in first approximation independent of the temperature. In fact, in the case of electrons one has to consider the Fermi–Dirac distribution instead of the Boltzmann distribution (as in the case of free atoms). The Fermi–Dirac distribution reads

$$f(E) = \left[e^{\frac{E - \xi}{k_{\rm B}T}} + 1 \right]^{-1},$$
 (1.25)

² The phenomenon of orbital momentum quenching is discussed for instance in [8,9].

with the chemical potential ξ , which is chosen such that the total number of electrons equals N. The Fermi energy is defined by $E_F = \xi(T = 0)$.

It is the peculiarity of the Fermi–Dirac distribution that for most electrons the probability to switch the spin upon application of a magnetic field is zero. Most states are already occupied. At finite temperatures, free states are available only within a very small region around $E_{\rm F}$, whose width is determined by the thermal energy $k_{\rm B}T$. The portion of electrons that can switch their spin is therefore of the order of $\frac{k_{\rm B}T}{E_{\rm F}}$. One expects thus a temperature-independent magnetic susceptibility:

$$\chi \approx \frac{N}{V} \frac{\mu_0 \mu_B^2}{k_B T} \cdot \frac{k_B T}{E_F} = \frac{N}{V} \frac{\mu_0 \mu_B^2}{E_F}.$$
 (1.26)

Moreover, at room temperature the magnetic susceptibility of a free electron system is by a factor of 100 smaller than that of a system of free atoms.

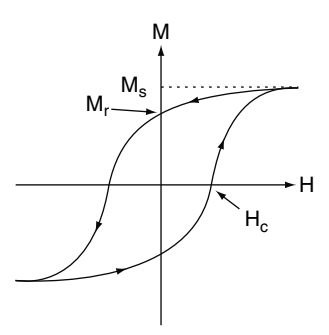
1.3 Ferromagnetism

The most characteristic property of ferromagnets is that once exposed to a magnetic field they retain their magnetization even when the field is removed. The retention of magnetization distinguishes ferromagnets from paramagnets which, although they acquire a magnetic moment in an applied magnetic field, cannot maintain the magnetization after the field is removed.

The most common way to represent the magnetic properties of a ferromagnetic material is by a plot of the magnetization M against the applied magnetic field H. In contrast to the non-hysteretic behavior of paramagnetic materials, which follows the Brillouin function (see Sect. 1.2.2), the magnetization M of a ferromagnetic material exhibits a hysteretic behavior as a function of the applied magnetic field H (see Fig. 1.7).

Important quantities determining an hysteresis loop are the coercive field H_c , the remanent magnetization M_r , and the saturation magnetization M_s . The area within the hysteresis loop is proportional to the work that has to be done to switch the magnetization from one direction to the opposite direction: $E = V\mu_0 \int H \, dM$.

Fig. 1.7 A typical hysteresis loop of a ferromagnetic material. M_s , M_r , and H_c are the saturation magnetization, the remanent magnetization, and the coercive field, respectively



What are the great differences between the behavior of a paramagnetic and a ferromagnetic material? (a) In a ferromagnet, the magnetization depends on the history of the magnetic field treatment. (b) A nonzero magnetization can be achieved in ferromagnets even in zero magnetic field. (c) In general, small magnetic fields of the order of 10^3 – 10^4 A m⁻¹ can induce in ferromagnets large magnetizations of the order of 10^6 A m⁻¹.

1.3.1 Molecular Field

To explain these properties, Pierre Weiss introduced (1907) the two following postulates [11, 12]:

- (1) A molecular field $H_{\rm m}$ exists within the ferromagnetic material that orders the magnetic moments against the thermal motion. It is so large that the ferromagnet can be saturated even without an external magnetic field. By a simple calculation one gets its order of magnitude. At the so-called Curie temperature $T_{\rm c}$ above which ferromagnetic order is lost, the thermal energy (that disorders the system) and the magnetic energy (that orders the system) must be of the same order of magnitude: $k_{\rm B}T_{\rm c} \approx \mu_0\mu_{\rm B}H_{\rm m}$. With a $T_{\rm c}$ of 1,043 K (Fe) one finds $H_{\rm m} \approx 10^9$ A m⁻¹.
- (2) A ferromagnetic material in its demagnetized state, that is, $M_r = 0$, is divided into a number of small regions, so-called magnetic domains. Within a single domain the magnetization is saturated, but different domains have different directions of the magnetization (see Fig. 1.8).

What is the origin of the molecular field? Can the dipole force between the magnetic moments be the origin? The interaction energy of two magnetic dipoles \mathbf{m}_1 and \mathbf{m}_2 that are separated by a distance r is given by

$$E_{\text{dip}} = \frac{1}{r^3} \left[\mathbf{m}_1 \mathbf{m}_2 - \frac{3}{r^2} \left(\mathbf{m}_1 \mathbf{r} \right) \left(\mathbf{m}_2 \mathbf{r} \right) \right]. \tag{1.27}$$

With atomic distances r one yields $E_{\rm dip}\approx 0.1$ –1 K. On the other hand, typical Curie temperatures are on the order of 1,000 K, so that the dipole force cannot explain the ferromagnetic order up to such temperatures.

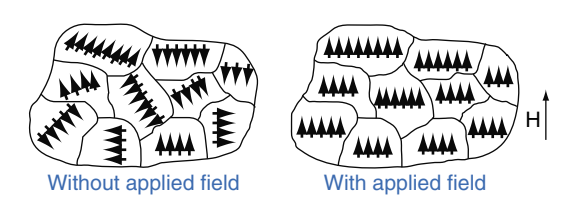


Fig. 1.8 Schematic domain configuration in a demagnetized state (*left*). Application of a sufficiently strong magnetic field leads to saturation (*right*)

1.3.2 Exchange Interaction as Origin of the Molecular Field

Let us consider two hydrogen atoms (proton "a" with electron "1" and proton "b" with electron "2") that are far from each other. The hamiltonian of this system reads

$$H = -\frac{\hbar^2}{2m_e} \left(\nabla_1^2 + \nabla_2^2 \right) + V(1, a) + V(2, b). \tag{1.28}$$

The potential is given by $V(r) = \frac{-e^2}{r}$, with r the distance between the electron and "its" proton.

The total wave function of the two electrons must be antisymmetric according to Pauli's principle: $\psi(1,2) = -\psi(2,1)$. With the single-electron wave functions $\psi_a(1), \psi_b(2), \psi_a(2)$, and $\psi_b(1)$, the total wave function reads

$$\psi(1,2) = \frac{1}{\sqrt{2}} \left[\psi_a(1)\psi_b(2) - \psi_a(2)\psi_b(1) \right]. \tag{1.29}$$

Now we factorize the total wave function into a spatial function ϕ and a spin function χ : $\psi(1,2) = \phi(1,2) \cdot \chi(1,2)$. We note that this factorization is justified only for systems in which the spin-orbit interaction is small. A total antisymmetric wave function can thus be achieved in two different ways:

- (1) By a symmetric spatial function ϕ and an antisymmetric spin function χ ,
- (2) By an antisymmetric spatial function ϕ and a symmetric spin function χ .

One obtains thus four wave functions:

$$\psi_{s}(1,2) = \frac{1}{\sqrt{2}} \left[\phi_{a}(1)\phi_{b}(2) + \phi_{a}(2)\phi_{b}(1) \right] \cdot \frac{1}{\sqrt{2}} \left(| \uparrow \downarrow \rangle - | \downarrow \uparrow \rangle \right),
\psi_{t}^{1}(1,2) = \frac{1}{\sqrt{2}} \left[\phi_{a}(1)\phi_{b}(2) - \phi_{a}(2)\phi_{b}(1) \right] \cdot | \uparrow \uparrow \rangle,
\psi_{t}^{2}(1,2) = \frac{1}{\sqrt{2}} \left[\phi_{a}(1)\phi_{b}(2) - \phi_{a}(2)\phi_{b}(1) \right] \cdot \frac{1}{\sqrt{2}} \left(| \uparrow \downarrow \rangle + | \downarrow \uparrow \rangle \right),
\psi_{t}^{3}(1,2) = \frac{1}{\sqrt{2}} \left[\phi_{a}(1)\phi_{b}(2) - \phi_{a}(2)\phi_{b}(1) \right] \cdot | \downarrow \downarrow \rangle.$$
(1.30)

The first wave function describes a singlet state, because S = 0. The other three wave functions describe a triplet state, because S = 1. The quantum numbers m_S of the S_Z operator for these three functions are +1, 0, and -1, respectively.

For large distances between the two hydrogen atoms, singlet and triplet states are energetically degenerated. When the distance becomes smaller the energies become different. The additional interactions upon approach of the atoms are given by $H_{12} = V(a,b) + V(1,b) + V(2,a) + V(1,2)$. The corresponding energies are

$$E_{s,t} = \int \psi_{s,t}^* H_{12} \psi_{s,t} \, dV = K_{12} \pm J_{12}, \tag{1.31}$$

with K_{12} the Coulomb integral:

$$K_{12} = \int \phi_a^*(1)\phi_b^*(2)H_{12}\phi_a(1)\phi_b(2)\,\mathrm{d}V_1\mathrm{d}V_2$$
 (1.32)

in which electron 1 (2) stays on site a (b), and with J_{12} the exchange integral:

$$J_{12} = \int \phi_a^*(1)\phi_b^*(2)H_{12}\phi_a(2)\phi_b(1)\,\mathrm{d}V_1\mathrm{d}V_2 \tag{1.33}$$

in which electron 1 (2) swaps to site b (a). We note that the use of single-atom wave functions (Heitler–London approach [13]) in the above equations is an approximation that is not always justified.

We emphasize that H_{12} is an operator without any spin dependence that acts, therefore, only on the spatial part of the wave function: $H_{12}\psi = H_{12}(\phi \cdot \chi) = \chi H_{12}\phi = \chi(E_{s,t}\phi) = E_{s,t}\psi$. The idea is now to construct a new hamiltonian $H_{\rm spin}$ that acts only on the spin part of the wave function yet yielding the same eigenvalues $E_{s,t}$. The following hamiltonian fulfills these requirements:

$$H_{\text{spin}} = K_{12} - \frac{1}{2}J_{12} - 2J_{12}\mathbf{S}_{1}\mathbf{S}_{2}. \tag{1.34}$$

Consequently, the system can be described by an effective spin–spin hamiltonian, that is, an effective spin–spin interaction exists, which is called exchange interaction [14, 15]. We note that the exchange interaction is the result of a combination of a pure electrostatic interaction and the Pauli principle and that no real magnetic field is involved.

By generalizing the above hamiltonian to a grid of atoms (one also shifts the zero of the energy), one obtains the Heisenberg hamiltonian: $H_{\text{Heis}} = -\sum_{i \neq j} J_{ij} \mathbf{S}_i \cdot \mathbf{S}_j$. It should be emphasized that the exchange interaction is very short-ranged. It is the overlap of wave functions between neighboring atoms that produces an effective interaction that propagates over large distances. Therefore, it is often sufficient to consider only the interaction between nearest neighbors (n.n.). Assuming the same value J of the exchange integral for all pairs of nearest neighbors, one finds

$$H_{\text{Heis}} = -J \sum_{i \neq i,n,n} \mathbf{S}_i \cdot \mathbf{S}_j. \tag{1.35}$$

Let us finish this section with a word of criticism. The most important problem of the above hamiltonian lies in the determination of the exchange integral J. We emphasize that the above expression for the exchange integral (1.33) has been obtained within the Heitler-London approach. A comparison of "experimental" values of J (from specific heat measurements and spin wave considerations) with those of calculations within this approach show strong discrepancies. It is in general not even possible to obtain the correct sign of J. Therefore, although the approach of Heitler-London and Heisenberg still provides a useful concept for discussing the spin-spin interaction of electrons, the method seems to be inadequate. One resorts to calculations of the total energy for different spin configurations. That with the lowest energy gives the spin order ground state.

1.3.3 Mean Field Approximation (MFA)

The total hamiltonian with the contribution due to the applied magnetic field **H** is

$$H_{\text{total}} = -J \sum_{i \neq j, n.n.} \mathbf{S}_i \cdot \mathbf{S}_j + g\mu_0 \mu_B H \sum_i S_{i,z}, \qquad (1.36)$$

where the magnetic field is supposed to be parallel to the z-direction. Now we want to know the behavior of the magnetization as a function of both the temperature and the applied magnetic field, that is, M(T, H). Unfortunately, it is not possible to calculate it exactly, and so one has to make an approximation. A reasonable approximation is done by using the thermal mean value of the spin operators, that is, replacing S_j by $S_j >$ and thus neglecting thermal fluctuations. This approximation is called mean field approximation (MFA). By applying the magnetic field along the z-direction, the only nonvanishing component of the mean value of the spin operator is the z-component. Moreover, because of translational symmetry, one obtains $S_{i,z} >$ $S_i >$ so that the total hamiltonian in MFA reads

$$H_{\text{MFA}} = -Jn < S_z > \sum_{i} S_{i,z} + g\mu_0 \mu_{\text{B}} H \sum_{i} S_{i,z}$$

$$= g\mu_0 \mu_{\text{B}} \left[H - \frac{Jn < S_z >}{g\mu_0 \mu_{\text{B}}} \right] \sum_{i} S_{i,z}, \qquad (1.37)$$

with *n* the number of nearest neighbors.

The above hamiltonian describes a system of independent magnetic moments that are under the influence of an external magnetic field H and a "molecular field" $H_{\rm m} = -\frac{Jn < S_z >}{g\mu_0\mu_{\rm B}}$. Replacing H in the Brillouin function for the paramagnetic case by $H+H_{\rm m}$ should therefore be a solution of our problem:

$$M_z^{\text{MFA}} = \frac{N}{V} g \mu_{\text{B}} S B_{\text{S}}(\alpha), \qquad (1.38)$$

with

$$\alpha = \frac{g\mu_0\mu_B S}{k_B T} \left[H - \frac{Jn \langle S_z \rangle}{g\mu_0\mu_B} \right]. \tag{1.39}$$

On the other hand, one has

$$M_z = -\frac{N}{V}g\mu_{\rm B} < S_z >, \tag{1.40}$$

so that the magnetization can be expressed in terms of α , H, and T as follows:

$$M_z = \frac{N}{V} \frac{k_{\rm B} T g \mu_{\rm B}}{J n S} \alpha - \frac{N}{V} \frac{(g \mu_{\rm B})^2}{J n} \mu_0 H. \tag{1.41}$$

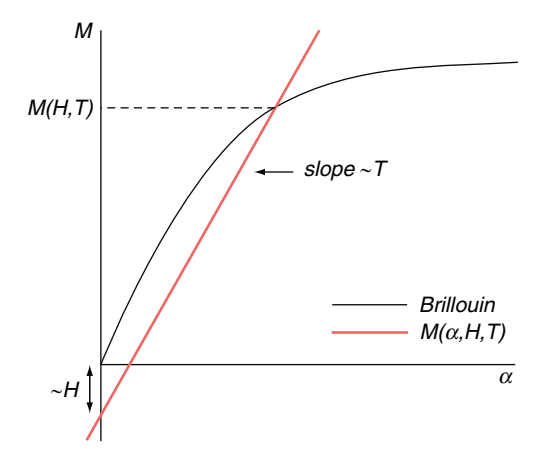


Fig. 1.9 The graphical determination of M(H,T) by plotting (1.38) (Brillouin) and (1.41) $(M(\alpha, H, T))$

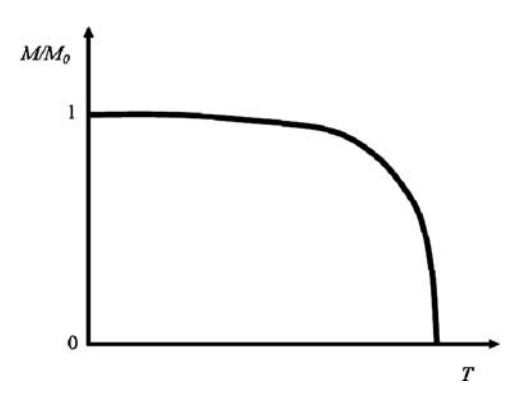


Fig. 1.10 Schematic representation of the magnetization as a function of temperature

Equations (1.38) and (1.41) are a pair of equations that can be resolved graphically (see Fig. 1.9).

For H > 0 one has always $M_z \neq 0$. For H = 0, a temperature T_c exists for which the straight line is a tangent to the Brillouin function. Above T_c , $M_z = 0$ is the only possible solution. One can show that M(T, H = 0) is nonanalytic at $T = T_c$ (see Fig. 1.10). There is a phase transition.

1.3.3.1 Curie Temperature in MFA

The Curie temperature in MFA can be calculated by equating the slope of the Brillouin function at $\alpha = 0$ and the slope of the straight line for H = 0:

$$\frac{N}{V}g\mu_{\rm B}S\frac{\partial B_{\rm S}}{\partial\alpha}(\alpha=0) = \frac{N}{V}\frac{k_{\rm B}T_{\rm c}g\mu_{\rm B}}{JnS}.$$
 (1.42)

As $B_S(\alpha << 1) = \frac{S+1}{3S}\alpha$, one obtains

$$T_{\rm c}^{\rm MFA} = \frac{JnS(S+1)}{3k_{\rm B}}.$$
 (1.43)

The Curie temperature is in particular proportional to the number of nearest neighbors n. Accordingly, a reduction in the Curie temperature for surface atoms – having a reduced coordination number – has been observed in many instances [16]. We note that MFA usually overestimates the Curie temperature.

1.3.3.2 Curie-Weiss Law [11]

For a paramagnetic material one finds a Curie law $M = \frac{C}{T}H$ with a constant C. For a ferromagnetic material in MFA, the magnetic field H has to be replaced by $H + H_m$ so that we obtain $M = \frac{C}{T}(H + H_m)$. On the other hand, the molecular field H_m can be expressed in terms of the magnetization: $H_m = N_m M$, with N_m a suitable number such that $H_m = -\frac{J_n < S_c >}{g \mu_0 \mu_B}$, leading us to $M = \frac{C}{T}(H + N_m M)$. The magnetic susceptibility is thus given by

$$\chi = \frac{C}{T - CN_{\rm m}} = \frac{C}{T - \theta},\tag{1.44}$$

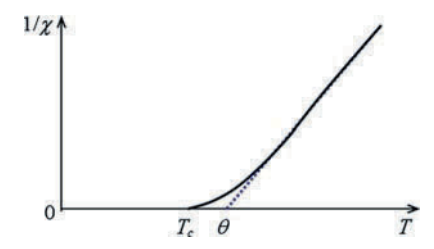
with $\theta = CN_{\rm m}$, the so-called paramagnetic Curie temperature. For ferromagnets one always has $\theta > T_{\rm c}$ (see Fig. 1.11).

We note that the susceptibility follows only the Curie–Weiss law in the paramagnetic region. For temperatures below $T_{\rm c}$, the material becomes ordered and the susceptibility behaves in a very complicated way.

1.3.3.3 The Behavior of M(T) Close to T_c

In the proximity of the Curie temperature T_c , one finds a power law behavior of the magnetization:

Fig. 1.11 Schematic representation of the inverse susceptibility of a ferromagnetic material as a function of temperature. $T_{\rm c}$ and θ are the Curie temperature and the paramagnetic Curie temperature, respectively



$$M(T) \propto \left(1 - \frac{T}{T_c}\right)^{\beta},$$
 (1.45)

with the critical exponent β (0 < β < 1) of the magnetization. Let us calculate β within the MFA. For the sake of simplicity we consider only the case with $S = \frac{1}{2}$. From the preceding discussion we know that the magnetization can be expressed in the following way:

$$M = \frac{N}{V}\mu_{\rm B}\tanh\left[\frac{1}{k_{\rm B}T}\left(\mu_{\rm 0}\mu_{\rm B}H + \frac{MVnJ}{4N\mu_{\rm B}}\right)\right]. \tag{1.46}$$

With $\sigma \equiv \frac{M}{M(T=0)} = \frac{M}{N\mu_B/V}$, one has

$$\sigma = \tanh\left[\frac{1}{k_{\rm B}T}\left(\mu_0\mu_{\rm B}H + \frac{\sigma nJ}{4}\right)\right]. \tag{1.47}$$

Using the expression for the Curie temperature T_c in MFA, one obtains

$$\sigma = \tanh\left(\frac{\mu_0 \mu_{\rm B} H}{k_{\rm B} T} + \sigma \frac{T_{\rm c}}{T}\right). \tag{1.48}$$

Applying $\tanh(x + y) = \left[\tanh(x) + \tanh(y)\right] / \left[1 + \tanh(x) \tanh(y)\right]$ and $T^* \equiv T/T_c$, one arrives at

$$h \equiv \tanh\left(\frac{\mu_0 \mu_{\rm B} H}{k_{\rm B} T}\right) = \frac{\sigma - \tanh\left(\sigma/T^*\right)}{1 - \sigma \tanh\left(\sigma/T^*\right)}.$$
 (1.49)

For H=0 and $T\approx T_{\rm c}$, one has $M\approx 0$, that is, $\sigma<<1$. Considering only terms up to third order in σ , one obtains

$$0 = \sigma \left(1 - \frac{1}{T^*} \right) + \frac{\sigma^3}{3T^{*3}} + 0 \left(\sigma^5 \right). \tag{1.50}$$

The solution for $T > T_c$ is trivial: $\sigma = 0$. The solution for $T < T_c$ is

$$\sigma = \sqrt{3} \frac{T}{T_c} \left(1 - \frac{T}{T_c} \right)^{\frac{1}{2}},\tag{1.51}$$

thus yielding a critical exponent β of 1/2.

Experiments, however, show that the critical exponent β differs quite sensibly from 1/2, that is, the MFA does not describe correctly the behavior in the vicinity of T_c . In fact, spin fluctuations, which have been neglected in the MFA, have to be taken into account to obtain the correct value of the exponent.

1.3.4 Spin Waves

A simple way to decrease the total magnetic moment of a ferromagnetic material might be to switch the direction of a particular magnetic moment (see Fig. 1.12).

The energy of the ground state is $E_0 = -NJS^2$, while that of the first localized excited state is given by $E_1 = -(N-2)JS^2 + 2JS^2 = -(N-4)JS^2$. For the normalized energy difference we thus find $(E_1 - E_0)/E_0 \propto 1/N$.

However, there is another way to reduce the magnetization, in which the excitation energy is distributed over the entire spin system. Most importantly, by exciting a collective excitation, the required amount of energy can be lowered. Such a collective excitation of the spin system is called spin wave (see Fig. 1.13).

Let θ be the angle between a spin and the z-axis around which the spins are precessing and ϕ the angle between two neighboring spins in the projection onto the xy plane. As the effective reduction of the total magnetic moment by a spin wave should be equal to that of a localized excitation as shown in Fig. 1.12, one has $N\theta = \pi$. The value of the angle ϕ is, however, not defined by the number of spins in the chain, but by the wavelength of the spin wave. For the sake of simplicity we consider a spin wave with the largest possible wavelength, that is, $N\phi = 2\pi$. The energy of the spin wave is then $E_1 = -NJS^2\cos(\varepsilon)$, with ε the angle between two neighboring spins. For large N, the angles θ , ϕ , and ε are very small and one finds $\varepsilon \approx \theta \cdot \phi$. Thus, one obtains $(E_1 - E_0)/E_0 = 1 - \cos(\varepsilon) \approx 1 - \cos(\theta \phi) \approx (\theta \phi)^2/2 \propto 1/N^4$. This shows that the excitation of a spin wave is much more favorable than a localized excitation if the number N of spins is large, that is, if the system is large.

Fig. 1.12 A linear chain of spins: ground state (*left*), a state with one spin antiparallel (*right*)





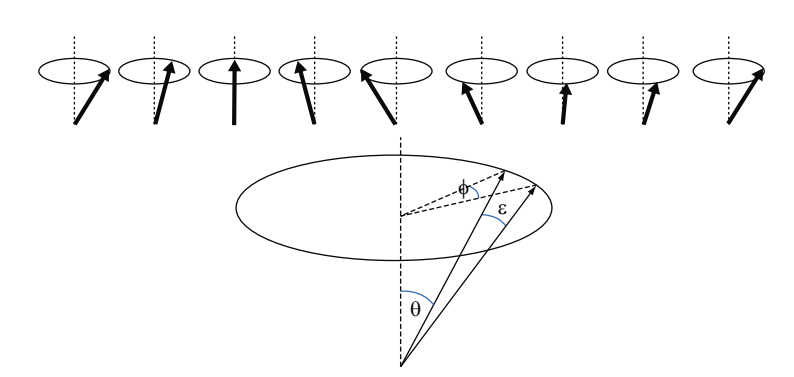


Fig. 1.13 A state of a chain of spins in which each successive spin is at an angle ε to its neighbors

1.3.4.1 Dispersion Relation of Spin Waves

Let us derive in the following the dispersion relation $\omega(k)$ in a semi-classical way for a line of spins. The exchange energy between one spin at a position pa (a being the lattice parameter) and its neighbors at the positions (p-1)a and (p+1)a is $E = -J\mathbf{S}_p(\mathbf{S}_{p-1} + \mathbf{S}_{p+1})$. The magnetic moment at the position pa is given by $\mathbf{m}_p = -g\mu_{\mathbf{B}}\mathbf{S}_p$ and one obtains

$$E = -\mathbf{m}_p \frac{-J}{g\mu_{\rm R}} \left(\mathbf{S}_{p-1} + \mathbf{S}_{p+1} \right) = -\mu_0 \mathbf{m}_p \cdot \mathbf{H}_p, \tag{1.52}$$

where \mathbf{H}_p can be identified as the molecular field or the "exchange" field. Classical mechanics demands now that $\frac{d}{dt}$ (angular momentum) = torque, resulting in

$$\frac{\mathrm{d}\left(\hbar\mathbf{S}_{p}\right)}{\mathrm{d}t} = \mu_{0}\mathbf{m}_{p} \times \mathbf{H}_{p}.\tag{1.53}$$

With the above identification of H_p as the molecular field, one obtains

$$\frac{\mathrm{d}\mathbf{S}_{p}}{\mathrm{d}t} = \frac{-g\mu_{0}\mu_{\mathrm{B}}}{\hbar}\mathbf{S}_{p} \times \mathbf{H}_{p} = \frac{J}{\hbar}\left(\mathbf{S}_{p} \times \mathbf{S}_{p-1} + \mathbf{S}_{p} \times \mathbf{S}_{p+1}\right). \tag{1.54}$$

Assuming small amplitudes of S_x and S_y , one can linearize the equations, that is, $S_z = S$, and all terms containing products of S_x and S_y can be neglected:

$$\frac{\mathrm{d}S_{p}^{x}}{\mathrm{d}t} = \frac{JS}{\hbar} \left(2S_{p}^{y} - S_{p-1}^{y} - S_{p+1}^{y} \right),\tag{1.55}$$

$$\frac{\mathrm{d}S_{p}^{y}}{\mathrm{d}t} = \frac{-JS}{\hbar} \left(2S_{p}^{x} - S_{p-1}^{x} - S_{p+1}^{x} \right),\tag{1.56}$$

$$\frac{\mathrm{d}S_p^z}{\mathrm{d}t} = 0. \tag{1.57}$$

In analogy to lattice vibrations, one looks for solutions of the following form:

$$S_p^x = A e^{i(pka - \omega t)}$$
 and $S_p^y = B e^{i(pka - \omega t)}$ (1.58)

with A and B complex numbers. This ansatz leads to the following equations:

$$-i\omega A = \frac{2JS}{\hbar} [1 - \cos(ka)] B \quad \text{and} \quad -i\omega B = -\frac{2JS}{\hbar} [1 - \cos(ka)] A.$$
(1.59)

Vanishing of the coefficient determinant yields the dispersion relation

$$\hbar\omega = 2JS[1 - \cos(ka)]. \tag{1.60}$$

For $ka \ll 1$ one has a parabolic behavior

$$\hbar\omega = JSa^2k^2. \tag{1.61}$$

1.3.4.2 Thermal Excitation of Spin Waves

Analog to the case of lattice vibrations (or phonons) spin waves (or magnons) are quantized. n_k is the number of magnons having a wave vector k. In thermal equilibrium, the average value of n_k is determined by the Bose–Einstein distribution

$$\langle n_k \rangle = \frac{1}{e^{\frac{\hbar \omega_k}{k_{\rm B}T}} - 1}.$$
 (1.62)

Now we are interested in the total number of spin waves that are excited at the temperature T. As the excitation of one spin wave reduces the total spin by one unit, we get information about the temperature-dependent magnetization. First, let us calculate the number of possible k-states between k and k + dk:

density-of-states
$$\cdot dk = D^*(k) dk = \frac{V}{8\pi^3} \cdot 4\pi k^2 dk$$
, (1.63)

where the first factor is the density of wave vectors and the second the volume of a shell of radius k and thickness dk in reciprocal space. By exploiting the above dispersion relation (1.61) (for ka << 1) one yields

$$D^*(k) dk = \frac{V}{4\pi^2} \left(\frac{\hbar}{JSa^2}\right)^{\frac{3}{2}} \sqrt{\omega} d\omega = D(\omega) d\omega, \qquad (1.64)$$

with $D(\omega)$ the density-of-states as a function of ω .

Now we can calculate the total number of excited spin waves (only k values of the first Brillouin zone (BZ) contribute):

$$\sum_{k \in 1.BZ} n_k = \int_0^{k_{ZB}} D(\omega) < n(\omega) > d\omega, \tag{1.65}$$

with $k_{\rm ZB}$ the k-value of the zone boundary. At low temperatures, $< n(\omega) >$ approaches zero exponentially as ω goes to infinity, thus allowing us to integrate from 0 to infinity:

$$\sum_{k \in 1.BZ} n_k = \int_0^\infty D(\omega) < n(\omega) > d\omega = \frac{V}{4\pi^2} \left(\frac{\hbar}{JSa^2}\right)^{\frac{3}{2}} \int_0^\infty \frac{\sqrt{\omega}}{e^{\frac{\hbar\omega}{k_BT}} - 1} d\omega$$
$$= \frac{V}{4\pi^2} \left(\frac{k_BT}{JSa^2}\right)^{\frac{3}{2}} \int_0^\infty \frac{\sqrt{x}}{e^x - 1} dx. \tag{1.66}$$

Thus the reduction of the magnetization as a function of temperature is

$$\Delta M(T) = M(T=0) - M(T) = \sum_{k \in 1.BZ} n_k \propto T^{\frac{3}{2}}, \tag{1.67}$$

which is known as Bloch's law [17].

1.3.5 Itinerant Ferromagnetism

Why there are only few metals that exhibit ferromagnetic b ehavior? To answer this question we have to consider the competition between exchange energy and kinetic energy. Let us consider a free electron gas with the Fermi wave vector $k_{\rm F} =$ $(3\pi^2 n)^{\frac{1}{3}}$, where n = N/V is the electron density. In the paramagnetic case, each state is occupied by a spin up electron and a spin down electron. The kinetic energy $E_{\rm kin}$ is proportional to $k_{\rm F}^2$. If we consider the completely ferromagnetic case, that is, all spins are aligned parallel, one has to double the volume of the Fermi sphere because of the Pauli principle. Consequently, $k_{\rm F}$ is by a factor of $2^{\frac{1}{3}}$ larger such that the kinetic energy will be larger by a factor of $2^{\frac{2}{3}}$. This increase of the kinetic energy can in general not be overcompensated by a reduction of the exchange energy. Thus, in a free electron gas there is no ferromagnetic order. However, in systems that are more localized than a gas of free electrons, ferromagnetic order can appear. A localization leads to a reduction of the band width so that both the spin up and spin down density-of-states at the Fermi energy $E_{\rm F}$ become larger. For sufficiently large density-of-states at $E_{\rm F}$, $D(E_{\rm F})$, a "transfer" of electrons from the spin down to the spin up density-of-states (which corresponds to an alignment of moments) does not anymore lead to a strong increase of the kinetic energy. It is therefore the degree of localization that decides whether ferromagnetic order appears or not. This fact is expressed by the Stoner criterion [18] that will be derived in the following. The exchange energy is given by

$$E_{\rm ex} = J N_{\uparrow} N_{\downarrow}, \tag{1.68}$$

with $N_{\uparrow,\downarrow}$ the number of electrons with spin up and spin down, respectively. The total number of electrons is $N=N_{\uparrow}+N_{\downarrow}$. If we assume now – starting from the paramagnetic case with $N_{\uparrow}=N_{\downarrow}$ – that ΔN electrons are transferred from the spin down to the spin up band (see Fig. 1.14), then the exchange energy decreases by

$$-J(\Delta N)^2. \tag{1.69}$$

On the other hand, the kinetic energy increases by

$$\Delta E \cdot \Delta N = \frac{\Delta N}{D(E_{\rm F})} \Delta N. \tag{1.70}$$

Fig. 1.14 $D(E_{\rm F}) \cdot \Delta E$ spin down electrons are transferred to the spin up band

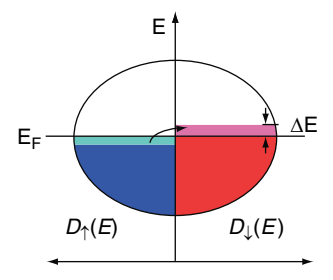


Table 1.1 The product $J \cdot D(E_{\rm F})$ and the sign of J are listed for six transition metals. Fe, Co, and Ni fulfill the Stoner criterion

Element	Cr	Mn	Fe	Co	Ni	Pd
$J.D(E_F)$	0.27	0.63	1.43	1.70	2.04	0.78
J	<0	<0	>0	>0	>0	>0

Thus, the transfer takes place spontaneously if the condition

$$J \cdot D\left(E_{\rm F}\right) > 1,\tag{1.71}$$

the Stoner criterion, is fulfilled. Table 1.1 shows the above product for a few elements.

1.4 Magnetization Curves M(H)

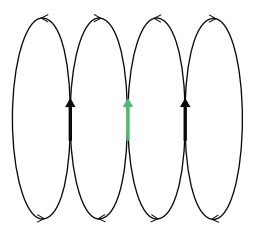
Based on an energy consideration and subsequent minimization of the total energy, M(H) can in principle be determined. First, one has to identify all relevant energy contributions. In the following, we will restrict our discussion to four contributions: exchange energy, field energy, magnetostatic energy, and magneto-crystalline anisotropy. As we know already, the expressions for the exchange and the field energy are

$$E_{\text{ex}} = -J \sum_{i \neq j, n.n.} \mathbf{S}_i \cdot \mathbf{S}_j, \qquad (1.72)$$

$$E_H = -\mu_0 \int_V \mathbf{M} \cdot \mathbf{H} \, \mathrm{d}V. \tag{1.73}$$

Let us discuss in the following section the magnetostatic energy.

Fig. 1.15 A magnetic moment (*green*) in the dipole field of its neighbors (*black*)



1.4.1 Magnetostatic Energy or Shape Anisotropy

The field inside a specimen is different from the applied magnetic field **H** because of the magnetization **M**. To understand this, let us consider a line of magnetic moments. Each magnetic moment creates a magnetic stray field at the positions of its neighbors that has to be added to the applied magnetic field (see Fig. 1.15).

As the sum of all these dipole fields is in a finite 3D-lattice on average always opposed to the magnetization, we will call it demagnetizing field:

$$\mathbf{H}_{d} = -N^{d}\mathbf{M},\tag{1.74}$$

with $N^{\rm d}$ the demagnetizing factor. This term leads to an energy contribution

$$E_{\rm d} = -\frac{\mu_0}{2} \int_V \mathbf{M} \mathbf{H}_{\rm d} \, \mathrm{d}V. \tag{1.75}$$

The demagnetizing factor is in general a tensor function of position and magnetization orientation within the sample. For ellipsoids, $N_{\rm d}$ is a diagonal tensor (with trace $N_{\rm d}=1$) and can be calculated because for those shapes the demagnetizing field turns out to be uniform. The most simple case is that of a thin film for which the thickness is much smaller than the lateral dimensions, so that there is only one nonvanishing coefficient. For a thin film in the xy-plane, for instance, the only nonvanishing coefficient is $N_{zz}^{\rm d}$ and equals to 1. Consequently, the demagnetizing field is

$$\mathbf{H}_{d} = -N^{d}\mathbf{M} = (0, 0, -M_{z}).$$
 (1.76)

For a magnetization in the plane of the film (xy-plane) the demagnetizing field is zero, while it is $-\mathbf{M}$ for an out-of-plane magnetization. That is the reason why thin films are usually magnetized in-plane. An out-of-plane magnetization would cost too much energy. However, there exists another energy contribution, the magnetocrystalline anisotropy (see Sect. 1.4.2), that favors particular directions in a crystal. In certain situations, this can lead to an out-of-plane magnetization (see Sect. 1.5.1).

We note that for a continuous magnetization distribution, the dipole fields may be expressed as due to magnetic pseudo-charges with a volume density $\rho_m = -\nabla \mathbf{M}$ and a surface density $\sigma_m = \mathbf{n} \cdot \mathbf{M}$, where \mathbf{n} is the normal to the surface. If the magnetization is uniform, then only the surfaces carry some pseudo-charges. One

can show that in this case the demagnetizing field is determined by the number of pseudo-charges on the external surface of the sample (see Fig. 1.16).

1.4.2 Magneto-Crystalline Anisotropy

In a solid, the electron orbitals of an atom are coupled to the crystal lattice, leading thus to a particular orientation of the electron orbitals with respect to the crystalline axes. As the associated orbital angular momentum (\mathbf{L}) is coupled to the spin angular momentum (\mathbf{S}) through the spin–orbit interaction ($E_{\rm so} = \xi \mathbf{L} \cdot \mathbf{S}$), the orientation of orbitals forces the spin magnetic moments in one or more particular directions, the so-called easy directions of magnetization. This phenomenon of magneto-crystalline anisotropy is the reason why a rotation of the spin direction relative to the crystalline axes changes both exchange energy and electrostatic interaction. Thus, the energies in the two configurations (a) and (b) in Fig. 1.17 are not identical. Usually, the configuration (a) is energetically more favorable, because in this configuration the electrons can be more easily delocalized, thanks to the overlap of neighboring electron distributions, while no overlap is realized in the configuration (b). On the other hand, the uncertainty principle of Heisenberg tells us that the uncertainty of the velocity is small when the uncertainty of the position is large, that is, the kinetic energy is much smaller in the configuration (a).

The anisotropy energy must reflect the symmetry of the lattice. It is usual to express the anisotropy energy in a power series of trigonometric functions of the angles ϕ_i the magnetization makes with the principal axes of the crystal (see Fig. 1.18). For the sake of ease, we define the direction cosine by $\alpha_i = \cos(\phi_i)$.

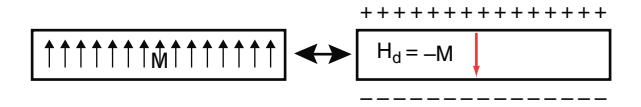
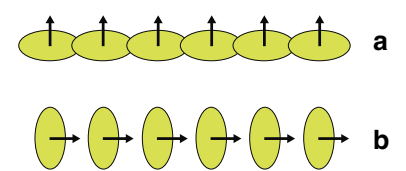


Fig. 1.16 The appearance of pseudo-charges on the upper and the bottom surface of a thin-film sample for an out-of-plane magnetization. The resulting demagnetizing field $H_{\rm d}$ is -M

Fig. 1.17 The asymmetric overlap of the electron distributions at neighboring positions is the origin of the magneto-crystalline anisotropy. Via the spin-orbit interaction this asymmetry is related to the magnetization direction; a change of the spin direction results thus in a change of the overlap energy



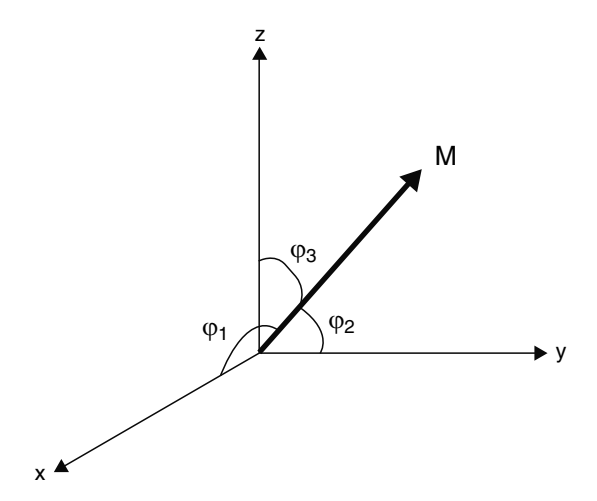


Fig. 1.18 The magnetization **M** and the angles ϕ_i between the magnetization and the principal axes i, i.e., x, y, and z

On the one hand, the energy must be invariant under time reversal. On the other hand, the axial vector \mathbf{M} changes sign under time reversal, so that we must have $E_{\mathbf{A}}(\mathbf{M}) = E_{\mathbf{A}}(-\mathbf{M})$. Thus, the energy expression must contain neither odd power terms of α_i nor cross terms such as $\alpha_i \alpha_j$ ($i \neq j$).

As an example let us consider the cubic case (sc, fcc, bcc). Consequently, the anisotropy energy must be independent of an interchange of the α_i . As a result, the c_i in the second order contribution $E_A = c_1\alpha_1^2 + c_2\alpha_2^2 + c_3\alpha_3^2$ are all identical. On the other hand, $\alpha_1^2 + \alpha_2^2 + \alpha_3^2 = 1$, so that no anisotropy results from it. The first nonvanishing anisotropy terms are of fourth and sixth order: $\alpha_1^2\alpha_2^2 + \alpha_2^2\alpha_3^2 + \alpha_3^2\alpha_1^2$ and $\alpha_1^2\alpha_2^2\alpha_3^2$. Thus, we obtain in the cubic case for the energy density

$$E_{\rm A}/V = K_1 \left(\alpha_1^2 \alpha_2^2 + \alpha_2^2 \alpha_3^2 + \alpha_3^2 \alpha_1^2 \right) + K_2 \alpha_1^2 \alpha_2^2 \alpha_3^2 + \cdots, \tag{1.77}$$

with K_1 and K_2 the anisotropy constants of fourth and sixth order, respectively. We note that the unit of the anisotropy constants is J m⁻³.

We note that beside the magneto-crystalline anisotropy, there is another important contribution leading to magnetic anisotropy via spin—orbit interaction, namely magnetostriction. The spin moments are coupled to the lattice via the orbital motion of the electrons. If the lattice is changed by strain, the distances between the magnetic atoms are altered and hence the interaction energies are changed. Thus, stressing or straining a magnetic material can produce a change in its preferred magnetization direction.

1.4.3 Magnetization Curves in the "Uniform Rotation" Model [19]

Let us consider as example a single-domain particle with an ellipsoidal shape and with negligible magneto-crystalline anisotropy (see Fig. 1.19). As in the "uniform rotation" model all spins in the particle are always aligned parallel to each other, the exchange energy contribution is a constant and can therefore be neglected. In the following, all magnetization curves will show the projection M_H of the magnetization \mathbf{M} onto the applied magnetic field \mathbf{H} :

$$M_H = M \cos(\theta). \tag{1.78}$$

Assuming the following form for the energy contribution of the shape anisotropy,

$$E_{\rm d} = K_{\rm u}V \sin^2(\alpha), \tag{1.79}$$

with $K_{\rm u} > 0$ the uniaxial anisotropy constant, the total energy $E_{\rm tot}$, being the sum of shape anisotropy and field energy contribution, reads

$$E_{\text{tot}} = E_{\text{d}} + E_{H} = K_{\text{u}}V \sin^{2}(\alpha) - \mu_{0}MHV \cos(\theta)$$
$$= K_{\text{u}}V \sin^{2}(\theta - \phi) - \mu_{0}MHV \cos(\theta). \tag{1.80}$$

Let us in the following consider three particular cases: $\phi = 0^{\circ}$, 45°, and 90°.

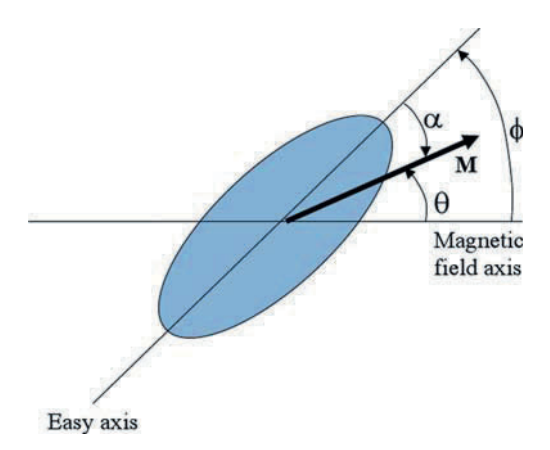


Fig. 1.19 A single-domain particle with ellipsoidal shape in an applied magnetic field \mathbf{H} . α is the angle between the easy axis of the particle and the direction of magnetization \mathbf{M} , θ is the angle between the magnetic field axis and \mathbf{M} , and $\phi = \theta - \alpha$ is the angle between the magnetic field axis and the easy axis of the particle

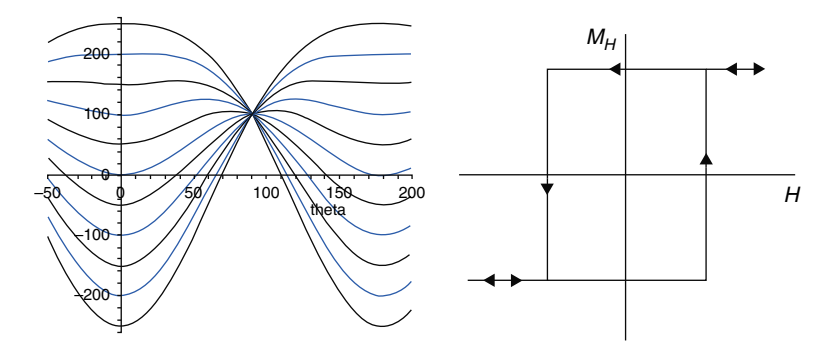


Fig. 1.20 The total energy (1.80) as a function of the angle θ for different values of the applied magnetic field H and $\phi = 0^{\circ}$ (*left*). Hysteresis loop obtained in this configuration (*right*)

1.4.3.1 $\phi = 0^{\circ}$ Case

In this case, (1.80) reduces to

$$E_{\text{tot}} = K_{\text{u}}V \sin^2(\theta) - \mu_0 MHV \cos(\theta). \tag{1.81}$$

Figure 1.20 (left) shows E_{tot} as a function of θ for different values of the applied magnetic field. Whatever the magnetic field, the minimum energy is always at one of the two positions $\theta = 0^{\circ}$ or 180° .

Let **H** be oriented to the right and **M** parallel to **H**. In this case, we find a minimum position at $\theta = 0^{\circ}$ and the magnetization will remain in this configuration for all positive values of the magnetic field (i.e., **H** remains oriented to the right). If we switch the direction of **H** (orientation to the left), $\theta = 0^{\circ}$ will remain a minimum of the energy for absolute values of the magnetic field smaller than the coercive field:

$$H_{\rm c} = \frac{2K_{\rm u}}{\mu_0 M}.\tag{1.82}$$

Crossing this value of the magnetic field, the minimum at $\theta=0^\circ$ becomes a maximum, so that this configuration can no longer be stable. Consequently, the magnetization will also switch to the left, so that the energy is again in a minimum (now at $\theta=180^\circ$). The magnetization will remain in this configuration now for all negative values of the magnetic field and it will need again a magnetic field of strength H_c in the opposite direction to make \mathbf{M} switch to the right. Figure 1.20 (right) shows M_H as a function of the applied magnetic field and we see that the magnetization curve exhibits a hysteretic behavior.

1.4.3.2 $\phi = 45^{\circ}$ case

Now (1.80) becomes

$$E_{\text{tot}} = K_{\text{u}}V \sin^2(\theta - 45^{\circ}) - \mu_0 MHV \cos(\theta).$$
 (1.83)

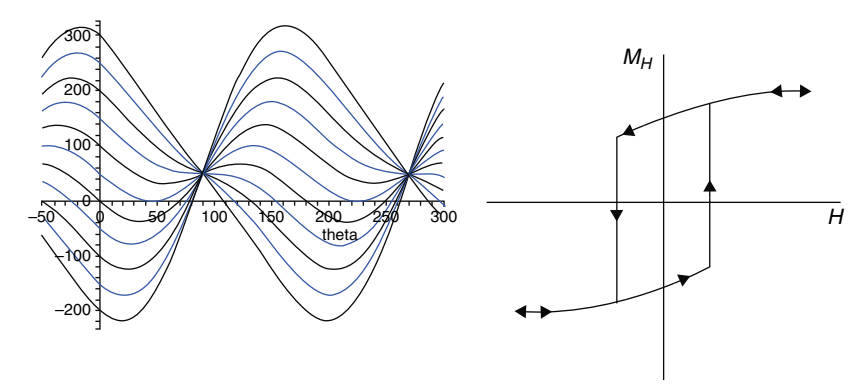


Fig. 1.21 As in Fig. 1.20, but for $\phi = 45^{\circ}$

Figure 1.21 (left) shows E_{tot} as a function of θ for different values of the applied magnetic field.

As in the first configuration, one obtains again a hysteresis loop (see Fig. 1.21, right). However, there are several important differences with respect to the preceding case: first, the coercive field $H_{\rm c}$ is half of that found for $\phi=0^{\circ}$; second, the remanent magnetization $M_{\rm r}$ is not equal to the saturation magnetization $M_{\rm s}$, $M_{\rm r}=M_{\rm s}/\sqrt{2}$; and third, saturation is never reached for finite magnetic fields, but is approached asymptotically.

1.4.3.3 $\phi = 90^{\circ}$ case

Now (1.80) becomes

$$E_{\text{tot}} = K_{\text{u}}V \cos^2(\theta) - \mu_0 MHV \cos(\theta). \tag{1.84}$$

Figure 1.22 (left) shows E_{tot} as a function of θ for different values of the applied magnetic field. In this configuration we obtain a completely different behavior of the magnetization as a function of the applied magnetic field. Although in the case $\phi=0^{\circ}$ only two minimum positions exist, namely $\theta=0^{\circ}$ and 180°, the minimum position varies continuously as a function of the magnetic field strength in the present case. In fact, M_H varies linearly with the magnetic field and saturates for absolute magnetic field values larger than $\frac{2K_u}{\mu_0 M}$. Figure 1.22 (right) shows M_H as a function of the applied magnetic field. In contrast to the two preceding cases, no hysteresis is found.

1.4.4 Domains and Domain Walls

In massive ferromagnetic samples, the obtained coercive fields are substantially lower, often by a factor of 10, than those found in the "uniform rotation" model.

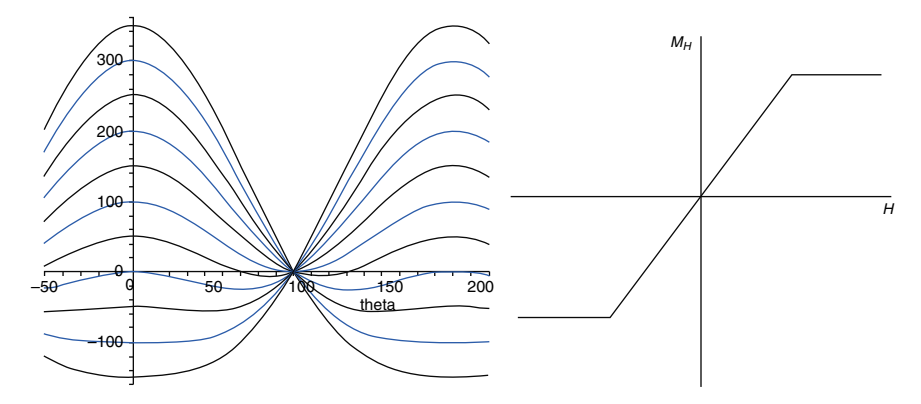


Fig. 1.22 As in Fig. 1.20, but for $\phi=90^\circ$. Note that in this particular case no hysteretic behavior is found

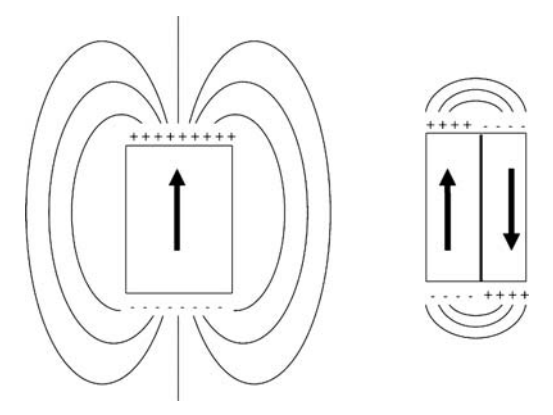


Fig. 1.23 The creation of magnetic domains leads to a decrease of the magnetic field energy $(\propto \int H^2 \, \mathrm{d}V)$

The reason for this is that there exists another magnetization-reversal mechanism that can proceed via considerably lower energy expenditure. The latter mechanism is based on the nucleation of domains, the motion of domain walls, and the growth of reversed domains.

1.4.4.1 Why Do Domains Exist?

Figure 1.23 shows two hypothetical domain configurations. In the left configuration both the exchange and the anisotropy energy are minimal. The first because all moments are aligned, and the second because the magnetization axis is an easy axis. However, the demagnetizing energy is not minimal. There are a lot of uncompensated magnetic "poles" at the surface of the ferromagnetic sample. This energy

contribution can be decreased by introducing domains as it is seen for the right configuration. However, a transition region between the two domains has been created in which the moments are not parallel to each other. Moreover, the moments in this region are not anymore parallel to the easy axis. Thus, both the exchange and the anisotropy energy are larger than in the left configuration. Nevertheless, in massive ferromagnets this domain configuration has a smaller total energy than in the single domain state, because a comparatively small number of moments are involved in increasing the exchange and the anisotropy energy.

1.4.4.2 Domain Wall Width

The transition region between the two domains has a finite width δ that is governed by the exchange and the anisotropy. While δ would become infinite without anisotropy, the anisotropy tries to make δ as small as possible. Thus, we have a competition between both energy contributions.

In the following we consider only 180°-walls as in Fig. 1.24, that is, the magnetization directions of the two neighboring domains are opposite. For the sake of simplicity, let us assume that the angle between two neighboring spins in the domain wall in the direction perpendicular to the domain wall be $\phi = \pi/N$, with N the number of spins along this direction in the domain wall of width δ . For large N, the angle ϕ is small and we find for the exchange energy per unit area

$$\sigma_{\rm ex} = -\frac{J}{a^2} S^2 N \cos(\phi) \approx -\frac{J}{a^2} S^2 N \left[1 - \frac{\phi^2}{2} \right],$$
 (1.85)

with a the lattice constant. Thus, the energy difference per unit area between the single-domain state and the configuration with domain wall is

$$\Delta \sigma_{\rm ex} \approx \frac{A}{2a} N \phi^2 = \frac{A}{2a} \frac{\pi^2}{N},\tag{1.86}$$

with $A = \frac{JS^2}{a}$ the exchange stiffness constant.

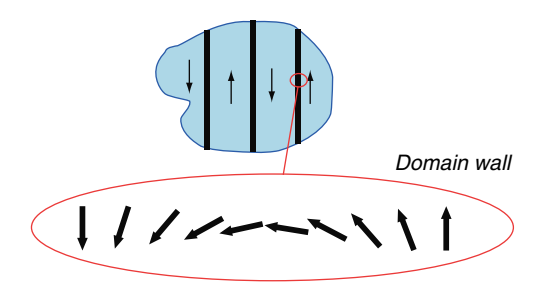


Fig. 1.24 A transition region, in which the spin direction varies, exists between two magnetic domains

Assuming a uniaxial magnetic anisotropy of the form $E_A = KV \sin^2(\theta)$, with K the anisotropy constant and θ the angle between the spin and the easy axis of magnetization, we obtain for the energy difference per unit area between the single-domain state and the configuration with domain wall:

$$\Delta \sigma_{\mathcal{A}} = Ka \sum_{n=1}^{N} \sin^2(n\phi) = K \frac{Na}{2}.$$
 (1.87)

To minimize the total wall energy per unit area, $\Delta\sigma_w=\Delta\sigma_{ex}+\Delta\sigma_A$, we have to demand

$$0 \equiv \frac{\mathrm{d}(\Delta\sigma_{\mathrm{w}})}{\mathrm{d}N} = -\frac{A}{2a} \left(\frac{\pi}{N}\right)^2 + \frac{Ka}{2},\tag{1.88}$$

resulting in

$$\delta = Na = \pi \sqrt{\frac{A}{K}}. (1.89)$$

For a 180° domain wall in massive Fe δ is about 85 nm. However, this is an approximate value for the domain-wall width in Fe. Actually the width depends on the type of domain wall, Bloch or Néel walls (see Sect. 1.4.4.5). In addition, there exists 180° and non-180° domain walls. In cubic materials with $K_1 > 0$, such as Fe, the non-180° walls are all 90° walls, so that the direction of the magnetic moments in neighboring domains are at right angles.

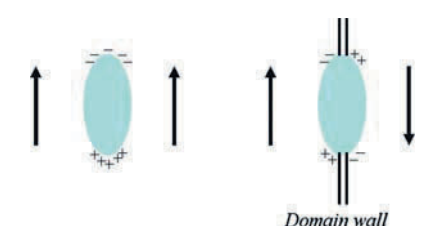
1.4.4.3 Nucleation of Reversed Domains

Reversed domains can be generated near all types of defect regions in which the local values of the exchange and the anisotropy are sufficiently small with respect to the bulk values to make the reversal of the local magnetization possible. The domain wall that has been created during such a reversal will spread into the ferromagnetic material and move across the whole sample until complete magnetization reversal has been established. Note that the energy required for this process is equal to the wall energy taken over the wall surface and thus involves only a very small volume compared to the total volume of the sample. This explains why actual coercive fields are much smaller than that found in the model of uniform rotation (see Sect. 1.4.3), in which the anisotropy energy over the whole sample volume has to be considered.

1.4.4.4 Pinning of Domain Walls

The changes in magnetization due to the application of a magnetic field can be either reversible or irreversible. In ferromagnetic materials, reversible changes occur only for small field increments. Two mechanisms are responsible for a magnetization change: first, domain rotation as discussed in Sect. 1.4.3, and second, domain wall motion. Both of these processes can be reversible or irreversible, which depends in

Fig. 1.25 The intersection of a nonmagnetic inclusion by a domain wall reduces the magnetostatic energy



both cases on the amplitude of the applied magnetic field. Domain wall motion is manifested in two different ways: bowing of the domain wall and translation, both of which become irreversible if the domain wall encounters a pinning site, preventing it from relaxation when the magnetic field is removed. There are two possible types of pinning sites:

- (a) Strain associated with dislocations in the material can pin domain walls through the magnetoelastic coupling. Therefore, the higher the density of dislocations, the stronger the pinning and the greater the impedance to domain wall motion.
- (b) The presence of inclusions in the material, which show different magnetic behavior (usually nonmagnetic) than the matrix material. The intersection of a nonmagnetic inclusion by a domain wall can strongly reduce the magnetostatic energy associated with the inclusion (see Fig. 1.25). Consequently, the domain wall will be pinned in this energetically favorable position unless a much higher magnetic field is applied to unpin it.

Defects that are most effective in pinning domain walls are those whose magnetic properties differ most from those of the matrix and whose dimensions are comparable to the domain wall width. Thus, in hard magnetic materials (i.e., high-coercivity materials) in which the domain wall width is of the order of a few nanometer, point defects and grain boundaries are very important. In soft magnetic materials (i.e., low-coercivity materials), on the other hand, the domain wall width is of the order of 100 nm so that long-range strain fields and larger precipitates are more effective in pinning domain walls.

1.4.4.5 Bloch or Néel Wall?

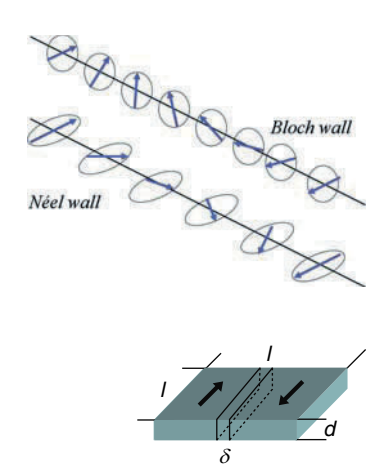
Up to now we have neglected the demagnetization energy due to a domain wall. If we take it into account, two different types of domain walls are possible: Bloch [20] and Néel walls [21] (see Fig. 1.26).

For a dimensional analysis of the energy, we consider a ferromagnet with the lateral dimensions l, the thickness d, and the domain wall width δ (see Fig. 1.27).

In the case of Bloch walls where the magnetic "poles" appear at the surface of the ferromagnet, the demagnetization energy due to the domain wall $E_{\rm d}^{\rm Bloch}$ is proportional to the product $\delta \cdot l$. In the case of Néel walls where the magnetic "poles" appear within the ferromagnet, the demagnetization energy due to the domain wall $E_{\rm d}^{\rm Neel}$ is proportional to the product $d \cdot l$.

Fig. 1.26 The two types of domain walls: Bloch wall (top); the moments rotate in a plane perpendicular to the plane defined by the magnetization directions in the neighboring domains. Néel wall (bottom); the moments rotate in the plane defined by the magnetization directions in the neighboring domains

Fig. 1.27 A two-domain state of a ferromagnet with lateral dimensions l, thickness d, and domain wall width δ



This analysis shows that the ratio δ/d determines whether a Bloch or a Néel wall is energetically more favorable. In thick films, in particular in massive ferromagnets, in which $d >> \delta$ is realized, Bloch walls are preferred. In thin films with $d << \delta$, however, Néel walls are energetically more favorable.

1.4.4.6 Why Small Particles are Always Mono-domain?

By the introduction of domains and hence of domain walls the demagnetizing energy is reduced while the wall energy is increased. By considering a ferromagnet with a linear dimension l, we obtain for the demagnetizing and the wall energy, $E_{\rm d}=Al^3$ and $E_{\rm w}=Bl^2$, respectively, with A and B constants. By defining a critical value of the linear dimension $l_{\rm c}=B/A$, one finds that for $l>l_{\rm c}$, the demagnetizing energy is larger than the wall energy, thus favoring a multidomain state, while for $l< l_{\rm c}$, the particle is in a mono-domain state because the energy of a single wall is now larger than the demagnetizing energy. Usually, critical values $l_{\rm c}$ are in the nanometer regime.

1.4.4.7 Superparamagnetism [22]

Assuming an uniaxial magnetic anisotropy for a small particle, in zero applied magnetic field an energy barrier separates the two possible orientations of the magnetization along the easy directions (see Fig. 1.28). The height of the energy barrier is E = KV, with K the anisotropy constant and V the volume of the particle. One observes superparamagnetic behavior when the energy barrier becomes comparable to the thermal energy $k_{\rm B}T$. Indeed, the characteristic time to overcome the barrier E is

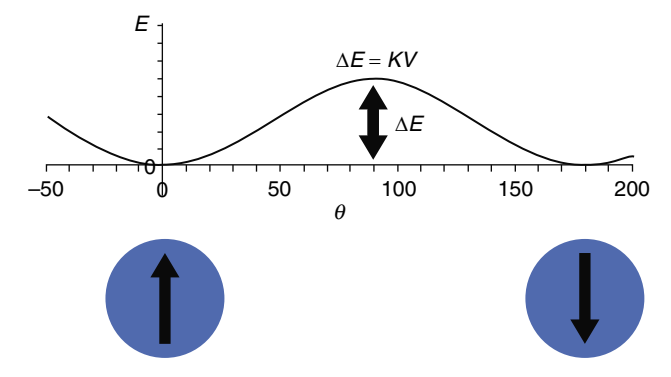


Fig. 1.28 A small particle with uniaxial magnetic anisotropy in zero magnetic field has two energy minima (at $\theta = 0^{\circ}$ and 180°). The energy barrier is given by $\Delta E = KV$

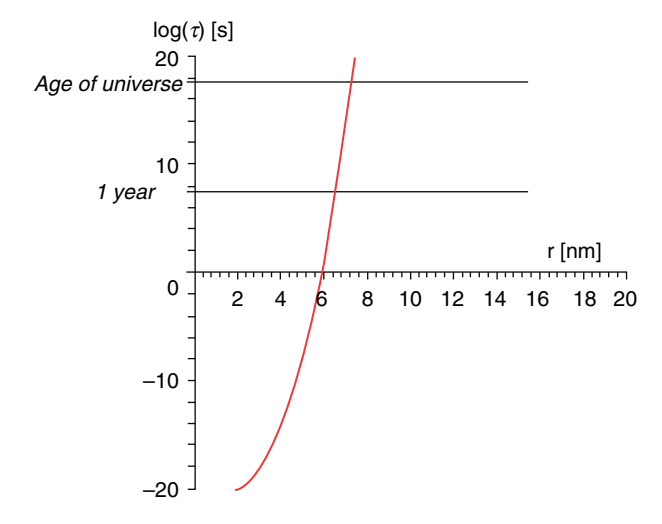


Fig. 1.29 The characteristic time τ as a function of the radius r for a spherical particle with a uniaxial magnetic anisotropy of $K = 10^5 \,\mathrm{J}\,\mathrm{m}^{-3}$ at room temperature

$$\tau = \tau_0 \, \mathrm{e}^{E/k_{\mathrm{B}}T},\tag{1.90}$$

where τ_0 is of the order 10^{-9} s. Thus, for particles of sufficiently large size, the characteristic time is extremely long so that the magnetization is stable. However, there exists a critical volume V_c of the particle below which the energy barrier will become so low that the magnetization will start to fluctuate on a very short time scale. While the magnetization is essentially uniform over the particle volume at any time, the time-averaged magnetization appears to be zero for $V < V_c$. Figure 1.29 shows the characteristic time τ as a function of the radius for a spherical particle with $K = 10^5 \, \mathrm{J} \, \mathrm{m}^{-3}$ at room temperature.

1.5 Thin Film Magnetism

The reasons to investigate thin films are manifold. On the one hand, new crystal-lographic structures can be realized for certain elements that cannot be found in the bulk (e.g. fcc Fe films). On the other hand, they can exhibit different (magnetic) behavior compared to bulk systems. The deposition of thin films on different substrates is an essential step in many fields of modern high technology, and applications range from large area optical coatings on windows and layers to improve friction and wear to the applications in microelectronics.

Among the many phenomena occurring in magnetic thin films, we will restrict ourselves in this last section to the discussion of only three of them: the appearance of a surface anisotropy, the indirect exchange coupling, and the giant magnetoresistance effect in multilayers.

1.5.1 Surface Anisotropy

Because of the symmetry breaking at the surface, the surface anisotropy K_s can have a different symmetry than the volume anisotropy K_v . The surface anisotropy, which is uniaxial by symmetry, may favor either an in-plane or an out-of-plane magnetization. An interesting case is that where the surface anisotropy favors the out-of-plane orientation, because it competes then with the magnetostatic energy that favors an in-plane orientation of the magnetization. Because of the definition of the surface anisotropy as an energy per unit area (unit is $J \, \mathrm{m}^{-2}$), the total anisotropy (energy/volume) of a magnetic film of thickness d is $K_{tot} = K_v + K_s/d$. Thus, for thicknesses below a critical value, the term K_s/d becomes dominant such that the magnetization will show a reorientation from in-plane to out-of-plane magnetization. Figure 1.30 shows an example of a film system in which the surface anisotropy favors an out-of-plane magnetization at low coverages.

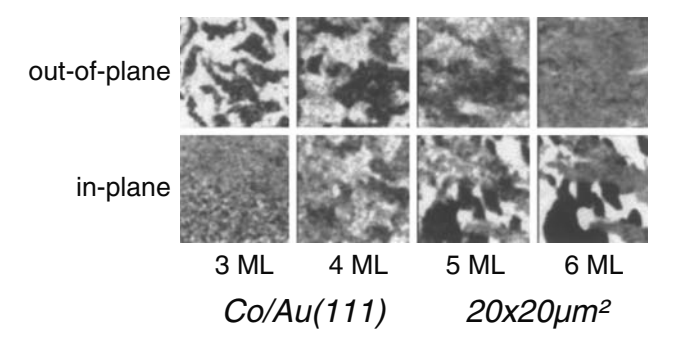


Fig. 1.30 The magnetic domains in ultrathin Co films grown on Au(111) show a transition from out-of-plane to in-plane between 4 and 5 monolayers. The images were taken with a spin-polarized scanning electron microscope. Adapted from [23]

1.5.2 Indirect Exchange Coupling in Multilayers

Between two ferromagnetic layers an indirect exchange coupling is observed, which oscillates as a function of the thickness of a nonmagnetic layer that separates the ferromagnetic layers (see Fig. 1.31).

What is the origin of this indirect exchange coupling? An explanation for this behavior is given within the RKKY theory (Ruderman, Kittel, Kasuya, Yosida) [25– 27]. It explains the ferromagnetic as well as the antiferromagnetic coupling in certain impurity systems where strongly localized moments (e.g., rare-earth ions) are embedded in a nonmagnetic host metal (e.g., Cu). Because of the negligible overlap of the wave functions of the localized moments, direct Heisenberg-exchange is not possible. However, there is a large overlap with the s-electrons of the host metal. The host metal tries to screen the localized moments by concentrating electrons with the opposite spin around the localized moment. The s-electron spin density tries to create Dirac peaks at the positions of the localized moments. To do so, k-values ranging between $-\infty$ to $+\infty$ are necessary. However, only k-values ranging between $-k_{\rm F}$ and $+k_{\rm F}$ are available. Thus, the Fourier series is truncated and the electron-spin density is left with oscillations characterized by $k \ge k_{\rm F}$ that are uncompensated. These oscillations are analogue to the Friedel oscillations of the charge density. The cutoff leads thus to an oscillatory structure with a wavelength of $\pi/k_{\rm F}$. Because these oscillations carry spin information away from the localized moment, they allow it to interact with other moments that are out of the reach of direct exchange coupling (see Fig. 1.32).

In the zero-dimensional case, the coupling is given by

$$J_{ij}^{\text{RKKY}} = \frac{1}{R^4} \left[\sin(2k_{\text{F}}R) - R\cos(2k_{\text{F}}R) \right]. \tag{1.91}$$

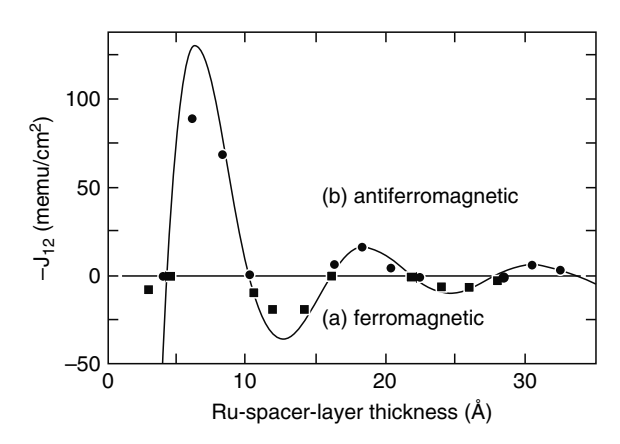
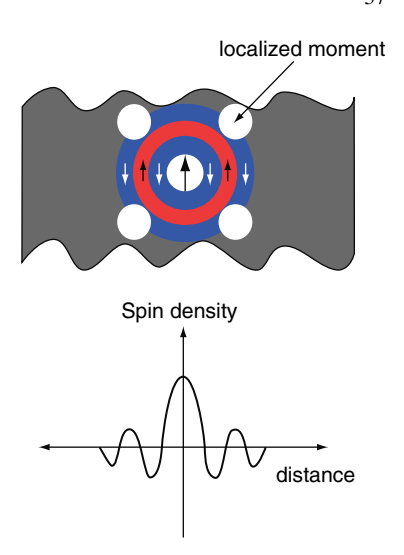


Fig. 1.31 The magnetic coupling between two ferromagnetic $Ni_{0.8}Co_{0.2}$ layers oscillates as a function of the Ru-spacer layer thickness. From [24]

Fig. 1.32 Oscillatory response of the spin density at the Fermi energy to a local magnetic moment



If we go to the case where two layers of localized moments are separated by a nonmagnetic metal, one obtains

$$J_{ij}^{\text{RKKY}} = \frac{1}{R^2} \sin(2k_{\text{F}}R),$$
 (1.92)

that is, the oscillations are much less damped in the two-dimensional case. Taking typical values for $k_{\rm F}$ (between 10 and 17 nm⁻¹), we expect a wavelength $\lambda = \pi/k_{\rm F}$ between 0.18 and 0.31 nm, that is, of the order of the lattice constant. However, this is not observed. For the above case of Ru as spacer layer, we expect $\lambda \sim 0.27$ nm while a wavelength of 1.2 nm is measured. How can one solve this contradiction? So far, it was assumed that the coupling J_{ij} is a continuous function of the distance between the ferromagnetic layers. However, the spacer layer is a solid material and the atoms are arranged at discrete lattice plans. Therefore, the spacer thickness and along with it the coupling function can only take discrete values. The consequences are elucidated in Fig. 1.33. The lattice plans intersect the coupling curve at the points. It is obvious that the new wavelength (continuous line) is much larger than the one in the original coupling curve (dashed line). This effect is called aliasing effect.

The aliasing approach is a first attempt to account for the discreteness of the crystal lattice. More accurately, the spatial distribution of the atoms reflects itself in the shape of the Fermi surface. The Fermi surfaces of crystalline materials are generally not spherical as for free electrons. As a consequence, $k_{\rm F}$ is directional dependent and the oscillation period depends on the direction, as has been experimentally verified. Generally, there exists more than one period for a given crystal direction. The periods in multilayers can be derived from the Fermi surface of the spacer layer by using the following procedure. Figure 1.34 shows the elliptical Fermi surface of a hypothetical spacer layer in a stack, with the stack normal i_z . One now looks for pairs of wave vectors $k_{\rm F}$ and $k_{\rm F}'$ for which the difference vector $\mathbf{Q} = k_{\rm F} - k_{\rm F}'$ is parallel

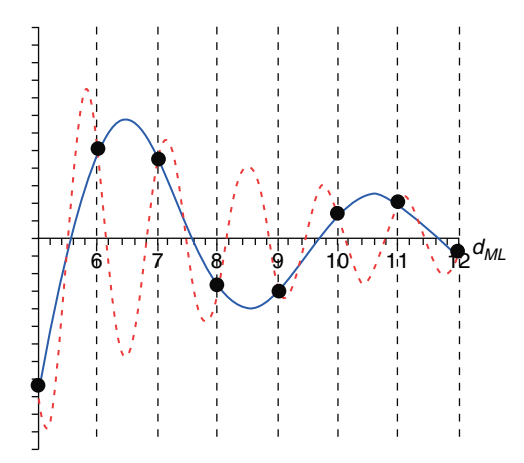


Fig. 1.33 The spin-density oscillations of wavelength $\lambda = \pi/k_F$ (dashed line) seem to have a longer wavelength (continous line) when measured at integer monolayer values $n\,d_{\rm ML}$ (dots), if $\lambda < 2\,d_{\rm ML}$

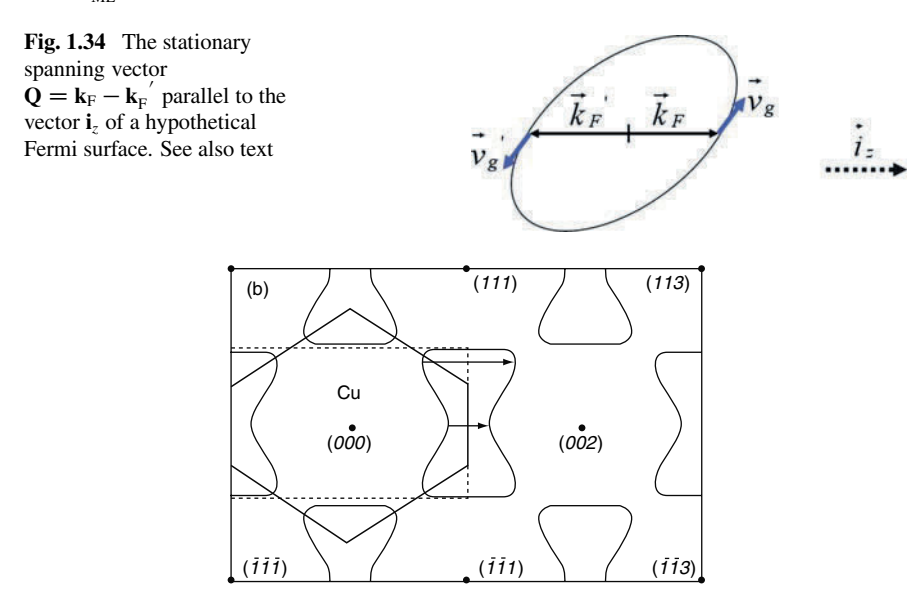


Fig. 1.35 Cross section of the Fermi surface of Cu along the $(1\overline{1}0)$ plane passing through the origin. The two stationary spanning vectors along the [001] direction are shown

to the stack normal and for which the group velocities \mathbf{v}_g and \mathbf{v}_g' are opposite. Only one such direction is found for each \mathbf{i}_z in the case of an elliptical Fermi surface. Figure 1.35 shows the famous dog-bone Fermi surface, being typical of cubic lattices. Using the same method one finds three solutions for the [100] direction of \mathbf{i}_z , two of which being equivalent. \mathbf{Q}_1 and \mathbf{Q}_2 represent a short and a long period, respectively.

1.5.3 Giant Magnetoresistance

Giant magnetoresistance (GMR) has been discovered in 1988 in multilayers of Fe (ferromagnetic metal) and Cr films (nonmagnetic metal) [28,29]. For Cr spacer layer thicknesses around 0.9 nm, a strong reduction of the resistivity is observed when a magnetic field is applied. Because of the indirect anti-ferromagnetic coupling that exists at this particular Cr spacer thickness between the ferromagnetic layers, the magnetic moments in the Fe films pass from an antiparallel alignment in zero field to a parallel one in high magnetic fields (Fig. 1.36). The giant magnetoresistance has also been observed in other multilayer systems containing ferromagnetic layers separated by nonmagnetic spacer layers.

Figure 1.37 shows in a schematic way the mechanism that is responsible for giant magnetoresistance in multilayers. For the sake of simplicity we assume that the mean free path λ (typically of the order of 10 nm in nonmagnetic metals and several nanometer in ferromagnetic metals) is much larger than the thickness of

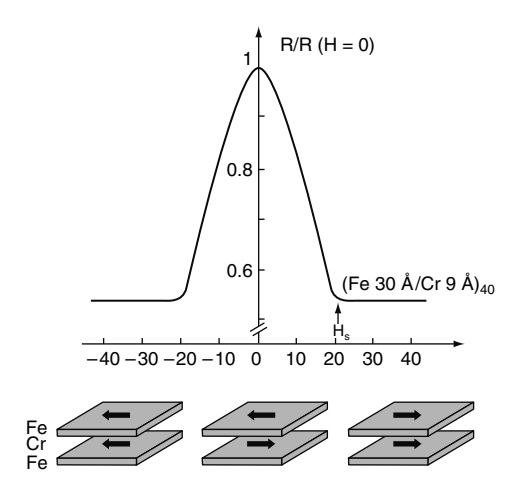


Fig. 1.36 The resistance of a Fe/Cr/Fe multilayer system as a function of the applied magnetic field. See text. Adapted from [28]

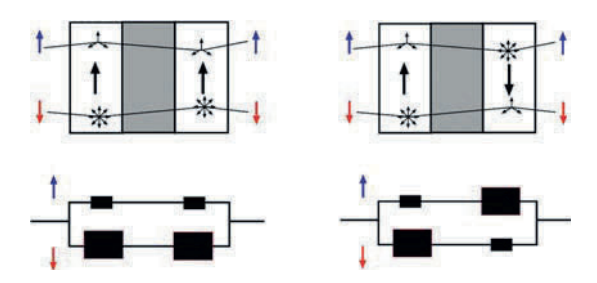


Fig. 1.37 Schematic description of the giant magnetoresistance by considering equivalent circuit diagrams. Parallel configuration (*left*), antiparallel configuration (*right*)

the layers. In this limit, one observes an average effect produced by the scattering over several periods. To understand the following discussion, we have to know that the scattering probability of an electron in a ferromagnetic material is not the same whether its spin is parallel or antiparallel to the local magnetic moment. This results in different mean free paths for up and down spin electrons, and is due to the fact that the densities-of-states of the two spin directions are very different. Consequently, the number of unoccupied states is also very different for the two spin directions. For example, in permalloy one finds spin-dependent mean free paths, which are separated by one order of magnitude.

Let us consider the case where spin up electrons have a larger mean free path than spin down electrons. The resistance of the up channel, r_{\uparrow} , is therefore smaller than that of the down channel, r_{\downarrow} . For the sake of simplicity we assume $r_{\downarrow} \gg r_{\uparrow}$. When the magnetic moments of the ferromagnetic films are in the parallel configuration (Fig. 1.37, left), the spin up electrons are little scattered in all magnetic films, while the spin down electrons are strongly scattered. The short-circuit in the up channel causes a small total resistance:

$$r_{\rm p} = \frac{2r_{\uparrow}r_{\downarrow}}{r_{\uparrow} + r_{\downarrow}} \approx 2r_{\uparrow}. \tag{1.93}$$

In contrast, in the antiparallel configuration of the magnetic moments (Fig. 1.37, right), both spin directions are strongly scattered in one ferromagnetic film and little scattered in the other. The total resistance reads

$$r_{\rm ap} = \frac{r_{\uparrow} + r_{\downarrow}}{2} \approx \frac{r_{\uparrow}}{2} \tag{1.94}$$

and hence $r_{ap} > r_p$.

The giant magnetoresistance characterizes therefore the progressive passage from the antiparallel alignment in zero magnetic field to the parallel alignment of the magnetic moments in a strong applied magnetic field (Fig. 1.36). The giant magnetoresistance can be expressed in terms of the spin asymmetry $\alpha = r_{\uparrow}/r_{\downarrow}$:

$$\left(\frac{\Delta r}{r}\right)_{GMR} = \frac{r_{ap} - r_p}{r_p} = \frac{(r_{\uparrow} - r_{\downarrow})^2}{4r_{\uparrow}r_{\downarrow}} = \frac{(\alpha - 1)^2}{4\alpha}.$$
 (1.95)

References

- 1. P. Langevin, Ann. Chem. Phys. 5, 70 (1905)
- 2. J. Larmor, Phil. Mag. 44, 503 (1897)
- 3. L. Brillouin, J. de Phys. Radium 8, 74 (1927)
- 4. P. Curie, Ann. Chem. Phys. 5, 289 (1895)
- 5. F. Hund, Linienspektren und periodisches System der Elemente (Springer, Berlin, 1927)
- 6. W. Pauli, Z. Phys. 31, 765 (1925)
- 7. J.H. van Vleck, The Theory of Electric and Magnetic Susceptibilities, (Oxford, 1952)

- 8. A.H. Morrish, The Physical Principles of Magnetism (Wiley, New York, 1965)
- 9. C. Kittel, Introduction to Solid State Physics (Wiley, New York, 1986)
- 10. W. Pauli, Z. Phys. 41, 81 (1926)
- 11. P. Weiss, Compt. Rend. 143, 1136 (1906)
- 12. P. Weiss, J. Phys. 6, 661 (1907)
- 13. W. Heitler, F. London, Z. Phys. 44, 455 (1927)
- 14. W. Heisenberg, Z. Phys. 49, 619 (1928)
- 15. P.A.M. Dirac, Proc. Roy. Soc. A123, 714 (1929)
- W. Dürr, M. Taborelli, O. Paul, R. Germar, W. Gudat, D. Pescia, M. Landolt, Phys. Rev. Lett. 62, 206 (1989)
- 17. F. Bloch, Z. Phys. 61, 206 (1930)
- 18. E.C. Stoner, Proc. Roy. Soc. A165, 372 (1938)
- 19. E.C. Stoner, E.P. Wohlfarth, Phil. Trans. Roy. Soc. A240, 599 (1948)
- 20. F. Bloch, Z. Phys. 74, 295 (1932)
- 21. L. Néel, Compt. Rend. **241**, 533 (1955)
- 22. L. Néel, Ann. Geophys. 5, 99 (1949)
- 23. R. Allenspach, M. Stampanoni, A. Bischof, Phys. Rev. Lett. 65, 3344 (1990)
- 24. S.S.P. Parkin, D. Mauri, Phys. Rev. **B44**, 7131 (1991)
- 25. M.A. Ruderman, C. Kittel, Phys. Rev. 96, 99 (1954)
- 26. T. Kasuya, Prog. Theor. Phys. 16, 45 (1956)
- 27. K. Yosida, Phys. Rev. 106, 893 (1957)
- M.N. Baibich, J.M. Broto, A. Fert, F. Nguyen Van Dau, F. Petroff, P. Etienne, G. Creuzet, A. Friederich, J. Chazelas, Phys. Rev. Lett. 61, 2472 (1988)
- 29. G. Binasch, P. Grünberg, F. Saurenbach, W. Zinn, Phys. Rev. **B39**, 4828 (1989)

Chapter 2

Spintronics: Conceptual Building Blocks

J.-Ph. Ansermet

Abstract The purpose of this introduction to spintronics is to provide some elementary description of its conceptual building blocks. Thus, it is intended for a newcomer to the field. After recalling rudimentary descriptions of spin precession and spin relaxation, spin-dependent transport is treated within the Boltzmann formalism. This suffices to introduce key notions such as the spin asymmetry of the conductivities in the two-current model, the spin diffusion length, and spin accumulation. Two basic mechanisms of spin relaxation are then presented, one arising from spin-orbit scattering and the other from electron-magnon collisions. Finally, the action of a spin-polarized current on magnetization is presented in a thermodynamics framework. This introduces the notion of spin torque and the characteristic length scale over which the transverse spin polarization of conduction electron decays as it is injected into a magnet.

2.1 Spin Precession

We begin by some simple reminders about how a spin evolves in a magnetic field, limiting the description to a spin 1/2 particle, as we will be concerned with transport phenomena for the electron spin exclusively.

Consider a particle with a magnetic moment **m** in an induction field **B**. The evolution of its angular momentum $\hbar S$ is, according to classical mechanics, given by

$$\frac{\mathrm{d}\left(\hbar\mathbf{S}\right)}{\mathrm{d}t} = \mathbf{m} \wedge \mathbf{B}.\tag{2.1}$$

Now in a semi-classical picture, we write that $\hbar S = \mathbf{m}/\gamma$. Then the evolution of the moment m can be written as

Insitut de Physique des Nanostructures, Ecole Polytechnique Fédérale de Lausanne, station 3, CH-1015 Lausanne-EPFL

J.-Ph. Ansermet

44 J.-Ph. Ansermet

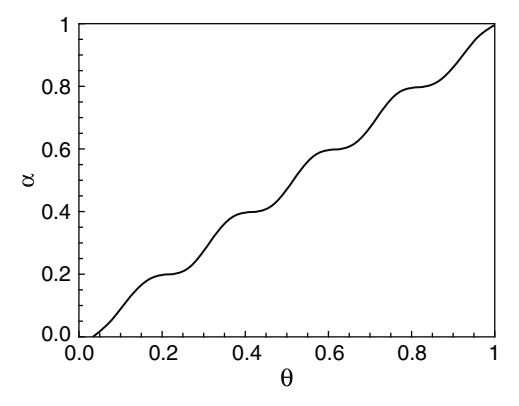


Fig. 2.1 Numerical integration of (2.2) for a **B** field rotating at an angular velocity 10 times smaller than the Larmor frequency of the spin precessing about this field. The x coordinate is the polar angle (in degrees) of the spin direction with respect to the vertical, and the y coordinate is the polar angle of the field (in radian)

$$\frac{\mathrm{d}\mathbf{m}}{\mathrm{d}t} = \boldsymbol{\omega} \wedge \mathbf{m},\tag{2.2}$$

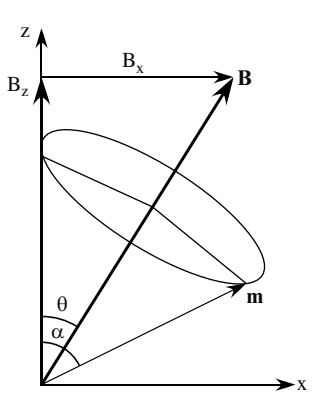
with $\omega = -\gamma \mathbf{B}$. This equation describes the precession of the vector \mathbf{m} about ω , $|\omega|/(2\pi)$ is called the Larmor frequency. The gyromagnetic factor γ of electrons is about $2\pi \times 2.8$ GHz kG⁻¹.

Using no more than (2.2), we can discuss the phenomenon known as *fast adiabatic passage*. The method is well-known in magnetic resonance spectroscopy and it has been invoked in discussing the dynamics of the electron spin when an electron crosses a domain wall. By simple integration, it can be shown that the magnetization will follow the applied field in its rotation, provided the period of rotation about the applied field is short compared to the time it takes the applied field to undergo the rotation. In Fig. 2.1, we show the result of a numerical integration. The time evolution of the angle between the magnetization and the applied field is shown for the case when the precession frequency is 10 times the angular velocity of the applied field. Hence, when the field changes direction suddenly, the spins do not follow whereas, when the spins have time to revolve about the field as the field tilts, the spins follow precessing tightly about the direction of the field.

When discussing the notion of spin mixing (Sect. 2.5), it will be useful to remember that in quantum mechanics the precession of spin can be thought of in terms of the probability of observing the spin being "up" and "down" alternatively. Consider a spin one-half particle at t=0 in the state $|+\rangle$ quantized in some "z" direction, possibly because it was exposed to a field B_z in this z direction. A transverse field is suddenly turned on along the x direction (by choice of x), B_x (Fig. 2.2). The total field is at an angle θ with respect to the z axis. The Hamiltonian is

$$H = -\gamma \mathbf{B} \cdot \hbar \mathbf{S} = \frac{-\gamma \hbar}{2} \begin{pmatrix} B_z & B_x \\ B_x & -B_z \end{pmatrix}. \tag{2.3}$$

Fig. 2.2 A spin initially along the z axis precesses about a field **B**



It is a standard example of elementary quantum mechanics to calculate the probability for the state $|\psi(t)\rangle$ of the system to be in the opposite *z*-spin direction. The result is known as the Rabi formula:

$$P_{+-}(t) = \frac{1}{2}\sin^2\theta\cos(\omega t),$$
 (2.4)

where ω is the Larmor frequency for the total field.

2.2 Spin Relaxation

The principle of detailed balance applied to spin 1/2 brings out the notion of spin relaxation time in the most concise fashion. We will see in particular that transition rates from "up" to "down" must be distinct from those of transitions from "down" to "up" if the spin system is to reach thermal equilibrium. Consider an ensemble of spin 1/2 particles. Under the effect of a static homogeneous magnetic field $\mathbf{B}_0 = \hat{\mathbf{k}} B_0$, the energy levels $m = \frac{1}{2}$, $m = \frac{-1}{2}$ are split (Fig. 2.3):

We apply an alternative field $B_x(t) = B_{x0} \cos(\omega t)\hat{x}$, and the Hamiltonian con-

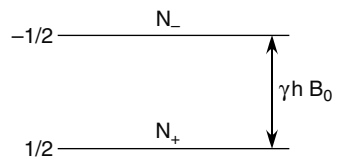
We apply an alternative field $B_x(t) = B_{x0} \cos(\omega t)\hat{x}$, and the Hamiltonian contains a time-dependent term: $H(t) = -\gamma \hbar B_{x0} \cos(\omega t) I_x$. If one were to apply time-dependent perturbation theory, we would have a probability of transition per unit time:

$$P_{a\to b} = \frac{2\pi}{\hbar} \left| \langle a | H(t) | b \rangle \right|^2 \delta \left(E_a - E_b - \hbar \omega \right). \tag{2.5}$$

This result implies that the transition rates going from a to b and b to a are equal: $P_{a\to b}=P_{b\to a}\equiv W$. We consider the populations of both levels, N+ and N-. Under the influence of the oscillating field, N+ and N- vary. As the transition rates are equal, we denote them as W. The principle of detailed balance states in this

46 J.-Ph. Ansermet

Fig. 2.3 Zeeman splitting under a field **B** defining a two-level system



case are

$$\frac{dN_{+}}{dt} = W(N_{-} - N_{+}), \tag{2.6}$$

$$\frac{dN_{-}}{dt} = W(N_{+} - N_{-}). \tag{2.7}$$

This implies, as it should, that the total population $N = N_+ + N_-$ is constant. The population difference $n = N_+ - N_-$ follows

$$\frac{\mathrm{d}n}{\mathrm{d}t} = -2Wn. \tag{2.8}$$

This differential equation for n integrates as $n(t) = n_0 e^{-2Wt}$. Note that if the initial population difference (or polarization) $n_0 > 0$, then the effect of the oscillating field is to make the populations equal. The absorption of energy by the ensemble of the system is given by

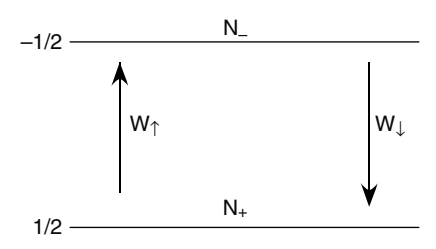
$$\frac{\mathrm{d}E}{\mathrm{d}t} = N_{+}W\hbar\omega - N_{-}W\hbar\omega = Wn\hbar\omega. \tag{2.9}$$

Therefore, we expect that the adsorption of energy drops to zero in a time of the order of 1/W. Likewise, if there is no time-dependent field applied, we get no evolution of n. Indeed, when the spins precess according to (2.2), the angle between the field and the spin is constant, and so the energy is constant. However, we know that when we apply a static field $\mathbf{B}_0 = B_0\hat{\mathbf{k}}$, the spins will eventually align in the field and $N_+ > N_-$. If we start with $N_+ = N_-$, we need a net excess of transitions $(-) \rightarrow (+)$. Where does the energy go? What is missing in our model so far is the coupling to a thermal bath. We have to describe the process by which N_+ and N_- evolve until they reach the equilibrium value given by

$$\frac{N_{-}^{0}}{N_{+}^{0}} = e^{-\Delta E/kT}.$$
 (2.10)

We must therefore assume a coupling of the spins to another system that constitutes a bath. We represent the effect of the coupling to the bath by the probability per unit time of transitions from $(-) \rightarrow (+)$ and $(+) \rightarrow (-)$: the transition rates W_{\downarrow} and W_{\uparrow} (Fig. 2.4).

Fig. 2.4 Two-level system with distinct up-down and down-up transition rates



We apply the principle of detailed balance once again, yielding here

$$\frac{\mathrm{d}N_{+}}{\mathrm{d}t} = W_{\downarrow}N_{-} - W_{\uparrow}N_{+}.\tag{2.11}$$

At equilibrium we have $dN_+/dt = 0$, which sets a condition on the ratio of the rates in order to reach the proper equilibrium populations:

$$\frac{N_{-}^{0}}{N_{+}^{0}} = \frac{W_{\uparrow}}{W_{\downarrow}} = e^{-\Delta E/kT}.$$
(2.12)

Why is it that the transition rates are not equal in this case, whereas the Fermi Golden Rule would make them equal? In a proper treatment, such as that found using the formalism of Bloch–Wangness–Redfield [1], these rates do not depend only on the matrix elements $|\langle a|H(t)|b\rangle|^2$ but also on the population of the levels of the bath.

We can solve for n using (2.11) and

$$N_{-} = \frac{1}{2}(N - n) \quad N_{+} = \frac{1}{2}(N + n). \tag{2.13}$$

Hence,

$$\frac{\mathrm{d}n}{\mathrm{d}t} = \frac{n_0 - n}{T_1},\tag{2.14}$$

with the spin-lattice relaxation rate

$$\frac{1}{T_1} = W_{\uparrow} + W_{\downarrow} \tag{2.15}$$

and

$$n_0 = \frac{W_{\downarrow} - W_{\uparrow}}{W_{\uparrow} + W_{\downarrow}} N, \tag{2.16}$$

the equilibrium value of n. T_1 is known as the spin-lattice relaxation. The integration for n is straightforward (Fig. 2.5):

$$n(t) = n_0 \left(1 - e^{-t/T_1} \right).$$
 (2.17)

48 J.-Ph. Ansermet

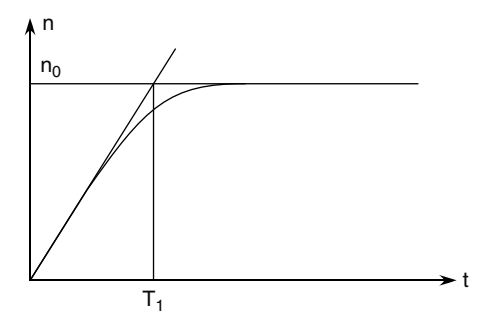


Fig. 2.5 Exponential relaxation, such as it might occur when a spin system, coupled to a bath, reaches equilibrium in an applied magnetic field

2.3 Spin-dependent Transport: The Collinear Case

In this section, we put in place the key ingredients for understanding giant magnetoresistance, relying on the Boltzmann formalism for describing transport perpendicular to interfaces between ferromagnetic layers in which the magnetization is always along a set direction of space. This allows us to introduce spin-dependent conductivities and chemical potentials. The derivation introduces a diffusion equation for the chemical potential difference, with the spin diffusion length as the characteristic length scale.

We assume that we can define a statistical distribution of the points in the phase space of positions and momentum of one electron states (\mathbf{r}, \mathbf{p}) . We assume that we can define a statistical distribution for each spin. This does not preclude transfers between the spin channels, but these transfers must be slow enough that an equilibrium per channel can be defined. Thus we consider

$$f_s(\mathbf{r}, \mathbf{p}, t)$$
 $(s = \uparrow, \downarrow)$.

This is justified by experimental data. It turns out that the mean distance between two collisions (which contribute to the momentum relaxation) is much less than the mean distance between two spin flips, and so we can think of the electrical current as being either of "up" spins or "down" spins. The scattering events may differ in these two channels (Fig. 2.6 top). We have to distinguish also the two types of spin-flip events: those that take place in collisions, which also relax the momentum of the electrons, and those that do not (Fig. 2.6 bottom).

We assume that we can define a local equilibrium distribution:

$$f_{0s}(\mathbf{r}, \mathbf{p}) = f_{FD}\left(\frac{E_s(\mathbf{p}) - \mu_s(\mathbf{r})}{k_B T}\right). \tag{2.18}$$

Here, f_{FD} is the Fermi–Dirac distribution, μ_s (**r**) is the position-dependent, spin-dependent, chemical potential, k_{B} is Boltzmann constant, and T is the temperature.

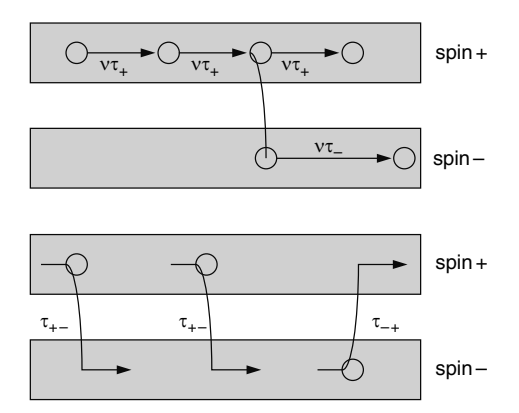


Fig. 2.6 (*Top*) The two types of events, collisions with or without loss of momentum. Electrons are accelerated in between collisions, and stopped fully at each inelastic collisions. (*Bottom*) Another type of spin flip is considered, where the spin flips without a change of its momentum

We learn from the semi-classical theory of electrons that $\mathbf{p} = \hbar \mathbf{k}$, with \mathbf{k} the wave vector of the Bloch state, and that $\mathrm{d}\mathbf{p}/\mathrm{d}t = \mathbf{F}$ applies, where \mathbf{F} is the force on the electron. The present approach presupposes that we describe electrons not as plane wave (Bloch) states, but as wave packets [2]. We describe the energy of the electron wave packets $E_s(\mathbf{p})$ with an accuracy sharper than kT. We invoke the uncertainty relation $\delta r \, \delta p \approx \hbar$ to see what this implies on the length scale over which the system changes. From $E = \frac{1}{2}mv^2$, we get $\delta E = mv\delta v = v\delta p$, which we want to be of the order of kT, implying $\delta p \cong kT/v$. Consider for the sake of the argument what would happen if we took δr as if we wanted to describe collisions with the field of an ion. Then we would have $\delta E \approx 10 \, E_{\rm F}$. This is way too big! Therefore, by this approach, we can hope to describe inhomogeneities over macroscopic scales only. To account for collisions with ions, for example, one must work them out in another framework, namely, with a quantum mechanical calculation. The effect of such collisions is then included as a distinct contribution to the time evolution of the probability distribution:

$$0 = \frac{\mathrm{d}f_s}{\mathrm{d}t} = \frac{\partial f_s}{\partial t} + \frac{\partial f_s}{\partial \mathbf{r}} \frac{\mathrm{d}\mathbf{r}}{\mathrm{d}t} + \frac{\partial f_s}{\partial \mathbf{p}} \frac{\mathrm{d}\mathbf{p}}{\mathrm{d}t} + \frac{\partial f_s}{\partial t} \bigg|_{\mathbf{r} \in \mathbb{N}}.$$
 (2.19)

We seek the linear response to an electric field $\mathbf{F} = -e\mathbf{E} = e\partial V/\partial \mathbf{r}$. So we write $f_s(\mathbf{r}, \mathbf{p}, t) = f_{0s}(\mathbf{r}, \mathbf{p}) + f_{1s}(\mathbf{r}, \mathbf{p}, t)$, where the last term is a small perturbation. In (2.19), we have for the momentum term, to first order,

$$\frac{\partial f_s}{\partial \mathbf{p}} \frac{\mathrm{d} \mathbf{p}}{\mathrm{d} t} \approx \frac{\partial f_{0s}}{\partial E} \frac{\partial E_s (\mathbf{p})}{\partial \mathbf{p}} \left(e \frac{\partial V}{\partial \mathbf{r}} \right). \tag{2.20}$$

In (2.19), the position term gives

$$\frac{\partial f_s}{\partial \mathbf{r}} \frac{d\mathbf{r}}{dt} \approx -\mathbf{v} \frac{\partial f_{0s}}{\partial E} \frac{\partial \mu_s (\mathbf{r})}{\partial \mathbf{r}}.$$
 (2.21)

50 J.-Ph. Ansermet

Here also, we keep only the distribution at equilibrium because the spatial variation of the chemical potential comes from the application of the electric field, and so it is of the order of the electric field. Now we simply assume that we have parabolic bands, the same for each spin orientation: $E_s(\mathbf{p}) = p^2/2m$. We are considering a stationary regime, that is, $\partial f_s/\partial t = 0$. From (2.19), there remains now

$$\frac{\mathbf{p}}{m} \frac{\partial \left(\mu_{s} \left(\mathbf{r}\right) - eV\left(\mathbf{r}\right)\right)}{\partial \mathbf{r}} \frac{\partial f_{0s}}{\partial E} = \left. \frac{\partial f_{s}}{\partial t} \right|_{\text{coll}}.$$
(2.22)

As usual, the chemical potential and the electrostatic potential come together. We combine them into a *spin-dependent electrochemical potential*: $\bar{\mu}_s(\mathbf{r}) = \mu_s(\mathbf{r}) - eV(\mathbf{r})$. Finally, our linearized spin-dependent Boltzmann equation has become

$$\frac{\mathbf{p}}{m} \frac{\partial \bar{\mu}_s \left(\mathbf{r} \right)}{\partial \mathbf{r}} \frac{\partial f_{0s}}{\partial E} = \left. \frac{\partial f_s}{\partial t} \right|_{\text{coll}} \qquad (s = \uparrow, \downarrow). \tag{2.23}$$

2.3.1 Collisions

As for the collision term, we assume that a quantum mechanical calculation has provided us with scattering rates $P(\mathbf{k}, i; \mathbf{k}', j)$ with or without spin flips, that is, $i, j = \uparrow, \downarrow$. We construct the collision term $\frac{\partial f_s}{\partial t}\Big|_{\text{coll}}$ of (2.23) by counting events that bring spins to the s channel at \mathbf{k} and events that remove from spin s at this same \mathbf{k} , for $s = (\uparrow, \downarrow)$:

$$\frac{\partial f_s}{\partial t} \Big|_{\text{coll}} = \sum_{i=\uparrow}^{\downarrow} \sum_{\mathbf{k}'} \left\{ f_i \left(\mathbf{k}' \right) \left(1 - f_s \left(\mathbf{k} \right) \right) P \left(\mathbf{k}', i; \mathbf{k}, s \right) - f_s \left(\mathbf{k} \right) \left(1 - f_i \left(\mathbf{k}' \right) \right) P \left(\mathbf{k}, s; \mathbf{k}', i \right) \right\}.$$
(2.24)

We could improve on this picture if we introduced the statistical weight of the initial state. This would introduce a difference in transition rates from "up" to "down" and its converse. This refinement is used below when treating collisions with magnons.

The Born approximation or the Fermi Golden rule gives the symmetry $P(\mathbf{k}', i; \mathbf{k}, s) = P(\mathbf{k}, s; \mathbf{k}', i)$. The collision terms for $s = (\uparrow, \downarrow)$ simplify to

$$\left. \frac{\partial f_s}{\partial t} \right|_{\text{coll}} = \sum_{i=\uparrow}^{\downarrow} \sum_{\mathbf{k}'} \left\{ \left[f_i \left(\mathbf{k}' \right) - f_s \left(\mathbf{k} \right) \right] P \left(\mathbf{k}', i; \mathbf{k}, s \right) \right\}. \tag{2.25}$$

In anticipation of later developments, when we work out the spin-dependent currents, we pay special attention to the collisions that leave the momentum unchanged. We refer to them as *spin mixing* term. We see that these terms give rise to

off-diagonal elements in the matrix that expresses the linear relationship between the spin-dependent currents and the gradients of the electrochemical potentials. We decompose also the sum over spin orientations, so as to render explicit the collisions with spin flips, and those without. Hence we rewrite (2.25) as

$$\frac{\partial f_s}{\partial t}\Big|_{\text{coll}} = \left[f_{-s}\left(\mathbf{k}\right) - f_s\left(\mathbf{k}\right)\right] P\left(\mathbf{k}, -s; \mathbf{k}, s\right)
+ \sum_{\mathbf{k}'} \left\{ \left[f_s\left(\mathbf{k}'\right) - f_s\left(\mathbf{k}\right)\right] P\left(\mathbf{k}', s; \mathbf{k}, s\right) \right\}
+ \sum_{\mathbf{k}'} \left\{ \left[f_{-s}\left(\mathbf{k}'\right) - f_s\left(\mathbf{k}\right)\right] P\left(\mathbf{k}', -s; \mathbf{k}, s\right) \right\}.$$
(2.26)

In view of the form of (2.23), we make an "educated guess" as to the form of the perturbation $f_{1s}(\mathbf{r}, \mathbf{pr}, \mathbf{p}, t)$ of the distribution functions. We write

$$f_s(\mathbf{r}, \mathbf{p}, t) = f_{0s}(\mathbf{r}, \mathbf{p}) + \alpha_s \mathbf{k}.$$
 (2.27)

So long as α_s is not specified, there is no loss of generality in writing the perturbation this way. Recall that we assumed $E_s(k) = E_s(|k|)$. We further assume that the collisions are elastic, |k| = |k'|. Then in (2.26), $f_{0s}(\mathbf{r}, \mathbf{k}) = f_{0s}(\mathbf{r}, \mathbf{k}')$. Thus, substituting (2.26) and (2.27) into (2.23) yields for $s = \uparrow, \downarrow$

$$\frac{\mathbf{p}}{m} \frac{\partial \bar{\mu}_{s} (\mathbf{r})}{\partial r} \frac{\partial f_{0s}}{\partial E} = \left[f_{-s} (\mathbf{k}) - f_{s} (\mathbf{k}) \right] P (\mathbf{k}, -s; \mathbf{k}, s)
+ \sum_{\mathbf{k}'} \left\{ \alpha_{s} \left[\mathbf{k}' - \mathbf{k} \right] P (\mathbf{k}', s; \mathbf{k}, s) \right\}
+ \sum_{\mathbf{k}'} \left\{ \left[\alpha_{-s} \mathbf{k}' - \alpha_{s} \mathbf{k} \right] P (\mathbf{k}', -s; \mathbf{k}, s) \right\}.$$
(2.28)

We assume the scattering potential to be spherically symmetric, so that the scattering probability $P(\mathbf{k}', i; \mathbf{k}, j)$ for any given i and j depends only on the angle θ between \mathbf{k}' and \mathbf{k} . For every \mathbf{k}' in the development above, there is a \mathbf{k}'' , which has the same angle θ to \mathbf{k} and cancels out the contribution of \mathbf{k}' normal to \mathbf{k} . So we can replace in the sum \mathbf{k}' by $\mathbf{k} \cos \theta$:

$$\frac{p}{m} \frac{\partial \bar{\mu}_{s} (\mathbf{r})}{\partial \mathbf{r}} \frac{\partial f_{0s}}{\partial E} = [f_{-s} (\mathbf{k}) - f_{s} (\mathbf{k})] P (\mathbf{k}, -s; \mathbf{k}, s)
- \sum_{\mathbf{k}'} \{ [1 - \cos \theta_{\mathbf{k}\mathbf{k}'}] \alpha_{s} \mathbf{k} P (\mathbf{k}', s; \mathbf{k}, s) \}
+ \sum_{\mathbf{k}'} \{ [\cos \theta_{\mathbf{k}\mathbf{k}'} \alpha_{-s} \mathbf{k} - \alpha_{s} \mathbf{k}] P (\mathbf{k}', -s; \mathbf{k}, s) \}. (2.29)$$

52 J.-Ph. Ansermet

Noting that (2.27) tells us that $\alpha_s \mathbf{k} = [f_s(\mathbf{r}, \mathbf{p}, t) - f_{0s}(\mathbf{r}, \mathbf{p})]$, we get then

$$\frac{\mathbf{p}}{m} \frac{\partial \bar{\mu}_{s} (\mathbf{r})}{\partial \mathbf{r}} \frac{\partial f_{0s}}{\partial E} = \left[f_{-s} (\mathbf{k}) - f_{s} (\mathbf{k}) \right] P (\mathbf{k}, -s; \mathbf{k}, s)$$

$$- \sum_{\mathbf{k}'} \left\{ \left[1 - \cos \theta_{\mathbf{k}\mathbf{k}'} \right] P (\mathbf{k}', s; \mathbf{k}, s) \right\} \left[f_{s} (\mathbf{r}, \mathbf{p}, t) - f_{0s} (\mathbf{r}, \mathbf{p}) \right]$$

$$- \sum_{\mathbf{k}'} \left\{ \left[-\cos \theta_{\mathbf{k}\mathbf{k}'} \frac{\alpha_{-s}}{\alpha_{s}} + 1 \right] P (\mathbf{k}', -s; \mathbf{k}, s) \right\}$$

$$\left[f_{s} (\mathbf{r}, \mathbf{p}, t) - f_{0s} (\mathbf{r}, \mathbf{p}) \right].$$
(2.30)

We define the following relaxation rates:

$$\frac{1}{\tau_{\uparrow\downarrow}} = P\left(\mathbf{k}, -s; \mathbf{k}, s\right),\tag{2.31}$$

$$\frac{1}{\tau_s} = \sum_{\mathbf{k}'} \left\{ \left[1 - \cos \theta_{\mathbf{k}\mathbf{k}'} \right] P\left(\mathbf{k}', s; \mathbf{k}, s\right) \right\}, \tag{2.32}$$

$$\frac{1}{\tau_{sf}} = \sum_{\mathbf{k}'} \left\{ \left[1 - \cos \theta_{\mathbf{k}\mathbf{k}'} \frac{\alpha_{-s}}{\alpha_{s}} \right] P\left(\mathbf{k}', -s; \mathbf{k}, s\right) \right\}. \tag{2.33}$$

The relaxation times, thus defined, are implicit functions of the momentum **k**. The end result is, for $s = \uparrow, \downarrow$,

$$\frac{p}{m}\frac{\partial \bar{\mu}_{s}\left(\mathbf{r}\right)}{\partial \mathbf{r}}\frac{\partial f_{0s}}{\partial E} = -\left(\frac{1}{\tau_{s}} + \frac{1}{\tau_{sf}}\right)\left(f_{s} - f_{0s}\right) + \frac{f_{-s} - f_{s}}{\tau_{\uparrow\downarrow}}.$$
(2.34)

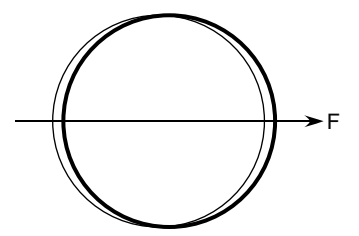
This is the result stated by Fert and Campbell in their analysis of spin-dependent transport in Nickel and Iron [3].

2.3.2 Calculation of the Currents

We define the current for each spin channel as $\mathbf{j}_s(\mathbf{r}) = \sum_k (-e/m)\hbar\mathbf{k} f_s(\mathbf{r}, \mathbf{p})$. We note that the equilibrium distribution does not contribute to the current (there is no net current at zero applied field). We take (2.34), with $\mathbf{p} = \hbar\mathbf{k}$, multiply it by $(-e/m)\hbar\mathbf{k}$ and sum over all \mathbf{k} 's:

$$\sum_{\mathbf{k}} (-e) \frac{\hbar \mathbf{k}}{m} \left(\frac{\hbar \mathbf{k}}{m} \cdot \frac{\partial \bar{\mu}_{s} (\mathbf{r})}{\partial \mathbf{r}} \right) \frac{\partial f_{0s}}{\partial E} = -\sum_{\mathbf{k}} \left(\frac{1}{\tau_{s}} + \frac{1}{\tau_{sf}} \right) (-e) \frac{\hbar \mathbf{k}}{m} f_{s} (\mathbf{k}) + \sum_{\mathbf{k}} \frac{1}{\tau_{\uparrow\downarrow}} (-e) \frac{\hbar \mathbf{k}}{m} (f_{-s} (\mathbf{k}) - f_{s} (\mathbf{k})).$$
(2.35)

Fig. 2.7 Under the effect of the electric field, the Fermi sphere is displaced slightly, so the average **k** no longer vanishes and lies in the direction of the applied field



As commonly done in transport under the framework of the Boltzmann equation, we take into account that only the terms near the Fermi level (the chemical potential) contribute to the current. As graphically put by Mott and Jones in their wonderful book [4], we are considering the contribution from the slight distortion of the Fermi surface due to the applied current (Fig. 2.7). So, we have

$$\sum_{\mathbf{k}} (-e) \frac{\hbar \mathbf{k}}{m} \left(\frac{\hbar \mathbf{k}}{m} \cdot \frac{\partial \bar{\mu}_{s} (\mathbf{r})}{\partial \mathbf{r}} \right) \frac{\partial f_{0s}}{\partial E} = -\left(\frac{1}{\tau_{s}} + \frac{1}{\tau_{sf}} + \frac{1}{\tau_{\uparrow\downarrow}} \right) \mathbf{j}_{s} (\mathbf{r}) + \frac{1}{\tau_{\uparrow\downarrow}} \mathbf{j}_{-s} (r).$$
(2.36)

We consider that we have Bloch waves quantized in a cube, and so the density of points in k space is $1/(2\pi)^3$, and we transform the left-hand-side above into an integral. We assume that the electric field, as well as all the gradients, are in the z direction. Then only the k_z terms contribute. As the other terms of the sum depend only on |k|, $k_z^2 = k^2 \cos^2 \theta$ is the only nonvanishing term.

Hence, the left-hand side of (2.36) becomes

$$\frac{\partial \bar{\mu}_{s}\left(\mathbf{r}\right)}{\partial z} \int_{0}^{2\pi} \mathrm{d}\varphi \int_{-\pi/2}^{\pi/2} \mathrm{d}\theta \, \sin\theta \int_{0}^{k_{\mathrm{F}}} \frac{k^{2} \mathrm{d}k}{\left(2\pi\right)^{3}} (-e) \frac{\hbar^{2}k^{2}}{3m^{2}} \, \cos^{2}\theta \, \frac{\partial f_{0s}}{\partial E}.$$

We recall that at reasonable temperatures, $\frac{\partial f_{0s}}{\partial E} \approx \delta(E - \mu_s)$, and so the k integral is trivial. The angular integral gives a factor of $4\pi/3$. In summary, for $s = \uparrow, \downarrow$,

$$-\frac{\partial \bar{\mu}_{s}(\mathbf{r})}{\partial z} \frac{4\pi}{3} \frac{k_{F}^{4}}{(2\pi)^{3}} (-e) \frac{\hbar^{2}}{m^{2}} = \left(\frac{1}{\tau_{s}} + \frac{1}{\tau_{sf}} + \frac{1}{\tau_{\uparrow\downarrow}}\right) j_{s}(r) - \frac{1}{\tau_{\uparrow\downarrow}} j_{-s}(r) . \quad (2.37)$$

At this point, we want to manipulate algebraically the form of this result so as to identify coefficients that can be equated with resistivity terms. Thus, we bring forth a term $-\frac{dV}{dz}$, which is the applied electric field. Hence, we write $\bar{\mu}_s(\mathbf{r}) = (-e) \left(V(r) - \frac{1}{e} \mu_s(\mathbf{r})\right)$ in (2.37):

$$-\frac{\mathrm{d}}{\mathrm{d}z}\left(V\left(\mathbf{r}\right)-\frac{1}{e}\mu_{s}\left(\mathbf{r}\right)\right)\frac{e^{2}k_{\mathrm{F}}^{2}E_{\mathrm{F}}}{3\pi^{2}m}=\left(\frac{1}{\tau_{s}}+\frac{1}{\tau_{sf}}+\frac{1}{\tau_{\uparrow\downarrow}}\right)j_{s}\left(\mathbf{r}\right)-\frac{1}{\tau_{\uparrow\downarrow}}j_{-s}\left(\mathbf{r}\right).$$

Now we can identify the resistivity terms:

$$\rho_s = \frac{3\pi^2 m}{e^2 k_{\rm F}^2 E_{\rm F}} \left(\frac{1}{\tau_s} + \frac{1}{\tau_{sf}} \right),\tag{2.38}$$

$$\rho_{\uparrow\downarrow} = \frac{3\pi^2 m}{e^2 k_{\rm F}^2 E_{\rm F}} \frac{1}{\tau_{\uparrow\downarrow}}.$$
 (2.39)

The two equations contained in (2.37) can now be written as

$$\begin{pmatrix} -\frac{d}{dz} \left(V \left(r \right) - \frac{1}{e} \mu_{\uparrow} \left(\mathbf{r} \right) \right) \\ -\frac{d}{dz} \left(V \left(r \right) - \frac{1}{e} \mu_{\downarrow} \left(\mathbf{r} \right) \right) \end{pmatrix} = \begin{pmatrix} \rho_{\uparrow} + \rho_{\uparrow\downarrow} & -\rho_{\uparrow\downarrow} \\ -\rho_{\uparrow\downarrow} & \rho_{\downarrow} + \rho_{\uparrow\downarrow} \end{pmatrix} \begin{pmatrix} j_{\uparrow} \left(\mathbf{r} \right) \\ j_{\downarrow} \left(\mathbf{r} \right) \end{pmatrix}. \tag{2.40}$$

This matrix is readily inverted, giving

$$\begin{pmatrix}
j_{\uparrow}(\mathbf{r}) \\
j_{\downarrow}(\mathbf{r})
\end{pmatrix} = \frac{1}{\rho_{\uparrow}\rho_{\downarrow} + \rho_{\uparrow\downarrow}\left(\rho_{\uparrow} + \rho_{\downarrow}\right)} \begin{pmatrix}
\rho_{\downarrow} + \rho_{\uparrow\downarrow} & \rho_{\uparrow\downarrow} \\
\rho_{\uparrow\downarrow} & \rho_{\uparrow} + \rho_{\uparrow\downarrow}
\end{pmatrix}$$

$$\begin{pmatrix}
-\frac{d}{dz}\left(V(\mathbf{r}) - \frac{1}{e}\mu_{\uparrow}(\mathbf{r})\right) \\
-\frac{d}{dz}\left(V(\mathbf{r}) - \frac{1}{e}\mu_{\downarrow}(\mathbf{r})\right)
\end{pmatrix} (2.41)$$

In (2.41), we find off-diagonal terms in the conductivity matrix. These express a contribution to the current of one spin channel by the gradient of the electrochemical potential of the *other* channel. We refer to these as *spin mixing* terms. We recall that they arise from collision terms for which the initial and final states have the same **k** (see (2.31)).

As will be seen, the spatial dependence of the chemical potential dies down over a characteristic distance, the spin diffusion length. If we are deep into a homogeneous material, then the terms containing the chemical potentials drop out and the total current is deduced from (2.41) to be

$$j = \frac{\rho_{\downarrow} + \rho_{\uparrow} + 4\rho_{\uparrow\downarrow}}{\rho_{\uparrow}\rho_{\downarrow} + \rho_{\uparrow\downarrow} \left(\rho_{\uparrow} + \rho_{\downarrow}\right)} \left(-\frac{\mathrm{d}}{\mathrm{d}z}V\right). \tag{2.42}$$

This is one of the earliest results on spin-dependent transport. It refers to bulk materials, while giant magnetoresistance arose when it became possible to make metal superlattices (needed when the current runs parallel to the interfaces) or nanostructures (when the current is driven perpendicular to the interfaces). This result for bulk samples is interesting, as it contains both the notion of spin-dependent conductivity and the notion of spin mixing.

The spin mixing term will be discussed later on for the case of the collision of electrons to magnons. In most situations, it is negligible compared to the interface effects. So, in what follows, in conformity with the standard literature on spin-dependent transport, we drop out this term. We have then Ohm's law for each spin channel:

$$j_s(\mathbf{r}) = \sigma_s \left[-\frac{1}{dz} \left(V(\mathbf{r}) - \frac{1}{e} \mu_s(\mathbf{r}) \right) \right],$$
 (2.43)

with $\sigma_s = 1/\rho_s$ given by (2.38).

2.3.3 Diffusion Equation and the Spin Accumulation

We can write a continuity equation for each electron spin current. The divergence of each spin current is equal to the source of electrons in this channel, which is equal to the rate of spin flips producing electrons coming into the channel minus the rate of electrons leaving it:

$$\operatorname{div}(\mathbf{j}_s) = \frac{\partial j_s}{\partial z} = \int \frac{1}{\hbar^3} \, \mathrm{d}^3 p \left(-\frac{f_s - f_{-s}}{\tau_{sf}} \right) (-e) \,. \tag{2.44}$$

We need to consider $f_{0+}-f_{0-}$. We neglect the term $-(f_{1,s}-f_{1,-s})/\tau_{sf}$ of (2.36), as both terms of this difference are small, they are expected to be quite similar, and they arise from the electric field. Graphically, the integral of $f_{0+}-f_{0-}$ is the area in between two step-like Fermi–Dirac functions at a distance $2\Delta\mu$ from one another (Fig. 2.8), defining a narrow energy slice and one expects to be able to approximate $f_{0+}-f_{0-}$ with a delta function.

Indeed, developing to first order, writing u for the argument of $f_{\pm s}$, we have

$$f_{0}\left(\frac{E+\varepsilon}{kT}\right) = f_{0}(u),$$

$$= f_{0}(\varepsilon = 0) + \frac{\partial f_{0}}{\partial u} \varepsilon \frac{1}{kT},$$

$$= f_{0}(\varepsilon = 0) + \frac{\partial f_{0}}{\partial u} \varepsilon \frac{\partial u}{\partial E} = f_{0}(\varepsilon = 0) + \frac{\partial f_{0}}{\partial E} \varepsilon.$$

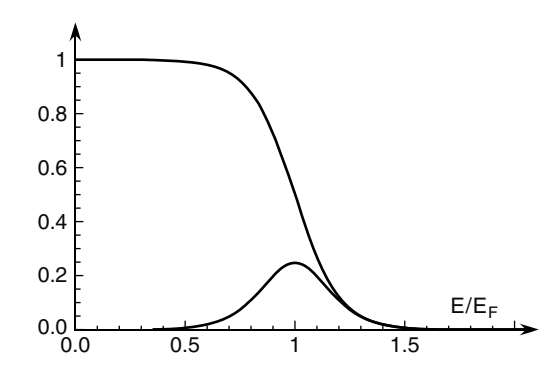


Fig. 2.8 Qualitative aspect of the Fermi–Dirac distribution and its energy derivative for finite T>0

Hence,

$$f_{0+} - f_{0-} = f_0 \left(\frac{E - \mu_0 - \Delta \mu}{kT} \right) - f_0 \left(\frac{E - \mu_0 + \Delta \mu}{kT} \right) = -\frac{\partial f_0}{\partial E} 2\Delta.$$
 (2.45)

Thus the integral for the current gives

$$\frac{\partial j_s}{\partial z} = \frac{\sigma_s}{\frac{1}{3} \left(\tau_s^{-1} + \tau_{\rm sf}^{-1} \right)^{-1} v_{\rm F}^2 e} \left(\frac{(\bar{\mu}_s - \bar{\mu}_{-s})}{\tau_{\rm sf}} \right). \tag{2.46}$$

We distinguish in this expression the electron mean free path and another length, which we call the electron spin-flip mean free path:

$$\lambda_{\rm sf} = \nu_{\rm F} \, \tau_{\rm sf}. \tag{2.47}$$

We denote by

$$l_s^2 = \frac{1}{3}\tau_{\rm sf} \left(\tau_s^{-1} + \tau_{\rm sf}^{-1}\right)^{-1} v_{\rm F}^2 \tag{2.48}$$

the square of some coherence length of each spin band. Finally, for each spin current we have

$$\frac{e}{\sigma_s} \frac{\partial j_s}{\partial z} = \left(\frac{\bar{\mu}_s - \bar{\mu}_{-s}}{l_s^2}\right) \tag{2.49}$$

and Ohm's law (2.43)

$$j_s = \sigma_s \frac{1}{e} \left(\frac{\partial \bar{\mu}_s}{\partial z} \right). \tag{2.50}$$

We can then show that the chemical potential difference

$$\Delta \mu = (\bar{\mu}_s - \bar{\mu}_{-s}) = (\mu_s - \mu_{-s}) \tag{2.51}$$

follows a diffusion equation. Indeed, we have

$$\begin{split} \mu_{\pm} &= \mu_0 \pm \Delta \mu, \\ \bar{\mu}_{\pm} &= \mu_{\pm} - eV, \\ \frac{j_+}{\sigma_+} - \frac{j_-}{\sigma_-} &= \frac{1}{e} \left(\frac{\partial \Delta \bar{\mu}}{\partial z} \right), \\ \frac{1}{e} \frac{\partial^2 \Delta \bar{\mu}}{\partial z^2} &= \frac{1}{\sigma_+} \frac{\partial j_+}{\partial z} - \frac{1}{\sigma_-} \frac{\partial j_-}{\partial z} = \frac{1}{e} \frac{\Delta \bar{\mu}}{l_+^2} - \frac{1}{e} \frac{\Delta \bar{\mu}}{l_-^2}. \end{split}$$

In short,

$$\frac{\partial^2 \Delta \bar{\mu}}{\partial z^2} = \frac{\Delta \bar{\mu}}{l_{sf}^2},\tag{2.52}$$

with the spin diffusion length $l_{\rm sf}$ defined by

$$\frac{1}{l_{\rm sf}^2} = \frac{1}{l_+^2} + \frac{1}{l_-^2}. (2.53)$$

If we take $\lambda_+ = \lambda_- = \lambda_e$, then

$$l_{\rm sf}^2 = (1/6)\lambda_{\rm sf}\lambda_e. \tag{2.54}$$

Spin up electrons transform into spin down electrons and vice versa. So the sum of both currents is spatially uniform. Indeed we find

$$\frac{\partial}{\partial z}(j_{+}+j_{-}) = \frac{\partial^{2}}{\partial z^{2}}(\sigma_{+}\mu_{+}-\sigma_{-}\mu_{-})\frac{1}{e} = \frac{\sigma_{+}}{l_{+}^{2}}(\mu_{+}-\mu_{-}) + \frac{\sigma_{-}}{l_{-}^{2}}(\mu_{-}-\mu_{+}) = 0.$$

As a final consideration, we turn now to the concept of *spin accumulation*. This terminology is used because the spin dependent chemical potential *difference* $\Delta \bar{\mu}$ is closely linked to the spin polarization in the system. To make this clear, we introduce the density of states g(E) of the conduction electrons. The spin accumulation creates an imbalance in population, though the spin bands are assumed identical, thus the spin-dependent densities of states:

$$g_{\pm}^{a}(E) = \frac{1}{2}g(E).$$
 (2.55)

The spin populations are given by

$$N_{\pm}^{a} = \int dE g_{\pm}^{a}(E) f_{FD}(E, \mu_{0} \pm \Delta \mu/2),$$
 (2.56)

where the second argument of f_{FD} is the Fermi level. We can change the integration variable to $E' = E \mp \Delta \mu/2$:

$$N_{\pm}^{\rm a} = \int dE' \frac{1}{2} g(E' \mp \Delta \mu/2) f_{\rm FD}(E, \mu_0).$$
 (2.57)

We can compare this result with the one that is obtained when deriving Pauli paramagnetism. In this case, the spin bands are shifted by the Zeeman splitting due to an applied field H, so that their densities of states are

$$g_{\pm}^{P}(E) = \frac{1}{2}g(E \mp \mu_{B}H).$$
 (2.58)

The Fermi level remains μ_0 for both spin bands because the spin system is assumed to have reached equilibrium in the field H. Thus, in the Pauli paramagnetism case, we have the spin populations

$$N_{\pm}^{P} = \int dE \frac{1}{2} g(E \mp \mu_{\rm B} H) f_{\rm FD}(E, \mu_{\rm 0}).$$
 (2.59)

Comparison of (2.57) and (2.59) demonstrates the similarity in both calculations. The calculation is carried out further assuming small shifts in energies compared to the Fermi energy (see e.g., [2]). Thus, for Pauli paramagnetism, one finds

$$M^{P} = -\mu_{B} \left(N_{+}^{P} - N_{-}^{P} \right) = \mu_{B} \left(\mu_{B} H \right) g(\mu_{0}). \tag{2.60}$$

By analogy, for the spin accumulation, we deduce

$$M^{a} = -\mu_{B} \left(N_{+}^{a} - N_{-}^{a} \right) = \mu_{B} \left(\Delta \mu / 2 \right) g(\mu_{0}). \tag{2.61}$$

As the Pauli susceptibility is found from (2.60) to be $\chi^P = \mu_B^2 g(\mu_0)$, the spin accumulation can be expressed as

$$M^{\rm a} = \frac{1}{2} \frac{\Delta \mu}{\mu_{\rm B}} \chi^{\rm P}. \tag{2.62}$$

Valet and Fert [5] gave one of the clearest accounts of the application of this form of Boltzmann transport analysis using spin-dependent Boltzmann distributions. The authors begin with integrating the diffusion equation for the chemical potential under the presence of a current crossing an infinitely sharp interface between two ferromagnetic layers. This is experimentally not achievable, but the result brings out an important point. When the magnetization of the two layers is set antiparallel, the spins of the electrons must relax in order for the electrons to cross the interface. This is a dissipative process that leads to a so-called *spin-coupled interface resistance*. The resistance of a unit area is

$$r_{\rm SI} = 2\beta^2 \rho_{\rm F}^* l_{\rm sf}^{\rm F}$$

where β is defined by $\rho_s = \rho_F^* (1 \pm \beta)$. Furthermore, they find that the difference in chemical potentials $\Delta \mu$ at the interface is given by

$$\Delta \mu = \beta \rho_{\rm F}^* j l_{\rm sf}^{\rm F} \tag{2.63}$$

where j is the current density. This result can be used to get an estimate of the order of magnitude of the spin accumulation. Hence, one finds that the spin accumulation M^a due to a current density of 10^6 A cm⁻², assuming a resistivity of 10^{-5} Ohm cm, is ten times less than the Pauli spin polarization M^P of the same conduction electron band in a field of 1 tesla.

Valet and Fert [5] also considered a trilayer: two ferromagnetic layers separated by a nonmagnetic layer (Fig. 2.9). The first line shows the spatial variation of the difference in chemical potential. Given the above relations of chemical potential and electron spin polarization, this graph shows in a way the spin-accumulation effect. The second line is the effective spin-dependent electric field (i.e., the gradient of the

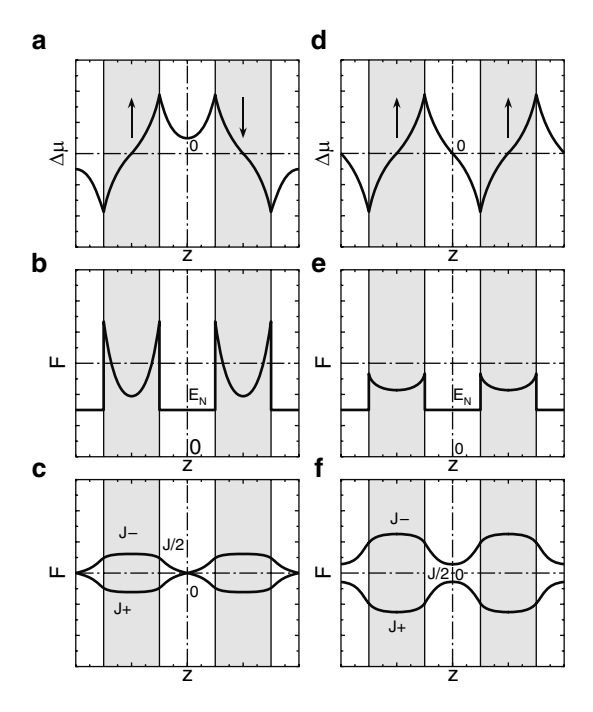


Fig. 2.9 (*Top*) Valet and Fert calculation of spin-dependent transport, with current perpendicular to the layers. (*Left*) The magnetization is in the anti-parallel configuration; (*right*) the parallel configuration. From *top* to *bottom* on each side: the chemical potential difference $\delta\mu$, the gradient of the chemical potential, and the spin currents

chemical potential) and the last line shows each spin current. We must keep in mind that the spin polarization that is referred to here is driven by the current.

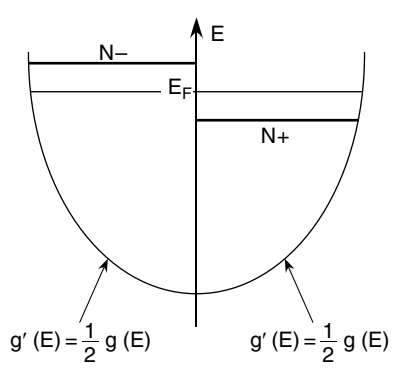
2.4 Spin Relaxation of Conduction Electrons

The Boltzmann description of transport, in the relaxation time approximation, leaves out the question of the mechanisms determining those relaxation times. Here we consider two mechanisms: spin—orbit scattering and electron—magnon collisions.

2.4.1 Spin-Lattice Relaxation Time for Conduction Electrons

We consider here a nonmagnetic metal, and so the spin-up and spin-down bands have the same structure. The density of states at the energy level E will be $g'(E) = \frac{1}{2}g(E)$ for both spin directions, $\rho(E)$ is the total density of states. We will assume later on that the surfaces in k-space of constant energy are spheres.

Fig. 2.10 Density of states for up and down spins just after a field has been turned off. The population difference shown is the initial state from which the system will relax. This imbalance may have been produced at zero current by an applied field that is suddenly turned off



We ask ourselves how fast the electrons reach equilibrium if they have been initially prepared in a state away from equilibrium. We mean that the population N_+ of up spins differs from that, N_- , of down spins (Fig. 2.10). This initial state could be achieved, for example, by switching off an applied field in a short time compared to the relaxation time of the electrons. In spintronics, such a fast turn-off of the field occurs when spin polarized electrons are injected in a normal metal, for example, electrons going from Co to Cu in a Co/Cu multilayer. Here we assume that the system is uniform. We avoid the effects specific of spin transport and focus on spin-lattice relaxation mechanisms as they intervene in a magnetic resonance experiment. This amounts to considering relaxation times as in (2.32) and (2.33), but without the $\cos(\theta)$ terms. The electrons are in states $|\mathbf{k}s\rangle$ of energy $E_{\mathbf{k}s}$. To make explicit the assumption of uniform system, we write the Fermi–Dirac distribution (2.18) with the notation

$$f_{\pm}(E) = \frac{1}{1 + e^{(E - E_{\pm})/kT}}$$

and likewise for the down spins. E_{\pm} is defined by

$$N_{\pm} = \sum_{\mathbf{k}} f_{\pm}(E_{\mathbf{k}}) = \int_{0}^{\infty} dE g'(E) \int_{A_{-}} d\Omega \frac{1}{1 + e^{(E_{\mathbf{k}} - E_{\pm})/kT}}$$
(2.64)

and likewise for E_{-} . In writing this, we assume that the electrons of each spin-band are brought to a thermal equilibrium much faster than the spins relax among each other.

Now we want to evaluate the spin lattice relaxation rate $1/T_1$ introduced in Sect. 2.2. Here it is sufficient to make the approximation $W_{\uparrow} = W_{\downarrow} = W$ and we draw W from (2.6). We express W in terms of the scattering amplitudes of single electrons interacting with the potential V of an impurity. The probability per unit time for an electron in a state $|\mathbf{k}s\rangle$ to scatter into a state $|\mathbf{k}'s'\rangle$ is calculated with the Born formula [6]:

$$W\left(\mathbf{k}s,\mathbf{k}'s'\right) = \frac{2\pi}{\hbar} \left| \langle \mathbf{k}s | V | \mathbf{k}'s' \rangle \right|^{2} \delta\left(E_{\mathbf{k}s} - E_{\mathbf{k}'s'}\right).$$

Because we are dealing with electrons and must take care of the exclusion principle, a scattering event from state $|\mathbf{k}s\rangle$ to a state $|\mathbf{k}'s'\rangle$ occurs with a probability proportional to the probability that the state $|\mathbf{k}s\rangle$ is occupied, and the final state $|\mathbf{k}'s'\rangle$ is not, which is given by the product $f_s(E_\mathbf{k})(1-f_{s'}(E_\mathbf{k'}))$. The spin flip rate WN_- feeding N_+ as expressed in the detailed balance (2.6) can be expressed as

$$WN_{-} = \sum_{\mathbf{k},\mathbf{k}'} W(\mathbf{k}_{-},\mathbf{k}'+) f_{-}(E_{\mathbf{k}}) \left(1 - f_{+}(E_{\mathbf{k}'})\right).$$

The converse process can be expressed as

$$WN_{+} = \sum_{\mathbf{k},\mathbf{k}'} W(\mathbf{k}+,\mathbf{k}'-) f_{+}(E_{\mathbf{k}}) (1 - f_{-}(E_{\mathbf{k}'})),$$

= $\sum_{\mathbf{k}',\mathbf{k}} W(\mathbf{k}'+,\mathbf{k}-) f_{+}(E_{\mathbf{k}'}) (1 - f_{-}(E_{\mathbf{k}})).$

We could swap the summation indices, thanks to the fact that the sums are carried over all **k**s. Then using $W(\mathbf{k}-,\mathbf{k}'+)=W(\mathbf{k}'+,\mathbf{k}-)$ we get

$$\frac{\mathrm{d}N_{+}}{\mathrm{d}t} = WN_{-} - WN_{+} = \sum_{\mathbf{k},\mathbf{k}'} W\left(\mathbf{k}-,\mathbf{k}'+\right) \left(f_{-}\left(E_{\mathbf{k}}\right) - f_{+}\left(E_{\mathbf{k}'}\right)\right).$$

The sum is transformed into an integral over spherical surfaces of constant energy:

$$\frac{\mathrm{d}N_{+}}{\mathrm{d}t} = \int \mathrm{d}E \int \mathrm{d}E' \int_{4\pi} \frac{\mathrm{d}\Omega}{4\pi} \int_{4\pi} \frac{\mathrm{d}\Omega'}{4\pi} W\left(\mathbf{k}-,\mathbf{k}'+\right) g'$$

$$(E_{\mathbf{k}})\rho'(E_{\mathbf{k}'}) \left(f_{-}\left(E_{\mathbf{k}}\right) - f_{+}\left(E_{\mathbf{k}'}\right)\right).$$

The Born formula imposes $E_{\bf k} - E_{\bf k'} = 0$. The term $(f_{-}(E) - f_{+}(E))$ is nonzero over a narrow range of energy only (Fig. 2.8 and (2.45)). Over this range, the rest of the integrand can be considered approximately constant, equal to its value at the Fermi level. Hence we have

$$\frac{dN_{+}}{dt} = \frac{2\pi}{\hbar} \langle V^{2} \rangle_{F} g'(E_{F})^{2} (E_{-} - E_{+}), \qquad (2.65)$$

with

$$\left\langle V^{2}\right\rangle_{\!F} = \frac{2\pi}{\hbar} \int\limits_{4\pi} \frac{\mathrm{d}\Omega}{4\pi} \int\limits_{4\pi} \frac{\mathrm{d}\Omega'}{4\pi} \left| \left\langle \mathbf{k}_{F} - \mid V \mid \mathbf{k}_{F}' + \right\rangle \right|^{2}.$$

We have, according to (2.64) and using (2.45),

$$N_{-} - N_{+} = \sum_{\mathbf{k}} (f_{-}(E_{\mathbf{k}}) - f_{+}(E_{\mathbf{k}})) = (E_{-} - E_{+}) g'(E_{F}).$$

Thus, with W given by $1/T_1 = 2W$, the relaxation rate is

$$\frac{1}{T_1} = \frac{2\pi}{\hbar} \left\langle V^2 \right\rangle_{\!\!\!F} g(E_{\rm F}).$$

If there is an atomic concentration c of impurities, N electrons and the density of state is defined as a number per energy and per electrons, then

$$\frac{1}{T_1} = Nc \frac{2\pi}{\hbar} \left\langle V^2 \right\rangle_{\mathcal{F}} g(E_{\mathcal{F}}). \tag{2.66}$$

This last step amounts to assuming that the scattering events are independent (incoherent scattering), which is the case at sufficiently low impurity concentrations.

2.4.2 The Bottleneck Regime

The spin-lattice relaxation as detected in electron spin resonance experiments depends strongly on spin-orbit scattering at impurities or crystalline defects in a normal metal. In the 1950s, some 10 years after the discovery of magnetic resonance, researchers of the caliber of Bloombergen at Harvard [7] and Kittel at Berkeley [8] investigated the electron spin resonance of ferromagnets (now called ferromagnetic resonance, FMR). The line width of the resonance gave a measure of the relaxation time for magnetic excitations to relax to equilibrium. The rf field excited long wavelength spin waves of wavelength comparable to the skin depth. Soon the picture arose that in metals the magnetization does not relax efficiently to the lattice. Instead, it couples efficiently to conduction electrons, and those relax fast via the spin-orbit coupling (Fig. 2.11) [9]. Thus, the relaxation mechanism for localized moments is closely linked to one of the central themes of spintronics: the coupling of the spin of the conduction electrons with the magnetization. The case can be

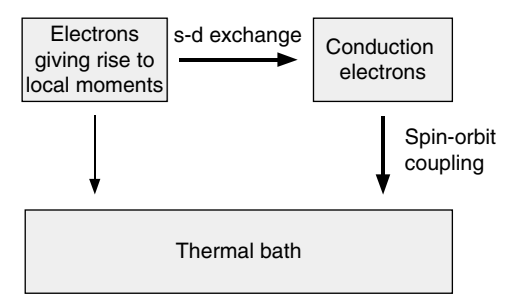


Fig. 2.11 Localized electron of predominant d character do not couple strongly to the thermal bath. However, via exchange, they strongly interact with the conduction electrons. These experience a strong spin-orbit scattering at impurities, owing to their nonvanishing probability to be at the nuclei

made that some of the recent considerations on the action of a spin polarized current on magnetization have origins that can be traced back to conduction electron spin resonance experiments [10].

2.4.3 Spin-Orbit Scattering

It is sometimes useful to remember that the spin-orbit coupling is essentially a coupling of the electron spin with the electric field:

$$V = \frac{e\hbar}{2m^2c^2}\mathbf{S} \cdot (\mathbf{E} \times \mathbf{p}). \tag{2.67}$$

In alkali metals, the electric field is negligible and there is practically no spin—orbit effect, in general. However, to the extent that phonons induce an electric field, the spin—orbit coupling can produce a spin—phonon coupling [11]. Basic reference on spin—orbit coupling in solids can be found in reviews and research articles (Yafet 1963, Friedel 1964, Elliott 1953). The spin—orbit coupling is the strongest when the electron is near the nucleus. There, the electric field can be assumed to be radial, thus a factor $\mathbf{r} \wedge \mathbf{p}$ appears in (2.67), which is the orbital moment of the electron **l**. Then we can write the customary expression

$$V = \lambda(r) \mathbf{S} \cdot \mathbf{l}$$
.

To calculate T_1 in (2.66), we need to estimate $\langle V^2 \rangle_F$ and according to (2.65) we need to consider:

$$\begin{aligned} \left| \langle \mathbf{k}_{F} - | V | \mathbf{k}_{F}' + \rangle \right|^{2} &= \langle \mathbf{k}_{F} - | V | \mathbf{k}_{F}' + \rangle \langle \mathbf{k}_{F}' + | V | \mathbf{k}_{F} - \rangle \\ &= \langle + | \mathbf{S} | - \rangle \langle - | \mathbf{S} | + \rangle \langle \mathbf{k}_{F} | \lambda(r) \mathbf{l} | \mathbf{k}_{F}' \rangle \langle \mathbf{k}_{F}' | \lambda(r) \mathbf{l} | \mathbf{k}_{F} \rangle \\ &= \sum_{\alpha\beta = x, y} \langle + | S_{\alpha} | - \rangle \langle - | S_{\beta} | + \rangle \langle \mathbf{k}_{F} | \lambda(r) l_{\alpha} | \mathbf{k}_{F}' \rangle \langle \mathbf{k}_{F}' | \lambda(r) l_{\beta} | \mathbf{k}_{F} \rangle. \end{aligned}$$

$$(2.68)$$

As $\langle V^2 \rangle_{\!\!F}$ requires summing over all possible states, we write this sum as

$$\begin{split} \frac{1}{2} \sum_{\alpha\beta = x,y} \left\langle + \mid S_{\alpha} \mid - \right\rangle \left\langle - \mid S_{\beta} \mid + \right\rangle \\ & \left[\left\langle \mathbf{k}_{\mathrm{F}} \right| \lambda(r) l_{\alpha} \mid \mathbf{k}_{\mathrm{F}}' \right\rangle \left\langle \mathbf{k}_{\mathrm{F}}' \mid \lambda(r) l_{\beta} \mid \mathbf{k}_{\mathrm{F}} \right\rangle + \left\langle \mathbf{k}_{\mathrm{F}} \mid \lambda(r) l_{\beta} \mid \mathbf{k}_{\mathrm{F}}' \right\rangle \left\langle \mathbf{k}_{\mathrm{F}}' \mid \lambda(r) l_{\alpha} \mid \mathbf{k}_{\mathrm{F}} \right\rangle \right]. \end{split}$$

As $\langle + | S_{\alpha} | + \rangle = \langle - | S_{\alpha} | - \rangle = 0$ ($\alpha = x, y$), we can add $\langle + | S_{\alpha} | + \rangle \langle - | S_{\beta} | - \rangle$ to this sum without changing it. Then we make use of the closure relation to replace the spin part with $\langle + | S_{\alpha} S_{\beta} | + \rangle$. Again as the sum is carried over both α and β , we can write it as

$$\begin{split} \frac{1}{4} \sum_{\alpha\beta = x,y} \left\langle + \mid S_{\alpha} \; S_{\beta} \; + S_{\beta} \; S_{\alpha} \mid + \right\rangle \\ & \left[\left\langle \mathbf{k}_{\mathrm{F}} \right| \lambda(r) l_{\alpha} \; \middle| \mathbf{k}_{\mathrm{F}}' \right\rangle \left\langle \mathbf{k}_{\mathrm{F}}' \right| \lambda(r) l_{\beta} \; \middle| \mathbf{k}_{\mathrm{F}} \rangle \; \left\langle \mathbf{k}_{\mathrm{F}} \right| \lambda(r) l_{\beta} \; \middle| \mathbf{k}_{\mathrm{F}}' \right\rangle \left\langle \mathbf{k}_{\mathrm{F}}' \right| \lambda(r) l_{\alpha} \; \middle| \mathbf{k}_{\mathrm{F}} \rangle \right]. \end{split}$$

As $S_{\alpha}S_{\beta} + S_{\beta}S_{\alpha} = 0$ if $\alpha \neq \beta$, the sum reduces to

$$\frac{1}{4}\left\{\left\langle +|\,2S_{x}^{2}\,|+\right\rangle \left(2\left|\left\langle \mathbf{k}_{\mathrm{F}}|\,\lambda(r)l_{x}\,\left|\mathbf{k}_{\mathrm{F}}^{\prime}\right\rangle \right|^{2}\right)+\left\langle +|\,2S_{y}^{2}\,|+\right\rangle \left(2\left|\left\langle \mathbf{k}_{\mathrm{F}}|\,\lambda(r)l_{y}\,\left|\mathbf{k}_{\mathrm{F}}^{\prime}\right\rangle \right|^{2}\right)\right\}$$

This expression is to be integrated over all possible \mathbf{k}_{F} , and the l_{x} and the l_{y} terms give the same contributions, and so

$$\left\langle V^{2}\right\rangle_{\!\!F} = \int\limits_{4\pi} \frac{\mathrm{d}\Omega}{4\pi} \int\limits_{4\pi} \frac{\mathrm{d}\Omega'}{4\pi} \frac{1}{4} \left\{ \left\langle + \left| 2S_{x}^{2} + 2S_{y}^{2} \right| + \right\rangle \left(2 \left| \left\langle \mathbf{k}_{\!\!F} \right| \lambda(r) l_{x} \left| \mathbf{k}_{\!\!F}' \right\rangle \right|^{2} \right) \right\}.$$

Finally, using $\langle + | S_x^2 + S_y^2 | + \rangle = \langle + | S^2 - S_z^2 | + \rangle = \frac{1}{2}$, we get

$$\langle V^{2} \rangle_{F} = \frac{1}{2} \int_{4\pi} \frac{\mathrm{d}\Omega}{4\pi} \int_{4\pi} \frac{\mathrm{d}\Omega'}{4\pi} \left| \langle \mathbf{k}_{F} | \lambda(r) l_{x} | \mathbf{k}_{F}' \rangle \right|^{2}. \tag{2.69}$$

We proceed further with the purpose of a given explanation as to why it is that one finds in the literature the spin–orbit scattering expressed in terms of core states. This may seem paradoxical as we just stated that the conduction electrons were the most strongly subject to spin–orbit scattering. In (2.69), we have got rid of the spin part, and we are left with the description of the orbital part of the electron wave function. We consider here a model that turns out to account reasonably well of the spin-lattice measurements when the impurity has no excess charge compared to its host [12]. We need to make a good choice to express the $|\mathbf{k}_F\rangle$ states so that the electronic state near the nucleus is well approximated. Our choice is suggested by the following considerations [13]. The tight binding approach is acceptable if there are not too many overlaps, that is, for narrow bands. When the bands broaden too much, they cross, and the simplest scheme of tight binding is not applicable. We assume that we are preparing to apply a variational principle to find an approximate solution to the Schroedinger equation. We consider a trial wave function, which is a superposition of wave functions that are orthogonal to the core states of the system.

Here, we work out a set of wave functions for conduction electrons in a crystal with a single impurity at $\mathbf{R}=0$. We consider an impurity that has p core states. We take into consideration only the core p-states $|b_i\rangle=|x_i\rangle=x_i\,f(\mathbf{r})$ $x_i=x,y,z$. The directions numbered with i refer to crystalline directions. The conduction electron states are taken to be

$$|\mathbf{k}_{\mathrm{F}}\rangle = |\mathbf{e}^{i\,\mathbf{k}\mathbf{r}}\rangle - \sum_{i} \beta_{i\,\mathbf{k}} |x_{i}\rangle,$$

with

$$\beta_{i\mathbf{k}} = \langle e^{i\mathbf{k}\mathbf{r}} | x_i \rangle$$

in order to satisfy the condition of orthogonality. Consider coordinate axes X, Y, Z such that the Z axis is along \mathbf{k}_F . We can write $|x_i\rangle = \sum_j c_{ij} |X_j\rangle$. Then $\beta_{i\mathbf{k}} = \sum_j c_{ij} |X_j\rangle$.

$$\langle e^{ikZ} | x_i \rangle = \sum_j c_{ij} \langle e^{ikZ} | X_j \rangle$$
. We have $\langle e^{ikx} | xf \rangle = \langle e^{iky} | yf \rangle = \langle e^{ikz} | zf \rangle$,

equal to a constant a. We have also $\langle e^{ikz} | xf \rangle = \langle e^{ikz} | yf \rangle = 0$. Then $\beta_{i\mathbf{k}} = a \, c_{i\mathbf{k}}$. Let $\cos(i,\mathbf{k})$ be the cosine of the angle between the crystalline direction designated by i and the direction of \mathbf{k} . As $zf(r) = Z \cos(i,\mathbf{k}) f(r)$, we have $c_{i\mathbf{k}} = \cos(i,\mathbf{k})$ and

$$|\mathbf{k}_{\mathrm{F}}\rangle = |\mathbf{e}^{i\mathbf{k}\mathbf{r}}\rangle - \sum_{i} a \cos(i, \mathbf{k}) |x_{i}\rangle.$$

In calculating $\langle V^2 \rangle_{\!\!F}$, four terms appear (plane wave in, plane-wave out, core in, core out, crossed terms plane wave-core state). Calculations show that the core–core terms are by far the largest. We will neglect the others. Thus,

$$\langle V^2 \rangle_{\rm F} = \frac{1}{2} \int\limits_{4\pi} \frac{{\rm d}\Omega}{4\pi} \int\limits_{4\pi} \frac{{\rm d}\Omega'}{4\pi} \sum_{ii'i''i''} a^4 c_{ik} c_{i'k'} c_{i''k} c_{i'''k'}$$

$$\langle x_{i'} | \lambda(r) l_x | x_i \rangle \langle x_{i''} | \lambda(r) l_x | x_{i'''} \rangle$$

If i and i'' differ, we have $\int\limits_{4\pi} \frac{\mathrm{d}\Omega}{4\pi} c_{ik} c_{i''k} = 0$, while if i = i'', then $\int\limits_{4\pi} \frac{\mathrm{d}\Omega}{4\pi} c_{ik}^2 = \frac{1}{3}$. We are left with

$$\langle V^2 \rangle_{\mathrm{F}} = \frac{1}{2} \frac{a^4}{9} \sum_{iii} |\langle x_{ii} | \lambda(r) l_x | x_i \rangle|^2,$$

and we see how the scattering is finally expressed as matrix element with core state! The spin-orbit parameters such as $a^2\lambda(r)$ are tabulated from measurements of X-ray spectra.

2.4.4 Electron-Magnon Scattering

Starting around 1999, research on spin transport was concerned with the effect of a current on the magnetization, the possibility of exciting spin waves by current, or driving a magnetization flip by a spin-polarized current. Here we focus on a corollary effect, the spin flip of electrons that scatter with spin-waves. Long before spintronics research, this interaction of conduction electron and magnetization at an interface between a ferromagnet and a metal was examined by electron spin resonance [14]. Here we examine simply the effect of electron–magnon collisions on spin mixing (see Sect. 2.3, (2.31)). Another mechanism for spin mixing would be elastic electron–electron scattering.

The following description is meant to approximate the situation for 3d ferromagnets Fe, Co, Ni [15]. A very crude picture is used, by which conduction electrons form a sea of s electrons, while 3d electrons are responsible for the localized moments. Our main concern here is to obtain the qualitative form of the interaction between conduction electrons and magnetization. We consider the scattering of a single conduction electron spin with N electrons forming the local moments. These localized electrons are described by Wannier functions $w_s^{\pm}(\mathbf{r}-\mathbf{R}_s)$, where \mathbf{R}_s is a lattice vector. The conduction electron is specified by a Bloch function $\psi_k^{\pm}(\mathbf{r})$, which can be thought of as composed of Wannier functions $\phi_s(\mathbf{r})$:

$$\psi_{\mathbf{k}}^{\pm}(\mathbf{r}) = \frac{1}{\sqrt{N}} \sum_{s} e^{i \mathbf{k} \mathbf{R}_{s}} \phi_{s}(\mathbf{r}).$$

The state of the system composed of N+1 electrons must be an antisymmetric linear combination of these states. There are many possible states of the system, corresponding to all the spin configurations. The interaction of the conduction electron with the moment-forming electrons is given by the Hamiltonian

$$\sum_{i < j}^{N+1} \frac{e^2}{r_{ij}}.$$

A perturbation calculation carried out to estimate the effect of the Coulomb interaction needs to work out the matrix elements of this Hamiltonian between these antisymmetric states of N+1 electrons. When all is done [15], it is possible to construct a Hamiltonian that would give the same matrix elements, where we to consider simple products of one-electron wave functions instead of the fully antisymmetric ones. This Hamiltonian has the form

$$H(\mathbf{k}', \mathbf{k}) = -2 \sum_{j=1}^{N} J_j(\mathbf{k}', \mathbf{k}) \mathbf{S}_j \cdot \mathbf{s},$$

where

$$J_j(\mathbf{k}', \mathbf{k}) = \int \int d\tau_{12} \frac{e^2}{r_{12}} \psi_{\mathbf{k}'}^*(1) w_j(1) w_j^*(2) \psi_{\mathbf{k}}(2)$$

is a typical exchange integral. Now, by expressing the expansion of the Bloch wave function of the conduction electron in terms of Wannier functions, we have

$$J_j(\mathbf{k}',\mathbf{k}) = \frac{1}{N} e^{i(\mathbf{k}-\mathbf{k}')\mathbf{R}_j} \int \int d\tau_1 d\tau_2 \frac{e^2}{r_{12}} \phi^*(\mathbf{r}_1) w_j(\mathbf{r}_1) w_j^*(\mathbf{r}_2) \phi_s(\mathbf{r}_2).$$

In this expression, the w_j are the localized wave functions of those electrons that give rise to the ferromagnetic moments, they are presumed to be 3d-electrons, while the ϕ_s represent a 4s-type electron, and so the exchange integral is a so-called s-d

exchange integral. Atomic physics provides tabulated values for these integrals. In solid, one must expect these integrals to take on different values because of screening effects (Zener et al. 1953). We write

$$J_j(\mathbf{k}',\mathbf{k}) = \frac{1}{N} e^{i(\mathbf{k}-\mathbf{k}')\mathbf{R}_j} J_{\text{sd}}$$

and treat $J_{\rm sd}$ as a phenomenological parameter. The end result [15] for the form of the exchange interaction between a conduction electron and localized moment is then

$$H(\mathbf{k}', \mathbf{k}) = -2J_{\text{sd}}\left(\frac{1}{N}\sum_{j} e^{i(\mathbf{k} - \mathbf{k}')\mathbf{R}_{j}} \mathbf{S}_{j}\right) \cdot \mathbf{s}.$$
 (2.70)

As this Hamiltonian commutes neither with $\sum_{i,j} \mathbf{S}_i \mathbf{S}_j$ nor with $\sum_{i,j} S_{i,z}$, it provides a coupling mechanism that can change the magnitude and the *z*-component of the localized moments. Thus, this interaction specifies how magnetization is transferred between *s* and *d* electrons. The total angular momentum of *s* and *d* electrons is conserved in this Hamiltonian description. This conservation rule is dictated by the invariance under rotation of the coupling $\mathbf{S} \cdot \mathbf{s}$ [6].

Note that scattering with $\mathbf{k}' = \mathbf{k}$, $\sum_{i} S_{i,z}$ does not commute with $H(\mathbf{k}', \mathbf{k})$, but $\sum_{i,j} \mathbf{S}_i \mathbf{S}_j$ does commute with it, implying that the magnitude of the d moments is constant, that is, the d moments undergo a rotation under the effect of this "spinonly" scattering.

2.4.5 Spin Mixing by Collisions with Magnons

Here we look at the contribution of electron—magnon collisions to spin-mixing, that is, to spin-dependent transport. It turns out that it is the difference in spin-mixing rates from majority to minority vs. minority to majority that plays a crucial role in some measurements, such as the spin-dependent thermoelectric effect [16] and the temperature derivative of the low-temperature resistance of metallic ferromagnets [17]. Consequently, we distinguish the two directions of spin flips.

The electron–magnon scattering was initially discussed by Kasuya [18], Mannari [19], and Goodings [20]. They focused there attention on its contributions to the transport relaxation. Fert emphasized the role of electron–magnon collisions in the spin-mixing [21]. We can find useful insight about how to calculate this by examining the treatment of collisions with phonons [22]. Mahan derives as well the mean time between collisions (not the transport relaxation time) for collisions with acoustic phonons [23]. For spin-mixing, we seek in effect the mean time between spin flips due to collisions with magnons, and ignore any momentum relaxation due to electron–magnon collision, as they are quite negligible. We will use the notation

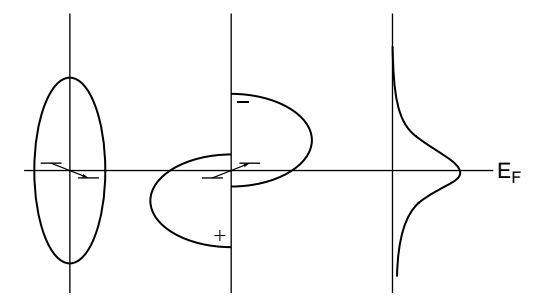


Fig. 2.12 From *left* to *right*: density of states for conduction electrons, for localized electrons, and f(E)(1-f(E)) product

 τ_{+-} and τ_{-+} instead of the spin-mixing time $\tau_{\uparrow,\downarrow}$ defined in (2.31) to signal that here we keep track of the difference between the two spin-flip directions.

The time τ_{-+} refers to the process in which the polarization of the conduction electrons *gains* one Bohr magneton. In view of the form (2.70) of the electron—magnon interaction, this gain must correspond to a loss of one Bohr magneton on the part of the magnetization. This is equivalent to saying that one magnon is *created* (Fig. 2.12). We use the modified Fermi golden rule in which we add the statistical weight of the initial state [1] so as to take into account the difference between τ_{+-} and τ_{-+} . For the electrons, we insure that the electronic final state is empty and the electronic initial state is occupied. This gives, after summing over all possible magnon wave vectors,

$$\frac{1}{\tau_{-+}} = \frac{2\pi}{\hbar} \int \frac{\mathrm{d}^3 q}{(2\pi)^3} |M_q|^2 N_q f(E_-) (1 - f(E_+)) \delta(E_- - (E_+ + \hbar\omega_q)),$$

where $|M_q|^2$ symbolizes the square of the matrix element of the interaction hamiltonian (2.70), N_q is the number of magnons of wave vector of module q, and $\hbar\omega_q$ is their frequency. In creating a magnon, the electrons loose some energy, and so this integral contains a product of the form $f_0(E)(1 - f_0(E - \Delta E))(\Delta E > 0)$.

For the converse process, a magnon is annihilated and the rate of such a process is given by

$$\frac{1}{\tau_{+-}} = \frac{2\pi}{\hbar} \int \frac{\mathrm{d}^3 q}{(2\pi)^3} |M_q|^2 (N_q + 1) f(E_+) (1 - f(E_-))$$
$$\delta (E_+ - (E_- - \hbar \omega_q)).$$

The magnetization restitutes some energy to the electrons in this process, and so the integrand contains a term of the form $f_0(E)(1 - f_0(E + \Delta E))(\Delta E > 0)$. The graph of Fig. 2.13 shows that these two factors, namely $f_0(E)(1 - f_0(E + \Delta E))$ and $f_0(E)(1 - f_0(E - \Delta E))$, may be noticeably different. Hence, we expect that

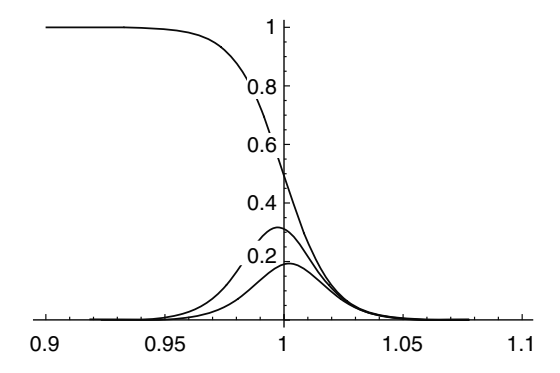


Fig. 2.13 Fermi–Dirac distribution f(E) and product $f(E)(1 - f(E \pm \Delta E))$

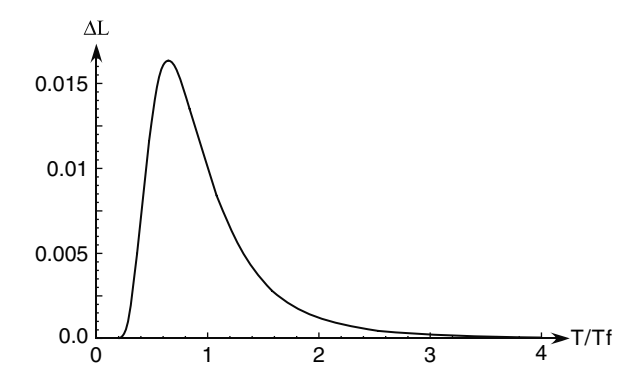


Fig. 2.14 Temperature difference in the $(+) \rightarrow (-)$ and $(-) \rightarrow (+)$ rates due to collision with magnons (arbitrary units)

the spin mixing rates differ depending on whether transitions are from majority to minority spins or vice versa.

To proceed further with an estimate of the temperature dependence of the difference between τ_{+-} and τ_{-+} , we take a magnon dispersion $\omega_q = Dq^2$. We assume that there is a splitting of the majority and minority bands, the energies of which are E_+ , E_- . Then the magnon energies must have at least the value of this gap in order for them to induce transitions between the two bands. We call this splitting k T_F . This defines a lower bound for q. The largest q would be k_F , but this corresponds to magnon energies that have zero occupancy N_q , and so we can set the upper bound to infinity. After some algebra and integration, it can be found that the mixing rates vary about as T^2 at high temperatures. As T goes below T_F , they drop sharply to zero. In Fig. 2.14, we report the quantity

$$\Delta L = \frac{L_{+-} - L_{-+}}{\sigma_s} \cong \frac{\tau_0}{\tau_{+-}} - \frac{\tau_0}{\tau_{-+}},$$

where τ_0^{-1} is the mean collision rate (see (2.38)) averaged over both spin channels. This quantity ΔL appears in the analysis of spin-dependent transport when spin mixing is included [24]. Thus, we find that ΔL , though it is small, presents a sharp temperature dependence around the temperature $T_{\rm F}$.

A recent paper asserts that the contribution of the s-d interaction to the magnetic resistivity via electronic spin-flip transitions remains poorly known [25]. These authors deduce from their very high field magnetoresistance data that the freezing temperature ($T_{\rm F}$) of the electron–magnon process is of about 15 K for Nickel and 250 K for Co. Thus, details of the band structure give rise to very large differences in the temperature dependence of electron–magnon collision effects, even though the magnetic excitation dispersion at low q are not very different in these two metals.

2.5 Spin-dependent Transport: The Non-collinear Case

The notion that a spin-polarized current can act on the magnetization was introduced by two seminal papers by Berger [26] and Slonczewski [27]. There is by now a general consensus that a torque arises when the conduction electrons enter a layer where the magnetization is not aligned with their spin polarization, because this transverse spin moment relaxes onto the magnetization. We saw that this spin polarization, or spin accumulation, is an out-of-equilibrium property that arises when a current is driven through a magnetic nanostructure. When the magnetization directions in the two layers of a spin valve are not collinear, the spin accumulation of the incoming electrons is at an angle with respect to the magnetization. For Slonczewski [28], the length over which this transverse component decays is of the order of one atomic unit, owing to the $\mathbf{k}_{\uparrow,\downarrow}$ averaging over the Fermi surface. Instead, Shpiro et al. [29] described this decay in a diffusive model and estimated this decay length to be in the range of a few nanometers [30].

Here, the idea that a spin-polarized current can exert a torque on the magnetization that it traverses is introduced by means of a simple approach. We use a thermodynamics description of transport, with Pauli matrices to account for the full spin dynamics. As reported by other groups, we describe the spin and charge currents as tensorial quantities using Pauli matrices [31]. We follow the notation of Zhang et al. [32]. Thermodynamic descriptions of spin-dependent transport was initiated by Johnson and Silsbee [33]. This formalism allowed Wegrowe et al. [34] to express the details of s and d electron spin relaxation processes. Quite generally, the Onsager matrix defines linear relationships between generalized currents and generalized forces, which are the gradients of their associated potentials [35]. This approach is convenient to describe spin relaxation and spin-dependent transport, including spin mixing effect [24].

In spin valves, when a conduction electron enters a magnetic layer from a non-magnetic metal, we can consider that its spin experiences a sudden turn-on of a magnetic field (see Sect. 2.2). The spin dynamics regime is the extreme opposite to the adiabatic fast passage as found, most notably, when an electron crosses a domain wall. Following Shpiro et al. [29], we express this with a Bloch equation for the

transverse spin accumulation. A more appropriate approach is that of Brataas et al. [36]. These authors treat transport through the interface using quantum mechanics, thus obtaining spin mixing conductivities of interfaces. This sets for them the boundary conditions for diffusive transport in each layer. Recently, they extended their calculations in order to include thermal currents [37]. However, the simple thermodynamic description adopted here is sufficient to introduce the concept of spin torque and to analyze some basic experiments [38].

2.5.1 Toward a Semi-classical Description of Spin Dynamics in Transport

It is possible to infer the form of the basic properties of spin-dependent transport, in particular spin current, by starting from a quantum-mechanical description of the conduction electrons. The treatise on transport of Smith and Jensen [39] shows that a system of N electrons can be described by a density matrix. When statistical averages are carried out, it results in a Hamiltonian equation of evolution for a Boltzmann distribution in the space of 2×2 matrices that accounts for the spin dynamics of one electron.

Gliesche et al. [40] discussed in detail under what conditions an equation of evolution for a density matrix for one electron can be derived from the full density matrix of a system of N electrons, which are weakly coupled among themselves and also weakly coupled to a thermal bath. Thus they obtain an equation of evolution for the one-electron density matrix D with relaxation terms

$$\frac{\mathrm{d}D}{\mathrm{d}t} = \frac{i}{\hbar} [D, H] + \Gamma D, \tag{2.71}$$

where H is the one-electron hamiltonian and Γ a superoperator. Such equations are often referred to as master equations and correspond to a generalization of the detailed balance (2.6). In a follow-up paper, the same authors [41] show under what conditions it is possible to derive from (2.71) a semi-classical Boltzmann equation, including relaxation terms.

At this point of the semi-classical approach, one has a Boltzmann distribution defined in terms of 2×2 matrices. Those can be projected in terms of the unit matrix and the Pauli matrices. This is, for example, the starting point of the development of Zhang et al. [30]. Spin and charge currents can then be deduced from D, with the appropriate tensorial character.

2.5.2 Constitutive Equations

We consider a 1D model of a magnetic multilayer with current flow perpendicular to the interfaces (the variable x will be used as the spatial coordinates). In

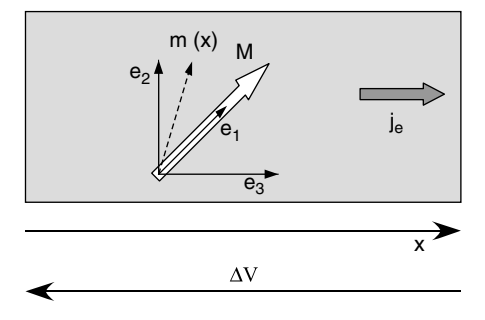


Fig. 2.15 Spin polarization m, magnetization M, and unit vectors of the reference frame

Fig. 2.15, we have represented one magnetic layer for which we define the following properties.

The Onsager reciprocal relations including the thermal current are written in the Pauli space as follows [42]:

$$\hat{j}(x) = \hat{C}\left(E(x)\hat{\mathbf{I}} + \frac{1}{e}\frac{\partial\hat{\mu}}{\partial x}\right),\tag{2.72}$$

where E is the electric field and $\hat{\mathbf{I}}$ the 2×2 identity matrix. Here, the generalized current \hat{j} , the chemical potential $\hat{\mu}$, and the Onsager coefficient \hat{C} are 2×2 tensors. The latter ones can be decomposed upon the Pauli spin matrix σ and the identity matrix

$$\hat{C} = c_0 \hat{\mathbf{I}} + c \mathbf{M} \cdot \boldsymbol{\sigma}, \tag{2.73}$$

$$\hat{\mu} = \mu_0 \hat{\mathbf{I}} + \mathbf{m} \cdot \boldsymbol{\sigma}. \tag{2.74}$$

The electric current and the spin current are derived from the generalized current following

$$j_e = \text{Re}(Tr(\hat{j})), \tag{2.75}$$

$$\mathbf{j_m} = \text{Re}(Tr(\hat{j}\boldsymbol{\sigma})). \tag{2.76}$$

M is the unit vector representing the direction of local magnetization. In this notation, the projections of **m** have the dimensions of a chemical potential. The generalized charge and spin accumulation \hat{n} is proportional to the chemical potential

$$\hat{n} = \int e\hat{N}(E)\hat{f}(E) dE = e\hat{N}(\varepsilon_{\rm F})\hat{\mu}$$
 (2.77)

with $N(\varepsilon_{\rm F})$ the density of states at the Fermi level. For convenience, we note the electric field augmented by the chemical potential gradient as

$$F = E(x) + \frac{1}{e} Tr\left(\frac{\partial \hat{\mu}}{\partial x}\right). \tag{2.78}$$

2.5.3 Spin Diffusion in Non-collinear Configurations

We express now the equations of continuity for the currents in the stationary regime. The continuity of the charge current reads, as usual,

$$\frac{\mathrm{d}j_e}{\mathrm{d}x} = 0. \tag{2.79}$$

We assume a Block equation for the spin accumulation \hat{n} from which we deduce an equation of evolution for \mathbf{m} . \hat{n} evolves under the combined effect of a relaxation process, with a spin-lattice relaxation time $t_{\rm sf}$ and an exchange field $J\mathbf{M}$. There is a corresponding Bloch equation for the chemical potential vector \mathbf{m} , according to (2.74) and (2.77), with a relaxation time $\tau_{\rm sf} = t_{\rm sf}/eN(\varepsilon_{\rm F})$ and an angular velocity term $g = JeN(\varepsilon_{\rm F})/\hbar$. Thus, we obtain the continuity equation for the spin current:

$$\frac{\mathrm{d}\mathbf{j_m}}{\mathrm{d}x} = \frac{\mathbf{m}}{\tau_{\mathrm{sf}}} + g\mathbf{M} \wedge \mathbf{m}. \tag{2.80}$$

The constitutive equations together with the continuity equations imply a set of diffusion equations. In nonmagnetic layers, the Onsager coefficient \hat{C} is diagonal. We write $\hat{C} = c_N \hat{\mathbf{I}}$. Then the transport equation and the continuity equations together imply a diffusion equation for the generalized chemical potential:

$$\frac{c_{\rm N}}{e} \frac{\mathrm{d}^2 \mathbf{m}}{\mathrm{d}x^2} = \frac{\mathbf{m}}{2\tau_N}.\tag{2.81}$$

Writing the spin-diffusion length as $q^{-1} = \sqrt{2\tau_{\rm N}c_{\rm N}\,e^{-1}}$, the general solution of (2.81) is

$$\mathbf{m} = \mathbf{m}_{(+)} \exp(qx) + \mathbf{m}_{(-)} \exp(-qx).$$
 (2.82)

In magnetic layers, we consider that the magnetization **M** is uniform. Substituting (2.73) and (2.74) into the transport equations (2.72), we can decompose \hat{j} into currents of charge and spins:

$$j_e = 2 \left[c_0 F + \frac{c}{e} \mathbf{M} \cdot \frac{\mathbf{dm}}{\mathbf{d}x} \right]$$

$$\mathbf{j_m} = 2 \left[cF\mathbf{M} + \frac{c_0}{e} \frac{d\mathbf{m}}{dx} \right].$$

When these linear relations are substituted into the continuity equations, we obtain a diffusion equation for the part of the chemical potential \mathbf{m}_{\perp} , which is perpendicular to the magnetization \mathbf{M} :

$$\frac{c_0}{e} \frac{\mathrm{d}^2 \mathbf{m}_{\perp}}{\mathrm{d}x^2} = \frac{\mathbf{m}_{\perp}}{2\tau_{\mathrm{sf}}} + \frac{g}{2} \mathbf{M} \wedge \mathbf{m}_{\perp}. \tag{2.83}$$

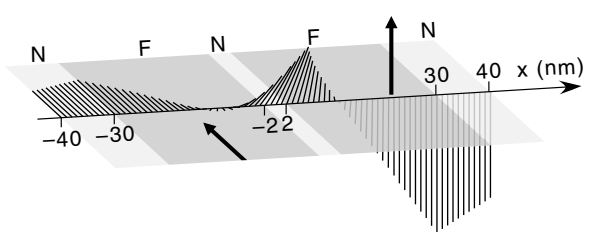


Fig. 2.16 Chemical potential **m** (appearing like a comb) as a function of position along the axis of a nanowire comprising a Co–Cu–Co spin valve contacted with Cu leads. The electrons flow from *right* to *left*. **m** is roughly upward as it is injected from the N spacer into the second magnetic layer, and soon becomes parallel to its magnetization as the electrons travel deeper into it

This is the key result of this section. Typically, we expect the second term to dominate the diffusion process. We define a new characteristic length of spintronics:

$$\lambda_J = \sqrt{c_0/ge}. (2.84)$$

This is the decay length associated with the relaxation process of the transverse spin polarization. A diffusion equation for the component of the chemical potential $m_{//}$ can also be obtained [38].

We could at this point set out to calculate spin transport through a set of layers of nonmagnetic and magnetic layers in non-collinear configurations. The boundary conditions at the ends of the structure and the continuity of currents at each interface would determine the coefficients of the solutions for each diffusion equation in each layer. An example is shown in Fig. 2.16 for a nanowire of square cross-section, $100 \times 100 \, \mathrm{nm}^2$, comprising a spin valve in its middle.

The torque that the spin-polarized current exerts on a given layer can be calculated by determining how much the spin current has changed as it traverses this layer, that is,

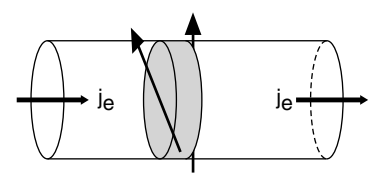
$$\Delta \tau = \frac{\mu_{\rm B}}{e} (\mathbf{j_m}(L) - \mathbf{j_m}(l)) S, \qquad (2.85)$$

where S is the cross-section of the magnetic layer, μ_B is the Bohr magneton. In a pillar with a cross-section less than $100 \, \mathrm{nm}$ in diameter, the torque produced by a current density of about $10^7 \, \mathrm{A \, cm^{-2}}$ is equivalent to a field strength of about $10 \, \mathrm{mT}$ applied to the magnetization. In comparison, the field induced by this current would be less than $0.01 \, \mathrm{mT}$!

2.5.4 Domain Walls

When a spin-polarized current goes through a domain wall, the spin dynamics is quite different from that of a spin valve. In the reference frame of the electron, the spin injection into a magnetic layer is equivalent to a sudden passage in magnetic

Fig. 2.17 Spin polarized current flowing in the z direction through a domain wall. The incoming spin current at z and at z + dz differ, implying a torque on the magnetization of the pill-box



resonance. To the contrary, when an electron goes through a domain wall, the effective field (in a sd exchange picture) rotates at a rate slow enough that the spin tracks the field [43]: we are in a situation of adiabatic fast passage (see Sect. 2.2).

In this approximation, the effect of a spin-polarized current on the magnetization can be thought of as follows. We work out an equation for the time evolution of the magnetization in a small pill box in the domain wall (Fig. 2.17). The evolution of the magnetization inside the pillbox (Fig. 2.17) can be described with a Laudau–Lifshitz equation. The pill-box also experiences an incoming flow of spins parallel to $\mathbf{M}(x)$ on its face at position x, and an outgoing flow parallel to $\mathbf{M}(x+dx)$ on its face at position x+dx. Therefore, there is a change per unit time of the total angular momentum of the pill-box proportional to $d\mathbf{M}/dx$ [44–46]. Hence, we infer an equation of the form

$$\frac{\partial \mathbf{M}}{\partial t} = \gamma \mathbf{M} \times \mathbf{H} + D \mathbf{M} \times \nabla^2 \mathbf{M} + \frac{1}{2} g \mu_{\rm B} \frac{j}{e} \frac{\partial}{\partial x} \left(\frac{\mathbf{M}}{M_{\rm s}} \right). \tag{2.86}$$

In general, the spin current is not fully polarized and the tracking of the exchange field is not perfect [47]. This gives rise to an additional term, as discussed in the recent literature [44, 48, 49]. Kläui has shown (see his contribution to this volume) that this effect is critical in pushing walls [50].

References

- F.A. Reuse, K. Maschke, V. de Coulon, J. van der Klink, J.-Ph. Ansermet, Eur. Phys. J. B 36, 573 (2003)
- 2. W. Harrison, Place Name Solid Place Type State Theory (Dover, NY, 1979)
- 3. A. Fert, I.A. Campbell, Phys. Rev. Lett. **21**(16), 1190 (1968)
- 4. N.F. Mott, H. Johns, The Theory of Metals and Alloys (Oxford University, London, 1936)
- 5. T. Valet, A. Fert, Phys. Rev. B 48, 7099-7113 (1993)
- 6. L.E. Ballentine, Quantum Mechanics (Prentice Hall, NJ, 1990)
- 7. N. Bloombergen, Phys. Rev. 78, 572 (1950)
- 8. C. Kittel, A.H. Mitchell, Phys. Rev. **101**, 1611 (1956)
- 9. S.E. Barnes, Adv. Phys. 30, 801–938 (1981)
- J.-Ph. Ansermet, in Frontiers in Nanosciences. Spintronics with Metallic Nanowires (Oxford University Press, London, 2009)
- 11. J. R. Asik, M.A. Ball, C.P. Slichter, Phys. Rev. Lett. 16(17), 740 (1966)
- 12. J.R. Asik, M.A. Ball, C.P. Slichter, Phys. Rev. 137, A512(1965)

13. J.M. Ziman, *Principle of the Theory of Solids* 1st edn. (Cambridge University Press, London, 1964), p. 93

- 14. R.H. Silsbee, A. Janossy, P. Monod, Phys. Rev. **B** 19, 4382 (1979)
- 15. A.H. Mitchell, Phys. Rev. 105, 1439 (1957)
- L. Piraux, A. Fert, P.A. Schroeder, R. Loloee, P. Etienne, J. Magn. Magn. Mater. 119, L247–253 (1992)
- 17. L. Gravier, S. Serrano-Guisan, F. Reuse, J.-Ph. Ansermet, Phys. Rev. B 73, 024419 (2006)
- 18. Kasuya, Prog. Theor. Phys. 22, 227 (1959)
- 19. I. Mannari, Prog. Theor. Phys. 22, 335 (1959)
- 20. A. Goodings, Phys. Rev. 132(2), 542 (1963)
- 21. A. Fert, J. Phys. C (Solid State Phys.), 2(2), 1784 (1969)
- 22. O. Madelung, Solid State Phys. Ser. 2 (1978)
- 23. G.D. Mahan, Many-Particle Physics (Kluwer Academics, New York, 2000)
- 24. J.-Ph. Ansermet, IEEE Trans. mag. 44, 329-335 (2008)
- B. Racquet, M. Viret, E. Sondergard, O. Cespecdes, R. Manmy, Phys. Rev. B 66, 024433 (2002)
- 26. L. Berger, Phys. Rev. **B** 54, 9353 (1996)
- 27. J.C. Slonczewski, J. Magn. Magn. Mater. 159, L1 (1996)
- 28. J.C. Slonczewski, J. Magn. Magn. Mater. 247, 324 (2002)
- 29. A. Shpiro, P. Levy, S. Zhang, Phys. Rev. **B** 67, 104430 (2003)
- 30. J. Zhang, P. Levy, S. Zhang, V. Antropov, Phys. Rev. Lett. 93, 256602 (2004)
- 31. M.D. Stiles, A. Zangwill, Phys. Rev. B 66, 014407 (2002b)
- 32. S. Zhang, P.M. Levy, A. Fert, Phys. Rev. Lett. 88, 236601 (2002)
- 33. M. Johnson, R.H. Silsbee, Phys. Rev. Lett. 55, 1790 (1985)
- 34. J.-E. Wegrowe, M.C. Ciornei, H.-J. Drouhin, J. Phys. Condens. Matter 19, 165213 (2007)
- 35. Blundell and Blundell, Concepts in Thermal Physics (Oxford University Press, London, 2006)
- 36. A. Brataas, F.E.W. Bauer, P.J. Kelly, Phys. Rep. 427, 157 (2006)
- 37. H. Moosa, G.E.W. Bauer, Q. Zhang, P.J. Kelly, Phys. Rev. Lett. 99, 066603 (2007)
- 38. J. Dubois and J.-Ph. Ansermet, Phys. Rev. B78, 184430 (2008)
- 39. H. Smith, H.H. Jensen, *Transport Phenomena* (Clarendon Press, Oxford, 1989)
- 40. A. Gliesche, K, Maschke, F.A. Reuse, Phys. Rev. **B** 77, 245104 (2008a)
- 41. A. Gliesche, K, Maschke, F.A. Reuse, Phys. Rev. B 77, 214301 (2008b)
- 42. Z.C. Wang, G. Su, S. Gao, Phys. Rev. B 63, 224419 (2001)
- J.F. Gregg, W. Allen, S.M. Thompson, M.L. Watson, G.A. Gehring, J.Appl. Phys. 79(8), 5593 (1996)
- 44. G. Tatara, H. Kohno, Phys. Rev. Lett. 92(8), 86601 (2004)
- 45. J.-Ph. Ansermet, IEEE Trans. Mag. 40(2), 358 (2004)
- 46. X. Waintal, M. Viret, Europhys. Lett. **65**(3), 427–433(2004)
- 47. P.M. Levy, S. Zhang, Phys. Rev. Lett. 79(25), 5110 (1997)
- 48. Z. Li, S. Zhang, Phys. Rev. Lett. **92**(20), 207203 (2004)
- 49. S. Zhang, Z. Li, Phys. Rev. Lett. 93, 127204 (2004)
- 50. D. Backes, C. Schieback, M. Kläui, Appl. Phys. Lett. 91, 112502 (2007)
- 51. C. Zeener, R.R. Heikes, "Exchange Interactions", Rev. Mod. Phys. 25(1), 191 (1953)
- 52. Yafet, Y. in Solid state physics, Academic Press, N.Y., 14, (1963)
- 53. J. Friedel, P. Lenghart, G. Leman, J. Phys. chem. Solids, 25, 781 (1964)
- 54. R.J. Elliot, Phys. Rev. 89(4), 689 (1953)
- 55. J. Dubois and J.-Ph. Ansermet, Phys. Rev. B78, 184430 (2008)

Chapter 3 Interaction of Polarized Light with Matter

Y. Joly

Abstract This chapter is devoted to the interaction of light, mainly in the X-ray range, with matter. The subject is introduced by some experimental evidences of X-ray absorption, emission, or scattering processes in different kinds of materials. The ways of describing the electromagnetic wave field are then briefly presented before developing its interaction with an electron in an atom. They are then applied in the context of X-ray spectroscopies. Absorption, dichroism, and resonant diffraction are specifically discussed before giving some key elements to manage monoelectronic simulations.

3.1 Introduction

When an electromagnetic wave interacts with matter, many processes can be observed. The incoming wave can simply be partially, or completely, absorbed by the sample. It can be scattered elastically or inelastically, coherently or incoherently. We can also observe emission of photons at specific wavelengths and of electrons also at characteristic energies. From the explanation of the photoelectric effect by Einstein, huge progress in the understanding of the physical processes involved in all these phenomena have been done. Moreover, enormous developments in the use of these processes, often spectroscopies, have been made. They permit to analyze all kinds of material, solid, liquid, or gaseous, ordered or disordered, used in many fields, like biology, geology, chemistry, or condensed matter physics. It is impossible to give an exhaustive overview of such a subject. We shall focus mainly on the X-ray regime and consider essentially the absorption and elastic scattering of the photons. To introduce the subject, we first present some of the basic observations. Then, we give the main concepts of the electromagnetic waves before developing their interaction with matter: first from a microscopic point of view and second using terminology used for the study of dielectrics to make the connection between

Institut Néel, CNRS and Université Joseph Fourier, BP 166, 38042 Grenoble Cedex 9, France e-mail: yves.joly@grenoble.cnrs.fr

Y. Joly

78 Y. Joly

both approaches. The microscopic point of view will concern mainly the transition process between two electronic levels and not the full multielectronic aspect. The last part will concern the X-ray spectroscopies, mainly absorption, including dichroism and resonant diffraction.

3.2 Experimental Observations of X-Ray Interaction with Matter

Here we give some important measurements showing general aspects connected to the X-ray absorption/scattering by matter. We shall see that the absorption depends on energy, polarization, chemical species, and geometrical environment.

3.2.1 Absorption

From its discovery by Roentgen in 1896, the most important use of X-ray comes probably from its high penetration depth in matter with different absorption rates depending on its constituents. It is thus an exceptional tool to investigate the structure and the composition of all types of samples. For an homogeneous isotropic material, there is a simple exponential decrease of the transmitted beam intensity I in terms of the sample thickness D:

$$I = I_0 \exp\left(-\mu D\right),\tag{3.1}$$

where I_0 is the incident intensity. This equation, equivalent to the Beer–Lambert law $\ln(I_0/I) = \mu D$, introduces the total linear absorption coefficient μ . This coefficient, for a crystalline solid, is related to the absorption cross section, σ_i , of the n different chemical elements of the unit cell [1]:

$$\mu = \frac{1}{V} \sum_{i=1}^{n} \sigma_i,\tag{3.2}$$

where V is the volume of the unit cell. It is usually expressed in square centimeters or in megabarns (1 Mbarn = 10^{-18} cm²).

3.2.2 Dependence on Energy

When measuring the energy dependence of the photoelectric absorption cross section for the interaction of X-rays with matter, one can see a decrease from some megabarns at low energy down to some barns at around 1 MeV [2]. At some energies, there are strong and abrupt increases in the cross section. For example, in Fig. 3.1, we show the energy dependence of the photoabsorption cross section in

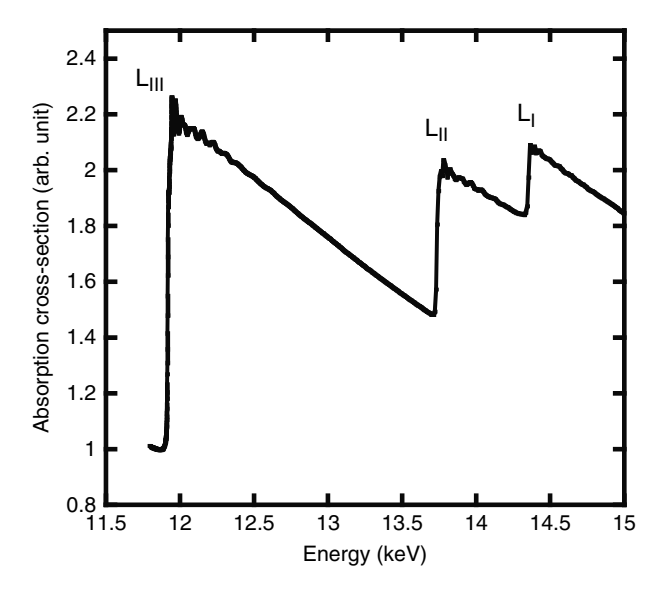


Fig. 3.1 X-ray absorption spectrum of a gold metallic foil in a 2.5 keV energy range around 13 keV. The experiment by Proux and Hazemann [3] shows the abrupt increases (called edges) in the absorption cross section at energies characteristic of the chemical element. Note that the $L_{\rm III}$ edge is two times higher than the $L_{\rm II}$ edge. Note also the so-called EXAFS oscillations after each edge

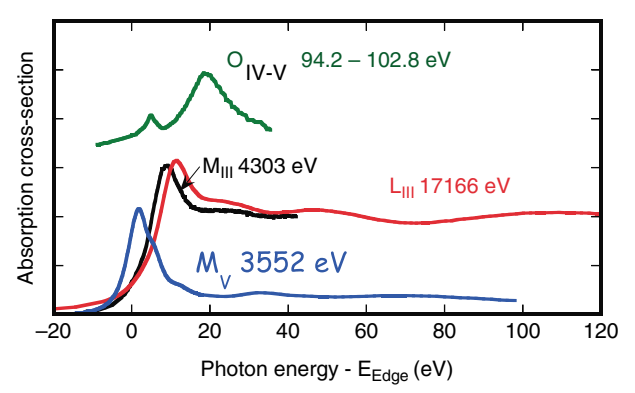


Fig. 3.2 X-ray absorption spectra at different edges of uranium in the uranyl ion UO_2^{2+} . All the edges are shifted by the value of the ionization energy of the corresponding edge in order to compare their shapes. The $L_{\rm III}$ and $M_{\rm III}$ are step like and very similar. The other edges have a very different shape. This difference is due to the selection rule imposed on the electronic transition

the $11.8-15\,\mathrm{keV}$ energy range for a gold metallic foil [3]. One can see three edges labeled $L_{\rm I}$, $L_{\rm II}$, and $L_{\rm III}$. Note also the EXAFS oscillations after the edges, which are very rich in information on the close neighborhood of the absorbing atoms, as it will be seen further on.

When looking at the different edges of a same element in the same material, as for instance the uranium edges in uranyl ion UO_2^{2+} (Fig. 3.2) in the experiment

80 Y. Joly

performed by Fillaux et al. [4], we can see the different kinds of shape of the edges. In this case, we see that the $L_{\rm III}$ and $M_{\rm III}$ have a very similar step-like shape. The M_V , $O_{\rm IV}$, and O_V spectra present only a single peak, more or less broad. We shall see, Sect. 3.4.6, that this is due to *selection rules* in the transition. Another observation which is often done is that, as in Fig. 3.1, the $L_{\rm III}$ edge is two times higher than the $L_{\rm II}$ edge.

The energy of the edges is a signature of the absorbing atom and its chemical bonding. A closer look at the spectra shows that small shifts (up to a few eV) can be observed in the threshold energy for a same element but in different chemical environments. When increasing the oxidation state, the edge tends to shift toward higher energy. This fact is often used to check the valence state of a metal atom in an oxide.

3.2.3 Dependence on the Atomic Environment

Now let us have a look at the oscillations above a typical edge. We compare two different surroundings of a same element, as, for example, the Cu K edge in pure copper and in $YCuO_{0.25}$. In Fig. 3.3, we can observe very different oscillations. From other measurements in the gas phase or in disordered materials, we also know that these oscillations do not need a long-range order. They are thus a signature of the close environment of the absorbing atoms. The connection between the spectral shape and the neighborhood will be discussed in Sect. 3.6.

3.2.4 Dependence on the Light Polarization

Pleochroism or dichroism is the change in color when a mineral is observed at different angles under plane-polarized light. Because of the absorption of particular wavelengths, the transmitted light appears colored depending on the thickness and the particular chemical and crystallographic nature of the mineral.

Fig. 3.3 X-ray absorption spectra at the Cu K edge in (*top*) a copper metallic foil and (*bottom*) in YCuO_{0.25}. The edges are roughly at the same energy, but the oscillations are very different

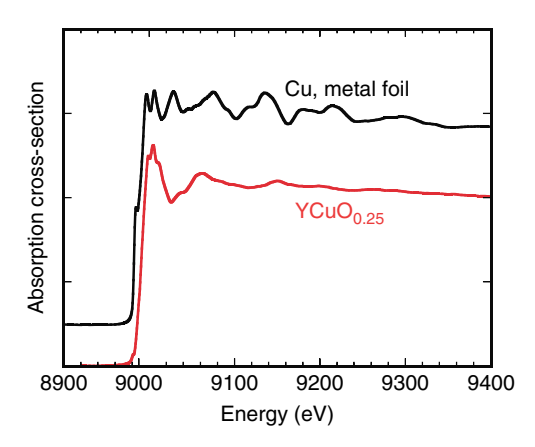
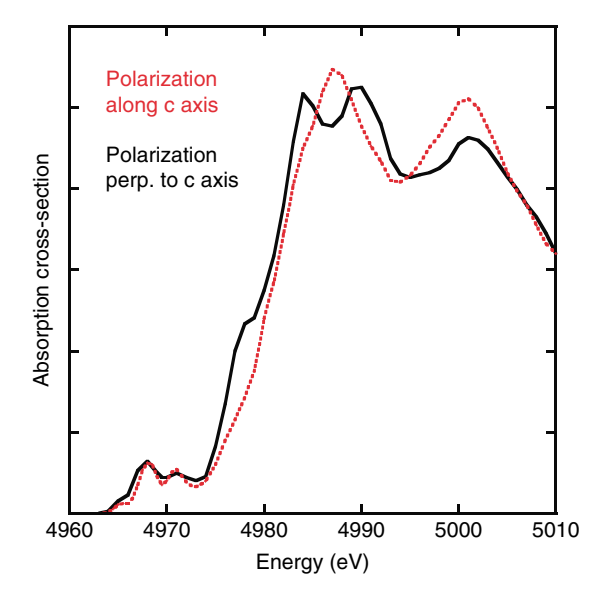


Fig. 3.4 X-ray absorption spectra of TiO₂ (rutile) around the Ti K edge. The experiment by Poumellec et al. [5] is performed using a single crystal under two orientations of the sample in front of the incoming linear wave field. The difference shown in the figure is called linear dichroism. It is relatively strong when the sample is not cubic



By extension, the difference of absorption, under rotation only, is called dichroism. This phenomenon is also observed in the X-ray energy range. To observe this, one needs a single crystal of a noncubic material (note that very small dichroism can also be observed in cubic material). For example, Poumellec et al. [5] measured the absorption along three orientations of a TiO₂ single crystal; two are shown in Fig. 3.4. The effect of the tetragonal symmetry of the material can be easily checked.

These studies are performed with linearly polarized light (the concepts of linearly or circularly polarized light are given in Sect. 3.3). As in the visible range, the use of circularly polarized light in the X-ray regime also gives useful information. Special interest comes from experiments where one looks at the difference between two spectra recorded, respectively, with left and right circular polarization. At the $L_{II,III}$ edges of magnetic material, the dichroic signal can reach several percent of the total absorption edge. For example, at the Er L_{III} edge in ErZn (Fig. 3.5), we see an oscillating behavior around the rising edge energy. At K edges, on the contrary, these kinds of observations are always very small.

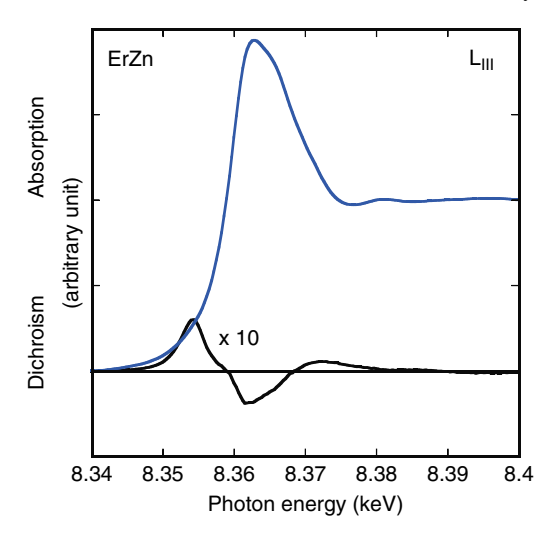
The explanation of these polarization phenomena comes from the dependence of the absorption spectroscopies on the electronic structure around the absorbing atoms. This is detailed in Sect. 3.6.

3.2.5 Diffraction Around Edges

Another kind of experiment increasingly popular at the different synchrotron facilities concerns the measurement of diffraction peaks in a more or less wide energy range around some edges. The technique called diffraction anomalous fine structure (DAFS) or resonant X-ray Scattering (RXS) [7] gives sets of spectra rich in

82 Y. Joly

Fig. 3.5 X-ray absorption spectra of ErZn and the circular dichroic signal at the Er $L_{\rm III}$ edge. The latter is a signature of magnetism of the 5d orbitals on the Er atom. The experiment was performed at the ESRF ID12 beamline by Galéra et al. [6]



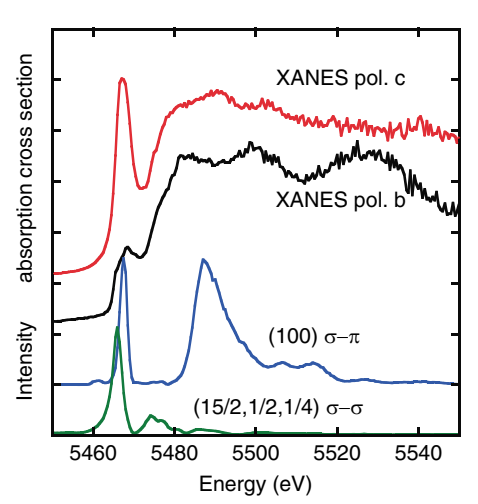


Fig. 3.6 Two diffraction peaks measured by Grenier et al. [8] around the V K edge in NaV_2O_5 at 13 K. Their intensity is nearly zero far from the edge and shows strong variations around the edge. The spectra also strongly depend on the polarization conditions. For comparison, the absorption spectra are also shown for two linear polarizations. The pre-peak visible in these spectra is also present but slightly shifted in the diffraction spectra

information on the crystalline material studied. For example, in Fig. 3.6 are shown two spectra of diffraction peaks in NaV_2O_5 compared with two absorption spectra measured for two orientations of the sample. The diffracted intensity becomes highly energy-dependent around the absorption edges. In some cases, the intensity is nearly zero; but close to the edge, the intensity variations have similarities with what is observed in the absorption spectra. This spectroscopy is indeed very similar to absorption spectroscopy. It is explained for the photon–matter interaction process in Sect. 3.4 and in an unified scheme to get the final amplitudes in Sect. 3.6.

3.3 The Light

Before considering the interaction of light with matter, one has to recall the basic definitions used to describe the electromagnetic waves.

3.3.1 Definitions and Notations

The vector potential, **A**, the electric and magnetic field, **E** and **B**, of the electromagnetic waves are obtained from the Maxwell equations. These equations lead first to the *propagation equations* in vacuum:

$$\Delta \mathbf{A} = \varepsilon_0 \mu_0 \frac{\partial^2 \mathbf{A}}{\partial t^2}, \ \Delta \mathbf{B} = \varepsilon_0 \mu_0 \frac{\partial^2 \mathbf{B}}{\partial t^2}, \ \Delta \mathbf{E} = \varepsilon_0 \mu_0 \frac{\partial^2 \mathbf{E}}{\partial t^2}. \tag{3.3}$$

A *plane wave* is a wave with infinitely long and wide wave front. From the propagation equations, it can be shown that in this case:

- The vector potential depends only on time (t) and coordinate corresponding to the propagation direction z
- A, E, and B are perpendicular to the propagation direction
- E and B are perpendicular to each other
- \bullet E = cB

The solutions of the propagation equations are necessarily of the form

$$s(z,t) = f(z-ct) + g(z+ct),$$
 (3.4)

where f and g are scalar functions.

Progressive plane waves are such that either f or g is always zero. That is,

- s(z,t) = f(z-ct) is a traveling plane wave propagating along +z
- s(z,t) = g(z+ct) is a traveling plane wave propagating along -z.

Monochromatic traveling plane waves can be written as

$$A_{x}(z,t) = A_{0x} \cos \left[2\pi v \left(\frac{z}{c} - t \right) + \varphi_{0x} \right],$$

$$A_{y}(z,t) = A_{0y} \cos \left[2\pi v \left(\frac{z}{c} - t \right) + \varphi_{0y} \right],$$
(3.5)

where the amplitudes, A_{0x} and A_{0y} , and the phases, φ_{0x} and φ_{0y} , can have peculiar relations.

Linearly polarized plane waves have both components in phase, that is, $\varphi_{0x} = \varphi_{0y}$. **E**, **B**, and **A** are thus in phase. **E** and **A** are moreover collinear.

Circularly polarized plane waves are such that $A_{0x} = A_{0y}$ and $\varphi = \varphi_{0y} - \varphi_{0x} = \pm 90^{\circ}$. The sign plus and minus are, respectively, for left and right circular polarizations.

84 Y. Joly

Complex notations are more tractable. A, E, and B are then given by

$$\mathbf{A} = \mathbf{A}_0 \, \mathbf{e}^{\mathbf{i}(\mathbf{k} \cdot \mathbf{r} - \omega t)}, \quad \mathbf{E} = \mathbf{E}_0 \, \mathbf{e}^{\mathbf{i}(\mathbf{k} \cdot \mathbf{r} - \omega t)}, \quad \mathbf{B} = \mathbf{B}_0 \, \mathbf{e}^{\mathbf{i}(\mathbf{k} \cdot \mathbf{r} - \omega t)}, \tag{3.6}$$

where **k** is the wave vector, which is collinear to the propagation direction, and $\omega = 2\pi v$ is the pulsation. Moreover, we have the relations $\mathbf{E} = -\mathrm{i}\omega \mathbf{A}$, $\mathbf{B} = -\mathrm{i}\mathbf{k} \times \mathbf{A}$, and $k^2 = \omega^2/c^2$.

In this context, we define the polarization vector by

$$\boldsymbol{\varepsilon} = \mathrm{i}\frac{\mathbf{E}_0}{E_0}.\tag{3.7}$$

The polarization vector of a circularly polarized wave propagating along z is thus

$$\varepsilon = \frac{1}{\sqrt{2}} \begin{pmatrix} 1\\ \pm i\\ 0 \end{pmatrix}. \tag{3.8}$$

In diffraction, the terms of σ (or s) and π (or p) polarizations are often used. They designate the orientation of the polarization relative to the scattering plane. When the polarization is perpendicular to the scattering plane, it is called σ ; when it is parallel, it is called π . In classical diffraction, most of the intensity of the diffraction peaks is obtained in the σ -in- σ -out channel (one says directly σ - σ). With magnetism or around the absorption edge, one can get important σ - π contributions. The information obtained from the polarization analysis of the diffraction peaks can be very rich.

3.3.2 Stokes Parameters

There is another way to characterize the polarization. It is the use of the *Stokes parameters*. They are used in many contexts: in astrophysics, in instrumentation to validate the quality of the beam lines, and in X-ray physics to describe with common tools the effect of the interaction with matter. The Stokes parameters describe completely the polarization state of an electromagnetic wave through a four component vector **S**:

$$\mathbf{S} = \begin{pmatrix} S_0 \\ S_1 \\ S_2 \\ S_3 \end{pmatrix} = \begin{pmatrix} |E_x|^2 + |E_y|^2 \\ |E_x|^2 - |E_y|^2 \\ 2\Re\left(E_x E_y^*\right) \\ 2\Re\left(E_x E_y^*\right) \end{pmatrix}. \tag{3.9}$$

The polarization itself (or rate of polarization) is thus given by

$$p = \frac{\sqrt{S_1^2 + S_2^2 + S_3^2}}{S_0}. (3.10)$$

For practical purposes, one normalizes by S_0 and thus one gets the following for example:

• (1, 0, 0, 0): unpolarized

• (1, 1, 0, 0): linearly polarized along x

• (1, -1, 0, 0): linearly polarized along y

• (1,0,1,0): linearly polarized at 45°

• (1,0,0,1): left-hand circularly polarized

• (1,0,0,-1): right-hand circularly polarized.

3.3.3 Quantization of the Electromagnetic Field

In the next section, we give the expression of the interaction between the electromagnetic wave and an electron in an atom. For this purpose, we have to first derive the quantization of the electromagnetic field. When it is confined in a volume V, the potential vector $\mathbf{A}(\mathbf{r},t)$ is expressed using the previous expressions and the annihilation $a_{\varepsilon,\mathbf{k}}$ and creation $a_{\varepsilon,\mathbf{k}}^+$ operators:

$$\mathbf{A}(\mathbf{r},t) = \sum_{\boldsymbol{\varepsilon},\mathbf{k}} \mathbf{A}_{0,\mathbf{k}} \left[a_{\boldsymbol{\varepsilon},\mathbf{k}} e^{\mathrm{i}(\mathbf{k}\cdot\mathbf{r} - \omega t)} \boldsymbol{\varepsilon} + a_{\boldsymbol{\varepsilon},\mathbf{k}}^{+} e^{-\mathrm{i}(\mathbf{k}\cdot\mathbf{r} - \omega t)} \right], \tag{3.11}$$

with

$$\mathbf{A}_{0,\mathbf{k}} = \sqrt{\frac{\hbar}{2\varepsilon_0 V \omega_k}}.\tag{3.12}$$

The Hamiltonian of the field is given by

$$H_{\rm R} = \sum_{\epsilon, \mathbf{k}} \hbar \omega_{\mathbf{k}} \left(a_{\epsilon, \mathbf{k}}^{+} a_{\epsilon, \mathbf{k}} + \frac{1}{2} \right). \tag{3.13}$$

3.4 Interaction of Light with an Electron in an Atom

Having defined the electromagnetic waves, one can now consider how they interact with matter. In this section, we consider the interaction of a photon with one electron, making a transition between two atomic levels. From the interaction Hamiltonian, we shall have, at the end of this chapter, the important processes involved in the absorption, resonant, and nonresonant scattering phenomena.

86 Y. Joly

3.4.1 Linear and Nonlinear Interactions

A first distinction between the linear and nonlinear interactions should be carried out. When there is a single incoming or a single outgoing photon in the interaction, the process is said to be linear. With more photons, one gets the nonlinear physics involved, for example, in frequency doubling. The subject, extensively studied in the infrared, visible, and ultraviolet regimes, very rarely deals with X-ray physics. Indeed, it needs huge radiation power (typically $1\,\mathrm{kW\,mm^{-2}}$). This can be reached by lasers but not at a synchrotron radiation facility, even with the very high brilliance one gets now [$\sim 10^{20}$ photons (s $^{-1}\,\mathrm{mm^{-2}mrad^{-2}0.1\%\,bw^{-1}}$)]. In a near future, with the free electron laser, which gives X-ray pulses with a brilliance 1,000 times higher than the synchrotron, the radiation power will be probably sufficient to reach nonlinear phenomena in the X-ray regime. For the moment it is not yet done, and thus the following sections are limited to the linear response.

3.4.2 Interaction Hamiltonian

The nonrelativistic Hamiltonian¹ for one photon and one particle of mass m and charge q is given by [9, 10]

$$H = \frac{1}{2m} (\mathbf{P} - q\mathbf{A})^2 + qV - g_{L} \frac{q}{2m} \mathbf{S} \cdot \mathbf{B} + H_{R}, \tag{3.14}$$

where g_L is the Landé factor (2 here), and **P** and **S** are, respectively, the momentum operator and the spin vector. H_R is the Hamiltonian of the field already seen in Sect. 3.3.3. The relativistic Hamiltonian brings terms resulting in a spin-orbit component, which can be neglected in the X-ray regime.² The nonrelativistic Hamiltonian can be split between its noninteraction part H_0 and a perturbation V_1 :

$$H_0 = \frac{p^2}{2m} + qV + H_{\rm R},\tag{3.15}$$

$$V_{\rm I} = -\frac{q}{m} \mathbf{P} \cdot \mathbf{A} + \frac{q^2}{2m} \mathbf{A}^2 - g_{\rm L} \frac{q}{2m} \mathbf{S} \cdot \mathbf{B}.$$
 (3.16)

We consider a transition between an initial state and a final state. The initial state contains one photon with wave vector \mathbf{k}_i and polarization $\boldsymbol{\varepsilon}_i$ and one electron in the state φ_g . In the same way, the final state contains the photon $(\mathbf{k}_s, \boldsymbol{\varepsilon}_s)$ and the electron

 $^{^1}$ The Hamiltonian is in SI units. When expressed in CGS units, there is a 1/c extra factor in front of ${\bf A}$.

² This spin-orbit component must not be confused with that of the electronic structure in the material, particularly strong for the atomic core states and which makes magnetism detectable using X-rays.

in state φ_f . The solutions of H_0 can be written as

$$|\phi_{g}\rangle = |\varphi_{g}; \mathbf{k}_{i}, \boldsymbol{\varepsilon}_{i}\rangle, \ H_{0} |\phi_{g}\rangle = \mathcal{E}_{g} |\phi_{g}\rangle \text{ with } \mathcal{E}_{g} = E_{g} + \hbar\omega_{i},$$
 (3.17)

$$|\phi_{\rm f}\rangle = |\varphi_{\rm f}; \mathbf{k}_{\rm s}, \boldsymbol{\varepsilon}_{\rm s}\rangle, \quad H_0 |\phi_{\rm f}\rangle = \mathcal{E}_{\rm f} |\phi_{\rm f}\rangle \quad \text{with } \mathcal{E}_{\rm f} = E_{\rm f} + \hbar\omega_{\rm s},$$
 (3.18)

where \mathcal{E}_g (\mathcal{E}_f) is the total initial (final) energy, E_g (E_f) is the electron initial (final) energy and $\hbar\omega_i$ ($\hbar\omega_s$) the initial (final) photon energy. For practical purposes, we shall use this formulation in the context of transition from one electronic localized state up (or down) to some unlocalized state. We shall thus ascribe a density of states ρ_f to the final state, which is supposed to be not zero on some energy range. In this context the transition probability from $|\phi_g\rangle$ to $|\phi_f\rangle$ is given by

$$W_{\rm fg} = \frac{2\pi}{\hbar} \left| \langle \phi_{\rm f} | T_{\rm I} | \phi_{\rm g} \rangle \right|^2 \rho_{\rm f}, \tag{3.19}$$

where $T_{\rm I}$ is the transition operator given by

$$T_{\rm I} = V_{\rm I} + V_{\rm I}G\left(\mathcal{E}_{\rm g}\right)V_{\rm I}.\tag{3.20}$$

 $G\left(\mathcal{E}_{\mathrm{g}}\right)$ is the resolvent (Green's function) of the total Hamiltonian, that is,

$$G\left(\mathcal{E}_{g}\right) = \lim_{\eta \to 0^{+}} \frac{1}{\mathcal{E}_{g} - H + i\eta}.$$
(3.21)

The zero-order approximation using $T_1 \approx V_I$ gives the second golden rule. In the following, we shall use the first-order approximation where we replace the Green's function of the total Hamiltonian by that of the ground state Hamiltonian. The transition probability we get is the first golden rule, where

$$T_{\rm I} \approx V_{\rm I} + V_{\rm I} G_0 \left(\mathcal{E}_{\rm g} \right) V_{\rm I}.$$
 (3.22)

Inserting in (3.22) the expression of $V_{\rm I}$ given in (3.16) and using q = -e, $g_{\rm L} = 2$, and $\mathbf{B} = -i\,\mathbf{k}\times\mathbf{A}$, one gets to the second order in an e/m expansion

$$T_{\rm I} \approx \frac{e}{m} \left(\mathbf{P} \cdot \mathbf{A} - i \mathbf{S} \cdot \mathbf{k} \times \mathbf{A} \right)$$

$$+ \left(\frac{e}{m} \right)^{2} \left[\frac{m}{2} \mathbf{A} \cdot \mathbf{A} + \left(\mathbf{P} \cdot \mathbf{A} - i \mathbf{S} \cdot \mathbf{k} \times \mathbf{A} \right) G_{0} \left(\mathcal{E}_{\rm g} \right) \left(\mathbf{P} \cdot \mathbf{A} - i \mathbf{S} \cdot \mathbf{k} \times \mathbf{A} \right) \right]$$

$$+ O\left(\frac{e^{3}}{m^{3}} \right).$$

$$(3.23)$$

In this expression, the terms containing just one A reveal processes with one photon, that is, absorption or emission. The terms with two A reveal situations with two photons, one photon in and one photon out, that is, a scattering process. Let us now introduce the expression of the potential vector given in (3.11).

88 Y. Joly

3.4.3 Absorption and Emission

When keeping the annihilation term alone, one gets the operator corresponding to the absorption process:

$$T_{\text{I,abs}} = \frac{e}{m} \sum_{\epsilon, \mathbf{k}} A_{0, \mathbf{k}} a_{\epsilon, \mathbf{k}} \left(\epsilon \cdot \mathbf{P} - i \mathbf{S} \mathbf{k} \times \epsilon \right) e^{i(\mathbf{k} \cdot \mathbf{r} - \omega t)}. \tag{3.24}$$

To get the absorption cross section, one introduces this operator in (3.19) and we divide by the incoming flux (c/V). We get,

$$\sigma_{\text{abs}} = \frac{V}{c} \sum_{f} \frac{2\pi}{\hbar} \left| \langle \phi_f | T_{\text{I,abs}} | \phi_g \rangle \right|^2 \rho_f$$
 (3.25)

$$= \frac{4\pi^2 \alpha \hbar}{m^2 \omega} \sum_{f} \left| \left\langle \varphi_f \left| \hat{O} \right| \varphi_g \right\rangle \right|^2 \rho_f \left(E_f = E_g + \hbar \omega \right), \tag{3.26}$$

where $\alpha = e^2/(2\varepsilon_0 hc) \approx 1/137$ is the fine structure constant, and the operator \hat{O} is given by

$$\hat{O} = (\boldsymbol{\varepsilon} \cdot \mathbf{P} - i\mathbf{S}\mathbf{k} \times \boldsymbol{\varepsilon}) e^{i\mathbf{k} \cdot \mathbf{r}}.$$
 (3.27)

The total energies are given by

$$\mathcal{E}_{g} = E_{g} + \hbar\omega, \quad \mathcal{E}_{f} = E_{f}.$$
 (3.28)

Very often the term corresponding to the magnetic field can be neglected in the X-ray energy range. This means that we use $\hat{O} \approx \epsilon \cdot \mathbf{P} \, \mathrm{e}^{\mathrm{i} \mathbf{k} \cdot \mathbf{r}}$.

The emission is treated identically by keeping the only creation operator. There is no incident flux and the normalization depends on the peculiar process. For a coupling between the continuum and a discrete final level, one gets an emission cross section proportional to the absorption cross section, but with the total energies given by

$$\mathcal{E}_{\rm f} = E_{\rm f} + \hbar\omega, \quad \mathcal{E}_{\rm g} = E_{\rm g}.$$
 (3.29)

3.4.4 Scattering

Now one considers the two photon case. For a scattering process, to get the intensity, one has to divide by the incoming flux (c/V) and multiply by the density of photon in the final state $V(\hbar\omega_{\rm s})^2/(2\pi\hbar c)^3$. One thus multiplies and divides the matrix element $\langle \phi_{\rm f} | T | \phi_n \rangle$ by the square root of the previous factors. To get the scattering amplitude in the conventional unit scale, that is, in number of electrons, one also divides by the classical electron radius $r_0 = e^2/\left(4\pi\varepsilon_0 mc^2\right) = 2.82\times 10^{-5}\,{\rm \mathring{A}}$. We have thus to calculate

$$f = \frac{V\hbar\omega_{\rm s}}{(2\pi\hbar c)^{3/2} r_0} \langle \phi_{\rm f} | T | \phi_{\rm g} \rangle. \tag{3.30}$$

3.4.4.1 Thomson Scattering

We consider the first term with $\mathbf{A} \cdot \mathbf{A}$ in (3.24). The corresponding amplitude is

$$f = \frac{V\hbar\omega_{\rm s}}{(2\pi\hbar c)^{3/2} r_0} \frac{e^2}{2m} \langle \phi_{\rm f} | \mathbf{A} \cdot \mathbf{A} | \phi_{\rm g} \rangle$$
 (3.31)

$$= \frac{\omega_{s}}{\omega_{i}} \boldsymbol{\varepsilon}_{s}^{*} \boldsymbol{\varepsilon}_{i} \left\langle \phi_{f} \left| e^{i(\mathbf{k}_{i} - \mathbf{k}_{s}) \cdot \mathbf{r}} \left(a_{i} a_{s}^{+} + a_{s}^{+} a_{i} \right) \right| \phi_{g} \right\rangle. \tag{3.32}$$

In the elastic case, one gets the Thomson scattering

$$f_{0} = \boldsymbol{\varepsilon}_{s}^{*} \cdot \boldsymbol{\varepsilon}_{i} \left\langle \varphi_{g} \left| e^{i(\mathbf{k}_{i} - \mathbf{k}_{s}) \cdot \mathbf{r}} \right| \varphi_{g} \right\rangle = \boldsymbol{\varepsilon}_{s}^{*} \cdot \boldsymbol{\varepsilon}_{i} \int |\varphi(\mathbf{r})|^{2} e^{-i\mathbf{Q} \cdot \mathbf{r}} d^{3}\mathbf{r},$$
(3.33)

where $\mathbf{Q} = \mathbf{k}_{s} - \mathbf{k}_{i}$.

We now compare this result with the classical demonstration. Then, Thomson scattering is the elastic interaction with a free electron. The vibrating electron acts as a source and the ratio of the radiated field $E_r(r)$ to the incoming field E_i is

$$\frac{E_{\rm r}(r)}{E_{\rm i}} = -r_0 \frac{\mathrm{e}^{\mathrm{i}kr}}{r} \cos \psi,\tag{3.34}$$

 ψ being the angle between the incoming polarization and the outgoing one. It is the scattering angle only when the polarizations are parallel with the scattering plane. One has $\cos \psi = \varepsilon_s^* \cdot \varepsilon_i$. The scattering amplitude expressed in number of electrons is then

$$f = \boldsymbol{\varepsilon}_{s}^{*} \cdot \boldsymbol{\varepsilon}_{i}. \tag{3.35}$$

For one atom with a distribution of charge $\rho(r)$, one just has to integrate over it, taking into account the phase difference between the paths (Fig. 3.7), which is given by

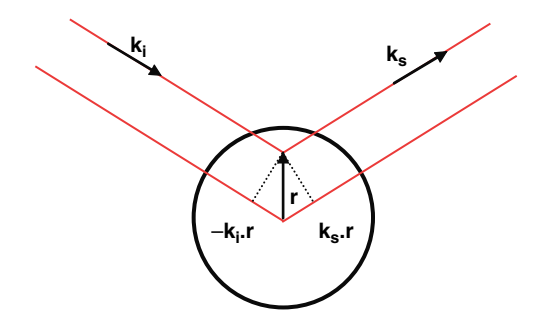
$$\Delta \phi (\mathbf{r}) = (\mathbf{k}_{i} - \mathbf{k}_{s}) \cdot \mathbf{r} = -\mathbf{Q} \cdot \mathbf{r}, \tag{3.36}$$

and the scattering amplitude is thus

$$f(\mathbf{Q}) = \int \rho(\mathbf{r}) e^{-i\mathbf{Q}\cdot\mathbf{r}} d^3\mathbf{r}, \qquad (3.37)$$

that in the limit $\mathbf{Q} \to 0$ yields $f(\mathbf{Q} = 0) = Z$. Finally just multiplying by the scattering amplitude for one electron (3.35), one gets again the formula giving the Thomson scattering amplitude (3.33).

Fig. 3.7 Thomson scattering where the incoming beam with wave vector \mathbf{k}_i is shown scattered at the center and at a point \mathbf{r} in the atom, giving thus a phase difference



In periodic systems, the diffracted peaks are mainly due to this effect. The phase difference between the atoms of the unit cell is taken into account by the Bragg factor, $e^{i\mathbf{Q}\cdot\mathbf{R}_a}$, in such a way that the intensity is given by

$$I(\mathbf{Q}) \propto \left| \boldsymbol{\varepsilon}_{s}^{*} \cdot \boldsymbol{\varepsilon}_{i} \sum_{a} e^{i\mathbf{Q} \cdot \mathbf{R}_{a}} f_{0a}(\mathbf{Q}) \right|^{2},$$
 (3.38)

where \mathbf{R}_a and f_{0a} are, respectively, the position and Thomson scattering amplitude of the atom a. The summation is over all the atoms of the unit cell. From this equation, one sees that there is no σ - π Thomson scattering. Often the electronic density can be considered as spherical around the atoms. Consequently, the Thomson scattering for a specific diffraction vector \mathbf{Q} is mostly isotropic. Note finally that a temperature dependent Debye–Waller factor must also be included in the Bragg factor to take into account the thermal disorder.

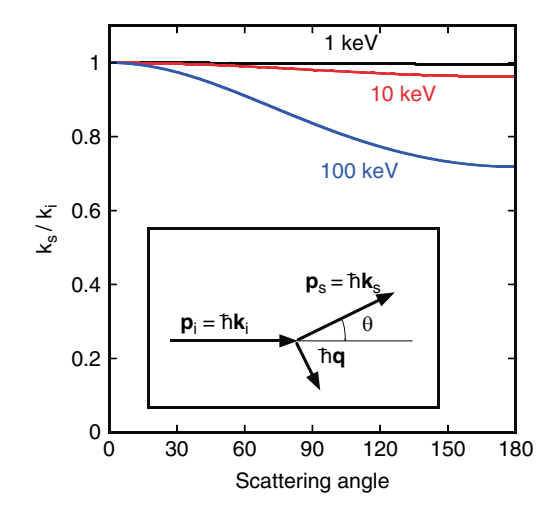
3.4.4.2 Compton Scattering

For completeness one has to touch on the Compton scattering. It corresponds to the inelastic interaction with a free electron. Contrary to Thomson scattering, it cannot be explained purely with light as a wave phenomenon. One has to consider the relativistic energy and momentum conservation laws (Fig. 3.8), and we get then

$$\frac{k_{\rm i}}{k_{\rm s}} = \frac{\hbar\omega_{\rm i}}{\hbar\omega_{\rm s}} = \frac{\lambda_{\rm s}}{\lambda_{\rm i}} = 1 + \lambda_{\rm C}k_{\rm i}\left(1 - \cos\theta\right),\tag{3.39}$$

where θ is the scattering angle and $\lambda_C = \hbar/mc$ is the Compton wavelength. Compton scattering is incoherent and it is often seen as a simple background. This one is small in the X-ray range but increases at higher energy (see Fig. 3.8) and with the scattering angle. For electrons in solids, it gives nevertheless information on the electronic momentum distribution (see Chap. 8).

Fig. 3.8 Compton scattering with the ratio of the outgoing and incoming photon wave vectors vs. the scattering angle and at different energies. The diagram in the inset shows the momenta of the particles



3.4.4.3 Resonant Scattering

Now we consider the second term in the two photon process, the one containing $G_0(\mathcal{E}_g)$ in (3.24). This Green's function applied on the state $|\varphi_n\rangle$ is

$$G_{0}\left(\mathcal{E}_{g}\right)\left|\varphi_{n}\right\rangle = \lim_{\eta \to 0^{+}} \frac{\left|\varphi_{n}\right\rangle\left|\boldsymbol{\varepsilon}_{n}, \mathbf{k}_{n}\right\rangle}{\mathcal{E}_{g} - H_{0} + i\eta}.$$
(3.40)

There are two possibilities. In the first one, the intermediate state already contains the photon of energy $\hbar\omega_s$. In other words, the emitted photon is created before the annihilation of the incoming one. We thus have $\mathcal{E}_g=E_g$ and

$$\mathcal{E}_n = E_n + \hbar \omega_{\rm s}. \tag{3.41}$$

In the second case, there is no photon in the intermediate state. The emitted photon is created after the annihilation of the incoming one. In this case one gets

$$\mathcal{E}_n = E_n. \tag{3.42}$$

One also has for the initial state $\mathcal{E}_{\rm g}=E_{\rm g}+\hbar\omega_{\rm i}$. Consequently, the expression of the scattering amplitude becomes *Resonant case*:

$$f_{(a)} = \frac{\omega_{\rm s}}{\omega_{\rm i}} \frac{1}{m} \lim_{\eta \to 0^{+}} \sum_{n} \frac{\left\langle \varphi_{\rm f} \left| \hat{O}_{\rm s}^{*} \right| \varphi_{n} \right\rangle \left\langle \varphi_{n} \left| \hat{O}_{\rm i} \right| \varphi_{\rm g} \right\rangle}{E_{\rm g} - E_{n} + \hbar \omega_{\rm i} + i \eta}.$$
 (3.43)

Nonresonant case with the photon in the intermediate state:

$$f_{(b)} = \frac{\omega_{\rm s}}{\omega_{\rm i}} \frac{1}{m} \sum_{n} \frac{\left\langle \varphi_{\rm f} \left| \hat{O}_{\rm i} \right| \varphi_{n} \right\rangle \left\langle \varphi_{n} \left| \hat{O}_{\rm s}^{*} \right| \varphi_{\rm g} \right\rangle}{E_{\rm g} - E_{n} - \hbar \omega_{\rm s}}.$$
 (3.44)

In these expressions, the operator $\hat{O}_{i,s}$ has now subscripts corresponding to the incoming and outgoing photons and thus their corresponding wave vector and polarization. Note that for the expression of $f_{(b)}$, one does not need the limit with η because $E_g - E_n$ and $\hbar \omega_s$ are generally of the same sign. On the contrary, $f_{(a)}$ is a resonant process because we can have $E_g - E_n + \hbar \omega_s = 0$. We get a virtual transition because there is an uncertainty on the energy during the interval Δt , such that $\Delta t \Delta E = \hbar$, with $\Delta E = |E_n - E_g - \hbar \omega_s|$. One can also remark that around an absorption edge, the denominator of the resonant term is nearly zero. On the contrary, the denominator of $f_{(b)}$ is around two times the energy edge. Thus $f_{(b)}$ is nearly always negligible in comparison with $f_{(a)}$.

The resonant term is used in many spectroscopies. Depending on the wavelength, different properties of the material can be investigated. Section 3.6 is partly devoted to the use of the resonant term in the X-ray regime.

3.4.4.4 Nonresonant Magnetic Scattering

To end up this part on scattering, one can consider the nonresonant magnetic scattering. This scattering was explained by Blume and Gibbs [11] and first observed in 1981 by de Bergevin and Brunel [12]. It contains the interaction between the magnetic field of the incoming wave with the spin of the electron. It contains also an angular momentum part, which comes from the expansion to first order in $\hbar\omega/\left(E_n-E_g\right)$ of the resonant $f_{(a)}$ and nonresonant $f_{(b)}$ scattering amplitudes. At high energy, one then gets a magnetic scattering amplitude given by

$$f_{\rm m} = -\frac{\hbar\omega}{mc^2} \left[\frac{1}{2} \mathbf{L} \left(\mathbf{Q} \right) \cdot \mathbf{a} + \mathbf{S} \left(\mathbf{Q} \right) \cdot \mathbf{b} \right], \tag{3.45}$$

where **a** and **b** are two vectors depending on the incoming and outgoing wave vectors and polarizations:

$$\mathbf{a} = 2\left(1 - \mathbf{u}_{i} \cdot \mathbf{u}_{s}\right) \boldsymbol{\varepsilon}_{s} \times \boldsymbol{\varepsilon}_{i} - \left(\mathbf{u}_{i} \times \boldsymbol{\varepsilon}_{i}\right) \mathbf{u}_{i} \cdot \boldsymbol{\varepsilon}_{s} + \left(\mathbf{u}_{s} \times \boldsymbol{\varepsilon}_{s}\right) \mathbf{u}_{s} \cdot \boldsymbol{\varepsilon}_{i}, \tag{3.46}$$

$$\mathbf{b} = \boldsymbol{\varepsilon}_{s} \times \boldsymbol{\varepsilon}_{i} - (\mathbf{u}_{i} \times \boldsymbol{\varepsilon}_{i}) \, \mathbf{u}_{i} \cdot \boldsymbol{\varepsilon}_{s} + (\mathbf{u}_{s} \times \boldsymbol{\varepsilon}_{s}) \, \mathbf{u}_{s} \cdot \boldsymbol{\varepsilon}_{i} - (\mathbf{u}_{s} \times \boldsymbol{\varepsilon}_{s}) \times (\mathbf{u}_{i} \times \boldsymbol{\varepsilon}_{i}) \, . (3.47)$$

where $\mathbf{u} = \mathbf{k}/k$ and $\mathbf{S}(\mathbf{Q})$ is the Fourier transform of the spin density, that is of $\rho(r)^{\uparrow} - \rho(r)^{\downarrow}$. The term $\mathbf{L}(\mathbf{Q})$ is related to the Fourier transform of the orbital momentum. It is often a good approximation to take $\mathbf{L}(\mathbf{Q})$ and $\mathbf{S}(\mathbf{Q})$ in the same direction.

The amplitude of the nonresonant magnetic scattering is very small, and neutron diffraction is most often far more sensitive to measure magnetic ordering. Nevertheless, when studying magnetic material using resonant processes, because this term interferes with the other terms, it can gives notable effects on the intensity of some peaks.

3.4.5 Transition Matrix

To obtain the absorption and emission cross sections and the resonant scattering amplitudes, matrix elements of the form $\left\langle \varphi_f \left| \hat{O} \right| \varphi_g \right\rangle$ have to be evaluated. The exponential in the operator can be expanded in terms of $\mathbf{k} \cdot \boldsymbol{\varepsilon}$ and we get to second order for, respectively, its electric and magnetic part:

$$\hat{O}_{e} = \boldsymbol{\varepsilon} \cdot \mathbf{P} e^{i\mathbf{k} \cdot \mathbf{r}} = \boldsymbol{\varepsilon} \cdot \mathbf{P} \left[1 + i\mathbf{k} \cdot \mathbf{r} - \frac{1}{2} (\mathbf{k} \cdot \mathbf{r})^{2} + \cdots \right], \tag{3.48}$$

$$\hat{O}_{\rm m} = -i\mathbf{S}\mathbf{k} \times \boldsymbol{\varepsilon} \, e^{i\mathbf{k}\cdot\mathbf{r}} = -i\mathbf{S}\mathbf{k} \times \boldsymbol{\varepsilon} \left[1 + i\mathbf{k}\cdot\mathbf{r} - \frac{1}{2} \left(\mathbf{k}\cdot\mathbf{r}\right)^2 + \cdots \right]. \quad (3.49)$$

In (3.48), the first term of the expansion is called the *electric dipole* or E1 term. The corresponding operator $\boldsymbol{\varepsilon} \cdot \mathbf{P}$ can be rewritten, thanks to its relation with the commutator, as

$$\boldsymbol{\varepsilon} \cdot \mathbf{P} = \frac{m}{i\hbar} \left[\boldsymbol{\varepsilon} \cdot \mathbf{r}, H_0 \right]. \tag{3.50}$$

Using the relation

$$\langle \varphi_{\rm f} | [\boldsymbol{\varepsilon} \cdot \mathbf{r}, H_0] | \varphi_{\rm g} \rangle = (E_{\rm g} - E_{\rm f}) \langle \varphi_{\rm f} | \boldsymbol{\varepsilon} \cdot \mathbf{r} | \varphi_{\rm g} \rangle,$$
 (3.51)

one gets

$$M_{\rm fg,E1} = \langle \varphi_{\rm f} | \boldsymbol{\varepsilon} \cdot \mathbf{P} | \varphi_{\rm g} \rangle = i \frac{m}{\hbar} (E_{\rm f} - E_{\rm g}) \langle \varphi_{\rm f} | \boldsymbol{\varepsilon} \cdot \mathbf{r} | \varphi_{\rm g} \rangle.$$
 (3.52)

Let us calculate now the second term of the expansion of the electric operator. To get the corresponding matrix, one sets the polarization along the y-axis and the wave vector along z. Then we use

$$\frac{m}{2\hbar} [zy, H_0] = \frac{m}{2\hbar} ([z, H_0] y + z [y, H_0]) = \frac{i}{2} (P_z y + z P_y)
= \frac{i}{2} (2P_z y - P_z y + z P_y) = i P_z y - \frac{i}{2} L_x,$$
(3.53)

where L_x is the x component of the orbital angular moment L. For any direction, we thus get

$$i \mathbf{P} \cdot \boldsymbol{\varepsilon} \mathbf{k} \cdot \mathbf{r} = \frac{m}{2\hbar} \left[\boldsymbol{\varepsilon} \cdot \mathbf{r} \mathbf{k} \cdot \mathbf{r}, H_0 \right] + \frac{i}{2} \mathbf{k} \times \boldsymbol{\varepsilon} \cdot \mathbf{L}.$$
 (3.54)

The first term of the second member of this expression gives the *electric quadrupole* or E2 contribution:

$$M_{\text{fg},E2} = i \frac{m}{\hbar} \left(E_{\text{f}} - E_{\text{g}} \right) \frac{i}{2} \left\langle \varphi_{\text{f}} \left| \boldsymbol{\varepsilon} \cdot \mathbf{r} \right| \mathbf{k} \cdot \mathbf{r} \right| \varphi_{\text{g}} \right). \tag{3.55}$$

The second term of the second member depending on orbital moment **L** is magnetic. Consequently, it is grouped with the zero order of the expansion coming from the spin contribution. The new term is called the *magnetic dipole* or M1 term:

$$M_{\text{fg},M1} = \frac{1}{2} \langle \varphi_{\text{f}} | \mathbf{k} \times \boldsymbol{\varepsilon} \cdot (\mathbf{L} + 2\mathbf{S}) | \varphi_{\text{g}} \rangle. \tag{3.56}$$

The M1 contribution is very small in the X-ray energy range because it involves a nearly zero radial integral (it acts only on m and σ , the corresponding selection rule being $\Delta \ell = 0$).

3.4.6 Selection Rules

We have to calculate

$$\langle \varphi_{f} | \hat{o} | \varphi_{g} \rangle_{\sigma} = \sigma \int \varphi_{f}^{*}(\mathbf{r}, \sigma) \, \hat{o}(\mathbf{r}) \, \varphi_{g}(\mathbf{r}, \sigma) \, d^{3}\mathbf{r}.$$
 (3.57)

When considering only the E1 and E2 transitions, there is no possibility of spin flip during the transition; thus the sum on the spin is reduced to one index, σ , set outside. Here the operator just contains the terms inside the matrix of (3.52) for E1 and (3.55) for E2, that is,

$$\hat{o} = \boldsymbol{\varepsilon} \cdot \mathbf{r} \left(1 + \frac{1}{2} i \mathbf{k} \cdot \mathbf{r} \right). \tag{3.58}$$

The core state g is localized, thus the integral has to be performed only inside the absorbing atom. The expansion of f, \hat{o} , and g in spherical harmonics is consequently very convenient because it singles out the angular momentum quantum numbers explicitly, and separates the radial and angular dependences.

3.4.6.1 Final States

In the nonmagnetic case, the final (or intermediate) state can be written as

$$\bar{\varphi}_{f}(\mathbf{r}) = \sum_{\ell,m} a_{\ell,m}^{f}(E) \,\bar{b}_{\ell}(E,r) \, Y_{\ell}^{m}(\Omega) \,, \tag{3.59}$$

where $\mathbf{r} = (r, \Omega)$ is expressed in spherical coordinates and $\bar{b}_{\ell}(E, r)$ is the radial component of the wave function inside the atom. It is obtained by solving the radial Schrödinger equation in the atom. It weakly depends on the photoelectron energy E. The bar is to show a specific normalization, which will be seen in Sect. 3.7.2. The $a_{\ell,m}^f(E)$ are the amplitudes.³

In the magnetic case, if one neglects the spin–orbit coupling, a single sum over σ is to be included:

$$\bar{\varphi}_{f}(\mathbf{r}) = \sum_{\ell,m,\sigma} a_{\ell,m,\sigma}^{f}(E) \,\bar{b}_{\ell,\sigma}(E,r) \, Y_{\ell}^{m}(\Omega) \, \chi_{\sigma}, \tag{3.60}$$

where the spin state is given by

$$\chi_{\frac{1}{2}} = \begin{pmatrix} 1 \\ 0 \end{pmatrix}, \quad \chi_{-\frac{1}{2}} = \begin{pmatrix} 0 \\ 1 \end{pmatrix}. \tag{3.61}$$

When one considers the spin-orbit coupling, the final state is written as

$$\bar{\varphi}_{f}(\mathbf{r}) = \sum_{\ell, m, s} a_{\ell, m + \frac{1}{2} - s, s}^{f}(E) \bar{b}_{\ell, m + \frac{1}{2} - \sigma, s}^{\sigma}(E, r) Y_{\ell}^{m + \frac{1}{2} - \sigma}(\Omega) \chi_{\sigma}.$$
 (3.62)

Note that in this case, the spherical harmonics are necessarily the complex ones. This expression comes from the solution of the Dirac equation for the atom. σ is not anymore a good quantum number. We replace it by the index s. Because of the spin-orbit coupling, the $(\ell, m, \frac{1}{2})$ and $(\ell, m+1, -\frac{1}{2})$ components are part of the same state. This is what gives the eventual spin flip during the photoelectron scattering.

3.4.6.2 Initial States

Now let us look at the initial states. They are localized and the expansion seen in the previous expression is limited to one or two components. For example, at the K edge, one has $\ell=0$ and two initial states

$$\left|\frac{1}{2}, -\frac{1}{2}\right| = b_{0\frac{1}{2}}(r) Y_0^0 \chi_{-\frac{1}{2}}, \tag{3.63}$$

$$\left|\frac{1}{2}, \frac{1}{2}\right| = b_{0\frac{1}{2}}(r) Y_0^0 \chi_{\frac{1}{2}}.$$
(3.64)

³ When using the monoelectronic approach, the $a_{\ell,m}^f(E)$ contain the main dependence on the energy E. They are obtained using the continuity of the wave function and its derivative between the atom and its surrounding. In the other approaches, they are just normalization coefficients, and the energy dependence is put outside the transition matrix. At this stage, whatever is the method, our demonstration is general.

At the L_{II} edge, one has $\ell = 1$, j = 1/2, and two initial states

$$\left|\frac{1}{2}, -\frac{1}{2}\right\rangle = b_{1\frac{1}{2}}(r) \left(-\sqrt{\frac{2}{3}} Y_{1}^{-1} \chi_{\frac{1}{2}} + \sqrt{\frac{1}{3}} Y_{1}^{0} \chi_{-\frac{1}{2}}\right),$$

$$\left|\frac{1}{2}, \frac{1}{2}\right\rangle = b_{1\frac{1}{2}}(r) \left(-\sqrt{\frac{1}{3}} Y_{1}^{0} \chi_{\frac{1}{2}} + \sqrt{\frac{2}{3}} Y_{1}^{1} \chi_{-\frac{1}{2}}\right).$$

$$(3.65)$$

At the L_{III}- edge, one has $\ell = 1$, j = 3/2, and four initial states

$$\begin{vmatrix} \frac{3}{2}, -\frac{3}{2} \end{pmatrix} = b_{1\frac{3}{2}}(r) Y_{1}^{-1} \chi_{-\frac{1}{2}}, \qquad (3.66)$$

$$\begin{vmatrix} \frac{3}{2}, -\frac{1}{2} \end{pmatrix} = b_{1\frac{3}{2}}(r) \left(\sqrt{\frac{1}{3}} Y_{1}^{-1} \chi_{\frac{1}{2}} + \sqrt{\frac{2}{3}} Y_{1}^{0} \chi_{-\frac{1}{2}} \right), \qquad \qquad \begin{vmatrix} \frac{3}{2}, \frac{1}{2} \end{pmatrix} = b_{1\frac{3}{2}}(r) \left(\sqrt{\frac{2}{3}} Y_{1}^{0} \chi_{\frac{1}{2}} + \sqrt{\frac{1}{3}} Y_{1}^{1} \chi_{-\frac{1}{2}} \right), \qquad \qquad \qquad \begin{vmatrix} \frac{3}{2}, \frac{3}{2} \end{pmatrix} = b_{1\frac{3}{2}}(r) Y_{1}^{1} \chi_{\frac{1}{2}}.$$

In general, when using complex harmonics, one can just write

$$\varphi_{\mathbf{g}} = \sum_{\sigma} G_{\mathbf{g}}^{\sigma} b_{\mathbf{g}}(r) Y_{\ell_{\mathbf{g}}}^{m_{\mathbf{g}} + \frac{1}{2} - \sigma} \chi_{\sigma}. \tag{3.67}$$

3.4.6.3 Operator

The operator can also be expanded in spherical harmonics:

$$\hat{o} = \boldsymbol{\varepsilon} \cdot \mathbf{r} \left(1 + \frac{1}{2} i \mathbf{k} \cdot \mathbf{r} \right) = \sum_{\ell_0, m_0} \left(\frac{i}{2} k \right)^{\ell_0 - 1} c_{\ell_0, m_0} r^{\ell_0} Y_{\ell_0}^{m_0} \left(\Omega \right), \tag{3.68}$$

where the c_{ℓ_0,m_0} are specific coefficients with their operator quantum numbers (ℓ_0,m_0) . For example, for a polarization along z and a wave vector along x, one gets

$$\boldsymbol{\varepsilon} \cdot \mathbf{r} = z = r \cos \theta = \sqrt{\frac{4\pi}{3}} r Y_1^0, \tag{3.69}$$

$$\frac{\mathrm{i}}{2}\boldsymbol{\varepsilon} \cdot \mathbf{r} \ \mathbf{k} \cdot \mathbf{r} = \frac{\mathrm{i}}{2}kzx = \frac{\mathrm{i}}{2}kr^2 \sin\theta\cos\varphi = \frac{\mathrm{i}}{2}k\sqrt{\frac{4\pi}{15}}r^2Y_2^1, \tag{3.70}$$

where we have used the real spherical harmonics, which if needed can be expressed in terms of the complex spherical harmonics.

3.4.6.4 The Transition Matrix

We can now gather (3.62), (3.67), and (3.68). The transition matrix for each spin σ is then

$$\langle \varphi_{f} | \hat{o} | \varphi_{g} \rangle_{\sigma} = \sum_{o} \left(\frac{i}{2} k \right)^{\ell_{o} - 1} c_{\ell_{o}, m_{o}} \sum_{\ell, m} \Gamma_{\ell, m + \frac{1}{2} - \sigma}^{\ell_{g}, m_{g} + \frac{1}{2} - \sigma, \ell_{o}, m_{o}} \times \sum_{s} \mathcal{R}_{\ell, m + \frac{1}{2} - \sigma, s}^{g, \ell_{o}, \sigma} (E) a_{\ell, m + \frac{1}{2} - s, s}^{f} (E),$$
(3.71)

where

$$\mathcal{R}_{\ell,m+\frac{1}{2}-\sigma,s}^{g,\ell_0,\sigma}(E) = \int_0^R \bar{b}_{\ell,m+\frac{1}{2}-s,s}^{\sigma*}(E,r) \, b_{\rm g}(r) \, r^{2+\ell_0} \mathrm{d}r, \tag{3.72}$$

is the radial integral performed up to the atom radius R, and

$$\Gamma_{\ell,m}^{\ell_{g},m_{g},\ell_{o},m_{o}} = G_{g}^{\sigma} \int_{\text{sphere}} Y_{\ell}^{m*} \left(\Omega\right) Y_{\ell_{o}}^{m_{o}} \left(\Omega\right) Y_{\ell_{g}}^{m_{g}} \left(\Omega\right) d\Omega \tag{3.73}$$

is the angular integral or Gaunt coefficient multiplied by the factor G_{g}^{σ} coming from the initial state. It is usually expressed in terms of Clebsch-Gordan coefficients. The angular integral is not zero only for peculiar value of ℓ , m:

- ℓ must have the same parity than $\ell_g + \ell_o$
- $\left|\ell_{g}-\ell_{o}\right| \leq \ell \leq \left|\ell_{g}+\ell_{o}\right|$
- $m = m_0 + m_g$.

The last condition on m is when using complex spherical harmonics. When using the real ones the conditions are

- When $m_0 m_g = 0, m = m_0 + m_g$
- When $m_0 m_g > 0$, $m = |m_0 + m_g|$ and $m = |m_0 m_g|$ When $m_0 m_g < 0$, $m = -|m_0| |m_g|$ and $m = -|m_0 + m_g|$.

For the dipole and quadrupole components, we have, respectively, $\ell_{\rm o}=1$ and $\ell_0 = 2$. Thus, the difference on ℓ between the initial and the final state is

- Dipole: $\Delta \ell = \pm 1$
- Quadrupole: $\Delta \ell = 0, \pm 2.$

The orbitals probed at the different edges are summarized in Table 3.1.

At the K edge, the initial state is 1s and the Gaunt coefficients are equal to $(1/\sqrt{4\pi}) \, \delta_{\ell,\ell_0} \delta_{m,m_0}$. The corresponding effect of the selection rule on the probed orbital is shown in Fig. 3.9. One considers an atom in an octahedral surrounding, for

Edge	Dipole probed state	Quadrupole probed state		
$\begin{array}{c} K, L_{I}, M_{I}, N_{I}, O_{I} \\ L_{II}, L_{III}, M_{II}, M_{III}, N_{III}, N_{III}, O_{II}, O_{III} \\ M_{IV}, M_{V}, N_{IV}, N_{V}, O_{IV}, O_{V} \end{array}$	p s-d p-f	s-d p-f s - d-g		

Table 3.1 Probed states for the dipole and quadrupole transition for the different edges

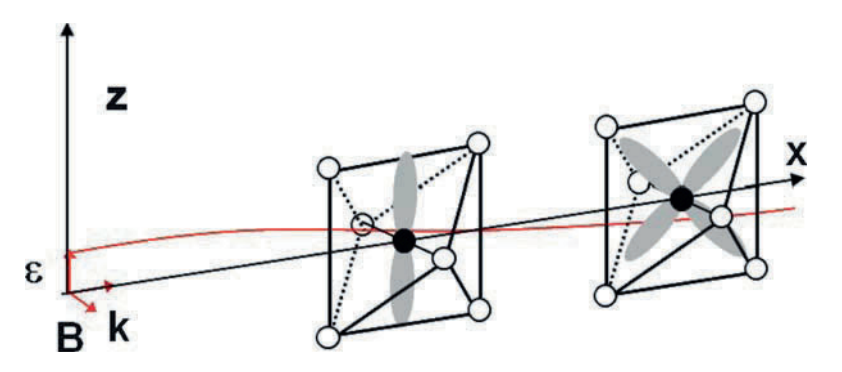


Fig. 3.9 Selection rule in the K-edge case. An octahedron is surrounding a 3d element. When the polarization is along z and the wave vector along x, the dipole probed orbital is p_z and the quadrupole probed orbital is $3d_{xz}$. When rotating the sample by 90° , the probed 3d state by the E2 channel can correspond to an e_g state or to a t_{2g} state

instance, a 3d element. It is oriented in a specific way with respect to the incoming electromagnetic wave, which has its polarization along z and its wave vector along x. The electric field of the wave makes the core 1s electron vibrating to first order (for the dipole) in the vertical direction, like a p_z . The core electron can thus jump into the empty $4p_z$ state above the Fermi level. When the energy is sufficiently high, or the wave length sufficiently short in comparison with the 1s orbital radius, the vibration is not anymore exactly along z. There is a phase difference along x, resulting in a d_{xz} -like vibration component. The core electron can thus jump into the $3d_{xz}$ final state. This is a quadrupole transition.

3.5 Dielectric Function or Macroscopic Point of View

We briefly recall the definitions of the values permitting to describe macroscopically a dielectric. The aim is to connect the susceptibility, the permittivity, and the refractive index with the scattering factor used in the microscopic point of view.

A dielectric is a nonconducting substance where any volume element $d\tau$ has a dipole electric moment $d\mathcal{M}$. It can be permanent or induced by an external electric fields **E**. The polarization vector **P** is defined by

$$d\mathcal{M} = \mathbf{P}d\tau. \tag{3.74}$$

The electric displacement at a point M is defined by

$$\mathbf{D}(\mathbf{M}) = \varepsilon_0 \mathbf{E}(\mathbf{M}) + \mathbf{P}(\mathbf{M}). \tag{3.75}$$

For a linear (see Sect. 3.4.1) dielectric medium, the relation between the electric displacement and the electric field is

$$\begin{pmatrix} D_{x} \\ D_{y} \\ D_{z} \end{pmatrix} = \begin{pmatrix} \varepsilon_{xx} & \varepsilon_{xy} & \varepsilon_{xz} \\ \varepsilon_{yx} & \varepsilon_{yy} & \varepsilon_{yz} \\ \varepsilon_{zx} & \varepsilon_{zy} & \varepsilon_{zz} \end{pmatrix} \begin{pmatrix} E_{x} \\ E_{y} \\ E_{z} \end{pmatrix}, \tag{3.76}$$

where ε is the dielectric constant. Defining the electric susceptibility χ and the relative permittivity ε_r by $\varepsilon = \varepsilon_0 \varepsilon_r = \varepsilon_0 (1 + \chi)$, one gets

$$\mathbf{P} = \varepsilon_0 \chi \mathbf{E}. \tag{3.77}$$

For an isotropic material, the refractive index is given by

$$n = \sqrt{\varepsilon_r}. (3.78)$$

For an anisotropic material, the refractive index is a vector defined by

$$\mathbf{n} = \frac{c}{\omega}\mathbf{k},\tag{3.79}$$

where \mathbf{k} is the wave vector, c the speed of light, and ω the pulsation. One gets the components of the refractive index from the Maxwell equations. For a plane wave, we find

$$\mathbf{D} = \mathbf{n}^2 \mathbf{E} - (\mathbf{n} \cdot \mathbf{E}) \,\mathbf{n}. \tag{3.80}$$

Using the matrix relation between $\bf D$ and $\bf E$ and substituting $\bf D$ by (3.80), one obtains the Fresnel equation

$$\mathbf{n}^{2} \left(\widehat{\varepsilon}_{x} n_{x}^{2} + \widehat{\varepsilon}_{y} n_{y}^{2} + \widehat{\varepsilon}_{z} n_{z}^{2} \right) - n_{x}^{2} \widehat{\varepsilon}_{x} \left(\widehat{\varepsilon}_{y} + \widehat{\varepsilon}_{z} \right) - n_{y}^{2} \widehat{\varepsilon}_{y} \left(\widehat{\varepsilon}_{x} + \widehat{\varepsilon}_{z} \right) - n_{z}^{2} \widehat{\varepsilon}_{z} \left(\widehat{\varepsilon}_{x} + \widehat{\varepsilon}_{y} \right) + \widehat{\varepsilon}_{x} \widehat{\varepsilon}_{y} \widehat{\varepsilon}_{z} = 0,$$

$$(3.81)$$

where $(\widehat{\varepsilon}_x, \widehat{\varepsilon}_y, \widehat{\varepsilon}_z)$ are the eigenvalues of the permittivity matrix, defining the principal axis.

3.5.1 Complex Permittivity

In this section, we use classical equations to define a resonant system. When comparing with the quantum mechanical scattering factor calculated in Sect. 3.4.4, we shall see that the resulting expressions have strong similarities. First we consider the

differential equation of motion for an electron in a molecule:

$$m\frac{\mathrm{d}^2\mathbf{r}}{\mathrm{d}t^2} = -k\mathbf{r} - \frac{m}{\tau}\frac{\mathrm{d}\mathbf{r}}{\mathrm{d}t} - e\mathbf{E}_{\mathrm{l}},\tag{3.82}$$

where $\mathbf{E}_{l} = \mathbf{E} + \mathbf{P}/3\varepsilon_{0}$ is the local field, τ some damping, m, e, and \mathbf{r} the mass, the absolute charge, and the position of the electron, respectively. Putting $\mathbf{P} = 2Ne\mathbf{r}$, where N is the number of electrons per unit volume, we find the relation between \mathbf{E} and \mathbf{P} , and the electric susceptibility is given by

$$\chi = \frac{\chi_0 \omega_1^2}{\omega_1^2 - \omega^2 + i\frac{\omega}{\tau}},\tag{3.83}$$

where

$$\chi_0 = \frac{2Ne^2}{\varepsilon_0 m\omega_1^2} \tag{3.84}$$

is the susceptibility at $\omega=0$. From the (3.83), the complex relative permittivity (or dielectric function) can be expressed as

$$\varepsilon_{\rm r}(\omega) = \varepsilon_{\rm r}'(\omega) + i\varepsilon_{\rm r}''(\omega),$$
 (3.85)

where its real and imaginary parts are given by

$$\varepsilon_{\rm r}'(\omega) - 1 = \frac{\chi_0 \omega_1^2 \left(\omega_1^2 - \omega^2\right)}{\left(\omega_1^2 - \omega^2\right)^2 + \frac{\omega^2}{\tau^2}}, \quad \varepsilon_{\rm r}''(\omega) = \frac{\chi_0 \omega_1^2 \frac{\omega}{\tau}}{\left(\omega_1^2 - \omega^2\right)^2 + \frac{\omega^2}{\tau^2}}.$$
 (3.86)

When plotting (Fig. 3.10) these quantities, we find the typical resonant shapes for the imaginary and real part of the amplitude. From this simple consideration and

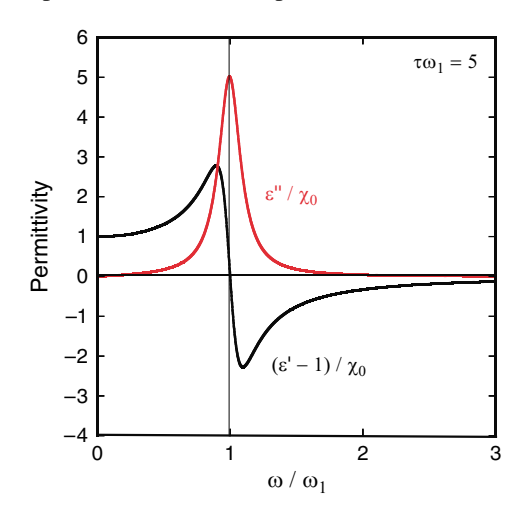


Fig. 3.10 Real and imaginary part of the permittivity for $\tau\omega_1 = 5$. At high frequency, corresponding to the X-ray range, the real part is negative. The refractive index is thus less than unity

taking into account that the main resonance pulsation ω_1 is in the ultraviolet range, one gets the Cauchy formula giving the dependence of the refractive index on the wavelength at low frequency (i.e., in the visible):

$$n^2 = n_0^2 + \frac{A}{\lambda^2},\tag{3.87}$$

with $A = 4\pi^2 \chi_0 c^2/\omega_1^2$. We also obtain the value inferior to unity for the refractive index at high frequency, that is, in the X-ray range.

3.5.2 Complex Refractive Index

With a complex permittivity, one also gets a complex refractive index and a complex wave vector. We have

$$k^2 = \frac{\omega^2}{c^2} \left(\varepsilon_{\rm r}' + i \varepsilon_{\rm r}'' \right). \tag{3.88}$$

Setting k = k' + ik'', one gets

$$k'^2 - k''^2 = \frac{\omega^2}{c^2} \varepsilon_{\rm r}', \quad k'k'' = \frac{\omega^2}{c^2} \varepsilon_{\rm r}''.$$
 (3.89)

So, for a plane wave along z, there is a damping given by $e^{ikz} = e^{ik'z}e^{-k''z}$. The complex refractive index is simply defined by

- $n' = k'c/\omega$ is the refractive index
- $n'' = k''c/\omega$ is the extinction index.

Around ω_1 , there is an absorption and an *anomalous* dispersion. Far from ω_1 , there is no absorption and a *normal* dispersion.

From these relations, reflection and transmission coefficients can be calculated for an incident electromagnetic wave when interacting with a surface separating two media of different refractive indices. It is then possible to get a relation between the orientation of the polarization of an electromagnetic wave after reflection by a surface in terms of the permittivity. In the visible range, it is one of the goals of *ellipsometry*. Another one is, knowing the refractive index, to determine the thickness and roughness of a surface. For magnetic materials, the equivalent technique is called *Kerr effect*.

At higher energy, in the soft X-ray range, reflectivity is a tool to get magnetic moment and thickness as a function of depth in a material. The connection with resonant scattering factor $f(\mathbf{Q}, \omega)$ is effective in this technique, and we can write the relation between the refractive index n and $f(\mathbf{Q}, \omega)$:

$$n\left(\mathbf{Q},\omega\right) = 1 - \frac{2\pi N_{\mathrm{a}} r_{\mathrm{0}}}{k^{2}} f(\mathbf{Q},\omega),\tag{3.90}$$

with r_0 the classical electron radius, N_a the number of atom per unit volume, and **Q** the diffraction vector. For a magnetic system, the scattering factor itself depends, as seen previously, on a nonresonant and a resonant part. The \mathbf{Q} dependence of nshows its angular dependence.

3.6 X-Ray Spectroscopies

In Sect. 3.4, we have seen the case of the interaction of a photon with an electron, making a transition between two levels. It is implied that the electron is in some atom. In this section, we focus on the X-ray spectroscopies. The corresponding energies make that the transition is necessarily between a core level and some other unoccupied level above the Fermi energy (or above the highest molecular occupied orbital to adopt the chemistry terminology).

The series of ionization edges gives evidence of the existence of the electronic energy levels in the atom. They are labeled by a letter K, L, M, N, and O according to the principal quantum number, n = 1, 2, 3, 4, and 5. The atomic levels are also split according to the orbital momentum quantum number ℓ and to $j = |\ell + s|$, where $s = \pm \frac{1}{2}$ is the spin. These sublevels are labeled using the subscripts I, II, III, IV, and V (see Table 3.2).

The expressions of the core level wave functions corresponding to the K, L_{II}, and L_{III} edges were given in Sect. 3.4.6. The energies spread from 13.6 eV for the K edge of hydrogen (defining the Rydberg unit) up to 115, 606 eV for the K edge of uranium. The K edges of the light elements and the $L_{II\,III}$ edges of the 3d elements are in the soft X-ray energy range.

In fact, the atom is embedded in a molecule or in a solid and, often, the final states for the photoelectron cannot be considered as completely localized. The description is very different depending upon the localization of the final states (atom-like or band-like). For the moment, we remain with a final (or intermediate state) at least partially nonlocalized and thus with some hybridization with the environment. The transition probability depends on the transition matrix seen in Sect. 3.4, which itself depends on the final states. X-ray spectroscopies are thus necessarily a direct probe of the density of states, or at least its projection on the absorbing atom. This density of states depends on the position of the atoms in the neighborhood and thus

Table 3.2 Corresponde	nce between	the edge nam	es and the quantum numb	pers of the core states
Edge	ℓ	j	Spectro. notat.	No. of electrons
K, L_I, M_I, N_I, O_I	0	1/2	S _{1/2}	2
$L_{II}, M_{II}, N_{II}, O_{II}$	1	1/2	$p_{1/2}$	2

3/2

3/2

5/2

1

2

2

 L_{III} , M_{III} , N_{III} , O_{III}

 M_{IV} , N_{IV} , O_{IV}

 M_V, N_V, O_V

The two last columns give the corresponding spectroscopic notation and the number of electrons

 $p_{3/2}$

 $d_{3/2}$

 $d_{5/2}$

4

4

6

absorption spectroscopies are also indirect probes of the geometrical surrounding (interatomic distances and symmetry).

The transition can be observed by different detection modes. One can simply measure the attenuation, that is, the damping, of the X-ray beam through a sample. This is the most frequent measurement of X-ray absorption fine structure spectra for powder samples. For monocrystalline samples or for surface sensitive measurements, fluorescence or secondary electron emission measurements can be preferred. They are in principle nearly proportional to the transition process but, due to experimental reasons (self-absorption, for instance), strong divergence can be observed.

Irrespective of the detection mode, X-ray absorption spectroscopies are local spectroscopies. They are chemically selective because of the energy of the edges. They are also selective on the second (or total) angular quantum number of the final states. However, the processes involved are complex. There is no single transition of one electron from one level to another level. The scheme is more complex because during this transition, all the other electrons would have to be included in the process. The photoelectron probes final states, which see a core hole. When the interaction with the hole is too strong, it must be taken into account within a multi-electronic scheme. The other electrons tend also to screen the core hole. In any case, the probed density of states is not the ground density of states but an excited one.

3.6.1 Characteristic Times

The main interaction of light with matter, at least in the energy range considered here, is the photon absorption, in which a core (for X-rays) electron is promoted to some higher level. The transition process is not limited to this single electron; it is a multielectronic process that involves a complete reorganization of the electronic (and vibrating, . . .) configuration. The limit of validity of the monoelectronic approach can be understood by looking at the various characteristic times in the absorption process:

- Duration of the photon absorption process. It is given by $t_1 = 1/W_{\rm fg}$, where $W_{\rm fg}$ is the transition rate. We have $t_1 < 10^{-20}$ s.
- Lifetime of the core hole. It is given by $t_2 = \hbar/\Delta E_{\rm g}$, where $\Delta E_{\rm g}$ is the core level width. For the 1s level and for Z=20 up to Z=30, $\Delta E_{\rm g}\approx 1\,{\rm eV}$; thus, $10^{-16}\,{\rm s} < t_2 < 10^{-15}\,{\rm s}$.
- Relaxation time of the electrons. It is the effect on all the electrons of the field created by the hole and the photoelectron. It is intrinsically a multielectronic effect. The associated time is also 10^{-16} s < $t_3 < 10^{-15}$ s.
- Traveling time of the photoelectron outward from the atom. It depends on the photoelectron kinetic energy E_c . For $1 < E_c < 100 \,\mathrm{eV}$, we have $10^{-17} \,\mathrm{s} < t_4 < 10^{-15} \,\mathrm{s}$.
- Thermal vibration. The time scale associated to the thermal displacements extends from about 10^{-11} down to 10^{-14} s.

We see that the thermal time scale is far larger that the other ones; thus, in most cases the thermal aspect can be seen as independent of the other phenomena. For this adiabatic approximation, it is often said that the photon sees a rigid but slightly disordered arrangement of atoms. Nevertheless, in the soft X-ray range, for example, at the K edge of carbon in small molecules, the vibrational modes can sometimes be observed.

More interestingly, it can be noted that t_2 , t_3 , and t_4 can be of the same order. It is the condition to have multielectronic processes involved. For this, the first condition is that the photoelectron has a very low kinetic energy. The second condition, as stated earlier, is that the final state is localized. We know that it is typically the case of the $L_{II,III}$ edges of the 3d elements and even more of the $M_{IV,IV}$ edges of the 4f elements. Nevertheless, there is an experimental way to check when it is the case. One just has to look at the edge shape. When the edge is more or less step-like, the final states are not localized. It is the case at K edges (except for some light elements where the electron probes unoccupied molecular orbitals) and at the L_{II III} edges of the heavy elements. On the contrary, the edge shape can be more or less peak-like, that is, that some electron volt after the usual increase, the absorption cross section decreases sharply, to go back to nearly zero. This means that the probed states are localized in energy as well as in space. In the first case, the simulation of such spectra can be performed using monoelectronic simulations. The difficulties are that, the state being not localized, the electronic structure must be evaluated in a sufficiently large volume around the absorbing atom. In the second case, multielectronic calculations are necessary. When the localization is very high, atomic multiconfiguration calculations where the surrounding symmetry breaking is just parametrized are often sufficient. It is the domain of multiplet theory. Unfortunately, it exists in intermediate situations where the edge starts with an intense peak, the absorption cross section then decreasing rather strongly but not completely vanishing above the edge. In these cases, multielectronic and multiatomic calculations are mandatory. The theories that account for these multiprocesses are presently in progress. There are three main tracks: the multichannel approach [13], the use of the Bethe-Salpeter equation [14], and the time-dependent density functional theory (TDDFT) [15, 16].

3.6.2 The Different Spectroscopies

We treat the spectroscopies related to the transition of a core level up to some excited level. We recall that this transition that involves a photon absorption can be real or virtual.

3.6.2.1 Real Absorption

X-ray absorption spectroscopy (XAS) is the general name for the techniques measuring in some way the photon absorption. A distinction is first made according to

the energy range under study. In the wide range from around 50 eV after the edge up to several hundredth (or even some thousands) of electron volt, the spectroscopy is called EXAFS for Extended X-ray Absorption Fine Structure. This spectroscopy is particularly sensitive to the radial distances of the different shells of neighboring atoms (two shells, sometimes more) around the absorbing atom. It also gives the number of atoms by shell albeit with less precision, because this number is correlated with the thermal disorder. The data analysis is performed by comparison with simulations where the calculated spectra is built by simple superposition of outgoing and backscattered electron waves by the different shells. It is the interference phenomena on the absorbing atom that depend on the shell distances from the central atom and on the photoelectron energy, which are responsible for the oscillating aspect of the spectra [18] and thus of the sensitivity of the method. Actual analysis go farther than the single scattering process by considering a multiple scattering phenomena limited to some paths between the atoms.

At low kinetic energy of the photoelectron, that is, from the rising edge up to around 100 eV, the absorption spectroscopy is called XANES for *X-ray absorption near edge spectroscopy*. This spectroscopy is sensitive to the three-dimensional aspect of the geometry around the absorbing atom. As stated earlier, it is also directly sensitive to the electronic structure around the absorbing atom.

In the XANES energy range, analysis as a function of the polarization are often done. Using a single crystal of a material with some preferential arrangement, as on a surface, one can perform studies with different orientations of the sample. When the incoming electromagnetic wave field is linearly polarized, the corresponding spectroscopy is called *linear dichroism*. When it is circularly polarized, the difference between the absorption spectra recorded using right and left polarizations is measured (Fig. 3.5). This technique is very useful to study ferromagnetic or ferrimagnetic systems (in antiferromagnetic systems, it gives no intensity!). It is called *X-ray magnetic circular dichroism* (XMCD). Without magnetism, this technique also exists for materials of peculiar symmetry. It gives a small but detectable signal. It is called *natural circular dichroism*. More recently, a new technique has surged with the time analysis of the rotation of orbitals under magnetic field. It is called *X-ray detected magnetic resonance* (XDMR).

From the absorption techniques, one derives many other techniques as *X-ray photoelectron spectroscopy* (XPS) and, with angular resolution on the emitted electron, *photodiffraction*. At lower energy and with a better resolution, it is called *angle-resolved photoelectron spectroscopy* (ARPES) [21]. It is particularly well adapted to study tiny details in the band structure and is presently extensively used for the analysis of superconducting materials.

It can be noted that an equivalent absorption spectroscopy is performed in the electronic microscope. It is the *electron energy loss spectroscopy* (EELS) where the incoming photons are replaced by an incoming energetic electron beam. The measured spectra are very similar (but with a slightly lower resolution) to the X-ray absorption spectra obtained with synchrotron radiation. The main dipolar contribution is equivalent. The smaller quadrupolar contribution obtained when increasing

the electron scattering angle is different. Recent studies claim for Ångström lateral resolution, thanks to the Ångström-size electron beam.

3.6.2.2 Virtual Absorption

When the transition is virtual, or as is more usually said, for a resonant scattering process, different spectroscopies are used. In the context of elastic scattering in diffraction mode, a distinction is made depending on the energy range, as in the XAS case. The equivalent to EXAFS is called *diffraction anomalous fine structure spectroscopy* (DAFS). The diffraction peaks are then measured along a wide energy range. On the contrary, when measuring spectra just around the edge (as in XANES), the DAFS is called *diffraction anomalous near edge structure* (DANES) or *resonant X-ray scattering* (RXS) or *resonant X-ray diffraction* (RXD). There is a third technique where the intensity of the reflections is recorded only at some points in energy around the edge. This is a way to increase the sensitivity of the diffraction technique on some specific atoms (corresponding to the energy edge). This technique is called *multi-wavelength anomalous diffraction* (MAD). It is often used for complex materials, particularly in biology, to help with structure resolution.

3.6.3 Fluorescence and Auger Spectroscopies

Two spectroscopies are a direct consequence of the photoelectric effect. Because of the expulsion of the electron from an atomic energy level E_1 , a hole remains in the atom. The atom is thus excited and two main concurrent channels can put back the atom in a less excited state. Both channels involve the transition of another electron with energy E_2 down to the hole left behind (Fig. 3.11). The resulting energy gain $E_1 - E_2$ can be used either through the emission of a photon with energy $\hbar\omega =$ $E_1 - E_2$ (X-ray fluorescence) or through the ejection of an electron from an atomic energy level E_3 , with a kinetic energy around $E_1 - E_2 - E_3$ (Auger effect). Both effects give typical signature of the material by the energy of their appearance and sometimes by the shape of the resulting spectra. The first gives the X-ray emission spectroscopy (XES) or UPS in the ultra-violet regime; the second, gives the auger electron spectroscopy (AES).4 The relative weight of these phenomena depends on the atomic number of the element. The Auger emission is always dominating, except for K shell decay in elements with an atomic number larger than \approx 30. Note also that because of the difference in the detected particle, an electron having a much shorter mean free path than a photon with the same energy, the Auger technique is surface

⁴ Note that the first core hole can also be created by an incident energetic electron (and not by a photon).

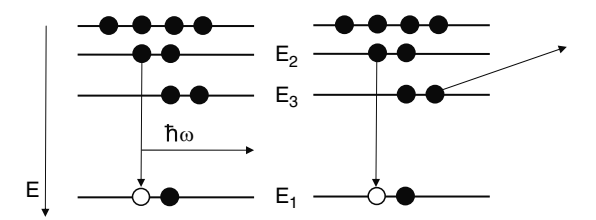


Fig. 3.11 The two channels for the desexcitation of an atom in which a hole is left after the ejection of a core electron. In the *left* panel, the transition of an electron from level E_2 down to the core level E_1 gives directly a photon of energy $\hbar\omega=E_1-E_2$ (fluorescence). In the *right* panel, the corresponding energy is given to an electron with energy E_3 . In this Auger effect, an electron is ejected with a kinetic energy $\approx E_1-E_2-E_3$

sensitive. Indeed, it is one of the most popular technique to check the cleanliness of a surface.

3.6.4 XANES and RXS Formula

The initial and final states must contain all the electrons of the system and one would have to calculate matrix terms of the form

$$\langle \Phi_{\rm f}(r_1, r_2, r_3, \ldots) | \hat{o} | \Phi_{\rm g}(r_1, r_2, r_3, \ldots) \rangle,$$
 (3.91)

where r_1, r_2, r_3, \ldots are the positions of the different electrons and Φ is the multielectronic states. Such a general formulation is developed in the ligand field multiplet scheme. All the possible transitions from all the multielectronic states up to all the multielectronic final states are then summed up. They occur at different energies and have amplitudes related to the multiplicity of the states. The resulting comb figure is then convoluted with a relevant spectral profile for comparison with the experimental data. In the monoelectronic approach, we write $\Phi(r_1, r_2, r_3, \ldots) = \varphi_1(r_1)\varphi_2(r_2)\varphi_3(r_3)\cdots$. One also assumes that there is a specific electron that makes the transition, the others being spectators. The different states are seen through a continuum and with a density of states that can be calculated. Then, the general formula seen in Sect. 3.4 is still valid. The effect of the other electrons is then a simple multiplicative factor:

$$S_0 = \prod_{i=2,N} \langle \varphi_i^{f}(r_i) | \varphi_i^{g}(r_i) \rangle.$$
 (3.92)

 S_0 is typically of the order of 0.8 and is supposed to be energy independent. It comes from the fact that the core hole screening induces a contraction of the final state atomic orbitals, resulting in a scalar product less than unity. The screening also makes the energies of the other atomic levels change so that in the transition one has

$$\hbar\omega \approx \mathcal{E}_{\rm f} - \mathcal{E}_{\rm g} = E_{\rm f} - E_{\rm g} + \Delta E_{\rm a},$$
 (3.93)

where ΔE_a is the sum of the differences between the initial and final energies of the other electrons. This fact is mostly often forgotten and ΔE_a is not written. Nevertheless, it can represent several hundredth of electron volt at typical K edges.

With this simplification, we can use the matrix product that appears in both absorption (3.26) and RXS (3.43) formulas:

$$A = \sum_{f,g} \langle \varphi_{g} | \hat{o}_{s}^{*} | \bar{\varphi}_{f} \rangle \langle \bar{\varphi}_{f} | \hat{o}_{i} | \varphi_{g} \rangle.$$
 (3.94)

In the absorption case, one just has to impose $\hat{o}_s = \hat{o}_i$. Using moreover (3.72) of Sect. 3.4.6 on the selection rules, which expresses the transition matrix in terms of the radial and angular integrals and of the atomic amplitudes, one gets

$$A = \sum_{o_{i},o_{s}} c_{\ell_{o_{i}},m_{o_{i}}} c_{\ell_{o_{s}},m_{o_{s}}} \sum_{\sigma,g} \sum_{\ell,m,\ell',m'} \Gamma_{\ell,m+\frac{1}{2}-\sigma}^{\ell_{g},m_{g}+\frac{1}{2}-\sigma,\ell_{o_{i}},m_{o_{i}}} \Gamma_{\ell,m'+\frac{1}{2}-\sigma}^{\ell_{g},m'_{g}+\frac{1}{2}-\sigma,\ell_{o_{s}},m_{o_{s}}} \times \sum_{s,s'} \mathcal{R}_{\ell,m+\frac{1}{2}-\sigma,s}^{g,\ell_{o_{i}},\sigma}(E) \mathcal{R}_{\ell,m+\frac{1}{2}-\sigma,s'}^{g,\ell_{o_{s}},\sigma}(E) \sum_{f} a_{\ell,m,s}^{f}(E) a_{\ell',m',s'}^{f*}(E), \quad (3.95)$$

where we omit the index f on the energy because, in this summation, they all have the same value.

The density of states does not appear explicitly because it is included in the atomic amplitudes and in the normalization of the radial wave functions. They are built by continuity with an outer sphere where the potential is constant. There the solutions are the Bessel and Hankel functions normalized by the density of states in vacuum, that is, by $\sqrt{k/\pi}$, where k is the photoelectron wave vector. One thus gets the normalized radial solutions $\bar{b}_{\ell}(E,r)$ instead of the $b_{\ell}(E,r)$, which are normalized to unity. Thus one replaces in the formulas $\langle \varphi_{\rm g} | \hat{o}_{\rm s}^* | \varphi_{\rm f} \rangle \langle \varphi_{\rm f} | \hat{o}_{\rm i} | \varphi_{\rm g} \rangle \rho(E)$ by $\langle \varphi_{\rm g} | \hat{o}_{\rm s}^* | \bar{\varphi}_{\rm f} \rangle \langle \bar{\varphi}_{\rm f} | \hat{o}_{\rm i} | \varphi_{\rm g} \rangle$.

In many cases this expression can be simplified. For example, when quadrupole transitions are negligible, as at the $L_{II,III}$ edges of the 3d elements, the summation on the operators often reduces to one element. In the absorption case where $\hat{o}_s = \hat{o}_i$, we can write

$$\sigma = 4\pi^{2}\alpha\hbar\omega c_{\ell_{o},m_{o}}^{2} \sum_{\sigma,g} \sum_{\ell,m,s} \left[\Gamma_{\ell,m+\frac{1}{2}-\sigma}^{\ell_{g},m_{g}+\frac{1}{2}-\sigma,\ell_{o},m_{o}} \mathcal{R}_{\ell,m+\frac{1}{2}-\sigma,s}^{g,\ell_{o_{i}},\sigma}(E) \right]^{2} \times \sum_{f} \left| a_{\ell,m,s}^{f}(E) \right|^{2}.$$

$$(3.96)$$

To get a signal equivalent to the measured one, a broadening due to the corehole and final-state lifetimes has to introduced in this equation. This is achieved by convoluting (3.96) by a Lorentzian profile having a width which increases with energy. At the Fermi energy, it is typically the initial state width. At higher energy, plasmons and other phenomena contributes also to the damping. Often the width follows an arctangent-like function vs. the photoelectron kinetic energy. Note that new measurements improve the resolution by selecting sub-channel using the fluorescence detection. This limit the hole width to smaller value.

For the RXS, the infinitely small η in (3.43) is replaced by a finite value equivalent to the width broadening in absorption. The summation on the intermediate states n can be made in two steps. We first group, as in XANES, the states of same energy (we shall call them now f of energy E, to be consistent with the XANES formula), which we still sum in a discrete form. The sum over the states of different energies is performed in a second step through an integral spreading from the Fermi level up to infinity. In the elastic case where we are supposed to have $E - E_{\rm g} + \Delta E_{\rm a} \approx \hbar \omega$, the resonant or anomalous scattering amplitude is given by

$$f' - if'' \approx m\omega^2 \int_{E_F}^{\infty} \frac{\sum_{f,g} \langle \varphi_g | \hat{o}_s^* | \bar{\varphi}_f \rangle \langle \bar{\varphi}_f | \hat{o}_i | \varphi_g \rangle}{\hbar\omega - (E - E_g + \Delta E_a) + i\Gamma/2} dE, \tag{3.97}$$

where $E_{\rm F}$ is the Fermi energy and Γ is the broadening. Note the minus sign in front of the imaginary part of the scattering amplitude to get the conventional way where f' is negative and f'' positive.⁵ When the incoming and outgoing polarizations are parallel, the absorption cross section is nearly proportional to $\hbar\omega$ f''.

The RXS and XANES formula we have derived stand for an atom embedded in some surrounding. In fact the absorption or scattering comes from all the atoms in the molecule or in the unit cell. Thus one has to sum over them eventually using the symmetry operations of the space group. For the XANES this gives

$$\sigma_{\text{cell}} = \sum_{a=1}^{N} \sigma_a = \sum_{a=1}^{N_e} \sum_{b=1}^{n_a} S_b(\sigma_a),$$
(3.98)

where N is the number of atoms, b is the index of the n_a equivalent atoms related by the symmetry operation S_b to the prototypical atom a. N_e is the number of nonequivalent atoms. We see in this way that the tensor dependence (or anisotropy) of the absorption cross section depends not on the individual point group but on that of the unit cell. On the contrary, the shape of the spectra is related to the individual surroundings and symmetries.

For RXS, one uses the same summation, but now taking into account the Bragg factors and the nonresonant contributions. The intensity for a diffraction peak of diffraction wave vector \mathbf{Q} is then given by

$$I = \frac{K}{V^2} \left| \sum_{a=1}^{N_e} \sum_{b=1}^{n_a} S_b \left\{ (e^{i\mathbf{Q} \cdot \mathbf{R}_a} \left[f_{0a} + i f_{ma} + f_a'(\omega) + i f_a''(\omega) \right] \right\} \right|^2, \quad (3.99)$$

⁵ This sign as well as the plus sign in the exponent of the Bragg factor of (3.38) and (3.99) comes from a different convention in the time arrow between the crystallographic community and the theoreticians of quantum mechanics.

where we have the nonresonant Thomson f_{0a} and nonresonant magnetic scattering amplitude f_{ma} of the atom a and the resonant terms f_a' and f_a'' . The latter terms contain the eventual magnetic resonant contribution, sometimes written in separate terms. In the formula, K is a constant, V is the volume of the unit cell, and \mathbf{R}_a is the position of the atom a.

In this context, during the last years there has been a strong interest in the so-called forbidden reflections, which are nearly zero far from the absorption edges but with sharp intensity around the edge (as in the example of Fig. 3.6). These reflections are such that the sum of the Bragg terms are zero, and the intensity can be nearly proportional to $|f_a - f_b|^2$, where a and b are the two atoms possibly related by a symmetry operation (a rotation-translation or a glide plane). Thus the isotropic contributions disappear and one remains with the anisotropic ones, giving the so-called Templeton effect [25]. Very weak peaks often come from a slight symmetry breaking, thus they are, let say, *nearly* forbidden. These reflections can give information on the change occurring during the transition between two previously equivalent atoms. In XANES, one measures always a sum (and no f' neither). It is clear that the sensitivity is enhanced when measuring a difference. It is what has been used in the study of charge ordering in different compound, for instance in magnetite [26].

In Fig. 3.12, typical resonant scattering amplitudes for isolated atoms and for iron atoms in magnetite are shown. The relative amplitude of these terms with the Thomson scattering amplitude (which is typically equal to the atomic number) shows the importance of the anomalous effect around the absorption edge. The effect of the surrounding atoms is shown when comparing the atomic and the atom embedded in real structure spectra. For magnetite there are two different iron sites, one in octahedral environment, the other in tetrahedral environment. They have also very different shapes. Note also that their f'' is typical of the XANES spectral shapes.

3.6.4.1 Relation with the Density of States

With the same notation, but without spin for simplicity, the density of states (or its projection on the atom) is given by

$$\rho_{\ell,m}^{\ell',m'}(r,E) = \left| \sum_{f} a_{\ell,m}^{f}(E) a_{\ell',m'}^{f*}(E) \bar{b}_{\ell}(r,E) \bar{b}_{\ell'}^{*}(r,E) \right|. \tag{3.100}$$

One can integrate the radial part up to the atom radius and we get

$$n_{\ell,m}^{\ell',m'}(r,E) = \left| \sum_{f} a_{\ell,m}^{f}(E) a_{\ell',m'}^{f*}(E) \right| R_{\ell,\ell'}(E),$$
(3.101)

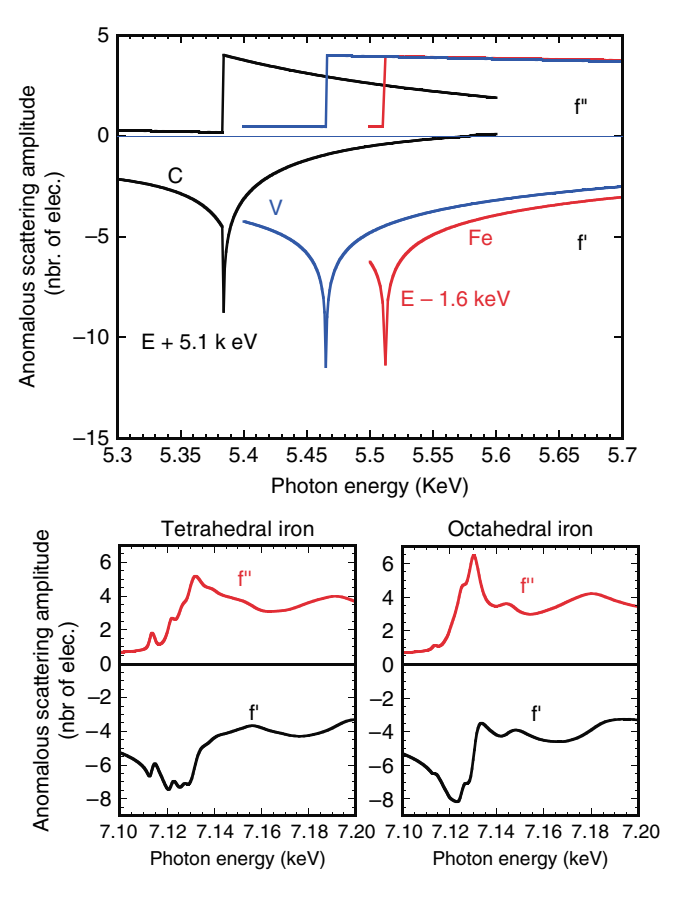


Fig. 3.12 Anomalous scattering amplitudes. Top: atomic spectra for carbon, vanadium, and iron atoms. Bottom: spectra for the iron atom in its octahedral and tetrahedral sites in magnetite at room temperature. The imaginary parts, f'', of the amplitudes have shapes similar to the XANES. The spectra are calculated using the FDMNES code [27]

where $R_{\ell,\ell'}(E)$ is the radial integral:

$$R_{\ell,\ell'}(E) = \int_0^R \left| \bar{b}_{\ell}(r,E) \, \bar{b}_{\ell'}^*(r,E) \, 4\pi r^2 \mathrm{d}r \right|. \tag{3.102}$$

The diagonal term is the number of electrons per unit of energy in the atom:

$$n_{\ell,m}(E) = \sum_{f} \left| a_{\ell,m}^{f}(E) \right|^{2} R_{\ell,\ell}(E).$$
 (3.103)

The formulas for the absorption cross section and for RXS contain the same $a_{\ell,m}^f(E) \, a_{\ell',m'}^{f*}(E)$ terms than the density of states formula. The difference is in the radial integral and other constant parameters. We thus see that the expressions

are nearly proportional in most cases, except for the radial part, which depends only slightly on energy. Note also that the proportionality coefficient is different for dipole and quadrupole transitions, the dipole one being much stronger. From all this we can confirm that absorption spectroscopy measures the projection of the density of states on the absorbing atoms. Because of the selection rules, it is even a peculiar projection of the density of states, resolved in ℓ and eventually also in m, which is measured. When playing with the polarization and sometimes with the magnetic field, more selective processes can be taken into account. A good example is the measurement of circular magnetic dichroism. What is measured is then the magnetic momentum as is seen in Sect. 3.6.6.

3.6.5 Multipole Analysis

We have seen in the previous section that we have access to specific projection of the density of states. The access to a particular component can be obtained by playing with the polarization and taking into account the symmetry of the material. Depending on this symmetry, the different terms can be zero or nonzero. The consequence is that the measurement under specific conditions can give information on the symmetry, including the magnetic state of the material. The mathematical tools, Cartesian and spherical tensor algebra, which permits to make a complete analysis of these terms are seen in the following.⁶

3.6.5.1 Cartesian Tensors

We have seen that the matrix elements can be expanded into dipole and quadrupole components:

$$\langle \bar{\varphi}_f | \hat{o}_i | \varphi_g \rangle = D_i^f + i \frac{k}{2} Q_i^f + \cdots$$
 (3.104)

The signal amplitude can thus be written as

$$\langle \varphi_{\mathbf{g}} | \hat{o}_{s}^{*} | \bar{\varphi}_{\mathbf{f}} \rangle \langle \bar{\varphi}_{\mathbf{f}} | \hat{o}_{i} | \varphi_{\mathbf{g}} \rangle \approx D_{s}^{f*} D_{i}^{f} + i \frac{k}{2} \left(D_{s}^{f*} Q_{i}^{f} - Q_{s}^{f*} D_{i}^{f} \right) + \frac{k^{2}}{4} Q_{s}^{f*} Q_{i}^{f}.$$

$$(3.105)$$

We can then introduce three Cartesian tensors. The dipole–dipole or E1–E1 rank 2 tensor:

$$D_{\alpha\beta} = \sum_{f,g} \langle \varphi_{g} | r_{\alpha} | \bar{\varphi}_{f} \rangle \langle \bar{\varphi}_{f} | r_{\beta} | \varphi_{g} \rangle, \qquad (3.106)$$

where r_{α} and r_{β} represent x, y, or z.

⁶ Using other tools, Ch. Brouder gives, in a very useful paper [28], the relation between the angular dependence of the absorption cross section and the point group of the studied system.

In the same way, we get the dipole–quadrupole or E1–E2 rank 3 tensor and the quadrupole–quadrupole or E2–E2 rank 4 tensor:

$$I_{\alpha\beta\gamma} = \sum_{f,g} \langle \varphi_{g} | r_{\alpha} r_{\beta} | \bar{\varphi}_{f} \rangle \langle \bar{\varphi}_{f} | r_{\gamma} | \varphi_{g} \rangle, \qquad (3.107)$$

$$Q_{\alpha\beta\gamma} = \sum_{f,g} \langle \varphi_{g} | r_{\alpha}r_{\beta} | \bar{\varphi}_{f} \rangle \langle \bar{\varphi}_{f} | r_{\gamma}r_{\delta} | \varphi_{g} \rangle.$$
 (3.108)

where α , β , γ , and δ label the three directions of space in Cartesian coordinates.

With this, the signal amplitude (but the multiplicative factor in the absorption cross section and the denominator in RXS) is given by

$$A = \sum_{\alpha,\beta} \varepsilon_{\alpha}^{s*} \varepsilon_{\beta}^{i} D_{\alpha\beta} + i \frac{k}{2} \sum_{\alpha,\beta,\gamma} \varepsilon_{\alpha}^{s*} \varepsilon_{\beta}^{i} \left(u_{\gamma}^{i} I_{\alpha\beta\gamma} - u_{\gamma}^{s} I_{\alpha\beta\gamma}^{*} \right)$$

$$+ \frac{k^{2}}{4} \sum_{\alpha,\beta,\gamma,\delta} \varepsilon_{\alpha}^{s*} \varepsilon_{\beta}^{i} u_{\gamma}^{s} u_{\delta}^{i} Q_{\alpha\beta\gamma\delta} .$$

$$(3.109)$$

To fix the idea, the E1–E1 amplitude is given by

$$A_{\text{E1E1}} = \left(\varepsilon_{x}^{s*}, \varepsilon_{y}^{s*}, \varepsilon_{z}^{s*}\right) \begin{pmatrix} D_{xx} & D_{xy} & D_{xz} \\ D_{yx} & D_{yy} & D_{yz} \\ D_{zx} & D_{zy} & D_{zz} \end{pmatrix} \begin{pmatrix} \varepsilon_{x}^{i} \\ \varepsilon_{y}^{i} \\ \varepsilon_{z}^{i} \end{pmatrix}. \tag{3.110}$$

The matrix is hermitic $(D_{\alpha\beta} = D_{\beta\alpha}^*)$ and off-diagonal elements are complex when the material is magnetic. For example, the D_{xx} term is proportional to the absorption cross section when the polarization is along x.

The E1-E2 terms can be observed only for peculiar symmetry. We can remark that, for a same final state f, one has a product of a dipole and a quadrupole term. Because of the different selection rules ($\Delta \ell$ odd for the first and $\Delta \ell$ even for the second), this means that f must have at the same time odd and even components. In other words, f must be an hybridized state between odd and even components. This is possible only when the atom is not at a center of symmetry. In absorption, because of the sum on the equivalent atoms, it is sufficient to have a center of symmetry anywhere (and not necessarily on the atom) to make the E1-E2 signal zero. In RXS, on the contrary, for some reflections such that the Bragg factor is opposite on two equivalent atoms related by inversion, the signal can be observed only for the E1-E2 term, the E1-E1 and E2-E2 contributions being zero. When there is no center of symmetry, the signal can also be observed using the natural circular dichroism [29, 30]. The subtraction between the spectra obtained with the left and right polarized light eliminates the E1-E1 and E2-E2 contributions as in the diffraction technique given above. In his chapter, A. Rogalev develops examples of optical activities using the E1–E2 process (see also [31]).

3.6.5.2 Spherical Tensors

The use of Cartesian tensor is rather natural. Nevertheless, the spherical tensors are often preferred. The reason is that their components can be related to specific observable values as, for example, the orbital occupancy, the magnetic moment, or the toroidal moment. These tensors are also separated in E1–E1, E1–E2, and E2–E2 contributions. The amplitude can be written as

$$A = \sum_{\substack{0 \le \ell \le 2 \\ -\ell \le m \le \ell}} (-1)^{\ell+m} T_{\ell}^{m} D_{\ell}^{m} + i \sum_{\substack{1 \le \ell \le 3 \\ -\ell \le m \le \ell}} (-1)^{\ell+m} U_{\ell}^{m} I_{\ell}^{m}$$

$$+ \sum_{\substack{0 \le \ell \le 4 \\ -\ell \le m \le \ell}} (-1)^{\ell+m} V_{\ell}^{m} Q_{\ell}^{m},$$
(3.111)

where D_ℓ^m , I_ℓ^m , and Q_ℓ^m are the components of the absorption-scattering tensors and T_ℓ^m , U_ℓ^m , and V_ℓ^m are the same for the polarization-wave vectors.

All these spherical coefficients are related to the Cartesian ones. For example, for the E1–E1 tensor, the relations are

$$D_0^0 = \frac{1}{\sqrt{3}} \left(D_{xx} + D_{yy} + D_{zz} \right), \quad D_1^0 = -\frac{i}{\sqrt{2}} \left(D_{xy} - D_{yx} \right),$$

$$D_1^{-1} = -\frac{i}{\sqrt{2}} \left(D_{yz} - D_{zy} \right), \quad D_1^{-1} = \frac{1}{\sqrt{2}} \left(D_{xz} - D_{zx} \right),$$

$$D_2^0 = \frac{i}{\sqrt{6}} \left(2D_{zz} - D_{xx} - D_{yy} \right), \quad D_2^{-1} = -\frac{1}{\sqrt{2}} \left(D_{xz} + D_{zx} \right),$$

$$D_2^{-1} = -\frac{i}{\sqrt{2}} \left(D_{yz} + D_{zy} \right), \quad D_2^{-2} = \frac{i}{\sqrt{2}} \left(D_{xy} + D_{yx} \right),$$

$$D_2^{-1} = \frac{i}{\sqrt{2}} \left(D_{xx} - D_{yy} \right), \quad D_2^{-1} = \frac{i}{\sqrt{2}} \left(D_{xy} + D_{yx} \right),$$

$$D_2^{-1} = \frac{i}{\sqrt{2}} \left(D_{xx} - D_{yy} \right), \quad D_2^{-1} = \frac{i}{\sqrt{2}} \left(D_{xy} + D_{yx} \right),$$

$$D_2^{-1} = \frac{i}{\sqrt{2}} \left(D_{xx} - D_{yy} \right), \quad D_2^{-1} = \frac{i}{\sqrt{2}} \left(D_{xy} + D_{yx} \right),$$

$$D_2^{-1} = \frac{i}{\sqrt{2}} \left(D_{xy} - D_{yy} \right), \quad D_2^{-1} = \frac{i}{\sqrt{2}} \left(D_{xy} - D_{yy} \right),$$

$$D_2^{-1} = \frac{i}{\sqrt{2}} \left(D_{xy} - D_{yy} \right), \quad D_2^{-1} = \frac{i}{\sqrt{2}} \left(D_{xy} - D_{yy} \right),$$

$$D_2^{-1} = \frac{i}{\sqrt{2}} \left(D_{xy} - D_{yy} \right), \quad D_2^{-1} = \frac{i}{\sqrt{2}} \left(D_{xy} - D_{yy} \right),$$

$$D_2^{-1} = \frac{i}{\sqrt{2}} \left(D_{xy} - D_{yy} \right), \quad D_2^{-1} = \frac{i}{\sqrt{2}} \left(D_{xy} - D_{yy} \right),$$

$$D_2^{-1} = \frac{i}{\sqrt{2}} \left(D_{xy} - D_{yy} \right),$$

where we have used for all the tensors the transformation

$$T_{\ell}^{\pm} = \frac{1}{\sqrt{2}} \left(T_{\ell}^{m} \pm T_{\ell}^{-m} \right),$$
 (3.113)

which gives

$$T_{\ell}^{m} D_{\ell}^{m} = T_{\ell}^{+} D_{\ell}^{+} - T_{\ell}^{-} D_{\ell}^{m} . \tag{3.114}$$

The $\ell=1$ components are directly proportional to the magnetic moment vector per unit energy, **m**:

$$\mathbf{m} = \begin{pmatrix} \bar{D}_1^1 \\ + \\ i \ D_1^1 \\ D_1^0 \end{pmatrix}, \tag{3.115}$$

where we omitted the proportionality coefficient. To get the polarization spherical tensor, one first writes the polarization in the matrix form

$$T = \begin{pmatrix} \varepsilon_x^{s*} \varepsilon_x^i, & \varepsilon_x^{s*} \varepsilon_y^i, & \varepsilon_x^{s*} \varepsilon_z^i \\ \varepsilon_y^{s*} \varepsilon_x^i, & \varepsilon_y^{s*} \varepsilon_y^i, & \varepsilon_y^{s*} \varepsilon_z^i \\ \varepsilon_z^{s*} \varepsilon_x^i, & \varepsilon_z^{s*} \varepsilon_y^i, & \varepsilon_z^{s*} \varepsilon_z^i \end{pmatrix}.$$
(3.116)

The spherical components of the polarization are then calculated with the same transformation than in (3.112). For example,

$$T_0^0 = \frac{1}{\sqrt{3}} \left(\varepsilon_x^{s*} \varepsilon_x^i + \varepsilon_y^{s*} \varepsilon_y^i + \varepsilon_z^{s*} \varepsilon_z^i \right) = \frac{1}{\sqrt{3}} \varepsilon_s \cdot \varepsilon_i,$$

$$T_1^0 = -\frac{i}{\sqrt{2}} \left(\varepsilon_x^{s*} \varepsilon_y^i - \varepsilon_y^{s*} \varepsilon_x^i \right) = -\frac{i}{\sqrt{2}} \left(\varepsilon_s^* \times \varepsilon_i \right)_z. \tag{3.117}$$

Using all these relations, one gets for the E1–E1 signal

$$A_{\text{EIEI}} = \frac{1}{3} \varepsilon_{s} \cdot \varepsilon_{i} \text{Tr}(D) - \frac{i}{\sqrt{2}} \left(\varepsilon_{s}^{*} \times \varepsilon_{i} \right)_{z} \cdot \mathbf{m} + T_{2}^{0} D_{2}^{0} - T_{2}^{1} D_{2}^{1} + T_{2}^{1} D_{2}^{1} + T_{2}^{1} D_{2}^{1} + T_{2}^{2} D_{2}^{2} - T_{2}^{2} D_{2}^{2},$$

$$(3.118)$$

where Tr(D) is the trace of D.

The first term in this equation does not depend on the polarization orientation in XANES because the scalar product is just one (it is also the case in RXS when keeping the relative orientation of ε_i and ε_s). It is thus called the electric monopole component because it probes only the electronic density and not its magnetic part. It gives the E1–E1 isotropic part of the signal in the absorption cross section and in RXS for the σ - σ polarization (there is also an E2–E2 isotropic part). It is the main contribution to the XANES cross section. When the final states are rather localized, one gets the so-called white line at the beginning of the edge. Because the electric monopole measures the charge of the nonoccupied states, the surface of this white line is roughly proportional to the number of hole in the corresponding state of the atom (e.g., the 3d state in a $L_{\text{II,III}}$ edge). By difference, one thus can get an idea of the electron occupancy in the atom: larger is the white line, less electrons are in the atom.

⁷ Note that another factor can give an idea of the atom valence state. It is the energy shift of the edge. Indeed, when an atom is a higher oxidation state, its electrons tend to leave the atom. Consequently, the potential at the core of the atom decreases and the core level becomes deeper. The incoming photon needs thus more energy to eject the electron from its core level and the edge is shifted towards higher energy. This phenomena is stronger at the K edges. Typically a change by one in the oxidation number corresponds to a shift of several electron volt.

The second term is strictly magnetic. One sees that it is proportional to the magnetic moment through a scalar product with $\varepsilon_s^* \times \varepsilon_i$. It can thus be probed with circular polarization. The last terms are the electric quadrupole components. They are, as the first term, purely electric. They measure the anisotropy of the electric cloud around the absorber and are responsible for the main part of the linear dichroism (see Fig. 3.4). A smaller part in the pre-edge region can comes from the E2–E2 contribution. Note that the present terms, *magnetic dipole* and *electric quadrupole*, must not be confused with the *dipole* and *quadrupole electric transitions* E1 and E2.

To illustrate this more, one can have a look to three formal examples following three different point group on the absorbing atom. We use a polarization $\varepsilon = \varepsilon_s = \varepsilon_i$, that is, like in the absorption or in σ – σ RXS.

3.6.5.3 m3m Symmetry (O_h)

This cubic symmetry is for instance the case of a 3d atom surrounded by a nondistorted octahedron. Let us put the six surrounding atoms at the same distance along the positive and negative directions of the three axes. Because of the symmetry plane perpendicular to Ox, Oy, and Oz, the off-diagonal components of the E1–E1 Cartesian tensor are zero; because of the threefold axis its diagonal elements are equal. The amplitude of the signal is in this case

$$A_{\text{E1E1}} = \boldsymbol{\varepsilon}^{+} \begin{pmatrix} D_{zz} & 0 & 0 \\ 0 & D_{zz} & 0 \\ 0 & 0 & D_{zz} \end{pmatrix} \boldsymbol{\varepsilon} = \frac{1}{3} \boldsymbol{\varepsilon} \cdot \boldsymbol{\varepsilon} Tr(D) = D_{zz}. \tag{3.119}$$

The signal amplitude is isotropic. It does not depend on the polarization orientation.

3.6.5.4 4/m m m Symmetry (D_{4h})

This symmetry can be obtained for instance by a single elongation of the previous octahedron along the z-axis. There is no more threefold axis but a fourfold axis around z, which makes $D_{xx} = D_{yy}$. One thus gets

$$A_{\text{EIEI}} = \boldsymbol{\varepsilon}^{+} \begin{pmatrix} D_{xx} & 0 & 0 \\ 0 & D_{xx} & 0 \\ 0 & 0 & D_{zz} \end{pmatrix} \boldsymbol{\varepsilon} = \frac{1}{3} (2D_{xx} + D_{zz}) + \frac{1}{3} (D_{zz} - D_{xx}) (3\cos^{2}\theta - 1).$$
(3.120)

Here we used the spherical coordinate for the polarization:

$$\boldsymbol{\varepsilon} = \begin{pmatrix} \sin \theta \cos \phi \\ \sin \theta \sin \phi \\ \cos \theta \end{pmatrix}. \tag{3.121}$$

We get a polarization orientation dependence equivalent to the harmonics Y_2^0 . The signal is not anymore isotropic.

$3.6.5.5 \quad 4/m'm'm$ Symmetry

Let us consider now a magnetic case with spin-orbit. We start again from the nondistorted octahedron and assume a magnetic moment along the z-axis on the central atom. The diagonal threefold axes are broken as in the previous example. Because of the magnetic moment, the symmetry planes perpendicular to Ox and Oy are now multiplied by time reversal; thus, one gets the 4/m'm'm symmetry. The Cartesian tensor contains now off-diagonal imaginary terms, which are proportional to the magnetic moment per energy unit:

$$A_{\text{EIEI}} = \boldsymbol{\varepsilon}^{+} \begin{pmatrix} D_{xx} & iD_{xy}^{i} & 0 \\ -iD_{xy}^{i} & D_{xx} & 0 \\ 0 & 0 & D_{zz} \end{pmatrix} \boldsymbol{\varepsilon} = \frac{1}{3} (D_{xx} + 2D_{zz}) - \frac{i}{\sqrt{2}} \boldsymbol{\varepsilon}^{*} \times \boldsymbol{\varepsilon} \cdot \mathbf{m} + T_{2}^{0} D_{2}^{0}.$$

$$(3.122)$$

We get a new magnetic term, which can be directly measured with X-ray circular dichroism, using polarizations:

$$\boldsymbol{\varepsilon} = \frac{1}{\sqrt{2}} \begin{pmatrix} 1\\ \pm i\\ 0 \end{pmatrix},\tag{3.123}$$

such that

$$A_{\text{E1E1}}^{+} - A_{\text{E1E1}}^{-} = D_{xy}^{i} = m_{z}. \tag{3.124}$$

For linear polarization, one gets the same angular dependence as with the 4/mmm symmetry, but probably with a smaller amplitude. This term reveals a nonspherical electric cloud. It is not magnetic. Nevertheless, it is present even without elongation along the z-axis. Its presence comes from the spin-orbit coupling, which makes that the orbital electric cloud tends to align along the spin direction. It can then be said that, though electric, it is an indirect signature of the magnetic moment. Note that when there is also an elongation along z, this anisotropy reveals both phenomena together. All this means that such a linear measurement cannot be considered as a proof of a magnetization. One really needs circular polarization.

The expansion in spherical tensors can be performed also for the E1–E2 and E2–E2 terms. All the components have a specific physical significance. They are classified in Table 3.3. The different terms change in sign with time reversal when they are magnetic and with inversion when they are E1–E2. This allows peculiar measurements on specific reflections or/and with peculiar polarization conditions. Time reversal can be obtained by inverting the magnetic field, making a measurement in one way and another in the other way. The different contributions can be often measured separately playing with the incoming (and outgoing in RXS)

ℓ		E1–E1	E1–E2 elec.	E1-E2 magn.	E2–E2
0	Monopole	$++ ch_{\ell+1}$			$++ \approx ch_{\ell+2}$
1	Dipole	$-+ m_{\ell+1}$	+-n	t	$-+ \approx m_{\ell+2}$
2	Quadrupole	++	+-(t,m)	(n,m)	++
3	Octupole		+-(n,m,m)	(t,m,m)	-+
4	Hexadecapole				++

Table 3.3 List of the spherical tensor components with some of their physical significance

The couple of signs (++, +-, -+,and --) gives the change in sign under time reversal for the first and inversion for the second. The magnetic terms are odd by time reversal. The E1–E2 components are odd by inversion. The electric monopole term measures the charge density $ch_{\ell+1}$ in E1–E1 and a part of it $ch_{\ell+2}$ for E2–E2. The magnetic dipole terms measure the magnetic moment density $m_{\ell+1}$ in E1–E1 and a part of it $m_{\ell+2}$ for E2–E2. The magnetic dipole E1–E2 measures the toroidal moment (or anapole) t. The electric quadrupole E1–E2 measures the toroidal axis (t,m). Other components measure higher order of electric charges or magnetic moments

polarizations, the choice of the reflections in RXS, the orientation of the magnetic field and that of the sample.

To finish this part, we recall that the magnetic dipole transition M1 term can also exist. Thus one can get M1–M1 or E1–M1 components. Nevertheless, these ones are necessarily very small, when not zero. In the X-ray range, a definite proof of their measurement remains to be given.

3.6.6 X-Ray Magnetic Circular Dichroism

When making the difference between spectra recorded with left and right circular polarization, one measures the circular dichroism. In the X-ray range and applied to magnetic materials, this technique is called XMCD. We have already seen in the previous section that it is a way to measure the magnetic moment on the atoms. Let us see in more detail how the measurements can give a quantitative evaluation and how, using *sum rules*, one can in many cases separate the orbital and the spin magnetic moments. The X-ray sum rules were derived at the beginning of the 1990s by Thole, Carra et al. [32, 33] from magneto-optics sum rules. Numerous experimental and theoretical studies were aimed at investigating their validity for itinerant magnetic systems. The adequacy of the sum rules varied from very good to poor. It is with the experimental work of Chen et al. [34], where a special care of the experimental artifacts has been taken, that their validity was proved.

For the $L_{II,III}$ edges of the 3d elements, we can use the simplified (3.96) because the quadrupolar transition is negligible. We choose polarizations such that:

$$\boldsymbol{\varepsilon} \cdot \mathbf{r} = \sqrt{\frac{4\pi}{3}} r Y_1^{\pm 1},\tag{3.125}$$

using the complex harmonics and with $m=\pm 1$ for the left and right circular polarized light. There are four $p_{3/2}$ initial states corresponding to the $L_{\rm III}$ edge and two $p_{1/2}$ states corresponding to the $L_{\rm II}$ edge.⁸ From the different values of the Gaunt coefficients for the $L_{\rm II}$ and $L_{\rm III}$ edges and from the different values of the $G_{\rm g}^{\sigma}$ in (3.66) and (3.67), it can be shown that the transition probability for the XMCD is not the same for the orbital and spin part at $L_{\rm II}$ and $L_{\rm III}$ edges.

We use also the fact that the 3d states are *rather* localized. This means that they spread over a narrow energy range and thus integration in an energy range containing all the empty 3d states is possible. When measuring the absorption cross section, whatever is the polarization, one probes the unoccupied states. The idea is that, by integration, one measures the number of unoccupied states in electron unit, the occupied states being given by the difference with the total number of electrons per atom in a 3d band, that is, 10. The difficulties are that d states are present in the continuum. The photoelectron mainly probes the 3d states and also all the (n > 3)d states. Thus, before making the integration, a double step like function, with each height equal to the absorption after each white line, is subtracted. For practical purposes, the integrations are performed over a range extending typically from $20 \, \text{eV}$ below the L_{III} edge up to $40 \, \text{eV}$ above the L_{III} edge.

From all this, one gets two equations for the two unknowns. The normalization is performed with the absorption edge, which is, as we know, a measurement of the density of states. At the end, one gets the sum rules

$$m_{\text{orb}} = -\frac{4}{3N} (10 - n_{3d}) \int_{L_{\text{II}} + L_{\text{III}}} (\sigma^+ - \sigma^-) dE$$
, (3.126)

$$m_{\text{spin}} = -\frac{2}{N} (10 - n_{3d}) \left(1 + \frac{7 \langle T_z \rangle}{2 \langle S_z \rangle} \right)^{-1} \times \left[3 \int_{L_{\text{III}}} (\sigma^+ - \sigma^-) dE - 2 \int_{L_{\text{II}} + L_{\text{III}}} (\sigma^+ - \sigma^-) dE \right],$$
(3.127)

with the normalization

$$N = \int_{L_{II} + L_{III}} (\sigma^{+} + \sigma^{-}) dE, \qquad (3.128)$$

where $m_{\rm orb}$ and $m_{\rm spin}$ are, respectively, the orbital and spin magnetic moments in unit of Bohr magneton per atom. n_{3d} is the 3d electron occupation number of the transition metal atom under study. $L_{\rm II}$ and $L_{\rm III}$ denote the integration ranges. $\langle T_z \rangle$ is the expectation value of the magnetic dipole operator and $\langle S_z \rangle$ is equal to $m_{\rm spin}$ in atomic units (Rydberg). The ratio $\langle T_z \rangle / \langle S_z \rangle$ can be estimated by first-principles

⁸ The relative number of states (and so of electrons) in the initial state gives the often observed ratio of 2 between these edges. Note also that the ratio is exactly equal to 2 when there is no multielectronic effect and no spin–orbit interaction in the final state. Getting the good *branching ratio* is one of the challenges for the multielectronic theories.

calculations; it is only a few percents and thus, for practical purposes, this term can often be neglected. On the contrary, one has to estimate n_{3d} . These sum rules are sufficient to extract $m_{\rm orb}$ and $m_{\rm spin}$ from experiment.

3.7 Monoelectronic Simulations

As stated earlier, simulations can be very helpful in the interpretation of the experiments. Moreover, to quantitatively access to parameters such as atom positions, charges, or magnetic moments, they can be absolutely necessary. We have seen that in some cases ligand field multiplet theory is necessary. Here we focus on the monoelectronic simulations. They often give satisfactory results for the K and $L_{II,III}$ edges of heavy elements.

Monoelectronic simulations use the local (spin) density approximation [L(S)DA] of the density functional theory (DFT). There are two groups of calculation methods: one solving the Schrödinger (or Dirac, or Dyson) equation in a cluster centered around the absorbing atom; the other usually derived from band structure calculations, using the 3D periodicity of the material. The calculations can be performed with or without self-consistency.

Whatever the method, the first thing needed is a potential. This is seen briefly discussed in the next section. Among the different methods of calculation [(full-potential) linearized augmented plane wave (F)LAPW [35], tight-binding, linear combination of atomic orbitals (LCAO), pseudopotential [36], linear muffin-tin orbital (LMTO), Korringa–Kohn–Rostoker (KKR) [38], finite difference, ...], the most used for practical purposes is the multiple scattering theory (MST), which is discussed a bit more in Sect. 3.7.2. At the end, a table shows the different codes available.

3.7.1 The Potential

It is often said that all the methods are equivalent, at the end. Although it might be true, in fact, they give different results... This is due to the fact that, inside each method, approximations are done. Expansions in spherical harmonics or in plane waves are limited; there are interpolations in the building of the potential; calculations are in single or double precision. But, in particular, there are the potential problems. The first problem comes from the approximation done on the potential shape. The second is related to the choice of the exchange—correlation potential.

MST, as LMTO, usually makes an approximation on the potential shape. To make the calculation simpler, the potential is taken as spherically symmetric in the atoms and constant between them, in the interstitial region. This is the so-called muffin-tin approximation. The radius of the atoms (of the spherical part) is thus a technical difficulty, each code author having its own recipe. Often a small overlap is allowed

because, pragmatically, this improves the agreement with the experiments. Nevertheless, from a mathematical point of view, this trick is not justified. Now, using the finite difference method (FDM), pseudopotential or FLAPW techniques, for example, it is possible to have shape-free (or full) potential. The price to pay is that calculations are heavier. Nevertheless, for open structures, when there are few symmetry elements or when the absorbing atom is relatively light, important differences are observed due to the muffin-tin approximation [27]. A recent work has shown, however, that the MST, up to now always using the muffin-tin approximation, can also be applied with a full-potential shape [39].

In the LSDA, the exchange–correlation problem is treated with a local potential, which depends only on the local density of electrons (i.e., at the point where one calculates the potential). In the magnetic case, it depends as well on the local difference between the spin-up and spin-down density. This density can have different forms. Presently, the most used forms are the Hedin–Lundqvist [40] and Perdew–Wang [41] forms. Globally they give an attractive potential of increasing amplitude with increasing electron density. For XAS, it is important to consider the energy dependence of this potential, as proposed by von Barth and Hedin [42]. Indeed, the amplitude of the potential decreases with increasing electron kinetic energy. In a relatively narrow energy range around the plasmon energy, that is, between 10 and 30 eV, this potential changes by several electron volt. Without considering this phenomenon, one gets structures in the spectra shifted by the same amount. Because the position of the oscillations are related to the inter atomic distances, this could lead to false agreement with wrong fit of the corresponding parameters.

3.7.2 The Multiple Scattering Theory

Explaining this theory in a single paragraph is difficult. Readers can find detailed description by Natoli and coworkers [43] or Brouder [44]. There are two ways to explain it. The first way uses the Green's function approach, and the second uses the scattering wave approach. Let us use the second one.

First, one considers just one atom. We build a complete basis in the surrounding vacuum. There, the potential is constant and the solutions of the radial Schrödinger equation are the Bessel, j_{ℓ} , Neumann, and Hankel functions. Using the phase shift theory, one looks how the atom scatters all the Bessel functions. One uses the continuity of the wave function and its derivative at the border. For simplicity, we keep the nonmagnetic case; we can write

$$a_{\ell}b_{\ell}(R)Y_{\ell}^{m} = \sqrt{\frac{k}{\pi}} \left[j_{\ell}(r) - it_{\ell}h_{\ell}^{+}(R) \right] Y_{\ell}^{m}$$
 (3.129)

for the wave function at the muffin-tin radius R. $h_{\ell}^+(r)$ is the Hankel outgoing function, t_{ℓ} is the atomic scattering amplitude, b_{ℓ} the solution of the radial Schrödinger equation in the atom, k the electron wave vector, and a_{ℓ} the amplitude inside the

atom. All these terms depend on the electron kinetic energy. We have introduced the normalization by the density of states in vacuum $\sqrt{k/\pi}$. By continuity, this normalization makes the density of states included in the atomic amplitudes. Using the two equations of continuity (function and derivative), one gets a_{ℓ} and t_{ℓ} .

Now the atom is embedded in a cluster. Thus the incoming wave is not anymore included in a simple Bessel function, but the superposition of this Bessel function and all the other waves of Hankel type is backscattered by the other atoms. The problem is thus not anymore spherical, and the scattering and atomic amplitudes will also depend on the quantum number m (and eventually on the spin index). One has to consider all the scattering processes from one atom to any other atom. To do that, one fills a (big) multiple scattering matrix, containing, for all the atoms, all their individual expansion in spherical harmonics. Its diagonal contains the atomic scattering amplitudes. The off-diagonal part contains the propagation terms connecting the scattering from the (ℓ, m) of an atom a to the (ℓ', m') of another atom a. The inversion of this matrix gives the multiple scattering amplitudes, $\tau_{\ell,m,a}^{\ell',m',a'}$, by the relation

$$\tau_{\ell,m,a}^{\ell',m',a'} = \left[\frac{1}{1-TH}T\right]_{\ell,m,a}^{\ell',m',a'}.$$
(3.130)

T is a diagonal matrix containing the atomic scattering amplitudes. H is the matrix containing the propagation terms.

Most of the computing time is devoted to the inversion of this matrix. When we are not interested in the low photoelectron energy range, it is possible to perform a Taylor expansion (this is the so-called path expansion):

$$\tau_{\ell,m,a}^{\ell',m',a'} \approx \left[T + THT + (TH)^2 T + (TH)^3 T + \dots \right]_{\ell,m,a}^{\ell',m',a'},$$
(3.131)

where the number of paths increases with the power of TH. The limitation of this number is one of the key point in the IFEFFIT [45] and GNXAS [46] codes. At the rising edge, it is not possible to perform this path expansion, because terms in the denominator are bigger than 1 and the series never converge [47].

Using a = a' and skipping the atom index, the optical theorem gives

$$-\Im\left(\tau_{\ell,m}^{\ell',m'}\right) = \left|\sum_{f} a_{\ell,m}^{f*} a_{\ell',m'}^{f}\right| \tag{3.132}$$

when the potential is real. Introducing this in the XANES formula, one gets

$$\sigma = -4\pi^{2}\alpha\hbar\omega\sum_{g}\sum_{\ell,m,\ell',m'}\Im\left(\left\langle\varphi_{g}\left|\hat{o}^{*}\right|\bar{b}_{\ell}Y_{\ell}^{m}\right\rangle\tau_{\ell,m}^{\ell',m'}\left\langle\bar{b}_{\ell'}Y_{\ell'}^{m'}\left|\hat{o}\right|\varphi_{g}\right\rangle\right). \quad (3.133)$$

The central term $\left|\bar{b}_{\ell}Y_{\ell}^{m}\right\rangle au_{\ell,m}^{\ell',m'}\left\langle\bar{b}_{\ell'}Y_{\ell'}^{m'}\right|$ is the Green's function.

Authors	Name	Technique	3D	SCF	Fit	Reference and note
Natoli et al.	CONTINUUM	MST	Cl			[43] The first
Benfatto et al.	MXAN	MST	Cl		\checkmark	[51]
Ankudinov et al.	FEFF	MST	Cl	\checkmark		[52] The most used
Joly	FDMNES	MST & FDM	Cl	\checkmark	\checkmark	[27]
Ebert	SPRKKR	KKR	3D	\checkmark		[38]
Blaha et al.	WIEN2k	FLAPW	3D	\checkmark		[35]
Cabaret et al.		Pseudo	3D	\checkmark		[36]
Saint-Amant et al.	StoBe	LCAO	3D	\checkmark		[53]
Vedrinskii et al.	XKDQ	MST	Cl			[54]
Yaresko et al.	Py-LMTO	LMTO	3D	\checkmark		[55]

Table 3.4 Some of the most used monoelectronic codes for absorption spectroscopy

Cl and 3D means, respectively, cluster and 3D approach, SCF means self-consistent calculation, Fit means there is a fit procedure with experimental spectra to get parameters. Note that a FEFF version used in the intermediate energy range called IFEFFIT [45] and the code GNXAS [46] use the path expansion in the MST framework and allow a fitting procedure to get geometrical parameters. Cabaret et al. use a pseudopotential approach, having modified first the PARATEC code and more recently the PWSCF code

One can do the same for the RXS case. To be more complete, we have written the equation with inclusion of the spin—orbit interaction:

$$f' - if'' = \frac{\pi}{2} \frac{2m}{\hbar^2} (\hbar \omega)^2$$

$$\times \sum_{g,\sigma} \sum_{\substack{\ell,m,s \\ \ell',m',s'}} \left\langle \varphi_g^{\sigma} \left| o_s^* \right| \bar{b}_{\ell,m+\frac{1}{2}-\sigma,s}^{\sigma} Y_{\ell}^{m} \right\rangle \tau_{\ell,m+\frac{1}{2}-s,s}^{\ell',m'+\frac{1}{2}-s',s'} \left\langle \bar{b}_{\ell',m'+\frac{1}{2}-\sigma,s'}^{\sigma} \left| o_i \right| \varphi_g^{\sigma} \right\rangle.$$
(3.134)

When the potential is complex, the expression contains more terms because the irregular solutions of the radial Schrödinger equation have to be considered, as well.

3.7.3 Available Codes

There are a number of codes that permits to perform monoelectronic simulations of the absorption spectra. We present a probably nonexhaustive list of them in Table 3.4. Some use the 3D periodicity of the solid, and some others use the cluster approach. One has first to recall that the first theories are due to Dill and Dehmer in 1974 [48] and Lee and Pendry in 1975 [49]. The first calculations using a cluster MST approach are due to Natoli et al. [43] and those using a band structure approach were first performed by Mattheiss and Dietz [50], both in 1980.

3.8 Conclusion

We have reviewed the different phenomena governing the X-ray spectroscopies related to the transition of an electron from a core level up to some other level. The number of applications of these processes is huge. They permit a precise

understanding of spectroscopies, giving different pieces of information on the materials. Because the processes involved in the transition are complex, the interpretations are not always direct. Some of them need multiplet calculations (see, e.g., [56]). Some others can use monoelectronic simulations as presented here. Some of the spectroscopic techniques are presented in details in the following chapters of this book. These are the inelastic X-ray scattering by J.-P. Rueff, the X-ray detected magnetic resonance by J. Goulon and coworkers, and the resonant X-ray scattering by S.P. Collins and A. Bombardi. A. Rogalev also develops examples of optical activities.

Acknowledgements All my gratitude goes to C. Natoli for his constant help. Most of the community has benefited of his enormous knowledge kindly shared. I also specially thank Ch. Brouder, D. Cabaret, E. Lorenzo, S. Grenier, H. Tolentino, and D. Sébilleau for their support and their useful advices.

References

- 1. E. N. Maslen, in *International Tables for Crystallography*, Vol. C: Mathematical, Physical and Chemical Tables, ed. by E. Prince (Kluwer, Dordrecht, 2006), pp. 599–608
- V. V. Balashov, in *Interaction of Particles and Radiation with Matter* (Springer, Berlin, 1997),
 p. 136
- 3. O. Proux and J.-L. Hazemann, measured at the FAME beamline at the ESRF, private communication
- C. Fillaux, C. Den Auwer, D. Guillaumont, D. K. Shuh, T. Tyliszczak, J. Alloys Comp. 444–445, 443 (2007)
- 5. B. Poumellec, R. Cortes, G. Tourillon, J. Berthon, Phys. Stat. Sol. (b) 164, 319 (1991)
- 6. R.-M. Galéra, Y. Joly, A. Rogalev, N. Bingelli, J. Phys.: Condens. Matter 20, 395217 (2008)
- 7. M. Blume, in *Resonant Anomalous X-ray Scattering: Theory and Applications*, ed. by G. Materlik, J. Sparks, K. Fischer (North-Holland, Amsterdam, 1994), p. 495
- S. Grenier, A. Toader, J. E. Lorenzo, Y. Joly, B. Grenier, S. Ravy, L. P. Regnault, H. Renevier, J. Y. Henry, J. Jegoudez, A. Revcolevschi, Phys. Rev. B 65, 180101 (2002)
- 9. M. Blume, J. Appl. Phys. 57, 3615 (1985)
- C. Cohen-Tannoudji, J. Dupont-Roc, G. Grynberg, in *Processus d'Interaction entre Photons et Atomes*, Chapitre 2 (EDP Sciences & CNRS Editions, Les Ulis, 1988)
- 11. M. Blume, D. Gibbs, Phys. Rev. B **37**, 1779 (1988)
- 12. F. de Bergevin, M. Brunel, Acta Cryst. A 37, 314 (1981)
- 13. P. Kruger, C. R. Natoli, Physica Scripta **T115**, 146 (2005)
- 14. J. A. Soininen, E. L. Shirley, Phys. Rev. B **64**, 165112 (2001)
- Time-Dependent Functional Theory, ed. by M. A. L. Marques, C. A. Ullrich, F. Nogueira, A. Rubio, K. Burke, E. K. U. Gross, Lecture Notes in Physics, Vol. 706 (Springer, Berlin, 2006)
- 16. A. L. Ankudinov, A. I. Nesvizhskii, J. J. Rehr, Phys. Rev. B 67, 115120 (2003)
- 17. F. M. F. de Groot, Inorganica Chimica Acta **361**, 850 (2008)
- 18. P. A. Lee, Phys. Rev. B 13, 5261 (1976)
- 19. J. L. Erskine, E. A. Stern, Phys. Rev. B 12, 5016 (1975)
- C. D. Wagner, W. M. Riggs, L. E. Davis, J. F. Moulder, G. E. Mullenberg, in *Handbook of X-ray Photoelectron Spectroscopy* (Perkin-Elmer Corp., Eden Prairie, 1979)
- S. V. Borisenko, A. A. Kordyuk, V. Zabolotnyy, J. Geck, D. Inosov, A. Koitzsch, J. Fink, M. Knupfer, B. Büchner, V. Hinkov, C. T. Lin, B. Keimer, T. Wolf, S. G. Chiuzbăian, L. Patthey, R. Follath, Phys. Rev. Lett. 96, 117004 (2006)

- R. F. Egerton, Electron Energy Loss Spectroscopy in the Electron Microscope, 2nd ed. (Plenum, New York, 1996)
- 23. Resonant Anomalous X-ray Scattering: Theory and Applications, ed. by G. Materlik, C. J. Sparks, K. Fischer (North-Holland, Amsterdam, 1994)
- M. A. Walsh, G. Evans, R. Sanishvili, I. Dementieva, A. Joachimiak, Acta Cryst. D 55, 1726 (1999)
- 25. D. H. Templeton, L. K. Templeton, Acta Cryst. A 41, 365 (1985)
- E. Nazarenko, J. E. Lorenzo, Y. Joly, J.-L. Hodeau, D. Mannix, C. Marin, Phys. Rev. Lett. 97, 056403 (2006)
- 27. Y. Joly, Phys. Rev. B **63**, 125120 (2001) http://www.neel.cnrs.fr/fdmnes
- 28. Ch. Brouder, J. Phys.: Condens. Matter 2, 701 (1990).
- C. R. Natoli, Ch. Brouder, Ph. Sainctavit, J. Goulon, C. Goulon-Ginet, A. Rogalev, Eur. Phys. J. B 4, 1 (1998)
- J. Goulon, C. Goulon-Ginet, A. Rogalev, V. Gotte, C. Malgrange, Ch. Brouder, C. R. Natoli J. Chem. Phys. 108, 6394 (1998)
- 31. A. Rogalev, J. Goulon, F. Wilhelm, Comptes Rendus Physique 9, 642 (2008)
- 32. B. T. Thole, P. Carra, F. Sette, G. van der Laan, Phys. Rev. Lett. 68, 1943 (1992)
- 33. P. Carra, M. Altarelli, Phys. Rev. Lett. 64, 1286 (1990)
- 34. C. T. Chen, Y. U. Idzerda, H.-J. Lin, N. V. Smith, G. Meigs, E. Chaban, G. H. Ho, E. Pellegrin, F. Sette, Phys. Rev. Lett. 75, 152 (1995)
- 35. P. Blaha, K. Schwarz, G. Madsen, D. Kvasicka, J. Luitz, WIEN2k: An Augmented Plane Wave + Local Orbitals Program for Calculating Crystal Properties (Technische Universität Wien, Wien, 2001)
- D. Cabaret, E. Gaudry, M. Taillefumier, P. Sainctavit, F. Mauri, Physica Scripta T115, 131 (2005)
- 37. O. K. Andersen, O. Jepsen, M. Sob, in *Electronic Band Structure and its Applications*, ed. by M. Yussouff, Lecture Notes in Physics, Vol. 283 (Springer-Verlag, Berlin, 1987), p. 1
- 38. H. Ebert, in *Electronic Structure and Physical Properties of Solids: the Uses of the LMTO Method*, ed. by H. Dreyssé, Lecture Notes in Physics, Vol. 535 (Springer Berlin, 2000), p. 191.
- 39. K. Hatada, K. Hayakawa, M. Benfatto, C. R. Natoli, Phys. Rev. B 76, 060102 (2007)
- 40. L. Hedin, S. Lundqvist, J. Phys. C: Solid State Phys. **4**, 2064 (1971)
- 41. J. P. Perdew, Y. Wang, Phys. Rev. B 45, 13244 (1992)
- 42. U. von Barth, L. Hedin, J. Phys. C: Solid State Phys. 5, 1629 (1972)
- 43. C. R. Natoli, D. K. Misemer, S. Doniach, F. W. Kutzler, Phys. Rev. A 22, 1104 (1980)
- 44. Ch. Brouder, in *Magnetism and Synchrotron Radiation*, ed. by E. Beaurepaire, B. Carrière, J.-P. Kappler (Les Editions de Physique, Les Ulis, 1997), p. 33
- 45. http://cars9.uchicago.edu/ifeffit/
- 46. http://gnxas.unicam.it/
- 47. C. R. Natoli, M. Benfatto, J. Phys. C: Solid State Phys. 8, 11 (1986)
- 48. D. Dill, J. L. Dehmer, J. Chem. Phys. **61**, 692 (1974)
- 49. P. A. Lee, J. B. Pendry, Phys. Rev. B 11, 2795 (1975)
- 50. L. F. Mattheiss, R. E. Dietz, Phys. Rev. B 22, 1663 (1980)
- 51. M. Benfatto, S. Della Longa, J. Synchrotron Rad. 8, 1087 (2001)
- A. L. Ankudinov, B. Ravel, J. J. Rehr, S. D. Conradson, Phys. Rev. B 58, 7565 (1998) http://leonardo.phys.washington.edu/feff/
- 53. http://w3.rz-berlin.mpg.de/ hermann/StoBe/
- R. V. Vedrinskii, V. L. Kraizman, A. A. Novakovich, Sh. M. Elyafi, S. Bocharov, Th. Kirchner, G. Dräger, Phys. Stat. Sol. (b) 226, 203 (2001)
- A. N. Yaresko, V. N. Antonov, H. Eschrig, P. Thalmeier, P. Fulde, Phys. Rev. B 62, 15538 (2003)
- F. de Groot and A. Kotani, in Core Level Spectroscopy of Solids, eds. Taylor and Francis, New-York(2008)

Chapter 4 Synchrotron Radiation Sources and Optical Devices

D. Cocco and M. Zangrando

Abstract This chapter will briefly describe the photon transport system, from the sources to the experimental stations, including an overview of the characteristics of the synchrotron radiation (SR). The target of this chapter is to give, to an occasional user of the SR source, a general overview on the possible different available sources and the different possible optical systems, with particular emphasis to the soft X-ray region, without entering too much into details. If one wish to have a deep knowledge on the subjects treated here, there are four books that can answer almost all the possible questions on SR sources and optical devices, and they are reported in the references [W.B. Peatman, *Gratings, Mirrors, and Slits* (Gordon and Breach Science Publishers, New York, 1997); D. Attwood, *Soft X-rays and Extreme Ultraviolet Radiation* (Cambridge University Press, Cambridge, 1999); H. Wiedemann, *Synchrotron Radiation* (Springer, Heidelberg, 2002); A. Erko, M. Idir, T. Krist, A.G. Michette, *Modern Developments in X-ray and Neutron Optics*, Springer Series in Optical Science, vol. 137 (Springer, Heidelberg, 2008)].

4.1 Optics for UV and X-Ray

The synchrotron radiation emitted from the sources that will be described in the next sections (bending magnets, undulators, and wigglers) typically ranges from the infrared (IR) to the Hard X-rays (HXR) regions. Consequently, the emitted wavelengths go from microns (IR) to fractions of nanometers (HXR), and the energy goes from fractions of electron-volt (eV) to tens of kilo electron-volt (keV). Within this range there is a very interesting region going from vacuum ultraviolet (VUV) to HXR, where most of the low- and intermediate-Z elements absorption edges are present. So photons covering these energies are a very sensitive tool for elemental and chemical identification. Unfortunately, these regions are difficult to access, and the corresponding photons are not easy to handle and transport to the experiments

Sincrotrone Trieste ScpA, SS14 Km 163.5 in Area Science Park, 34012 Trieste, Italy e-mail: daniele.cocco@elettra.trieste.it

D. Cocco (⊠)

through mirrors and diffraction gratings. This difficulty mainly arises from the fact that the radiation from Soft X-rays (SXR) to extreme UV (EUV) is characterized by very small reflection coefficients for most of the angles of incidence. This limitation is caused by the fact that the refractive index is almost 1 ($n=1-\delta+i\beta$), causing only little changes on the field amplitudes across the interface. Nevertheless, for certain angles of incidence, namely grazing incidence (far from the surface normal), this behavior changes, leading to an enhancement of the reflectivity. As a matter of fact, total external reflection takes place, enabling the use of dedicated optics for transport, deflection, focusing, and filtering of the EUV-XR radiation. This effect can be understood from Snell's law.

$$\sin \phi' = \frac{\sin \phi}{n},\tag{4.1}$$

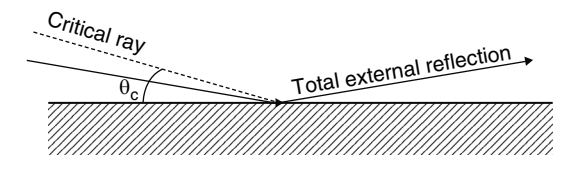
where n is the complex index of refraction, and ϕ and ϕ' are the incidence and refraction angles, respectively (Fig. 4.1). For EUV and XR, the real part of the refractive index is slightly less than unity and consequently the radiation is refracted in a direction slightly further from the surface normal ($\sin \phi'$ slightly larger than $\sin \phi$). Thus for near-grazing incidence (ϕ close to $\frac{\pi}{2}$), the refraction angle ϕ' can equal $\frac{\pi}{2}$, leading to a refracted wave propagating along the interface rather than penetrating into the material (Fig. 4.1).

In reality, the total external reflection is not completely realized due to the presence of the finite coefficient β . As a portion of the field extends into the medium, even if only in an evanescence manner, losses are incurred and total reflection is not achieved. Nonetheless, it is possible to calculate the reflectivity vs. photon energy of different materials simply by knowing δ and β of the material of interest, across the photon energies of interest, for the incident angles relevant to the experiment. The values for δ and β are tabulated by Henke et al. [1] and the resultant reflectivity curves are interesting as they relate to real materials and include the effects of absorption edges (as well as other effects such as oxidation and multi-elements). Some examples of reflectivity curves for selected materials are reported in Fig. 4.2.

Typically, instead of having an optical element completely made of the selected material, it is common to put a thin coating of the material used for reflection on the polished surface. In this way the radiation, which penetrates the surface only for some nanometers, will optically behave as if the whole mirror was made by the right material.

The choice of the coating material depends on the energy of the photons to be used. In normal incidence mode, in the UV range, a typical coating is aluminium

Fig. 4.1 Grazing incidence radiation and total external reflection. $\theta_{\rm c}$ in figure is equal to $\frac{\pi}{2}-\phi$



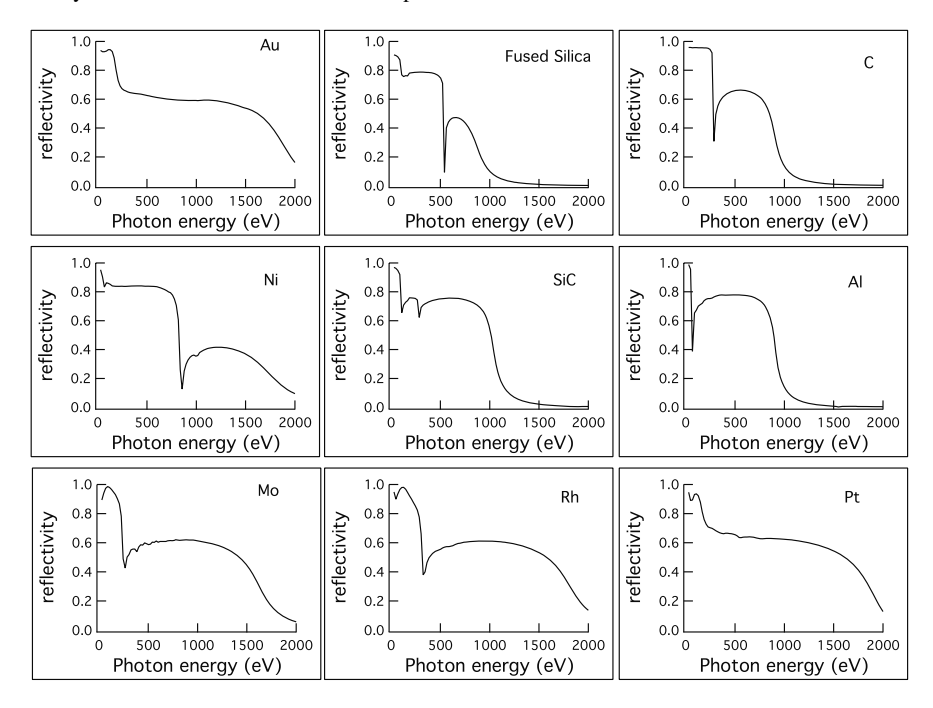


Fig. 4.2 Grazing incidence reflectivity vs. photon energy for incidence angle of 2° for different materials

with an MgF_2 over-coating protecting the aluminium from oxidation. In the lower part of the soft X-ray range, carbon, gold, nickel, platinum, and some other metallic layers are the good choices. Nevertheless, when higher energies are necessary, only gold and platinum remain good choices due to the absence of absorption edges.

Another element to take into account is the dependence of the reflectivity upon the angle of incidence. As the penetration depth of the photons into the matter increases as the incidence angle goes towards the surface normal, the absorption increases too. In Fig. 4.3, the behavior of the reflectivity as a function of the incidence angle is reported for a gold-coated mirror.

To select the proper material for the bulk of the optical element (mirror or grating), some considerations have to be made. The main problem is to find a material that can be polished and manufactured to produce the required shape with the required precision, and in the meantime this material must satisfy some requirements: it has to be UHV-compatible, it has to be characterized by a limited thermal expansion (to avoid deformation under the synchrotron radiation beam), it has to be rigid enough not to be deformed by the clamping system, and in many cases it must be cooled. Depending on the chosen material, the roughness and the slope errors can be reduced to acceptable values. Some widely used materials are summarized in Table 4.1.

From Table 4.1 it is evident that silicon carbide (SiC) is a good material when it is needed to cool the mirror/grating. It is in fact rigid enough not to be deformed by

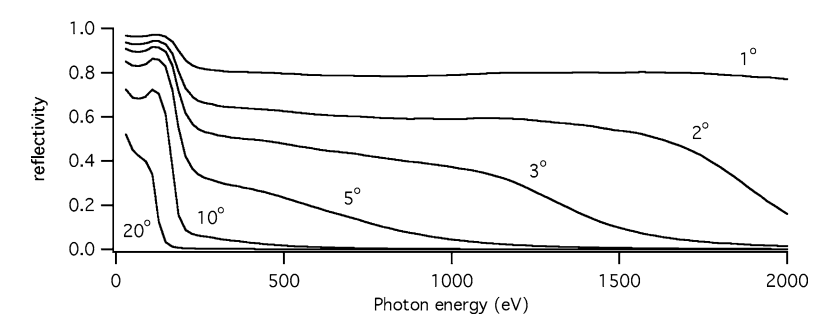


Fig. 4.3 Reflectivity vs. photon energy for gold at different grazing angles of incidence

Table 4.1 List of typically used material for the synchrotron radiation mirrors and some useful characteristics

Material	Density	Young's	Thermal	Thermal	Figure of
	$(g cm^{-3})$	modulus	expansion (α)	conductivity (k)	merit $(k \alpha^{-1})$
		(GPa)	$(ppm K^{-1})$	$(W m^{-1} K^{-1})$	
Si	2.33	131	2.6	156	60
SiC	3.21	461	2.4	198	82.5
Glidcop	8.84	130	16.6	365	22
Mo	10.21	324	4.8	142	29.6
Fused silica	2.17	73	0.5	1.4	2.8
Zerodur	2.53	92	0.05	1.6	32

the clamping and it has a high figure of merit, that is, a limited thermal expansion together with a good thermal conductivity. This means that, with a cooling system made by a cool object put in tight contact with the edge of the optic, it is possible to dissipate the heat induced by the synchrotron radiation light. Another advantage of its stiffness is the possibility to polish it with a very good surface finishing. In this way the final roughness can be of the order of 0.1 nm rms. The same statement is valid for silicon and glass materials in general, while this is not true for metals. As a matter of fact, metals are typically malleable, and therefore the friction with the polishing tools always produces some particles of material that damage the surface. If the optics need to be cooled, another possible solution is the use of Glidcop (Copper and/or Molybdenum) but with the option of internal cooling. To realize such internally cooled optics, it is necessary to manufacture them with particular care. In particular, as the materials for this kind of optical elements are metals, it is feasible to weld them. The only difference with normal welding is that the procedure should be vacuum-compatible. This causes some complications, but nonetheless it is possible, and it is called brazing. In this way it is possible to create some channels close to the optical surface inside the blank and let the water circulate inside them. Therefore, even if the thermal conductivity of the material is poor with respect to silicon or SiC, the cooling channels are very close to the optical surface and the cooling procedure is efficient.

Besides the above-mentioned characteristics of the optical elements to be used along a beamline (materials, angles of incidence, cooling, etc.), the most important requirement to be fulfilled is the shape of the optical surface reflecting/diffracting the radiation. The need is to carry the photon beam to the experimental endstations and to meet the users' requirements in terms of fluxes, spot sizes, energy resolutions, and so on. To perform these tasks, the optical designer must select the proper shape and parameters for each optical element.

The typical shapes for synchrotron mirrors and gratings vary from plane to more exotic aspherical ones (e.g., paraboloid, ellipsoid, toroids, etc.). Moreover, the parameters of these mirrors are rather variable. Ellipsoidal and toroidal optical surfaces, with radius (or equivalent radius) of curvature from 10–20 m up to some kilometer in the tangential direction and close to few centimeters in the sagittal one (perpendicular to the incoming beam), are typically specified.

On the other hand, for small grazing incidence angles, every imperfection on the optical surfaces will result in drastically reduced overall performance of a multicomponent beamline, designed to monochromatize and focus synchrotron light.

It is possible to distinguish between two types of errors related to the optical surface: those with a period comparable to the dimensions of the optical element itself, and those with a much shorter period. A further subdivision is then possible for the second type: errors that contribute to the specular image are called (along with those of the first type) figure or tangent errors, while the others that contribute to scattered light are ascribed to surface roughness [2]. Figure (slope) errors of a few micro-radian rms and surface roughness exceeding few Å rms can be sufficient to reduce substantially both the energy resolution and the photon density required for the experiments.

Going into detail, the slope errors can be thought as imperfections that locally change the direction of the normal to the optical surface, and therefore change the direction of the reflected radiation. In Fig. 4.4, $\delta\theta$ is the change in the normal direction and $2\delta\theta$ (the angle is doubled by the reflection) is the change in the reflected beam.

The plane reported in Fig. 4.4 is called the tangential plane, and it is determined by the normal to the optical surface and the incoming radiation direction. In this plane, the effect of the enlargement of the spot Δs_{tan} at a distance r' from the mirror is easily estimated by

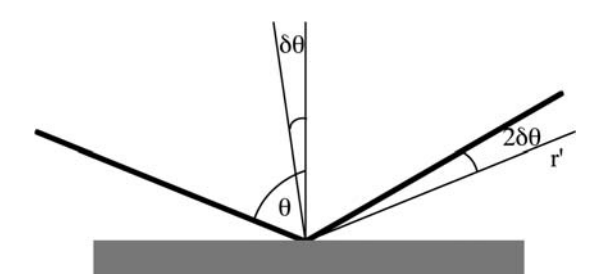


Fig. 4.4 Effect of a surface error on the tangential plane of a mirror

$$\Delta s_{\text{tan}} = 2r'\delta\theta_{\text{tan}}.\tag{4.2}$$

In the plane perpendicular to the tangential one, the so-called sagittal plane, the effect of the enlargement on the spot is reduced. By applying simple geometry relation, it is easy to see that the enlargement of the spot in the sagittal direction is

$$\Delta s_{\text{sag}} = 2r'\delta\theta_{\text{sag}}\cos\theta. \tag{4.3}$$

As in a synchrotron typically the source is smaller in the vertical direction and the monochromators have vertical dispersing planes, it is clear that optical elements producing a horizontal (sagittal for the monochromator) deflection need not be of as high quality as those producing a vertical (tangential for the monochromator) deflection. In particular, to produce the same Δs on the image, in the case of θ equal to 88°, the relative magnitudes of the figure errors should be related in the following way: $\delta_{\rm sag} = 29\delta_{\rm tan}$. It is straightforward that the tangential figure errors are more effective in disturbing the image with respect to the sagittal ones.

The second kind of error, the roughness, can be thought as a random distribution of small imperfections. In this way the final effect is a reduction of the intensity in the reflected peaks because the rays are dispersed all around the reflected beam direction and the dispersion profile follows a Gaussian distribution. The parameters of this Gaussian profile depend on the ratio σ/λ , where σ is the amplitude of the roughness and λ is the wavelength of the incoming radiation: smaller is the wavelength higher is the effect of the roughness.

The intensity of the reflected radiation I is reduced with respect to the ideal reflected radiation intensity (I_0) by a factor proportional to the above mentioned ratio, and precisely

$$I = I_0 \exp\left(-\frac{4\pi\sigma \cos\theta}{\lambda}\right)^2. \tag{4.4}$$

As stated earlier, the shapes of the optical surfaces are the most important feature to take into account when designing a beamline. Depending on these shapes, in fact, the focusing and monochromatizing properties of a beamline may change, and so it is important to choose the proper shape according to the experimental needs.

The different shapes can be described by means of simple formulas relating the object distance r, the image distance r', and the angle of incidence θ . Typical shapes are toroidal, cylinder, ellipsoid, parabola besides the most used, spherical and plane. Toroidal mirrors are spherical mirrors in the tangential direction and cylinder, with a shorter radius of curvature, in the sagittal one. They are used commonly because they are easily available on the market at reasonable prices, and moreover they offer the advantage of reducing the number of optical elements in a beamline. However, the quality of the produced image is poorer than that produced by ellipsoidal or paraboloidal surfaces due to the presence of astigmatic coma. The latter ones, on the other hand, are more difficult to manufacture due to the presence of aspheric

surfaces (the ellipsoid will be described later in the refocusing section). They typically cost much more than plane and spherical/toroidal surfaces. However, it may be convenient to select in any case ellipsoidal surfaces as they are almost free from aberrations, which counterbalances the slightly poorer optical quality with respect to simpler shapes.

4.2 Sources, Beamlines, and Monochromators for Soft X-Ray

To preserve the particular characteristics of the synchrotron radiation sources and carry the light to the experiments, adapting the shape and selecting a particular wavelength over the entire available spectrum, it is necessary to use a *beamline*. A sketch of a typical beamline is reported in Fig. 4.5. It can be divided into three parts that can be present altogether or just one or two of them.

The first part is called *prefocusing* or sometimes *preconditioning* or *heat load* section. The main purpose of it is to adapt the source characteristics to the need of the following section. The second part, usually the most important and expensive one, is the *monochromator*, used to select a particular wavelength within the spectrum provided by the SR sources. The third part is the *refocusing* section and it is used to adapt the beam dimensions or divergence to the needs of the experiment.

4.2.1 SR Sources and Prefocusing or Heat Load Section

The purpose of the first part of a beamline is double. The most evident task is to adapt the source size to the need of the following section, the monochromator. The reason will be clear later on when the monochromator will be described. Practically, to have high energy resolution or to have a flexible system (for instance in a Follath

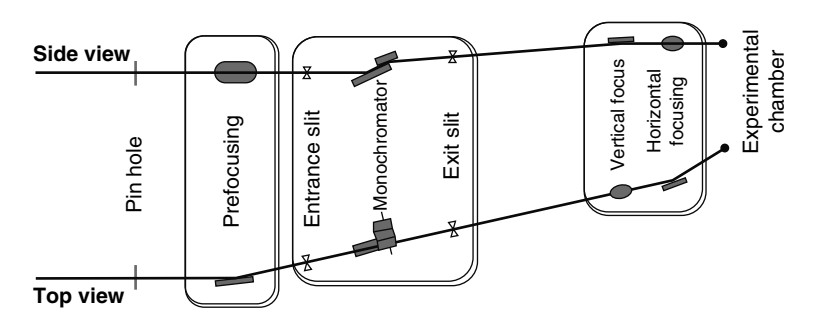


Fig. 4.5 Layout of a soft X-ray beamline. From left to right one can find the prefocusing section, the monochromator, and the refocusing section

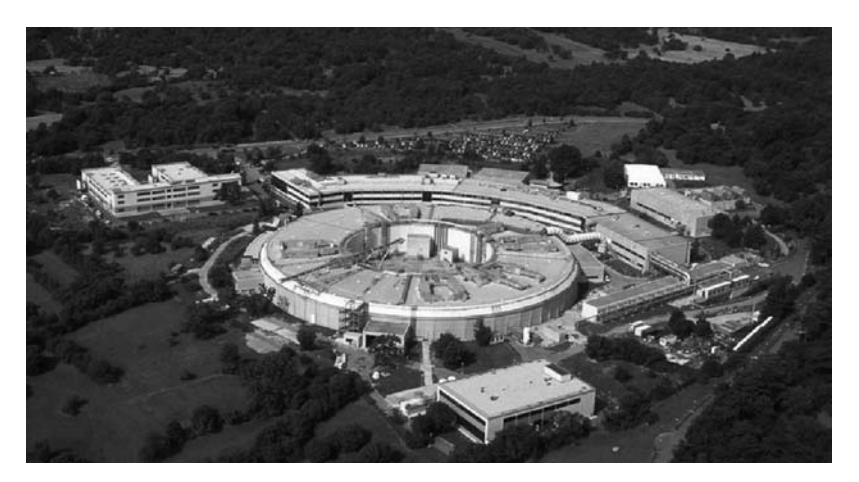


Fig. 4.6 Areal view of the third generation synchrotron radiation Source Elettra in Trieste, Italy

type monochromator[3]), one needs to demagnify the SR source to create a new source for the monochromator into the dispersive direction or to generate a collimated beam, if needed. Moreover, there is a second reason to have a prefocusing section, that is, the *heat load*. To understand this, we have to make a short review on the characteristics of the radiation emitted by a synchrotron radiation source, also called storage ring.

As stated at the beginning, the SR source is very well described in several text-books [4,5]. It consists of a circular ring (Fig. 4.6) where electrons are accelerated up to a relativistic speed and maintained at a fixed energy of few Giga-electron-volt. The electrons travel in an ultrahigh vacuum ring on a closed loop, maintained in orbit by means of strong magnetic fields. Every time an electron is forced by a magnet to change its trajectory (Lorentz force), it loses energy by emitting radiation. This is the first and most simple way to extract radiation from a storage ring, and this kind of source is called Bending Magnet. The radiation emitted by an accelerated electron is the typical dipole radiation but, in the laboratory frame, thanks to the very high speed, it suffers from a relativistic contraction, resulting in a very forward peaked beam, and the energy of the radiation shifts to the X-ray region.

The radiation emitted by a bending magnet has a continuous energy spectrum ranging from the infrared to the hard X-ray (see Fig. 4.7), with a peak at a wavelength depending on the energy of the circulating electrons and the magnetic field of the bending magnets. The higher is the energy of the electrons, the higher (in photon energy) will be the position of this peak. This is the reason why the storage rings are classified according to the energy of the circulating electrons. Typical energies for the modern rings range from 2 to 8 GeV with very few exceptions. The peak photon energy changes accordingly to the ring energy, from few keV to 50 keV or more.

The radiation emitted by a bending magnet is concentrated in a narrow cone (Fig. 4.8) in the vertical plane and it is linearly polarized with the electric field

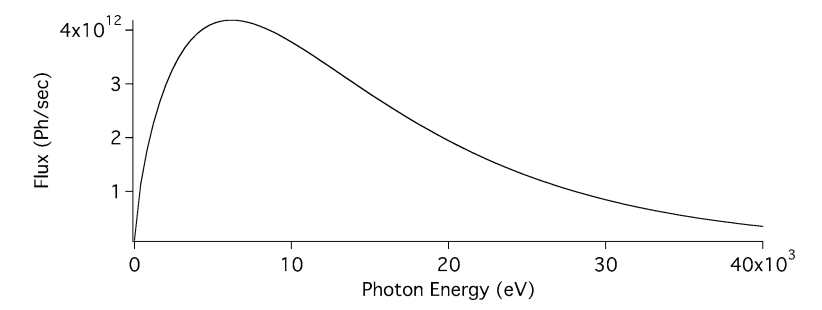


Fig. 4.7 Bending magnet spectrum

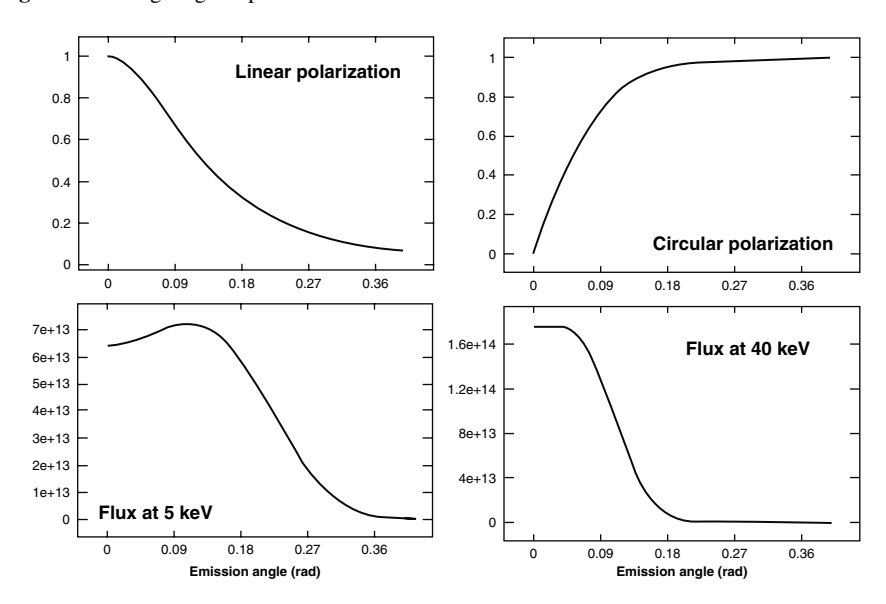
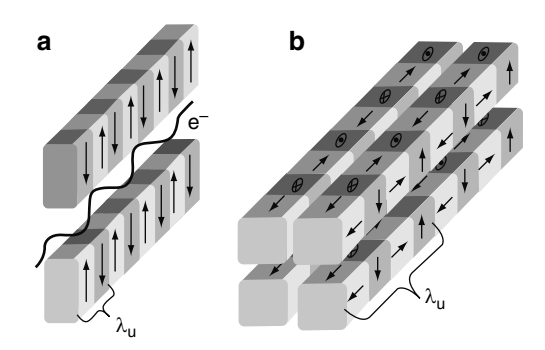


Fig. 4.8 Distribution of the BM radiation for a 6 GeV ring. *Top left*: Typical normalized distribution of the linearly polarized light in the vertical plane (perpendicular to the electron orbit plane). *Top right*: Normalized distribution of the circularly polarized light in the vertical plane. *Bottom left*: Flux (ph/s) distribution of the 5 keV radiation in the vertical plane (energy lower than the peak emission energy). *Bottom right*: Flux (ph/sec) distribution of the 40 keV radiation (energy higher than the peak one) in the vertical plane

parallel to the plane of the orbit. In reality, the linear polarization degree is 1 only in the plane of the orbit (Fig. 4.8). If one looks at the emitted radiation from an angle extending outside the plane of the orbit, the linearly polarized light contribution decreases while the circularly polarized one increases (Fig. 4.8).

A very useful concept widely used in the SR community is the brilliance, sometimes also called brightness. The brilliance is the number of emitted photons per second in a narrow energy bandwidth BW (usually 0.1%) per unit solid angle. Practically, while the flux is a measure of the total intensity, integrated in the total

Fig. 4.9 Periodic array of magnets with the direction of the magnetic field. (a) The typical magnet array of a planar undulator, producing linear polarized light. (b) The arrangement needed to produce elliptically polarized light



accepted solid angle, the brilliance takes into account the "ability" of the storage ring to generate a very narrow cone of radiation out of a very small source dimension. Therefore, the brilliance can be written as

Brilliance =
$$\frac{N_{\text{photons}}}{\sigma_x \sigma_y \sigma_x^t \sigma_y^t \text{BW}_{0.1\%}}$$
, (4.5)

where $\sigma_x \sigma_y$ are the source spatial divergences and $\sigma_x^t \sigma_y^t$ are the source angular divergences. Even if the bending magnets are sources with very high flux, in terms of brilliance, the *undulators* are some orders of magnitude higher. The undulators, as well as the *wigglers*, are periodic arrays of magnets positioned along the straight sections of the storage ring. In fact, between two consecutive bending magnets there are several devices needed to maintain the electrons in the proper orbit with the right energy and spatial characteristics, and machine designers typically let some long empty spaces available to insert the so-called *insertion devices* (IDs). In this long straight section, with length going from 1–2 m up to 10–12 m, one can insert, as said, a periodic set of magnets (Fig. 4.9) arranged such that the traveling electrons are wiggled producing an interference effect.

The resulting emitted energy spectra are not continuous as for the bending magnet (Fig. 4.10) but peaked on well defined wavelengths, depending on the period of the magnetic array (λ_u), the energy of the electrons (E), and the magnetic field (B). The radiation wavelength is determined by

$$\lambda = \frac{\lambda_u}{2\gamma^2} \left(1 + \frac{K^2}{2} \right),\tag{4.6}$$

where γ is the relativistic factor $\left(1 - \frac{v^2}{c^2}\right)^{-\frac{1}{2}}$ and K, called deflection parameter, is a term taking into account the magnetic field, and it is

$$K = \frac{eB\lambda_u}{2\pi mc} \approx 0.934\lambda_u(\text{cm})B(T). \tag{4.7}$$

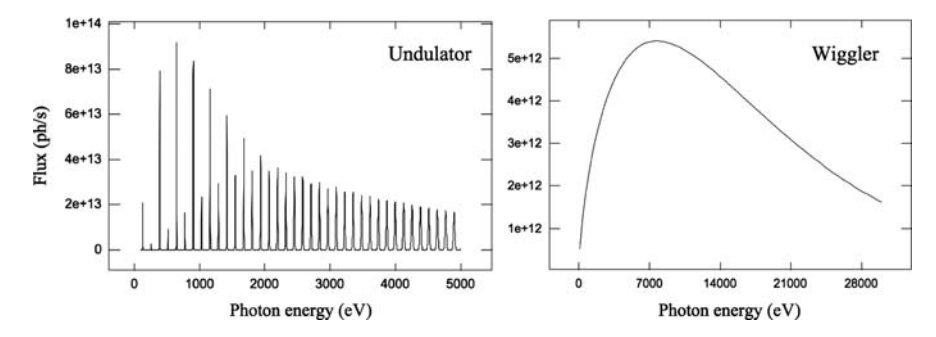


Fig. 4.10 Typical energy spectrum of the radiation emitted by an undulator (*left*) and a wiggler (*right*) collected after a beam-defining aperture. The units are eV for the energy and photons per seconds for the intensity

The radiation is emitted in a very narrow cone, whose divergence is inversely proportional to γ and to the number of periods into the undulator, which further increases the brilliance of the undulator sources.

The undulators, of course, do not have a fixed magnetic field, which would produce a single wavelength. On the contrary, K can be varied producing different values of λ . The easiest way to do it is to change the vertical distance between the magnets (undulator gap) or, in the electromagnetic undulators and wigglers, to change the magnetic field by varying the flowing current.

Typical values of K for undulators range from more or less 1 to 3–4 or maximum of 5, but never too much higher. If K increases further, the deflection becomes very strong and the effect becomes similar to the "sum" of a series of bending magnets. In this case, one works in the wiggler regime and the insertion devices are therefore called wigglers. The emitted spectrum is no longer similar to the one produced by an undulator but it is something closer to that produced by a bending magnet, with higher brilliance and flux. Also the divergence of the emitted radiation becomes larger than that emitted by the undulators. For this reason, the brilliance of the wigglers is lower than the one of the undulators, even if the total flux can be higher. For both insertion devices, there is the possibility to generate circularly polarized light. The way to do it is to force the electrons to oscillate not only in the horizontal plane (Fig. 4.9a) but also in the vertical plane (Fig. 4.9b). In this case, a single ID can produce, depending on the mechanical complexity of the system and or on the magnetic arrangement, linear horizontal, linear vertical, circular, or elliptical polarization. In some cases, it is also possible to rotate the main axis of polarization, so that it is possible to have a linearly or elliptically polarized light with the axis oriented in any given direction.

From Figs. 4.7 and 4.10, it is evident that these sources deliver a lot of photons in very large spectra, even in the case of an undulator. As typically only one wavelength, with narrow or large bandwidth, has to be selected, this means that the biggest part of the emission must be cut. In particular, a high amount of power load has to be absorbed and dissipated. While the selection is made into the

monochromator, the power heat load is adsorbed by the first optical element encountered by the radiation, due to the fact that the reflectivity is not perfect, and so the radiation is absorbed. The power carried by the radiation can be of the order of tens of watts to kilo-watts. To avoid deformation of the mirror, one has to cool down the optics and maintain the surface almost at a constant temperature. To do this, one needs a mirror having a good thermal conductivity and also a low thermal expansion coefficient. Moreover, to produce a good profile, it is necessary to have a quite large Young's modulus, meaning that the optic is quite stiff. Some widely used materials are silicon or silicon carbide (SiC), both satisfying all the above mentioned characteristics. In particular, SiC is slightly better but it is also much more expensive. Therefore, the most used material in SR optics is silicon. Sometimes people use metallic substrates, which have the advantage to be easily workable. In this way it is possible to produce internally cooled mirrors, but the surface quality never reaches that obtained with silicon or glass-based materials.

The list of the commonly used materials with their principal thermal and mechanical properties is reported in Table 4.1.

Of course, the mentioned materials are used to make the mirror body. On its optical surface, typically there is a thin layer of a proper coating to increase the reflectivity, as described at the beginning of this chapter. The reflectivity drops down with increase in the photon energy, and so the high energy part of the source spectrum is adsorbed by the first optics. This fact preserve from deformation the following mirrors and diffraction gratings, the heart of the soft X-ray monochromators.

4.2.2 Soft X-Ray Monochromators and Diffraction Gratings

The central part of a beamline, typically the most expensive and the most complicated, is the monochromator, which is dedicated to select the proper photon energy.

Soft X-ray monochromators are based on the use of diffraction gratings in reflection mode. These are artificial periodic structures generated on substrates polished as mirrors. The grating profiles are shown in Fig. 4.11. They can be laminar, a sort of square profile, or blaze, like a saw tooth. The incident light is dispersed at different angles depending on the wavelength, and the equation describing this effect is

$$\frac{n\lambda}{d} = \sin(\alpha) - \sin(\beta),\tag{4.8}$$

where d is the grating period, n is the diffraction order, and α and β are the angles of incidence and diffraction, respectively (see Fig. 4.11).

The grating, therefore, disperses all the different wavelengths at different angles, and the way to select just one of them over the entire spectrum is described in the following. The radiation has to be focused by the grating or by a curved mirror

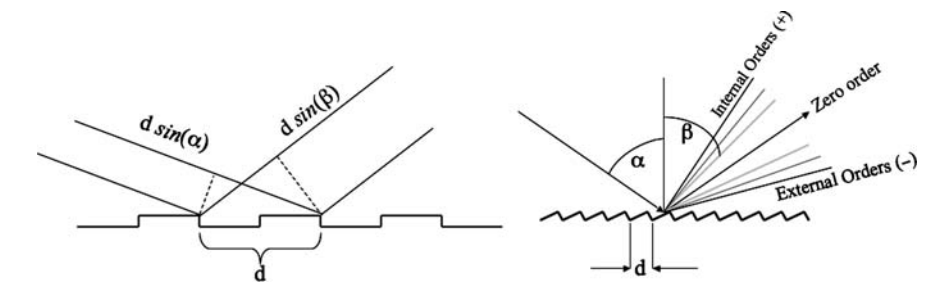


Fig. 4.11 Possible grating profiles and principle of operation. *Left*: Laminar grating with the evidence of the path difference between two rays impinging on the grating at two consecutive grooves. *Right*: Blaze grating with the description of different diffraction orders

into a slit, which lets only "one" wavelength to pass through stopping the others. This slit is generally called *exit slit*, and clearly it cannot select just a single wavelength but rather an extended bandwidth $\Delta\lambda$ (or ΔE in terms of photon energy). The ratio between the selected wavelength or energy and the passing bandwidth $(E/\Delta E = \lambda/\Delta\lambda)$ is called *resolving power*. Let us highlight the relation between the wavelength and the photon energy, namely

$$\lambda(\text{nm}) = \frac{1239.852}{E(\text{eV})}.$$
 (4.9)

How much should the resolving power be? This, of course, strongly depends on the need of the experiment. One thing that have to be kept in mind, when a beamline and therefore a monochromator is designed, is that, by increasing the resolving power by a factor of 2, the flux will very likely decrease by more than a factor of 2. Another important factor is that the resolving power calculated analytically or by simulation (ray tracing) is higher than the real one. So, if an experimentalist needs a resolving power of 10,000 one must try to design beamline to have 11,000 or slightly more. The resolution needed in third generation storage rings must let one study the detail of, for instance, core level shifts, dichroic effects on magnetic sample, different chemical bonding of surface species, and so on. To study these kind of effects, it is necessary to distinguish electrons coming out with difference in energies of the order of few milli-electron-volt. If the incoming radiation has a photon energy of 600 eV (around the Cr edge, for instance), it means that the resolving power $E/\Delta E$ must be of the order of 600/0.01=60,000. Is it an acceptable request? Let us consider the (4.8). To select the proper bandwidth, one has to use a slit. If we call s the slit aperture in the direction of dispersion of the grating, this aperture can also be addressed by

$$s = r' \cdot \Delta \beta,\tag{4.10}$$

where r' is the focal distance of the grating or of the focusing mirror, and β is the angle of diffraction. By deriving 4.8, it follows that

$$\frac{\partial \lambda}{\partial \beta} = \frac{d \cos \beta}{n} \to \Delta \lambda = \frac{d s \cos \beta}{n r'} \to \frac{\lambda}{\Delta \lambda} = \frac{E}{\Delta E} = \frac{n r' \lambda}{d s \cos \beta}.$$
 (4.11)

It is important to underline that *s* can be varied by opening or closing the slit, but it is useless to close it less than the *monochromatic spot dimension* of the focused radiation. This is the dimension of the spot into the exit slit if the incoming radiation is perfectly monochromatic. If one sets the exit slit at lower values, there is no gain in resolution but just a loss of flux.

On the other side, d, the d-spacing, cannot be made as small as possible. Typical values are of the order of 1 or half micrometer, corresponding to groove density of the order of $1,200-1,8001\,\mathrm{mm}^{-1}$. Companies like Jobin Yvon [6] or Zeiss [7] are able to produce larger groove density, but losing the precision of such a grating to a certain extent. The typical groove density for high resolution monochromators is $1,2001\,\mathrm{mm}^{-1}$ corresponding to $0.833\,\mu\mathrm{m}\,d$ -spacing. The angle of diffraction can be also very high, close to 90° but, for efficiency and acceptance reasons, it is practical to set it smaller than 89° . Therefore, from (4.11), to reach a resolution of 60,000 in the first diffraction order at $600\,\mathrm{eV}$, one should have a monochromatic image of $11\,\mu\mathrm{m}$ at a focal distance of $3\,\mathrm{m}$. The problem, consequently, is to generate a monochromatic image of $11\,\mu\mathrm{m}$.

Typical values for undulators or bending magnet sources can range from 30–40 to more than $100\,\mu m$. If the SR sources are of the order of $30\,\mu m$ like in the new high brilliance storage rings, one has to demagnify the source size by a factor 3, which can be made inside the monochromator. When, vice versa, the source size is larger, it is necessary to use an optic before the monochromator that pre-demagnifies the source to transform it into a relatively small value, let us say 20–30 μm . In practice, only in the new third generation SR sources and only on some insertion devices, it is possible to have a monochromator without a prefocusing optics still obtaining quite high resolution.

It is important to note that, in reality, to have a reasonable amount of flux and a limited number of gratings, typical resolution are of the order of 10,000 or 20,000 with very few cases of higher values.

It is out of the scope of this introductive chapter to describe the different kinds of monochromators. We wish just to highlight that one could divide the monochromators in terms of the grating used: the plane grating monochromator (PGM) and the spherical grating monochromators (SGM). In the first class, the most used is the SX700 [8], originally designed by Petersen and modified to work without entrance slit by Naletto and Tondello [9] and further on by Follath [3]. This kind of monochromator needs a refocusing optic after the grating to focus the radiation into the exit slit. It has the great advantage of using a single grating to cover a very large energy range, maintaining the resolving power quite high (see Fig. 4.12). In the case of the SGM, the most used configurations are the variable included angle SGM, also called Padmore [10], and the Dragon [11], working with fixed included angle

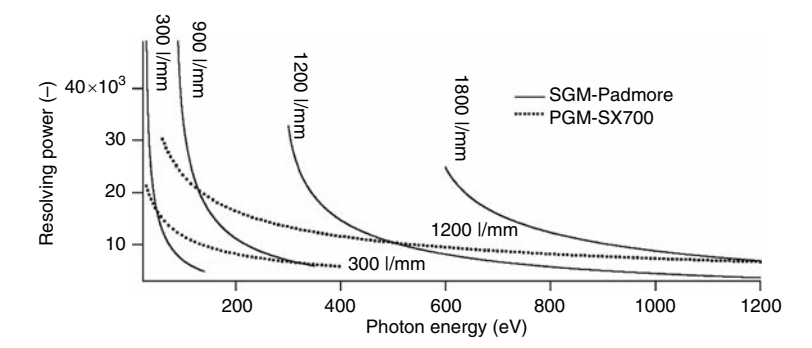


Fig. 4.12 Resolving power of a variable included angle SGM (Padmore like) monochromator (*full line*) and of a variable included angle PGM (SX700) (*dotted line*). The numbers represent the groove densities for the different needed gratings. The distance from the spherical gratings to the exit slit is equal to the distance from the focusing optics of the SX700 to the exit slit, and is 3 m. All the other parameters are identical

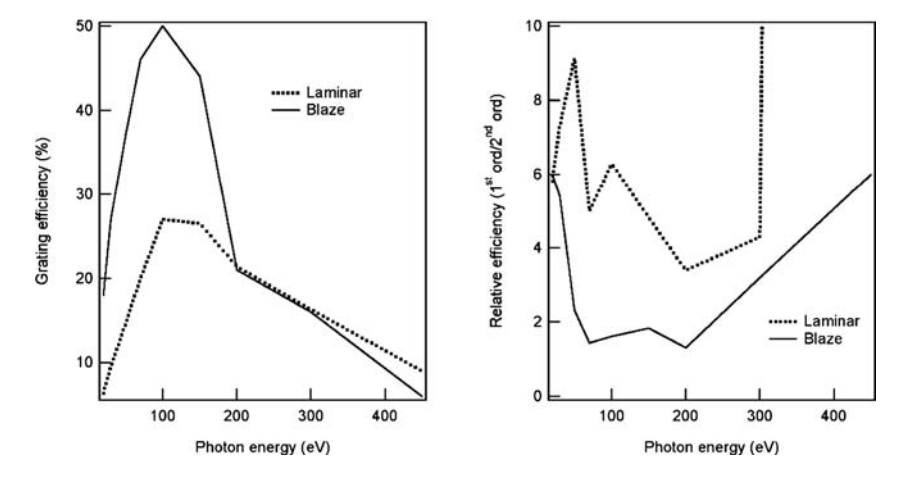


Fig. 4.13 Calculated efficiency for a blaze profile (*full line*) and a laminar profile (*dotted line*) for a PGM. The left figure is the first diffraction order efficiency, while the right one is the ratio between the efficiency in first and second order. It represents the "ability" of the grating to suppress the second diffraction order with respect to the first one

and movable exit slit. These solutions have the advantage of a very high resolving power, but with the drawback of needing several gratings to cover the same energy range as that covered by a single grating in the SX700 case (Fig. 4.12).

Before closing this section, let us spend few words on the efficiency, the quantity of photons of a particular wavelength diffracted into a particular order. Let us consider the groove profile. The blaze profile (Fig. 4.13) has usually the highest efficiency, as the light "sees" a mirror at each groove. But the efficiency is high also for the higher orders of diffraction. In fact, from 4.8 it is evident that if a particular wavelength λ is diffracted at an angle β in the first diffraction order, the wavelength

 $\lambda/2$ is diffracted at the same angle but in second order. What happens is that the experimental chamber will receive radiation at 200 eV together with 400 eV, 600 eV, and so on, even if with higher and lower efficiency. With a laminar profile, the efficiency are usually lower but the *higher order suppression* is slightly better. This is another thing to consider when a beamline is designed, for example, if the flux is the only parameter to be optimized or if the presence of higher orders can be a problem for the experimental program.

Because of the different kind of procedure for the realization of the gratings, the different profiles can also affect the resolution. The laminar profiles, in fact, are produced holographically and this procedure generates a very good distribution of the grooves along the grating. Precision of the order of 1 part over 1,00,000 was measured. The blaze gratings are, on the contrary, produced mechanically and this procedure suffers from nonuniformity of the movement of the *ruling machine*, which can generate some lacks in the homogeneity. These errors reduce the resolving power, in the same way in which the slope errors will degrade the performance of a mirror.

Therefore, even if a great improvement in the mechanical production and density measurement [12] was made in the recent years, the laminar gratings can deliver the highest resolution and are the most used. Recently, Zeiss developed blaze gratings with very shallow blaze angle [13], capable of reaching very high photon energies [14], extending quite a lot the range of utilization of the soft X-ray monochromators.

4.2.3 Refocusing Optics

What was mentioned in the first part of this chapter is valid also for the last part of a beamline, the refocusing section. This part has to adapt the photon dimension and divergence to the needs of the experiment. Very often, a spot of 20 µm or more is required. As the SR sources, nowadays, are already quite small at the beginning (from 20 to 200 µm), this is not a big challenge and, according to the divergence of the beam, one can use two spherical mirrors mounted perpendicularly with respect to the other (KB configuration [15]) to focus the radiation as well as a toroidal or an elliptical mirror. The last one is the best approach, but producing an elliptical mirror with very good slope errors is not an easy task. Therefore, if one wishes to have very small spot (of the order of $1-2 \mu m$ roughly) or to preserve the wavefront or coherence of the propagating radiation, it is mandatory to use a different approach. As a matter of fact, the manufacturers are able to produce plane or spherical mirrors with residual slope errors of the order of half a micro-radian. When, on the contrary, an aspherical surface, like a toroid or an ellipsoid, is required, the residual errors increase. These errors deteriorate the final spot and therefore the advantage of using an ellipsoidal shape is lost.

A way to overcome such a limit is the use of *active optics* or *bendable mirrors*. This technology is in use in astronomy since the 1980s, but it is just a decade that it became popular in the SR community. The idea is the following: as the perfect optic is an ellipsoid, but the easiest to do is the plane or spherical one, why don't we bend a plane surface to an elliptical profile? It actually works, but first of all we can

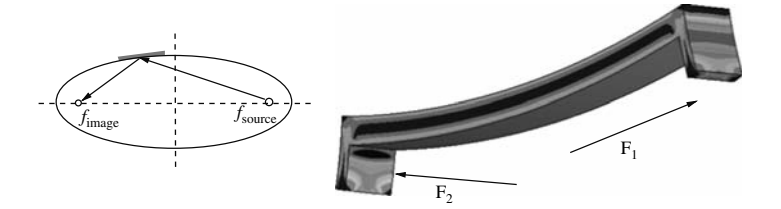


Fig. 4.14 Elliptical profile of a mirror. *Left*: Just a part of the whole ellipsoid is used as mirror. It produces a perfect image in one foci as if the rays come from the other foci. *Right*: A way to produce an elliptical profile starting from a flat surface. Two unequal moments are applied at the end of the substrate. This is not enough to have a good ellipsoid. One needs to correct the higher orders

bend it only in one direction (forcing people to adopt the KB configuration), and second, the ellipsoidal surface has to be approximated as much as possible not to introduce artificial slope errors. If we rewrite the equation describing the ellipsoid profile as a Fourier series, we need to approximate the ellipsoid up to the third or fourth order not to introduce a too large residual shape error. So we need to act on the starting flat mirror with, at least, three independent actuators. Two of them are common to almost all the solutions and are shown in Fig. 4.14 (right). In practice, two unequal moments are applied at the edge of the flat substrate to bend it toward the elliptical profile. If the two moments are identical, one produces a symmetric spherical profile. A proper difference between the two forces guarantees the required elliptical profile, approximated to the second order.

The third order can be corrected in a different way. One can introduce a variable thickness or width [16] of the flat substrate, which produce a variation of the moment of inertia. Alternatively, one can polish this higher order into the initial process [17]. An alternative method is the use of piezoelectric actuators positioned at the back of the mirror acting as local pushers or pullers. This solution permits the control of a very high number of degrees of freedom so that the lateral forces are sometimes no longer needed. The most successful use of piezoelectric actuators can be found in the *bimorph mirrors* [18]. These are made by a thin silicon layer (3 mm more or less) glued on a polarized piezoceramic. By applying a proper voltage, one can obtain almost any surface with a spatial frequency control down to the distance of three consecutive electrodes.

Some other focusing elements are the zone plates, the capillary optics, the photon sieves, the X-ray lenses, the waveguides, and so on. These and other solutions can be adopted according to the needs of the experiment. A description of most of these elements can be found in dedicated books [4, 19].

References

- 1. B.L. Henke, E.M. Gullikson, J.C. Davis, Atomic and Nuclear Data Tables 54, 181–342 (1993)
- W.B. Peatman, Gratings, Mirrors, and Slits (Gordon and Breach Science Publishers, New York, 1997)
- 3. R. Follath, Nucl. Instrum. Methods Phys. Res. A 467-468, 418-425 (2001)

- 4. D. Attwood, Soft X-Rays and Extreme Ultraviolet Radiation (Cambridge University Press, Cambridge, 1999)
- 5. H. Wiedemann, Synchrotron Radiation (Springer, Heidelberg, 2002)
- 6. http://www.HORIBA.com/US/EN/SCIENTIFIC/PRODUCTS/OPTICS-TUTORIAL/DIFFRACTION-GRATINGS/
- 7. http://www.zeiss.de/spectral
- 8. H. Petersen, Opt. Commun. 40, 402 (1982)
- 9. G. Naletto, G. Tondello, J. Eur. Opt. Soc. A 1(6), 347–358 (1992)
- 10. H.A. Padmore, Rev. Sci. Instrum. 60(7), 1608–1615 (1989)
- 11. C.T. Chen, F. Sette, Rev. Sci. Instrum. 60, 1616 (1989)
- 12. D. Cocco, G. Sostero, M. Zangrando, Rev. Sci. Instrum. 74(7), 3544–3548 (2003)
- 13. K.F. Heidemann, B. Nelles, R. Lenke, *Gratings with Blaze Angles down to 0.1r for Photon Energies up to 10 keV*, AIP Conference Proceedings, vol. 879, pp. 485–488, 2007
- D. Cocco et al., From Soft to Hard X-ray with a Single Grating Monochromator, AIP Conference Proceedings, vol. 879, pp. 497–500, 2007
- 15. P. Kirkpatrick, A.V. Baez, J. Opt. Soc. Am. 38, 766–774 (1948)
- 16. O. Hignette et al., Submicron Focusing of Hard X-rays with Reflecting Surfaces at the ESRF, Proceedings of SPIE, Vol. 4499, pp. 105–116, 2001
- 17. J.J. Fermé, Nucl. Instrum. Meth. A **467–468**, 279–282 (2001)
- 18. R. Signorato, O. Hignette, J. Goulon, Journal of Synchrotron Radiation 5(3), 797–800 (1998)
- 19. A. Erko, M. Idir, T. Krist, A.G. Michette, *Modern Developments in X-ray and Neutron Optics*, Springer Series in Optical Science, vol. 137, (Springer, Heidelberg, 2008)

Chapter 5 X-Ray Magnetic Dichroism

H. Wende and C. Antoniak

Abstract An introduction is given to the X-ray magnetic dichroism focusing on X-ray magnetic circular dichroism (XMCD). The standard analysis of XMCD spectra by using the sum rules is elucidated. Additionally, aspects of the experimental realization and the data analysis are presented. By means of experimental examples of light 3d metal films, rare earth single crystals, and Fe-porphyrin molecules, the assets and drawbacks of the XMCD technique are illustrated. It is shown that the comparison of ab initio calculated spectra to the experimental results can provide the magnetic properties of the samples if the standard analysis fails.

5.1 Introduction

Ever since the discovery of X-rays by Röntgen in 1895, the field of spectroscopy using this regime of the electromagnetic spectrum has shown a dramatic development. Nowadays, it is relatively easy to measure X-ray absorption spectra (XAS) or X-ray photoelectron spectroscopy (XPS) at modern synchrotron radiation facilities with excellent X-ray energy resolution. In a simplified picture, the XPS technique investigates the occupied electronic states, while the XAS investigates the unoccupied states (see, e.g., [1]). In contrast to the XPS measurements, where the focus is, for example, the band dispersion by analyzing the dependence of the spectra on the photoelectron k-value, the analysis of the integral unoccupied densities of states vs. energy is one of the major interests in XAS. Because of these differences with respect to k-resolved or k-integral measurements, the X-ray absorption spectroscopy can be used to determine magnetic moments, which can be compared with the established methods such as vibrating sample or superconducting quantum interference device (SQUID) magnetometry. As the history of X-ray absorption spectroscopy, especially focusing on magnetic dichroism, can be found in various

Fachbereich Physik and Center for Nanointegration Duisburg-Essen (CeNIDE), Universität Duisburg-Essen, Lotharstraße 1, 47048 Duisburg, Germany

e-mail: heiko.wende@uni-due.de

H. Wende (⊠)

works (see e.g., [2, 3]), we want to start here directly with the discussion of state-of-the-art X-ray absorption spectroscopy at third generation synchrotron radiation facilities. It is certain that in modern electronic devices, magnetic systems play a vital role especially for data storage. But also the vision of utilizing the electron spin in addition to the charge in the so-called spintronics demonstrates the demand for advanced magnetometries. It will be shown below that with the X-ray magnetic circular dichroism (XMCD), element- and shell-selective magnetic properties can be probed. The technique is highly sensitive, allows for the disentanglement of spin and orbital magnetism, and probes local (atomic) properties. Thereby, the fields of fundamental investigations as well as applied material science can be advanced. Despite the fact that the extended energy regime in XAS (namely EXAFS) played a more important role in the past, the investigation of the near edge regime (near edge X-ray absorption fine structure (NEXAFS) or X-ray absorption near edge spectroscopy (XANES)) is a boom. One of the reasons is that it is quite straight forward to determine magnetic moments by means of standard analysis procedures (sum rules). However, as we show below, the handiness of the analysis as well as the availability of highly brilliant synchrotron radiation might lead to a misinterpretation of the data if the limits of the applicability of these procedures are not considered.

To present the amenities and also the dangers of false analysis of the XMCD spectra, we structured the chapter as follows. An introduction to the X-ray absorption spectroscopy is given in Sect. 5.2, which is followed by a detailed discussion of the XMCD in Sect. 5.3. Some details of the actual experiments and the data analysis including the sum rules are presented in Sects. 5.4 and 5.5. In Sect. 5.6, examples of recent investigations in the soft X-ray as well as the hard X-ray regime are presented. Especially, the examples for the XMCD of light 3d elements as well as the measurements for the rare earth elements show that the failure of the standard analysis procedures can be overcome by comparison of the experimental results with ab initio calculations. The chapter ends with Sect. 5.7 giving a conclusion and an outlook.

5.2 X-Ray Absorption Spectroscopy

In XAS, core-level electrons with their element-specific binding energies are excited by incident X-rays. It is the generic term for the spectroscopic measurement of the following:

- XANES that contains information about the unoccupied electronic states and the chemical environment
- EXAFS for determination of type and distance of atoms in the local environment of the absorbing atom
- Dichroism in X-ray absorption with linearly polarized light, that is, X-ray natural linear dichroism (XNLD) and X-ray magnetic linear dichroism (XMLD), or with circularly polarized light, that is, X-ray natural circular dichroism (XNCD) and

X-ray magnetic circular dichroism (XMCD). The latter being explained in more detail in the next section.

5.2.1 X-Ray Absorption Near-Edge Structure

As known from visible light, the intensity of X-rays after passing through matter of thickness x is described by the Lambert–Beer law:

$$I(E, x) = I_0(E) \exp[-\mu(E) \cdot x],$$
 (5.1)

where μ is the photoabsorption coefficient. In the case of energies below $20 \,\mathrm{keV}$, the photoeffect is the dominating interaction between photons and electrons. Both elastic Rayleigh scattering and inelastic Compton scattering is negligible. The photoabsorption coefficient is proportional to the absorption cross section, that is, the transition probability per unit time P_{fi} and photon flux I_{ph} :

$$\mu \propto \sigma_{\rm abs} = P_{\rm fi}/I_{\rm ph}.$$
 (5.2)

The transition probability per unit time can be described using Fermi's Golden Rule:

$$P_{\rm fi} \propto \sum_{f,i} M_{\rm fi}^2 \cdot \left(1 - n(E_f)\right) \cdot \delta\left(\hbar\omega - (E_f - E_i)\right),\tag{5.3}$$

where $(1 - n(E_f))$ is the density of unoccupied final states and the δ -function reflects the conservation of energy in the absorption process. The transition matrix element $M_{\rm fi}^2$ can be written within electric dipole approximation (E1) as $M_{\rm fi}^2 = |\langle f|P{\bf A}|i\rangle|^2$, where P is the momentum operator of the electron and ${\bf A}$ is the vector of the electric field containing the polarization of X-rays.

Within this approximation, transitions are allowed according to the dipole selection rules

$$\Delta m_s = 0, \ \Delta m_l = \pm 1. \tag{5.4}$$

For instance, transitions from the 2p states to d states at the L_{3,2} absorption edges and transitions from the 1s to p states at the K absorption edge are included in the dipole approximation. In the electric quadrupole (E2) approximation, for example, transitions from the 1s state to d states are described ($\Delta m_l = 2$). Interference terms between dipolar and quadrupolar contributions may lead to special types of dichroism in X-ray absorption (cf. next section).

5.2.2 Dichroism in X-Ray Absorption Spectroscopy

A polarization dependent absorption behavior is called "dichroism." In a microscopic picture, this dependence is caused by an anisotropy of the charge or spin distribution. If the dichroism is due to a charge anisotropy only, it is called "charge dichroism" or "natural dichroism" like the XNLD and XNCD. In the case of an anisotropic spin distribution, it is called "magnetic dichroism" like XMLD and XMCD. The latter is the focus of this whole chapter and will be discussed in detail in the next section. In the following, we give a short introduction to the different types of dichroism mentioned earlier.

The XNLD is due to an anisotropic charge distribution. Measuring the X-ray absorption of linearly polarized light for different angles of incidence, the electric field vector of the X-rays acts like a search light for the maximum and minimum unoccupied states. This can be used to study the orientation of molecules [4]. But this effect can be detected also for solids. For instance, at the L_{3,2} absorption edges, the unoccupied d states are probed and the X-ray absorption intensity vanishes if the vector of the electric field lies along the d orbital nodal axis. One example of the XNLD effect measured at the Cu L_{3.2} absorption edges of La_{1.85}Sr_{0.15}CuO₄ can be found in [5]. The X-ray magnetic linear dichroism occurs if the charge anisotropy is induced by an axial spin alignment. A first measurement yielding a significant XMLD was performed at the M_{4.5} absorption edges of Tb in Tb₃Fe₅O₁₂ [6]. The existence of the effect at the M_{4.5} absorption edges of rare earths was predicted one year before, in 1985 [7]. The XNLD and XMLD signals are even, under both time reversal and spatial inversion. In contrast, the X-ray natural circular dichroism effect has odd parity, as it is caused by a charge anisotropy lacking a center of inversion. The first experimental evidence of the XNCD in a gyrotropic crystal of α -LiIO₃ was reported in [8], where the occurrence of a large XNCD effect at the I L₁ edge and a smaller effect at the I L_{2,3} absorption edges was ascribed to the electric dipole (E1)-electric quadrupole (E2) interference terms. Breaking inversion symmetry by magnetoelectric ordering yields the effect of X-ray non-reciprocal linear dichroism, which is a parity odd and time reversal odd property. Another type of dichroism that is odd under both spatial inversion and time reversal is the X-ray magnetochiral dichroism (XM χ D) due to a chiral charge distribution and an axial spin alignment. The latter two types of dichroism are more complicated cases but have been experimentally proven [9, 10].

Here we focus on XMCD that arises from a directional spin alignment and is even with respect to parity and odd with respect to time reversal. The XMCD effect was predicted in 1975 by Erskine and Stern, who performed band structure calculations for the $M_{3,2}$ absorption edges of Ni [11]. The first experimental results were reported in 1987 by Schütz et al., who detected a significant XMCD effect at the K absorption edge of an Fe foil [12]. A more detailed historical overview can be found, for example, in [2]. The theoretical background of the XMCD will be summarized in the following sections.

5.3 X-Ray Magnetic Circular Dichroism

In this section, we focus on XMCD. After an explanation for the occurrence of this effect in a simple two-step model, the so-called sum rules are presented, which can be used for the determination of spin and orbital magnetic moments with some limitations as mentioned at the end of Sect. 5.3.1.

Let us consider an X-ray photon with helicity +1 absorbed by an electron from a spin-orbit-split core-level, for example, $2p_{3/2}$ and $2p_{1/2}$. This may lead to the electron transitions listed in Table 5.1. The excitation probabilities are given by the Clebsch-Gordon coefficients and do not take into account the number of unoccupied final states. These excitations with their related probabilities yield an orbital polarization of excited electrons, which is the same for electrons from the $2p_{1/2}$ or $2p_{3/2}$ core levels. By simply summing up all possible excitations weighted by their probabilities, one finds a spin polarization of the excited electrons. From the $2p_{3/2}$ state, 62.5% of excited electrons carry a spin of $m_s = -1/2$. From the $2p_{1/2}$ state, 75% of excited electrons carry a spin of $m_s = -1/2$ and only 25% of $m_s = +1/2$. Note that the sign of spin polarization is different for the different 2p states. If there were no spin-orbit-splitting, that is, no energy gap between $2p_{3/2}$ and $2p_{1/2}$ states, the averaged spin polarization would be zero.

Consideration of an X-ray photon with helicity -1 instead of +1 leads to the same results, but with reversed signs.

With this spin and orbital polarized excited electrons, the polarization of the unoccupied final states is probed in the second step of this model. Any imbalance in either spin or orbital momentum in the final states will give rise to a dichroic effect. This is shown schematically in Fig. 5.1 for X-ray photons with helicity +1, that is, transitions from the $2p_{3/2}$ state with a positive spin polarization into 3d final states. For a simplification of the discussion, let us consider first the cases of magnetic saturation at T=0, each with the final unoccupied states containing electrons of one spin direction only. In the left panel of Fig. 5.1, the spin polarization of the unoccupied final states is positive, that is, has the same sign as the spin polarization of the excited electrons. Therefore, the transition probability $P_1=P_{1,\uparrow}$ is quite large. Note that in this example $P_{1,\downarrow}=0$ as all final d states of electrons with spin down are occupied. After reversal of the magnetization direction, the spin polarization of the unoccupied final states is negative and the probability for transitions of the excited electrons with their positive spin polarization is smaller: $(P_{2,\downarrow}=P_2< P_1=P_{1,\uparrow})$. The resulting difference in

Table 5.1 Possible electron transitions from a 2p state induced by an photon with helicity +1 and the related relative excitation probabilities

m_l	Fraction
$1 \rightarrow 2$	60%
$0 \rightarrow 1$	30%
$-1 \rightarrow 0$	10%

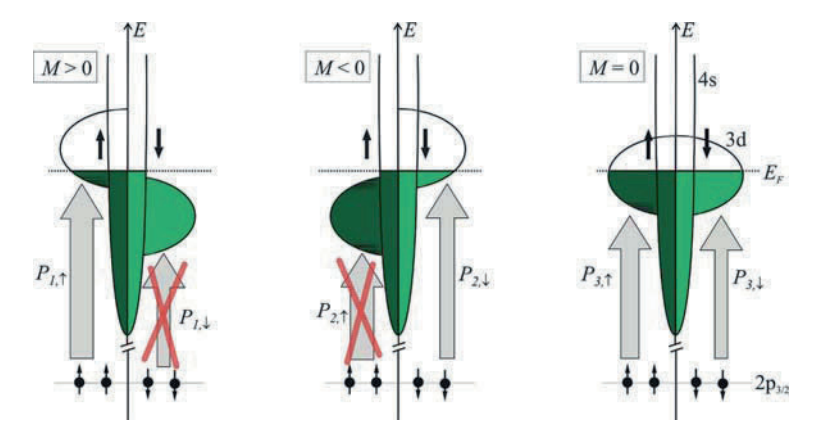


Fig. 5.1 Schematic depiction of the electronic transitions from a $2p_{3/2}$ level of a 3d ferromagnet for two reversed directions of magnetization and zero magnetization

the absorption strength is the so-called XMCD effect at the L₃ absorption edge. Considering transitions at the L₂ absorption edge yields an XMCD with reversed sign. For a vanishing magnetization (right panel of Fig. 5.1), the total transition probability ($P_3 = P_{3,\uparrow} + P_{3,\downarrow}$) is independent of the helicity of X-ray photons and no dichroism can be obtained. The dependence of the dichroism on the magnetization gives the possibility to measure field-dependent magnetization curves element-specifically.

In the following, μ_+ denotes the absorption coefficient in the case of the same sign of spin polarization of excited electrons from the $2p_{1/2}$ state and unoccupied final states. Otherwise, the absorption coefficient is called μ_- .

5.3.1 Determination of Orbital and Spin Magnetic Moments: Sum Rules

As the spin polarization of excited electrons from the $2p_{3/2}$ and $2p_{1/2}$ states exhibit different signs in contrast to the orbital polarization, which has the same sign, it is possible to distinguish between spin and orbital contributions to a dichroic signal. Via the so-called sum rules derived by Thole [13] and Carra [14] for spin–orbit split absorption edges, it is possible to determine both spin and orbital magnetic moment, that is, $\mu_S = -2\mu_B \langle S_z \rangle /\hbar$ and $\mu_l = -\mu_B \langle L_z \rangle /\hbar$ per unoccupied final state n_h :

$$\frac{\mu_{s}}{n_{h}} = -\frac{6 \int_{L_{3}} (\mu_{+} - \mu_{-}) dE - 4 \int_{L_{3} + L_{2}} (\mu_{+} - \mu_{-}) dE}{\int_{L_{3} + L_{2}} (\mu_{+} + \mu_{-}) dE} \cdot \left(1 + \frac{7 \langle T_{z} \rangle}{2 \langle S_{z} \rangle}\right)^{-1} \mu_{B},$$
(5.5)

$$\frac{\mu_l}{n_h} = -\frac{3}{4} \frac{\int_{13+L_2} (\mu_+ - \mu_-) dE}{\int_{13+L_2} (\mu_+ + \mu_-) dE} \cdot \mu_B,$$
 (5.6)

where $\langle T_z \rangle$ is the expectation value of the intra-atomic magnetic dipole operator, accounting for a possible asphericity of the spin density distribution. Usually, this value is much smaller than the spin moment and can be neglected. Nevertheless, it is widespread to use the term *effective* spin magnetic moment $\mu_S^{\text{eff}} = \mu_S + 7\mu_T$, which consists of both the spin magnetic moment and the magnetic moment of $\langle T_z \rangle$.

With

$$p = \int_{L_3} (\mu_+ - \mu_-) \, \mathrm{d}E, \tag{5.7}$$

$$q = \int_{L_3 + L_2} (\mu_+ - \mu_-) \, \mathrm{d}E, \tag{5.8}$$

$$r = \frac{1}{2} \int_{L_3 + L_2} (\mu_+ + \mu_-) \, dE, \tag{5.9}$$

(5.5) and (5.6) can be written as [15]

$$\frac{\mu_l}{n_h} = -\frac{2}{3} \frac{q}{r} \cdot \mu_{\rm B},\tag{5.10}$$

$$\frac{\mu_s^{\text{eff}}}{n_h} = \frac{-3p + 2q}{r} \cdot \mu_{\text{B}}.\tag{5.11}$$

Originally the sum rules are derived in an atomic framework. However, using the density matrix formalism, Ankudinov and Rehr demonstrated that the application of the sum rules is not only restricted to these atomic systems [16]. To derive the sum rules, various assumptions and approximations were made in addition. For example, the exchange splitting for the core-levels was ignored as well as any energy dependence of the wave functions. Many-body effects are neglected, and for a proper application of the sum rules, L_3 and L_2 absorption edges have to be clearly separated energetically. In any case, it could be shown that the determination of the magnetic moments via sum-rule based analysis leads to reasonable results, for example, in the case of Fe and Co [15].

A different approach to determine spin and orbital moments is the so-called multipole moment analysis [17]. It is based on a calculation of the fine structures in experimental XMCD spectra. Thereby, the focus is on the actual spectroscopic details, which are not taken into account in the integral sum-rule analysis method

discussed earlier. Nevertheless, the multipole moment analysis yields the same values for the magnetic moments. A detailed discussion of this method can be found in [18] and is not a scope of the present manuscript.

5.4 Experimental Setup

It is possible to measure the absorption directly for thin samples by the analysis of the intensity of transmitted X-rays, but this is not possible for thick samples such as substrate-supported films. For the latter case, the absorption can be measured via photon detection or current measurements as described later.

If a core electron is excited by an absorbed X-ray photon, the core-hole will be reoccupied by an electron from an energetically higher state accompanied by the emission of either a photon or an Auger electron. The absorption coefficient measured by the detection of the emitted photons is called the fluorescence yield (FY) mode. The detection of Auger electrons and cascade secondary electrons with an energy high enough to leave the sample is called the total electron yield (TEY) mode. The emission of electrons may be facilitated by an electric field, for example, by putting a positively charged electrode near the sample or by applying a negative voltage on the sample with respect to ground. In both cases, the sample drain current can be used as a measure of the absorption coefficient with some limitations as discussed in the following section. Usually, the absorption signal of a gold grid in the path of light is used as a reference for the intensity of the incident X-rays.

5.5 Data Analysis

5.5.1 Self-absorption and Saturation Effects in Electron Yield

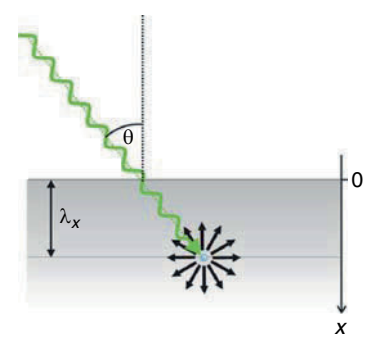
In total electron yield (TEY) mode, the X-ray absorption is measurable only if secondary electrons escape from the sample. The probability of an electron reaching the surface becomes smaller with larger distance to the surface, and the number of electrons that may escape is given by [19]

$$dY_e = dY_0 \exp[-x/\lambda_e], \qquad (5.12)$$

where λ_e is the electron escape depth, which is usually in the range of a few nanometers and dY_0 is the number of secondary electrons created in a layer of thickness dx at depth x from the surface (cf. Fig. 5.2). It is given by [20]

$$dY_0 = I_0 G \frac{\mu}{\cos \theta} \exp[-\mu x/\cos \theta] dx, \qquad (5.13)$$

Fig. 5.2 Emission of an Auger electron in various possible direction after absorption of an X-ray photon under grazing incidence on a semi-infinite sample



with the angular-dependent absorption coefficient $\mu(\theta, E) = \mu(E)/\cos\theta = \mu/\cos\theta$. The factor G represents the averaged number of secondary electrons released in a cascade caused by a single Auger electron. As can be seen from (5.12), the TEY mode is a surface sensitive method to measure the X-ray absorption. The TEY intensity can be calculated by simple integration over dx from x=0 to $x=\infty$. Thus, the TEY intensity can be written as

$$I_{\text{TEY}} = \frac{I_0 G \mu \lambda_e}{\cos \theta} \frac{1}{\mu \lambda_e / \cos \theta + 1} = \frac{I_0 G \mu \lambda_e}{\lambda_x} \frac{1}{\lambda_e / \lambda_x + 1}, \quad (5.14)$$

using $\lambda_x = \cos\theta/\mu$, which describes the attenuation depth of incident X-rays along x direction. For $\lambda_x \gg \lambda_e$, the measured TEY intensity is proportional to the absorption coefficient, $I_{\text{TEY}} = I_0 G \lambda_e \mu/\cos\theta$. For $\lambda_x \ll \lambda_e$, the TEY intensity can be approximated by $I_{\text{TEY}} \approx I_0 G \lambda_e/\cos\theta$. In the latter case, the measured TEY is independent of the absorption coefficient, that is, the signal is saturated. This occurs for measurements of samples under grazing incidence or at photon energies equal to the energy of an absorption edge.

One example of a XANES spectrum that suffers from saturation is shown in Fig. 5.3 on the left hand side. Simply assuming a proportional dependence of the TEY intensity on the absorption coefficient μ leads to too small values of μ , especially at the absorption edges (see also [21]). At the L₃ absorption edge with its larger intensity, the saturation effect is larger than that for the L₂ intensity. For samples exhibiting XMCD, the dichroic signal is also strongly influenced by saturation effects as can be concluded from Fig. 5.3, where the deviation from the proportional relation between the TEY signal and μ is shown for the μ_+ and μ_- spectrum. The analysis of TEY spectra which have not been corrected for saturation effects always underestimates the dichroism and the magnetic moments, respectively. Especially, the orbital magnetic moment is underestimated as it corresponds to the difference between the areas of the dichroism at the L₃ and L₂ absorption edges, while the spin magnetic moment corresponds to the sum of these areas. A detailed discussion of these effects in Fe, Ni, and Co samples is given in [19]. For instance, the calculated spin magnetic moment of Fe atoms in a Fe bulk sample from a saturated

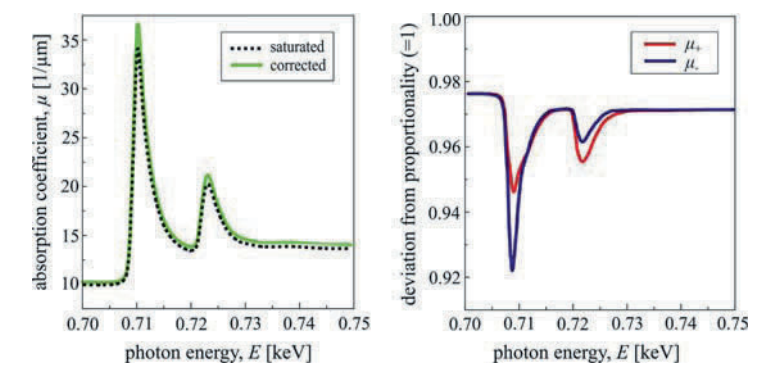


Fig. 5.3 Example of a XANES spectrum at the Fe $L_{3,2}$ absorption edges of an FePt sample before and after saturation correction (left) and the deviation from a proportional dependence of the TEY signal from the absorption coefficient as a function of photon energy for reversed directions of sample magnetization

spectrum is only about 92% of the real value at $\theta=0$ and about 80% when $\theta=70^\circ$. The orbital magnetic moment determined from saturated spectra is only half of the real value at $\theta=0$ and vanishes at grazing incidence around $\theta=65^\circ$. Going to more grazing incidence ($\theta=70^\circ$) will even lead to the wrong sign of the calculated orbital magnetic moment. For thin Fe films with thicknesses of a few nanometers, the saturation effects are smaller but nevertheless they cannot be neglected.

5.5.2 Standard Analysis

To analyze an experimentally obtained XANES spectrum or XMCD spectrum, respectively, the spectra are first normalized to the total photon flux, which usually shows an energy and time dependence. This dependence is usually measured by the absorption of a gold mesh brought into the beam in front of the sample. The absorption signal of the gold reference is often called the " I_0 signal." This method is much more precise than, for example, normalization simply using the current of the storage ring or the current of one of the mirrors in the beamline.

Second, the slope of the pre-edge region can be subtracted and the post-edge region should be normalized to unity. Before application of the sum rules it is necessary to separate the absorption intensity due to the electron transitions we are interested in, for example, $2p \rightarrow d$ states at the L_{3,2} absorption edges, from transitions into higher unoccupied states or into the continuum. In the case of the 3d transition metals, the latter can be described by a two step-like function. If there are less pronounced absorption maxima at the absorption edges, a reference spectrum of a similar element with a well-known number of unoccupied states should be subtracted. In Fig. 5.4 are two examples shown. In the left panel, an absorption

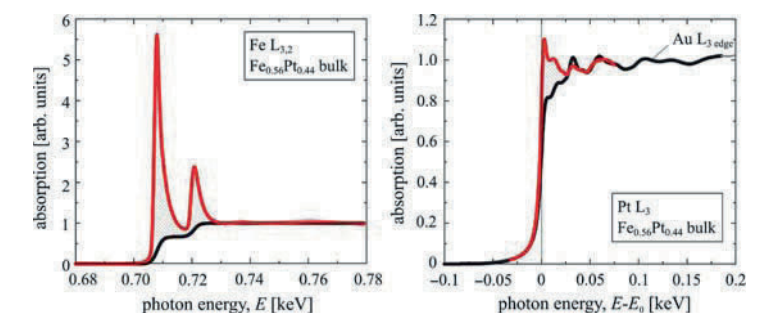


Fig. 5.4 XANES at the $L_{3,2}$ absorption edges of Fe and two-step-like function accounting for transitions into continuum (*left panel*) and XANES at the Pt L_3 absorption edge with Au reference spectrum shifted and stretched in energy. See text for details

spectrum measured at the Fe $L_{3,2}$ -edges is shown with the transitions into higher unoccupied states than the 3d levels approximated by a two step-like function. In the right panel, an absorption spectrum of Pt at the $L_{3,2}$ absorption edges is shown which was normalized to an Au reference spectrum.

In the case of Fe, the L_3 and L_2 absorption edges are not clearly separated energetically, which lead to larger errors in the determination of spin and orbital magnetic moments as, for example, in the case of Pt.

5.6 Examples of Recent Research

In the next three sections we give examples for the advantages and also the difficulties in the XMCD analysis. At first, we turn to the investigation of induced moments in ultrathin films of light 3d elements at the interface with Fe films. For the light 3d elements, the reduced splitting of the L₃ and L₂-edge leads to a failure of the standard analysis, resulting in a large underestimation of the induced spin moments. In the second example, we turn to the analysis of the L_{3,2}-edge XMCD of rare earth elements. Here, a spin-dependence of the transition matrix elements has the effect that applying the XMCD sum rules would even lead to the wrong sign of the 5d moments for the rare earth elements. The limits of the applicability of the sum rules have already been discussed in the original presentation of these rules [13, 14]. This raises the question in which way these systems can be analyzed. For both examples we show that the magnetic moments can be determined by comparing the experimental XMCD spectra to ab initio calculations. In the last example we demonstrate the strength of combining XNLD and XMCD. For a monolayer of Feporphyrin molecules adsorbed on epitaxially grown Co and Ni films, XNLD clarifies the orientation of the molecules on the surface, and the XMCD spectra allow for the determination of the element-specific magnetic properties and the corresponding magnetic coupling phenomena.

5.6.1 Failure of Sum Rule-based Analysis for Light 3d Elements

To exemplify the breakdown of the XMCD standard analysis and to look at the XMCD fine structures in the light 3d elements in a more systematic way, we investigate the induced or uncompensated moments in prototype Fe/light 3d/Fe trilayers on a Cu(100) single crystal. Such a trilayer is presented in Fig. 5.5 for the case of vanadium as the light 3d element. Indeed, an induced magnetic moment in V can be revealed by the XMCD spectroscopy. The X-ray absorption coefficients for right and left circularly polarized X-ray are shown at the V and Fe L_{3,2}-edges in Fig. 5.5b. The dichroic signal at the Fe edges is quite obvious as it stems from bulklike 50 monolayer (ML) buffer layer and the 5 ML on top of the in situ prepared structure. At the V L_{3,2}-edges, the X-ray absorption coefficients μ^+ and μ^- are very similar. But because of the excellent performance of modern third generation synchrotron radiation facilities, even tiny induced moments can be revealed. This can be seen in the small dichroic signal (please note the enlargement factor $\times 15$), which presents a large signal-to-noise ratio. The positive sign of XMCD at the V L₃edge in comparison to the negative signal at the Fe L₃-edge shows that the induced moment in V is aligned antiparallel to Fe. Furthermore, the V XMCD signal exhibits many more fine structures as compared to the Fe case, for example, an asymmetric contribution at both L-edges can be determined.

Unfortunately, a quantitative analysis is more problematic. To discuss this in greater detail, we present the XMCD signal of Ti, V, and Cr recorded for the same trilayer setup in Fig. 5.6. The dichroic signal in the transition metals (TM) Ti and V stems from induced moments at the Fe/TM interface, while it originates in Cr from uncompensated moments in the layerwise antiferromagnetic structure. To compare the systematics in the XMCD fine structures, the dichroic signals of bulk-like Fe, Co, and Ni films are also presented in Fig. 5.6. The spin moments of the light 3*d* elements Ti, V, and Cr are oriented antiparallel to those of the Fe films in the trilayers.

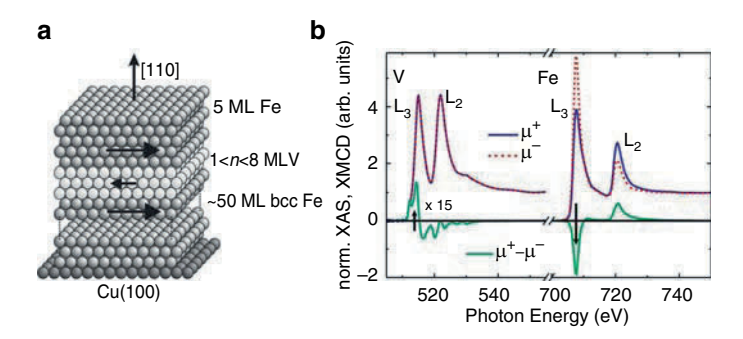


Fig. 5.5 (a) Schematic picture of the prototype Fe/V/Fe(110) trilayer on Cu(100). The *bold arrows* indicate the direction of the total Fe and V moments, respectively. (b) Normalized XAS for *right* (μ^+) and *left* (μ^-) circularly polarized X-rays (*top*) and the corresponding XMCD at the V and Fe L_{3,2}-edges of a Fe/V₄/Fe trilayer [32]. For a clearer representation, the V XMCD was multiplied by a factor 15. Figure taken from [3]

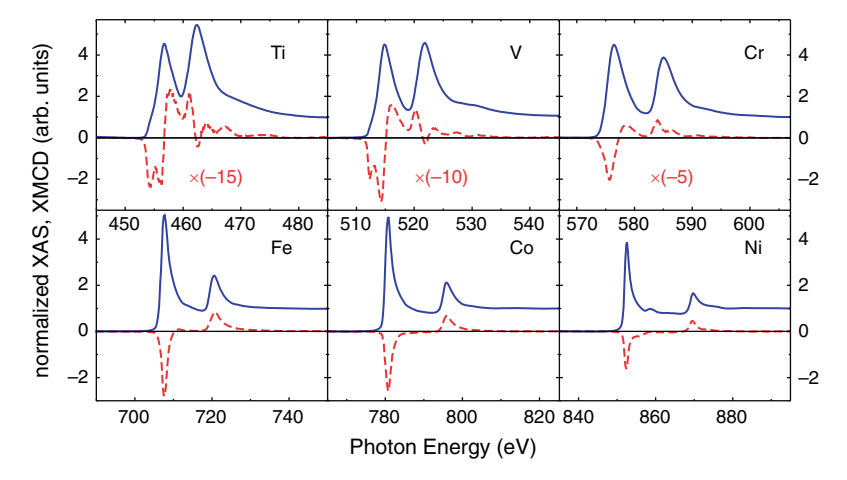


Fig. 5.6 Normalized isotropic spectra (*solid lines*) and corresponding XMCD spectra (*dotted lines*) for light 3d transition metals (*upper panel*) in comparison to the heavy 3d ferromagnetic transition metals Fe, Co, and Ni (*lower panel*) [30] at the L_{3,2}-edges. The XMCD spectra for the light 3d transition metals (TM) are obtained for Fe/TM/Fe(110) trilayers, whereas the Fe, Co, and Ni spectra are recorded for bulk-like films on Cu(100). The direction of magnetization for the light 3d metals is defined with respect to the one of Fe in the trilayer. For a clearer presentation of the systematics, the sign of the Ti, V, and Cr XMCD spectra was changed (negative enlargement factors). Figure taken from [30]

However, to study the systematics in the XMCD fine structures, we multiplied them by negative scaling factors. When inspecting the spectra from the heavier element Ni towards the lighter element Ti, the effect of the reduction of the $L_{3,2}$ -edge splitting is revealed. First of all, the intensity ratio of the L_3 -edge whiteline to the L_2 -edge whiteline clearly changes. For the case of Fe, nearly the statistical ratio of 2:1 (originating from the electron occupancy of the $2p_{3/2}$ and $2p_{1/2}$ core levels) is seen, while for the lighter 3d elements this ratio becomes about 1:1.

These changes in the isotropic spectra have been analyzed in the past experimentally as well as theoretically [22–24]. Here, we want to focus on the dichroic spectra. When traversing the 3d series towards the lighter elements, the XMCD spectra become more and more asymmetric. An onset of this trend is already detected for the element Fe. At a photon energy of about 711 eV in the Fe spectra, a small positive XMCD signal is seen at the L₃-edge. This contribution increases clearly for Cr, V, and Ti. A reason for this asymmetry is the effective exchange field splittings of the initial 2p and final 3d sublevels [25, 26]. Furthermore, for these light 3d elements, an obvious overlap of the L₃-edge signal with the one at the L₂-edge is seen.

Despite the fact that all fine structures in the XMCD are nicely resolved and hardly any noise can be detected by eye, the quantitative analysis turns out to be problematic because the sum rule analysis fails for Ti, V, and Cr. The reason is that for these elements, the initial j, m_j elements are mixed [27] and therefore the standard analysis procedure cannot be applied any more. For V the induced spin moment

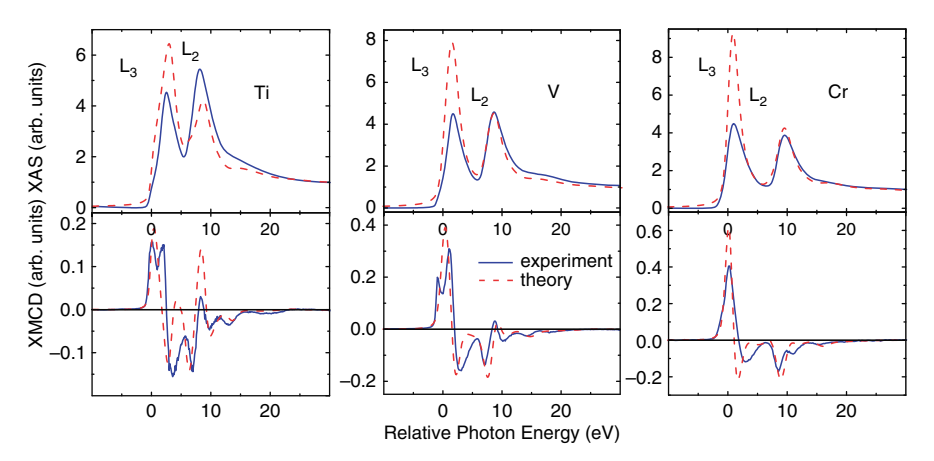


Fig. 5.7 Normalized XAS (*above*) and XMCD spectra (*below*) for the light 3d TM's Ti, V, and Cr at the $L_{3,2}$ -edges: (*solid lines*) experimental data vs. (*dashed lines*) ab initio calculations. There are no scaling factors between theory and experiment. Figure taken from [29]

determined by sum rule analysis is wrong by about a factor of 5 [3,28–31]. To overcome this difficulty, we compared the experimental results to ab initio calculations. For this purpose, an Fe_{0.9}V_{0.1} alloy was prepared by co-evaporation of Fe and V to create an experimental standard. Furthermore, Fe/Ti/Fe(110) and Fe/Cr/Fe(110) trilayers were prepared on a Cu(100) crystal [30]. During the preparation of the Fe/Ti trilayers, it turned out that the Ti XMCD signal did not depend on the deposited thickness of the Ti film up to 15 Å. An explanation could be that all the Ti atoms were polarized by Fe. This would be the case if a TiFe₂ compound was formed as it has been reported for Fe/Ti multilayers [33]. The SPR-KKR calculations have been performed in the group of H. Ebert (LMU Munich, Germany) for a FeTi₂ compound, and Fe_{0.9}V_{0.1} and Fe_{0.9}Cr_{0.1} alloys. The results are presented in Fig. 5.7. As the interaction of the excited electron with the created core hole is not taken into account, the calculated isotropic spectra assume the statistical branching ratio in contrast to the experimental spectra. However, the calculated XMCD spectra agree with the experimental reasonably well with respect to the intensity and the detailed fine structures. For the case of Ti and V, the magnetic moments were directly taken from the SPR-KKR calculations, while the Cr moment was determined by downscaling (factor 0.6) the calculated results. The reason for the downscaling is that Fe/Cr/Fe(110) trilayers were measured in the experiment, which were compared with calculations of an Fe_{0.9}Cr_{0.1} alloy to account for some intermixing at the interface of the trilayer [3, 29]. By comparison to the ab initio calculations, the following spin moments were obtained: $\mu_S(\text{Ti}) = -0.7 \ \mu_B, \ \mu_S(\text{V}) = -1.0 \ \mu_B$, and $\mu_{\rm S}({\rm Cr}) = -0.6 \ \mu_{\rm B}$. The negative sign indicates that these moments are aligned antiparallel to the Fe moments. The apparent moments for the experimental spectra determined by sum rule analysis for Ti and V are about a factor of four to five too small, whereas for the case of Cr, the spin moment is underestimated by about a factor of two using the same analysis [29]. Interestingly, the agreement between experiment and theory for the XMCD seen in Fig. 5.7 is an indication that the problem for the standard analysis is related to the isotropic spectra that are needed for the normalization in the sum rule analysis. Therefore, we established a two-pole approximation within a time-dependent density functional theory [34] in collaboration with E.K.U. Gross (Freie Universität Berlin, Germany) to analyze the change of the branching ratio for the light 3d elements for metallic systems.

In this work, we applied a simple three-level model to explain the origin of the strong deviations from the one-particle branching ratio and determined the matrix elements of the unknown exchange-correlation kernel directly from experiment by utilizing the experimentally determined branching ratios. It turns out that because of the reduced 2p spin-orbit coupling, the two poles couple due to interaction of the excited electron with the created core hole. In the future, the effect of the coupling of the two poles on the dichroic spectra will be studied in detail.

5.6.2 Spin-dependence of Matrix Elements in Rare Earths

In the previous section it was demonstrated that the decrease of the separation between the L_3 - and the L_2 -edges results in the breakdown of the standard sum rule analysis because of the reduced spin-orbit splitting of the $2p_{3/2}$ and $2p_{1/2}$ core levels. This standard analysis can also yield erroneous results even if the L_{3,2}-edges are well separated, as it is the case for rare earth metals. The magnetic properties of the rare earth metals are determined by the localized 4f moments. However, the magnetic ordering of these metals originates from the polarized 5d band. We show below that the 4f as well as the 5d magnetic moments can be probed by the analysis of the L_{3,2}-edge XMCD: in addition to the electric dipole transitions (E1: $2p \to 5d$), electric quadrupole transitions can be identified (E2: $2p \to 4f$). However, even after separating the two contributions, the application of the sum rules to the electric dipolar contributions yields the wrong sign of the induced 5d moments [3,35,36]. This is due to a spin-dependence of the transition matrix elements. For the standard XMCD analysis, it is assumed that the XMCD signal $\Delta \mu$ is proportional to the difference in the spin-dependent density of states (DOS): $\Delta \mu \propto \rho^{\uparrow} - \rho^{\downarrow}$. However, this is not the case for the rare earth L_{3,2}-edge XMCD as the dipole transition matrix elements μ^{\uparrow} and μ^{\downarrow} are spin-dependent. The exchange potential of the 4 f electrons is attractive for spin up and repulsive for spin-down electrons [37]. Therefore, the 5d spin up radial wave function is compressed while the 5d spin-down wave function is pushed out. This leads to a larger dipole-dipole transition matrix element for the spin-up electrons $(\mu^{\uparrow} > \mu^{\downarrow})$.

Consequently, the XMCD spectra cannot be directly related to the difference in the DOS, but the spin-dependence of the transition matrix elements must be included [36]: $\Delta\mu \propto [\mu^{\uparrow}\rho^{\uparrow} - \mu^{\downarrow}\rho^{\downarrow}]$. To analyze the effect of this spin-dependence, we defined a dimensionless spin asymmetry parameter [36]:

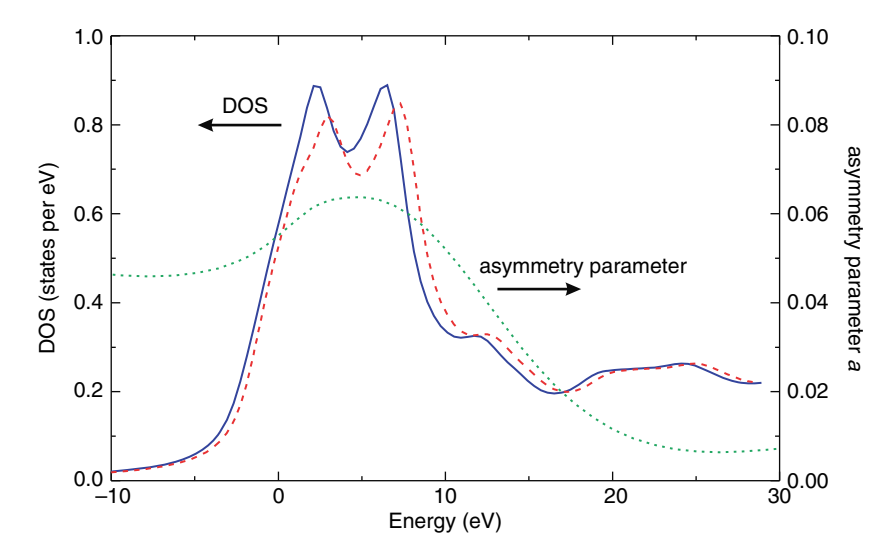


Fig. 5.8 Unoccupied (E < 0) and occupied (E > 0) 5d density of states for spin-up (solid line) and spin-down (dashed line) electrons in Tb as calculated with the FEFF8 code [36]. The asymmetry parameter a (dotted line) characterizes the difference from unity of the ratio between spin-up and spin-down matrix elements (5.15). Figure taken from [36]

$$a_{j} \equiv \frac{R_{j,nl\uparrow} - R_{j,nl\downarrow}}{R_{i,nl\uparrow} + R_{i,nl\downarrow}}, \qquad (5.15)$$

where $R_{j,nl\uparrow}$ denotes the matrix element for the majority spin and $R_{j,nl\downarrow}$ that for the minority spin. The asymmetry parameter a_j is presented in Fig. 5.8 together with the spin-dependent 5d density of states as calculated by the FEFF8 code [36]. The effect of the spin-dependent transition matrix elements can be depicted as follows: the integral of the empty states of the 5d majority band is smaller than the integral of the minority band (there are more empty states in the minority band). However, in the vicinity of the Fermi energy, the asymmetry parameter has a sizable value of about 0.06. Therefore, one probes apparently more empty majority states. The effect is so dramatic that even the sign of XMCD signal is changed (positive L₃-edge XMCD signal) and thereby the moment determined from the sum rule analysis exhibits the wrong sign.

The total moment of bulk Tb is known to be 9.34 μ_B [38]. According to Hund's rules, one expects that the 4f spin contribution to this moment is $\mu_S(4f) = 6.0 \, \mu_B$, while the orbital contribution is $\mu_L(4f) = 3.0 \, \mu_B$. This simple calculation suggests that the remaining $0.34 \, \mu_B$ is due to the induced 5d moments. However, as mentioned earlier, the sum rule analysis even yields the wrong sign, namely an induced moment of $\mu_S^{\text{sumrule}}(5d) = -0.27 \, \mu_B$ is determined from the experimental XMCD results for a Tb single crystal by this standard analysis procedure. To overcome this difficulty, we included the spin-dependence of the matrix elements in a generalized form of the sum rules as presented in [36]. Using these corrections, a spin moment

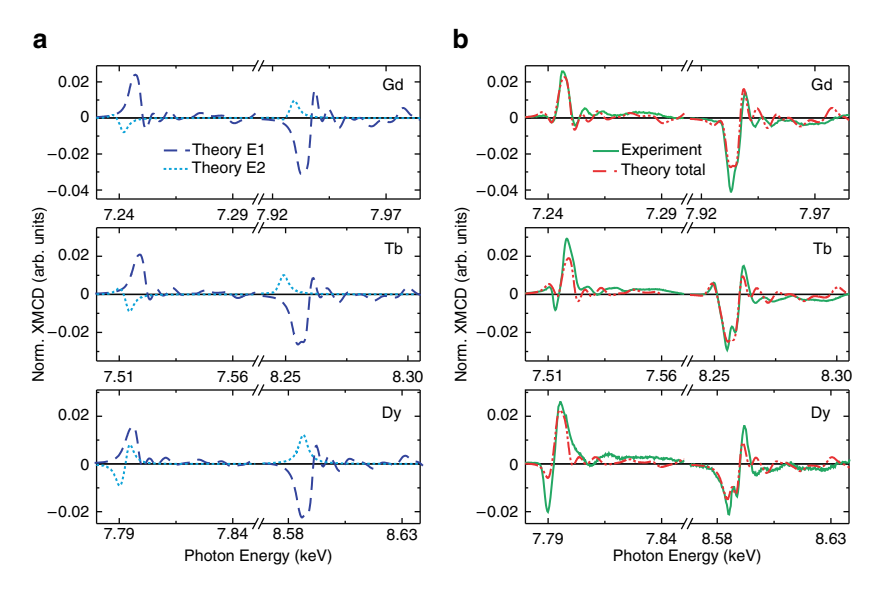


Fig. 5.9 (a) Calculated E1 and E2 contributions to the $L_{3,2}$ -edge XMCD spectra of Gd, Tb, and Dy. (b) Comparison of the measured XMCD spectra of rare earth single crystals at low temperature to the total spectra obtained from calculations. Figure taken from [40]

of $\mu_S(5d) = +0.37 \ \mu_B$ is determined, which is consistent with the results expected (see above).

To display spectroscopic features of the electric dipole (E1) and quadrupolar contributions (E2) in a more systematic manner, we show Gd, Tb, and Dy single crystal L_{3,2}-edge XMCD results together with ab initio calculations (utilizing the SPR-KKR code) in Fig. 5.9 (for details see [39, 40]). The theoretical calculations have the advantage that individual contributions can be easily switched on and off. This allows for the separation of the E1 and the E2 contributions as presented on the left hand side (Fig. 5.9a). The consequence of the spin dependence of transition matrix elements is obvious in the different signs of the calculated E1 and E2 signals: the 4 f states probed by the E2 transitions basically yield a negative contribution to the L_3 -edge XMCD, whereas mainly a positive contribution is detected at the L_2 -edge. This is different for the E1 transitions that probe the polarized 5d band: the E1 transitions are mainly positive at the L₃-edge and negative at the L₂-edge. Furthermore, it is interesting to see that clear dichroic fine structures can be identified in the extended energy regime that originate from the E1 transitions. Figure 5.9b presents that these calculations indeed nicely reproduce the experimental results, where the sum of the calculated E1 and E2 contributions is shown together with the experimental XMCD results of the rare earth single crystals (see [40] for details). The different signs of the E1 and the E2 contributions result in a very pronounced fine structure of the XMCD, where the contribution from the 4 f states (E2 transitions) is essentially located in the pre-edge regime. The reason for this energy shift is the stronger Coulomb interaction of the 4 f states with the 2 p core hole [37]. Another interesting effect on the spectral form of the XMCD can be seen in Fig. 5.9b. Although a clear double structure is identified in the empty 5d density of states (Fig. 5.8), a double structure is seen only at the L₂-edges. This is due to the fact that the final states at the respective edges are not identical. The L₃-edge is dominated by the $2p_{3/2} \rightarrow 5d_{5/2}$ transitions. However, the $5d_{5/2}$ states cannot be probed at the L₂-edge. To test this, the spin–orbit coupling (SOC) in the final states was switched on and off in [40]. It was found for the case with SOC switched on that the splitting of the double structure decreases as compared to the case without SOC and cannot be resolved any more. The results presented in this section again demonstrate that a direct comparison of the experimental data to ab initio calculations helps to interpret the experimental results – especially if the standard analysis procedure fails.

5.6.3 Paramagnetic Biomolecules on Ferromagnetic Surfaces

In this last section, various advantages of the X-ray absorption spectroscopy will be utilized to unravel the secrets of Fe-porphyrin molecules adsorbed on ferromagnetic surfaces. In addition to offering the possibility of an element-specific magnetic analysis, the XMCD-technique has the advantage of an amazing high sensitivity that allows for the detection of tiny magnetic signals as, for example, of magnetic molecules with sub-monolayer coverages on surfaces. Additionally, the orientation of the molecules on the surface is analyzed using linearly polarized X-rays to study the angular dependence of the near-edge X-ray absorption fine structures (NEX-AFS), which is also referred to as the XNLD. The combination of these X-ray absorption spectroscopies provides a deeper insight into the important interactions of the molecules with the surface.

Fe-porphyrin molecules are important biomolecules, for example, as a part of the heme group these molecules are essential components of hemoglobin, which is responsible for the transport of oxygen in blood. However, recently porphyrins have also been discussed with the prospect of realizing the vision of molecular spintronics. One of the reasons for this recent revival of these molecules in surface science is connected to the immense stability of these molecules. This allows one to sublimate porphyrin molecules under ultra-high vacuum conditions. Thereby, the molecules can be adsorbed on the surface with well-defined coverages, which is vital to gain insight into the interaction of the molecules with the surface. Here, we focus on possible coupling phenomena of the Fe spin in the porphyrin molecule (schematically shown in Fig. 5.10) to ferromagnetic surfaces [41,42]. To start with structurally well defined surfaces, Ni and Co ferromagnetic films were grown epitaxially on a Cu(100) single crystal. The use of Ni and Co films has also the advantage that by the choice of the film thickness the easy direction of magnetization can be tuned to the in-plane (5 ML Co/Cu(100)) or out-of-plane (15 ML Ni/Cu(100)) direction. By sublimation at 485 K of octaethylporphyrin Fe(III) chloride (OEP), a coverage of one monolayer on the ferromagnetic films could be achieved (see [42, 43] for further experimental details).

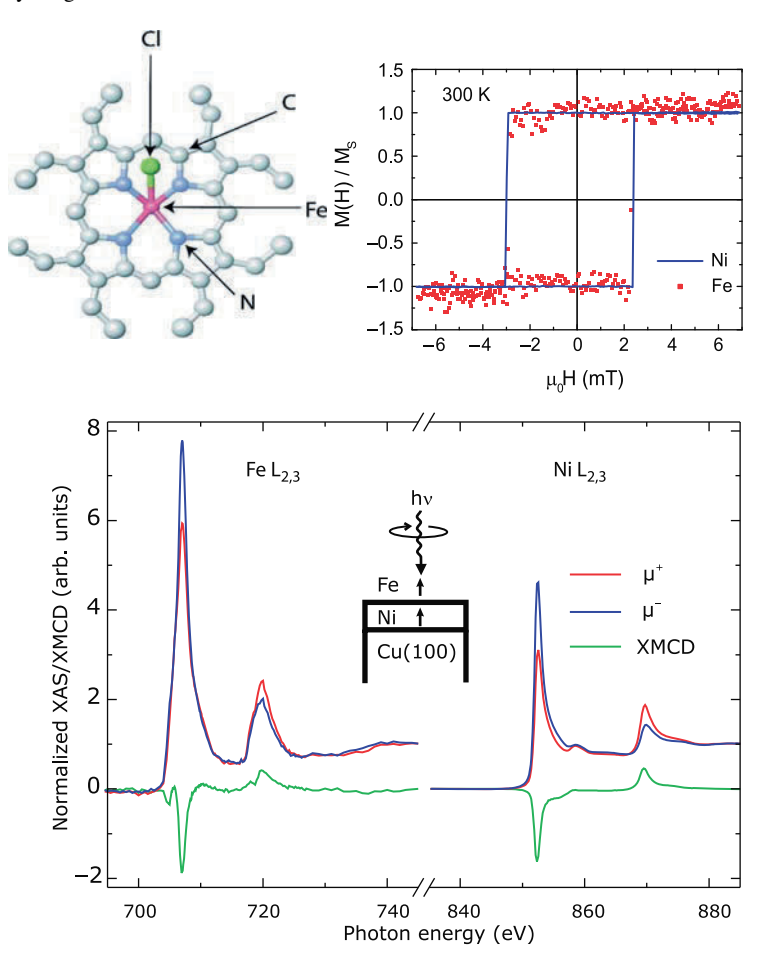


Fig. 5.10 Top left: schematic illustration of the Fe-OEP-chloride molecule. Top right: element-specific hysteresis curves of the Fe atoms (filled squares) and Ni (full line) obtained at the L₃-edge XMCD maxima of Fe OEP on Ni/Cu(100) at 300 K [42]. Bottom: normalized X-ray absorption coefficients for right and left circularly polarized X-rays $\mu^+(E)$ (red) and $\mu^-(E)$ (blue) and XMCD (green) at the L_{3,2}-edges of the central Fe atoms of the OEP molecules and the Ni film (300 K, 10 mT)[42]. The inset depicts the orientation of the sample to the incident X-rays. The arrows for the Fe and the Ni film show the alignment of the spins. Figure taken from [44]

In contrast to the single molecule magnets that exhibit magnetic ordering by intra-molecular exchange phenomena as, for example, described by R. Sessoli et al. in this book, the porphyrin molecules studied here are paramagnetic. Hence, a crucial question is if the paramagnetic molecules show a magnetic coupling to the ferromagnetic films, and in that case what would be the nature of the coupling. One could think of direct exchange phenomena, for example, by hybridization, but also indirect exchange mechanisms like superexchange are imaginable. Therefore, we studied the magnetism of the porphyrin molecules and the ferromagnetic

films separately by the XMCD technique. The results for the Ni film substrate are given in Fig. 5.10 (bottom). Clear dichroic signals are revealed at the Ni as well as the Fe L_{3.2}-edges. This means that the Fe spins in the molecules present an obvious ordering. The data are recorded at room temperature and at an applied field of 10 mT only. At these conditions, a paramagnet would hardly exhibit such ordering of the spins. Hence, there must exist a ferromagnetic coupling to the Ni film. By means of density functional theory, the nature of this coupling was investigated. It turned out that a 90° indirect exchange mechanism via the N-atoms is responsible for this coupling [42]. Furthermore, the strength of the coupling was studied by temperature-dependent XMCD measurements [43]. Thereby, it was found that the coupling to the Ni films is considerably weaker than that to the Co film. Interestingly, we could show that the coupling of the porphyrin molecules to the ferromagnetic films can be changed from ferromagnetic coupling to antiferromagnetic coupling if the Ni or Co film is covered by 0.5 ML of atomic oxygen. To achieve a more detailed experimental understanding of the ferromagnetic coupling, we investigated the magnetic hysteresis loops element specifically by tuning the photon energy to the maximum of the dichroic signals at the Fe and Ni L₃edges. To record the hysteresis loops, the XMCD signal was measured as a function of the applied field. The result is presented in Fig. 5.10 (top right). Obviously, the two curves coincide, which shows that the Fe-spins can be switched by reversing the magnetization of the subjacent ferromagnetic films. The hysteresis loop at the Fe L₃-edge is more noisy than the one at the Ni L₃-edge. The reason is the small amount of material: one monolayer of Fe-porphyrins corresponds to an effective Fe-coverage of about 1/100 ML. But because of the high sensitivity of the XMCD spectroscopy, the dichroic signal and the hysteresis can be clearly resolved as shown in Fig. 5.10.

For the analysis of the coupling of the porphyrin molecules to the ferromagnetic films, the orientation of the molecules on the surface is crucial. Therefore, we studied the X-ray absorption spectra with linearly polarized X-rays at the nitrogen and carbon K-edges in the near-edge regime (NEXAFS). Spectra were taken at normal (90°) and grazing incidence (20°). The results shown in Fig. 5.11 present a prominent difference in angular dependence – the so-called XNLD. The NEXAFS spectra show clear excitations into the antibonding π^* and σ^* molecular states. At normal X-ray incidence, the σ^* resonances dominate the spectra. As these resonances stem from the scattering of the photoelectron at the surrounding atoms, it can be concluded that the molecules are basically oriented flat on the surface. Accordingly, at grazing incidence the π^* resonances are detected. The angular dependence is more pronounced at the N K-edge compared to the C K-edge. The reason is that not all the carbon atoms, as for example, in the ethyl groups, are located in the molecular plane. Therefore, angular dependence at the C K-edge is diminished by averaging. Hence, XNLD at the N and the C K-edges shows that the molecules are lying flat on the surfaces, which enables the coupling of the Fe spins to the ferromagnetic films.

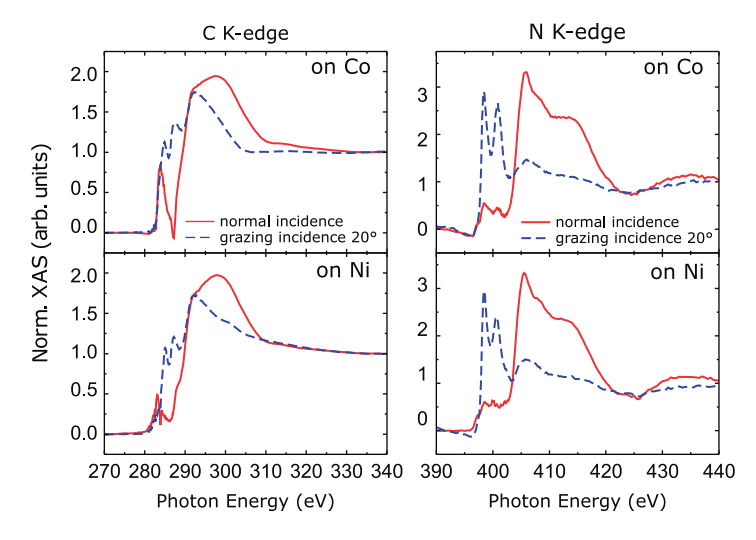


Fig. 5.11 Angular dependence of the NEXAFS (linear polarization) of Fe OEP at the C K-edge (*left*) and N K-edge (*right*) for the Co and Ni substrates at 300 K. X-rays were applied at normal and grazing incidence (20°). After [42]

5.7 Conclusions and Outlook

In this article we presented the advantages and possible misinterpretations of XMCD investigations. We provide insight into the theoretical background, the standard analysis procedures, as well as the corrections of the data for specific detection schemes. The danger of an incorrect analysis by the standard procedures was exemplified by XMCD measurements of magnetic systems of current interest: the effect of the reduced spin-orbit splitting in the initial states leading to a deviation of the branching ratio from its statistical value was shown for the induced moments in light 3d elements. Furthermore, the strong spin-dependence of the transition matrix elements for the electric dipolar transitions of rare earth elements at the L_{3,2}-edges was described. The neglect of this effect even yields the wrong sign of the 5d moments for these elements. The comparison of the experimental data with ab initio calculations avoids the pitfalls of the sum rule analysis. In contrast, the investigation of paramagnetic biomolecules on ferromagnetic surfaces demonstrates the beauty of the XMCD technique: the magnetic properties of the Fe-porphyrin molecules can be studied separately from the ferromagnetic surfaces. Even the element-specific hysteresis curves can be taken, which show that the Fe spins in the molecules can be switched by reversing the ferromagnetic film. This high sensitivity together with the possibility to analyze spin and orbital moments in an element-selective way will definitely advance modern magnetism research.

Acknowledgements Some of the results shown here are parts of the following PhD theses: the investigation of the induced moments in light 3d elements is a major part of the PhD thesis of A. Scherz, and the results for the rare earth XMCD are a part of the PhD thesis of C. Sorg. These two dissertations were supervised by K. Baberschke at the Freie Universität Berlin, Germany. The measurements of the paramagnetic porphyrin molecules on the ferromagnetic surfaces contribute to the PhD thesis of M. Bernien, who is supervised by W. Kuch at the Freie Universität Berlin, Germany. We thank the group leaders H. Ebert (LMU, Munich, Germany), J.J. Rehr (University of Washington, Seattle, USA), O. Eriksson (Uppsala University, Uppsala, Sweden), and their group members for the enlightening ab initio calculations. We thank R. Brand (Universität Duisburg-Essen, Germany) for proofreading the manuscript. Furthermore, we want to acknowledge the help of the staff members at the synchrotron radiation facilities BESSY (Berlin, Germany) and ESRF (Grenoble, France) for their help during the experiments. These works are supported by BMBF (05 KS1 KEB/4, 05 KS4 KEB/5 and 05 ES3XBA/5) and DFG (SFB 290, SFB 491, SFB 658 and Heisenberg program).

References

- S. Hüfner, Photoelectron Spectroscopy (Springer Series in Solid-State Sciences 82, Springer-Verlag, Berlin, Heidelberg, New York, 1995)
- A. Rogalev, F. Wilhelm, N. Jaouen, J. Goulon, and J.-P. Kappler, X-ray Magnetic Circular Dichroism: Historical Perspective and Recent Highlights ed. by E. Beaurepaire et al., Lecture Notes in Physis 697, (Springer, Berlin Heidelberg, 2006) pp. 71
- 3. Heiko Wende, Rep. Prog. Phys. 67, 2105 (2004)
- 4. J. Stöhr, K. Baberschke, R. Jaeger, R. Treichler and S. Brennan, Phys. Rev. Lett. 47, 381 (1981)
- C.T. Chen, L.H. Tjeng, J. Kwo, H.L. Kao, P. Rudolf, F. Sette, and R.M. Fleming, Phys. Rev. Lett. 68, 2543 (1992)
- G. van der Laan, B.T. Thole, G.A. Sawatzky, J.B. Goedkoop, J.C. Fuggle, J.-M. Esteva, R. Karnatak, J.P. Remeika, and H.A. Dabkowska, Phys. Rev. B 34, 6529 (1986)
- 7. B.T. Thole, G. van der Laan, G.A. Sawatzky, Phys. Rev. Lett. **55**, 2086 (1985)
- 8. J. Goulon, C. Goulon-Ginet, A. Rogalev, V. Gotte, C. Malgrange, and C. Brouder, J. Chem. Phys. 108, 6394 (1998)
- J. Goulon, A. Rogalev, C. Goulon-Ginet, G. Benayoun, L. Paolasini, C. Brouder, C. Malgrange, and P. A. Metcalf, Phys. Rev. Lett. 85 4385 (2000)
- J. Goulon, A. Rogalev, F. Wilhelm, C. Goulon-Ginet, P. Carra, D. Cabaret, and C. Brouder, Phys. Rev. Lett. 88, 237401 (2002)
- 11. J.L. Erskine and E.A. Stern, Phys. Rev. B 12, 5016 (1975)
- 12. G. Schütz, W. Wagner, W. Wilhelm, P. Kienle, R. Zeller, R. Frahm, and G. Materlik, Phys. Rev. Lett. 58, 737 (1987)
- 13. B.T. Thole, P. Carra, F. Sette and G. van der Laan, Phys. Rev. Lett. **68**, 1943 (1992)
- 14. P. Carra, B.T. Thole, M. Altarelli and X. Wang, Phys. Rev. Lett. 70, 694 (1993)
- C.T. Chen, Y.U. Idzerda, H.-J. Lin, N.V. Smith, G. Meigs, E. Chaban, G.H. Ho, E. Pellegrin and F. Sette, Phys. Rev. Lett. 75, 152 (1995)
- 16. A.L. Ankudinov and J.J. Rehr, Phys. Rev. B **51**, 1282 (1995)
- 17. G. van der Laan, Phys. Rev. B 55, 8086 (1997)
- G. van der Laan, Hitchhiker's Guide to Multiplet Calculations ed. by E. Beaurepaire et al., Lecture Notes in Physis 697, (Springer, Berlin Heidelberg, 2006) pp.143
- 19. R. Nakajima, J. Stöhr, Y.U. Idzerda, Phys. Rev. B **59**, 6421 (1999)
- 20. J. Stöhr, NEXAFS spectroscopy, 1st edn. (Springer Berlin 1992), pp. 122
- L. Tröger, D. Arvanitis, K. Baberschke, H. Michaelis, U. Grimm and E. Zschech Phys. Rev. B 46, 3283 (1992)
- J. Fink, Th. Müller-Heinzerling, B. Scheerer, W. Speier, F.U. Hillebrecht, J.C. Fuggle, J. Zaanen, and G.A. Sawatzky, Phys. Rev. B 32, 4899 (1985)

- 23. J. Schwitalla and H. Ebert, Phys. Rev. Lett. **80**, 4586 (1998)
- 24. G. van der Laan and B.T. Thole, Phys. Rev. Lett. 60, 1977 (1988)
- 25. H. Ebert, Rep. Prog. Phys. 59, 1665 (1996)
- 26. G. van der Laan, J. Phys.: Condens. Matter 9, L259 (1997)
- 27. E. Goering, Phil. Mag. 85, 2895 (2005)
- A. Scherz, PhD thesis, Freie Universität Berlin (2004), http://www.dissertation.de/buch.php3?buch=3463
- A. Scherz, H. Wende, C. Sorg, K. Baberschke, J. Minár, D. Benea, H. Ebert, Physica Scripta T115, 586 (2005)
- 30. A. Scherz, H. Wende, K. Baberschke, Appl. Phys. A 78, 843 (2004)
- A. Scherz, H. Wende, K. Baberschke, J. Minár, D. Benea and H. Ebert, Phys. Rev. B 66, 184401-1 (2002)
- A. Scherz, P. Poulopoulos, H. Wende, G. Ceballos and K. Baberschke, J. Appl. Phys. 91, 8760 (2002)
- A. Fnidiki, J. Juraszek, J. Teillet, N.H. Duc, T.M. Danh, C. KaabouchiMand Sella, J. Appl. Phys. 84, 3311 (1998)
- A. Scherz, E.K.U. Gross, H. Appel, C. Sorg, K. Baberschke, H. Wende, and K. Burke, Phys. Rev. Lett. 95, 253006 (2005)
- H. Wende, Z. Li, A. Scherz, G. Ceballos, K. Baberschke, A. Ankudinov, J.J. Rehr, F. Wilhelm,
 A. Rogalev, D.L. Schlagel and T.A. Lograsso, J. Appl. Phys. 91, 7361 (2002)
- A.L. Ankudinov, J.J. Rehr, H. Wende, A. Scherz, K. Baberschke, Europhys. Lett. 66, 441 (2004)
- 37. X. Wang, T.C. Leung, B.N. Harmon and P. Carra, Phys. Rev. B 47, 9087 (1993)
- 38. D.E. Hegland, S. Legvold, and F.H. Spedding, Phys. Rev. **131**, 158 (1963)
- 39. C. Sorg, PhD thesis, Freie Universität Berlin (2005), http://www.dissertation.de/buch.php3?buch=4610
- C. Sorg, A. Scherz, K. Baberschke, H. Wende, F. Wilhelm, A. Rogalev, S. Chadov, J. Minár, and H. Ebert, Phys. Rev. B 75, 064428 (2007)
- 41. M. Bernien, PhD thesis, Freie Universität Berlin (2005)
- 42. H. Wende, M. Bernien, J. Luo, C. Sorg, N. Ponpandian, J. Kurde, J. Miguel, M. Piantek, X. Xu, Ph. Eckhold, W. Kuch, K. Baberschke, P. M. Panchmatia, B. Sanyal, P. M. Oppeneer and O. Eriksson, Nature Materials 6, 516 (2007)
- M. Bernien, X. Xu, J. Miguel, M. Piantek, Ph. Eckhold, J. Luo, J. Kurde, W. Kuch, K. Baberschke, H. Wende and P. Srivastava, Phys. Rev. B 76, 214406 (2007)
- 44. H. Dürr, T. Eimüller, H.-J. Elmer, S. Eisebitt, M. Farle, W. Kuch, F. Matthes, H.-C. Mertins, P.M.Oppeneer, L. Plucinski, C.M. Schneider, H. Wende, W. Wurth, H. Zabel, IEEE Transactions on Magnetics 45, 15 (2009)
- M. Bernien, J. Miguel, C. Weis, Md. E. Ali, J. Kurde, B. Krumme, P. M. Panchmatia, B. Sanyal, M. Piantek, P. Srivastava, K. Baberschke, P. M. Oppeneer, O. Eriksson, W. Kuch, and H. Wende, Phys. Rev. Lett. 102, 047202 (2009)

Chapter 6 X-Ray Detected Optical Activity

A. Rogalev, J. Goulon, F. Wilhelm, and A. Bosak

Abstract The detection of optical activity (OA) with X-rays became possible with third generation synchrotron radiation sources. X-ray detected OA stems mainly from electric dipole–electric quadrupole interference terms, which mix multipoles of opposite parity: this implies that these effects can be observed only in systems with broken inversion symmetry. *Natural* OA refers to effects that are *even* with respect to time-reversal symmetry, while *nonreciprocal* OA is concerned with time-reversal *odd* contributions. Various types of X-ray dichroisms related to either natural or nonreciprocal OA were measured at the ESRF and are briefly reviewed in this chapter.

6.1 Introduction

Natural optical activity (OA) was discovered in 1811 by Arago and Biot [1, 2], who observed the rotation of the plane of polarization of visible light in a crystal of quartz. In 1845, Faraday [3] found that the plane of polarization could also be rotated when a beam of visible light propagated through a medium subject to a strong magnetic field: he just discovered magneto-optical activity. Even though what was measured was in both case a rotation of the plane of polarization of light, the underlying mechanisms involved in those two experiments are fundamentally different.

Magneto-optical (MO) effects arise as a consequence of *frequency dispersion*: with an external magnetic field or an internal exchange field, one may induce an unbalanced shift of the density of states involved in optical transitions caused by either right- and left-circularly polarized light. MO effects are currently described within quantum theory as the interaction of circularly polarized photons with electron spins through spin—orbit interaction. The leading terms in MO effects are thus proportional to pure electric dipole (*E*1.*E*1) transitions. MO activity then requires

A. Rogalev (⊠)

European Synchrotron Radiation Facility (ESRF)B.P.-220, F-38043 Grenoble Cedex, France e-mail: rogalev@esrf.fr

time-reversal symmetry breaking, but it does not require the sample to satisfy any specific symmetry condition.

On the other hand, OA is a consequence of *spatial dispersion* [4], that is, it implies a dependence of the transition probabilities on a space variable **r** and on the light wavevector **k**. As a first order spatial dispersion effect linear in **k**, OA is inherently associated with transition probabilities that mix multipoles of opposite parity, for example, electric dipole–magnetic dipole (E1.M1) or electric dipole–electric quadrupole (E1.E2). The Curie symmetry principle states that this can occur only in systems with broken inversion symmetry. OA effects that are even with respect to time reversal symmetry, such as optical rotation or circular dichroism, are commonly referred to as *natural* OA or *reciprocal* OA. Time-reversal odd OA phenomena do also exist, even though the subject is not so-well documented: the corresponding phenomena are most often referred to as *nonreciprocal* OA effects. Let us stress that these new effects are fundamentally different from MO effects and can only be observed in parity-odd magneto-electric media.

Shortly after its discovery, OA of visible light has developed as one of the most powerful spectroscopic tool in physics, chemistry, and biology, and this technique has fascinated many successive generations of scientists. The existence of OA in the X-ray range was questioned for nearly one century, that is, until X-ray natural circular dichroism (XNCD) was unambiguously detected at the ESRF in a series of non-centrosymmetric crystals [5–8]. Such pioneering experiments became feasible, thanks to the recent availability of intense beams of circularly polarized X-rays at third-generation synchrotron radiation sources. Let us emphasize, however, that the origin of OA is not identical in optical and in X-ray spectral regions. This is because the E1.M1 interference terms, which dominate OA measured with visible light, become vanishingly small in X-ray spectroscopy because magnetic dipole transitions (M1) from deep core levels are forbidden, at least in nonrelativistic theories. Fortunately, in the X-ray range there is a significant contribution from the E1.E2 interference term [9], which, in contrast, plays only a marginal role at optical wavelengths. It is now well documented (see, e.g., [10]) that the E1.E2 terms are responsible for most OA features detected in the X-ray range. Various types of X-ray dichroisms related to either natural or nonreciprocal OA were measured at the ESRF and are reviewed in the present chapter.

In the next section, the gyration tensor formalism is used to discriminate between several types of dichroisms related to OA: this formalism is most helpful to identify various effects that can be observed in a non-centrosymmetric crystal. In Sect. 6.3, we shall draw attention onto instrumentation developments related to the measurements of OA with X-rays. In the following sections, we have selected some typical results that provide us with good illustrations of either natural or nonreciprocal OA in the X-ray regime. In the last section, we introduce briefly edge-selective sum rules [11], which made it possible to identify the effective operators responsible for X-ray detected OA.

6.2 X-Ray Detected OA Tensor Formalism

X-ray detected OA can be most easily described using a complex *gyration* tensor, which takes into account spatial dispersion effects, that is, the breakdown of the usual electric dipole approximation in radiation–matter interactions. A quick way to introduce this tensor is to use the theory of refringent scattering which was elaborated by Buckingham and his colleagues [12, 13] to describe OA measured with visible light. We have reported elsewhere an extension of this theory into the X-ray regime [14]. The starting point of this approach is that all modes propagating inside a crystal should be parallel to the wavevector of the incident beam: this requirement is quite acceptable in the X-ray range where the real part of the refractive index $n = 1 - \delta$ is very close to unity ($\delta \le 10^{-5}$): this explains why the critical angles for X-ray reflection $\Theta_C = \sqrt{2\delta}$ usually do not exceed a few micro-radian.

For a transverse polarized wave of wavevector \mathbf{k} , the forward scattered amplitude is most conveniently described with a complex tensor \mathbf{a}^{\star} , which can be expanded in series as

$$a_{ij}^* = \alpha_{ij}^* + \zeta_{ijl}^* k_l + \left(\frac{1}{4} Q_{illj}^* + \frac{1}{6} \eta_{illj}^*\right) k_l 2 + \dots$$
 (6.1)

The first term refers to the rank-2 electric dipole complex polarizability tensor ($\alpha^* \propto E1.E1$). This term is fully symmetric and describes natural linear birefringence as well as natural linear dichroism effects. In an external magnetic field or in the presence of spontaneous magnetic order, this tensor has an antisymmetric part that is nonzero: the latter component is at the origin of the Faraday effect and of the magnetic *circular* dichroism. There are as well additional "magnetic" contributions to the symmetrical part, but the latter contributions are quadratic in the magnetization: the corresponding terms describe the Cotton–Mouton effect and magnetic *linear* dichroism.

The last term in (6.1) involves two complex rank-4 tensors: the pure electric quadrupole polarizability tensor $(Q^* \propto E2.E2)$ and the electric dipole–electric octupole interference term $(\eta^* \propto E1.E3)$. Many experimental results have accumulated over these recent years [15], which support the view that the electric quadrupole (E2.E2) contribution should not be neglected in X-ray absorption spectroscopy because they are responsible for weak natural X-ray linear dichroisms and for additional signatures in X-ray magnetic linear or circular dichroism spectra [16]. Typically, the electric quadrupole contribution can give rise to a detectable optical anisotropy in cubic crystals, which can be measured either with visible light [17,18] or with X-rays [19,20]. It may be worth emphasizing here that the electric dipole–electric octupole interference term mixes multipole moments of the *same* parity and hence cannot give rise to any OA effect.

In the present paper we want to focus on the second term of (6.1), which is often identified as the complex, rank-3 gyration tensor ($\zeta^* \propto E1.E2$ or E1.M1). In the absence of any external magnetic field (or spontaneous magnetic order), ζ^* is fully antisymmetric and describes *natural* OA effects, that is, the reciprocal rotation

of the plane of polarization, circular birefringence, and natural circular dichroism. One should emphasize here again that the elements of the gyration tensor ζ^* are associated with transition probabilities that mix multipoles of opposite parity: those terms vanish except in non-centrosymmetric systems.

The gyration tensor has three irreducible representations with respect to the symmetry operations of the rotation group SO_3 [21]:

- A pseudo-scalar part associated only with the *E*1.*M*1 interference term, which is responsible for the rotatory strength measured at optical wavelengths in enantiomorphous (chiral) systems
- A polar vector part involving both E1.M1 and E1.E2 interference terms: it is responsible for a (very) weak longitudinal component of electrical polarization that is a typical property of pyroelectric materials
- A rank-2 pseudo-deviator part to which both E1.M1 and E1.E2 interference terms contribute.

As far as X-ray absorption spectroscopy (XAS) is concerned, magnetic dipole transitions (M1) are forbidden by standard "nonrelativistic" selection rules. However, as first pointed out by Goulon [9], the interference between electric dipole and electric quadrupole E1.E2 can still contribute to X-ray detected OA. This was confirmed later on by more recent theories [22–24]. Thus, at this stage, we expect both the vector-like and the pseudo-deviator representations to contribute to X-ray detected OA. As a pseudo-deviator is a traceless object, it immediately appears that there is a priori no hope to measure any sizeable X-ray detected OA in a sample that would lack orientational order, for example, a powder or a solution. It then becomes quite obvious that enantiomorphism (or chirality) and optical activity are two distinct concepts that should not be confused. Moreover, not all non-centrosymmetric crystals are suitable to detect OA in the X-ray range. Following Jerphagnon and Chemla [21], we have summarized in Table 6.1 which ones of the 21 classes of non-centrosymmetric crystals should be compatible with the detection of natural OA with X-rays: only 13 crystal classes that admit a pseudo-deviator as rotational invariant in SO(3) may exhibit XNCD due to the $\zeta^* \propto E1.E2$ gyration tensor; on the other hand, the so-called Voigt-Fedorov dichroism might be observed only in ten crystal classes, which admit a polar vector as irreducible representation.

When a crystal is odd with respect to both space parity and time-reversal, the gyration tensor ζ^* then exhibits an additional symmetric part. This is the latter term that is at the origin of a variety of nonreciprocal OA effects such as nonreciprocal or gyrotropic birefringence, nonreciprocal linear dichroism, magneto-chiral birefringence, and dichroism. Systems in which both the temporal and spatial inversion symmetry are broken belong to the remarkable class of magneto-electric materials. Dzyaloshinskii [25] was the first to point out that magnetoelectric solids had precisely time- and parity-odd properties, but which should remain invariant with respect to the product of both operations. There are only 58 Shubnikov groups that are compatible with magnetoelectric effects [26]. We have analyzed elsewhere [11] which nonreciprocal OA effect could be measured for a given magnetoelectric group.

Crystal classes	Point groups	Pseudo scalar	Polar vector	Pseudo-deviator
		Enantio-morphism	Voigt/Fedorov	XNCD
		(E1.M1)	(E1.M1) & (E1.E2)	(E1.M1) & (E1.E2)
$\overline{43}m \ \overline{6}m \ \overline{6}$	$T_d D_{3h} C_{3h}$	No	No	No
432 23	ΟT	Yes	No	No
622 32 422	$D_6 D_3 D_4$	Yes	No	Yes
$6mm\ 3m\ 4mm$	$C_{6\nu}C_{3\nu}$ $C_{4\nu}$	No	Yes	No
6 3 4	$C_6 C_3 C_4$	Yes	Yes	Yes
$\bar{4}2m$	D_{2d}	No	No	Yes
4	S_4	No	No	Yes
mm2	$C_{2\nu}$	No	Yes	Yes
222	D_2	Yes	No	Yes
2	C_2	Yes	Yes	Yes
m	C_s	No	Yes	Yes
1	C_1	Yes	Yes	Yes

Table 6.1 Irreducible components of the gyration tensor in non-centrosymmetric crystals

If we restrict ourselves to dichroism experiments, it can be shown that every component of the Stokes polarization vector of the incoming X-ray beam is associated with a well identified dichroism related to OA:

- $S_0 \Rightarrow X$ -ray magnetochiral dichroism $(XM\chi D)$ [27]
- $S_1 \Rightarrow$ nonreciprocal X-ray magnetic linear dichroism (nr-XMLD) [28]
- $S_2 \Rightarrow$ Jones nonreciprocal cross XMLD (Jones XMLD)¹
- $S_3 \Rightarrow X$ -ray natural circular dichroism (XNCD) [5] and Voigt-Fedorov dichroism [29]

6.3 Instrumentation and Experimental Considerations

X-ray dichroism can be defined as the difference in the X-ray absorption cross sections measured for two orthogonal polarization states of the incident X-ray beam: right- and left-handed polarizations for circular dichroism, and vertical and horizontal polarizations for linear dichroism measurements. Given that the amplitude of the dichroic signal can be as small as a few parts in 104 compared to the polarization averaged edge jump signal, the experimental setup should be carefully optimized if one wants to record such tiny dichroic effects free of artifacts. All experiments reported in this paper were carried out at the ESRF beamline ID12, which was designed for spectroscopic applications requiring a full control of the polarization of X-ray photons of energy ranging between 2 and 15 keV. Given that the performances of this beamline were already discussed in details elsewhere [30, 31], we shall focus hereafter on a few key points that concern OA experiments.

¹ To the best of our knowledge this dichroism had not been detected with X-rays as yet.

The X-ray source consists of three helical undulators, which are inserted in the ID12 straight section of the storage ring: (1) the HELIOS-II (HU-52) undulator [32], (2) the APPLE-II (HU-38) undulator, and (3) the so-called "ElectroMagnet Permanent Magnet Hybrid Undulator" (EMPHU) [33]. All of them can produce either circularly or linearly polarized X-ray photons, but the three devices were carefully optimized to complement each other. Typically, (3) is most appropriate for experiments at low photon energies ($E \ll 4 \, \text{keV}$) and benefits of the advantage that one can flip very rapidly (in $\approx 160 \, \text{ms}$) the circular polarization of the emitted photons from left to right. The HU-52 and HU-38 undulators can deliver a much higher photon flux over a broad energy range but one cannot flip the polarization as fast.

The monochromator is the most critical component of a beamline designed for XAS. This is because the quality of the spectra can be dramatically spoiled by a poor energy resolution, by the transmission of unwanted harmonics, or by instabilities of the exit beam during energy scans, etc. The beamline ID12 is equipped with a UHV compatible, fixed-exit, double-crystal monochromator manufactured by KoHzu Seiki Co. following specifications imposed by the ESRF. The exceptional quality of the mechanics, in particular the high precision of the translation stages, allows one to obtain a fixed exit beam (within $\pm 5\,\mu$ m) over the whole range of Bragg angles that are accessible (6°–80°). The monochromator is most often equipped with a pair of Si <111> crystals. Note that the temperature of each individual crystal is kept at $-140^{\circ}C$ ($\pm 0.2^{\circ}$) using a cryogenic cooling system developed in-house and which proved to be totally free of undesirable vibrations. The stability of the maximum of the rocking curve was shown to be better than 0.1 arcsec over periods of several hours. For two consecutive scans, we obtained an excellent reproducibility of typically 1 meV or even better.

As far as we are concerned with X-ray circular dichroism experiments, one should keep in mind that the double crystal monochromator does not preserve the initial degree of polarization of the undulator beam, except for σ or π linearly polarized beams. Numerical simulations were performed to simulate the transfer of polarization by a Si <111> double-crystal monochromator. The polarization rates (i.e., the Stokes–Poincaré components P_1' , P_2' , P_3') were calculated as a function of the energy of the incident photons over the range 2–10 keV. Typical results are reproduced in Fig. 6.1.

Such calculations were performed on assuming that the incoming undulator beam was entirely circularly polarized ($P_3=1$). At photon energies around ca. 2.8 keV, P_3' drops down to very low values: this implies that X-ray circular dichroism measurements should be most difficult in the corresponding energy range. Indeed, this behavior is typical of the Brewster's angle ($\Theta_B=45^\circ$), where the monochromator acts as a linear polarizer ($P_1'=1$). There is an additional problem that stems from the fairly different reflectivity of the σ and π -components: linearly polarized components with the polarization vector rotated by $\pm 45^\circ$ can possibly be generated by the monochromator, even though the incident beam is perfectly circularly polarized. In critical cases, the unwanted P_2' component can even be fairly intense (nearly 20% at 2.2 keV) with the important point that it is proportional to the P_3 component of the incident X-ray beam. This can have a dramatic consequence: whenever the helicity

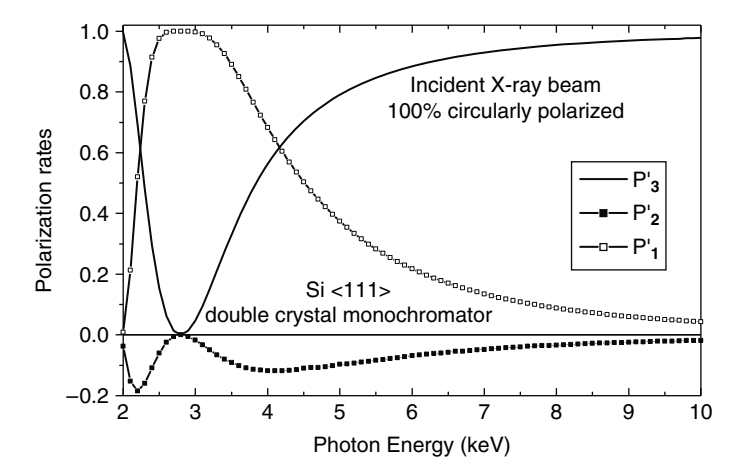


Fig. 6.1 Calculated polarization rates of the exit beam of a Si <111> double-crystal monochromator. It was assumed that the incident X-ray beam was circularly polarized with typically $P_3=1$

of the undulator beam is reverted, the Stokes components P_2' and P_3' get simultaneously reverted, whereas P_1' remains unaffected. In practice, this will spoil all types of circular dichroism measurements (i.e., XMCD as well as XNCD) carried out on biaxial crystals because a weak circular dichroim signal can easily be masked by a much stronger linear dichroism signal [34, 35]. One should also worry about similar difficulties experienced with uniaxial crystals whenever the optical axis of the sample is not strictly parallel to the direction of propagation of the X-rays.

As it was highly desirable to fully characterize the polarization state of the monochromatic beam, we found most convenient to insert downstream with respect to the monochromator a UHV compatible quarter wave plate (QWP) chamber equipped with a diamond single crystal [36]. It is also very convenient to exploit a QWP for X-ray linear dichroism (XLD) experiments [30]: the QWP makes it easy to convert a circularly polarized X-ray beam into a linearly polarized beam with a full control of the orientation of the polarization vector. Moreover, it is straightforward to switch rapidly from one linear polarization to the orthogonal one, with the advantage that one can flip the polarization vector several times for each data point of an energy scan. Obviously, such measurements become much less sensitive to low-frequency instabilities of the source, and small linear dichroism signals can be measured more accurately.

So far, all OA experiments carried out at the ESRF beamline ID12 concerned thick single crystals, which were much too absorbing for measurements in the transmission mode. All spectra were then systematically recorded in the total fluorescence yield mode using photodiodes as detectors. The backscattering geometry of these detectors was found most attractive as it makes it possible (1) to set the optical axis of the crystal either parallel or at a given angle with respect to the wavevector k of the incident X-ray photons; (2) to rotate the crystal around the direction of the

wavevector k. The latter option is crucial for OA experiments on biaxial systems. Last but not least, in the case of magnetoelectric solids, the sample can be inserted inside the bore of a superconducting electromagnet so that a magnetic field \mathbf{H} and an electric field \mathbf{E} both parallel to the wavevector k can be applied simultaneously for the magnetoelectric annealing process.

6.4 Natural Optical Activity Detected with X-Rays

6.4.1 X-Ray Natural Circular Dichroism

X-ray natural circular dichroism (XNCD) refers to the difference in X-ray absorption cross-sections measured with left- and right-circularly polarized photons independently of the presence or absence of any external magnetic field. The first experiment, which firmly established the existence of natural circular dichroism in the X-ray range, was performed at the ESRF in 1997 using a uniaxial laevorotatory crystal of α-LiIO₃, which belongs to the enantiomorphous crystal class 6 [5]. A rather large XNCD signal (up to 6% of the edge jump) was observed at the iodine L_1 absorption edge. At the L_2 and L_3 absorption edges, the recorded XNCD spectra were found to have very similar spectral shapes and the same sign: this observation is at variance with XMCD spectra, which most often exhibit opposite signs at spin-orbit split edges. This can easily be understood as the spin-orbit and exchange splitting are the driving forces in XMCD, while this is not the case in XNCD, as long as the signal is to be assigned to electric dipole–electric quadrupole E1.E2 interference terms. Our interpretation was supported by a direct comparison of the experimental spectra with ab initio simulations carried out in the framework of the multiple scattering theory [22, 24].

The existence of a well-resolved pre-edge feature assigned to $1s \rightarrow 3d$ quadrupolar transitions is often found on the low energy side of the K-edge X-ray absorption spectra of transition metals [15]. The presence of this signature is often retained as a favorable circumstance to detect a large XNCD signal. As an example, we have reproduced in Fig. 6.2 the XAS and XNCD spectra recorded at the nickel K-edge using an enantiomeric single crystal of a α -NiSO₄ × 6H₂O. This uniaxial crystal (with four formula units per unit cell) belongs to the enantiomorphpous tetragonal space groups, $P4_12_12$ or $P4_32_12$ [37]. This compound has long been known to exhibit a natural OA only in the crystalline state, due to the chiral arrangement of nonchiral units: four (nearly) perfect Ni(H₂O)₆²⁺ octahedrons are located along a screw axis, which is parallel to the tetragonal axis of the crystal, that is, the crystallographic c axis, which is the optical axis. OA measurements on this crystal date back to the 1940s [38] and were reported from the infrared up to the UV range. There was even an attempt to detect some natural optical rotatory power in the X-ray range [39] using Cu K_{α} radiation. The latter experiment had, however, very little chance to yield any positive result, because it was performed far from the absorption edges of the atoms constituting the crystal.

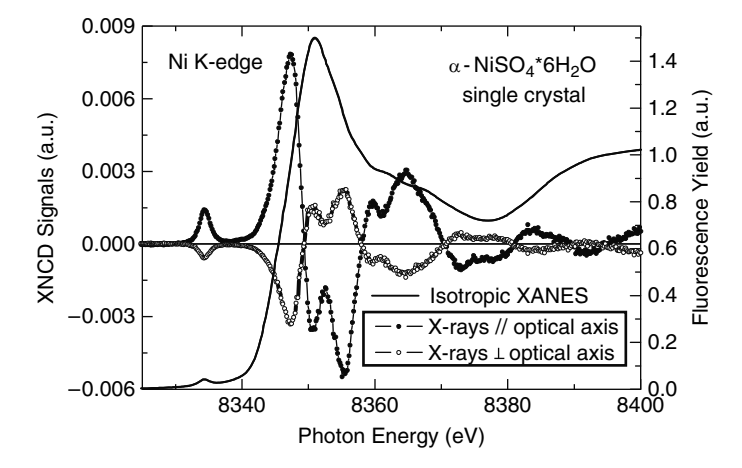


Fig. 6.2 Ni K-edge XNCD of a dextro-rotatory uniaxial single crystal of α -NiSO₄×6H₂O. The XNCD spectrum was recorded with the wavevector of the incident X-ray photons taken either parallel or perpendicular to the optical axis of the crystal. A polarization averaged XANES spectrum was added for the sake of comparison. Note that the XNCD signatures recorded for two different orientations may have the opposite sign

As one can judge from Fig. 6.2, the XNCD signal recorded at the Ni K-edge is not marginally small: its amplitude is of the order of 1% of the edge jump. Surprisingly, we did not observe the maximum of the XNCD signal in the pre-edge region but at much higher energy, and the XNCD spectrum was found to extend well above the absorption edge. This is at variance with what was previously reported regarding the XNCD spectra of chiral transition metal complexes, for example, for XNCD measurements carried out at the Co K-edge with a single crystal of the propeller-like organometallic complex 2[Co(en)₃Cl₃]·NaCl·6H₂O [8] or at the Cu K-edge with a single crystal of CsCuCl₃ [40]. To check whether the XNCD spectrum measured at the Ni K-edge was really to be assigned to the E1.E2 interference term, we decided to carry out further measurements for several orientations of the crystal, in particular on setting the optical axis either parallel or perpendicular to the Xray wavevector. From symmetry considerations [22], one would expect that, for such a uniaxial crystal, the angular dependence of the XNCD signal should vary as $3\cos 2\theta - 1$, where θ denotes the angle between the X-ray wavevector and the optic axis of the crystal. This is exactly what we found as illustrated with Fig. 6.2: the XNCD spectrum recorded with the X-ray wavevector perpendicular to the optic axis is typically twice weaker and, interestingly, it has the opposite sign with respect to the XNCD spectrum recorded in the parallel configuration. This result provided us with an excellent illustration of the fact that the E1.E2 mechanism can be very efficient at the K-edge of transition metals. It also leaves very little hope to detect easily any significant contribution of the pseudo-scalar E1.M1 interference term under such experimental conditions.

Let us nevertheless assume that a weak E1.M1 XNCD signal may exist. The only chance to detect it is when the optic axis of the crystal is set at the magic angle, ca. 54.73° with respect to the X-ray wavevector. This is because the XNCD signal due to E1.E2 interference term should vanish in this geometry so that only the isotropic pseudo-scalar E1.M1 term could ultimately contribute to the XNCD spectrum. We have performed a whole series of angle dependent XNCD measurements for both the enantiomers. The results are shown on Fig. 6.3, where we focused on the XNCD spectra recorded in the pre-edge region of the Ni XANES. For the first time we succeeded in measuring a very weak XNCD signal that may reasonably be assigned to the E1.M1 interference term: the corresponding spectra are reproduced on Fig. 6.3a. As expected the XNCD spectra have the opposite sign for the two enantiomers and their amplitudes are as small as 3×10^{-5} with respect to the edge-jump. To the best of our knowledge, this appears to be the smallest static circular dichroism signal ever measured in the X-ray range. For the sake of comparison, we have also reproduced in Fig. 6.3b the XNCD spectra recorded with the X-ray wavevector

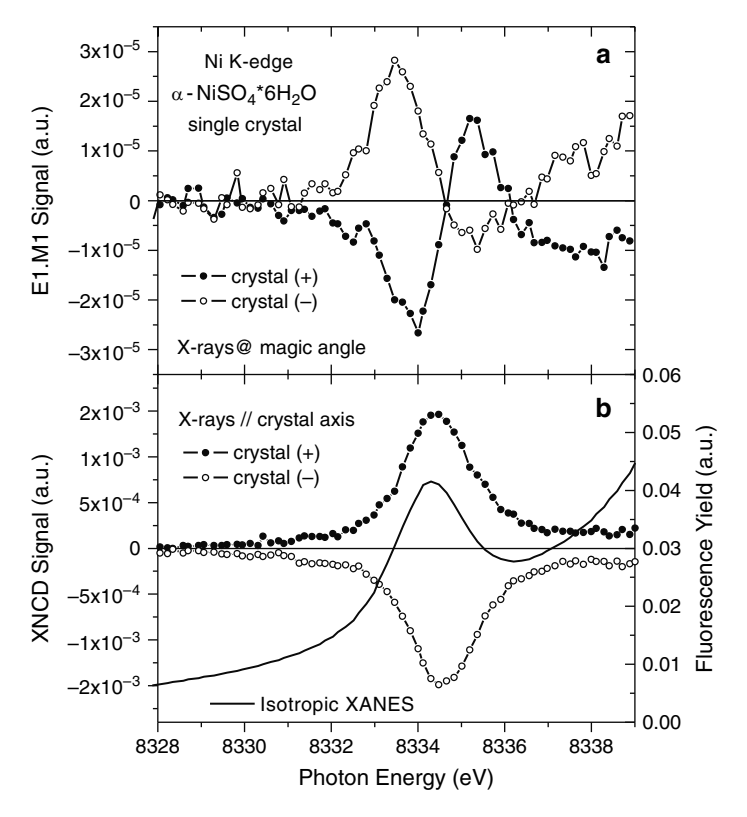


Fig. 6.3 The pre-edge part of the Ni K-edge XNCD spectra for two enantiomeric uniaxial single crystals of α -NiSO₄×6H₂O. (a) XNCD spectra assigned to the E1.M1 interference term, measured at the magic angle. (b) XNCD spectra recorded with the X-ray wavevector parallel to the optic axis. The XANES spectrum was added for the sake of comparison. Note that the E1.M1 XNCD signal is ca. 60 times smaller than the signal assigned to the dominant E1.E2 mechanism

parallel to the optic axis, which are ca. 60 times larger and are indeed dominated by the E1.E2 interference term. It is quite noteworthy that the latter spectra have systematically the opposite sign with respect to the E1.M1 signatures measured with a crystal of the same enantiomer. This result supports a tentative interpretation we gave elsewhere for a weak XNCD signal measured at the Co K-edge on a pellet of a powdered sample of $2[Co(en)_3Cl_3]\cdot NaCl\cdot 6H_2O$ chiral organometalic complexes[11]. Recall that monoelectronic M1 transitions from a 1s core level to 3d states are strictly forbidden in a nonrelativistic approach, but they become weakly allowed in a relativistic theory[41]. That is why the E1.M1 contribution to the X-ray natural circular dichroism is so weak.

Therefore, the experiment reproduced in Fig. 6.3 sets the highest limit for the E1.M1 contributions to natural OA in the hard X-ray range. When no single crystal is available, we found another way to recover a well-detectable XNCD signal assigned to the E1.E2 interference term: our strategy was simply to break artificially the orientational isotropy of space, for example, dissolving the chiral compound of interest in a liquid crystal aligned in a high magnetic field [11].

Given that the XNCD signal is not restricted to the near-edge region of the XAS spectrum, one may question whether it can extend over a wider energy range where EXAFS oscillations are usually observed. The existence of such oscillations in the XNCD spectrum was predicted by theory: those oscillations currently referred to as Chiral-EXAFS (γ -EXAFS) signatures could be seen as the analog of Magnetic-EXAFS signatures for XNCD. The key point is that γ-EXAFS oscillations originate only from symmetry allowed multiple-scattering paths, because all single scattering paths are intrinsically achiral: vertical mirror planes would transform them back into themselves. Chiral-EXAFS oscillations were unambiguously detected at the L_I -edge of Te using a uniaxial crystal α -TeO₂[35]: taking full advantage of the capability of the EMPHU source to flip rapidly the helicity of X-rays, we were able to detect a tiny XNCD signal over a wide energy range. This positive result prompted us to try to identify the multiple-scattering paths contributing most substantially to the measured γ -EXAFS signal. Simulations carried out with the multiple scattering formalism revealed that chiral paths involving the nearest oxygen neighbors represented the dominant contribution, while chiral paths involving heavy Te would suffer from a heavy Debye-Waller damping. These results led to the conclusion that most of the XNCD signal could be accounted for by the chiral arrangement of the low-Z oxygen atoms around the Te atom.

The experiments carried out at the ESRF contributed to establish that X-ray detected natural OA is not necessarily a weak or marginal effect: we proved that XNCD can readily be measured in oriented non-centrosymmetric systems. Moreover, the sign of the XNCD signature can a priori be correlated with the absolute configuration of chiral structures via either the E1.E2 interference term or the E1.M1 contribution if the latter is measurable. XNCD is an element selective probe of local chirality that could be used as a unique tool to extract quantitative information regarding the mixing of orbitals of different parity at a given atom. The knowledge of the amount of mixing should be of direct interest to explain and predict the nonlinear optical properties of acentric crystals.

6.4.2 Vector Part of X-Ray-detected OA

In this section, we focus on crystals in which the gyration tensor has an irreducible part that transforms as a polar vector in O(3). There are three classes of non-centrosymmetric crystals $(4\,m\,m,\,3\,m,\,6\,m\,m)$, which look particularly attractive because their gyration tensor have only an irreducible part that transforms as a vector. Crystals that belong to those classes do not exhibit any optical rotation or any natural circular dichroism in absorption: this is why such crystals have long been (improperly) quoted as optically inactive.

In 1905, Voigt [42] was the first to suggest that these crystals should exhibit OA. In 1959, Fedorov [43] proposed a new way to detect such a peculiar type of OA: his idea was that, under oblique incidence, a linearly polarized light should be reflected as an elliptically polarized light by a crystal at suitable symmetry. Shortly later, Fedorov and his colleagues [44] refined their proposal and discussed specific geometries aimed at maximizing the amplitude of this new OA effect at optical wavelengths. Unfortunately, the reality of this effect was firmly established only in 1978 when Ivchenko and coworkers measured the OA of an hexagonal crystal of cadmium sulfide (CdS) on investigating its optical properties in the exciton resonance region [45].

The theory of reflectivity in non-centrosymmetric uniaxial crystals was carefully revisited more recently by Graham and Raab [46]. A major outcome of this work was to show that one could easily access to the vector part of OA using circular intensity differential reflectivity measurements when the optical \mathbf{c} axis is perpendicular to the reflection plane and when the angle of incidence is close to 45°. Unfortunately, specular reflectivity of X-rays cannot be used for such measurements because the off-diagonal terms responsible for OA just vanish at glancing angles. However, we suggested that the vector part of OA could still be measured in the X-ray resonant diffraction regime using circularly polarized X-rays at Bragg angles near 45°, that is, under conditions where the crystal behaves just like a linear polarimeter.

The first experiment of this type [29] was performed by the ESRF ID12 team using a UHV compatible reflectometer/diffractometer featuring an excellent mechanical reliability and a high level of reproducibility [47]. The crystal that we selected for this challenging experiment was a high-quality single crystal of zincite (ZnO), which exhibits the hexagonal structure of Würtzite. We decided to exploit the strong (300) reflection characterized by a Bragg angle varying from 43.13° to 42.69° over the whole Zn K-edge XANES range (9655–9735 eV). Under such conditions, the angular width of the reflection was measured to be typically 5.4 arcsec. Note that the Zn atoms contribute for 80% of the structure factor of this reflection.

The results of this experiment are displayed in Fig. 6.4. A typical Zn K-edge DANES (diffraction anomalous near edge structure) spectrum of the zincite crystal is reproduced in Fig. 6.4a, in which we plotted the integrated area below the (300) diffraction peak as a function of the incident photon energy. Note that the crystal **c** axis was kept strictly perpendicular to the scattering plane. The CID spectra shown on Fig. 6.4b were obtained as a direct difference of the DANES spectra recorded

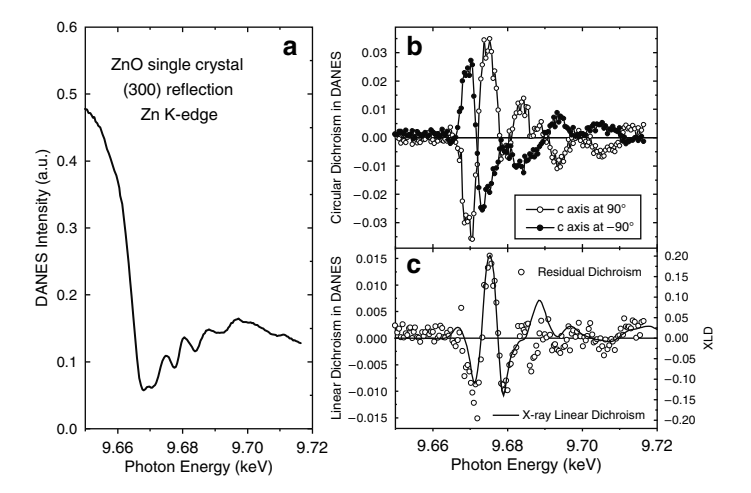


Fig. 6.4 Circular intensity differential scattering measured at the Zn K-edge using the (300) reflection by a single crystal of zincite: (a) Polarization averaged DANES spectrum. (b) Circular intensity differential scattering measured in DANES spectra for two orientations of the crystal. (c) Comparison of the residual signal with the XLD spectrum

with left- and right-circularly polarized incident photons. Graham and Raab pointed out that the sign of the circular dichroism should be reversed if the crystal was rotated by 180° around the normal to the reflection planes, that is, when the angle between the **c** axis of the crystal and the reflection plane changed from $+90^{\circ}$ to -90° . This is precisely what is observed in Fig. 6.4b. Note that such a 180° rotation should leave the unwanted linear dichroism unchanged, provided that the diffraction planes are strictly perpendicular to the rotation axis. In the absence of any experimental artifact, the sum of two circular dichroism spectra should reproduce the X-ray linear dichroism (XLD) spectrum expected as a consequence of the existence of a small P'_2 polarization component in the exit beam of the monochromator: the corresponding amplitude of the component was estimated to be of the order of 2% at $9.7 \, \text{keV}$. As illustrated with Fig. 6.4c, this residual spectrum matches perfectly the XLD spectrum that could be measured simultaneously in the total fluorescence yield detection mode.

This is the first example of X-ray detected OA measured in DANES spectra using an acentric single crystal. This experiment clearly supports our view that the vector part of OA can perfectly be measured in the X-ray range as well as with visible light. Given that ZnO belongs to a very important class of pyroelectric materials, let us suggest that this type of experiment could open a new field of applications for X-ray spectroscopy, in which element- and orbital-selective studies could bring new information on the ferroelectric properties of single crystals.

6.5 Nonreciprocal X-Ray-detected OA

6.5.1 Nonreciprocal X-Ray Linear Dichroism

In this section, we draw attention on the possible existence of a nr-XMLD, that is, a difference in the relative absorption of the σ and π components of a linearly polarized X-ray beam. Recall that this effect is expected to be odd with respect to the time-reversal symmetry and that it can be observed only in magnetoelectric crystals with broken inversion symmetry. Let us stress once again that this peculiar OA is fundamentally different from the more common magneto-optical XMLD effect discovered by Van der Laan et al. [48]. which was shown to be a time-reversal even effect.

As first suggested by Birss and Shrubsall [49] and confirmed by several authors [50,51], nonreciprocal OA should be detected only in crystals that are *magnetoelectric*. Recall that magnetoelectric systems form a special class of magnetic ordered materials in which time-reversal and parity are simultaneously broken, while the product of the two operators should leave the measured properties unchanged. The predicted nonreciprocal magnetic linear dichroism is notoriously very small in the visible region and it took some time before theory could be corroborated with rather challenging experiments [52,53].

Even though there are as much as 58 non-centrosymmetric magnetoelectric crystal classes, it does not mean that nr-XMLD can be observed in any experimental geometry. The geometrical and symmetry requirements to detect such a small effect with X-rays were discussed in deeper details elsewhere[11]. Unfortunately, most magnetoelectric crystals are antiferromagnetic, with the additional difficulty that we have to deal with multidomain states. To observe a nonreciprocal XMLD effect in an antiferromagnet, one has to grow a single antiferromagnetic domain and should have the capability to switch from one type of domain to the other. This is usually achieved with a so-called "magnetoelectric annealing" procedure. Most frequently, it consists in heating up first the crystal in the paramagnetic phase; then after some delay time, both an electric and a magnetic field are applied to the sample before one starts to cool slowly the systems across its antiferromagnetic phase transition.

The first nonreciprocal X-ray magnetic linear dichroism spectrum was tentatively recorded at the ESRF ID12 beamline [28] using a Cr-doped crystal of vanadium sesquioxide, that is, $(V_{1-x}Cr_x)_2O_3$. According to neutron diffraction data [54], the space–time group of the AFM monoclinic low temperature phase below T_N was expected to be 2 due to the transfer of magnetic moments towards the oxygen atoms. As far as this interpretation is correct, the low temperature monoclinic phase of V_2O_3 should be magnetoelectric. We have to admit that we are not aware of any successful measurements of the magnetoelectric susceptibility in V_2O_3 . The reason for the failure of the first experiment reported by Astrov [55] seems to be related to the fact that the first order transition from the corundum phase to the monoclinic phase in pure V_2O_3 is crystal-destructive. This is why we concentrated our efforts on a Cr-doped $(V_{1-x}Cr_x)_2O_3$ single crystal for which x=0.028. At this concentration,

not only $T_{\rm N}$ raises from 150 K to ca. 181 K, but also the electric resistivity is substantially increased in the paramagnetic phase. Here, we reused the same crystal as for previous resonant X-ray scattering experiments carried out at the ESRF beamline ID20[56]: this Cr-doped crystal $(1.0\times0.8\times0.05\,{\rm mm^3})$ was initially assumed to have been cleaved perpendicularly to the hexagonal ${\bf c}$ axis, but it was realized later that it was slightly miscut. Neutron diffraction experiments tend to suggest that, in the low temperature (monoclinic) phase, the magnetic moments $(1.2\,\mu_{\rm B}$ per V atom) could be rotated by ca. 71° with respect to the hexagonal ${\bf c}$ axis: the system should then exhibit a nonreciprocal XMLD signal.

As illustrated with Fig. 6.5, we observed a rather intense nr-XMLD signal at the vanadium K-edge (ca. 1% of the edge jump) after magnetoelectric annealing. For the sake of comparison, we added on the same plot a XANES spectrum recorded at the V K-edge but deconvoluted to compensate for the effect of the core-hole lifetime broadening. The nonreciprocal XMLD spectra reproduced in Fig. 6.5 were recorded after a magnetoelectric annealing process conducted in the geometry $\mathbf{E} \| \mathbf{H} \| \mathbf{k}$ with \mathbf{c} tilted away from \mathbf{k} by approximately 10° . Given that the signal was found to change its sign when the annealing was performed with parallel or antiparallel electric and magnetic fields and that it was clearly found to vanish above the Néel temperature $T_{\rm N} = 181\,\mathrm{K}$, we keep thinking that there is very little doubt left regarding the nonreciprocal character of this signal. Let us emphasize that the true orientations of the crystallographic axes \mathbf{a} and \mathbf{b} were unfortunately unknown in this experiment: this makes it impossible to clarify whether the nonreciprocal dichroism that was measured is to be interpreted as the Jones dichroism cross XMLD or as a true nonreciprocal XMLD. In any case, the observed nonreciprocal effect can

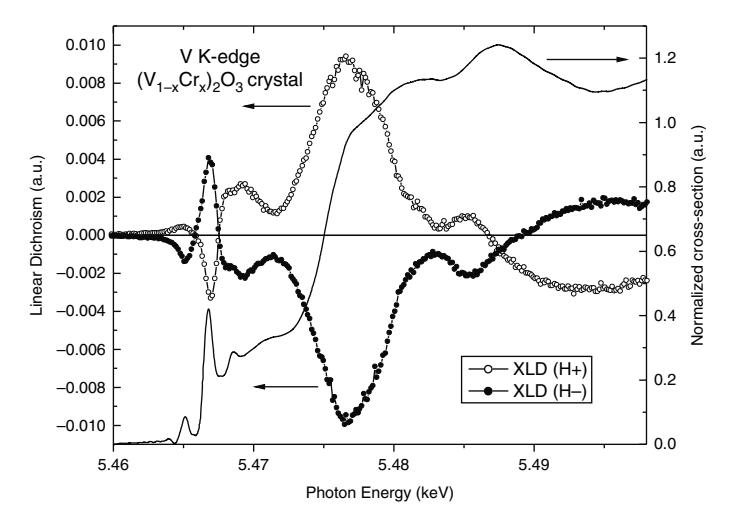


Fig. 6.5 Nonreciprocal XLD spectra recorded at the V K-edge in the monoclinic AFI phase of the $(V_{1-x}Cr_x)_2O_3$ crystal. Magneto-electric annealing was performed either with parallel (+) or antiparallel (-) electric and magnetic fields. A deconvoluted V K-edge XANES spectrum was added again for the sake of comparison

only be understood if the inversion symmetry is broken by the magnetic order as expected in the space–time magnetoelectric group 2. Thus, our result would support the interpretation proposed by Word and his colleagues [54]. In this respect, nonreciprocal XMLD experiments could develop as a useful technique to unravel hidden space–time symmetry in magnetoelectric systems.

Let us draw attention onto the fact that the existence of nr-XMLD effect was confirmed more recently by Kubota et al. [57], who were able to detect a typical nr-XMLD signal on recording the XANES spectra of a *polar* ferrimagnetic crystal of GaFeO₃ at the Fe K-edge. These authors, however, gave a different name to this effect, which they called *X-ray non-reciprocal directional dichroism* (XNDD), thus referring to the fact that the sign of the effect depends on whether the direction of propagation of X-rays is either parallel or antiparallel to the outer product of the magnetization and electric-polarization vectors in the sample.

6.5.2 X-Ray Magnetochiral Dichroism: XM χD

Let us focus below onto another nonreciprocal effect that we tentatively called X-ray magnetochiral dichroism ($XM\chi D$) by analogy with a long anticipated OA effect [58, 59] that was finally observed in 1997 in the visible by Rikken and Raupach [60]. A somewhat surprising aspect of this new type of dichroism is that it can be measured with an *unpolarized* X-ray beam propagating in a magnetochiral medium when the sign of the magnetization is inverted at the absorbing site. Once more, inversion and time-reversal symmetries should be broken in those magneto-chiral systems. Indeed, magnetoelectric systems appear here again as good candidates to measure a magnetochiral dichroism. However, only 31 magnetoelectric groups [61] out of 58 are compatible with the existence of the magnetochiral effect. Those groups have all in common the characteristic property that their rank-2 ME tensor should have *antisymmetric* off-diagonal terms.

The first $XM\chi D$ spectrum was measured with a single crystal of chromium sesquioxyde (Cr_2O_3) cooled down to the antiferromagnetic phase. This experiment required us again to obtain single domains using the well established magneto-electric annealing procedure. Recall that Cr_2O_3 is the generic example of magnetoelectric solids with a convenient transition temperature of 307 K. The $XM\chi D$ spectra were measured at 50 K on exploiting XAS spectra recorded at the Cr K-edge in the fluorescence excitation mode using the usual backscattering configuration. We produced artificially an unpolarized X-ray beam by incoherent superposition of fluorescence excitation spectra recorded with right and left circularly polarized incident photons: $F_0 = F_{rcp} + F_{lcp}$. The Cr K-edge $XM\chi D$ spectra displayed in Fig. 6.6 were obtained in comparing the *pseudo*-unpolarized XANES spectra recorded for 180° domains grown under the condition of time-reversality after magnetoelectric annealing. For the sake of comparison, we have reproduced on the sample plot a deconvoluted, unpolarized XANES spectrum recorded with an equidomain crystal: in this experiment, the wavevector \mathbf{k} was carefully set parallel to the \mathbf{c} axis of the

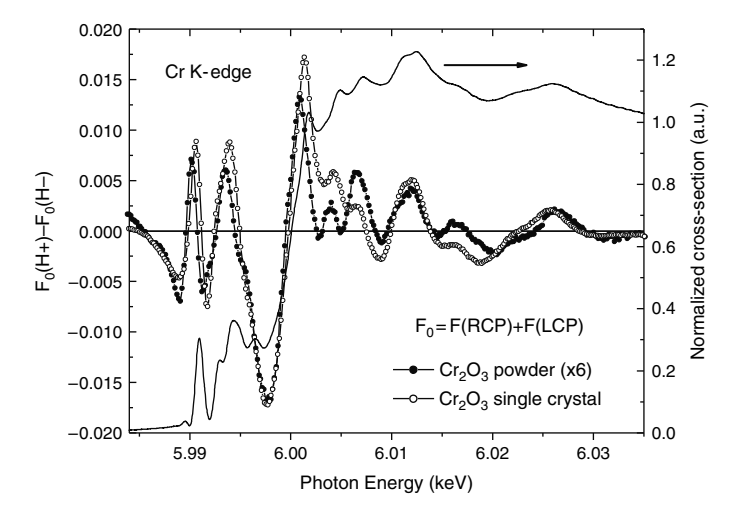


Fig. 6.6 Cr K-edge $XM\chi D$ spectra recorded either with a (001) single crystal of Cr_2O_3 or with a powdered pellet of the same material. In both experiments, we had $\mathbf{k}||\mathbf{c}||\mathbf{E}||\mathbf{H}$. The signal measured with the powdered pellet was tentatively multiplied by a factor 6. $XM\chi D$ spectra refer to the difference of isotropic spectra measured on two 180° domains grown by magnetoelectric annealing. For the sake of comparison, we added again a deconvoluted XANES spectrum recorded with a equidomain crystal

crystal. As the rotational isotropy of space is broken when single domains are grown after magnetoelectric annealing along the direction of (E, H), one may anticipate that $XM\chi D$ spectra could be recorded with powdered samples. This was confirmed experimentally: using a pellet of Cr_2O_3 powder, we were able to record $XM\chi D$ spectra, which look very similar to the previous ones, except that the intensity of the dichroism was reduced by a factor of the order of 6, such a reduction being nicely consistent with the theory as discussed in the next section.

Surprisingly, we realized that the magnetic group $\bar{3}'m'$ which is most often assumed for Cr_2O_3 was not in the list of the 31 groups that are compatible with the existence of magnetochiral effects. Thus, our result tend to suggest that the true magnetic group of Cr_2O_3 may not be $\bar{3}'m'$ as usually considered on the basis of early neutron data: in reality, the level of symmetry should be somewhat lower and we suggested that the true magnetic group might be only $\bar{3}'$. Several interpretations can be formulated to explain such a lower magnetic symmetry. It is our own interpretation that the configuration of the chromium spins should be quite correct, but we expect again some magnetic polarization of the oxygen atoms affecting the *orbital* magnetism. This was already envisaged by Shirane and his colleagues [62] more than 30 years ago: it was precisely suggested by these authors that the covalent character in the Cr-O bonds should involve a small spin transfer from the chromium 3d-orbitals to the oxygen 2p shell, but they noted that such transferred moment should be much too small to be detected in neutron diffraction experiments. Recall that an asymmetric twist of the oxygen planes is already responsible for a reduction

of the local symmetry of the Cr atoms from $C_{3\nu}$ to C_3 [63]. As pointed out in [64], the angular momentum unquenched by covalent bonding, with a different quantization axis than the spins, must be a widespread phenomenon in antiferromagnetic solids. Therefore, one may perfectly envisage that some orbital contribution to the magnetoelectric tensor (which could not be measured so far) could well explain a symmetry reduction.

As far as our interpretation is correct, we must seek for a magnetoelectric group consistent with the newly measured X-ray detected OA and with more standard magnetoelectric susceptibility measurements. The only magnetic group that can reconcile all published results regarding magnetic properties of Cr_2O_3 is $\bar{3}'$. We, therefore, propose this group as the true magnetic group describing the spin and orbital magnetoelectric effects in $Cr_2O_3[27]$.

6.6 Effective Operators for X-Ray Detected OA

The success of X-ray magnetic circular dichroism is, to a large extent, associated with the availability of the magneto-optical sum rules [65,66]. This is because these rules made it possible to correlate the integrated XMCD spectra with the expectation value of the z component of several magnetic operators: < L_z >, < S_z >, and < T_z >. A similar approach was first envisaged by Natoli [22] for X-ray natural circular dichroism, but no clear physical meaning was found for the effective operator responsible for XNCD. Using the powerful method of group generators, Carra and collaborators derived a whole set of the sum rules applicable to X-ray OA [67–70]. A key achievement was to show that all effective operators responsible for X-ray OA could be built from a triad of mutually orthogonal vector operators:

- $\mathbf{n} = \mathbf{r}/r$, which is a time-reversal *even*, polar vector associated with the electric dipole moment
- the orbital angular momentum L, which is a time-reversal odd axial vector
- the toroidal vector $\Omega = [(\mathbf{n} \times \mathbf{L}) (\mathbf{L} \times \mathbf{n})]/2$, which is odd with respect to both parity and time-reversal.

Interestingly, Ω was rapidly identified with the orbital *anapole* moment as defined in textbooks [71]. Recall that the concept of an anapole was first introduced in 1958 by Zel'dovich[72], who started from symmetry considerations but proposed it as a useful tool to describe parity-violating interactions.

Up to five spherical operators are required for a full description of the effects related to X-ray OA:

- The ground state expectation value of the z component of the orbital anapole moment < Ω_z > is found to be the key effective operator for XM χD.
- As long as one consider only the transition probabilities associated with the E1E2 interference terms, the effective operator responsible for XNCD is the time-reversal *even* rank-2 pseudo-deviator built from the tensor product of two time-reversal *odd* vectors $[\mathbf{L} \otimes \Omega]^{(2)}$. The XNCD signal associated with the

- *E*1.*M*1 rotatory strength would refer to more complex two-electron operators: an orbital pseudo-scalar and an orbital pseudo-deviator, both tensors being clearly two-particle electron operators [73].
- Regarding the vector part of OA, the effective operator is a polar vector (L2 · n) which, according as to Marri and Carra [70], may well be responsible for ferroelectric ordering
- The time-reversal odd rank-2 pseudo-deviator defined as $[\mathbf{L} \otimes \mathbf{n}]^{(2)}$ is another effective operator responsible for nonreciprocal XMLD.
- An additional operator should still be introduced: it concerns the orbital septor $\left[\left[L\otimes L\right]^{(2)}\otimes\Omega\right]^{(3)}$. Its expectation value is involved in the XM χ D sum rule as well as in the nonreciprocal XMLD sum rule.

The significance of the corresponding sum rules and the practical conditions of their exploitation have been discussed elsewhere [11]. The case of Cr₂O₃ looks most interesting. Recently, Di Matteo and Natoli [74] claimed that the largest contribution should come from the septor terms. This is, however, strongly contradicted by our experiment carried out with the powdered sample (see Fig. 6.6). If we assume that the effective operator for the magneto-chiral dichroism is Ω , then one may easily predict [11] that the XM χ D signal should be reduced by a typical factor ≈ 5.5 in the powdered sample as compared to the signal measured with the single crystal; if the effective operator was the septor, then the XM χ D signal should be hardly measurable with a powdered pellet as the sum-rule would predict a dramatic reduction factor (<0.05). This consideration strongly supports our interpretation and our view that the $XM\chi D$ sum rule may offer a unique possibility to quantify the expectation value of the *orbital* anapole moment in Cr_2O_3 : $\langle \Omega_z \rangle \approx 0.03$ a.u. This is a rather small value when compared to the values currently admitted for spin anapoles [11]. Indeed, this confirms that it would be very difficult – if not simply impossible – to access the orbital part of the magnetoelectric tensor using conventional magnetoelectric susceptibility measurements.

There is another interesting implication of the XNCD sum rule: the effective operator associated with natural X-ray detected OA should be the time-reversal *even* direct product of two time-reversal *odd* operators that are both related to orbital magnetism. This result establishes a direct link between OA and magnetism. Let us recall that Pasteur tried very hard for many years to show that chirality and magnetism were connected [75], but he could never prove his view within the knowledge of his time.

In conclusion, we believe that our work contributed to establish X-ray detected OA as a new, *element*- and *orbital*-selective spectroscopy, which appears as a unique tool to study orbital magnetism in parity nonconserving solids. As far as the sum rules may give us access to the ground state expectation values of orbital operators, the nonreciprocal X-ray detected OA might reveal hidden space–time symmetry properties in magnetoelectric crystals whenever the partially unquenched angular momentum has a quantization axis slightly different from the quantification axis of the spins.

Acknowledgements The authors wish to acknowledge a long standing and very fruitful collaboration with Ch. Brouder and P. Carra. The authors are particularly indebted to E. Katz for many stimulating discussions over the past years. Acknowledgements are also due to Y. Petroff for his permanent encouragement.

References

- 1. D.F.M. Arago, Mémoires de l'Institut de France 12, 93 (1811)
- 2. J.-B. Biot, Mémoires de l'Institut de France 13, 218 (1812)
- 3. M. Faraday, Phil. Trans. 3, 1 (1846)
- 4. L.D. Landau, E.M. Lifshitz, *Electrodynamics of Continuous Media*, (Pergamon Press, New York, 1960)
- J. Goulon, C. Goulon-Ginet, A. Rogalev, V. Gotte, C. Malgrange, C. Brouder, C.R. Natoli, J. Chem. Phys. 108, 6394 (1998)
- L. Alagna, T. Prosperi, S. Turchini, J. Goulon, A. Rogalev, C. Goulon-Ginet, C.R. Natoli, R.D. Peacock, B. Stewart, Phys. Rev. Lett. 80, 4799 (1998)
- J. Goulon, C. Goulon-Ginet, A. Rogalev, G. Benayoun, C. Brouder, C.R. Natoli, J. Synchrotron. Radiat. 6, 673 (1999)
- 8. B. Stewart, R.D. Peacock, L. Alagna, T. Prosperi, S. Turchini, J. Goulon, A. Rogalev, C. Goulon-Ginet, J. Am. Chem. Soc. **121**, 10233 (1999)
- 9. J. Goulon, in *Rayonnement Synchrotron Polarisé, Electrons Polarisés et Magnétisme*, ed. by E. Beaurepaire, B. Carriére, J.P. Kappler, (Strasbourg: IPCMS 1990), p. 333
- J. Goulon, A. Rogalev, F. Wilhelm, N. Jaouen, C. Goulon-Ginet, C. Brouder, J. Phys. Condens. Matter 15, S633 (2003)
- J. Goulon, A. Rogalev, F. Wilhelm, C. Goulon-Ginet, P. Carra, I. Marri, Ch. Brouder J. Exp. Theor. Phys. 97, 402 (2003)
- 12. A.D. Buckingham, Adv. Chem. Phys. 12, 107 (1968)
- 13. L.D. Barron, *Molecular Light Scattering and Optical Activity*, (Cambridge University Press, Cambridge, 1982)
- J. Goulon, C. Goulon-Ginet, A. Rogalev, V. Gotte, C. Brouder, C. Malgrange, Eur. Phys. J. B Condens Matter 12, 373 (1999)
- 15. Ch. Brouder, J. Phys. Condens. Matter **2**, 701 (1990)
- 16. R.-M. Galera, Y. Joly, A. Rogalev, N. Binggeli, J. Phys. Condens. Matter 20, 395217 (2008)
- 17. H.A. Lorentz, Proc. Acad. Amsterdam 24, 333 (1921)
- 18. J. Pastrnak, K. Vedam, Phys. Rev. B 3, 2567 (1971)
- 19. G. Dräger, R. Frahm, G. Materlick, O. Brümmer, Phys. Status. Solidi. B 146, 287 (1988)
- D. Cabaret, C. Brouder, M.-A. Arrio, Ph. Sainctavit, Y. Joly, A. Rogalev, J. Goulon, J. Synchrotron Radiat. 8, 460 (2001)
- 21. J. Jerphagnon, D.S. Chemla, J. Chem. Phys. 65, 1522 (1976)
- C.R. Natoli, Ch. Brouder, Ph. Sainctavit, J. Goulon, C. Goulon-Ginet, A. Rogalev, Eur. Phys. J. B 4, 1 (1998)
- 23. M. Okutani, T. Jo, P. Carra, J. Phys. Soc. Jpn. 68, 3191 (1999)
- Ch. Brouder, C.R. Natoli, Ph. Sainctavit, J. Goulon, C. Goulon-Ginet, A. Rogalev, J. Synchrotron Radiat. 6, 261 (1999)
- 25. I.E. Dzyaloshinskii, Soviet Phys. JETP **10**, 628 (1960)
- A. J. Freeman, H. Scmhid(eds.), Magnetoelectric Interaction Phenomena in Crystals, (London, Gordon and Breach, 1975)
- J. Goulon, A. Rogalev, F. Wilhelm, C. Goulon-Ginet, P. Carra, D. Cabaret, Ch. Brouder, Phys. Rev. Lett. 88, 237401 (2002)
- J. Goulon, A. Rogalev, C. Goulon-Ginet, G. Benayoun, L. Paolasini, Ch. Brouder, C. Malgrange, P.A. Metcalf, Phys. Rev. Lett. 85, 4385 (2000)

- J. Goulon, N. Jaouen, A. Rogalev, F. Wilhelm, C. Goulon-Ginet, Ch. Brouder, Y. Joly, E.N. Ovchinnikova, V.E. Dmitrienko, J. Phys. Condens. Matter 19, 156201 (2007)
- J. Goulon, A. Rogalev, C. Gauthier, C. Goulon-Ginet, S. Pasté, R. Signorato, C. Neuman, L. Varga, C. Malgrange, J. Synchrotron Radiat. 5, 232 (1998)
- 31. A. Rogalev, J. Goulon, C. Goulon-Ginet, C. Malgrange, in *Magnetism and Synchrotron Radiation (Springer Lecture Notes in Physics)* ed. by E. Beaurepaire et al., vol. 565(Springer, Berlin, 2001), p. 60
- 32. P. Elleaume, J. Synchrotron Radiat. 1, 19 (1994)
- A. Rogalev, J. Goulon, G. Benayoun, P. Elleaume, J. Chavanne, C. Penel, P. Van Vaerenbergh, Proc. SPIE 3773, 275 (1999)
- 34. J. Goulon, C. Goulon-Ginet, A. Rogalev, V. Gotte, Ch. Brouder, C. Malgrange, Eur. Phys. J. B 12, 373 (1999)
- J. Goulon, C. Goulon-Ginet, A. Rogalev, G. Benayoun, Ch. Brouder, C.R. Natoli, J. Synchrotron Radiat. 7, 182 (2000)
- 36. C. Malgrange, L. Varga, C. Giles, A. Rogalev, J. Goulon, Proc. SPIE 3773, 326 (1999)
- 37. K. Stadnicka, A.M. Glazer, M. Koralewski, Acta Crystallogr. **B43**, 319 (1987)
- 38. L.R. Ingersoll, P. Rudnick, F.G. Slack, N. Underwood, Phys. Rev. 57, 1145 (1940)
- 39. M. Hart, A.R.D. Rodrigues, Phil. Mag. B 43, 321 (1981)
- A. Rogalev, J. Goulon, F. Wilhelm, K.A. Kozlovskaya, E.N. Ovchinnikova, L.V. Soboleva, A.F. Konstantinova, V.E. Dmitrienko, Crystallogr. Rep. 53, 384 (2008)
- 41. J. Kaniauskas, Liet. Fiz. Rink. 14, 463 (1974)
- 42. W. Voigt, Ann. Phys. 18, 651 (1905)
- 43. F.I. Fedorov, Optic. Spectros. **6**, 237 (1959)
- 44. F.I. Fedorov, B.V. Bokut, A.F. Konstantinova, Sov. Phys. Crystallogr. 7, 738 (1963)
- 45. E.L. Ivchenko, S.A. Permogorov, A.V. Sel'kin, J. Exp. Theor. Phys. Lett. 27, 24 (1978)
- 46. E.B. Graham, R.E. Raab, Proc. Roy. Soc. A Lond. 430, 593 (1990)
- N. Jaouen, F. Wilhelm, A. Rogalev, J. Goulon, J.M. Tonnerre, Am. Inst. Phys. Conf. Proc. 705, 1134 (2004)
- 48. G. Van der Laan, B.T. Thole, G.A. Sawatzky, J.B. Goedkoop, J.C. Fuggle, J.M. Esteva, R. Karnatak, J.P. Remeika, H.A. Dabkowska, Phys. Rev. B **34**, 6529 (1986)
- 49. R.R. Birss, R.G. Shrubsall, Phil. Mag. 15, 687 (1967)
- 50. R.M. Hornreich, S. Shtrikman, Phys. Rev. 171, 1065 (1968)
- 51. E.B. Graham, R.E. Raab, Phil. Mag. 66, 269 (1992)
- 52. V.A. Markelov, M.A. Novikov, A.A. Turkin, JETP Lett. 25, 378 (1977)
- B.B. Krichevtsov, V.V. Pavlov, R.V. Pisarev, V.N. Gridnev, J. Phys. Condens. Matter 5, 8233 (1993)
- R.E. Word, S.A. Werner, W.B. Yelon, J.M. Honig, S. Shivashankar, Phys. Rev. B 23, 3533 (1981)
- 55. B.I. AlÃŕ£Â; shin, D.N. Astrov, Sov. Phys. JETP **17**, 809 (1963)
- L. Paolasini, C. Vettier, F. de Bergevin, F. Yakhou, D. Mannix, A. Stunault, W. Neubeck, M. Altarelli, M. Fabrizio, P. A. Metcalf, J. M. Honig, Phys. Rev. Lett. 82, 4719 (1999)
- M. Kubota, T. Arima, Y. Kaneko, J.P. He, X.Z. Yu, Y. Tokura, Phys. Rev. Lett. 92, 137401 (2004)
- 58. N.B. Baranova, B.Ya. ZelÃr£Â;dovich, Mol. Phys. 38, 1085 (1979)
- 59. L.D. Barron, J. Vrbancich, Mol. Phys. 51, 715 (1984)
- 60. G.L.J.A. Rikken, E. Raupach, Nature **390**, 493 (1997)
- 61. V.M. Dubovik, Sov. Phys. Crystallogr. **32**, 314 (1988)
- 62. E.J. Samuelsen, M.T. Hutchings, G. Shirane, Physica 48, 13 (1970)
- 63. M. Vallade, Ph.D. Thesis, Grenoble: Université J Fourier, Chapt. IV, 1968
- 64. V.P. Plakthy, Solid State Comm. **79**, 313 (1991)
- 65. B.T. Thole, P. Carra, F. Sette, G. van der Laan, Phys. Rev. Lett. 68, 1943 (1992)
- 66. P. Carra, B.T. Thole, M. Altarelli, X. Wang, Phys. Rev. Lett. 70, 694 (1993)
- 67. P. Carra, R. Benoist, Phys. Rev. B **62**, R7703 (2000)
- 68. P. Carra, J. Magn. Magn. Mater. 233, 8 (2001)
- 69. P. Carra, A. Jerez, I. Marri, Phys. Rev. B 67, 045111 (2003)

- 70. I. Marri, P. Carra, Phys. Rev. B 69, 113101 (2004)
- 71. I.B. Khriplovich, *Parity Non-Conservation in Atomic Phenomena* (Gordon and Breach, New York, 1991)
- 72. Ya.B. Zel'dovich, Sov. Phys. JETP, **6**, 1184 (1958)
- 73. I. Marri, P.Carra, C.M. Bertoni, J. Phys. A Math. Gen. 39, 1969 (2006)
- 74. S. Di Matteo, C.R. Natoli, Phys. Rev. B 66, 212413 (2002)
- 75. L. Pasteur, Rev. Sci. 7, 2 (1884)

Chapter 7 X-Ray Detected Magnetic Resonance: A New Spectroscopic Tool

J. Goulon, A. Rogalev, F. Wilhelm, and G. Goujon

Abstract We discuss the information content of X-ray detected magnetic resonance (XDMR), that is, a novel spectroscopy that uses X-ray magnetic circular dichroism to probe the resonant precession of local magnetization components in a strong microwave pump field. As XDMR is element- and edge-selective, it appears as a unique tool to resolve the magnetization dynamics of spin and orbital components at any absorbing site. We compare different experimental configurations that we used to get access to element-selective information such as the opening angle and the phase of precession in iron garnet films or single crystals. In YIG thin films, *orbital* magnetization components measured at the iron sites were shown to couple to *magnetostatic* waves. We also detected a change in the chirality of the precession of the Fe orbital magnetization components at the compensation temperature of GdIG. Extending XDMR up to sub-THz frequencies would considerably enlarge the range of potential applications of this new spectroscopic tool.

7.1 Introduction

X-ray detected magnetic resonance (XDMR) can be seen as a *Pump* and *Probe* experiment in which X-ray magnetic circular dichroism (XMCD) is used to *probe* the resonant precession of either spin or orbital magnetization components in a strong microwave *pump* field. XDMR is not just another exotic way to record ferromagnetic or ferrimagnetic resonance (FMR) spectra: given the rather poor sensitivity of the method, this approach would have a fairly limited interest. It is the aim of the present chapter to show that new and unique information can be extracted from element- and edge-selective XDMR experiments performed in a variety of experimental configurations. What stimulated our own interest in such experiments was the prospect of resolving locally the precession dynamics of *induced spin* or *orbital* magnetization components. Regarding FMR of *3d* transition metals, it has

European Synchrotron Radiation Facility, B.P. 220, F-38043, Grenoble, France e-mail: goulon@esrf.fr

J. Goulon (⊠)

192 J. Goulon et al.

long been considered that orbital magnetization components were either quenched or so strongly coupled to the lattice that they had little or no contribution to FMR due to ultra-fast damping processes. Using XDMR experiments carried out at the Fe K-edge in yttrium iron garnet (YIG) thin films, we produced the first experimental evidence [1–3] that orbital magnetization components were clearly precessing and that XDMR was a quite appropriate tool to study their precession dynamics. In this chapter, we lay emphasis on a few new results: the orbital magnetization components at the Fe sites in YIG thin films will be shown to couple to *magnetostatic* modes (MSM) through dipole–dipole interactions. On the other hand, using a single crystal of ferrimagnetic gadolinium iron garnet (GdIG), we observed the inversion of the *chirality* of the precession of the Fe orbital magnetization components at the compensation temperature.

Recall that the XMCD signal at the K-edge of 3d transition metals is unfortunately one or two orders of magnitude weaker than the XMCD signatures measured at the corresponding L-edges in the soft X-ray range. The enhanced difficulty of XDMR experiments at K-edges is, however, partly counter-balanced by one decisive advantage to be discussed in Sect. 7.2: the effective operator responsible for K-edge XMCD is entirely of orbital nature while our capability to disentangle spin and orbital contributions in XDMR measurements at L-edges would rely on the questionable validity of extended dynamical sum rules. The stronger XMCD signals expected at L-edges can nevertheless be turned out into a valuable gain of XDMR sensitivity: actually, the first successful attempt to probe the precession dynamics with X-rays was reported by Bailey and coworkers [4] who, initially, combined soft X-ray differential circular reflectometry with time-domain pulsed induction magnetometry (PIM) at the L-edges of Fe and Ni in permalloy. Further work in the soft X-ray range tends to show that continuous wave (CW) XDMR measurements carried out in the soft X-ray range either in a transmission geometry [5-7] or in the fluorescence excitation detection mode [8, 9] were preferable.

A risky choice made by the ESRF was to develop XDMR experiments on beamline ID12, which was optimized for XMCD measurements at higher X-ray excitation energies (2–20 keV). There are numerous arguments supporting this strategy: (1) there is potentially much to be learned from L-edge XDMR of 4d or 5d transition elements (e.g., Pd, Pt, etc.) and rare-earths (RE), as well as from M-edge XDMR of actinides; (2) still very little is known regarding the magnetization dynamics at nonmetal sites (e.g., at the K-edges of S, Se, Te, P, As, or Ge); (3) above 2 keV, XDMR studies definitely probe bulk properties, while soft X-ray measurements are rather surface sensitive: this can result in major differences regarding the excitation of magnetostatic modes or the investigation of dilute paramagnets. The choice made at the ESRF was indeed most demanding from the performances of the whole instrumentation and required us to invest much time and effort as reflected by the high quality of the XDMR spectra reproduced in Sect. 7.3. In Sect. 7.4, we introduce an even more challenging project, which is to extend XDMR experiments up to sub-THz pumping frequencies.

7.2 Precession Dynamics Probed with X-Rays

7.2.1 Phenomenological Equation of Motion

Let us consider a ferromagnetic sample with its equilibrium magnetization \mathbf{M}_{eq} not necessarily aligned along the static magnetic bias field \mathbf{H}_0 as most conveniently sketched in Fig. 7.1. If one adds a microwave pump field \mathbf{h}_p , which is time-dependent and oscillates in a direction perpendicular to \mathbf{H}_0 , then the magnetization vector $\mathbf{M}(\mathbf{r},t)$ should transform according to the equation of motion [2]

$$\frac{\partial \mathbf{M}(\mathbf{r},t)}{\partial t} = -\gamma \mathbf{T}(\mathbf{r},t) = -\gamma \mathbf{M} \times \mathbf{B_e},\tag{7.1}$$

where $\gamma = g\mu_B/\hbar$ denotes the gyromagnetic ratio. It was recognized by Landau and Lifshitz that (7.1) described a precession of the magnetization vector \mathbf{M} around an *effective*, instantaneous field $\mathbf{B_e}(\mathbf{r},t)$ defined as the functional derivative of the free energy (F) with respect to the magnetic moment $\mathbf{M}(\mathbf{r},t)$:

$$\mathbf{B_{e}}(\mathbf{r},t) = \mu_0 \mathbf{H_{e}}(\mathbf{r},t) = -\frac{\delta F}{\delta \mathbf{M}(\mathbf{r},t)}.$$
 (7.2)

In (7.1), $\mathbf{T}(\mathbf{r},t)$ is the total torque acting on $\mathbf{M}(\mathbf{r},t)$: it includes contributions from external and internal magnetic fields. External fields encompass both the static (bias) field \mathbf{H}_0 and the microwave (pump) field \mathbf{h}_p . Internal fields include the exchange field \mathbf{H}_{ex} , the demagnetizing field \mathbf{H}_D due to long range dipolar interactions, and the magnetocrystalline anisotropy field \mathbf{H}_A . The exchange field \mathbf{H}_{ex} combines terms proportional to both \mathbf{M} and $\nabla^2 \mathbf{M}$, but (7.1) implies that only the inhomogeneous exchange term ($\nabla^2 \mathbf{M}$) can contribute to a nonvanishing torque as $\mathbf{M} \times \mathbf{M} \equiv 0$.

A phenomenological damping torque should be added to drive the magnetization back towards its equilibrium state with M_{eq} parallel to H_e . The Landau–Lifshitz–Gilbert (LLG) torque is most frequently preferred because it does not depend on the effective field B_e [10]:

$$\mathbf{T}_{\mathrm{LLG}} = +\frac{\alpha}{\gamma M_{\mathrm{s}}} \mathbf{M} \times \frac{\partial \mathbf{M}}{\partial t},\tag{7.3}$$

 α being a dimensionless, scalar constant. Note that the LLG formulation is fully consistent with the fluctuation–dissipation theorem [11], whereas this is not true for the Bloch–Bloembergen (BB) torque: $\mathbf{T}_{\mathrm{BB}} = (\omega_r/\gamma)[\mathbf{M} - \mathbf{M}_{\mathrm{eq}}]$ which, moreover, does not conserve the length of \mathbf{M} [10]. The corresponding BB equation of motion can, however, be associated with two distinct relaxation times [12,13]: a longitudinal relaxation time T_1 parallel to the direction of $\mathbf{H_0}$ and a transverse relaxation time T_2 perpendicular to the direction of $\mathbf{H_0}$. This was found more convenient because T_2

194 J. Goulon et al.

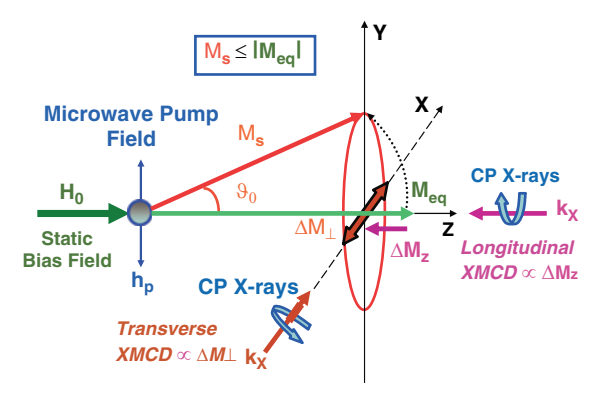


Fig. 7.1 XDMR detection in *longitudinal* and *transverse* geometries. ΔM_z is time invariant only if $M_s = |\mathbf{M}_{eq}|$. Decreasing M_s would *increase* $|\Delta M_z|$

is more sensitive to collective processes that couple the uniform precession mode $(\mathbf{k} = 0)$ to thermally excited magneto-exchange modes or spin-waves $(\mathbf{k} \neq 0)$ [13].

As illustrated with Fig. 7.1, one may then envisage two distinct configurations for the XDMR experiment:

- In the *transverse* geometry, the wavevector \mathbf{k}_X of the incident, circularly polarized (CP) X-rays would be taken perpendicular to both \mathbf{H}_0 and \mathbf{h}_p : what should then be measured is an XMCD signal proportional to the transverse magnetization ΔM_{\perp} which oscillates at the microwave frequency. The obvious difficulty is that such an experiment requires a fast detection system with a high dynamic range.
- In the *longitudinal* geometry, the wavevector \mathbf{k}_X of the incident CP X-rays could alternatively be chosen parallel to the static bias field \mathbf{H}_0 . As far as the length of the equilibrium magnetization vector remains invariant in precession, that is, $M_s = |\mathbf{M}_{eq}|$, one would expect a steady-state change of the projection of the magnetization along the direction of \mathbf{H}_0 , and the whole challenge of such an XDMR experiment is precisely to probe ΔM_z using XMCD. The difficulty arises from the fact that ΔM_z is only a second order effect with respect to the opening angle of precession. Note that any information related to the precession phase should implicitly be lost. Actually, ΔM_z is time invariant only for circular precession.

For a ferromagnetic thin film with true uniaxial anisotropy and near-normal magnetization, the opening angle of precession is a constant of motion – even in the foldover regime [14]. This consideration led us to propose [1,2] to determine the opening angle θ_0 on simply combining together normalized XDMR cross-sections with *static* XMCD cross-sections measured under identical conditions. For an XDMR experiment performed in the longitudinal detection geometry ($\mathbf{k}_X = \mathbf{k}_{\parallel}$) on a perpendicularly magnetized film, one easily obtains

$$[\Delta \sigma_{\text{XDMR}}(k_{\parallel})]/[\Delta \sigma_{\text{XMCD}}(k_{\parallel})] \simeq -1/2 \tan^2 \theta_0. \tag{7.4}$$

Similarly, for an XDMR experiment performed in the transverse geometry ($\mathbf{k}_X = \mathbf{k}_{\perp}$) with the same film,

$$[\Delta \sigma_{\text{XDMR}}(k_{\perp})]/[\Delta \sigma_{\text{XMCD}}(k_{\parallel})] \simeq \tan \theta_0 \sin[\omega t + \phi_0]. \tag{7.5}$$

Here, the various $\Delta \sigma_j$ refer to differential X-ray absorption cross-sections. What stimulated our interest is the consideration that not only the opening angle of precession (θ_0) but also the phase (ϕ_0) could be element selective probes of the micromagnetic dynamics inside the sample. Let us insist that both (7.4) and (7.5) rely on the LLG equation and the assumption that the norm of the local magnetization vector (M_s) is invariant in the forced precession.

7.2.2 Precession Dynamics of Orbital and Spin Magnetization Components

What makes the specificity of XDMR as compared to optically detected magnetic resonance (ODMR) is indeed the element-selectivity of XMCD measurements. We already pointed out earlier that the effective operator responsible for XMCD at a K-edge had a pure *orbital* nature. For electric dipole transitions, this immediately appears with a differential formulation of the XMCD sum-rules at K-edges [15–18]:

$$[\Delta \sigma]_K = 3C_p \frac{\mathrm{d}}{\mathrm{d}\Delta E} \langle L_z \rangle_p = 3C_p \langle \ell_z \rangle_p, \tag{7.6}$$

in which $\Delta E = E_{\rm RX} - E_0$ is the energy of the photoelectron excited by an X-ray photon of energy $E_{\rm RX}$ from a core level with the binding energy of E_0 ; C_p is a constant factor. The effective operators responsible for XMCD in electric quadrupole transitions were also derived by Carra and coworkers [19]: again, it was clearly established that the terms contributing only at a K-edge were of orbital nature. Thus, the effective operator accounting for XMCD at the Fe K-edge in YIG could be decomposed as a sum of two terms [1,2]: $\{\langle \ell_z \rangle_{4p} + \varepsilon \langle \ell_z \rangle_{3d} \}$.

At spin-orbit split $L_{2,3}$ -edges, one can similarly make use of differential operators [15, 18]

$$[\Delta\sigma]_{L_3} = \frac{C_d}{3N_b} \frac{\mathrm{d}}{\mathrm{d}\Delta E} \{ \langle L_z \rangle_d + \frac{2}{3} \langle S_z \rangle_d + \frac{7}{3} \langle T_z \rangle_d \},$$

$$= \frac{C_d}{3N_b} \{ \langle \ell_z \rangle_d + \frac{2}{3} \langle s_z \rangle_d + \frac{7}{3} \langle t_z \rangle_d \}, \tag{7.7}$$

$$[\Delta\sigma]_{L_2} = \frac{C_d}{6} \frac{d}{d\Delta E} \{ \langle L_z \rangle_d - \frac{4}{3} \langle S_z \rangle_d - \frac{14}{3} \langle T_z \rangle_d \},$$

$$= \frac{C_d}{6} \{ \langle \ell_z \rangle_d - \frac{4}{3} \langle s_z \rangle_d - \frac{14}{3} \langle t_z \rangle_d \}, \tag{7.8}$$

J. Goulon et al.

in which $N_b \simeq 2$ denotes the statistical branching ratio. Injecting (7.7) and (7.8) into the definition of ΔM_z allowed us to derive an extended formulation of the sumrules, which could make it possible to disentangle the precession dynamics of orbital and spin components, for example, at the yttrium L-edges of YIG [2, 3]

$$(1+3\eta)\tan^2\theta_0(L_3) = \tan^2\theta_s + 3\eta \tan^2\theta_\ell, \tag{7.9}$$

$$(2 - 3\eta) \tan^2 \theta_0(L_2) = 2 \tan^2 \theta_s - 3\eta \tan^2 \theta_\ell, \tag{7.10}$$

in which $\eta = \langle \ell_z \rangle_d/2 \langle s_z \rangle_d$, whereas $\langle t_z \rangle_d/2 \langle s_z \rangle_d$ was assumed here to be negligibly small. In (7.9) and (7.10), $\theta_0(L_3)$ and $\theta_0(L_2)$ are effective precession angles measured at the L₃ and L₂ edges, whereas θ_s and θ_ℓ are the precession angles for the relevant spin and orbital magnetization components. This clearly shows that, at spin–orbit split L-edges, one cannot resolve the precession dynamics of the spin and orbital components without resorting to questionable approximations. Let us point out first that (7.9) and (7.10) are basically a *quasi-static* extension of the (equilibrium) XMCD sum rules. Indeed, a pre-requisite to exploit (7.9) and (7.10) is that the corresponding XMCD sum rules should be fully applicable: in the soft X-ray range, difficulties will undoubtly happen whenever the L₂ and L₃ edges are poorly resolved (e.g., at the L_{2,3} edges of Ti, V, or Cr, etc.); at higher excitation energies, one may also expect some problems at the RE L-edges for other reasons [20].

7.2.3 Precession Under High Pumping Power

It should be kept in mind that under the standard conditions of FMR experiments, the opening angle of precession θ_0 is well below 1°: this makes the detection of the XDMR signal very difficult, especially in the longitudinal detection geometry where ΔM_z is proportional to $\tan^2\theta_0$. This sensitivity problem becomes particularly acute for K-edge XDMR experiments, given that the XMCD differential cross-section is itself very poor. A way to increase θ_0 may be to increase the microwave pumping power, but this option is fairly limited by the strong nonlinearity of the LLG equation as discussed below.

7.2.3.1 Foldover Effects

For brevity, we shall consider only the simplest case where the static bias field \mathbf{H}_0 is set perpendicular to a YIG thin film grown on a (111) GGG substrate:

$$\tan^2 \theta_0 = \frac{(\gamma b_{cp})^2}{P_0^2 + (\alpha \omega \cos \theta_0')^2},\tag{7.11}$$

in which

$$P_0 = -\omega + \gamma B_0 + \gamma \left[B_u - \frac{2}{3} B_{A1} \left(1 - \frac{7}{4} \sin^2 \theta_0 \right) \right] \cos \theta_0, \tag{7.12}$$

where B_u and B_{A1} refer to the uniaxial demagnetizing field and the cylindrical component of the magnetocrystalline anisotropy field, respectively. In the low microwave power limit, that is, when $\cos\theta_0 \rightarrow 1$, the resonance condition $P_0 = 0$ will obviously converge towards the well known Lorentzian lineshape of FMR. This is not anymore true at high microwave power as the resonance condition now depends on $\cos\theta_0$, that is, on the microwave power. Equation (7.11) finally yields a biquadratic equation in $\cos\theta_0$, with multivalued (unstable) solutions defining the foldover regime illustrated with Fig. 7.2, which reproduces anticipated lineshapes for a perpendicularly magnetized YIG film when the frequency of the pumping radiation is either 9.51 GHz or 354 GHz.

For such a ferrimagnetic film magnetized perpendicularly, the maximum precession angle at resonance should be given by $\theta_{0_{max}} \simeq (\gamma b_{cp})/\alpha \omega$, in which b_{cp} denotes the amplitude of the *circularly* polarized microwave field component. With a Gilbert damping parameter as small as $\alpha \simeq 6 \times 10^{-6}$, YIG films would look like excellent test samples. In reality, due to the foldover instability, the maximum precession angle $\theta_{0_{max}}$ is never reached (see Fig. 7.2a): at best, opening angles of the order of θ_{0C2} are obtained experimentally, especially if the microwave power is amplitude modulated. Thus, foldover effects will spoil the sensitivity of the XDMR experiments. In the specific case of YIG films in which the uniaxial anisotropy field B_{u} largely exceeds the contribution of the cubic anisotropy B_{A1} (7.12), let us expect that the foldover effects should be minimized when the film is rotated near the magic angle (i.e., $\beta = 54.73^{\circ}$). As illustrated with Fig. 7.2b, one may expect the foldover distortion to be heavily reduced at very high pumping frequency simply because

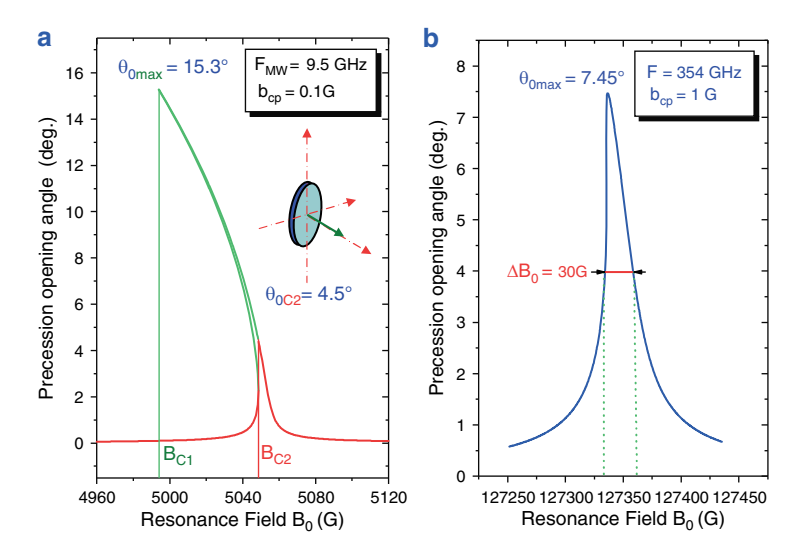


Fig. 7.2 Simulated lineshapes in the foldover regime for a perpendicularly magnetized YIG thin film; (a) CW Pumping in the microwave x-band at 9.5 GHz; (b) High power excitation at sub-THz frequency, e.g., at 354 GHz

198 J. Goulon et al.

the whole anisotropy field tends to become very small in comparison with the large resonance bias field ($B_0 \simeq 12.8 \,\mathrm{T}$ at 354 GHz).

7.2.3.2 Suhl's Instability Thresholds

As early as in 1959, Suhl predicted that the opening angle of precession of the uniform mode could hardly exceed some threshold value $\theta_{0S_{1,2}}$, beyond which parametric amplification of *exchange* spin-waves could also cause *foldover-like* FMR lineshapes [21]. As sketched in Fig. 7.3, he introduced two distinct instability thresholds associated with either a three-magnon or a four-magnon scattering process, respectively.

The first-order instability predicted by Suhl could cause a *subsidiary* microwave absorption off-resonance, for example, at $B_0/2$, but the corresponding process should have a limited influence on the XDMR spectra recorded on perpendicularly magnetized thin films as long as resonance truly occurs at the *bottom* of the magnon band, that is, far above $\omega/2$. In XDMR experiments, we might be more directly concerned with the second-order process that develops at resonance but only at fairly high microwave power [22]: the annihilation of two magnons should alter the norm of the magnetization vector M_s , but since the early work of Bloembergen and coworkers [12], it is well documented that this process should leave M_z and thus ΔM_z invariant. We shall produce experimental evidence in Sect. 7.3 that this does not hold true for magnetostatic modes.

A crude estimation of the saturation threshold field b_{S_2} is given by

$$b_{\rm S_2} \simeq \Delta B_{(0)} [\Delta B_{(k)}/\mu_0 M_{\rm s}]^{1/2}$$
 (7.13)

in which $\Delta B_{(0)}$ refers to the intrinsic FMR linewidth of the uniform mode (i.e., k=0), while $\Delta B_{(k)}$ would refer to the (poorly known) linewidth of the amplified spinwave with momentum k.

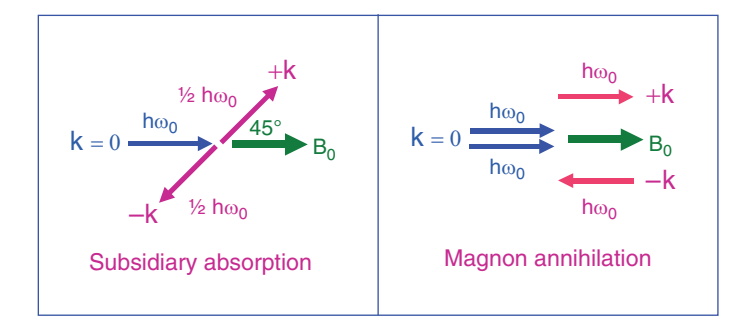


Fig. 7.3 First-order and second-order instability processes resulting in parametric amplification of exchange spin waves

7.2.4 Nonuniform Eigen Modes of Precession

It has long been recognized that one serious complication in the theory of FMR arose from the fact that the microdynamics of precession was driven by nonuniform, time-dependent fields:

$$\mathbf{h}(\mathbf{r},t) = \mathbf{h}_{p} + \mathbf{h}_{dd} + \mathbf{h}_{exch} + \mathbf{h}_{mca}, \tag{7.14}$$

because, in addition to the external pump field, one has to take into account a variety of time-dependent reaction fields, including a demagnetizing field (\mathbf{h}_{dd}) due to dipole–dipole interactions, an exchange field (\mathbf{h}_{exch}) due – again – to the anisotropic part of exchange interactions, and a dynamical reaction field (\mathbf{h}_{mca}) due to magnetocrystalline anisotropy. As a consequence, the magnetic system will be characterized by a number of orthogonal *eigen modes* of precession in which the precession speed (ω_j) would be everywhere the same but not the phase. In this section, we concentrate only on the excitation of magnetostatic modes (MSM) caused primarily by \mathbf{h}_{dd} . A classical approach is based on the so-called Walker's *quasi-static* approximation which consists in describing the space-time dependence of $\mathbf{h}(\mathbf{r},t)$ using Maxwell's equations in the magnetostatic limit, that is, by neglecting any time-dependence of the electric field [23]:

$$\nabla \times \mathbf{h} = 0,$$
$$\nabla \cdot [\bar{\mu}] \mathbf{h} = 0.$$

The first equation implies that $\mathbf{h} = -\nabla \psi(\mathbf{r}, t)$, while the second yields the wave equation $\nabla \cdot \bar{\mu} \nabla \psi(\mathbf{r}, t) = 0$. For a plane wave propagating in an *infinite* medium $\psi \propto \exp[i \mathbf{k} \cdot \mathbf{r}]$, one would easily check that the LLG equation can be solved within the Walker's approximation only if the following dispersion relation is satisfied [23]:

$$\omega_{\rm H} \le \omega = [\omega_{\rm H} \cdot (\omega_{\rm H} + \omega_{\rm M} \sin^2 \theta_k)]^{1/2} \le \omega_{\perp},\tag{7.15}$$

in which $\omega_{\rm H}=\gamma H_0$ and $\omega_{\rm M}=\gamma 4\pi M_{\rm s}$. Here, $\omega_{\rm H}$ and ω_{\perp} are resonance frequencies (ω) obtained for $\theta_k=0$ or $\theta_k=\pi/2$, respectively, that is, when the wavevector ${\bf k}$ is either parallel or perpendicular to the direction of the static bias field ${\bf H}_0$. In other terms, k will be real only if the dispersion relation is satisfied. Note that (7.15) does not depend on the magnitude of ${\bf k}$: this degeneracy will, however, be removed by considering the effects of either sample finite boundaries (e.g., in thin films) or exchange interactions in the so-called exchange spinwave regime.

Typically, for a perpendicularly magnetized YIG thin film of thickness d and vanishingly small aspect ratio, the dispersion relation becomes [10]

$$\omega^2 = \Omega_{\rm H} \cdot \left[\Omega_{\rm H} + \frac{\omega_{\rm M}}{1 + Z_n^2/(k_\perp d)^2} \right],\tag{7.16}$$

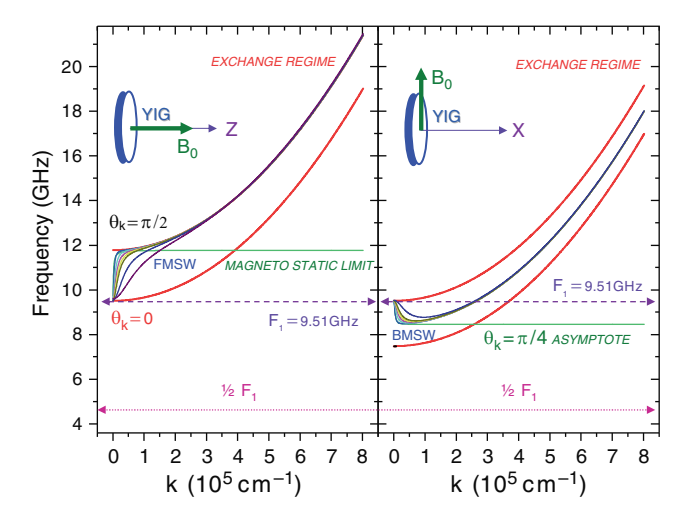


Fig. 7.4 Magneto-exchange dispersion spectrum for a thin film of YIG of vanishingly small aspect ratio. FMSW satellite resonances are expected for a perpendicularly magnetized film, while BMSW satellite resonances are expected for *in-plane* magnetization of the film

in which $Z_n \simeq n \times \pi = k_z d$, while $\Omega_{\rm H} = \omega_{\rm H} + \omega_{\rm M} [\eta_{\rm exch} k_z^2 + \eta_{\rm exch} k_\perp^2]$. As illustrated with Fig. 7.4, the resonance frequency (e.g., $F_1 = 9.51\,\rm GHz$) of the uniform mode is clearly located at the *bottom* of the whole magnon band. There should be, however, a series of satellite resonances associated with *bulk* forward magnetostatic waves (FMSW), all of them being characterized with a *positive* group velocity: $v_g = \partial \omega/\partial k > 0$. As a consequence, for a given microwave frequency $F_{\rm MW}$, FMSW satellites should systematically be observed in the FMR spectrum at *lower* resonance fields, for example, at $B_{0n}(F_{\rm MW}) < B_{01}(F_{\rm MW})$.

Similarly, if the same YIG thin film is magnetized *in-plane*, then the dispersion relation could be written [10] as

$$\omega^2 = \Omega_{\rm H} \cdot \left[\Omega_{\rm H} + \frac{\omega_{\rm M}}{1 + \cos^2 \theta_k / [\sin^2 \theta_k + X_n^2 / (k_\perp d)^2]} \right], \tag{7.17}$$

in which $X_n \simeq n \times \pi = k_x d$, while $\Omega_H = \omega_H + \omega_M [\eta_{\text{exch}} k_x^2 + \eta_{\text{exch}} k_\perp^2]$. As shown in Fig. 7.4, the resonance frequency (e.g., $F_1 = 9.51 \, \text{GHz}$) of the uniform mode is now located at the *top* of the whole magnon band. There should be, however, another series of satellite resonances associated this time with *bulk* backward magnetostatic waves (BMSW), all of them being characterized with a *negative* group velocity $v_g = \partial \omega / \partial k < 0$. As a consequence, for a given microwave frequency F_{MW} , BMSW satellites should now be observed at *higher* resonance fields, for example, at $B_{0n}(F_{MW}) > B_{01}(F_{MW})$. Damon and Eshbach [24] were the first to point out that a thin film magnetized in its plane could also exhibit *surface* MSW on top of the bulk magnon band, that is, with $\mathbf{k}^{\pm} \perp \mathbf{H_0}$, but with *opposite* directions at the two

film interfaces [23]. Surface magnetostatic waves offer an interesting example of *nonreciprocity* as \mathbf{k}^{\pm} would shift to the other interface on inverting the direction of \mathbf{H}_{0} .

The key question at issue is to know whether MSW satellites can be observed in XDMR spectra, especially at those sites where the precessing magnetic components are of *orbital* nature. In other terms, can orbital magnetization components couple to magnetostatic eigen modes. Conceptually, this may well be envisaged as orbital components are indeed subject to dipole–dipole interactions. In practice, the nature of the X-ray probe can cause problems. There is a priori no fundamental objection against the detection of MSW satellites in XDMR spectra recorded in the *longitudinal* geometry because the steady-state component ΔM_z is inherently insensitive to the phase of precession. In real practice, we show in Sect. 7.3 that this is not such an easy task because the foldover distortion at high pumping power is rapidly broadening the lineshape to the point where no satellite can be resolved anymore.

The situation is even more puzzling in the *transverse* detection geometry, given that the dispersion relations are invariant for plane-waves propagating with wavevectors \mathbf{k} and $-\mathbf{k}$, while the transverse components \mathbf{M}_{\perp} probed by XMCD can oscillate (locally) out of phase. Actually, one should keep in mind that the XMCD signal is *averaged* over the whole effective volume in which X-rays are absorbed. Moreover, in the X-ray excited fluorescence detection mode, the X-ray penetration depth distorts the weight of the averaged contributions of XMCD $\propto M_{\perp}$. As illustrated in Fig. 7.5, the detection of magnetostatic standing waves should be much more favorable for low order modes with an even number of nodes. In this respect, *quasi*-surface modes could be more easily detected. Note that electron yield detection in the soft X-ray range could be more exposed to surface pinning problems.

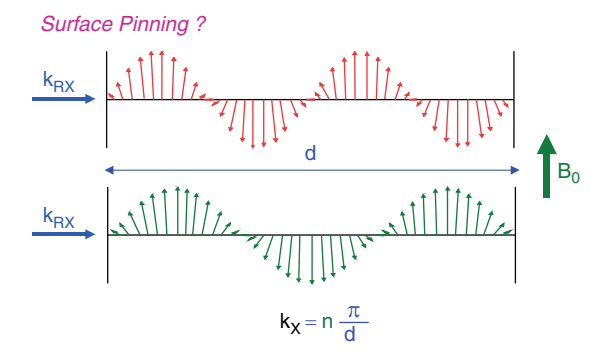


Fig. 7.5 Transverse XDMR should be only weakly sensitive to MSM standing waves, the detection sensitivity increasing for low-order modes with an even number of nodes

7.2.5 Longitudinal and Transverse Relaxation Times

We emphasize that an accurate determination of the opening angle of precession could, in principle, be turned into an indirect way to get access to the relaxation times T_1 and T_2 . For instance, far from saturation, (7.4) could be rewritten

$$\Delta \sigma_{\rm XDMR} / \Delta \sigma_{\rm XMCD} \simeq -\frac{1}{4} (\gamma b_{cp})^2 \cdot T_1 T_2 \ .$$
 (7.18)

Equation (7.18) was exploited in FMR by Fletcher and coworkers [13] but well below the foldover threshold, that is, under conditions that are hardly accessible to XDMR measurements. There is the additional difficulty that b_{cp} was never determined accurately enough in our XDMR experiments to let us access to the T_1T_2 product. This is why it looks desirable to develop specific methods to measure directly T_1 in XDMR.

Although T_1 describes how fast the magnetic energy is exchanged with the lattice due to magnetoelastic and spin-orbit coupling, T_2 is more sensitive to any loss of coherence due to the coupling of the uniform precession mode (k=0) with degenerated magneto-exchange modes or spinwaves $(k \neq 0)$. In the Landau–Lifschitz–Gilbert limit, one would expect $(T_2)^{-1} = (2T_1)^{-1}$, while the true relationship is rather

$$\frac{1}{T_2} = \frac{1}{2T_1} + \frac{1}{T_D},\tag{7.19}$$

in which $T_{\rm D}$ would encompass all magnon scattering processes that decrease the coherence of the precessing magnetization without altering the magnetic free energy: processes involving only direct or indirect coupling to the lattice phonons are energy dissipative. The various relaxation channels that are expected to contribute to XDMR relaxation are summarized in Fig. 7.6.

In YIG films, sample nonuniformities such as crystal defects, impurities, surface pits, etc. have long been shown to favor two-magnon scattering processes that increase the FMR linewidth, especially at low microwave frequencies.

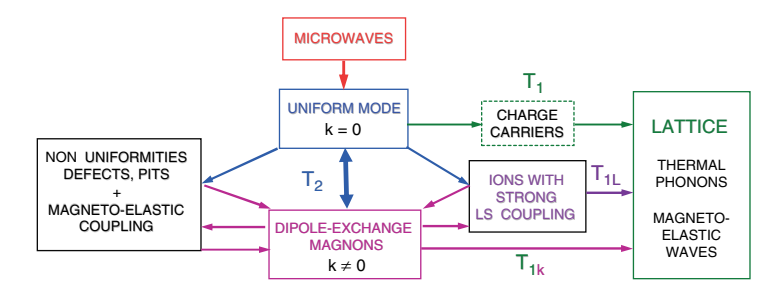


Fig. 7.6 Block diagram of the relaxation channels contributing to XDMR (adapted from [10]

Three-magnon scattering processes (either in momentum splitting or confluence modes) do not conserve the total number of magnons nor M_z . In four-magnon scattering processes, two (uniform) magnons are annihilated, but two magnons are created such that the total *number* of magnons remains unchanged (see Fig. 7.4).

Magnetoelastic interactions are the main cause of *direct* spin-lattice relaxation. In magnetically ordered systems, three-particle Cherenkov scattering processes involving two magnons plus one phonon are compatible with exchange interaction and form the most general basis of the analysis of direct spin-lattice relaxation mechanisms. In particular, the direct Cherenkov process (splitting of a magnon into another magnon plus one phonon) underlies the parametric excitation of magnetic and elastic waves under magnetic pumping [10]. In the case of *ferrimagnetic* insulators like YIG thin films, the Kasuya–LeCraw process [25] proved itself to be the most efficient mechanism to explain relaxation of magnetostatic magnons with very small k: it describes the confluence of a small k magnon with a phonon from the upper (optical) branch to produce a magnon with large k that can now relax much more efficiently by a Cherenkov process. In the first step, the energy transfer does not occur from the spin system towards the lattice, but in the opposite direction with the benefit that a low k magnon can be destroyed [10].

7.3 Experimental Results

7.3.1 Ferrimagnetic Iron Garnets

It is commonly admitted that the crystal structure of YIG is cubic with space group Ia $\bar{3}$ d (\mathcal{O}_h^{10} ; group N°230) [26]. The unit cell consists of eight formula units: $\{Y\}_3[Fe]_2(Fe)_3O_{12}$. This formulation emphasizes the role of two nonequivalent sites for iron: the first one (16a sites) has octahedral coordination with oxygen anions, while the second one (24d sites) has only tetrahedral coordination with O²⁻. Below the Curie temperature ($\simeq 550\,\mathrm{K}$), the two Fe sublattices get magnetized antiparallel to each other according to the ferrimagnetic model of Néel, with an unbalanced magnetization (ca. $5\,\mu_\mathrm{B}$) in favor of the tetrahedral sites. This is classically explained by a strong superexchange interaction between the two iron sublattices: the rather large Fe(a)–O–Fe(d) angle, 126.6°, is a clear indication that the wavefunctions of oxygen and iron have a substantial overlap so that superexchange may well be mediated by the oxygen anions.

This picture describes correctly the *spin* magnetization at the iron sites, but it does not preclude the existence of weaker, partially unquenched orbital moments that can hardly be seen in neutron diffraction. On the other hand, the detection of satellites in the ⁵⁷Fe NMR spectra has fed the presumption that induced magnetic moments could be carried by the nonmagnetic yttrium or other diamagnetic RE ions (e.g., Y³⁺, La³⁺, Lu³⁺, etc.): this is not totally unexpected as those cations (in 24c sites) have dodecahedral coordination to the same oxygen anions mediating

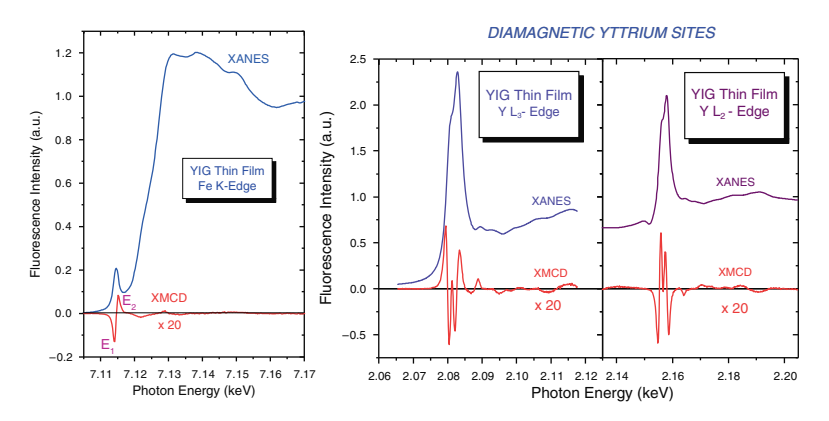


Fig. 7.7 XANES and XMCD spectra of a perpendicularly magnetized YIG/GGG thin film at the Fe K-edge and Y $L_{2.3}$ -edges

superexchange between the iron spins. This picture was confirmed by static XMCD measurements performed at the ESRF on a series of YIG and RE-substituted thin films such as, for example, [Y-La-Lu]IG = Y_{1.3}La_{0.47}Lu_{1.3}Fe_{4.84}O₁₂. The corresponding films grown by liquid phase epitaxy (LPE) on GGG single crystal substrates were all prepared and characterized for us by J. Ben Youssef at the *Lab. de Magnétisme de Bretagne* in Brest (France) [27].

We have reproduced in Fig. 7.7 typical XANES and XMCD spectra of such a perpendicularly magnetized YIG thin film (#520; 9.8 µm thick) grown on a GGG substrate cut parallel to the (111) planes. As the corresponding spectra were systematically recorded in the X-ray fluorescence detection mode, it should be mentioned that the spectra displayed in Fig. 7.7 are raw data, that is, uncorrected for fluorescence re-absorption and circular polarization rates. These spectra provided us with the clear evidence that *induced* spin components were present in the excited states of yttrium and related RE atoms, even though the integrated spin moments derived from the magneto-optic sum rules were extremely small. It will be shown that those induced spin components do participate as well to the forced precession in XDMR.

Even though the crystal structure of the gadolinium iron garnet (GdIG) is essentially the same as in YIG, the FMR spectra are considerably more complicate because, in addition to the strong exchange field acting on the iron sites, there is a much weaker, temperature-dependent effective antiferromagnetic coupling between the Fe³⁺ ions and the Gd³⁺ ions in the dodecahedral sites. Typically, the Gd magnetization is a Brillouin function for spin 7/2 in a field proportional to the net magnetization of the iron ions. In view of the weak coupling existing between the RE sites and the Fe³⁺ sites, as compared to the coupling of the two types of Fe³⁺ sites with each other, the two iron sublattices are most often treated as one in FMR experiments. Even with such a crude simplification, the problem remains quite complicate [33]. As illustrated with Fig. 7.8a, one should first take into account the possibility to excite two different precession modes that have opposite chirality: in

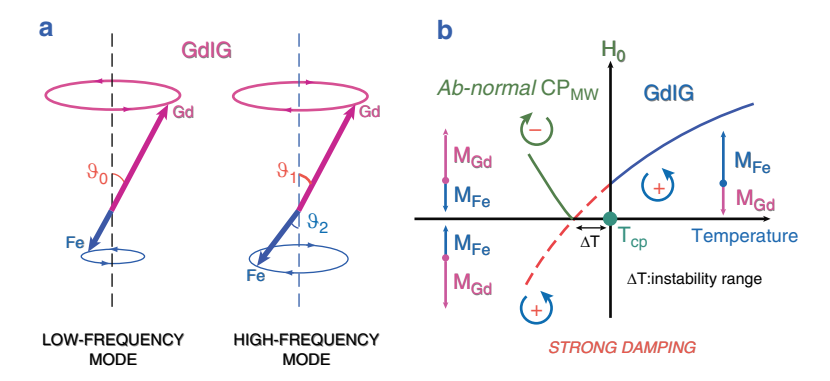


Fig. 7.8 (a) Low/high frequency precession modes in ferrimagnetic GdIG. Note that sublattices precess with opposite chirality; (b) Change of precession chirality at the compensation temperature [33]

the low-frequency mode that is not influenced by exchange, the two magnetization components would precess with the same opening angle (θ_0) and the same phase as in a ferromagnet, while this is not true for the high frequency (exchange coupled) mode. Figure 7.8b was inserted to remind the reader that there is an instability range near the compensation temperature (T_{cp}) at which the system behaves as an antiferromagnet, the FMR linewidth becoming extremely broad. Let us emphasize that the precession should have the opposite chirality on both sides of T_{cp} .

7.3.2 Modular XDMR Spectrometer

The modular spectrometer that is now permanently installed in the fourth experimental hutch of the ESRF beamline ID12 was designed to record XDMR spectra at high microwave pumping power over the whole frequency range 2–18 GHz. The microwave source is a wide-band tunable generator featuring an extremely low phase noise (Anritsu MG-3692A). Depending on the required pumping power, one may select the appropriate amplifier option:

- (1) A low noise amplifier (LNA: Miteq AMF-4B) can deliver up to 34 dBm (2.5 W) for standard experiments on YIG thin films
- (2) A micro-TWT power module (Litton: MPM-1020) can deliver up to $50\,\mathrm{dBm}$ (100 W)
- (3) Whenever higher pumping power is required, a powerful TWT amplifier operated in a pulsed mode can deliver up to $69\,\mathrm{dBm}$ (8 kW) peak power at ca. $9\,\mathrm{GHz}$ with 5% duty cycle.

As sketched in Fig. 7.9, the sample is inserted into a home-made TE_{102} rectangular waveguide cavity, which makes it possible to record magnetic resonance spectra in the usual Voigt configuration. The microwave power reflected back from

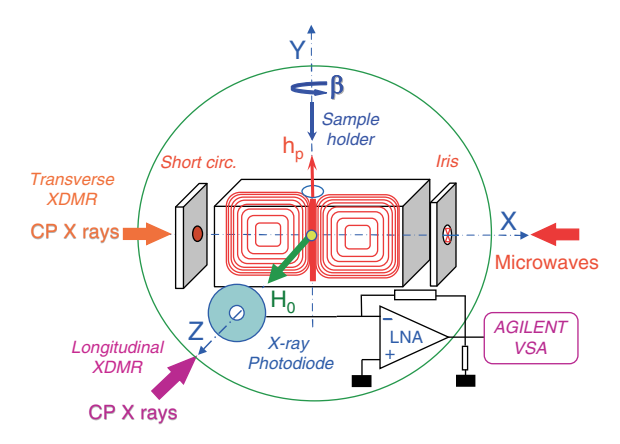


Fig. 7.9 Either *longitudinal* or *transverse* XDMR experiments can be performed in the Voigt configuration using the same rectangular TE_{102} cavity

the resonant cavity can be isolated using a circulator (Channel Microwave Inc.) that may work at high microwave peak power without any risk of damage. Standard FMR data can be recovered from this reflected signal. Whenever a phase information is needed, the reflected microwave signal can be fed into a microwave phase discriminator circuit (Anaren 20758).

As clearly shown by Fig. 7.9, one may use the same microwave resonant cavity to carry out XDMR experiments either in the longitudinal or transverse geometries, but this requires the resonance frequency of the cavity to be either adjustable or to be carefully optimized so as to lay very close to some selected harmonics of the RF frequency of the ESRF storage ring. A whole series of such cavities were thus machined to cover the microwave X-band ($F \simeq 24 \times RF$), C-band ($F \simeq 12 \times RF$; $F \simeq 16 \times RF$), or S-band ($F \simeq 8 \times RF$). Note that the cavity is itself inserted in a high-vacuum chamber made of amagnetic stainless steel and designed to critically match the rather narrow gap available between the magnetic poles of a commercial electromagnet. Waveguide cavities offer a few basic advantages over other resonant structures such as loop-gap or microstrip resonators: we can freely rotate the sample inside the cavity without modifying the relative orientation of H_0 and h_n , and we can easily cool the sample down to 10 K. Compared to a microstrip resonator, the waveguide cavity benefits of very low losses and of much higher factors of merit: typical loaded-Q in excess of 4,000 were easily achieved under critical coupling conditions. Actually, for YIG films featuring very narrow linewidths, this turned out to be even too high and required us to overcouple the cavity using a Gordon coupler or to carry out the measurements slightly off-resonance (e.g., with $\Delta F_{\rm cav} \leq$ 4 MHz).

The sensitivity and the performances of the XDMR spectrometer were quite significantly improved with a specific cavity design (see Fig. 7.9), which makes it possible to collect the X-ray fluorescence photons over a large solid angle using a large area photodiode located very close to the sample but *outside* the resonant

cavity. In this design, the electrical continuity of the X-ray transparent cavity wall was preserved using a polished Be window (\oslash 31 mm; thickness: 25 μm). Fast photodiodes were optimized for the XDMR experiments, which also require ultra-low noise performances: they have a large active area (300 mm²) and a 4 mm \oslash hole at their center, which is used to let the incident X-ray beam pass through the Si wafer and enter the microwave cavity when the XDMR experiment is to be performed in the longitudinal detection geometry [3].

7.3.3 XDMR in Longitudinal Geometry

7.3.3.1 Detection Issues

The incident microwave power is square-wave modulated using a fast switch featuring over 80 dB isolation with a very short rise/fall time (≤ 2 ns). The triggering signal is generated from the storage ring RF reference using a versatile digital frequency divider. As we are looking for a very weak XDMR signal, we have to make absolutely sure that no microwave modulation signal can indirectly interfere with the X-ray fluorescence signal detected by the photodiode. We found that a very high level of immunity against *artifact* could be achieved in exploiting the macrobunch time-structure of the incident X-ray beam, which results into a strong modulation of the X-ray fluorescence signal at the low order harmonics of the revolution frequency of the electrons in the storage ring, that is, $F_0 = \text{RF}/992 = 355.0427 \text{ kHz}$. Thus, experiments in longitudinal geometry were most easily carried out when the ESRF storage ring was operated either in the $2 \times 1/3$ or 7/8 filling modes. A time-chart of the data acquisition is illustrated with Fig. 7.10.

We found most convenient to modulate the microwave power at a frequency $F_{\rm mod} = 2F_0/p$ kHz, with typically p = 200. The XDMR signal should then show up as modulation sidebands at $F = F_{\rm RX} \pm F_{\rm mod}$, in which $F_{\rm RX} = n \times F_0$. The data acquisition was performed in the synchronous time-average mode of a high-performance vector spectrum analyzer driven by a triggering signal at $F_{\rm mod}$ or any appropriate sub-harmonics.

7.3.3.2 Element-selective Measurements on YIG Films

We have reproduced in Fig. 7.11 a typical power spectral density (PSD) such as that displayed with the Agilent VSA. The corresponding data were collected using an YIG film (#520) excited at $E_2 = 7115.1\,\mathrm{eV}$, that is, near the Fe K-edge. In those early experiments [3], the normal to the thin film was slightly tilted ($\beta_x \simeq 6^\circ$) with respect to the direction of the magnetic bias field B_0 . The incident microwave power was typically 28 dBm, while the microwave frequency was deliberately offset ($\Delta F_{cav} = 4\,\mathrm{MHz}$).

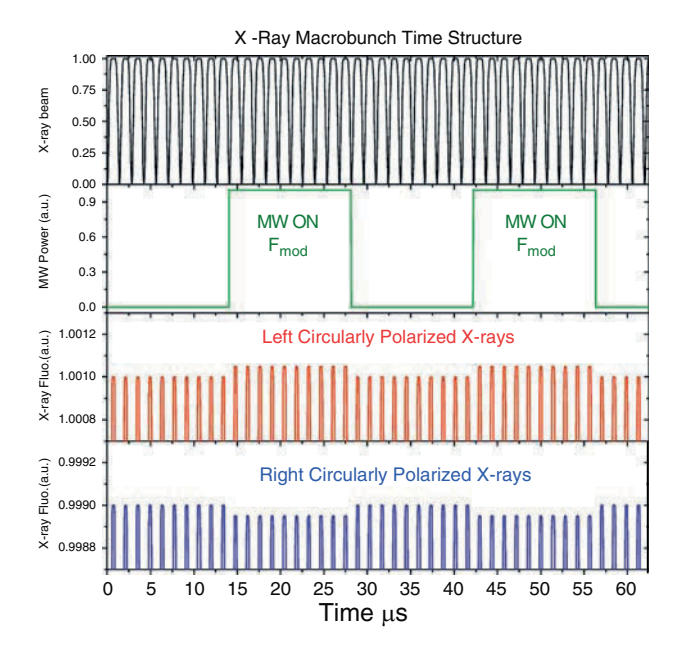


Fig. 7.10 Time-chart of the data acquisition: the modulation of the microwave power is fully synchronized with the time-structure of the X-ray macrobunches either in the $2 \times 1/3$ or 7/8 filling modes of the storage ring

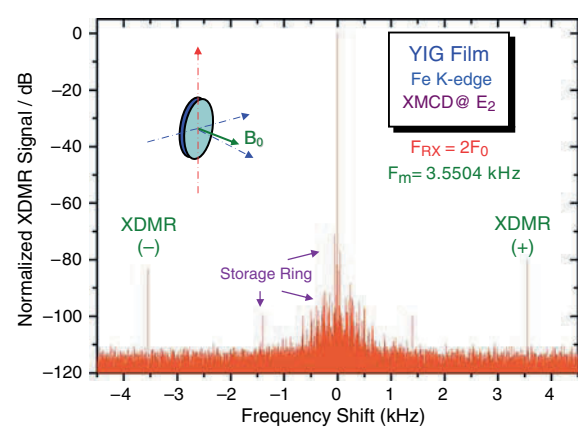


Fig. 7.11 Longitudinal XDMR signals measured at the characteristic excitation energy E_2 of the K-edge XMCD spectrum of the YIG/GGG thin film (#520). The XDMR signals clearly show up as two (\pm) modulation sidebands detected at: $F = F_{\rm RX} \pm F_{\rm mod}$

The Fe K_{α} fluorescence signal of the sample gave rise to a strong signal peaking at $F_{\rm RX}=2F_0=710.086\,{\rm kHz}$ and normalized to 0 dBV. The two XDMR satellites peak at ca. $-80\,{\rm dBV}$ but still benefit of a quite comfortable dynamic range because the noise floor could be kept below $-115\,{\rm dBV}$: this gives a nice illustration of the excellent performances of our detection system. The XDMR signals measured under

such conditions were converted into an ultra-low dichroism cross-section per atom: $\Delta\sigma_{\rm XDMR} \simeq 4.22 \times 10^{-5}$. In the time-average data acquisition mode of the VSA, each XDMR satellite has a complex vector character with a phase and an amplitude (modulus): it was carefully checked that the phase of the XDMR signal changed by 180° when the helicity of the incoming X-ray photons was switched from left to right [1] or when the energy of the X-ray photons was switched from E_1 to E_2 (see Fig. 7.7).

With the same YIG sample, we also measured the XDMR signals at the yttrium $L_{2,3}$ -edges [3]: this experiment turned out to be much more challenging because the circular polarization rate and the flux of the incident X-rays at 2.1 keV were not as favorable as at the Fe K-edge, whereas the X-ray fluorescence yield at the Y L-edges is fairly poor. Because of space limitation, we have reproduced in Fig. 7.12 only the (\pm) cross-correlated spectral densities of the XDMR signals measured at the yttrium L_3 - and L_2 -edges, when the energy of the X-ray photons was tuned to the first extremum (E_1) of each relevant XMCD spectrum. The geometry of the experiment, the incident microwave power, and the resonant field B_0 were all kept strictly identical to the configuration used for the Fe K-edge measurements.

In Fig. 7.12a, b, the (cross-correlated) XDMR signatures are still peaking ca. 18 dBV above the noise floor, which could be decreased down to -126 dBV, whereas the amplitude of the peak at $F_{\rm RX}=710.086$ kHz monitoring the fluorescence intensity is (as expected) quite significantly reduced. Precession angles were tentatively calculated from a series of XDMR measurements carried out either at the Fe K-edge or Y L_{2,3}-edges: for the orbital magnetization components precessing at the iron sites, we obtained $\theta_{\rm orbit}=(7\pm1)^{\circ}$, while for the *induced* spin components, which largely dominate the XDMR signal at the yttrium L-edges, we obtained $\theta_{\rm spin}\simeq (5.9\pm0.2)^{\circ}$.

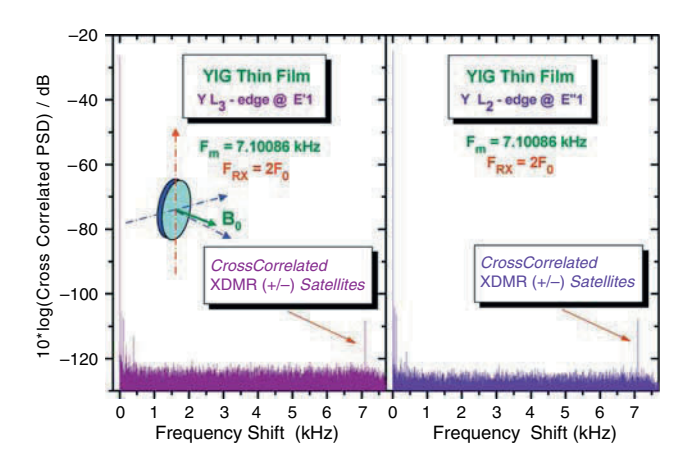


Fig. 7.12 Cross-correlated (\pm) XDMR intensities measured at the Y L_{2,3}-edges

7.3.3.3 Collective Effects in the Precession Dynamics of Orbital Components

Valuable new information was extracted from additional XDMR measurements carried out in longitudinal geometry on another iron garnet film, that is, [Y-La-Lu]IG, in which the yttrium was partially substituted with lanthanum and lutetium. The XDMR signal was not only measured at the Fe K-edge but also at the La and Lu $L_{2,3}$ -edges, the bias field B_0 being systematically kept strictly perpendicular to the film surface. What made those experiments quite puzzling was the huge discrepancy found between the precession angles calculated from the XDMR signals measured either at the Fe K-edge or at the RE $L_{2,3}$ -edges: for the orbital magnetization components precessing at the iron sites, we found $\theta_{\rm orbit} \simeq 19.1^{\circ}$, while for the *induced* spin components precessing at the La $L_{2,3}$ -edges, we found $\theta_{\rm spin} \simeq 4.7^{\circ}$.

FMR and XDMR spectra recorded simultaneously in the *field-scan* mode on the [Y-La-Lu]IG film are reproduced in Fig. 7.13. The foldover distortion of the microwave absorption spectrum $\chi''(B_0)$ and of the XDMR spectra results in fairly broad lineshapes ($\Delta B_0 \geq 400 \,\text{G}$). Most remarkable is, however, the very sharp increase of the XDMR signal very near the foldover jump, in a range where the

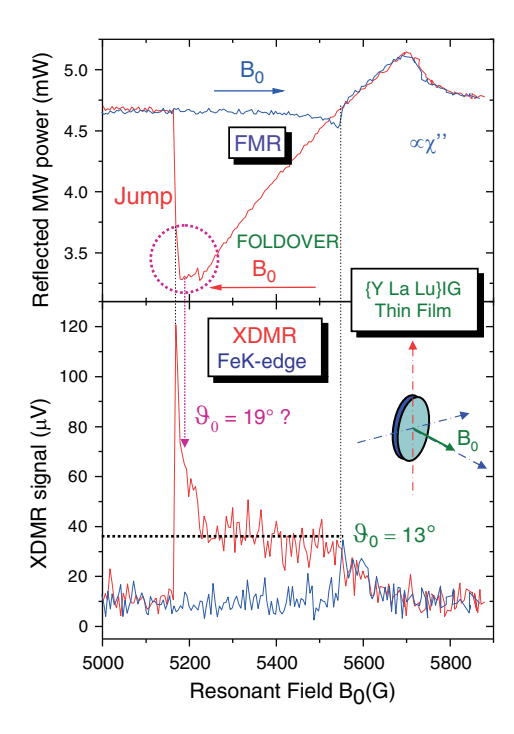


Fig. 7.13 XDMR and FMR foldover lineshapes of the [Y-La-LU]IG film recorded on scanning the magnetic bias field in both directions; the XDMR signal was measured at the Fe K-edge for the excitation energy E_1

FMR absorption spectrum seems to saturate. The observed XDMR lineshape confirms that what is measured in this experiment cannot be analyzed as the uniform precession of a magnetization vector with a constant length: everything looks as if the effective length (M_s) of the precessing magnetization vector would decrease and thus $|\Delta M_z|$ would increase. An interesting question is to know whether this would be consistent with the model of parametric amplification of spin waves as proposed by Suhl [21]. One certainly expects two-magnon annihilation processes to develop at resonance above the so-called second-order Suhl's instability threshold, but it is often claimed that those processes should have ultimately no effect on ΔM_z as the *total* number of magnons remains unchanged (see Fig. 7.3). Actually, this claim holds true only for exchange spin waves because the exchange Hamiltonian commutes with the operator associated with M_z [10]: it is false if one makes allowance for dipole-dipole interactions and the excitation of magnetostatic waves. This should precisely be the case for XDMR spectra recorded at the Fe K-edge because the precessing moments are of pure orbital nature: exchange interaction cannot play any role in those K-edge XDMR experiments, whereas, in contrast, exchange interaction may well play a key role in the XDMR measurements carried out at the L2,3-edges of RE in which the precessing components are essentially of spin character.

These considerations prompted us to look for any possibility to detect magneto-static wave satellites in the Fe K-edge XDMR spectra of YIG thin films. This was surely not a trivial task because the poor sensitivity of XDMR experiments in longitudinal geometry requires us to carry out such experiments at rather high microwave pumping power: under such conditions the strong foldover distortions of spectra recorded with either in-plane or perpendicular magnetization would make it totally hopeless to resolve MSW satellites. As illustrated with Fig. 7.14a, we found it nevertheless possible to minimize the foldover distortion on rotating the YIG film at the magic angle.

Actually, for an incident microwave power of 1.5 W, the foldover distortion was still quite significant and resulted in an apparent linewidth $\Delta H_0 \simeq 35$ Oe, but we found it possible to record the same XDMR spectrum with an incident power of only 150 mW, the linewidth of the uniform mode being now reduced down to only ca. 7 Oe. As illustrated with Fig. 7.14b, one could then resolve the very first satellites due to the excitation of backward magnetostatic waves (BMSW) and, perhaps, a surface mode. This was the first direct evidence that *orbital* magnetization components could perfectly couple to magnetostatic modes in YIG.

7.3.3.4 Direct Estimate of the Longitudinal Relaxation Time T_1

Owing to the difficulty to establish a fully reliable calibration of the microwave field h_p acting on the sample located inside the resonant cavity, we tried to explore a different approach to access the longitudinal relaxation time T_1 . This method, which looks promising, consists in analyzing the response of the precessing magnetization when the frequency (F_{mod}) of the amplitude-modulated (AM) microwave

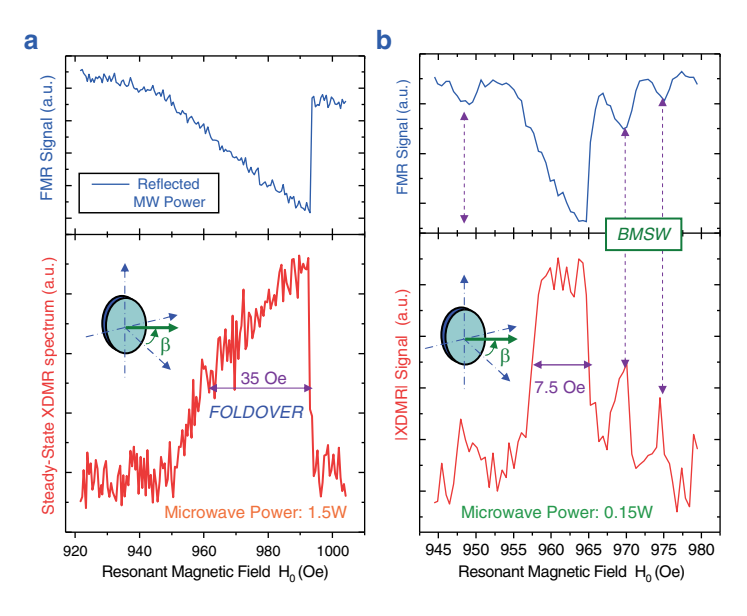


Fig. 7.14 (a) The XDMR foldover lineshape of the YIG/GGG thin film #520 was tentatively minimized on rotating the film at the magic angle but this was not enough to resolve any magnetostatic waves (MSW) satellite; the XDMR spectrum was recorded at the Fe K-edge with an incident microwave power of 1.5 W. (b) MSW satellites resolved at 150 mW pumping power

power is increased up to RF frequencies [13, 28, 29]. Recall that the XDMR signal which is analyzed in the Agilent VSA is a complex quantity defined by its phase and amplitude: we are precisely concerned below with careful measurements of the phase of the XDMR modulation satellites. Typically, in the Bloch–Bloembergen approach, the relaxation processes should contribute to the existence of an additional phase-shift at the modulation frequency $\omega_{\rm AM}$ [28]:

$$\tan \Delta \Phi_{\text{AM}} = -\omega_{\text{AM}} T_1 \left\{ (1 - \xi^2 T_1 T_2) \left[1 + \frac{T_2}{2T_1} \right] + \frac{1}{2} (\omega_{\text{AM}})^2 T_1 T_2 \left[1 + \frac{T_2}{2T_1} \right] + \cdots \right\},$$
(7.20)

in which $\xi = \frac{1}{2}h_{\rm p}$ now contributes only as a second order corrective term. With the latter YIG/GGG thin film again rotated at the magic angle, we measured the following phase-shifts: $\Delta \Phi_{\rm AM} \simeq 4.1^{\circ}$ at the modulation frequency $F_{\rm AM} = 71.0\,{\rm kHz}$; $\Delta \Phi_{\rm AM} \simeq 7.9^{\circ}$ at the modulation frequency $F_{\rm AM} = 142.0\,{\rm kHz}$. If one assumes that $T_2 = 2T_1$, as expected for the Landau–Lifschitz–Gilbert damping model, one obtains $T_1 \simeq 80\,{\rm ns}$. Given that this preliminary measurement was performed at the iron K-edge, this may be the first direct, element-selective measurement of an orbit–lattice relaxation time in the excited states. Much more work would still be needed to explore the whole potentiality of this method, which is nothing else than a peculiar adaptation of a technique known in optics as *phase fluorimetry*. One should try

to clarify to which extent such measurements would be affected by foldover distortions. It would be also desirable to check how far such T_1 measurements could really be exploited for sub-nanosecond relaxation times [30].

7.3.4 XDMR in Transverse Geometry

7.3.4.1 Super-Heterodyne Detection

The need for an X-ray fluorescence detector with a large active area is inherently conflicting with the additional requirement that we need to detect a weak XMCD signal oscillating at microwave frequencies. This led us to envisage an entirely new strategy to record XDMR spectra in the transverse geometry. The underlying concept can be easily understood if one keeps in mind that the time-structure of the excited X-ray fluorescence signal $I_f(T)$ consists of a series of discrete bunches, with a periodicity $\Delta T = 1/RF = 2.839 \, \text{ns}$ directly related to the RF frequency (352.202 MHz) of the storage ring, and with a FWHM length of ca. 50 ps at the ESRE.

$$I_{xf}(t) = I_{xf_0} \sum_{n} \delta(t - n\Delta T) \otimes \frac{1}{\sigma\sqrt{2\pi}} \exp\left[-\frac{t^2}{2\sigma^2}\right]. \tag{7.21}$$

On fourier transforming $I_{xf}(t)$, one obtains in the frequency domain a Gaussian envelope of RF frequency harmonics:

$$H_{xf}(F) = I_{xf_0} \cdot RF \sum_{n} \delta(F - n \cdot RF) \cdot \exp[-2(\pi \sigma F)^2]. \tag{7.22}$$

At the ESRF, the half-width at half maximum of the gaussian envelope corresponds typically to the 25th harmonics of the RF frequency: note that $25 \times RF = 8.79\,\mathrm{GHz}$ is typically in the microwave X-band. The proposed strategy was then to let the oscillating XMCD signal beat with the closest harmonics of the RF frequency. In other terms, the challenge was to adapt to XDMR the concept of heterodyne detection, which was quite popular in the early sixties: the difference is that we could benefit here of the tremendous advantage that synchrotron radiation directly provides us with a microwave local oscillator (LO) very near the desired XDMR frequency (Fig. 7.15). In this new approach of transverse XDMR, the resonance frequency of the microwave cavity should obviously match as closely as possible the frequency of selected RF harmonics. Special resonators were thus carefully optimized for these experiments, which also require a very high frequency stability and a very low phase noise. In the present paper, we shall report on a series of experiments carried out in the transverse geometry using the 24th harmonics of the RF frequency.

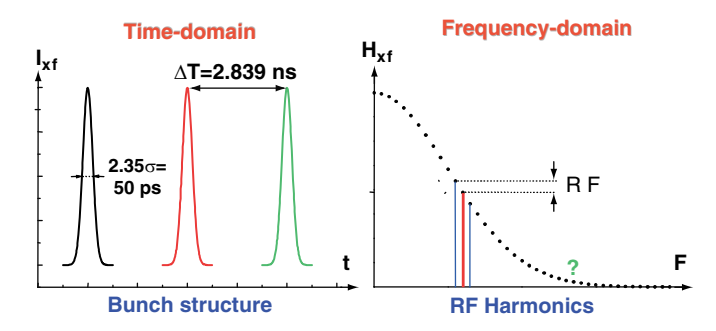


Fig. 7.15 X-ray fluorescence intensity measured in the time and frequency domains

Considerable improvement in the detection sensitivity was achieved recently with a super-heterodyne detection in which we exploit a 180° bi-phase modulation technique (BPSK). A block-diagram of the corresponding detection scheme is reproduced in Fig. 7.16. In this experiment, we found it essential to drive the microwave generator with the same (ultrastable) external 10 MHz reference clock as the one used to drive the RF generator of the storage ring. Moreover, the microwaves were phase-modulated at a very low modulation frequency: $F_{\text{bpsk}} = RF/(992 \times 10^{-5})$ 132) = 2.68948 kHz generated by the same ESRF PCI board (C-353) as used before. Defining next the XDMR resonance frequency as $F_{\text{MW}} = 24 \times \text{RF+IF}$, we are interested in measuring in the photodiode output not only the beating signal at the intermediate frequency IF, but also the modulation satellites at frequencies IF \pm F_{bosk} . It is the aim of some additional electronics to carry out a translation in the frequency domain of the detector output signal by a frequency shift strictly equal to IF. This was achieved by properly combining a comb generator delivering a reference signal for LO = $24 \times RF = 8.45266 \, \text{GHz}$, a microwave mixer with outputs in phase quadrature, and two RF mixers. Two distinct channels of the Agilent VSA are then used to carry out a vector decomposition of the XDMR signal, providing us with the whole phase information of the resonance. It is a major advantage of the proposed detection electronics to be now insensitive to any undesirable changes of the RF required to stabilize the electron beam in the storage ring [3].

7.3.4.2 Transverse XDMR Spectra of a YIG/GGG Thin Film Rotated at the Magic Angle

To illustrate the performance of the ESRF XDMR spectrometer in the transverse geometry, we used strictly the same YIG thin film (#520) rotated at the magic angle, which we used previously to carry out the XDMR experiments in the longitudinal geometry. The XDMR spectra displayed in Fig. 7.17a were recorded in the *field-scan* mode at the Fe K-edge, the X-ray monochromator being preset at energy E_1 , that is, the energy of the first extremum in the Fe K-edge XMCD spectrum (see Fig. 7.7).

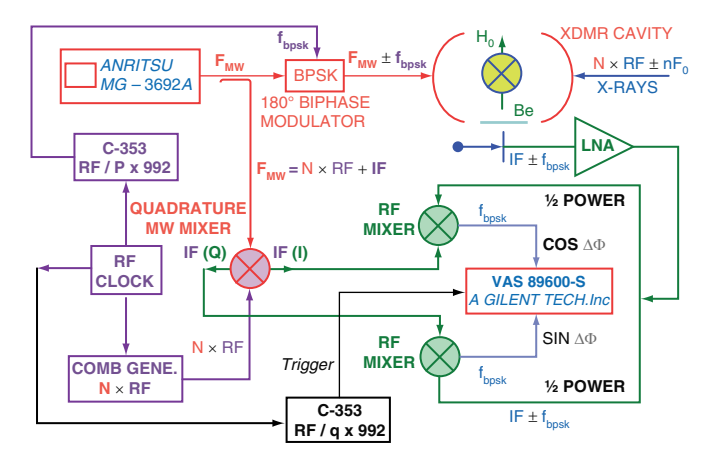


Fig. 7.16 Block-diagram of the superheterodyne detection of transverse XDMR exploiting BPSK

The absorptive and dispersive components of the resonances were obtained in exploiting the two VSA channels $\propto \sin \Phi$ and $\propto \cos \Phi$. Both spectra exhibit a rather impressive signal-to-noise ratio although the pumping power was only 10 mW, that is, two orders of magnitude smaller than in the experiments carried out in the longitudinal geometry and shown in Fig. 7.17a. With such a low pumping power, there is no significant foldover distortion and the linewidth was narrowed down to 7.5 Oe. The spectra reproduced in Fig. 7.17a obviously confirms the prediction made in Sect. 7.2.4, according to which one should expect only very weak contributions of magnetostatic wave satellites in Transverse-XDMR spectra. This is quite obvious regarding the (volume) BMSW satellites that are quite strong in the FMR absorption spectrum, but this not as clear regarding the eventual contribution of surface modes.

We also reproduced in Fig. 7.17b transverse-XDMR spectra recorded in the *energy-scan* mode using either left- or right-circularly polarized X-rays. As expected, the sign of the XDMR spectra recorded with orthogonal polarization is nicely inverted while the amplitude of the signal remains constant. This is a critical test, which establishes the full reliability of our measurements.

For the sake of comparison, we also added in Fig. 7.17b a rescaled plot of the *static* XMCD spectrum in the relevant Fe pre-edge region: interestingly, there is no significant difference between the reference XMCD spectrum and the Transverse-XDMR spectrum. One should nevertheless keep in mind that the orientation of the static bias field is fundamentally different in the two types of experiments: Fig. 7.18 was precisely added to remind the reader that the Bias field is rotated by 90° in transverse-XDMR experiment.

One important implication of the results displayed in Fig. 7.17b is that the opening angle of precession should remain constant over the whole band of final states probed by the excited photoelectrons. In other terms, θ_0 should be the same at energies E_1 or E_2 : this might cast doubt about the small variations of θ_0 , which we found in exploiting the measurements carried out in longitudinal geometry. It would

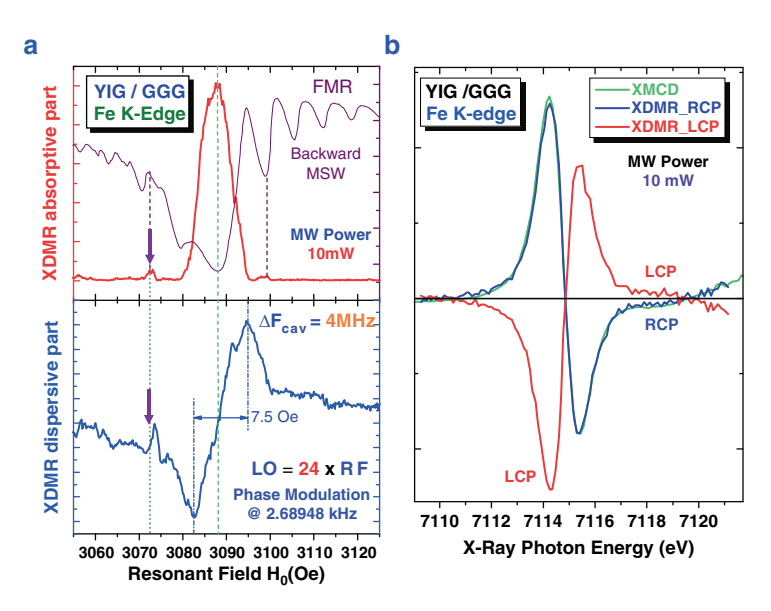
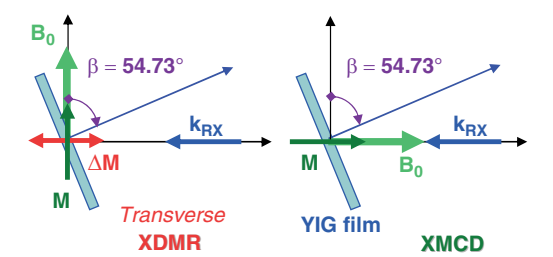


Fig. 7.17 (a) Absorptive and dispersive parts of the Transverse-XDMR spectra of a YIG film rotated at the magic angle; the spectra were recorded in the *field-scan* mode at the Fe K-edge; (b) Comparison of the static Fe K-edge XMCD spectrum with Transverse-XDMR spectra recorded in *energy-scan* mode for *left-* and *right-*circularly polarized X-rays

Fig. 7.18 Orientations of the magnetic bias field used for XMCD and transverse-XDMR measurements



be premature to draw such a conclusion because (1) the incident power was much lower; (2) there are strong arguments to suspect that the magnetization components M_{\perp} and M_z should not be affected in the same way by two-magnon annihilation processes [10, 28].

At this stage, let us point out that it is not a trivial exercise to extract the opening angle θ_0 from a transverse-XDMR signal measured with the proposed superheterodyne detection even though this signal is $\propto \sin \theta_0$: the difficulty arises from the fact that the proportionality factor depends on the amplitude of the 24th harmonics of the RF, the amplitude of which, in turn, depends on the *true* shape of the electron bunches in the machine, which we *assumed* (for simplicity) to be Gaussian with a constant bunch length.

What makes, nevertheless, the superheterodyne method quite attractive is its remarkable sensitivity, which allowed us to record Fe K-edge XDMR spectra of YIG

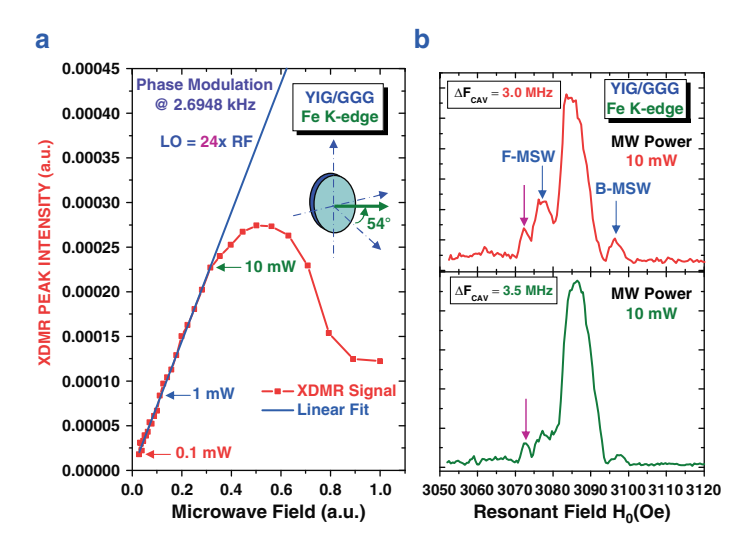


Fig. 7.19 (a) Saturation as a function of the microwave pump field $h_{\rm p}$ of the transverse-XDMR signal measured at the Fe K-edge in a YIG thin film rotated at the magic angle; (b) Growth of low-order magnetostatic waves satellites when the effective field is artificially increased by reducing $\Delta F_{\rm cav}$

thin films down to pumping powers as low as $100\,\mu\text{W}$. As illustrated with Fig. 7.19a, transverse-XDMR spectra could be recorded in a linear regime up to $10\,\text{mW}$, saturation being observed at ca. $40\,\text{mW}$. There are other ways to enter into the nonlinear regime: (1) one can decrease ΔF_{cav} , that is, tune the microwave frequency closer to the resonance of the cavity; (2) with overcoupled cavities, one can approach closer to the so-called critical coupling. In Fig. 7.19b, we have reproduced two XDMR spectra recorded in the saturation regime while keeping an incident power of $10\,\text{mW}$: we simply decreased ΔF_{cav} down to 3.5 and 3.0 MHz. Both forward- and backward-low order magnetostatic waves satellites now start growing and become rapidly rather broad. These spectra recorded in transverse geometry clearly confirm that orbital magnetization components precessing at the iron sites can couple to magnetostatic waves through dipole–dipole interactions.

7.3.4.3 Transverse XDMR Spectra of a Ferrimagnetic Single Crystal of GdIG Above and Below the Compensation Temperature

In this last subsection, we show that one may unravel additional information in looking at the precession phase. Basically, our idea was to check whether transverse-XDMR spectra could be used to detect a change in the chirality of the precession. We already mentioned in Sect. 7.3.1 that such a change of chirality is to be expected in a ferrimagnetic sample of GdIG if FMR or XDMR spectra are recorded either below or above the compensation temperature $T_{\rm cp} \simeq 285 \, {\rm K}$. What

makes such an experiment particularly challenging is the fact that the resonance linewidths are considerably broader than in the YIG thin films discussed in the previous sections: one would even expect the linewidth to diverge at $T_{\rm cp}$. Typically, the FMR linewidth measured with a GdIG single crystal cooled down to 200 K was of the order of 280 Oe; note that the microwave resonance measured at 450 K was considerably weaker and still fairly broad ($\Delta H_0 \simeq 135$ Oe).

Concentrating first on measurements carried out at the Fe K-edge on the GdIG crystal cooled down to $T\simeq 200$ K, we have reproduced in Fig. 7.20a XDMR spectra recorded in the *energy-scan* mode using either left- or right-circularly polarized X-rays. These spectra look obviously more noisy than the spectra recorded on the YIG film, but a simple comparison with the static XMCD spectrum would convince everybody that the information content of the XDMR spectra is still preserved. As illustrated with Fig. 7.20b, the XDMR spectrum recorded at the Gd L2-edge looks even worse: this is because X-rays are heavily absorbed in the sample due to the Fe K-edge and Gd L3-edge photoionization processes, which do not contribute to any XMCD signal. Note that the incident microwave power had to be kept below 1 W: the quality of the data could have been considerably improved on increasing the pumping power, for example, up to 10 W but, unfortunately, this turned out to be impossible during the allocated beam-time due to the accidental failure of one microwave component.

In Fig. 7.21, we have reproduced Fe K-edge XDMR spectra of GdIG recorded in the *field-scan* mode for two temperatures: $T \simeq 200 \,\mathrm{K}$ (below $T_{\rm cp}$: Fig. 7.21a), and $T \simeq 400 \,\mathrm{K}$ (above $T_{\rm cp}$: Fig. 7.21b). In these experiments, the monochromator of beamline ID12 was tuned to energy $E_1 \simeq 7114 \,\mathrm{eV}$ that corresponds to the largest

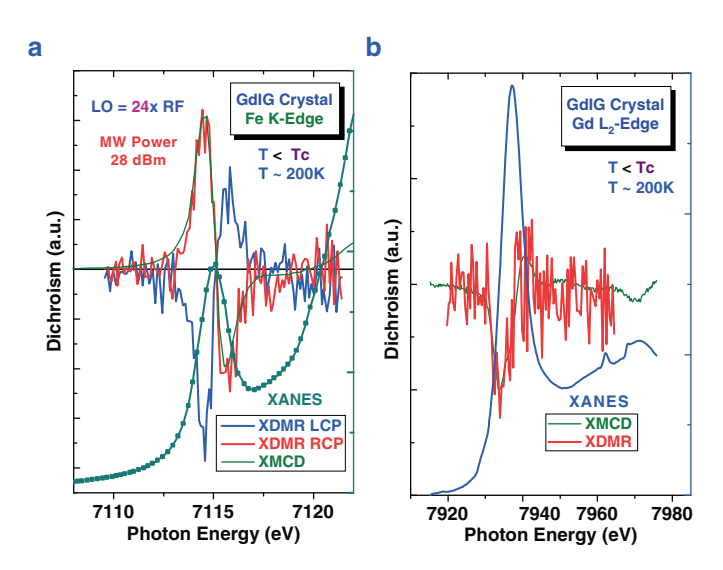


Fig. 7.20 Transverse XDMR spectra of GdIG recorded in the energy-scan mode at $T \simeq 200 \, \text{K}$: (a) at the Fe K-edge; (b) at the Gd L₂-edge

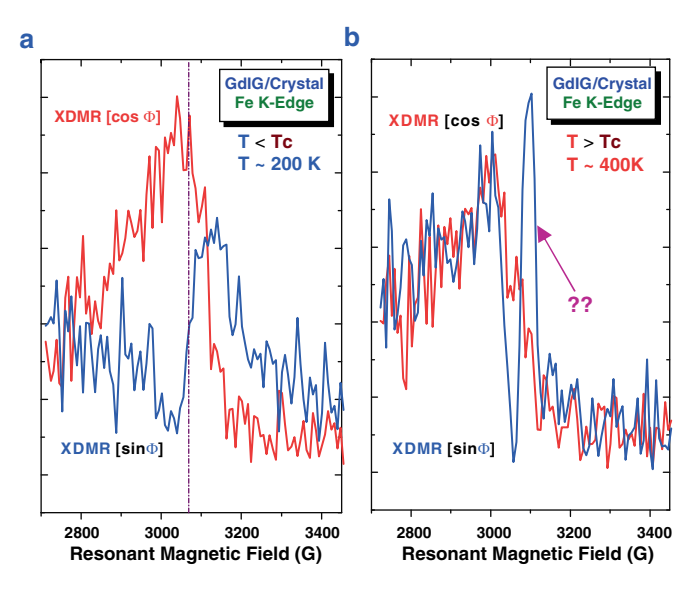


Fig. 7.21 Vector components of single-scan XDMR spectra recorded in the *field-scan* mode at the Fe K-edge of the GdIG single crystal: (a) below the compensation temperature, i.e., at $T \simeq 200 \, \mathrm{K}$; (b) above the compensation temperature, i.e., at $T \simeq 400 \, \mathrm{K}$. At $400 \, \mathrm{K}$, the broad XDMR signal $\propto \sin \Phi$ changes its sign, while there appears an (unexpected) additional signal with a narrow linewidth

XMCD signal in the Fe pre-edge region. Most important, we have reproduced in Fig. 7.21 the two vector components of the XDMR spectra, which are either $\propto \cos \Phi$ (absorptive-like) or $\propto \sin \Phi$ (dispersive-like). If there is a change in the chirality of the precession of the orbital magnetization components at the compensation temperature $T_{\rm cp}$, then one would expect *only one* vector component to have opposite signs at 200 K and 400 K, that is, that component $\propto \sin \Phi$. This seems to be clearly the case if one refers to the rather broad-band resonance of Fig. 7.21a, but what was totally unexpected is the appearance in Fig. 7.21b of a strong additional signature at resonance, this signature being quite intense and featuring a rather narrow linewidth.

In a further effort to figure out what could be the origin of this additional signature, we have also displayed in Fig. 7.22 the modulus |XDMR| calculated from the two vector components. Although the |XDMR| and |FMR| plots look rather similar at low temperature (200 K), this is not the case at high temperatures (e.g., $400 \, \text{K}$ or $450 \, \text{K}$), where it seems that the XDMR line is clearly split. At this stage, it should be kept in mind that the XDMR spectra recorded at the Fe K-edge here again result from two nonequivalent magnetic sublattices associated with Fe atoms in octahedral coordination (16a sites) or tetrahedral coordination (24d sites) and antiferromagnetically coupled. Indeed, the forced precession of the local *orbital* magnetization components should be fully coherent, but it is our interpretation that a destructive interference of the two oscillating XDMR signals could be envisaged under specific phase conditions.

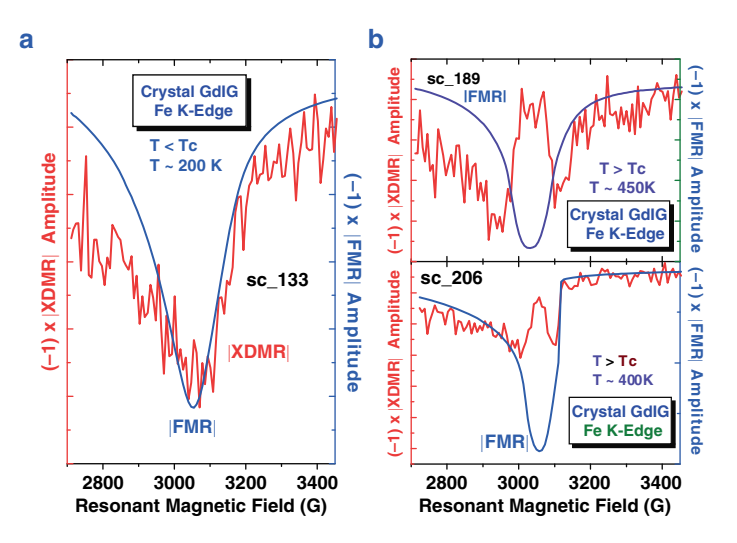


Fig. 7.22 Modulus of single-scan XDMR spectra recorded in the *field-scan* mode at the Fe K-edge of the GdIG single crystal: (a) below the compensation temperature, i.e., at $T \simeq 200\,\mathrm{K}$; (b) above the compensation temperature, i.e., at $T \simeq 400\,\mathrm{K}$ and 450 K. Split lines were systematically observed above the compensation temperature but not below

7.4 Facing New Challenges

In this contributed chapter, we tried to convince the reader that we have now the capability to record XDMR spectra both in the longitudinal or transverse geometries, either at the K-edge of 3d-transition metals or at the L_{2,3}-edges of rare earths. With a series of XDMR experiments carried out with YIG or RE-substituted YIG thin films, we produced clear evidence that, at the iron sites, *orbital* components of magnetized excited states with mixed p- or d-like symmetry are precessing; similarly, induced spin components located at the diamagnetic yttrium or RE sites are also precessing. Interestingly, the apparent opening angles of precession θ_0 measured at various absorbing sites can be fairly different and we suggested that this may well be the consequence of processes involving the annihilation of two uniform magnons: such a process is expected to develop at high pumping power whenever the precessing magnetization component can couple to collective modes, and more specifically to magnetostatic waves, via dipole-dipole interactions. We were precisely able to detect magnetostatic wave satellites in the Fe K-edge XDMR spectra of YIG thin films rotated at the magic angle: this appears to be the first direct evidence that orbital magnetization components can couple to magnetostatic waves. One clear advantage of XDMR experiments performed in transverse geometry is that one still preserves the capability to get access to additional information contained in the precession phase. As an example, we have shown that, in a ferrimagnetic single crystal of gadolinium iron garnet, the Fe K-edge XDMR spectra

were sensitive to the inversion of the precession chirality, which has long been predicted to take place at the compensation temperature $T_{\rm cp}$.

There is no doubt that the encouraging results obtained at the ESRF will stimulate further investigations of forced precession at *large* opening angle. One option would be to exploit ultra-short high power microwave pulses to study XDMR in a highly nonlinear regime. Another option would be to explore with XDMR what happens in the *SWASER* regime of spin valves in which, according to Slonczewki or Berger [31,32], electric currents flowing perpendicular to magnetic layers could result into creating a spin transfer torque opposing the LLG damping torque.

Extending XDMR measurements up to sub-THz frequencies would open a wide range of new applications. Let us recall, for example, that XMCD measurements on paramagnetic samples require high magnetic bias fields ($B_0 \geq 5\,\mathrm{T}$): this implies that the XDMR spectra should preferably be measured at high frequencies ($F \geq 70\,\mathrm{GHz}$). One should also keep in mind that many systems with integer spin are EPR-silent at microwave frequencies and can only be investigated in the sub-THz frequency range. In our opinion, XDMR at sub-THz frequencies would be a unique tool to study Van Vleck *orbital* paramagnetism, which is so far poorly known. The investigation of high frequency modes in ferrimagnetically coupled sublattices would be another interesting option, one famous example concerning the Kittel–Kaplan exchange modes in ferrimagnets. In this respect, one could even dream of recording high-frequency XDMR spectra in *antiferromagnetic* systems featuring a large anisotropy field.

Acknowledgements We are grateful to J. Ben Youssef and M.V. Indenbom (Laboratoire de Magnétisme de l'Université de Bretagne Occidentale) for providing us with YIG and related thin films grown in Brest. Invaluable technical assistance by M.-C. Dominguez, S. Feite, and P. Voisin are warmly acknowledged here. We greatly benefitted of the development of the C-353 PCI board by Ch. Hervé (ESRF/Digital Electronics group). Nothing would have been possible without the support and encouragements of Y. Petroff and F. Sette during the critical phase of the XDMR project.

References

- J. Goulon, A. Rogalev, F. Wilhelm, N. Jaouen, Ch. Goulon-Ginet, G. Goujon, J.B. Youssef, M.V. Indenbom, JETP Lett. 82, 791 (2005)
- J. Goulon, A. Rogalev, F. Wilhelm, N. Jaouen, Ch. Goulon-Ginet, Ch. Brouder, Eur. Phys. J. B 53, 169 (2006)
- J. Goulon, A. Rogalev, F. Wilhelm, Ch. Goulon-Ginet, G. Goujon, J. Synchrotron Rad. 14, 257 (2007)
- W.E. Bailey, L. Cheng, D.J. Keavney, C.-C. Kao, E. Vescovo, D.A. Arena, Phys. Rev. B 70, 172403 (2004)
- 5. D.A. Arena, E. Vescovo, C.-C. Kao, Y. Guan, W.E. Bailey, Phys. Rev. B 74, 064409 (2006)
- D.A. Arena, E. Vescovo, C.-C. Kao, Y. Guan, W.E. Bailey, J. Appl. Phys. 101, 09C109 (2007)
- 7. Y. Guan, W.E. Bailey, E. Vescovo, C.-C. Kao, D.A. Arena, JMMM 312 374 (2007)
- G. Boero, S. Rusponi, P. Bencock, R.S. Popovic, H. Brune, P. Gambardella, Appl. Phys. Lett. 87, 152503 (2005)

9. G. Boero, S. Mouaziz, S. Rusponi, P. Bencok, F. Nolting, S. Stepanow, P. Gambardella, New J. Phys. 10, 013011 (2008)

- 10. A.G. Gurevich, G.A. Melkov, *Magnetization Oscillations and Waves* (CRC Press, Boca Raton, 1996)
- 11. N. Smith, J. Appl. Phys. 92, 3877 (2002)
- 12. N. Bloembergen, S. Wang, Phys. Rev. 93, 72 (1954)
- 13. R.C. Fletcher, R.C. LeCraw, E.G. Spencer, Phys. Rev. 117, 955 (1960)
- 14. G. Bertotti, C. Serpico, I.D. Mayergoyz, Phys. Rev. Lett. 86, 724 (2001)
- 15. P. Strange, J. Phys. Condens. Matter **6**, L491 (1994)
- 16. H. Ebert, Rep. Prog. Phys. 59, 1665 (1996)
- 17. G.Y. Guo, J. Phys. Condens. Matter 8, L747 (1996)
- 18. H. Ebert, V. Popescu, D. Ahlers, Phys. Rev. B 60, 7156 (1999)
- 19. P. Carra, H. König, B.T. Thole, M. Altarelli, Physica B 192, 182 (1993)
- A. Rogalev, F. Wilhelm, N. Jaouen, J. Goulon, J.-P. Kappler, in *Magnetism: A Synchrotron Radiation Approach*, ed. by E. Beaurepaire, H. Bulou, F. Scheurer, J.-P. Kappler. Lectures Notes in Physics, vol 697 (Springer, Berlin, 2006) pp. 71–94
- 21. H. Suhl, J. Appl. Phys. 30, 1961 (1959); J. Appl. Phys. 31, 935 (1960)
- 22. A. Berteaud, H. Pascard, J. Appl. Phys. 37, 2035 (1966)
- 23. D.D. Stancil, *Theory of Magnetostatic Waves* (Springer, Berlin, 1993)
- 24. R.W. Damon, J.R. Eshbach, J. Phys. Chem. Solids 19, 308 (1961)
- 25. T. Kasuya, R.C. LeCraw, Phys. Rev. Lett. 5, 223 (1961)
- M.A. Gilleo, in Ferromagnetic Materials, vol 2, ed. by E.P. Wolfarth (North-Holland Publishing Company, Amsterdam, 1980) pp. 1–53
- A. Rogalev, J. Goulon, F. Wilhelm, Ch. Brouder, A. Yaresko, J. Ben Youssef, M.V. Indenbom, J. Magn. Magn. Mater. 321, 3945–3962 (2009)
- V. Charbois, Détection Mécanique de la Résonance Magnétique, Ph.D. thesis, Université Paris-VII Denis Diderot, 2003
- 29. J. Pescia, La Mesure des temps de relaxation spin-réseau très courts, *Thèse d'Etat*, Paris (1964); Ann. Phys. **10**, 389 (1965)
- 30. F. Murányi, F. Simon, F. Fülöp, A. Jánossy, J. Magn. Res. 167, 221 (2004)
- 31. J.C. Slonczewski, J. Magn. Magn. Mater. 159, L1-7 (1996)
- 32. L. Berger, Phys. Rev. B 54, 9353 (1996)
- 33. S. Geschwind, L.R. Walker: J. Appl. Phys. 30 (suppl), 163S (1959)

Chapter 8

Resonant X-Ray Scattering and Absorption

S.P. Collins and A. Bombardi

Abstract This chapter outlines some of the basic ideas behind nonresonant and resonant X-ray scattering, using classical or semiclassical pictures wherever possible; specifically, we highlight symmetry arguments governing the observation of X-ray optical effects, such as X-ray magnetic circular dichroism and resonant "forbidden" diffraction. Without dwelling on the microscopic physics that underlies resonant scattering, we outline some key steps required for calculating its rotation and polarization dependence, based on Cartesian and spherical tensor frameworks. Several examples of resonant scattering, involving electronic anisotropy and magnetism, are given as illustrations. Our goal is not to develop or defend theoretical concepts in X-ray scattering, but to bring together existing ideas in a pragmatic and utilitarian manner.

8.1 Absorption and Scattering: The Optical Theorem

Absorption is a special case of scattering. The mathematical relationship between the two, known as the optical theorem, is very general and fundamental. It can be written as

$$\gamma(E) = \left(\frac{4\pi n_0}{q}\right) \operatorname{Im} f(E, \mathbf{q}' = \mathbf{q}, \varepsilon' = \varepsilon), \tag{8.1}$$

where γ is the linear absorption coefficient and n_0 is the atomic density, \mathbf{q} , $\mathbf{q'}$, ε , ε' are the incident and scattered wavevectors and polarization, and E is the photon energy. We see that absorption scales with the imaginary part of the forward scattering amplitude for a scattered beam that is in the same state (energy, wavevector, polarization) as the incident wave. This can be understood very easily if we accept that the only way to diminish an electromagnetic wave is to add to it a wave that is the same but of opposite phase. Such a wave can be caused by scattering, and

S.P. Collins (\(\subseteq \)

Diamond Light Source Ltd., Diamond House, Harwell Science and Innovation Campus,

Didcot, Oxfordshire, OX11 0DE, UK

e-mail: steve.collins@diamond.ac.uk

so a relationship between absorption and the forward scattering amplitude is not surprising. What is, at first sight, surprising is that we need to take the imaginary component. The reason for this is that the optical theorem is written for a plane wave, while our scattering formalism describes scattering from a point into a spherical wave. It is therefore necessary to consider the scattering from every point on a plane representing the wavefront, and it is easy to show [1] that this procedure introduces a phase factor of $\pi/2$, which allows the imaginary part of the forward scattering amplitude to interfere destructively with the incident beam.

Because absorption is a special case of scattering, all the calculations described in this chapter can be applied trivially to absorption, simply by choosing $\mathbf{q}' = \mathbf{q}$, $\varepsilon' = \varepsilon$.

8.2 Symmetry and X-Ray Absorption

Before looking at the detailed physics behind a physical effect, it can be very informative to ask if there are any obvious symmetry arguments that will render the phenomenon impossible. Fundamental to modern physics is the assumption that there are no preferred directions or positions in space, leading to invariance with respect to spatial translation or rotation. Furthermore, all the forces of nature are exactly symmetrical with respect to the simultaneous reversal of charge, parity, and time (CPT). Electromagnetic interactions, which completely dominate the electronic and optical properties of materials, are symmetric with respect to C, P, and T separately. As a mirror reflection is equivalent to the combination of a rotation of π normal to the mirror plane and spatial inversion ($P(\mathbf{r}) = -\mathbf{r}$), it follows that all physical phenomena that are governed by electromagnetic interactions are symmetric with respect to any reflection. That is, if a measurement (the probability of detecting a photon that has passed through a material, e.g.) gives a certain result, then exactly the same result is expected if the entire experiment is reflected in a mirror plane. Here, we use this argument to show how some circular-dichroic effects are impossible, while others may be allowed.

We first consider magnetic circular dichroism, where the magnetism is described by an atomic vector. In Fig. 8.1 (top left), we arrange for the magnetic vector to be perpendicular to the beam of circularly polarized X-rays. Is it possible that reversing the direction of circular polarization will change the absorption to give circular dichroism? We know that reflecting the whole experiment in a mirror, as shown in the figure, must lead to the same result. The mirror reverses the circular polarization but leaves the magnetic vector (perpendicular to the mirror plane) unchanged, and so we can say that reversing the circular polarization cannot lead to different absorption and there can be no circular dichroism in this configuration. The mirror preserves the direction of the vector normal to it because it is an *axial* vector, conveniently visualized as a current loop, which is an appropriate representation of its physical origin. There are two types of vector: polar vectors and axial vectors. Polar vectors are examples of true tensors, which transform under spatial inversion as $(-1)^K$, where

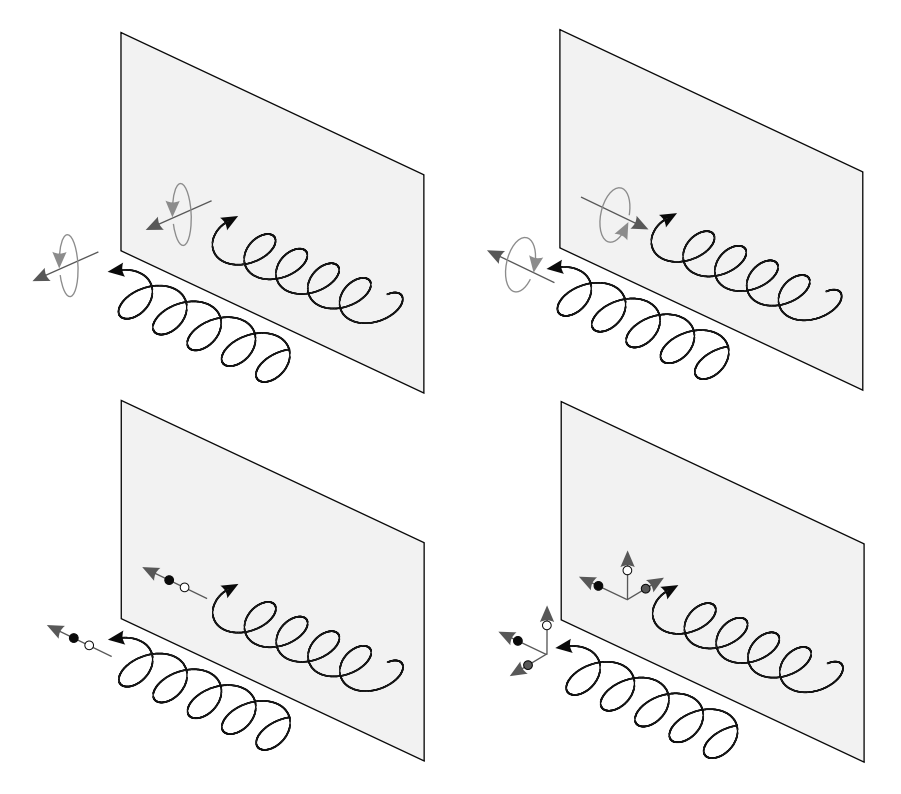
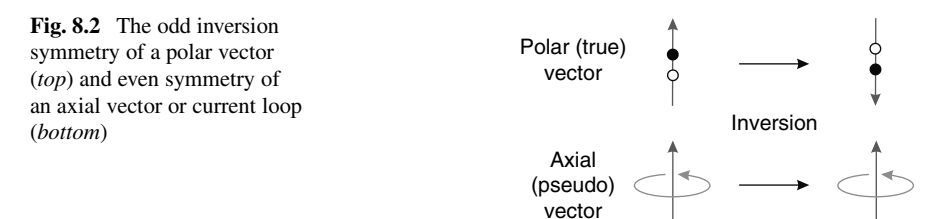


Fig. 8.1 Mirror planes constructed to give simple symmetry arguments to rule out circular dichroism from a magnetic vector perpendicular to the beam direction (*top left*) or a polar vector in any direction (*bottom left*). See text



K, the tensor rank, is one for a vector. Axial vectors are examples of pseudotensors, which transform under spatial inversion as $(-1)^{K+1}$. Thus, axial vectors are even under inversion (Fig. 8.2) and polar vectors are odd. This distinction is clearly of fundamental importance for understanding the symmetry properties of crystals that possess magnetic (axial) or electric (polar) dipoles. Turning to Fig. 8.1 (top right), we can ask if it is possible for circular dichroism to exist if the magnetic vector is parallel to the beam direction. In the mirror, we see that the magnetism reverses and so does the circular polarization. We can therefore say that reversing both can have no effect on the absorption, but there is no obvious symmetry argument to say that

reversing just the circular polarization (or magnetic direction) must lead to the same result, and so we cannot rule out circular dichroism if the magnetic vector is not perpendicular to the beam. Indeed, such a configuration is known to exhibit circular dichroism.

At first sight one might expect to observe similar effects with a polar vector (a ferroelectric, for example), but Fig. 8.1 (bottom left) shows that there can be no circular dichroism in the configuration shown. Moreover, as the X-ray beam is invariant (within a phase) to rotational about the beam direction, it is not hard to show that there is no orientation of the polar vector that can give circular dichroism.

The situation is more complicated with chiral sample symmetry, where the object (represented here by four points) is different from its mirror image, shown in Fig. 8.1 (bottom right). It is clear that reversing the chirality of the sample by reflection in the mirror, *and* the circular polarization, must give the same result, but there is no obvious reason why reversing only one must give the same result. Such a difference in absorption is weak for X-rays and requires a theory that goes beyond the electric dipole approximation, but it does exist.

The arguments demonstrated here can be applied to any measurement, including scattering, photoemission etc., but then one must pay attention to the symmetry properties of all of the vectors that are relevant to the experiment, such as the scattered beam or photoelectron trajectory. As a general rule, adding complexity in this way reduces the symmetry of the measurement and allows more optical effects to exist.

8.3 X-Ray Scattering and Multipole Matrix Elements

The theory of resonant X-ray scattering and absorption is treated in detail by several authors (see, e.g., [2–6]). The object of the exercise is the calculation of the quantum mechanical photon scattering amplitude, which is related to the classical electric field, and to the scattering cross-section via its squared magnitude. The scattering strength is given in terms of matrix elements of the perturbation energy, by Fermi's Golden Rule. A very important conceptual point is that, in the presence of an electromagnetic field (say a photon), the momentum $\bf p$ of an electron is modified by the vector potential, such that $\bf p \rightarrow \bf p - \frac{e}{c} \bf A$ [7]. Hence, the energy of the combined photon/electron system is

$$H = \frac{\left(\mathbf{p} - \frac{e}{c}\mathbf{A}\right)^2}{2m} = \frac{\mathbf{p}^2}{2m} + \frac{e^2}{2mc^2}\mathbf{A}^2 - \frac{e}{mc}\mathbf{p} \cdot \mathbf{A},\tag{8.2}$$

where the first and second terms are, respectively, the energies of the electron and the photon (relativistic effects are ignored), and the third term is the photon-electron interaction. In quantum mechanical calculations, \mathbf{p} and \mathbf{A} are operators. The \mathbf{A}^2 term is responsible for nonresonant scattering and can be used to give a sound interpretation of the vast majority of X-ray scattering data. The $\mathbf{p} \cdot \mathbf{A}$ term is responsible for resonant scattering (and absorption). For a scattering process, it must

be applied twice as the vector potential operator either creates or destroys a single photon, and the scattering amplitude is finally given by second-order perturbation theory as

$$f \propto \sum_{b} \frac{\langle a|\mathbf{O}^{+}|b\rangle\langle b|\mathbf{O}|a\rangle}{\Delta E - \frac{\mathrm{i}\Gamma}{2}},$$
 (8.3)

where $\mathbf{O} = \mathbf{p} \cdot \hat{\varepsilon} \mathrm{e}^{\mathrm{i}\mathbf{q}\cdot\mathbf{r}}$ (essentially, $\mathbf{p} \cdot \mathbf{A}$ with its time dependence removed, where \mathbf{q} is the photon wavevector, and $\hat{\varepsilon}$ is the polarization vector), a and b are the initial and virtual intermediate atomic states of energy $E_{a(b)}$, $\Delta E = \hbar\omega - E_b + E_a$ (the energy difference between the photon and the atomic excitation), and Γ is a small energy that is related to the lifetime of the intermediate state. The states a and b correspond to the initial atomic state (normally the ground state) and an excited state whereby a core electron is promoted into an empty valance level. The sum runs over all such empty states. The energy denominator, a characteristic of second-order perturbation theory, effectively selects only the state(s) of correct energy for the resonance.

It is worth pointing out that the resonant scattering and absorption described in this chapter involve excitation of a tightly bound atomic core electron at energies close to an X-ray "absorption edge," which marks the sudden increase in absorption as the core electron is given sufficient energy to fill an empty valence state. Close to such a resonance Γ is determined mainly by the lifetime of the core hole.

As the wavelength is long compared to the dimensions of the atomic core electrons, the exponential phase factor in the above expression can be expanded as a rapidly converging series,

$$\mathbf{O} = \mathbf{p} \cdot \hat{\varepsilon} + i(\mathbf{p} \cdot \hat{\varepsilon})(\mathbf{q} \cdot \mathbf{r}) + \cdots$$
 (8.4)

The transition operator is still not in a very convenient form as it involves both position and momentum. Conversion to a purely spatial form is facilitated by the use of commutation relations, such as,

$$\mathbf{p} = \frac{m}{\mathrm{i}\hbar}[\mathbf{r}, H] = \frac{m}{\mathrm{i}\hbar}(\mathbf{r}H - H\mathbf{r}), \qquad (8.5)$$

where the Hamiltonian operator, H, is simply replaced by the energies of the initial and final atomic states as they are energy eigenstates. Finally, we sidestep quantum mechanics and replace operators with their expectation values, whereby the product of the two terms in the numerator of (8.3) leads to a series of pure and mixed electric multipole transition amplitudes. We write, for example, the electric dipole–electric dipole (E1E1) amplitude as

$$f_{\text{EIE1}} = (\mathbf{r} \cdot \hat{\varepsilon})(\mathbf{r} \cdot \hat{\varepsilon}')^* = r_i r_j^* \varepsilon_i \varepsilon_j'^* = T_{ij} X_{ij}. \tag{8.6}$$

The last term introduces the widely used formalism of Cartesian tensors [8], where

$$T_{ij} = r_i r_i^*, \quad X_{ij} = \varepsilon_i \varepsilon_i^{\prime *} \tag{8.7}$$

are the "material" and "X-ray probe" tensors, respectively.

In the spirit of a phenomenological model, we take all constants and slowly varying functions into the expectation values, then restate and regroup the expression using Cartesian tensor formalism and Einstein implied summation notation (there is an implicit sum over three Cartesian basis vectors x, y, z, numbered 1–3). Finally, we combine the two vectors, or rank-one tensors, r_i etc., to give a matrix or rank-two tensor T_{ij} .

The tensor expressions for higher-order multipole transitions will be discussed again later when specific examples are given. For now, we focus on electric dipole (E1E1) transitions. Similar expressions can be derived for magnetic transitions, which have been shown to play an important role in some resonant scattering experiments [9], although they tend to be very weak at X-ray wavelengths [6] (Fortunately, magnetic properties can be probed with electric transitions, as we demonstrate in the next section).

While a proper calculation of the resonant amplitude requires a detailed knowledge of the electronic wavefunctions, the "geometrical" aspects of the resonance can be factored out as they depend only on the coupling of a set of unit vectors (polarization etc.) to the angular parts of the matrix elements. It is therefore possible to consider a phenomenological model of the scattering that can describe the polarization dependence, orientation dependence, and whether or not a particular optical effect, Bragg reflection, etc. can exist, without carrying out a detailed quantum-mechanical calculation. The remainder of this chapter deals with such geometrical properties.

8.4 Cartesian Tensors, Magnetism and Anisotropy

In the preceding section, we outlined the steps necessary to obtain a phenomenological model for resonant scattering (and absorption) based on Cartesian tensors. This may seem an unnecessary step but the separation of the sample and X-ray properties onto objects that have well-defined transformation properties proves to be an extremely powerful and elegant way of dealing with complex scattering process. The relationship between the scattering tensor and sample symmetries will be discussed in the next section. Here, we discuss a simple but widely used model of E1E1 resonant scattering, including magnetism and magnetically induced charge anisotropy.

We begin by selecting the most general form of the E1E1 scattering tensor:

$$T_{ij} = \begin{pmatrix} T_{11} & T_{12} & T_{13} \\ T_{21} & T_{22} & T_{23} \\ T_{31} & T_{32} & T_{33} \end{pmatrix} = \begin{pmatrix} r_1 r_1^* & r_1 r_2^* & r_1 r_3^* \\ r_2 r_1^* & r_2 r_2^* & r_2 r_3^* \\ r_3 r_1^* & r_3 r_2^* & r_3 r_3^* \end{pmatrix} = \begin{pmatrix} a & b & c \\ d & e & f \\ g & h & i \end{pmatrix},$$
(8.8)

where a, b, c, etc. are complex functions of energy. Now let us assume that all the interactions governing the atom of interest are (on average) either isotropic or have a direction that is fixed only by an applied magnetic field, which we take to lie

along the z-axis. This scenario corresponds to a free atom under the influence of a magnetic field. We assume as little as possible about the system, but one thing we can say with certainty is that the physical properties of the atom are invariant against any rotation about the field (z) axis. As each tensor component is an observable physical quantity (in principle, at least), then we must ensure that the tensor T_{ij} remains the same after rotation through some angle, ζ , that is,

$$T = R_{\xi}^{z}(T) = R_{\xi}^{z} T R_{\xi}^{z}^{T} = T_{ij} R_{\xi}^{z} {}_{iI} R_{\xi}^{z} {}_{jJ},$$
(8.9)

where the transformation is given in both tensor and matrix form, ^T represents a transpose and the rotation matrix is given by

$$R_{\zeta}^{z} = \begin{pmatrix} \cos \zeta - \sin \zeta \ 0\\ \sin \zeta & \cos \zeta \ 0\\ 0 & 0 & 1 \end{pmatrix}. \tag{8.10}$$

One can solve (8.9) for each tensor element, but it is a slightly tedious process. It is, however, a simple exercise to show that a tensor of the form

$$T_{ij} = \begin{pmatrix} a - \frac{1}{3}c & b & 0\\ -b & a - \frac{1}{3}c & 0\\ 0 & 0 & a + \frac{2}{3}c \end{pmatrix}$$
(8.11)

satisfies (8.9) and is therefore invariant against any rotation about the z-axis. On inspection of (8.11), we can identify three separate structures, characterized by the symbols a, b, and c. The first of these is a scalar, represented by the identity matrix multiplied by a. It is invariant with respect to any rotation and therefore describes the isotropic properties of the atom. The parts characterized by b and c are not isotropic, but are axially symmetric. One can show as another simple exercise that on rotation by π about the x axis, one obtains an identical tensor with the exception that the parameter b changes sign. We can therefore identify c with uniaxial anisotropy and b with a vector. In fact, this is an example of a well-established deconstruction of a second-rank Cartesian tensor into its irreducible components: a scalar, a vector, and a symmetric tensor that can be described by an ellipsoid.

To ascertain whether the vector part of the scattering tensor behaves like an axial or polar vector (see Sect. 8.2), we need to determine whether it is even or odd under inversion. For this we note that, under inversion, a Cartesian tensor of rank K changes only by the overall sign, $(-1)^K$, and so even rank tensors are even and odd rank tensors odd. A vector described by a rank-two Cartesian tensor is therefore even under inversion and behaves like a current loop rather than a polar vector. It is not a large step to associate the vector term with a magnetic dipole and to label this term in the scattering tensor as magnetic scattering. To add weight to this feasibility argument, we note that the tensor in (8.8) is symmetric if the expectation values r

are purely real. As complex conjugation (*) reverses the direction of time, we can deduce that the antisymmetric vector term is time-odd, that is, magnetic.

The uniaxial term does not change sign with time reversal (it is time-even) and so is not strictly magnetic, although the anisotropy is very often caused by magnetism.

To derive an explicit form for the polarization dependence of the above scattering process, we simply expand out the X-ray tensor in (8.7):

$$X_{ij} = \begin{pmatrix} \varepsilon_1 \varepsilon_1'^* & \varepsilon_1 \varepsilon_2'^* & \varepsilon_1 \varepsilon_3'^* \\ \varepsilon_2 \varepsilon_1'^* & \varepsilon_2 \varepsilon_2'^* & \varepsilon_2 \varepsilon_3'^* \\ \varepsilon_3 \varepsilon_1'^* & \varepsilon_3 \varepsilon_2'^* & \varepsilon_3 \varepsilon_3'^* \end{pmatrix}$$
(8.12)

and insert (8.11) and (8.12) into (8.6) to obtain

$$f_{\text{EIE1}} = T_{ij} X_{ij}$$

$$= a(\varepsilon_1 \varepsilon_1'^* + \varepsilon_2 \varepsilon_2'^* + \varepsilon_3 \varepsilon_3'^*) + b(\varepsilon_1 \varepsilon_2'^* - \varepsilon_2 \varepsilon_1'^*) + c \frac{1}{3} (2\varepsilon_3 \varepsilon_3'^* - \varepsilon_1 \varepsilon_1'^* - \varepsilon_2 \varepsilon_2'^*)$$

$$\equiv a(\hat{\varepsilon} \cdot \hat{\varepsilon}'^*) + b \hat{\mathbf{z}} \cdot (\hat{\varepsilon} \times \hat{\varepsilon}'^*) + c \left\{ (\hat{\varepsilon} \cdot \hat{\mathbf{z}})(\hat{\varepsilon}'^* \cdot \hat{\mathbf{z}}) - \frac{1}{3} (\hat{\varepsilon} \cdot \hat{\varepsilon}'^*) \right\}. \tag{8.13}$$

Here, we have used only very simple symmetry arguments to obtain a phenomenological expression for magnetic resonant scattering, within the electric dipole (E1E1) approximation, which reproduces the essence of the "standard" form [10, 11]

$$f_{\text{EIE1}} = (\hat{\varepsilon} \cdot \hat{\varepsilon}'^*) F^{(0)} + i \,\hat{z} \cdot (\hat{\varepsilon} \times \hat{\varepsilon}'^*) F^{(1)} + (\hat{\varepsilon} \cdot \hat{\mathbf{z}}) (\hat{\varepsilon}'^* \cdot \hat{\mathbf{z}}) F^{(2)}, \tag{8.14}$$

where the definitions of $F^{(n)}$ are given in the above references.

The Cartesian scattering tensor in (8.11) can be written equivalently, but more flexibly, by detaching the (magnetic) symmetry vector from the Cartesian axes. If we now represent the magnetic unit vector by $\hat{\mathbf{m}}$ (i.e., replace $\hat{\mathbf{z}}$ with $\hat{\mathbf{m}}$ in (8.13)), then resonant scattering tensor becomes

$$T_{ij} = a \begin{pmatrix} 1 & 0 & 0 \\ 0 & 1 & 0 \\ 0 & 0 & 1 \end{pmatrix} + b \begin{pmatrix} 0 & m_z & -m_y \\ -m_z & 0 & m_x \\ m_y & -m_x & 0 \end{pmatrix} + c \begin{pmatrix} m_x^2 - \frac{1}{3} & m_x m_y & m_x m_z \\ m_x m_y & m_y^2 - \frac{1}{3} & m_y m_z \\ m_x m_z & m_y m_z & m_z^2 - \frac{1}{3} \end{pmatrix}.$$
(8.15)

As $m_x^2 + m_y^2 + m_z^2 = 1$, the above tensor has a total of five independent parameters (four fewer than the most general case in (8.8)): one for the scalar term, three for the magnetic vector term, one extra parameter for the third term, describing the uniaxial anisotropy. The scalar and vector terms in (8.13) and (8.14) are completely general but the symmetric rank-two tensor is not. It is, therefore, clear that the standard expression for E1E1 resonant scattering, given by Hannon et al. [10] and reproduced in (8.14), is a complete description of the scalar and magnetic terms, but offers only a highly simplified model of anisotropic resonant scattering. Despite this limitation, it has proved extremely effective for the interpretation of resonant

scattering from magnetic systems, particularly in systems where the anisotropy of the electronic orbitals is dominated by magnetic (i.e., spin–orbit) interactions, rather than the electric field of a highly anisotropic crystalline environment.

Before leaving this section, we note that (8.14) encompasses both magnetic linear and circular dichroism. From the optical theorem (Sect. 8.1) and taking $\varepsilon = \varepsilon'$, we find the absorption cross-section to be

$$\gamma = F''^{(0)} + i \,\hat{\mathbf{m}} \cdot (\hat{\varepsilon} \times \hat{\varepsilon}^*) F''^{(1)} + |\hat{\varepsilon} \cdot \hat{\mathbf{m}}|^2 F''^{(2)}$$
(8.16)

where " indicates the imaginary part of the scattering amplitude. (It can be shown, as an exercise, that all the polarization factors in (8.16) are purely real, and so the requirement of the optical theorem to select the imaginary part of the scattering amplitude becomes a requirement to select the imaginary parts of $F^{(0,1,2)}$). The first term is the (normal) isotropic absorption. The third is magnetic linear dichroism [12] and depends in the direction of linear polarization relative to the magnetic vector, $\hat{\mathbf{m}}$. The only term that is linear in $\hat{\mathbf{m}}$, and changes sign with the magnetic vector direction, is the second term. This term vanishes if $\hat{\varepsilon}$ is real, and exists only when the beam is circularly polarized. For right- and left-hand circularly polarized beams, propagating along the z direction, we can write

$$\hat{\varepsilon}_{\pm} = \frac{1}{\sqrt{2}} \begin{pmatrix} 1\\ \pm i\\ 0 \end{pmatrix}, \tag{8.17}$$

which gives

$$\gamma_{\pm} = F''^{(0)} \pm \hat{\mathbf{m}} \cdot \hat{\mathbf{z}} F''^{(1)} + \frac{1 - (\hat{\mathbf{m}} \cdot \hat{\mathbf{z}})^2}{2} F''^{(2)},$$
 (8.18)

and so it is clear that X-ray magnetic circular dichroism (XMCD) requires both circularly polarized X-rays and a component of the magnetic vector along the beam direction, as we saw in Sect. 8.2.

8.5 Neumann's Principle and Symmetry-restricted Tensors

Derivation of properties of magnetic scattering from a material on the basis of symmetry, as discussed in Sects. 8.2 and 8.4, is an example of the application of Neumann's Principle. The principle has been couched in several ways but it is, essentially, that *Any symmetry of a material must also be possessed by any physical property of the material*. By *physical property* we mean any observable, and this includes the intensity, polarization, and relative phase of X-ray scattering. Thus, if we describe the scattering by a tensor, where each tensor component is potentially observable, then the tensor components must be invariant with respect to all the symmetries of the crystal.

In the tensor description of X-ray scattering, we obtain the scalar scattering amplitude by contracting a tensor describing the X-ray probe, X, [4] with one describing the scattering properties of the sample, T. As the resulting scalar quantity is invariant with respect to all symmetry transformations, it follows that any symmetry (or antisymmetry) of X is an effective symmetry (or antisymmetry) of T and vice versa. For example, a linearly polarized X-ray beam has mirror symmetry, which is effectively passed to the sample, making it impossible to probe chirality in an absorption measurement. Chiral properties can be probed only with a chiral probe. Similarly time-odd properties of T can only be accessed using a time-odd tensor X. The hand must fit the glove!

Throughout this chapter, we take the most general form of a scattering tensor as a starting point and "symmetrize" it by forcing it to be consistent with the sample symmetry operators. In some cases, these involve crystallographic (point- and space-group) symmetry operations, which are functions of spatial variables only. In other cases, the symmetry includes a description of magnetism (see Sect. 8.8), which is formalized by selectively including (or not) time-reversal with each of the crystallographic symmetry operators [13]. Often, the magnetic configuration is incompatible with the basic crystal symmetry, leading to very weak Bragg reflections that characterize this weak symmetry breaking. Sometimes, translation symmetry is partially or completely destroyed, leading to incommensurate modulations with wavevectors that have no rational relationship to the basic lattice parameters. All these phenomena are hugely important for studies of magnetic materials.

A final comment concerns the symmetry of a crystal that is interacting with an external field, such as a magnetic or electric field or uniaxial pressure. While the basic crystallographic symmetry remains unchanged (in the absence of a phase transition), the exact symmetry group of the crystal/field system is given by the *intersection* of the symmetry elements of the crystal and field. In practice, this means throwing away any symmetry element of the crystal that is not compatible with the field, such as rotations about any axis that is not the field direction or reflections in any plane that is not normal to the field. Although this is likely to be a minor perturbation, it may lead to a partial violation of glide-plane and screw-axis extinction rules, and allow weak Bragg reflections that characterize the interaction between the crystal and external field.

8.6 Scattering Matrix and Stokes Parameters

The scattering matrix [14] operates on a two-element polarization vector, rather than the three-element vector employed in the previous section, to give the amplitude and polarization of the scattered wave. Conventionally, the polarization basis states are those of σ and π polarization, that is, linear polarization perpendicular or parallel to the scattering plane. Scattering is completely described by the scattering amplitudes for the four polarization "channels," normally referred to as "sigma to pi" etc, and

we write

$$G = \begin{pmatrix} f_{\sigma-\sigma'} & f_{\pi-\sigma'} \\ f_{\sigma-\pi'} & f_{\pi-\pi'} \end{pmatrix}. \tag{8.19}$$

An advantage with this formalism is that it employs only the two possible polarization directions (transverse components of light are not, of course, allowed). A disadvantage is that this requires a special frame of reference for each beam, and the scattering matrix does not transform in a simple way, that is, as a tensor.

When the scattering intensity of interest corresponds to well-defined polarizations states, then the scattering matrix does not offer significant benefit. The scattering matrix approach comes into its own when combined with the polarization density matrix, which gives a complete description of the average state of polarization, including partially polarized beams. It can be written in terms of Stokes parameters [14]:

$$\mu = \frac{1}{2} \begin{pmatrix} 1 + P_3 & P_1 - iP_2 \\ P_1 + iP_2 & 1 - P_3 \end{pmatrix}$$
 (8.20)

where P_3 , P_1 , and P_2 are, respectively, the Stokes parameters for linear polarization perpendicular to the scattering plane, linear polarization at 45° to the plane, and circular polarization. The total polarization, P, which is unity for a completely polarized beam, is given by

$$P^2 = P_1^2 + P_2^2 + P_3^2 \le 1. (8.21)$$

One of the appeals of Stokes parameters is that they describe intensities and are closely related to measurements. Indeed, one can obtain a useful working definition of the Stokes parameters by considering the results of a measurement using a perfect polarization filter. For example, the value of P_3 could be obtained from a measurement of the ratio of transmitted to incident beam intensity through a perfect polarizing filter that transmits only linear polarization perpendicular to the scattering plane:

$$P_3 = 2\frac{I}{I_0} - 1. (8.22)$$

For complete (linear) polarization, $I = I_0$ and so $P_3 = +1$; for the opposite polarization (polarization parallel to the scattering plane), I = 0 and so $P_3 = -1$; and for an unpolarized beam, $I = I_0/2$ and so $P_3 = 0$. We can similarly define the other Stokes parameters.

With a knowledge of the incident beam polarization and scattering matrix, we can now take advantage of the very useful results [14]

$$I = \text{Tr}(G\mu G^+) \tag{8.23}$$

and

$$\mu' = \frac{1}{I} G \mu G^+, \tag{8.24}$$

where Tr is the trace (sum of diagonal elements), $^+$ indicates a Hermitian conjugate (transpose of complex conjugate), and μ' is the polarization density of the scattered beam.

The scattering matrix, G, can be thought of as an operator that transforms the initial beam into the final beam. If two sequential scattering processes are involved, then one can operate sequentially with two scattering matrices. A common example is when first the sample scatters the beam and then a polarization analyzer crystal scatters the secondary beam into an X-ray detector. We call the scattering matrix for the polarization analyzer the *analyzer matrix*, A, and for the common case of isotropic kinematical scattering from a crystal polarization analyzer, we find [15]

$$A = \begin{pmatrix} \cos \eta & -\sin \eta \\ \cos 2\phi \sin \eta \cos 2\phi \cos \eta \end{pmatrix}, \tag{8.25}$$

where η is the rotation angle of the analyzer about the scattered beam and ϕ is the analyzer crystal Bragg angle (note that this device is a perfect linear polarization analyzer only when $\phi = \pi/4$). The combined scattering matrix is simply the product of the two and we find

$$I = \text{Tr}(AG\mu G^+ A^+). \tag{8.26}$$

With this expression and the scattering matrix elements, we can calculate the intensity from an arbitrary, partially polarized incident beam, and nonideal linear polarization analyzer.

8.7 Diffraction Intensity and the Unit-Cell Structure Factor

X-ray diffraction intensities can, in all cases other than strong scattering from high-quality crystals, be interpreted within the framework of "kinematical diffraction," which is based on the Born approximation. One typically measures the ratios of Bragg reflections, integrated over the Bragg angle, θ . Expressions for such an integrated signal are given in the literature [16] and are of the form

$$\frac{I}{I_0} \propto |F|^2 \, \frac{N\lambda^3}{\nu} \frac{1}{\sin 2\theta},\tag{8.27}$$

where F is the unit cell structure factor (scattering amplitude) and N is the number of unit cells of volume v that are effective in scattering. The usual formulation includes a polarization factor, but we prefer to include this factor in the structure factor as we are interested in a range of processes, all with different polarization dependence. Often, all factors in (8.27) are constant and we typically associate the scattering intensity with $|F|^2$ directly. For comparisons between different reflections, some of the other factors may be required.

The unit cell structure factor is given by the sum or integral over all scatterers at positions \mathbf{r} within a unit cell, taking into account the phase factor at each point that arise from the path differences between beams scattered from different points:

$$F(\mathbf{k}) = \sum_{\text{cell}} f e^{i\mathbf{k}\cdot\mathbf{r}}.$$
 (8.28)

where $\mathbf{k} = \mathbf{q}' - \mathbf{q}$.

For nonresonant scattering, this expression becomes an integral over the continuous electron density. Resonant scattering is much simpler because the process requires a core electron, which exists only very close to the nucleus and is typically taken as a point in space. We therefore need to consider only the sum of a finite number of points, each representing the site of a resonant ion. Because of the point-like nature of the scattering, there is no form factor, but the Debye–Waller temperature factor [16] is still expected to be active.

Calculation of structure factors is greatly facilitated by adopting crystal (real and reciprocal space) coordinates, and one finds

$$F_{hkl} = \sum_{n=1}^{N} f_n e^{2\pi i (hx + ky + lz)},$$
 (8.29)

where hkl are the Miller indices of the reflection and xyz are the positions of the resonant ion in crystal coordinates. Finally, we note that (8.29) can equally well describe the relationship between the atomic resonant scattering tensor and the structure factor tensor.

In this chapter, we concern ourselves mainly with "forbidden reflections" where the structure factors and hence diffraction intensities are exactly zero by symmetry. There are other cases where the scattering from point-like (or spherical) atoms, as given by (8.29), is zero but the exact structure factor for the continuous electron density is small but not zero, as they are not ruled out by spacegroup symmetry. In other cases, the resonant scattering can be given by the sum of structure factors from different processes, leading to interference effects. We do not discuss these in this chapter.

8.8 Magnetic Symmetry, Propagation Vector, and the Magnetic Structure Factor

The goal of this section is to provide the reader with some basic ideas and references that can be useful when dealing with magnetic structure. Although the determination of complex magnetic structures using X-ray resonant scattering is not yet well developed, we are able to take competing models and consider the resulting resonant scattering signals. Here, we assume the structure to be known by other methods.

We have referred several times to the concept of invariance of the tensors under the symmetry operations of the space group. In the same way, it is natural to associate with a magnetic structure a new sets of symmetry elements, including transformation properties under time reversal. Several symbols have been adopted to define the operation of time reversal and here we use T or '. Shubnikov [17] considered the group of figures with "black and white" symmetries and called these "antisymmetry" groups. This terminology indicates that we are concerned with the connection between objects that are opposite (i.e., black and white or +1 and -1) rather than objects that are the same. The analogy between these groups and the symmetry element T is immediately seen. A black element is a space–time even symmetry and a white element is a space–time odd symmetry. Therefore, under a white symmetry, a black object will be transformed into a white object. Magnetic point groups can contain ordinary crystallographic symmetry elements like rotations and reflections, the element T, and their combination. The point groups where the element T enters only in combination with a crystallographic symmetry are called black and white. They represent magnetic systems. If T alone is a symmetry element, then the system is time-even and nonmagnetic.

While the concept of magnetic symmetry is sufficient to describe a large number of magnetic structures, there remain many that are not invariant under any of these groups, even though the atomic positions and charge density are described quite precisely by the underlying crystallographic space group. Two well-known cases where this framework is not useful are the description of the helical and/or semi-ordered (e.g., spin density wave) structures [18]. In the first case, the symmetry does not include spin rotations over non-crystallographic angles, and in the second, the required nonconservation of the absolute value of the ordered spin is not allowed.

Despite these limitations, even when dealing with semi-ordered structures, magnetic symmetry can be an useful approach when the deviation from a symmetry is small enough that its contribution to the scattering can be neglected, as we see in Sect. 8.13. A more general description of magnetism uses group representation theory and investigates the transformation properties of magnetic structures under the operations of the normal 230 space groups and searches for the irreducible representations and basis functions capable of describing them [18, 19]. This approach contains the magnetic (Shubnikov) groups as a special case.

While the point group of a material describes its macroscopic properties, the atomic-scale properties are determined by the space group, which includes translational symmetry. The structure of the ordered magnetic systems will be described by the corresponding magnetic space group. Several cases can occur:

- The magnetic ordering maps perfectly onto the crystallographic symmetry; therefore, there are no additional periodicities leading to new Bragg reflections, and there is no change to the crystal translational symmetry (e.g., a ferromagnet).
- The magnetic ordering introduces a new (larger) periodicity that is *commensurate* with the crystallographic unit cell, that is, the magnetic translation vectors are integer multiples of the crystallographic ones. In this case, if there is more than one magnetic ion in the crystallographic cell, the crystallographic unit cell *may* still be adequate to describe the magnetic ordering, but often multiple cells are required.

• The magnetic ordering introduces a new periodicity that is *incommensurate* with the crystal structure. In this case, exact crystallographic translational symmetry is destroyed in one or more directions and extra Bragg reflections are observed that have no rational relationship with the normal reflections.

The first two cases can be relatively easily accommodated even when the large number of cells required makes this description inconvenient. For the third case, it is necessary to introduce the concept of the magnetic propagation vector as a convenient way of describing the translational properties of the magnetic symmetry. In the following, we consider only magnetic configurations where the moments are attached to the ions defining the crystal structure. This is appropriate for the description of resonant X-ray scattering because it is a "local" probe that is sensitive only to magnetism in the vicinity of atomic core electrons. A complete description of the magnetic moment \mathbf{m}_n at any magnetic site n (assuming a single magnetic ion type) is given by

$$\mathbf{m}_n = \sum_{\{\mathbf{\tau}_m\}} \mathbf{S}_{\mathbf{\tau}_m} e^{-i\mathbf{\tau}_m \cdot \mathbf{R}_n}, \tag{8.30}$$

where the set of vectors $\{\tau_m\}$ are restricted to the first Brillouin zone, the vectors \mathbf{R}_n span the crystal lattice, and the complex \mathbf{S}_{τ_m} are the Fourier components describing the magnetic moment distribution in the material. Often the sum over $\{\tau_m\}$ reduces to a single or to a small number of symmetrically equivalent vectors, hugely simplifying this expression. Substituting this equation into the expression for the unit-cell structure factor, it is a straightforward exercise to show that $F(\mathbf{k}) = 0$ unless $\mathbf{k} = \mathbf{h} + \tau_m$, where \mathbf{h} is a vector of the reciprocal lattice and τ_m is a propagation vector. Therefore, the structure factor formula holds for the integrated intensity of a magnetic reflection if the appropriate changes are made:

$$F(\mathbf{h} + \boldsymbol{\tau}_m) = \sum_{j} \mathbf{S}_{\boldsymbol{\tau}_m} \, \mathrm{e}^{\mathrm{i}(\mathbf{h} + \boldsymbol{\tau}_m) \cdot \mathbf{R}_j}$$
 (8.31)

or, equivalently,

$$F(\mathbf{H} + \boldsymbol{\tau}) = \sum_{j} \mathbf{S}_{\boldsymbol{\tau}} e^{2\pi i (\mathbf{H} + \boldsymbol{\tau}) \cdot \mathbf{r}_{j}}, \qquad (8.32)$$

where the sum runs over all magnetic ions in the unit cell. The two expression above are equivalent, except that the second is written in terms of crystal coordinates, that is, \mathbf{r}_j is the atomic site vector expressed as fractions of the unit cell lengths, \mathbf{H} is the set of Miller indices (hkl values) of the reflection, and $\boldsymbol{\tau}$ is the modulation vector in reciprocal lattice units.

The same kind of description can be followed for every type of periodic order that is established in the crystal and leads to diffraction.

8.9 Crystal Coordinates and Azimuthal Rotations

The main topic of this chapter is the calculation of geometrical properties of resonant scattering, that is, polarization and rotation dependence. The most tedious part of the calculation involves making the rotations necessary to access the desired reflection, **h**, with the desired azimuthal angle, ψ . Here, we outline a method for performing these transformations, which may be skipped by those who are not concerned with such details. We adopt, where practical, the notation of Busing and Levy [20] and opt to rotate the relevant "X-ray probe" vectors to the coordinate system of the scattering tensor, rather than rotating the scattering tensor. While the two approaches are equivalent, the machinery for transforming the scattering tensor depends on rank, whereas the X-ray scattering "probe" is always constructed from known vectors. We define several coordinate systems, each denoted by a subscript character: X (crystal coordinates), C (crystal Cartesian coordinates), ψ (coordinate system attached to the diffraction geometry, with the azimuthal reference in the xy plane), and θ (general diffraction coordinate system, rotated by an azimuthal angle ψ about the scattering vector). Our goal is to transform everything to the crystal Cartesian system.

It is often convenient to consider the properties of the scattering tensor in the crystal Cartesian coordinate system, where symmetries can either be applied manually from a knowledge of the symmetry operations or transformed from those found in the *International Tables* [21], from crystal to crystal Cartesian coordinates via the **B** matrix, described below and in (8.61). Any (column) vector \mathbf{v} in the experimental θ coordinate system can then be transformed to the crystal Cartesian system via

$$\mathbf{v}_C = \mathbf{U}^{C\psi} \mathbf{v}_{\psi} = \mathbf{U}^{C\psi} \mathbf{U}^{\psi\theta} \mathbf{v}_{\theta} = \mathbf{U}^{C\psi} \mathbf{R}_{-\psi}^x \mathbf{v}_{\theta}, \tag{8.33}$$

where

$$\mathbf{U}^{\psi\theta} = \mathbf{R}^{x}_{-\psi} = \begin{pmatrix} 1 & 0 & 0 \\ 0 & \cos\psi & \sin\psi \\ 0 - \sin\psi & \cos\psi \end{pmatrix}$$
(8.34)

rotates the sample about $\hat{\mathbf{x}} (\equiv \hat{\mathbf{h}})$ from some general azimuthal angle, ψ , to $\psi = 0$ (the ψ coordinate system), and $\mathbf{U}^{C\psi}$ is the unitary transformation from the ψ to the crystal Cartesian system. This matrix, which is the key to the calculation, can be derived by noting that

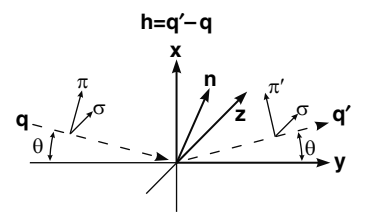
$$\mathbf{U}^{C\psi}\hat{\mathbf{z}}_{\psi} = \hat{\mathbf{h}}_{C} = \hat{\mathbf{x}}' = \widehat{\mathbf{Bh}}_{X}$$

$$\mathbf{U}^{C\psi}\hat{\mathbf{z}}_{\psi} = \widehat{\mathbf{h}}_{C} \times \widehat{\mathbf{n}}_{C} = \hat{\mathbf{z}}' = \widehat{\mathbf{Bh}}_{X} \times \widehat{\mathbf{Bn}}_{X}$$

$$\mathbf{U}^{C\psi}\hat{\mathbf{y}}_{\psi} = \hat{\mathbf{y}}' = \hat{\mathbf{z}}' \times \hat{\mathbf{x}}', \tag{8.35}$$

and we can adopt the definition of the **B** matrix which transforms from crystal (reciprocal lattice) to crystal Cartesian system, from [20]

Fig. 8.3 The θ coordinate system for scattering geometry. The ψ coordinate system differs only by a notation by ψ about $\hat{\mathbf{x}}$, which brings \mathbf{n} into the xy plane



$$\mathbf{B} = \begin{pmatrix} b_1 \ b_2 \cos \beta_3 & b_3 \cos \beta_2 \\ 0 \ b_2 \sin \beta_3 - b_3 \sin \beta_2 \cos \alpha_1 \\ 0 \ 0 \ 1/a_3 \end{pmatrix}, \tag{8.36}$$

where the a_i 's and α_i 's and the b_i 's and β_i 's are the direct and reciprocal lattice parameters, respectively [8, 20], and $\hat{\mathbf{n}}_X$ is the azimuthal reference hkl vector. The required transformation matrix can now be constructed from

$$\mathbf{U}^{C\psi} = (\hat{\mathbf{x}}', \hat{\mathbf{y}}', \hat{\mathbf{z}}'). \tag{8.37}$$

With reference to Fig. 8.3, we can write

$$\hat{\mathbf{h}}_{\theta} = \widehat{\mathbf{q}'_{\theta} - \mathbf{q}_{\theta}} = \begin{pmatrix} 1\\0\\0 \end{pmatrix} \hat{\mathbf{q}}_{\theta} = \begin{pmatrix} -\sin\theta\\\cos\theta\\0 \end{pmatrix} \hat{\mathbf{q}}'_{\theta} = \begin{pmatrix} \sin\theta\\\cos\theta\\0 \end{pmatrix},$$

$$\hat{\varepsilon}_{\sigma} = \hat{\varepsilon}'_{\sigma} = \begin{pmatrix} 0\\0\\1 \end{pmatrix} \hat{\varepsilon}_{\pi} = \begin{pmatrix} \cos\theta\\\sin\theta\\0 \end{pmatrix} \hat{\varepsilon}'_{\pi} = \begin{pmatrix} \cos\theta\\-\sin\theta\\0 \end{pmatrix}, \quad (8.38)$$

where

$$\sin \theta = \frac{\lambda}{2d} = \frac{\lambda |\mathbf{Bh}_X|}{2} = \frac{\lambda}{2} \left| \mathbf{B} \begin{pmatrix} h \\ k \\ l \end{pmatrix} \right|, \tag{8.39}$$

where h, k, and l are the Miller indices of the reflections. Armed with the definitions of these vectors and the means to transform them into the crystal Cartesian coordinate system, we can construct the required X tensors in the reference frame that is usually most convenient for considering the physical properties of the resonant scattering tensors.

8.10 Spherical and Cartesian Tensors

Spherical tensors, which are closely related to spherical harmonics and to the quantum mechanical treatment of angular momentum, are often used to describe resonant X-ray scattering [22]. They are useful partly because of their connection to atomic

properties but mainly because they are irreducible. That is, they do not contain within them tensors of lower rank. In Sect. 8.4, we saw that a Cartesian tensor of rank two, which contains $3^3 = 9$ components, can be split into three terms: one that transforms as a scalar (the identity matrix), one that transforms as an axial vector, and a symmetric rank-two tensor. These parts contain 1, 3, and 5 components, respectively. It is no coincidence that these are also the number (2J + 1) of projections of angular momentum J. As with angular momentum, a spherical tensor of rank K has 2K + 1 components. Using spherical tensor components to describe a tensor of rank K therefore has the advantages over the Cartesian equivalent, that its transformation properties are better defined and that it requires fewer numbers (5 rather than 9 in the rank-two case). The benefits in terms of economy of notation become more apparent as the tensor rank increases: a fourth-rank spherical tensor requires only nine components, compared to 81 for the Cartesian form.

The disadvantages of spherical tensors are that their manipulation tends to be more of a mathematical challenge than for Cartesian tensors, and there can be common pitfalls such as inconsistency of phase conventions between different authors. Moreover, they are less clearly related to the natural coordinate systems of crystals, some of which nature has even chosen to be Cartesian, that is, cubic!

Manipulation of spherical tensor components is straightforward if they are given in a form that has well-defined symmetry under inversion and time-reversal. Fortunately, most of the results of interest in X-ray scattering have already been derived in such a way [4, 23]. Tensors that are even (odd) under inversion simply have all components multiplied by +1 (-1) when this symmetry operator is applied, and likewise for time-reversal. The possible inversion/time-reversal symmetry of tensors describing multipole resonances up to E2E2 transitions is given in Table 8.1. It is interesting to note [4, 23] that for parity-even tensors, the time-reversal signature is given by $(-1)^K$, whereas for parity-odd tensors there is no such relationship and the tensors have no well-defined symmetry under time reversal. It is therefore convenient to split them into parts that are time-even (U) and time-odd (G).

To calculate the scattering amplitude and intensity for a resonant process described by some set of spherical tensor components, the tensor describing the atomic scattering must be contracted with a tensor of the same rank and inversion/time-reversal symmetry which describes the X-ray probe (X_Q^K) , to form a scalar [4]:

$$f = \sum_{K} \sum_{Q=-K}^{K} (-1)^{Q} X_{Q}^{K} F_{-Q}^{K}.$$
 (8.40)

The *X* tensors for E1E1 contributions to the scattering are written below in terms of projections of the polarization vectors in the coordinate system depicted in Fig. 8.3:

$$X_{\text{EIEI}}^{0} = \left(\frac{-\varepsilon_{x}\varepsilon_{x}' - \varepsilon_{y}\varepsilon_{y}' - \varepsilon_{z}\varepsilon_{z}'}{\sqrt{3}}\right) = -\frac{1}{3}\boldsymbol{\varepsilon} \cdot \boldsymbol{\varepsilon}', \tag{8.41}$$

K	P+T+	P+T-	Mpol	Ref	P-T+	P-T-	Mpol	Ref
0	T^0	×	E1E1 E2E2	a c	U^0	G^0	(E1M1)	b
1	×	T^1	E1E1 E2E2	a c	U^1	G^1	E1E2 (E1M1)	d b
2	T^2	×	E1E1 E2E2	a c	U^2	G^2	E1E2 (E1M1)	d b
3	×	T^3	E2E2	c	U^3	G^3	E1E2	d
4	T^4	×	E2E2	c	**			

Table 8.1 Tensor rank, symmetry under parity and time-reversal, and allowed multipole transitions

The references in the table give expressions for the X_Q^K (X-ray) spherical tensors for various processes. A detailed Cartesian treatment is given in [3]. E1M1 transitions are relatively obscure with X-rays and are shown in brackets

$$\begin{split} X_{\text{EIEI}}^{1} &= \left(\frac{\varepsilon_{z}\varepsilon_{x}^{\prime} - \mathrm{i}\varepsilon_{z}\varepsilon_{y}^{\prime} - \varepsilon_{x}\varepsilon_{z}^{\prime} + \mathrm{i}\varepsilon_{y}\varepsilon_{z}^{\prime}}{2}, \frac{-\mathrm{i}\varepsilon_{y}\varepsilon_{x}^{\prime} + \mathrm{i}\varepsilon_{x}\varepsilon_{y}^{\prime}}{\sqrt{2}}, \right. \\ &\left. \frac{\varepsilon_{z}\varepsilon_{x}^{\prime} + \mathrm{i}\varepsilon_{z}\varepsilon_{y}^{\prime} - \varepsilon_{x}\varepsilon_{z}^{\prime} - \mathrm{i}\varepsilon_{y}\varepsilon_{z}^{\prime}}{2} \right), \\ X_{\text{EIEI}}^{2} &= \left(\frac{\varepsilon_{x}\varepsilon_{x}^{\prime} - \mathrm{i}\varepsilon_{y}\varepsilon_{x}^{\prime} - \mathrm{i}\varepsilon_{x}\varepsilon_{y}^{\prime} - \varepsilon_{y}\varepsilon_{y}^{\prime}}{2}, \frac{\varepsilon_{z}\varepsilon_{x}^{\prime} - \mathrm{i}\varepsilon_{z}\varepsilon_{y}^{\prime} + \varepsilon_{x}\varepsilon_{z}^{\prime} - \mathrm{i}\varepsilon_{y}\varepsilon_{z}^{\prime}}{2}, \right. \\ &\left. \frac{-\varepsilon_{x}\varepsilon_{x}^{\prime} - \varepsilon_{y}\varepsilon_{y}^{\prime} + 2\varepsilon_{z}\varepsilon_{z}^{\prime}}{\sqrt{6}}, \frac{-\varepsilon_{z}\varepsilon_{x}^{\prime} - \mathrm{i}\varepsilon_{z}\varepsilon_{y}^{\prime} - \varepsilon_{x}\varepsilon_{z}^{\prime} - \mathrm{i}\varepsilon_{y}\varepsilon_{z}^{\prime}}{2}, \\ &\left. \frac{\varepsilon_{x}\varepsilon_{x}^{\prime} + \mathrm{i}\varepsilon_{y}\varepsilon_{x}^{\prime} + \mathrm{i}\varepsilon_{x}\varepsilon_{y}^{\prime} - \varepsilon_{y}\varepsilon_{y}^{\prime}}{2} \right). \end{split} \tag{8.42}$$

The X tensors can be transformed into the crystal coordinate system by rotating the vector component in the above expressions, as described in Sect. 8.9. Alternatively, one can keep the X tensor fixed and rotate the scattering tensor.

Having determined that inversion and time-reversal operations are rather trivial with suitably formed tensors, the only remaining symmetry operation required is rotation, which can be carried out with a Wigner D matrix. These are described in detail in the literature [4, 22, 24] and used in Sects. 8.12 and 8.13. We will not describe them further here, other than to say that they are $(2K+1)\times(2K+1)$ matrices that operate on a 2K+1 component tensor in much the same way that a Cartesian rotation matrix operates on a vector. The Wigner D matrices can be computed from a set of three Euler angles that represent the rotation [24]. However, as the Euler

^a [4] Equation (66)

^b [23] Equations (6.2) and (6.8)

^c [4] Equations (77) and (78)

^d [4] Equations (115), (116) and (119)

angles are referenced to a particular coordinate system, it can be tricky using this approach to apply crystallographic symmetry as one often encounters coordinate singularities. These are avoided with Cartesian tensors by working directly with the crystallographic unitary transformations, which no not require angles.

As there is sometimes real benefit in working with spherical tensors, and sometimes with Cartesian tensors, it can be convenient to convert between the two forms. This we do following the procedure of Stone [25] (This procedure can be particularly useful for applying symmetry constraints to spherical tensors based on Cartesian matrices. One can convert to Cartesian form, apply symmetry, and convert back to spherical form).

Conversion between spherical tensor components T_Q^K and corresponding Cartesian components $T_{ijk...}$ can be carried out using the following expressions:

$$T_{Q}^{K} = \sum_{ijk...} T_{ijk...} C_{Q;ijk...}^{K}$$
(8.44)

$$T_{ijk...} \sum_{Q} T_{Q}^{K} C_{Q;ijk...}^{K*},$$
 (8.45)

where the conversion coefficients are given in Tables 8.2–8.5. The coefficients are calculated using the Condon and Shortley phase convention, and we follow Stone's notation for the sequence of tensor coupling, that is, C^{1234} for rank four. For the present discussion, we consider only the special case where the coupling gives the maximum possible rank, although the same procedure can be used to carry out a complete decomposition of a general cartesian tensor into all of its irreducible spherical components.

To illustrate the use of the conversion coefficients, consider the spherical vector (i.e., spherical harmonic) (0,1,0), or $T_0^1=1, T_{-1}^1=T_1^1=0$. Conversion to Cartesian form gives (0,0,1), or $T_z^1=1, T_x^1=T_y^1=0$. Similarly, we find that the spherical components (0,0,1) transform into the Cartesian vector $\frac{1}{\sqrt{2}}(-1,i,0)$.

8.11 Example: HoFe₂

To illustrate some of the key points discussed in this chapter, we consider some specific examples. The first of these, the ferromagnet HoFe₂, is chosen because

Table 8.2 Cartesian-to-spherical conversion coefficients for rank-one tensors

$$C_{-1}^{1} = \frac{1}{\sqrt{2}}(1, -i, 0)$$

$$C_{0}^{1} = (0, 0, 1)$$

$$C_{1}^{1} = \frac{1}{\sqrt{2}}(-1, -i, 0)$$

Table 8.3 Cartesian-to-spherical conversion coefficients for rank-two tensors

$$C_{-2}^{12} = \frac{1}{2}((1, -i, 0), (-i, -1, 0), (0, 0, 0))$$

$$C_{-1}^{12} = \frac{1}{2}((0, 0, 1), (0, 0, -i), (1, -i, 0))$$

$$C_{0}^{12} = \frac{1}{\sqrt{6}}((-1, 0, 0), (0, -1, 0), (0, 0, 2))$$

$$C_{1}^{12} = \frac{1}{2}((0, 0, -1), (0, 0, -i), (-1, -i, 0))$$

$$C_{2}^{12} = \frac{1}{2}((1, i, 0), (i, -1, 0), (0, 0, 0))$$

 Table 8.4 Cartesian-to-spherical conversion coefficients for rank-three tensors

$$\begin{split} \overline{C_{-3}^{123}} &= \frac{1}{\sqrt{8}}(((1,-i,0),(-i,-1,0),(0,0,0)),((-i,-1,0),(-1,i,0),(0,0,0)),\\ & \qquad \qquad ((0,0,0),(0,0,0),(0,0,0))) \\ C_{-2}^{123} &= \frac{1}{\sqrt{12}}(((0,0,1),(0,0,-i),(1,-i,0)),((0,0,-i),(0,0,-1),(-i,-1,0)),\\ & \qquad \qquad ((1,-i,0),(-i,-1,0),(0,0,0))) \\ C_{-1}^{123} &= \frac{1}{\sqrt{120}}(((-3,i,0),(i,-1,0),(0,0,4)),((i,-1,0),(-1,3i,0),(0,0,-4i)),\\ & \qquad \qquad ((0,0,4),(0,0,-4i),(4,-4i,0))) \\ C_{0}^{123} &= \frac{1}{\sqrt{10}}(((0,0,-1),(0,0,0),(-1,0,0)),((0,0,0),(0,0,-1),(0,-1,0)),\\ & \qquad \qquad ((-1,0,0),(0,-1,0),(0,0,2))) \\ C_{1}^{123} &= \frac{1}{\sqrt{120}}(((3,i,0),(i,1,0),(0,0,-4)),((i,1,0),(1,3i,0),(0,0,-4i)),\\ & \qquad \qquad ((0,0,-4),(0,0,-4i),(-4,-4i,0))) \\ C_{2}^{123} &= \frac{1}{\sqrt{12}}(((0,0,1),(0,0,i),(1,i,0)),((0,0,i),(0,0,-1),(i,-1,0)),\\ & \qquad \qquad ((1,i,0),(i,-1,0),(0,0,0))) \\ C_{3}^{123} &= \frac{1}{\sqrt{8}}(((-1,-i,0),(-i,1,0),(0,0,0)),((-i,1,0),(1,i,0),(0,0,0)),\\ & \qquad \qquad ((0,0,0),(0,0,0),(0,0,0))) \end{split}$$

it has been shown [15] to exhibit relatively strong resonant forbidden scattering, which is adequately described within the electric dipole approximation. The material is cubic, with spacegroup $Fd\overline{3}m$ (same as diamond), with iron atoms situated on threefold axes at positions $(\frac{5}{8}, \frac{5}{8}, \frac{5}{8})$, etc. We concern ourselves only with the iron atoms, as the goal is to model the angle- and polarization-dependence of iron K-edge resonant forbidden diffraction. The most general form of the Cartesian atomic scattering tensor, within the dipole approximation and neglecting magnetic scattering, is a symmetric tensor with six independent elements:

$$\begin{split} \textbf{Table 8.5.} & \quad \text{Cartesian-to-spherical conversion coefficients for rank-four tensors} \\ \hline C_{-3}^{124} &= \frac{1}{4}((((1,-i,0),(-i,-1,0),(0.0,0)),((-i,-1,0),(-1,i,0),(0.0,0)),((0.0,0),(0.0,0),(0.0,0))), \\ &\quad (((-i,-1,0),(-1,i,0),(0.0,0)),((0.0,0),(0.1,0),(0.0,0)),((0.0,0),(0.0,0),(0.0,0)), \\ &\quad (((0,0,0),(0,0,0),(0.0,0)),((0.0,0),(0.0,0),(0.0,0)),((0.0,0),(0.0,0),(0.0,0))), \\ &\quad (((0,0,0),(0,0,0),(0.0,0)),((0.0,0),(0.0,0),(0.0,0)),((0.0,0),(0.0,0),(0.0,0)))) \\ \hline C_{-3}^{1234} &= \frac{1}{\sqrt{32}}((((0,0,1),(0.0-i),(-i,-1,0)),((0.0-i),(0.0-i),(0.0-i),(0.0-i),(-i,-1,0)),((1.-i,0),(-i,-1,0),(0.0,0))), \\ &\quad (((0,0,-i),(0.0-i),(0.0-i),(-i,-1,0)),((0.0,-i),(0.0,-i),(0.0,0)),((0.0,0),(0.0,0),(0.0,0),(0.0,0))), \\ &\quad (((1,-i,0),(-i,-1,0),(0.0,0)),((-i,-1,0),(-1,i,0),(0.0,0)),((0.0,0),(0.0,0),(0.0,0))), \\ &\quad (((i,0,0),(0.i,0),(0.0-2i)),((0.i,0),(0.0-2i),(0.0,0-2i),((0.0,-2i),(0.0,-2i),(0.0,-2i),(2.-2i,0))), \\ &\quad (((i,0,0),(0.i,0),(0.0-2i)),((0.i,0),(i.2,0),(0.0-2i),(0.0,-2i),(0.0,-2i),(0.0,-2i),(-2i,-2,0))), \\ &\quad (((0,0,2),(0.0-2i),(2.-2i,0),(0.0,-2i),(0.0,-2$$

$$T_{ij} = \begin{pmatrix} a & b & c \\ b & d & e \\ c & e & f \end{pmatrix}. \tag{8.46}$$

The steps required to calculate the diffracted intensity as a function of azimuthal rotation (rotation around the scattering vector at a fixed point in reciprocal space) and linear polarization are as follows: (1) deduce the simplified form of the atomic scattering tensor that is consistent with the symmetry of the atomic environment (this step is optional but informative), (2) calculate the symmetrized structure factor tensor for the reflection(s) of interest, (3) calculate the polarization vectors of interest, which vary with azimuthal angle, expressed in terms of the crystal

Cartesian coordinate system, (4) contract the polarization vectors with the structure factor tensor to produce a scalar amplitude and intensity.

Applying crystal symmetry to the scattering tensor can be carried out either by inspection or more mechanically by performing the symmetry operations mathematically. The first approach may be more intuitive; the latter better suited to computer programs. The iron atoms occupy sites of rhombohedral symmetry $(\overline{3}m)$ where the threefold axes point along the cube diagonals (Fig. 8.4). Recalling that the symmetric second-rank tensor can be represented by an ellipsoid, it is clear that the only ellipsoid compatible with this symmetry must have its unique axis along threefold axis. We have already encountered this symmetry in (8.15), and by taking $m_x = m_y = m_z$ (symmetry axis along a diagonal) and neglecting the antisymmetric term for magnetic scattering, we have

$$T_{ij} = \begin{pmatrix} a & b & b \\ b & a & b \\ b & b & a \end{pmatrix}. \tag{8.47}$$

Given that the scattering tensors from all the other 15 sites are related by symmetry to the first one, it is clear that no more than two independent tensor components will contribute to the scattering at any reflection. Moreover, as one of the components is a scalar (the identity matrix multiplied by a), it contributes only to "allowed" reflections and not to the resonant forbidden scattering driven by anisotropy. Such reflections are therefore determined entirely by a single tensor element b, making our task much easier. To carry out the above procedure in a more mechanical and mathematical way, two approaches are possible. The first is to identify one example of each type of symmetry operator, S, for the site in question and solve a set of equations of the form

$$T_{ij} = S_{Ii}S_{Jj}T_{IJ} (8.48)$$

or in matrix form

$$T = STS^+. (8.49)$$

where, for example, the symmetry operator $\overline{3}$ is given by

$$S = \begin{pmatrix} 0 & -1 & 0 \\ 0 & 0 & -1 \\ -1 & 0 & 0 \end{pmatrix}. \tag{8.50}$$

The second approach is to take the complete group of N symmetry operators for the site (12 in this case) and simply add the resulting tensors, that is,

$$T_{ij} = \sum_{n=1}^{N} S_{Ii}^{n} S_{Jj}^{n} T_{IJ}.$$
 (8.51)

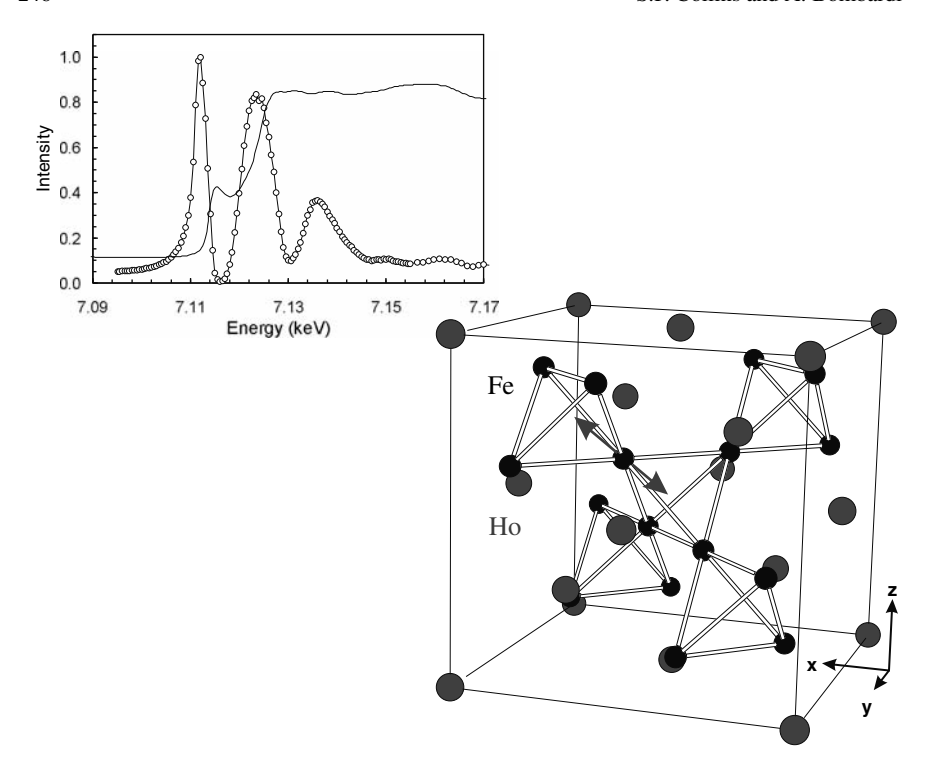


Fig. 8.4 *Top left*: the energy spectrum of resonant forbidden scattering from HoFe₂ (*circles*) superimposed on the absorption spectrum. As with all resonant forbidden scattering, the signal is only large close to the absorption edge. *Bottom right*: the crystal structure of HoFe₂ showing the diagonal threefold axis of one of the iron atoms

This approach is the least physically appealing but the easiest to automate. If magnetism is neglected, then the group of symmetry operators can be obtained in a straightforward way from standard references such as the *International Tables* [21]. Unfortunately, the situation tends to be less well documented when magnetism plays an important role.

The next step is to calculate the unit cell structure factor tensor for the (forbidden) reflection of interest. For this, we follow the procedure in Sect. 8.7, that is, we add the atomic tensor from each iron site within the unit cell, taking into account both the different (but related) configuration of each site and the phase factor, e^{ik.r}. For the (024) reflection, for example, we obtain

$$F_{024} = \begin{pmatrix} 0 & 0 & b \\ 0 & 0 & 0 \\ b & 0 & 0 \end{pmatrix}. \tag{8.52}$$

Again, the form of this tensor is not a surprise. The diagonal terms have vanished as they must for a forbidden reflection, and a single parameter describes the anisotropy.

Having established the form of the structure factor tensor, we must now contract it with the relevant X-ray probe tensor/vectors, which for E1E1 resonant scattering is simply the polarization vectors of the incident and scattered X-ray beam. The only real complication is that these rotate relative to the sample during an azimuthal scan. One must either compute the rotated properties of the scattering tensor or the experimental probe. In Sect. 8.9, we outline a procedure for latter, which fits well with the usual approach of taking the origin of the azimuthal angle with respect to a favored reciprocal lattice vector of the sample.

In [15], the (024) reflection intensity from HoFe₂, at the iron K-edge, was measured as a function of azimuthal rotation for scattered beam polarization states perpendicular to the scattering plane ($\hat{\varepsilon}_0 = \hat{\varepsilon}_\sigma$), perpendicular to the plane ($\hat{\varepsilon}_{90} = \hat{\varepsilon}'_{\pi}$), and at angles of 0 and 135° ($\hat{\varepsilon}_{45}$ and $\hat{\varepsilon}_{135}$). The incident polarization is perpendicular to the scattering plane, as is typical with a synchrotron diffraction experiment. In the experimental (θ) coordinate system shown in Fig. 8.3, the σ and π vectors are given in (8.38), with the vectors for 45 and 135° polarization easily obtained from sums and differences of these:

$$\hat{\varepsilon}_{45} = \frac{1}{\sqrt{2}} \begin{pmatrix} \cos \theta \\ -\sin \theta \\ 1 \end{pmatrix} \quad \hat{\varepsilon}_{135} = \frac{1}{\sqrt{2}} \begin{pmatrix} -\cos \theta \\ \sin \theta \\ 1 \end{pmatrix}. \tag{8.53}$$

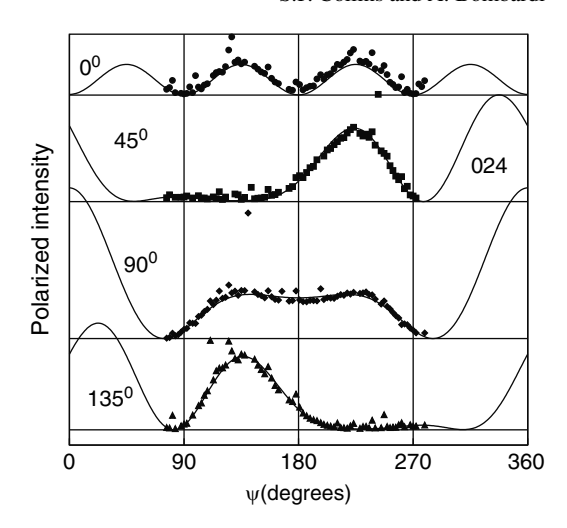
Before contracting these vectors (e.g., $\hat{\varepsilon}_{\sigma}$, $\hat{\varepsilon}'_{45}$ for 45° polarization) with the structure factor tensor, following (8.6) and (8.12), we select a sample hkl vector to define the azimuthal origin (we take the 010 vector), calculate the Bragg angle, θ , for the reflection and wavelength, and use (8.33) to calculate the polarization vectors for each azimuthal angle. Finally, we determine the X-ray intensity (to within an overall scale factor, as per this entire discussion),

$$I \propto |F|^2. \tag{8.54}$$

The resulting curves, reproduced in Fig. 8.5, show a remarkably rich angle and polarization dependence for this, the simplest of resonant scattering processes. The excellent agreement with the model calculations demonstrates that higher order processes, including magnetic scattering, quadrupole resonance, etc., play a negligible role in this case. One might reasonably ask what can be learnt from such an analysis beyond ruling out higher-order (and perhaps more interesting) scattering processes. In fact, "clean" examples such as these are vital for understanding more complex systems where there may be several competing processes. Moreover, pure dipole resonant forbidden scattering has been shown to be extremely sensitive to the atomic coordinates of resonant ions [5] and, recently, to be directly sensitive to chirality in enantiomorphic crystals [26].

Before concluding this example, we note that the results are strictly valid only for pure polarization states and a perfect polarization analyzer. States of partial

Fig. 8.5 Azimuthal dependence (intensity against rotation angle about the scattering vector) of the resonant forbidden (024) reflection in HoHe₂ for scattered beam linear polarization at angles of 0, 45, 90, and 135° with respect to the incident (σ) polarization



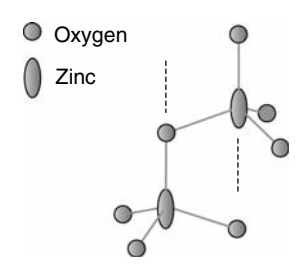
polarization can be dealt with by using Stokes parameter, as outlined in Sect. 8.6. With modern synchrotrons, the degree of polarization (typically linear unless a special insertion device or optic is employed) is usually very close to unity. A more significant source of error arises from the fact that the linear polarization analyzer, which relies on choosing an analyzer crystal with a d-spacing that gives a scattering angle (2θ) as close as possible to 90° with the X-ray energy at the resonance of interest. Calculations with an imperfect analyzer are described in Sect. 8.6 and illustrated in the next example.

8.12 Example: ZnO

Zinc oxide crystallizes in the polar hexagonal space group $P6_3mc$ with Zn atoms occupying sites of symmetry 3m (see Fig. 8.6). Resonant forbidden scattering from ZnO is of interest because it has been shown [27] to exhibit two interfering scattering processes described (in this case) by the same scattering tensor: one arising from mixed dipole–qaudrupole (E1E2) transitions and the other from thermal motion induced scattering, whereby one is sensitive to the evolution of the resonant anisotropy with atomic displacement. Here, we will not concern ourselves with the details of the physical processes, but concentrate again on the symmetry properties of the scattering tensor. For this example, we demonstrate two different approaches compared to our treatment of HoFe₂: we employ spherical tensors and use scattering and analyzer matrices.

While there is only one unique site for the Zn atoms, half of the Zn positions differ from the other half by a combination of a translation and a rotation or reflection (i.e., screw or glide symmetry). The fact that the symmetry operations are not purely translational suggests the possibility of observing resonant forbidden scattering.

Fig. 8.6 Two glide-plane related zinc atoms in ZnO, each located on a threefold axis



However, such forbidden reflections are ruled out for second-rank tensors (normal dipole–dipole resonant anisotropy) because the only allowed ellipsoids are identical for the two rotated Zn atoms and therefore cancel completely. The lowest order scattering tensor that survives symmetrization is of rank three. It is described by a true tensor, that is, parity = $(-1)^K = (-1)^3 = \text{odd}$. Just as we populated the Cartesian tensor components with arbitrary symbols in the previous example, here we do the same with the 2K + 1 = 7 (complex) components of the atomic spherical tensor:

$$T_S = (T_{Q=-3}^3, T_{Q=-2}^3, T_{Q=-1}^3, T_{Q=0}^3, T_{Q=1}^3, T_{Q=2}^3, T_{Q=3}^3) = (a, b, c, d, e, f, g),$$
(8.55)

which we treat as a column vector but write as a row vector to save space on the page. Our next task is to apply the constraints of crystal symmetry to the tensor components. Again, this can be done either by inspection or can be automated by a computer algorithm. We discuss both.

The simplest way to find the required tensor is to employ knowledge of the crystal symmetry and the transformation properties of spherical tensors. The latter is made considerably easier by following the approach of Lovesey et al. [4], whereby we adopt tensors with well-defined symmetry (odd or even) with respect to space and time reversal. Under these operations, even tensors are invariant and odd tensors change the sign of all components. As mirror reflections are equivalent to the combination of (spatial) inversion and a rotation of π normal to the mirror plane, we need concern ourselves only with rotations. Rotation of any set of spherical tensor components of rank K can be accomplished by the use of $(2K+1)\times(2K+1)$ Wigner D matrices which multiply the tensor. We will not consider the properties of Wigner D matrices here, but merely quote the results that we need from the literature [4,22,24]. In fact, the D matrix for rotations about the z-axis, which we take to be parallel to the threefold axes, takes on a particularly simple (diagonal) form for all K:

$$R_{\varepsilon}^{z}(T_{O}^{K}) = e^{iQ\xi}T_{O}^{K}. \tag{8.56}$$

Insisting on threefold ($\zeta=\frac{2\pi}{3}$) rotational invariance already eliminates most of the tensor components, leaving

$$T_S = (a, 0, 0, d, 0, 0, g).$$
 (8.57)

We next consider the effect of the mirror reflection, which we treat as an inversion (under which the tensor in question is odd) and a π -rotation normal to the mirror plane, which we call the y-axis, in keeping with our procedure for mapping crystal to Cartesian frames. In general, rotations about the x and y axes mix all the components. For rotations of π , however, the matrices have a rather simple (skew-diagonal) form, which exchanges +Q and -Q components, sometimes with a change of sign [4,24]

$$R_{\pi}^{x}(T_{Q}^{K}) = (-1)^{K} T_{-Q}^{K}, \quad R_{\pi}^{y}(T_{Q}^{K}) = (-1)^{K+Q} T_{-Q}^{K}. \tag{8.58}$$

By equating $T_S = T_Q^K$ with $-R_\pi^y(T_Q^K)$, one finds the atomic resonant scattering tensor to be

$$T_S = (a, 0, 0, d, 0, 0, -a).$$
 (8.59)

The final step is to derive the structure factor tensor by noting that allowed and (screw-axis) forbidden reflections are formed from the sum and difference of the atomic tensor and its equivalent form rotated by π about z. From (8.29) it is straightforward to show that

$$F_{\text{allowed}} = (0, 0, 0, d, 0, 0, 0), \quad F_{\text{forbidden}} = (a, 0, 0, 0, 0, 0, -a),$$
 (8.60)

and we note that the allowed reflections are invariant with respect to any rotation about the z axis.

Calculation of the (relative) scattering intensity for polarization and wave vectors, $\hat{\varepsilon}$, $\hat{\varepsilon}'$, $\hat{\mathbf{q}}$, $\hat{\mathbf{q}}'$, can now be carried out by contracting the structure factor tensor with the relevant X-ray tensor for the process of interest (8.64), using (8.40).

While this calculation is straightforward in principle, it can become tedious when dealing with arbitrary reflections, whose wavevectors bear no simple relationship to the Cartesian crystal axes, and with arbitrary azimuthal rotation angles, referenced to other arbitrary origin (usually given most conveniently in terms of an azimuthal reference reciprocal lattice vector). Dealing with beams of partial polarization and imperfect polarization analyzers will render the experience painful in the extreme. We therefore devote the remainder of this section to the description of a procedure whereby all of the steps, including symmetrization of the spherical tensor, can be automated.

Step 1: Obtain crystal information and symmetry, that is, lattice parameters (and therefore the **B** matrix), atomic coordinates of the resonant ion(s), and spacegroup symmetry operators. For nonmagnetic systems (or when magnetism plays only a minor role in the scattering process of interest), this may be obtained from a standard Crystallographic Information File (CIF file). Atomic coordinates and symmetry operators are given in terms of crystal coordinates. In hexagonal ZnO, for example, we find a Zn atom at $(\frac{1}{3}, \frac{2}{3}, 0)$ and 12 spacegroup symmetry operators (including the identity). These are conveniently expressed in terms of a set of "equivalent positions": (x, y, z) (x - y, -y, 1/2 + z) (-y, x - y, z) (-x, -y, 1/2 + z) (x, x - y, z) (-y, -x, z) (x - y, x, 1/2 + z) (-x + y, -x, z) (y, x, 1/2 + z) (-x, -x + y, 1/2 + z) (-x + y, y, z) where, for example, the first nontrivial element can be written in matrix/vector form as

$$\begin{pmatrix} 1 & -1 & 0 \\ 0 & -1 & 0 \\ 0 & 0 & 1 \end{pmatrix}, \quad \begin{pmatrix} 0 \\ 0 \\ \frac{1}{2} \end{pmatrix},$$

which corresponds to a reflection in the ac plane combined with a translation, c/2. While the hexagonal crystal coordinates are convenient for dealing with positions, applying symmetry transformation matrices is more straightforward using Cartesian coordinates. We therefore use the **B**-matrix, defined in (8.36), to transform from crystal to crystal-Cartesian coordinates:

$$\mathbf{S}_C = (\mathbf{B}^T)^{-1} \mathbf{S}_X \mathbf{B}^T. \tag{8.61}$$

The resulting Cartesian matrix for the above symmetry operator becomes,

$$\begin{pmatrix} \frac{1}{2} & -\frac{\sqrt{3}}{2} & 0\\ -\frac{\sqrt{3}}{2} & -\frac{1}{2} & 0\\ 0 & 0 & 1 \end{pmatrix}$$

corresponding to a reflection in the plane $x + \sqrt{3}y = 0$, which lies parallel to the z axis and at 30° to x.

Step 2: Select the scattering process and spherical tensor of interest (e.g., K = 3, time-even, parity-odd tensor describing E1E2 resonance, for the current example).

Step 3: Populate the 2K + 1 tensor components with objects that can keep track of the linear transformations applied to them. These might be symbols if a computer algebra program is adopted. Another choice is a set of 2K + 1 vectors, each of length 2K + 1. For simple cases with a single independent tensor component, such as the current example, random numbers are a very convenient choice.

Step 4: Convert the 2K + 1 components of the spherical tensor to 3^K components of the equivalent Cartesian tensor of rank K, using the conversion tables of Stone [25], described in Sect. 8.10 (Note that pseudotensors, whose parity is given by $(-1)^{K+1}$, will have the wrong properties under inversion following this procedure. This can be either corrected for when applying the symmetry transformations or one could adopt a Cartesian tensor of rank K+1, which will have opposite parity. We adopt the former approach). Conversion to Cartesian form is purely for convenience, but has the great advantage of avoiding the coordinate singularities that arise from the use of angles when constructing the rotation matrices for spherical tensors, for example.

Step 5 (optional): Calculate the symmetrized Cartesian atomic scattering tensor by transforming the original tensor with each of the symmetry operations in step 1 that preserves the atomic coordinates.

Step 6: Calculate the Cartesian resonant structure factor tensor by transforming the original tensor with each of the symmetry operations in step 1 and adding these together with the relevant phase factor:

$$T_{ijk...} = \sum_{n} \mathbf{S}_{Ii}^{n} \mathbf{S}_{Jj}^{n} \mathbf{S}_{Kk}^{n} ... T_{IJK...}^{0} e^{i\mathbf{k} \cdot (\mathbf{S}^{n} \mathbf{r}_{0} + \mathbf{v}^{n})}$$
(8.62)

where S^n and v^n are the matrix and vector parts of the *n*th symmetry operator, $T^0_{IJK...}$ is the original Cartesian tensor located at the atomic site vector \mathbf{r}_0 , and the symmetry matrix is applied K times – once for each tensor index. We noted in Step 4 that a factor must be applied to account for the incorrect transformation of pseudotensors under inversion (or reflections, which include inversion) using the above formalism. This simply requires multiplying each term in the above summation by the factor

$$\det(\mathbf{S}^n)^{\frac{1}{2}(3+P(-1)^K)},\tag{8.63}$$

where $P=\pm 1$ is the parity of the tensor of rank K and $\det(\mathbf{S}^n)=\pm 1$ depending on whether the symmetry operator is a pure rotation or includes inversion. For the ZnO 115 reflection, all 27 components of the resulting Cartesian tensor are zero except $F_{122}=F_{212}=F_{221}=-F_{111}$.

Step 7: Convert the Cartesian structure factor tensor (or atomic scattering tensor) back to spherical form using the conversion tables of Stone. For the ZnO 115 reflection, all seven components of the resulting spherical tensor are zero except $F_{-3} = -F_{+3}$.

Step 8: Calculate the scattering amplitudes for the four polarization channels of the scattering matrix. To do this, we take the polarization and wavevectors in (8.38) and rotate to the crystal Cartesian frame using (8.33), having first specified the azimuthal rotation angle and the azimuthal reference hkl vector. These rotated vector components are then inserted into the relevant expression for the X-ray tensor from the references in Table 8.1 (one for each of the four polarization channels) and finally, the X-ray and structure factor tensors are contracted, as per (8.40), to obtain the four components of the scattering matrix.

The expressions for the required X-ray tensors are given in [4], appropriate for time-even case (this example) and the time-odd case (next section), as,

$$X_{\text{E1E2}}^{U3} = \tilde{N}_{\text{E1E2}}^3 - N_{\text{E1E2}}^3 \tag{8.64}$$

and

$$X_{\text{EIE2}}^{G3} = \tilde{N}_{\text{EIE2}}^3 + N_{\text{EIE2}}^3, \tag{8.65}$$

respectively, where the tensors $\tilde{N}_{\rm E1E2}^3$ and $N_{\rm E1E2}^3$ are each obtained by coupling three vectors to form a rank-three tensor. A general expression for such a coupling of three vectors, A, B and C is given, in terms of the Cartesian vector components, as,

$$T_{3} = \left(\frac{(A_{x} - iA_{y})(iB_{x} + B_{y})(C_{x} - iC_{y})}{2\sqrt{10}}, \frac{A_{z}(iB_{x} + B_{y})(C_{x} - iC_{y}) + (iA_{x} + A_{y})(B_{z}(C_{x} - iC_{y}) + (B_{x} - iB_{y})C_{z})}{2\sqrt{15}}, \frac{2\sqrt{15}}{4A_{z}(iB_{z}C_{x} + B_{z}C_{y} + iB_{x}C_{z} + B_{y}C_{z}) - iA_{x}(3B_{x}C_{x} - iB_{y}C_{x} - iB_{x}C_{y} + B_{y}C_{y} - 4B_{z}C_{z})}{10\sqrt{6}}\right)$$

$$-\frac{A_{y}(B_{x}C_{x} + iB_{y}C_{x} + iB_{x}C_{y} + 3B_{y}C_{y} - 4B_{z}C_{z})}{10\sqrt{6}},$$

$$-i(A_{x}B_{z}C_{x} + A_{y}B_{z}C_{y} + A_{x}B_{x}C_{z} + A_{y}B_{y}C_{z} + A_{z}(B_{x}C_{x} + B_{y}C_{y} - 2B_{z}C_{z}))}{5\sqrt{2}},$$

$$\frac{4A_{z}(-iB_{z}C_{x} + B_{z}C_{y} - iB_{x}C_{z} + B_{y}C_{z}) + iA_{x}(3B_{x}C_{x} + iB_{y}C_{x} + iB_{x}C_{y} + B_{y}C_{y} - 4B_{z}C_{z})}{10\sqrt{6}}$$

$$+\frac{A_{y}(-(B_{x}C_{x}) + iB_{y}C_{x} + iB_{x}C_{y} - 3B_{y}C_{y} + 4B_{z}C_{z})}{10\sqrt{6}},$$

$$\frac{i(A_{z}(B_{x} + iB_{y})(C_{x} + iC_{y}) + (A_{x} + iA_{y})(B_{z}(C_{x} + iC_{y}) + (B_{x} + iB_{y})C_{z})}{2\sqrt{15}},$$

$$\frac{(A_{x} + iA_{y})(-iB_{x} + B_{y})(C_{x} + iC_{y})}{2\sqrt{10}}.$$

$$(8.66)$$

Careful inspection of the resultant tensor, T_3 , reveals that it is invariant with respect to any permutation of the vectors. This is generally true for the coupling of n vectors to form the tensor of maximum rank K = n (the *stretched* tensor) and leads to some useful results. For the present example, $\tilde{N}_{\text{E1E2}}^3$ is obtained by taking T_3 with ε , ε' and \mathbf{q} substituting for \mathbf{A} , \mathbf{B} , or \mathbf{C} , in any order. Similarly, N_{E1E2}^3 is given by replacing \mathbf{q} with \mathbf{q}' . An interesting consequence of the symmetry with respect to permutation of the vectors is that, for any stretched scattering tensor that involves ε and ε' once each, for example, for the rank-two E1E1 tensor, rank-three E1E2 tensor, and rank-four E2E2 tensor, the resulting 3×3 scattering matrix is always symmetric.

Step 9: Calculate the total scattering intensity for the required state of incident beam polarization, using (8.23), or the intensity scattered by the polarization analyzer, using (8.26).

The calculated azimuthal scans for various polarizer angles are given in Fig. 8.7 for the ZnO (115) reflection. We reiterate that the calculations outlined here are purely phenomenological and give intensities to within an overall scale factor. Moreover, in general, more than one tensor component survives the symmetrization process and the results depend on the (complex) ratios of the independent tensor components. Such an example is discussed in the next section.

8.13 Example: Ca₃Co₂O₆

For our final example we consider the azimuthal rotation dependence of resonant scattering from $Ca_3Co_2O_6$ – a complex incommensurate magnetic system that requires a number of resonant scattering tensors and illustrates most of the ideas described in this chapter. This compound has been studied extensively in recent years due largely to its fascinating properties under an applied magnetic field [28]. The role of X-ray diffraction has proved crucial in verifying long range magnetic order in this system [29]. Here, we discuss resonant X-ray scattering near the cobalt K-edge. In the following we are not going to discuss the physical properties of

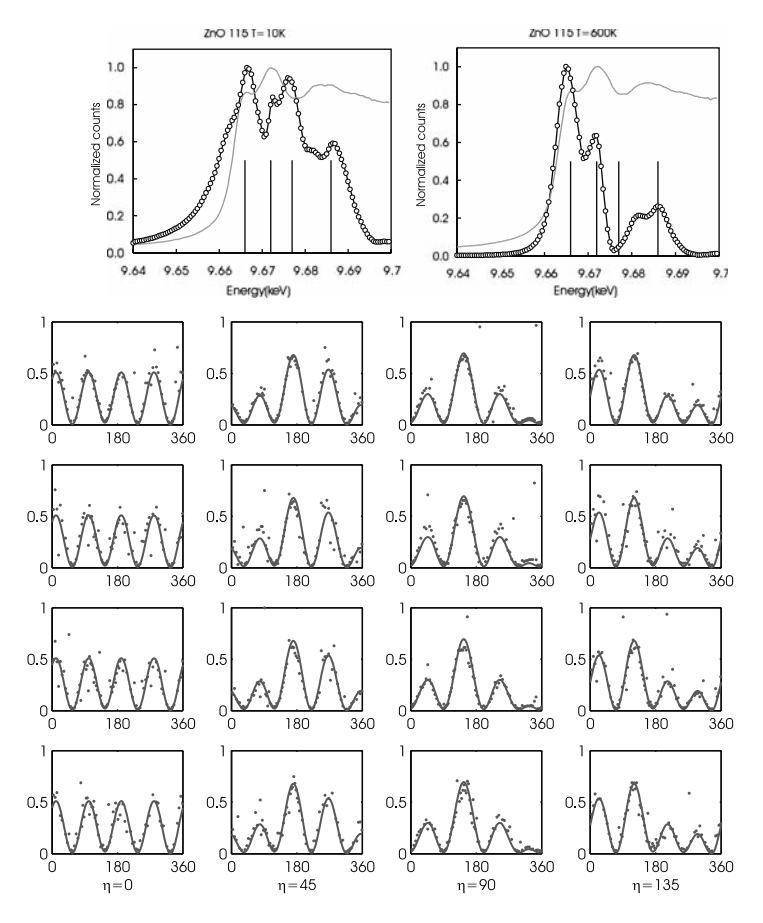


Fig. 8.7 The energy spectrum of the resonant forbidden (115) reflection in ZnO at $T=10\,\mathrm{K}$, where the scattering is dominated by E1E2 processes (top left), and at $T=600\,\mathrm{K}$, where the scattering is dominated by thermal motion induced scattering (top right). Azimuthal scans were performed at each of the energies marked by the vertical lines (energy increasing from top to bottom row). As all line shapes agree with the calculations, we conclude that scattering is well described by the same tensor at all temperatures and all energies (Data were obtained from Beamline I16, Diamond Light Source, UK)

 $Ca_3Co_2O_6$ but limit ourselves to the symmetry of the tensors that can contribute to the X-ray scattering processes [29, 30].

The system, shown in Fig. 8.8, consist of chains made up of alternating distorted octahedra and trigonal CoO_6 prisms sharing faces, running along the hexagonal c axis, and arranged in a triangular pattern within the ab plane [31]. The different local environments leave the Co^{3+} ions on the octahedral site (Co-I) in a lowspin (S=0) state and those on trigonal prism (Co-II) sites in the high-spin (S=2) state [32, 33]. The local anisotropy of the trigonal prism is very strong and forces the magnetic moments to point along the c axis as confirmed by a number

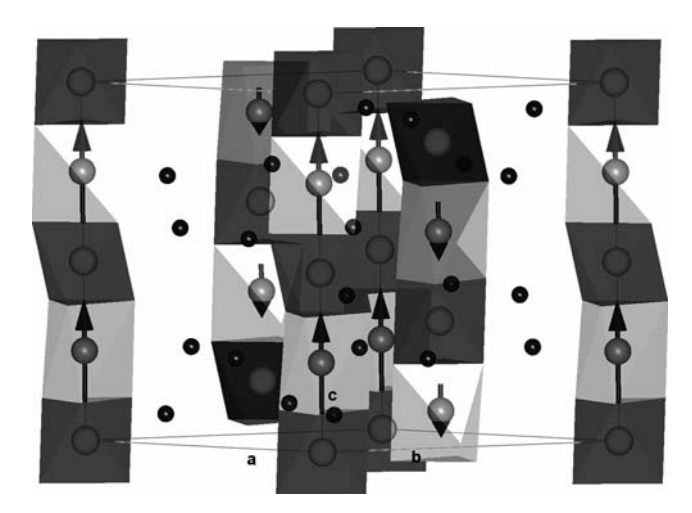


Fig. 8.8 Schematic of the unit cell of $Ca_3Co_2O_6$ in the hexagonal setting. The trigonal prisms are shown in *dark grey* and the octahedra in *light grey*. The magnetic moments at the center of the trigonal prism are also drawn. Moving along the hexagonal c-axis the role of the magnetic chains is exchanged

of experimental results. $Ca_3Co_2O_6$ is usually described in the hexagonal setting of the $R\bar{3}c$ space group, as this representation allows one to immediately identify the triangular arrangement of the CoO_6 chains within the ab planes. However, as this setting is nonprimitive, it makes both the description of the magnetic structure and the analysis of the symmetry of the tensors more difficult. For these reasons, in this section, rhombohedral coordinates are used throughout. In this setting, the unit-cell dimensions are $a = b = c = 6.274 \,\text{Å}$ and $\alpha = \beta = \gamma = 92.53^{\circ}$, and so we see that the system is very close to being cubic.

In the transition to the magnetically ordered phase, no changes are observed apart for the appearance of the magnetic reflections characterized by the propagation vector $\tau \simeq (\frac{1}{3}, \frac{1}{3}, \frac{1}{3})$, which is the parallel to the threefold symmetry axes. Only the Co-II ions contribute to the magnetic properties and we neglect all the other ions in the following discussion.

In the magnetically ordered state, in addition to the principal magnetic reflections, we observe a second class of reflections that also appear at the magnetic propagation vector $\tau \simeq (\frac{1}{3}, \frac{1}{3}, \frac{1}{3})$, but at positions where the magnetic structure factor is zero. These reflections are characterized by a completely different photon energy spectrum and azimuthal rotation dependence. We first demonstrate that unlike the principal magnetic reflections, they cannot be described within the dipole–dipole (E1E1) approximation but require dipole–quadrupole terms to provide a satisfactory description. The occurrence of higher rank scattering in the space group $R\overline{3}c$ has been treated by a number of authors [4,5,34,35].

The unit-cell scattering amplitude for the magnetic Co ions is obtained by summing over the two cobalt sites and is found to be

$$F(\mathbf{H}) = f_1 + P(f_1) e^{2\pi i \mathbf{H} \cdot (\frac{1}{2}, \frac{1}{2}, \frac{1}{2})},$$
(8.67)

where f_1 represents an atomic scattering tensor, defined in (8.40), where each tensor component is a complex function of energy, and P is the parity or inversion operator, which arises due to the fact that the two magnetic cobalt atoms occupy sites that are related by inversion.

The procedure that we follow is similar to the one adopted in the previous example of ZnO. The main difference stems from the fact that the signal that we are treating in this case is magnetic (i.e., time-odd). The first step will be to consider the point group symmetry of the magnetic cobalt site and to study the behavior of a given set of spherical tensors under this set of symmetries. Using the magnetic point group, we derive the linear combinations of tensor components that can contribute to the diffraction process. The third step will be to calculate the resonant structure factor. As described in the previous sections, one can write the (scalar) scattering amplitude as a contraction of two tensors: one (X_Q^K) built from the vectors describing the X-ray beams and the other (T_Q^K) arising from a multipole expansion of the atomic resonance.

This brings us to the technical steps described earlier in the chapter. While these tensors are relatively easy to write in appropriate reference frames, they become immediately very complex otherwise. (For example, a simple and intuitive form for the tensors T_Q^K is typically obtained when the quantization (z-axis) of the spherical tensor is taken parallel to a line of symmetry of the atom, such as a rotation axis or intersection of mirror planes). Unfortunately, convenient choices for the tensors T_Q^K and X_Q^K are not generally the same. Hence, it is useful to evaluate the tensors in two different reference frames and to rotate T_Q^K to the frame of X_Q^K . The latter is calculated in the reference frame given in [4] and shown in Fig. 8.3, while the reference frame for the resonant scattering tensor was chosen with the \hat{z} axis parallel to the (111) direction, the axis \hat{y} parallel to the ($\bar{1}01$) direction, and the axis \hat{x} parallel to $\hat{y} \times \hat{z}$. The required tensor rotations were performed using the Wigner D-matrices [24]. Elsewhere in this chapter a different but completely equivalent approach has been chosen, whose advantage is mainly that it requires only rotations of vector quantities.

The Neumann principle requires the T_Q^K tensors to be invariant under the point group symmetry of the magnetic cobalt site. The nonmagnetic point group is 32, that is, a twofold rotation axis perpendicular to a threefold axis. We note that maintaining this point group would lead to the absence of magnetism as 32 is not an admissible magnetic point group (one can show as an exercise that there is no possible vector direction that can satisfy the two rotations simultaneously). Hence, in order for the system to sustain a magnetic moment, the point group symmetry needs to be modified. The first admissible magnetic point group is 32'. The axis 3 is maintained, and as the proper rotations act on classical spins (axial vectors) in the same way as on polar vectors, we need to combine the action of the axis 2 with time reversal to allow a magnetic vector that is parallel to the threefold axis and compatible with the point group. Symmetry 3 would also be an admissible magnetic point group, but we

choose to maintain as much symmetry as possible to describe the properties of the system, as reducing the symmetry increases the number of parameters contributing to the scattering. This is a pragmatic approach and the possibility of reproducing the experimental data within this framework will provide a justification a posteriori for this approach. It is worth mentioning that even if the twofold symmetry is actually broken, we can assume that the deviation from this symmetry is relatively small and therefore terms related to its breaking can be neglected. A similar approach has been used in the past to reproduce the threefold modulation of reflections in Fe₂O₃[35].

The expressions describing the required spherical tensor rotations are given in the previous section:

$$R^z_{\zeta}(T_Q^K) = \mathrm{e}^{\mathrm{i} Q \zeta} T_Q^K \quad \text{and} \quad R^y_{\pi}(T_Q^K) = (-1)^{K+Q} T_{-Q}^K.$$

The tensors that "survive" the threefold symmetrization are as follows.

• E1E1 resonance: T_0^0 , \tilde{T}_0^1 , T_0^2 • E1E2 resonance: \tilde{T}_0^1 , \tilde{T}_0^2 , \tilde{T}_0^3 , $\tilde{T}_3^3 \pm \tilde{T}_{-3}^3$ and T_0^1 , T_0^2 , T_0^3 , $T_3^3 \pm T_{-3}^3$ • E2E2 resonance: T_0^0 , \tilde{T}_0^1 , T_0^2 , \tilde{T}_0^3 , $\tilde{T}_3^3 \pm \tilde{T}_{-3}^3$, T_0^4 , $T_3^4 \pm T_{-3}^4$

where indicates time-reversal-odd (i.e., magnetic) tensors. (Recall from Table 8.1 the relationship between tensor rank and time-reversal symmetry for the parity-even E1E1 and E2E2 tensors).

A further reduction in the number of the tensors contributing to the scattering is obtained by applying the symmetry 2' (equivalent to a twofold rotation for the nonmagnetic tensors). This symmetry rules out \tilde{T}_0^2 , T_0^1 and T_0^3 (E1E2) and $\tilde{T}_3^3 + \tilde{T}_{-3}^3$ and $T_3^4 + T_{-3}^4$ (E2E2). It is easy to see that the magnetic vector component \tilde{T}_0^1 is retained and that it corresponds to a magnetic moment along the trigonal (threefold) axis.

There are still a considerable number of contributions. An effective way to simplify the problem is to proceed to the calculation of the structure factor in (8.67) for the magnetic reflections $(h \pm \frac{1}{3}, k \pm \frac{1}{3}, l \pm \frac{1}{3})$, which are satellites of either allowed reflections, (h, k, l) with k + k + l = even or of the glide-plane-forbidden reflections with k + k + l = odd. A very elegant consequence of the modulation wavevector in Ca₃Co₂O₆ combined with the form of the structure factor in (8.67) means that the magnetic reflections fall neatly into two categories, which probe different aspects of the resonant scattering tensors. With $h \pm \frac{1}{3}$, $k \pm \frac{1}{3}$, $l \pm \frac{1}{3}$ = even (k + k + l) = odd) we have

$$F\left(h \pm \frac{1}{3}, k \pm \frac{1}{3}, l \pm \frac{1}{3}\right)_{k+k+l=\text{odd}} = T_Q^K + P\left(T_Q^K\right),$$
 (8.68)

whereby the scattering is determined by the parity-even tensors T_Q^K , that is, E1E1 and E2E2. Conversely, with k + k + l = even,

$$F\left(h \pm \frac{1}{3}, k \pm \frac{1}{3}, l \pm \frac{1}{3}\right)_{k+k+l=\text{even}} = T_Q^K - P\left(T_Q^K\right),$$
 (8.69)

and the scattering picks out the parity-odd tensors, that is, E1E2.

This result is very important as it relates (h, k, l) and the parity of the tensors. This is not something very common, but when it occurs it can allow a very easy distinction of the different scattering processes. The usual way to distinguish between different scattering processes is to look at their energy spectra, as the position of the resonances reflects the energy distribution of the projection of the empty density of states of well defined symmetry. In the 3d transition metals, the 3d (l = 2) electronic states, responsible for the magnetic properties, are usually well localized in energy within the much wider 4p (l=1) band. The symmetry of the local environment is crucial in allowing the hybridization of the parity-even $((-1)^l$ =even) and parity-odd $((-1)^l$ =odd) electronic states to occur. Again the presence or absence of an inversion at the scattering center makes a very important difference and in our case (32') allows the p and d states to hybridize and the 4p band become magnetically polarized. This is clearly seen in the complex photon-energy dependence around the Co *K*-absorption edge of the $(\frac{8}{3}, \frac{1}{3}, \frac{7}{3})$ reflection, shown in Fig. 8.9. In this case the main contribution comes from the E1E1 process that probes the *p* states, with a much weaker contribution from E2E2 processes. Usually the E2E2 contribution will occur in the pre-edge region where the 3d states are localized. Figure 8.9 also shows the energy spectrum of the much weaker $(\frac{8}{3}, \frac{8}{3}, \frac{5}{3})$ reflection. This reflection exhibits a very simple energy spectrum that can be described using a single oscillator, localized in the pre-edge region, which points to the E1E2 resonance being similarly localized. This is in good agreement with the fact that the p states will not be accessible through these higher rank processes. The reduced intensity ($\simeq \frac{1}{10}$) of the $(\frac{8}{3}, \frac{8}{3}, \frac{5}{3})$ reflection compared to the $(\frac{8}{3}, \frac{\overline{1}}{3}, \frac{\overline{7}}{3})$ reinforces the suggestion that the former originates from a higher order process.

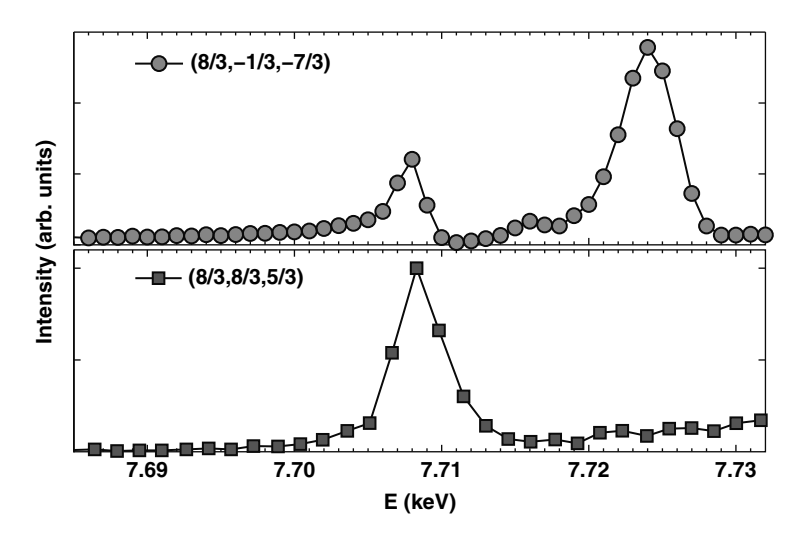


Fig. 8.9 The intensity vs. photon-energy dependence around the Co K-absorption edge of an E1E1 (top) and an E1E2 (bottom) magnetic reflection. The data were collected in the $\sigma\pi$ channel

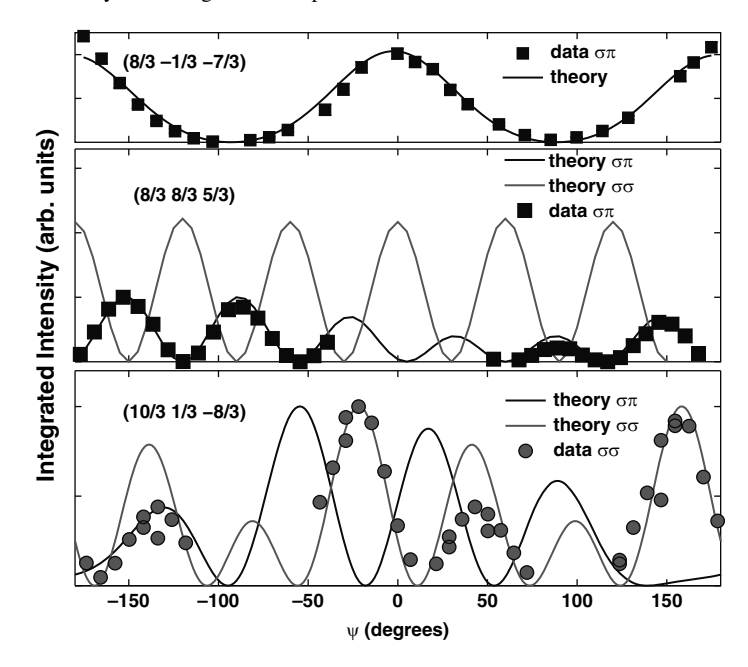


Fig. 8.10 Theoretical and experimental azimuthal dependence of three magnetic reflections at the Co K-absorption edge. In the first panel an E1E1 reflection is reported, whereas the central and bottom panels show reflections resulting from the E1E2 interference together with the model predictions. Two free parameters were used for the first plot while the amplitude is the only free parameter in the two E1E2 curves

The azimuthal dependence of the reflections reported in Fig. 8.10 confirms that the $(\frac{8}{3}, \frac{8}{3}, \frac{5}{3})$ and the $(\frac{10}{3}, \frac{1}{3}, \frac{8}{3})$ reflections are due to higher rank tensors. In fact, the $(\frac{8}{3}, \frac{1}{3}, \frac{7}{3})$ reflection due to E1E1 processes has an almost perfect twofold symmetry.

The **k**-vector of the latter is perpendicular to the quantization axis and form an angle of about 174° with the \hat{y} axis. The rotated tensor \tilde{T}_0^1 has all three components nonzero, but once contracted with the X-ray tensor only the rotated channel $\sigma\pi$, with periodicity $\cos\psi$, survives. An improved agreement with the experimental data is obtained if a small contribution coming from \tilde{T}_0^3 is considered. This contribution appears also in the nonrotated channel, but probably it is too small to be observed in the present case.

The $(\frac{8}{3}, \frac{8}{3}, \frac{5}{3})$ reflection, which has a **k**-vector $\approx 10^\circ$ from the threefold (111) axis, has six peaks with different intensities and with zeros that are not exactly 60° apart. For E1E2, only the term $\tilde{T}_3^3 - \tilde{T}_{-3}^3$ has a threefold periodicity with respect to a rotation about the quantization axis, whereas \tilde{T}_0^1 and \tilde{T}_0^3 are constant. Considering that the reflection is only slightly rotated from the (111) axis, they do not seem to provide an appropriate reproduction of the symmetry of the signal. Hence we neglect these contributions in the data analysis, and this will leave us with only one free coefficient instead of three to describe the azimuthal dependence.

To calculate the behavior of the reflections in the reference frame of X_Q^K , we apply again a sequence of coordinate rotations [4] to the structure factor tensor. As with the E1E1 tensor, E1E2 tensors $\tilde{T}_3^3 - \tilde{T}_{-3}^3$ are rotated into the new reference frame via the appropriate Wigner D-matrix, which produces a linear combination of the other rank 3 tensor components, with the dominant coefficient coming from the $\tilde{T}_3^3 - \tilde{T}_{-3}^3$ as the rotation is small with respect to the threefold axis. This operation, together with the contraction with the X-ray tensors X_Q^K [4] given in (8.65), produces the following expressions for the $(\frac{8}{3}, \frac{8}{3}, \frac{5}{3})$ intensity:

$$I_{\sigma-\sigma} = a_5 T_3^3 \left[a_6 + a_7 c_{2\psi} \right] c_{\theta} s_{\psi}, \tag{8.70}$$

$$I_{\sigma-\pi} = a_1 T_3^3 c_{\psi} c_{\theta} \left[a_2 c_{\theta} s_{\psi} + (a_3 + a_4 c_{2\psi}) s_{\theta} \right], \tag{8.71}$$

where a_i are complex numerical coefficients defined by the direction in the space of the reflection, $c_x(s_x)$ are shorthand for $\cos x(\sin x)$, θ is the Bragg angle, and ψ is the azimuthal angle. A similar expression is obtained in the case of the $(\frac{10}{3}, \frac{1}{3}, \frac{8}{3})$ reflection but with a different relative weight of the coefficients as this reflection forms a much larger angle with the threefold axis.

Violation of both parity and time-reversal symmetry at the Co-II sites in $Ca_3Co_2O_6$ might suggest that the material could exhibit the magneto-electric effect, because such (lack of) symmetry is an essential prerequisite. However, the system is *globally* centrosymmetric, which rules out the effect in the bulk (and, indeed, an E1E2 contribution to the bulk absorption). This highlights one of the strengths of resonant X-rays scattering: it is a local probe that can access atomic-scale phenomena even when they vanish macroscopically. The possibility of observing an E1E2 interference term in a globally centrosymmetric system has been demonstrated in V_2O_3 for the time-even case, arising from the absence of an inversion symmetry at the V position. At the Co-II site in $Ca_3Co_2O_6$, both the magnetic 32' and the nonmagnetic point groups 32 allow such "magneto-electric" tensors to occur. A useful classification of the multipole moments detected in resonant X-ray scattering, based exclusively on the linear magneto-electric effect, has been given in [36,37]. According to this scheme, the dominant term contributing to the scattering is a polar toroidal octupole.

The possibility of observing a polar toroidal moment has been widely discussed theoretically, but to date very few experimental observations of this quantity are available. V_2O_3 is certainly the most well known case [38] but in this instance the reflection structure factor allows an E2E2 term (the magnetic octupole) to occur together with the E1E2 terms [36]. More recently, a possible E1E2 signal has been reported in the ferroelectric phase of TbMnO₃ [39]. Here, both the E1E2 and the E1E1 contributions are symmetry allowed, but occur at different energies. So the tail of the E1E1, that is much stronger in intensity, can give a significant contribution at the lower energies where the E1E2 resonance is expected.

8.14 Conclusions

Resonant X-ray scattering is a complicated and rapidly evolving subject. Current interest in the subjects owes much to the wide variety of physical phenomena, such as magnetism, that can be probed by the various scattering tensors. Some of the key results of resonant scattering and absorption have a surprisingly simple, symmetry-based origin, and we have given feasibility arguments based on these ideas. Most of the remainder of the chapter is devoted to introducing the formalisms and language commonly applied by researchers in the field. In particular, we have focused on phenomenological models that employ Cartesian and spherical tensors to describe the sample response and the X-ray probe. Much effort is spent identifying simplified forms of the scattering tensors that obey the known symmetries of the sample. To illustrate these ideas, we have picked several examples of varying complexity.

The chapter exploits key results from a small set of authors – Lovesey, Blume etc – whose work is cited repeatedly. We do not elaborate on the results of these papers: the reader is encouraged to refer to them directly. While we have not developed the theory of resonant scattering, we have nonetheless brought together several established ideas and shown how they can be employed to compute scattering properties. Specifically, the formalism of Busing and Levy is employed to connect crystal and Cartesian coordinate systems, and the work of Stone to convert between Cartesian and spherical representations of tensors. The chapter therefore has the feel of a cook-book. As with its culinary counterparts, it is hoped that it is of interest both to budding practitioners and those with a passing interest and keen appetite.

Acknowledgements The authors are grateful to S. W. Lovesey for helpful comments on the manuscript.

References

- 1. R.P. Feynman, R.B. Leighton, M. Sands, *The Feynman Lectures on Physics*, vol 1, Ch. 30–37 (Addison-Wesley, Reading, MA, 1964)
- 2. S.W. Lovesey, S.P. Collins, X-Ray Scattering and Absorption from Magnetic Materials (Clarendon Press, Oxford, 1996)
- 3. M. Blume, *Resonant Anomalous X-Ray Scattering*, ed. by G. Materlik, C.S. Sparks, K. Fischer (North-Holland, Amsterdam, 1994)
- 4. S.W. Lovesey, E. Balcar, K.S. Knight, J.F. Rodríguez, Phys. Rep. 411, 233–289 (2005)
- 5. V.E. Dmitrienko, K. Ishida, A Kirfel, E.N. Ovchinnikova, Acta Cryst. A61, 481 (2005)
- 6. Ch. Brouder, J. Phys. Condens. Matter 2, 701–738 (1990)
- 7. R.P. Feynman, R.B. Leighton, M. Sands, *The Feynman Lectures on Physics*, vol 3, Ch. 21–23 (Addison-Wesley, Reading, MA, 1964)
- 8. D.E. Sands, Vectors and Tensors in Crystallography (Dover, New York, 1995)
- S. Turchini, N. Zema, S. Zennaro, L. Alagna, B. Stewart, R.D. Peacock, T. Prosperi, J. Am. Chem. Soc. 126, 4532–4533 (2004)
- 10. J.P. Hannon, G.T. Trammell, M. Blume, D. Gibbs, Phys. Rev. Lett. 61, 1245-1248 (1988)
- 11. J.P. Hill, D.F. McMorrow, Acta Cryst. **A52**, 236–244 (1996)
- G. van der Laan, B.T. Thole, G.A. Sawatsky, J.B. Goedkoop, J.C. Fuggle, J.-M. Esteva, R. Karnatak, J.P. Remeika, H.A. Dabkowska, Phys. Rev. B34 6529–6531 (1986)

- 13. R.R. Birss, Symmetry and Magnetism (North-Holland, Amsterdam, 1966)
- 14. S.W. Lovesey, Rep. Prog. Phys. **56**, 257–326 (1993)
- 15. S.P. Collins, D. Laundy, A. Stunault, J. Phys. Condens. Matter 13, 1891–1905 (2001)
- 16. B.E. Warren, X-Ray Diffraction (Dover, New York, 1990)
- A.V. Shubnikov, Symmetry and Antisymmetry of Finite Figures (in Russian) Moscow. Acad. Sci. USSR. English translation in A.V. Shubnikov, N.V. Belov, Colored Symmetry, ed. by W.T. Holster (Pergamon, Oxford, 1964)
- Yu.A. Izyumov, V.E. Naish, R.P. Ozerov, Neutron Diffraction of Magnetic Materials (Consultant Bureau, New York, 1991)
- 19. E.F. Bertaut, Acta Cryst. (1968) A24, 217
- 20. W.R. Busing, H.A. Levy, Acta. Cryst. 22, 457-464 (1967)
- 21. Th. Hahn (ed.), International Tables for Crystallography Volume A: Space-Group Symmetry (Kluwer, Dordrecht, 1987)
- 22. Ch. Brouder, A. Juhin, A. Bordage, M.-A. Arrio, J. Phys. Condens. Matter 20, 455205 (2008)
- 23. S.P. Collins, S.W. Lovesey, E. Balcar, J. Phys. Condens. Matter 19, 213201 (2007)
- 24. J.D. van Beek, J. Magn. Res. 187, 19–26 (2007)
- 25. A.J. Stone, Mol. Phys. 29, 1461–1471 (1975)
- Y. Tanaka, T. Takeuchi, S.W. Lovesey, K.S. Knight, A. Chainani, Y. Takata, M. Oura, Y. Senba, H. Ohashi, S. Shin, Phys. Rev. Lett. 100, 145502 (2008)
- S.P. Collins, D. Laundy, V.E. Dmitrienko, D. Mannix, P. Thompson, Phys. Rev. B 68, 064110 (2003)
- 28. A. Maignan, C. Michel, A.C. Masset, C. Martin, B. Raveau, Eur. Phys. J. B 15, 657 (2000)
- 29. S. Agrestini, C. Mazzoli, A. Bombardi, M.R. Lees, Phys. Rev. B 77, 140403(R) (2008)
- 30. A. Bombardi, C. Mazzoli, S. Agrestini, M.R. Lees, Phys. Rev. B 78, 100406(R) (2008)
- H. Fjellvåg, E. Gulbrandsen, S. Aasland, A. Olsen, B.C. Hauback, J. Solid State Chem. 124, 190 (1996)
- 32. E.V. Sampathkumaran, N. Fujiwara, S. Rayaprol, P.K. Madhu, Y. Uwatoko, Phys. Rev. B 70, 014437 (2004)
- T. Burnus, Z. Hu, M.W. Haverkort, J.C. Cezar, D. Flahaut, V. Hardy, A. Maignan, N.B. Brookes, A. Tanaka, H.H. Hsieh, H.-J. Lin, C.T. Chen, L.H. Tjeng, Phys. Rev. B 74, 245111 (2006)
- 34. P. Carra, B.T. Thole, Rev. Mod. Phys. 66, 1509 (1994)
- 35. S. Di Matteo, Y. Joly, A. Bombardi, L. Paolasini, F. de Bergevin, C.R. Natoli, Phys. Rev. Lett. 91, 257402 (2003)
- 36. S. Di Matteo, Y. Joly, R. Natoli, Phys. Rev. **B 72**, 144406 (2005)
- 37. I. Marri, P. Carra, Phys. Rev. B 69, 113101 (2004)
- L. Paolasini, S. Di Matteo, C. Vettier, F. de Bergevin, A. Sollier, W. Neubeck, F. Yakhou, P.A. Metcalf, J.M. Honig, J. Electron Spectrosc. Relat. Phenom. 120, 1 (2001)
- D. Mannix, D.F. McMorrow, R.A. Ewings, A.T. Boothroyd, D. Prabhakaran, Y. Joly,
 B. Janousova, C. Mazzoli, L. Paolasini, S.B. Wilkins, Phys. Rev. B 76, 184420 (2007)

Chapter 9

An Introduction to Inelastic X-Ray Scattering

J.-P. Rueff

Abstract The article provides a brief but up-to-date overview of inelastic X-ray scattering (IXS), a powerful spectroscopic probe of the electronic and dynamical properties. We introduce in first part the basic theoretical concepts for both resonant and nonresonant IXS, including resonant X-ray emission, absorption in the partial fluorescence yield mode, and X-ray Raman scattering. This formal section is followed by examples borrowed from the recent literature, with an emphasis on high pressure physics, strongly correlated materials, and new instrumentation.

9.1 Introduction

Inelastic X-ray scattering (IXS) is emerging as a powerful spectroscopic probe for investigating complex systems in physics or chemistry. Besides a somewhat complicated theoretical and experimental handling, IXS presents several, some times unique, advantages for the study of the electronic and dynamical properties of electrons in materials: acquiring soft X-ray spectra with high energy X-rays, revealing the fine structure within the white line, "imaging" the chemical environment, probing low energy excitations and their dispersion, measuring phonons, or performing spectroscopy in constrained sample environments are among the manifold possibilities offered by this technique.

The aim of the article is to provide a general yet selective overview of the IXS process through relevant examples in physics and chemistry of solids. The basic theoretical concept will be reviewed in first section for both resonant and non-resonant IXS. We address in second part emblematic examples of IXS borrowed from the recent literature.

For further reading, we encourage the reader to consult the books recently published on the subject [1, 2] and to browse through the review articles that have

Synchrotron SOLEIL, L'Orme des Merisiers, BP 48 Saint-Aubin, 91192 Gif sur Yvette e-mail: jean-pascal.rueff@synchrotron-soleil.fr and

Laboratoire de Chimie Physique–Matière et Rayonnement, CNRS-UMR 7614, Université Pierre et Marie Curie, F-75005 Paris, France

J.-P. Rueff

264 J.-P. Rueff

been devoted to inelastic X-ray scattering for electronic excitations [3–5], electron dynamics [6,7], and high-pressure physics [8]. The IXS development has been possible, thanks to the emergence of a new generation of synchrotron light sources and improved X-ray optics. The latter is described in some detail in [9].

9.2 Theoretical Concepts

9.2.1 Overview of the IXS Process

"There are only three basic actions to produce all the phenomena associated with light and electrons: A photon goes from place to place, an electron goes from place to place, an electron emits or absorbs a photon." (QED, Richard Feyman)

This beautifully concise definition of the interaction between light and matter by R. Feyman applies well to the IXS process: as depicted in Fig. 9.1, IXS involves the scattering of an incident photon defined by its wave vector, energy, and polarization $(\mathbf{k}_1, \hbar\omega_1, \boldsymbol{\varepsilon}_1)$ by the electron system; we use the same notation for the scattered photon defined by $(\mathbf{k}_2, \hbar\omega_2, \boldsymbol{\varepsilon}_2)$. Energy $(\hbar\omega)$ and momentum (\mathbf{q}) is transferred to the electrons during the scattering event according to

$$\hbar\omega = \hbar\omega_1 - \hbar\omega_2,\tag{9.1}$$

$$\mathbf{q} = \mathbf{k}_1 - \mathbf{k}_2. \tag{9.2}$$

For high energy X-ray, the change in the wave vector amplitude during the scattering process is negligibly small so that q is well approximated by

$$q \approx 2k_1 \sin(2\theta),\tag{9.3}$$

where 2θ is the scattering angle.

As discussed in the following, the denomination IXS embodies in fact many different spectroscopic techniques, which are summarized in Fig. 9.2. These can be mainly divided into two groups that branch out from the generic IXS process, depending on whether the incident photon energy is close or not to a resonance (absorption edge). Their definition will become clearer in the following when it comes to the IXS cross section.

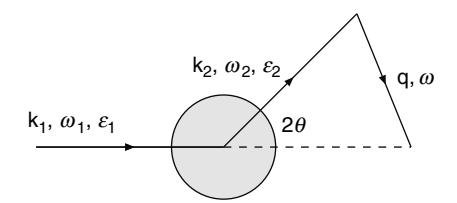


Fig. 9.1 Generic inelastic X-ray scattering (IXS) process

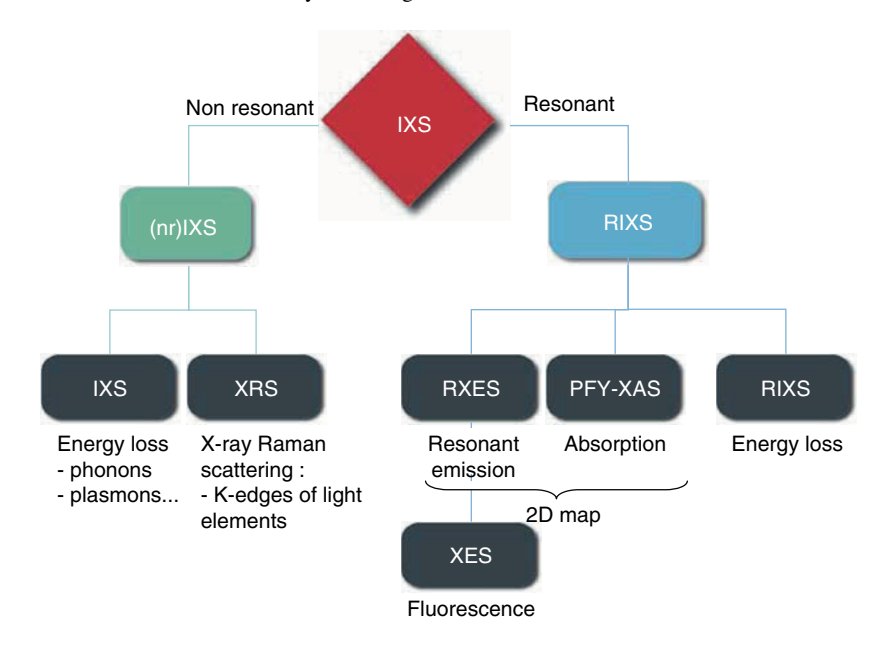


Fig. 9.2 Overview of IXS-derived techniques (cf text for details)

9.2.2 Interaction Hamiltonian

The interaction Hamiltonian \mathcal{H} is conventionally split into a noninteracting term \mathcal{H}_0 and an interacting term \mathcal{H}_{int} that is treated in perturbation theory:

$$\mathcal{H} = \mathcal{H}_0 + \mathcal{H}_{int}. \tag{9.4}$$

 \mathcal{H}_0 includes the electron kinetic and potential energies (9.5a), while \mathcal{H}_{int} describes the interaction between the incident electromagnetic field and the electrons (9.5b):

$$\mathcal{H}_0 = \sum_{j} \frac{1}{2m} \mathbf{p}_j^2 + \sum_{jj'} V(r_{jj'}), \tag{9.5a}$$

$$\mathcal{H}_{int} = \sum_{j} -\frac{e}{mc} \mathbf{A}(\mathbf{r}_{j}) \cdot \mathbf{p}_{j} + \sum_{j} \frac{e^{2}}{2mc^{2}} \mathbf{A}^{2}(\mathbf{r}_{j}). \tag{9.5b}$$

The sum is carried over all the electrons j in the system. We have omitted the spin dependent terms, which are smaller by a factor \hbar/mc^2 . The $(\mathbf{A} \cdot \mathbf{p})$ term in \mathcal{H}_{int} involves the photoelectric process between an incident photon and the electrons. It entails different phenomena such as photoemission, X-ray absorption or emission to the first order of perturbation, and resonant inelastic X-ray scattering (RIXS) to the second order of perturbation, all involving electronic transitions. The $\mathbf{p} \cdot \mathbf{A}$ term is

266 J.-P. Rueff

usually qualified as a *resonant* operator in contrast to the *nonresonant* A^2 term that gives rise to the Thomson scattering of photons by the valence electron, and more generally to the nonresonant IXS (nrIXS) process.

9.2.3 IXS Cross Sections and Fermi Golden Rule

The transition probability $w_{i \to f}$ between the ground state $|i\rangle$ (of energy E_i) and the final state $|f\rangle$ (of energy E_f) is given by the Fermi Golden rule applied to \mathcal{H}_{int} . In (9.6), it is developed up to the second order of perturbation:

$$w_{i \to f} = \frac{2\pi}{h} \left| \langle f | \mathcal{H}_{\text{int}} | i \rangle + \sum_{n} \frac{\langle f | \mathcal{H}_{\text{int}} | n \rangle \langle n | \mathcal{H}_{\text{int}} | i \rangle}{E_{n} - E_{i}} \right|^{2} \delta(E_{f} - E_{i}). \tag{9.6}$$

The sum is carried over all the intermediate states $|n\rangle$ (of energy E_n) and the δ function ensures energy conservation.

A typical scattering experiment consists of detecting the scattered photon within a certain solid angle $d\Omega$ and with a given resolution $d\hbar\omega_2$. The scattering cross section is then expressed by a double differential expression that is proportional to the transition probability w and the scattering volume V according to

$$\frac{\mathrm{d}^2 \sigma}{\mathrm{d}\Omega \mathrm{d}\omega_2} = \frac{wV^2 \omega_2^2}{8\pi^3 \hbar c^4} \tag{9.7}$$

9.2.4 Nonresonant IXS

9.2.4.1 Cross Section

To compute the nonresonant IXS double differential cross section (DDCS), it suffices to limit ourselves to the first-order of perturbation. The dominant term of the interaction Hamiltonian is A^2 ; using this operator in (9.6), we find

$$\frac{\mathrm{d}^2 \sigma}{\mathrm{d}\Omega \mathrm{d}\omega_2} = \frac{\omega_2}{\omega_1} \left(\frac{e^2}{mc^2} \right)^2 (\boldsymbol{\varepsilon}_1 \cdot \boldsymbol{\varepsilon}_2)^2 \sum_{i,f} \left| \langle f | \sum_j \exp(\mathrm{i} \mathbf{q} \cdot \mathbf{r}) | i \rangle \right|^2 \times \delta \left(E_f - E_i - \hbar \omega \right), \tag{9.8}$$

which can be simplified into

$$\frac{\mathrm{d}^2 \sigma}{\mathrm{d}\Omega \mathrm{d}\omega_2} = \left(\frac{\mathrm{d}\sigma}{\mathrm{d}\Omega}\right)_{\mathrm{Th}} S(\mathbf{q}, \omega),\tag{9.9}$$

where $(d\sigma/d\Omega)_{Th}$ is the Thomson scattering cross section and $S(\mathbf{q},\omega)$ the dynamical structure factor. In the adiabatic approximation, the electronic wave function in (9.9) can be factorized out from the ionic one. The DDCS then reads

$$\frac{\mathrm{d}^2 \sigma}{\mathrm{d}\Omega \mathrm{d}\omega_2} = \left(\frac{\mathrm{d}\sigma}{\mathrm{d}\Omega}\right)_{\mathrm{Th}} |f(\mathbf{q})|^2 S^*(\mathbf{q}, \omega), \tag{9.10}$$

where $f(\mathbf{q})$ is the electronic form factor and $S^*(\mathbf{q},\omega)$ the ionic contribution to the total dynamical structure factor. This expression is widely used when treating IXS of phonon excitations.

9.2.4.2 Expressions of the Dynamical Structure Factor

From (9.9) and (9.10), we find that the dynamical structure factor is expressed by

$$S(\mathbf{q}, \omega) = \sum_{i, f} \left| \langle f | \sum_{j} \exp(i\mathbf{q} \cdot \mathbf{r}) | i \rangle \right|^{2} \times \delta \left(E_{f} - E_{i} - \hbar \omega \right)$$
(9.11a)

$$= \frac{1}{2\pi} \int_{-\infty}^{\infty} dt \, e^{-i\omega t} \langle i | \sum_{jj'} e^{-i\mathbf{q}\cdot\mathbf{r}_{j'}(t)} \, e^{i\mathbf{q}\cdot\mathbf{r}_{j}(0)} | i \rangle. \tag{9.11b}$$

Equation (9.11a) links the dynamical structure factor to the excitations of the electron system from the ground state (E_i) to all the excited final states (E_f) that are allowed by energy and momentum conservation. The second expression follows the formulation of Van Hove [10] and expresses $S(\mathbf{q}, \omega)$ as the time dependent electron density fluctuation in the *ground state*. Everything happens as if the photons were not perturbing the electron systems. The equivalence between (9.11a) and (9.11b) is a manifestation of the well-known fluctuation—dissipation theorem.

Other known formulations of the dynamical structure factor connect $S(\mathbf{q}, \omega)$ to the imaginary part of electronic polarization function χ (9.12a) and to the inverse of the dielectric function $\varepsilon(\mathbf{q}, \omega)$ in (9.12b):

$$S(\mathbf{q},\omega) = -\frac{1}{\pi}(1+\eta_{\rm B})\chi''(\mathbf{q},\omega)$$
 (9.12a)

$$= (1 + \eta_{\rm B}) \frac{q^2}{4\pi e^2} \operatorname{Im} \left[\frac{-1}{\varepsilon(\mathbf{q}, \omega)} \right], \tag{9.12b}$$

with η_B , the Bose factor. These are mostly useful when it comes to the theoretical calculations of the nonresonant scattering process.

Thus, through the connection to the dynamical structure factor, IXS allows one to probe the low energy excitations of the electron system. As illustrated in Fig. 9.3a, this covers phonons at low energy, then excitons, plasmons in the mid-energy range to end up with excitation of core-electrons, which we discuss in the next section. Fig. 9.3b also compares IXS to other probing techniques of the electron dynamics

268 J.-P. Rueff

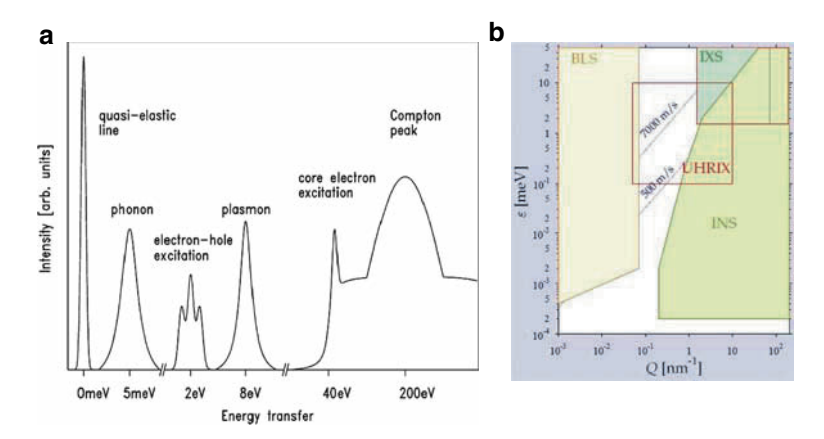


Fig. 9.3 (a) Excitations probed by nonresonant IXS as a function of the energy transfer; (b) accessible domain in the (\mathbf{q}, ω) phase space for IXS, inelastic neutron scattering (INS), and Brillouin light scattering (BLS) (source ESRF)

such as Brillouin light scattering (BLS) or inelastic neutron scattering (INS). Clearly enough, IXS can access a range in the (\mathbf{q}, ω) phase space not or only partly covered by those techniques.

9.2.4.3 X-Ray Raman scattering: Equivalence with Absorption

As shown in (9.11a), the nonresonant IXS cross section involves the matrix element of the transition operator $\exp(i\mathbf{q}\cdot\mathbf{r})$ taken between the initial and final states, $|i\rangle$ and $|f\rangle$. Using the series expansion of the exponential in the limit $qr \to 0$,

$$\exp(i\mathbf{q}\cdot\mathbf{r}) = 1 + i\mathbf{q}\cdot\mathbf{r} + (i\mathbf{q}\cdot\mathbf{r})^2/2 + \dots, \tag{9.13}$$

the nonresonant IXS matrix element simplifies to $|\langle f|\mathbf{q}\cdot\mathbf{r}\rangle|^2$ at the first order; the constant term does not contribute at low \mathbf{q} as $|i\rangle$ and $|f\rangle$ are orthogonal. This expression can be compared to the standard X-ray absorption cross-section:

$$\left(\frac{\mathrm{d}\sigma}{\mathrm{d}\Omega}\right)_{\mathrm{XAS}} = \left|\left\langle f|\boldsymbol{\epsilon}\cdot\mathbf{r}|i\right\rangle\right|^2 \times \delta\left(E_f - E_i - \hbar\omega\right). \tag{9.14}$$

In the limit $qr \ll 1$, (9.13) is valid and then the nonresonant IXS is equivalent to an absorption process with \mathbf{q} playing the role of the polarization vector $\boldsymbol{\varepsilon}$ [11]. When $qr \gg 1$, other terms of the series expansion may contribute to the X-ray Raman scattering (XRS) cross section, which then may contain monopolar or quadrupolar excitations channels in addition to the dipolar one [12].

9.2.5 RIXS

When the incident photon energy $\hbar\omega_1$ approaches the energy of an absorption edge, the $\mathbf{p} \cdot \mathbf{A}$ term of the interaction Hamiltonian dominates. As RIXS involves two photons, the Fermi golden rule (9.6) has to take into account the second order perturbation theory. In this case, the DDCS is given by the Kramers–Heisenberg formula,

$$\frac{\mathrm{d}^{2}\sigma}{\mathrm{d}\Omega\mathrm{d}\hbar\omega_{2}} = r_{0}^{2} \left(\frac{\omega_{2}}{\omega_{1}}\right) \sum_{f} \left| \left(\frac{\hbar}{m}\right) \sum_{n} \frac{\left\langle f \left| \left(\boldsymbol{\varepsilon}_{2}^{*} \cdot \mathbf{p}_{j}\right) e^{-\mathrm{i}\mathbf{k}_{2} \cdot \mathbf{r}_{j}}\right) \right| n \right\rangle \left\langle n \left| \left(\boldsymbol{\varepsilon}_{1} \cdot \mathbf{p}_{j'}\right) e^{\mathrm{i}\mathbf{k}_{1} \cdot \mathbf{r}_{j'}}\right) \right| i \right\rangle}{E_{i} - E_{n} + \hbar\omega_{1} - \mathrm{i}\Gamma_{n}/2} \right|^{2} \times \delta(E_{i} - E_{f} + \hbar\omega). \tag{9.15}$$

The sum is over the intermediate $|n\rangle$ and final $|f\rangle$ states; Γ_n is the energy broadening of the intermediate state.

The Kramers–Heisenberg formula highlights the main aspects of RIXS: one electron is absorbed (transition $|i\rangle \rightarrow |n\rangle$) and a secondary electron emitted (transition $|n\rangle \rightarrow |f\rangle$); interference may occurs between the different excitation channels; the denominator diverges at the resonance. The general RIXS process is schematized in Fig. 9.4 in a configuration level scheme, which shows the energy level of the ground state, intermediate state, and final states on a total energy scale (vertical axis). In this picture, the transfer energy can be directly visualized as the excitation energy of the final states.

To illustrate the physical content of the RIXS process, we have calculated the RIXS cross section from the energy diagram depicted in the Fig. 9.4, which more specifically applied to a resonant emission process. We consider both narrow energy levels and a broad flat band whose onset marks the absorption edge (or resonance

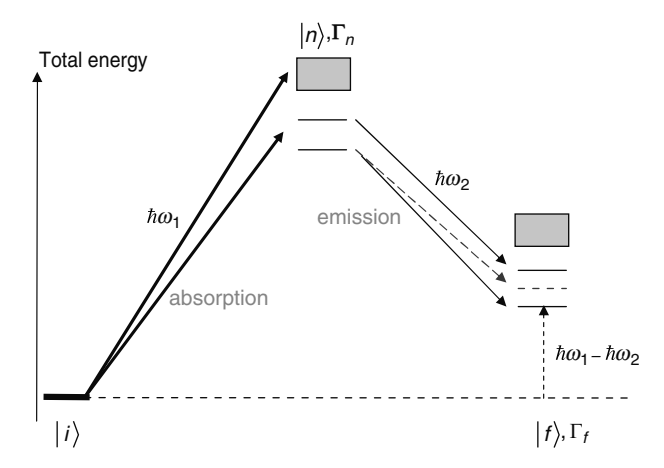


Fig. 9.4 RIXS process in a configuration level scheme; $|i\rangle$ is the initial state; $|n\rangle$ and $|f\rangle$ are the intermediate and final states of energy width Γ_n and Γ_f

270 J.-P. Rueff

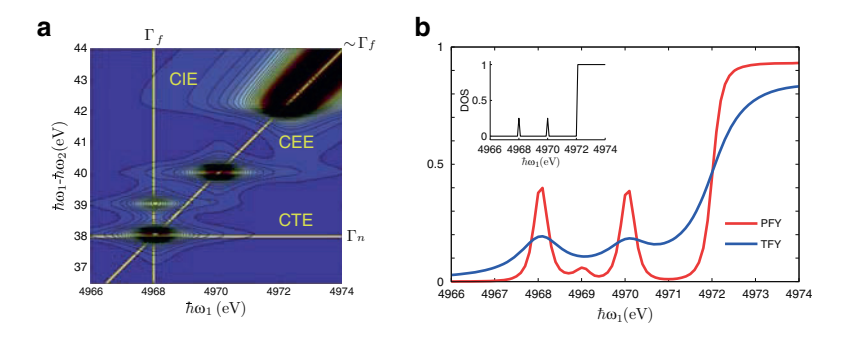


Fig. 9.5 (a) RIXS contour intensity map; lines are cuts at constant transfer energy (CTE), constant incident energy (CIE), and constant emission energy (CEE), also known as partial fluorescence yield (PFY); energy widths are indicated; (b) PFY XAS vs. standard XAS (TFY) spectra

energy). The cross-section was numerically computed using a simplified version of Kramers–Heisenberg formula (9.15) without interference effects and dropping the energy dependence of the matrix elements [13, 14]. The results are shown in Fig. 9.5a as an intensity contour map drawn as a function of the incident energy $\hbar\omega_1$ and transfer energy $\hbar\omega_1 - \hbar\omega_2$. Two types of spectral features can be recognized: patches stretched along $\hbar\omega_1$ and a broad diagonal structure. These reflect the RIXS process of, respectively narrow, levels and band states and give rise to different dispersive behaviors as a function of $\hbar\omega_1$: in the *fluorescence regime*, the features move with the incident energy while they appear at fixed transfer energy below the resonance in the so-called *Raman regime*. Notice, however, that the change of regime does not occur exactly at the resonance energy (vertical dashed lined in Fig. 9.5a), but slightly below as a consequence of the finite energy width of the intermediate and final states.

We now inspect different energy cuts through this intensity map which, as explained below, shows-up the spectral sharpening effect inherent to RIXS. Along $\hbar\omega_1$ at constant transfer energy (CTE), the spectra are dominated by the lifetime broadening of the core-hole Γ_n in the intermediate state; in contrast, cuts along the transfer energy (constant incident energy (CIE) or *resonant X-ray emission* spectroscopy (RXES)) probes the RIXS surface with a resolution of width Γ_f ; finally at 45° between these two are cuts at constant emission energy (CEE). They resemble an absorption spectrum but with an improved intrinsic resolution smaller than the core-hole lifetime broadening. This method is conventionally referred to as XAS in the *partial fluorescence yield* (PFY).

It can be shown that

$$\Gamma_{\text{PFY}} = \frac{1}{\sqrt{1/\Gamma_n^2 + 1/\Gamma_f^2}} \sim \Gamma_f \tag{9.16}$$

as $\Gamma_f \ll \Gamma_n$. This sharpening effect is clearly visible in Fig. 9.5b where the PFY XAS spectrum is compared to standard XAS. Another possibility that is not described in our model picture is when the lowest final state coincides with ground state energy. This recombination process (often called simply RIXS) yields a direct view of the low lying excited states. Besides the elastic peak at $\hbar\omega=0$, electronic excitations can be measured in the energy loss scale similarly to $S(\mathbf{q},\omega)$ but in resonant conditions.

9.3 Applications of IXS

We now turn to some examples of IXS borrowed from the recent literature. Needless to say that the choice among numerous results is somewhat arbitrary and biased by the author's experience. We have nevertheless selected examples in two fields of research where IXS has arguably attracted most interest and made the most significant impact in condensed matter physics: materials under extreme conditions and strongly correlated systems.

9.3.1 Extreme Conditions

As an all photon technique, IXS in the hard X-ray range is a penetrative bulk probe well suited to studying samples in constrained environments, amongst them diamond anvil cells for high pressure.

9.3.1.1 Absorption Edge of Light Elements Under Pressure

As discussed in Sect. 9.2.4, XRS offers the opportunity to probe the electronic core levels through the nonresonant scattering process. Under the condition $qr\ll 1$, XRS was found equivalent to an absorption process. In reality, this mostly applies to light elements whose binding energy falls in the soft X-ray region. Obviously, the main interest of XRS with respect to soft X-ray XAS is the use of high energy photon, which allows XRS to probe samples in highly absorbing environments. This is especially the case of diamond anvil cells.

Bonding changes and coordination has been investigated under high pressure in several C and B molecules by XRS. Figure 9.6b shows the C K-edge absorption spectra measured by XRS as a function of pressure in pyrolytic graphite [15]. The spectra were obtained in situ in a diamond anvil cell. The sample was loaded in a Be gasket partly transparent to X-rays, and the scattered X-rays was detected through the gasket. As depicted in Fig. 9.6a, the scattering process probes the C-p empty electronic states. These form π (σ) bonds that show up in the absorption spectra as distinct spectral features in the low (high) energy regions. The evolution of the XRS spectra upon compression indicates a progressive conversion of π to σ bonds under pressure, which reveals the densification of graphite – initially a layered 2D

272 J.-P. Rueff

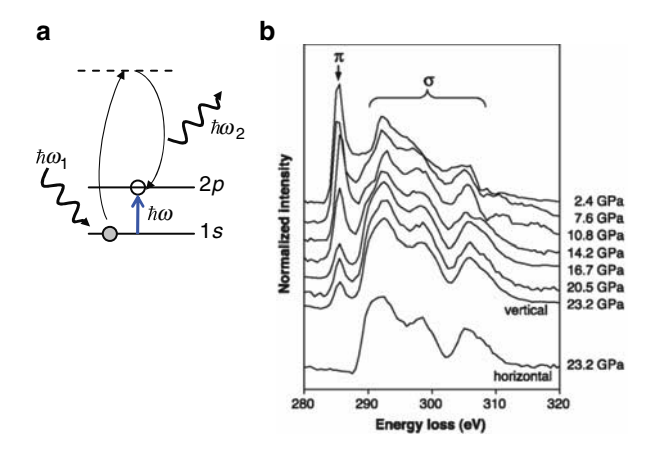


Fig. 9.6 (a) XRS process in light element; (b) C K-edge absorption spectra measured by XRS as a function of pressure in graphite (from [15])

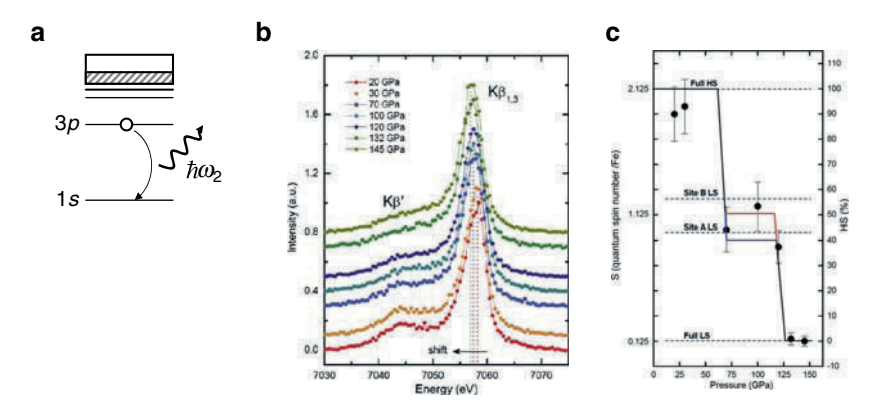


Fig. 9.7 (a) $K\beta$ emission process; (b) $K\beta$ emission line, and (c) spin state in $(Mg,Fe)SiO_2$ as a function of pressure (from [16])

material – into a hard 3D structure. The high pressure form of graphite was found to indent diamond.

9.3.1.2 Magnetic Collapse in Transition Metal

Thanks to the resonance, the RIXS scattering process discussed in Sect. 9.2.5 yields information about the electronic properties selective of the chemical species and electronic orbitals, a general feature of core-hole X-ray spectroscopic techniques. The conservation laws further ensure that energy and momentum are conserved during the scattering event and also the spin.

The sensitivity of RIXS to the spin state is best illustrated by the K β fluorescence line (3 $p \rightarrow 1s$ transition, cf Fig. 9.7a) in transition metal. The K β emission final

state is dominated by the Coulomb and exchange interactions between the 3p core hole and 3d electrons. The particularly strong multiplet effect splits of the final states into mainly two subsets of states, eventually leading to a main peak and a low energy satellite. The energy splitting between the two spectral features and their intensity ratio sensitively depends on the 3d spin polarization. K β XES therefore appears as a local probe of the 3d magnetism in transition metal. It can be easily applied to high pressure conditions since no magnetic field is required, and also in the absence of magnetic order.

Figure 9.7b shows the evolution of the $K\beta$ emission line in Fe-perovskite, a material assumed to be one of the components of the Earth mantle, as a function of pressure [16]. The low pressure spectra have a marked satellite structure characteristic of a high spin state of Fe. Upon pressure increase, the satellite intensity progressively declines as the main peak shifts to lower energies. This behavior is consistent with a change of the Fe spin state toward a low spin (or non magnetic) configuration. A detailed analysis (Fig. 9.7c) suggests a two-step decay of the Fe spin magnetic moment at about 50 and 125 GPa, which could reflect the successive magnetic collapse of the two Fe sites present in (Mg,Fe)SiO₂.

9.3.1.3 Valence Transition and Kondo Behavior

Pressure primarily affects electron delocalization as the overlap of the electron orbitals strengthens when the volume is reduced. Mixed valent rare-earth compound are very sensitive to this effect. Formally, the ground state of a mixed valent f-electron system can be written as a linear combination of different f-states,

$$|i\rangle = c_0|4f^n\rangle + c_1|4f^{n+1}\underline{\nu}\rangle + \cdots,$$
 (9.17)

where the c_i coefficients represent the weight of the $|4f^i\rangle$ components. The f-states are degenerated in the ground state, but this degeneracy can be lifted if a core-hole is created, thus making it possible to weight to the various f-states by core-hole spectroscopy.

These considerations have led to numerous studies in mixed-valent rare-earth compounds in the past performed by XAS or core-level photoemission. RIXS turns out to be a powerful alternative, thanks to the resonant enhancement and spectral sharpening effect, especially using the 2p3d-RIXS process. It consists of tuning the incident energy to the L_{2,3} edge and monitoring the L $\alpha_{1,2}$ emission line resonantly as schematized in Fig. 9.8a. A spectacular example of mixed valent transition occurs in $T_m T_e$. Figure 9.8b shows the results of a 2p3d-RIXS experiment in $T_m T_e$ under pressure: the spectra can be decomposed into a 2+ and 3+ replica that are signatures of the T_m mixed valent state. Through basic fitting, it is possible to extract the T_m valence v with a great accuracy and follow its evolution as a function of pressure (cf Fig. 9.8c). In $T_m T_e$, v increases progressively with pressure except for the jumps around 2 and 6 GPa that pinpoints the structural transition and a plateau from

274 J.-P. Rueff

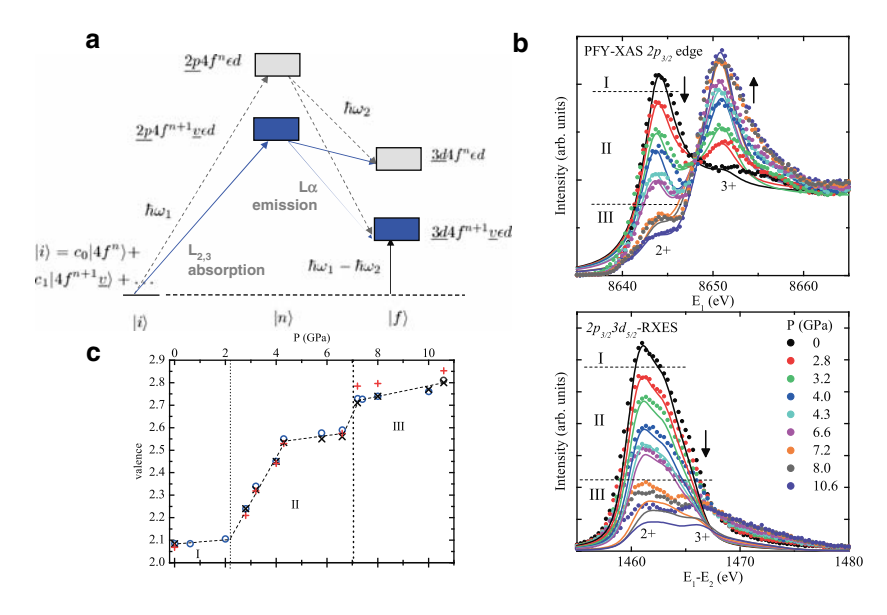


Fig. 9.8 (a) 3p3d-RIXS process; (b) PFY-XAS (top) and RXES (bottom) spectra measured in T_mT_e under pressure; (c) pressure-dependence of the T_m valence (from [17])

4-6 GPa. The latter is not expected in a normal delocalization picture of the f electron and was subsequently analyzed in terms of exotic Kondo effects in this material [17].

9.3.2 Strongly Correlated Materials

Strongly correlated electron systems embrace a vast family of materials that are of paramount interest for their wide implication in high $T_{\rm c}$ superconductivity, GMR effects, Kondo phenomena. Their properties rely on the interplay of charge, spin, and electronic of degrees freedoms, which has been addressed over the years by a massive experimental (and theoretical) effort. Among other spectroscopic techniques, RIXS has been applied to 3d transition metal oxides and f-electron systems. We briefly discuss in the following two examples that emphasize state-of-art IXS instrumentation for electronic excitation and electron dynamics.

9.3.2.1 dd-excitations in Transition Metal Oxides

The low energy excitations play a crucial role in many properties of transition metal systems. Especially, the dd excitations carry important information on local environment via the hybridization with ligands and magnetic interactions. They

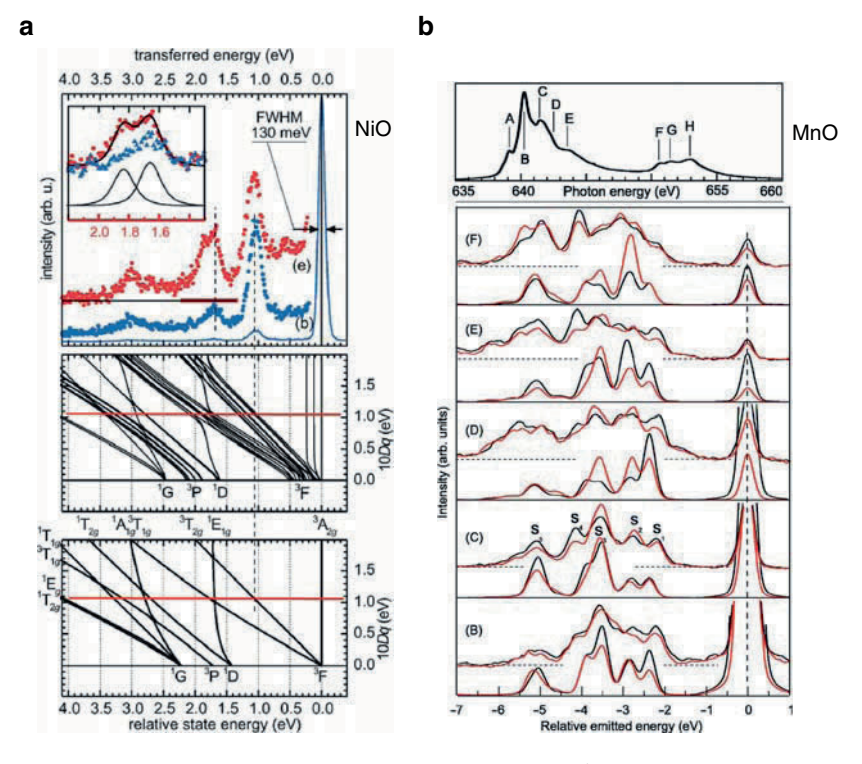


Fig. 9.9 Low energy excitations in NiO (a) and MnO (b) by 2p3d-RIXS (from [18, 19])

were traditionally the domain of optical absorption and electron energy loss experiments. More recently, however, it was shown that resonant inelastic X-ray scattering (RIXS) can also probe dd excitations, with the distinctive advantages of a resonant spectroscopy. Recent RIXS experiments were carried out on NiO and lately MnO, two model systems for correlated systems, in resonant conditions by tuning the incident energy to the metal $M_{2,3}$ and $L_{2,3}$ edges, respectively, in the soft X-ray region [18, 19]. The spectra displayed in Fig. 9.9 reveal well defined energy excitations in the 0–5 eV energy region that are ascribed to dd excitations. The complex spectral structure in MnO observed here with unprecedented details (Fig. 9.9b) is due to the multiplet effects in the RIXS final state between the 2p core hole and the 3d electrons. That these are not visible in NiO (Fig. 9.9a) illustrates the gain in resolving power attained by the new generation of RIXS instrumentation, now aiming for 10^4 in the soft X-ray range.

The MnO spectra can be well accounted for by calculations in the Anderson impurity model (upper curves in Fig. 9.9). The high quality of the experimental spectra permits a fine adjustment of the input parameters (charge transfer energy, crystal field strength) that are relevant for the physics of these materials.

276 J.-P. Rueff

9.3.2.2 Phonons in Plutonium

f-electrons in the early actinides are usually considered as a broad band states strongly hybridized with the 5d electrons. But starting from Am onwards, the f-electrons change their behavior to localized often correlated states. In this series, Pu stands out as a unique element as it lies at the border between localization–delocalization transition in presence of strong correlation. Such a valent (and magnetic) instability has major consequences for the electronic and structural properties and is likely to be at the origin of the intricate phase diagram of Pu and the superconductivity reported in several Pu compounds. The understanding of f correlated electrons remains a challenge for theoretical methods, though recent advances in this field allow one to consider how to make confrontation with precise experimental possible. The phonon spectrum especially is expected to be sensitive to details of the electronic distribution, influenced by the on-site Coulomb repulsion U.

Figure 9.10a displays the phonon spectrum of $PuCoGa_5$, an unconventional superconductor with a remarkably high transition temperature $T_c = 18 \, \mathrm{K}$ for an actinide material. The sample exists only in very small quantities, which hinders the use of neutron scattering. On the other hand, IXS benefits from the highly focused and intense X-ray beam generated by synchrotron light sources. The measurements were carried out by ultra-high resolution IXS on a single crystal of $PuCoGa_5$ [20]. A resolution of $\sim 1.5 \, \mathrm{meV}$ is achieved by using high orders of reflection of the monochromator and analyzer crystals, here $Si(11\ 11\ 11)$ at $21.7 \, \mathrm{keV}$, close to backscattering.

The phonon dispersion deduced from the IXS spectra is represented in Fig. 9.10b for different sections of the Brillouin zone. The results are confronted to first principle calculations (lines) with U left as the only adjustable parameter. Calculations with $U=3\,\mathrm{eV}$ match the experimental data best. This reveals the strongly correlated nature of the f-electrons in PuCoGa₅ while yielding an accurate estimation of the Coulomb repulsion in this system.

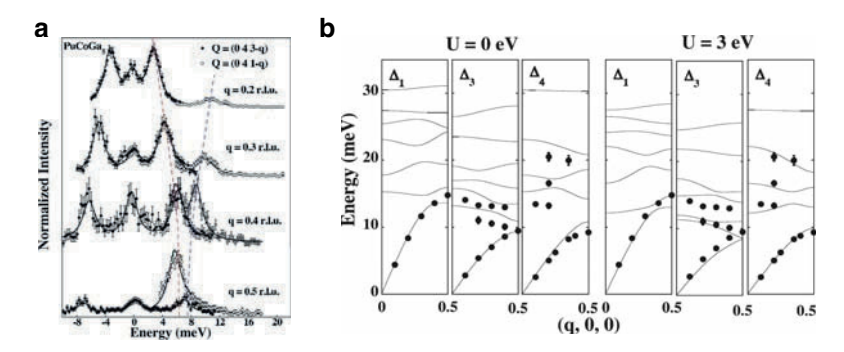


Fig. 9.10 (a) IXS phonon spectra in PuCoGa₅ and (b) phonon dispersion (from [20])

9.4 Conclusion

This short introduction to nonresonant and resonant inelastic X-ray scattering has not attempted to be exhaustive. Rather, we have provided the reader with the theoretical basics of IXS and discussed about few experimental results that underline the IXS specificities. We encourage the reader to consult the bibliography and the references therein for additional information.

Although IXS is a growing technique present nowadays in most of the new generation of synchrotrons, including the Synchrotron SOLEIL on the GALAXIES beamline, it is still in infancy with respect to other spectroscopic techniques. Our hope is that this contribution will trigger interest and motivate new directions of research using IXS.

References

- W. Schülke, Electron Dynamics by Inelastic X-Ray Scattering, Oxford Series on Synchrotron Radiation, Vol. 7 (Oxford University Press, USA, 2007)
- 2. F.M.F. de Groot, A. Kotani, Core Level Spectroscopy of Solids (Taylor and Francis, 2008)
- 3. A. Kotani, S. Shin, Rev. Mod. Phys. 73, 203 (2001)
- C.F. Hague, Magnetism: A Synchrotron Radiation Approach, Resonant Inelastic X-ray Scattering, (Springer, Hiedelberg, 2001), pp. 273–290
- 5. M. Altarelli, *Magnetism: A Synchrotron Radiation Approach*, Resonant X-ray Scattering: A Theoretical Introduction, (Springer, Hiedelberg, 2006), pp. 201–242
- 6. T. Scopigno, G. Ruocco, F. Sette, Rev. Mod. Phys. 77(3), 881 (2005)
- 7. F. Hennies, S. Polyutov, I. Minkov, A. Pietzsch, M. Nagasono, H. Agren, L. Triguero, M.N. Piancastelli, W. Wurth, F. Gel'mukhanov, A. Fohlisch, Phys. Rev. A **76**(3), 032505 (2007)
- 8. J.-P. Rueff, A. Shukla, Rev. Mod. Phys. (2009), under press
- 9. Y. Shvyd'ko, X-ray optics: High-energy-resolution applications, (Springer, Berlin, 2004)
- 10. L. Van Hove, Phys. Rev. 95, 249 (1954)
- 11. Y. Mizuno, Y. Ohmura, J. Phys. Soc. Jpn. 22, 445 (1967)
- 12. S. Doniach, P.M. Platzman, J.T. Yue, Phys. Rev. B 4, 3345 (1971)
- H. Hayashi, R. Takeda, Y. Udagawa, T. Nakamura, H. Miyagawa, H. Shoji, S. Nanao, N. Kawamura, Phys. Rev. B 68, 45122 (2003)
- P. Glatzel, M. Sikora & M. Fernández-García, Eur. Phys. J. Special Topics, 169, 207–214 (2009)
- W.L. Mao, H.K. Mao, P.J. Eng, T.P. Trainor, M. Newille, C.C. Kao, D.L. Heinz, J. Shu, Y. Meng, R.J. Hemley, Science 302, 425 (2003)
- 16. J. Badro, J.P. Rueff, G. Vankó, G. Monaco, G. Fiquet, F. Guyot, Science 305(5682), 383 (2004)
- I. Jarrige, J.P. Rueff, S.R. Shieh, M. Taguchi, Y. Ohishi, T. Matsumura, C.P. Wang, H. Ishii, N. Hiraoka, Y.Q. Cai, Phys. Rev. Lett. 101, 127401 (2008)
- S.G. Chiuzbaian, G. Ghiringhelli, C. Dallera, M. Grioni, P. Amann, X. Wang, L. Braicovich, L. Patthey, Phys. Rev. Lett. 95(19), 197402 (2005)
- G. Ghiringhelli, M. Matsubara, C. Dallera, F. Fracassi, A. Tagliaferri, N.B. Brookes, A. Kotani, L. Braicovich, Phys. Rev. B 73(3), 035111 (2006)
- S. Raymond, P. Piekarz, J.P. Sanchez, J. Serrano, M. Krisch, B. Janousova, J. Rebizant, N. Metoki, K. Kaneko, P.T. Jochym, A.M. Oles, K. Parlinski, Phys. Rev. Lett. 96(23), 237003 (2006)

Chapter 10 XAS and XMCD of Single Molecule Magnets

R. Sessoli, M. Mannini, F. Pineider, A. Cornia, and Ph. Sainctavit

Abstract Molecular magnetism is here presented with emphasis concerning the single molecule magnets (SMMs). The architecture of SMMs is reviewed as well as the various ingredients promoting magnetic anisotropy and the relation between magnetic anisotropy and the dynamics of magnetization. Then it is shown how XAS and XMCD can be unique tools to unravel the magnetic properties of SMM submonolayers grafted on clean surfaces. We bring a special attention to the spectral features associated with the magnetic anisotropy and magnetization dynamics.

10.1 Introduction

Molecular magnetism has covered in time a sort of cyclic pathway. In the days when X-ray diffractometers were not available, the magnetism of simple paramagnetic metal complexes was investigated to gather information on the coordination polyhedron around the metal center [1,2]. The investigation of pairs and oligomers of transition metal ions was the focus of the research in the early 1980s and allowed to establish useful correlations between the molecular structure and the efficiency of exchange interactions between the paramagnetic centers [3]. With this information in hand, chemists were able to construct extended structures that order magnetically close to room temperature [4–6]. The main advantage of the molecular approach to ordered magnetic materials resides in the possibility to combine properties brought in by the different building-blocks forming the molecular materials. A very recent example consists in the coexistence of magnetic order and optical chirality to yield a strong magneto-chiral effect [7].

The nineties were characterized by an intense research on a new class of molecular materials, known as single molecule magnets (SMMs) [8–10]. These are in general polynuclear coordination compounds of paramagnetic metal ions held

R. Sessoli (⊠)

Laboratory for Molecular Magnetism, Department of Chemistry and INSTM RU, University of Florence, 50019 Sesto Fiorentino, Italy

e-mail: roberta.sessoli@unifi.it

together by suitable organic ligands, which often provide an effective shielding between adjacent molecules in the solid state. They can be figured as tiny pieces of metal oxides or hydroxides, where the growth to form extended lattices has been blocked by capping ligand molecules. The most interesting aspect is that a few of these molecular clusters, featuring a combination of a large spin and an easy axis magnetic anisotropy, are characterized by a dramatic slowing down of the fluctuations of the magnetization at low temperature, and in some cases a magnetic hysteresis is observed [10]. At variance with more conventional magnetic materials, this type of hysteresis has a pure molecular origin and does not imply long range order. It was soon recognized that SMMs hold great potential to store information at the molecular level, even if the temperatures at which the hysteresis is observed remain prohibitive for technological applications. In fact, it is still confined to liquid helium region despite the many synthetic efforts devoted to its increase. This, however, has not diminished the interest in SMMs as model systems to investigate magnetism at the nanoscale and, in particular, the coexistence of quantum phenomena with the classical hysteretic behavior [11].

A key issue that has emerged in the last years is the possibility to address the magnetism of a single molecule, indeed a mandatory step to fully exploit the potential of SMMs and magnetic molecules in general. In its circular pathway, molecular magnetism is therefore focussing again on isolated magnetic objects. However, the environment is no longer a crystal lattice but a nanostructured surface or a miniaturized electronic device built using a single magnetic molecule. This gives the possibility to combine the rich quantum-dynamics of SMMs with transport properties, in the emerging field known as molecular spintronics [12]. The first step in this direction has been the organization of isolated SMMs on conducting and semiconducting surfaces [13] as a means of imaging single molecules and of measuring their transport properties with scanning probes techniques.

Synchrotron-based techniques, in particular X-ray absorption spectroscopy with circularly polarized light [14], have been used in molecular magnetism in all the different steps outlined above because of their unique capability to provide element-specific magnetic information [15–18], as well as to distinguish between orbital and spin contributions to the magnetism of the molecular material [19]. More recently, the great sensitivity of these techniques started to play a key role for the investigation of molecular adsorbates at surfaces [20–24]. Here, the challenge consists in clarifying the influence of the surface on the magnetic properties, and especially on the memory effect of a SMM, which is known to be dramatically environment-dependent [10].

The aim of this chapter is to present an overview of X-ray absorption (XAS) and X-ray magnetic circular dichroism (XMCD) in order to illustrate the great potential of these techniques as emerging from recent results [25–27]. This requires, however, a brief introduction about a few key concepts in molecular nanomagnetism, that is, magnetic exchange, magnetic anisotropy, and magnetization dynamics, all of them addressable with XAS-XMCD experiments. This overview is not intended to be exhaustive and the interested reader is addressed to more specialized literature.

10.2 Single Molecule Magnets

10.2.1 Building Up a Large Spin

If we exclude the fascinating case of mononuclear lanthanide complexes of high symmetry [28] or ions embedded in polyoxometallates [29], all other molecules presenting slow relaxation of the magnetization are constituted by polynuclear complexes of paramagnetic metal ions.

In the case of metal ions with a quenched orbital momentum, the leading term in the effective spin hamiltonian (SH) is isotropic exchange

$$H_{\text{ex}} = \sum_{i>j} J_{ij} \mathbf{S_i} \cdot \mathbf{S_j}, \tag{10.1}$$

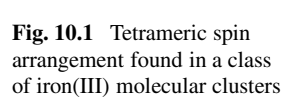
where i and j run over all metal sites of the cluster. Usually only interactions between nearest neighboring magnetic sites are considered, even if sizeable next nearest neighbor interactions are sometimes encountered. The resulting spin states are derived by following a vector coupling procedure and are characterized by a total spin state S_T , which in general varies from 0 or $^1/_2$, depending on the total number of unpaired electrons being even or odd, respectively, up to the sum of all individual spins [30, 31].

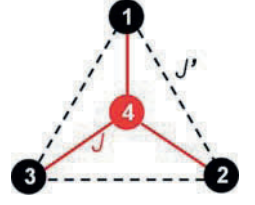
The energy of the different S_T states can be calculated analytically in some high symmetry cases, in particular when a central spin exhibits the same exchange interaction with the neighboring ones. This is also known as the Kambe approach [32] and spin systems comprising up to 13 coupled spins have been handled in this way [33]. A spin system that can be treated with this approach is the tetrameric unit schematized in Fig. 10.1.

This spin topology is encountered in a large family of tetranuclear iron(III) clusters, Fe₄ [34, 35], also known as *iron stars* [36]. Some of these clusters have also been widely investigated by XAS-XMCD techniques, as we show in Sect. 10.4.

We are using this spin topology to illustrate how the Kambe approach works. The SH that describes the exchange interactions in the system is

$$H_{\text{ex}} = J \left[\mathbf{S}_1 \cdot \mathbf{S}_4 + \mathbf{S}_2 \cdot \mathbf{S}_4 + \mathbf{S}_3 \cdot \mathbf{S}_4 \right] + J' \left[\mathbf{S}_1 \cdot \mathbf{S}_2 + \mathbf{S}_2 \cdot \mathbf{S}_3 + \mathbf{S}_1 \cdot \mathbf{S}_3 \right]. \quad (10.2)$$





Every spin state arising from the coupling of the four spins is defined by three quantum numbers $|S_a, S_{\text{ext}}, S_T\rangle$, where $S_a = S_1 + S_2$, $S_{\text{ext}} = S_a + S_3$, and $S_T = S_4 + S_{\text{ext}}$. There are many spin states with the same S_T but differing for the other quantum numbers. In the case of high symmetry, however, the total energy depends only on two of them, S_T and S_{ext} , according to

$$E(S_{T}, S_{\text{ext}}) = \frac{J}{2} \left[S_{T}(S_{T}+1) - S_{\text{ext}}(S_{\text{ext}}+1) - S_{4}(S_{4}+1) \right] + \frac{J'}{2} \left[S_{\text{ext}}(S_{\text{ext}}+1) - S_{3}(S_{3}+1) - S_{2}(S_{2}+1) - S_{1}(S_{1}+1) \right].$$
(10.3)

Considering that all terms involving local spins S_i introduce only an energy offset, (10.3) can be simplified as

$$E(S_{\rm T}, S_{\rm ext}) = \frac{J}{2} \left[S_{\rm T}(S_{\rm T} + 1) - S_{\rm ext}(S_{\rm ext} + 1) \right] + \frac{J'}{2} \left[S_{\rm ext}(S_{\rm ext} + 1) \right]. \quad (10.4)$$

Thus, it is necessary only to properly count all possible states arising from the coupling of four spins, in order to consider their correct degeneracy and to calculate their energy according to (10.4). Knowledge of the energy of the spin states then gives full access to the thermodynamic properties of the spin system.

In general, however, the diagonalization of big matrices is required and, as soon as the number of magnetic centers increases, the calculation of the energy of all resulting spin states becomes very demanding. Different approaches have been developed [37–39], and for moderate cluster sizes, a convenient method is based on irreducible tensor operators [40]. Codes are also available for the calculation of the thermodynamic properties of spin clusters.

The occurrence of a large spin ground state is a necessary, although not sufficient, condition to observe slow relaxation of the magnetization. At present a good control of the spin of the ground state has been achieved, thanks to many studies on magneto-structural correlations, such as those known as Goodenough and Kanamori rules [41–44]. They refer to the overlap of the wavefunction describing the unpaired electrons of two interacting fragments. It must be stressed that, in coordination compounds, the exchange interaction usually occurs through a "superexchange" mechanism, that is, mediated by the coordinating atoms of the bridging ligands, rather than arising from direct overlap of the metal d-orbitals. It is therefore more correct to refer to a molecular orbital of the metal fragment carrying the unpaired electron, which has a small, but significant, spin density on the bridging atom. The Goodenough and Kanamori rules tell us the following:

- An antiferromagnetic interaction is expected if the overlap integral between magnetic orbitals is different from zero.
- A ferromagnetic one is instead expected if the magnetic orbitals of the two interacting fragments are orthogonal.
- If a magnetic orbital shows a significant overlap with a fully occupied or with an empty orbital of the second fragment, the exchange interaction is ferromagnetic.



Fig. 10.2 Schematic view of the magnetic core of the heptanuclear cluster of formula $[Cr^{III}(CN-Ni^{II}-L)_6]^{9+}$, with the ferromagnetic alignment of the spin indicated by the *arrows*. The cyanide bridges are shown as *rods*, with the carbon atom in *pale grey*

From these simple rules it is clear that antiferromagnetism is the norm in polynuclear compounds and that strict orthogonality of the orbitals can be most easily achieved in highly symmetric molecules. An example is polycyanometallates, in which the central atom, for instance a chromium(III) ion in octahedral environment, is bridged by six CN⁻ ligands to other six metal ions, as schematized in Fig. 10.2 [45–48]. The unpaired electrons are occupying the d_{xy} , d_{yz} , and d_{xz} orbitals of Cr^{III} , which span the t_{2g} symmetry representation of the O_h group and are therefore orthogonal to the $d_{x^2-y^2}$ and d_{z^2} orbitals of the external ions, for instance, the magnetic orbitals of Ni^{II} ions. The compound of formula [Cr(CN-Ni-L)₆]⁹⁺, where L is the terminal ligand tetraethylenpentamine, has a ground state $S_T = 15/2$. Interestingly, if the outer metal ions are replaced by Mn^{II}, with unpaired electrons in each of the five 3d orbitals, the antiferromagnetic exchange through the overlapping orbitals of t_{2g} symmetry dominates to yield a ground spin state corresponding to $S_T = 6 \times 5/2 - 3/2 = 27/2$ [47,48]. This simple example tells us that, although ferromagnetic interactions in this type of insulators require strict conditions to be fulfilled, relatively high spin values can be achieved by simply playing with the noncompensation of the magnetic moments inside the molecule. This is by far the most commonly encountered case in SMMs, including the archetypal Mn₁₂ clusters [49]. Here, the $S_T = 10$ ground state results from exchange interactions that are antiferromagnetic and align the external spin S = 2 of Mn^{III} antiparallel to the S = 3/2 spins of the internal Mn^{IV} ions, as shown in Fig. 10.3 [8, 9, 38, 39]. In analogy to the uncompensated magnetism of different sublattices discovered by Néel, these types of spin clusters are often called ferrimagnetic, with the necessary clarification that they are zero-dimensional objects where the correlation is limited to a finite number of spins and does not diverge as in traditional magnets.

A significant number of spin clusters showing ferromagnetic interactions are however present in the literature. Noticeably, ferromagnetism is encountered in the case of the molecular system exhibiting the largest spin ground state, $S_T = 87/2$ [50], and in the hexanuclear manganese cluster holding the record temperature for the freezing of the magnetization [51].

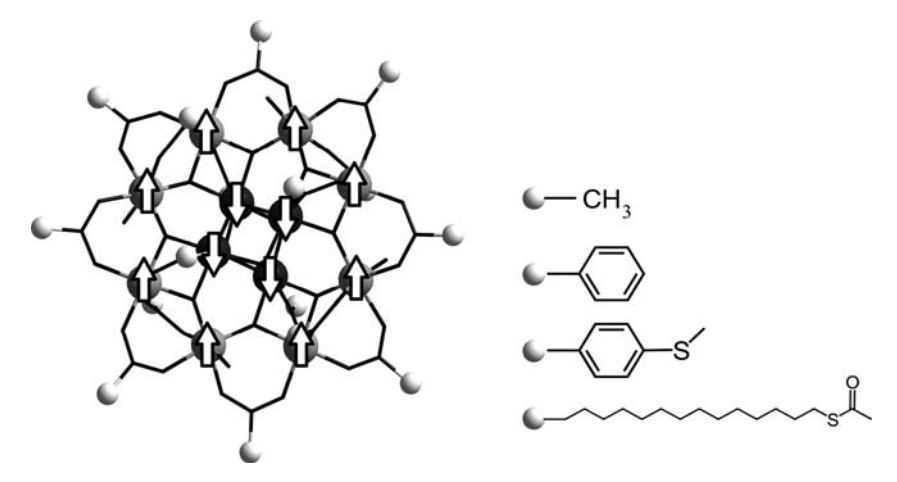


Fig. 10.3 View of the molecular structure of a Mn_{12} cluster along its tetragonal axis with the arrows representing the spin structure of the ground state. The dark spheres represent Mn^{IV} sites, while pale spheres stand for Mn^{III} ions. On the right, the ligand structure of the four different derivatives discussed in this chapter (Mn_{12} ac, Mn_{12} Bz, Mn_{12} BzSMe, and Mn_{12} C15SAc)

The spin structure of a SMM is strongly correlated to the dynamics of the magnetization and can be considered as a sort of fingerprint, which can be easily accessed through XMCD, as shown in the following.

10.2.2 Magnetic Anisotropy in Single Molecule Magnets

The second key ingredient in SMMs is magnetic anisotropy. In traditional magnets, three factors give equally important contributions to the anisotropy, namely surface, strain, and magnetocrystalline contributions. In SMMs, the only significant role is played by magnetocrystalline anisotropy and is brought in by a combination of spin—orbit coupling with the low-symmetry environment around the metal centers constituting the SMMs. Dipolar contributions are in most cases negligible. A quantitative treatment of the magnetic anisotropy is based on the effective spin-hamiltonian approach where only the spin variables appear, while the orbital contributions are introduced through parameters [52]. The magnetic anisotropy is treated with a multipolar expansion, which should be extended to the $2S^{th}$ order, where S is the spin of the system. Very often SMMs have a low symmetry and thus the lower terms of the expansion dominate.

For a system with no symmetry at all, the multipolar expansion up to the second order gives

$$H_{\text{an}} = \mathbf{S} \cdot \mathbf{D} \cdot \mathbf{S} = D \left[S_z^2 - \frac{1}{3} S(S+1) \right] + E(S_x^2 - S_y^2),$$
 (10.5)

where $D = D_{zz} - \frac{1}{2}D_{xx} - \frac{1}{2}D_{yy}$ represents the axial anisotropy and $E = \frac{1}{2}(D_{xx} - D_{yy})$ the transverse (or rhombic) one. The value of E is intrinsically limited to $\frac{1}{3}D$ because going beyond this limit indeed corresponds to a change in the axis of the leading anisotropy. The transverse term can be more conveniently rewritten in terms of ladder operators as $\frac{1}{2}E(S_+^2 + S_-^2)$.

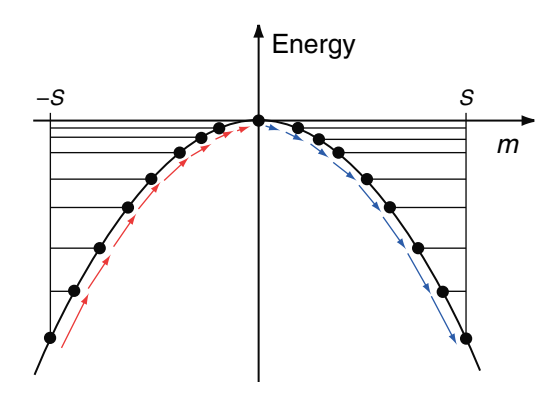
The effect of the magnetic anisotropy on the (2S+1) states of the spin multiplet is that of removing their degeneracy even in the absence of an external field, and thus is also named zero field splitting (ZFS), especially among spectroscopists. The term $\frac{1}{3}S(S+1)$ just introduces an offset of all levels to preserve the center of gravity of the energy spectrum and can be dropped off when dealing with the relative energies inside the S multiplet.

The same orbital contributions responsible for the ZFS are also affecting the anisotropy of the ${\bf g}$ tensor. However, as the ${\bf g}$ tensor describes the response to an applied magnetic field, it does not influence the dynamics of the magnetization in zero field after the system has been magnetized. For this reason it will not be further discussed in this context.

The effect of a negative D in (10.5) is that the system can be magnetized much more easily when the field is applied along the principal, that is, z, axis. In traditional magnets the anisotropy energy is quantified through the difference in the area spanned by the magnetization curves taken applying the field along the easy and hard axes. In SMMs the anisotropy energy is instead associated to the energy gap in zero field between the states characterized by the largest and smallest |m|, where m is the eigenvalue of S_z [10]. In the case of pure axial anisotropy, E=0, the gap corresponds to $|D|S^2$ and $|D|(S^2-1/4)$ for integer and half-integer S, respectively. A system showing easy axis magnetic anisotropy, D<0, has the ground doublet characterized by $m=\pm S$, which corresponds to two potential wells separated by an energy barrier, as reported in Fig. 10.4.

In the case of a spin system constituted by a single paramagnetic center carrying 2S unpaired electrons, the value of D can be experimentally determined through electron paramagnetic resonance (EPR) spectroscopy [53–56] or alternatively through inelastic neutron scattering [57]. Also magnetometry, especially if performed on a single crystal sample, can provide accurate values. The magnetic anisotropy can also be estimated theoretically, with a great variety of approaches.

Fig. 10.4 Splitting in zero field of the (2S + 1) levels due to an axial anisotropy described by (10.5) with D < 0. The application of a strong field populates selectively one of the wells and equilibrium in zero field is re-established by transferring population in the other well through a multiphonon process here depicted by the *arrows*



These range from simple perturbation theory, starting from a spectroscopic estimation of the energy separation of the partially filled d orbitals [58, 59] to a ligand field treatment based on the angular overlap model [60]. More recently ab initio calculations, either based on density functionals [61–64] or on post Hartree–Fock approaches [65, 66], have also shown a good predictive capability.

The situation is more complicated in the case of a polynuclear metal system, such as most SMMs. In general, when working with first row transition metal ions, it is found that the magnetic anisotropy is weaker than intramolecular exchange interactions. Hence, the resulting states are well described by the quantum number corresponding to the total spin state, as derived from (10.1), and the magnetic anisotropy is introduced as a perturbation. The magnetic anisotropy of a given total spin S_T can be related to the single ion contributions or to the anisotropic part of the interaction, either dipolar or exchange in nature, by using projection techniques [31]:

$$\mathbf{D}_{S_{\mathrm{T}}} = \sum_{i} d_{i} \mathbf{D}_{i} + \sum_{i>j} d_{ij} \mathbf{D}_{ij}, \qquad (10.6)$$

where i and j refer to the magnetic centers inside the SMM. The projection coefficients d_i and d_{ij} depend on how the individual spins project on the total spin state under consideration; \mathbf{D}_i are the single ion contributions, and \mathbf{D}_{ij} the anisotropy brought in by two-spin interactions. The calculation of d_i and d_{ij} is based on a relatively simple recursive algorithm, whose details are beyond the scope of this contribution and the interested reader is addressed to specific literature [10, 31]. However, to give a feeling to the reader, we provide the values of the projection coefficients for the simple $[\mathrm{Cr}(\mathrm{CN-Ni-L})_6]^{9+}$ cluster described in Sect. 10.2.1. The magnetic anisotropy of the state with the largest spin ($S_{\mathrm{T}}=15/2$) has $d_{\mathrm{Cr}}=0.028571$ and $d_{\mathrm{Ni}}=0.009524$. The small values of these coefficients clearly show that it is not straightforward to combine a large spin with a large magnetic anisotropy. Although apparently coupling more and more spins to increase S should lead to a quadratic effect on the height of the barrier, the projection of the anisotropies of the single ion makes the barrier to scale linearly with S [10, 67].

A second important aspect of (10.6) to be stressed here is its tensorial nature. In other words, it is not only the single ion anisotropy that matters, but also how the individual tensors are oriented inside the molecule. Let us again refer to the simple $[Cr(CN-Ni-L)_6]^{9+}$ cluster described in Fig. 10.2, and assume that the easy axis of the Ni ions is locally pointing along the CN^- group. These are orthogonal to each other because they are arranged in an octahedron around the Cr^{III} ion, thus resulting in a cancelation of the magnetic anisotropy [47].

Noncollinearity of the single ion anisotropy axes is a rather common phenomenon in molecular magnetism. It acts as a major source of high-order transverse anisotropy in symmetric clusters like the Mn_{12} SMM of Fig. 10.3 [68], which has tetragonal symmetry, and also gives rise to new phenomena like the spin chirality of a Dy^{III} triangle [69].

For the remaining part of this chapter we adopt the so-called *giant spin approximation*. In fact, at low temperature only the ground spin state is populated and the

dynamics of the magnetization is in first approximation well rationalized assuming that the whole molecule behaves like a unique large spin characterized by its axial and transverse anisotropies, derived according to (10.6).

10.2.3 The Dynamics of the Magnetization

Slow relaxation of the magnetization was first observed in $Mn_{12}ac$, thanks to ac susceptibility experiments [8]. By operating at sufficiently low temperature, the relaxation becomes so slow that an opening of the hysteresis is observable [70]. This dramatic slowing down of the fluctuations has its origin in the double well potential reported in Fig. 10.4, characteristic of a large spin with a negative D parameter. A similar double well potential characterizes single domain magnetic nanoparticles, which are the classical analogues of SMMs.

The application of a magnetic field has the effect of stabilizing and populating preferentially one of the two wells. Once the field is removed, an equal population of the two wells, corresponding to zero magnetization, is re-established only by transferring part of the population on the other well. Transitions from one state to the other are promoted by deformations of the metal coordination environment (rotations and geometrical strains), which can affect the spin degrees of freedom, thanks to spin orbit coupling. However, at a first level of approximation, these deformations are only able to induce transitions between states differing in m by ± 1 and ± 2 . To overcome the energy barrier, a multiphonon mechanism is therefore necessary, as shown in Fig. 10.4. In analogy to a chemical reaction involving many elementary processes, the overall rate is determined by the slowest step. In the case of a SMM, the slowest step is the one on top of the barrier, because at low temperature the highest states are less populated and also because of the quadratic energy spacing induced by (10.5). The combination of these two factors yields an exponential temperature dependence of the relaxation time, which is typical of a thermally activated mechanism:

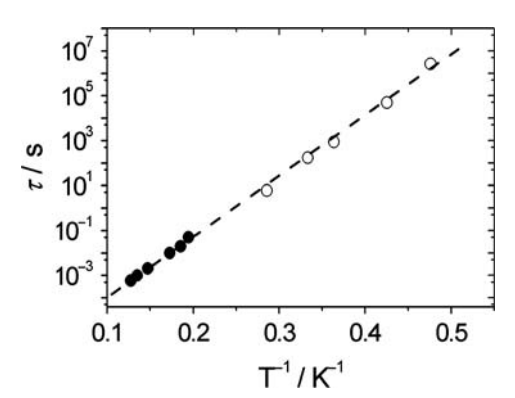
$$\tau = \tau_0 \exp(U_{\text{eff}}/k_{\text{B}}T). \tag{10.7}$$

Characteristically, the pre-exponential factor τ_0 , that is, the inverse of the frequency, is much longer than that observed in magnetic nanoparticles.

Figure 10.5 nicely shows the good agreement between the Arrhenius law (10.7) and the experimental behavior of the archetypal Mn₁₂ac SMM. $U_{\rm eff}/k_{\rm B}$ has been determined to be 62 K, thus not far from $100|D|/k_{\rm B}\approx 70$ K, and τ_0 amounts to ca. 10^{-7} s, which is about 3–4 orders of magnitude longer than in magnetic nanoparticles.

The question that immediately arises is why SMM behavior is not observable also in smaller clusters or even mononuclear complexes. The answer can be found in the quantum mechanics of angular momenta. In the case of pure axial symmetry, the eigenstates of (10.5) are pure $|m\rangle$ states, and transitions between states of the ground doublet with $m=\pm S$ can only occur through the multi-Orbach process schematized in Fig. 10.4 [71]. This is, however, an ideal case because in real systems

Fig. 10.5 Temperature dependence of the relaxation time of Mn_{12} ac measured with ac susceptibility (filled circles) and by time decay of the magnetization (empty circles). The broken line represents the best fit by using the Arrhenius law (10.7)



there are many mechanisms able to admix states on opposite sides of the barrier. A transverse anisotropy due to symmetry reduction or a transverse field, either externally applied or of intrinsic origin (dipolar or hyperfine), introduces in (10.5) terms in S_x and S_y that admix states with different m, so that m is no longer a good quantum number. The true eigenstates are now a linear combination of $|m\rangle$ states:

$$|\Psi_i\rangle = \sum_{m=-S}^{S} \varphi_i(m)|m\rangle. \tag{10.8}$$

In general, if the transverse term is a small perturbation of the axial anisotropy, one of the $|m\rangle$ states is dominant within each $|\Psi\rangle$. This is particularly true for the states lowest in the double well, because they are admixed only at a high order of perturbation, that is, at order Sth by a transverse anisotropy or at order 2Sth by a transverse field. In the case of a small spin, like the S=2 of a Mn^{III} ion, unavoidable transverse terms make the energy barrier depicted in Fig. 10.4 become transparent, and the low temperature divergence of the relaxation time responsible of the SMM behavior is not observed.

A quantitative estimation of the relaxation time can be obtained by writing a linear system of equations describing the change in population of each of the (2S+1) states. For simplicity, each state of the S multiplet will be labeled using the quantum number m, thus neglecting the above-described admixtures by transverse anisotropy or transverse fields. At a given time, t, the spin has a certain probability $p_m(t)$ to be in state $|m\rangle$. But in a short time dt, it has a certain probability to make a transition to some other state $|m'\rangle$. If the transitions are independent from each other, that is, assuming a Markov process, the probabilities $p_m(t)$ evolve according to equation

$$\frac{\mathrm{d}}{\mathrm{d}t}p_m(t) = \sum_{q} \left[\gamma_q^m p_q(t) - \gamma_m^q p_m(t) \right],\tag{10.9}$$

which is called *master equation* [10]. In the present case the master equation is a system of (2S + 1) equations. Finite transition probabilities $\gamma_m^{m'}$ arise from the interaction with phonons, but regardless of the interaction mechanism, (10.9) has

general properties. A simple one is that the equilibrium value for the populations $p_m^0 = exp(-E_m/k_BT)/Z$, with Z corresponding to the partition function, is a trivial solution of the master equation. Moreover, in (10.9) the relation known as detailed balance principle is satisfied:

$$\frac{\gamma_m^{m'}}{\gamma_{m'}^{m'}} = \frac{p_{m'}^0}{p_m^0} = \exp\left[(E_m - E_{m'})/k_{\rm B}T\right]. \tag{10.10}$$

The evolution of each $p_m(t)$ follows an exponential decay towards the equilibrium value and, consequently, $M(t) = \sum_m p_m(t) M_m$ has the form of a sum of exponentials, $\exp(-t/\tau_k)$, where the characteristic times, τ_k , coincide with the solutions of the master equation. This seems to contradict the experimental finding that the magnetization in SMMs decays with a single exponential law. However, of the (2S+1) values of τ_k one approaches ∞ , and indeed corresponds to the equilibrium state which persists for an infinite time. Concerning the remaining values, it has been demonstrated that at low temperature all τ_k but one are very short. This property is a consequence of the shape of the potential, more precisely of the existence of a potential barrier. Since the spin requires a very long time to jump over that barrier, one eigenvalue of the master matrix must be very large while the (2S-1) remaining ones correspond to much faster spin motions inside the left or right hand well.

To evaluate the relaxation time it is, however, necessary to know the transition probabilities γ_q^p . These can be expressed as

$$\gamma_{q}^{p} = \frac{3}{\pi \hbar^{4} \rho c_{s}^{5}} \frac{\left(E_{p} - E_{q}\right)^{3}}{\exp\left[\left(E_{p} - E_{q}\right) / k_{B} T\right] - 1} \\
\times \left\{\tilde{D}_{a}^{2} \left[\left|\left\langle p | S_{+}^{2} | q \right\rangle\right|^{2} + \left|\left\langle p | S_{-}^{2} | q \right\rangle\right|^{2}\right] \\
+ \tilde{D}_{b}^{2} \left[\left|\left\langle p | \left\{S_{+}, S_{z}\right\} | q \right\rangle\right|^{2} + \left|\left\langle p | \left\{S_{-}, S_{z}\right\} | q \right\rangle\right|^{2}\right]\right\}, \quad (10.11)$$

where ρ is density and c_s is the speed of sound. The spin-phonon coefficients $\tilde{D}_{a,b}$ are taken to be of the same order of magnitude as the uniaxial anisotropy, but are usually treated as adjustable parameters when trying to reproduce an experimental relaxation time.

At temperatures that are significantly smaller than the height of the barrier, the calculated relaxation time shows an exponential divergence on lowering the temperature:

$$\tau^{-1} \approx \frac{1}{\hbar^4 \rho c_s^5} |D|^3 (DS^2)^2 \exp\left[-\frac{|D|S^2}{k_B T}\right].$$
 (10.12)

Even if an accurate evaluation of the pre-exponential factor is hampered by the difficulty in estimating the speed of sound inside the crystal and the spin-phonon coupling parameters, here roughly assumed equal to D, the insertion in (10.12) of reference values, like the density of water and a sound speed of 10^3 m s⁻¹, yields for

 Mn_{12} $\tau_0 \approx 10^{-7}$ s, indeed an unusually large value that is, however, in agreement with the experimental finding.

Most SMMs, including the Fe₄ complex previously mentioned, at low temperature do not obey (10.7), but on decreasing the temperature the relaxation time levels off [35, 72, 73]. This suggests that under-barrier pathways not involving phonons are active. We have seen previously that transverse terms in the SH admix states on opposite sides of the barrier. In analogy to the quantum mechanical treatment of a particle in a double well potential, it is clear that such an admixture leads to a finite probability that a through-barrier transition may occur from one potential well to the other. In the case of spins, however, an additional factor enters the scenario: the magnetic field. A field applied along the anisotropy axis couples with the S_z component of the spin and induces opposite shifts on the levels lying on opposite sides of the barrier. Perturbation theory tells us that quantum state admixtures are most efficient when the unperturbed states are degenerate.

The case of zero field, reported in Fig. 10.4, is a special case where all unperturbed levels are degenerate in pairs. This is therefore expected to be a favorite situation for tunnel relaxation. However, this energy matching is re-established for other characteristic values of the applied field:

$$H_n = n \frac{|D|}{g\mu_{\rm B}}.\tag{10.13}$$

Figure 10.6a shows the Zeeman diagram for a spin S with uniaxial anisotropy when exposed to an axial field, while on the right, the aspect of the barrier at the resonance field, n = 1, is depicted.

This phenomenon, known as *resonant quantum tunneling* of the magnetization, has been first observed in the ac magnetic susceptibility of Mn₁₂ac SMM [74] and

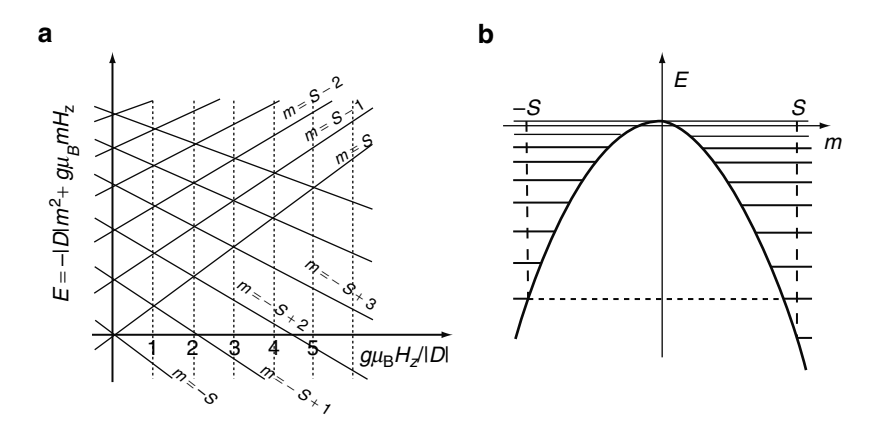


Fig. 10.6 (a) Field dependence of the levels of a spin multiplet characterized by a negative D parameter when the magnetic field is applied along the unique axis, z. (b) The shape of the double well potential at the first level crossing $H = |D|/g\mu_B$

then, more spectacularly, in the hysteresis curve [75, 76], which is characterized by steps at the resonant fields (see Fig. 10.7).

It is interesting to notice that quantum effects are also observed in a regime where phonons still play a role. In fact the admixing of levels is more efficient for states higher in the barrier, that is, smaller |m|, making quantum tunneling among these thermally populated states competitive even at intermediate temperatures. The mechanism is named *thermally activated resonant quantum tunneling* [77].

The vertical segments of the curve in Fig. 10.7 reflect accelerations of the relaxation rate and can be theoretically reproduced with the approach developed before, by taking into account that the true eigenstates of the system are not pure $|m\rangle$ states but they are described by (10.8). As an example, in Fig. 10.8 we report the calculated field dependence of the relaxation time for the Fe₄ cluster, or iron star, previously introduced to treat exchange interactions in symmetric molecules. The spin state has S = 5, $D/k_{\rm B} = -0.6$ K and E/D = 0.1.

As expected, the relaxation time shows a minimum in zero field, when tunneling is permitted. Three different cases are presented in Fig. 10.8. In the first calculation, a transverse term of the magnetic anisotropy is introduced with E/D=0.1. As this term couples states with even values of (m'-m), an admixing occurs for

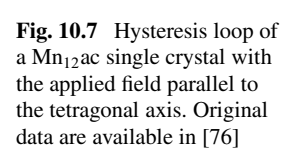
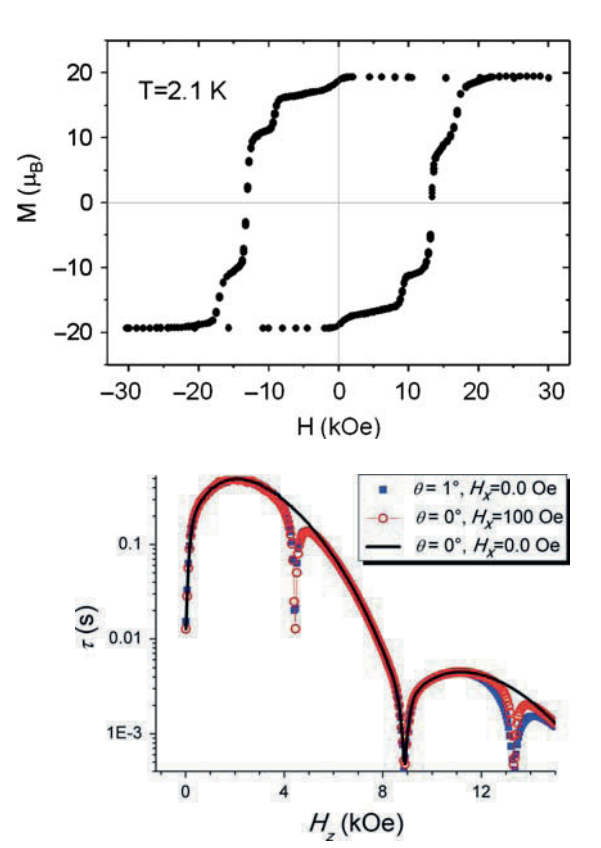


Fig. 10.8 Calculated field dependence of the relaxation time of a typical Fe_4 SMM with S=5 and at T=1 K by using the master matrix approach outlined in the text. θ is the angle that H forms with the z axis. The application of a transverse field has the striking effect of allowing tunneling also when $H_z = n|D|/g\mu_B$ with n being odd



every second crossing field value. The first acceleration is thus observed around $H_z = 0.9 \,\mathrm{T}$, which corresponds to n = 2. If a weak transverse field is added or is present due to a small misalignment of the crystal (which is difficult to avoid in a real experiment), the selection rule due to the symmetry of the transverse anisotropy operator is relaxed and also the first resonance at $H_z = 0.45 \,\mathrm{T}$ becomes observable.

The fascinating interplay between quantum and classical effects in the dynamics of the magnetization of molecular nanomagnets has attracted great interest among physicists and chemists and many other spectacular phenomena have been observed in the last 10 years [11], including topological interferences [78] and quantum coherence [79] to mention only two. However, what has been presented up to know is sufficient for the reader to understand the experiments with synchrotron light described in Sect. 10.4 and we will not go any further here, addressing the interested reader to more specialized literature [10].

10.3 Deposition of Single Molecule Magnets on Surfaces

The following step in the study of SMMs is the transposition of their unique properties to a nanoscale environment. Indeed, the assembling of magnetic molecules such as Mn_{12} and Fe_4 on surfaces and their addressing using scanning probe microscopy techniques has been the target of intensive research activity in last years. Many approaches have been followed to anchor such complex metallo-organic molecular units to surfaces, as described in a recent review [27]. In some cases, the structural and electronic intactness of deposited molecules could be ascertained only with the aid of sophisticated techniques for surface analysis.

The formation of arrays of SMMs on surface can be obtained following either elementary methods, like the deposition from the vapor phase or the drop casting of a dilute solution, or more complex ones, such as chemical adsorption. In this last case, the selection of a specific linker for a given surface [27] is a fundamental issue, and in Table 10.1 we list functional groups that can be used to graft molecules to representative surfaces.

A technique of widespread use relies on the formation of self-assembled monolayers, SAMs. We adopt here the definition of self-assembly given by Whitesides et al. [80]: A process that involves pre-existing components (separate or distinct parts of a disordered structure), is reversible and can be controlled by proper design of the components. Reversibility requires that the surface—molecule interactions are not too strong but comparable to thermal energy. The combination of reversibility with the fact that the building blocks are free to move allows the reparation of errors and thus the formation of ordered structures. Furthermore, weaker interactions like intermolecular van der Waals forces may play a crucial role [27].

So far grafting of SMMs on surfaces has been carried out by following the three main schemes depicted in Fig. 10.9. Interactions between molecules and the surface can be either nonspecific (case a, physisorption) or specific, being induced by proper functionalization of the magnetic molecule (b) or of the surface (c).

Linking group	Substrate	-
-SH	Au	•
-RS-SR		
-S-Ac ^a		
-RSR'		^a Ac stands for acetyl ((O)CCH ₃), a group that replaces H in thiols to
-SCN		
-OH	Pt	protect the otherwise too reactive S
$-NH_2$		atom
-COOH	Al_2O_3	
$-OPO_3H_2$	TiO_2	
	ITO	
-SiCl ₃	SiO_2	
-CH=CH ₂	Si(-H)	

Table 10.1 Commonly employed combinations of linker-substrate for the formation of self-assembled monolayers

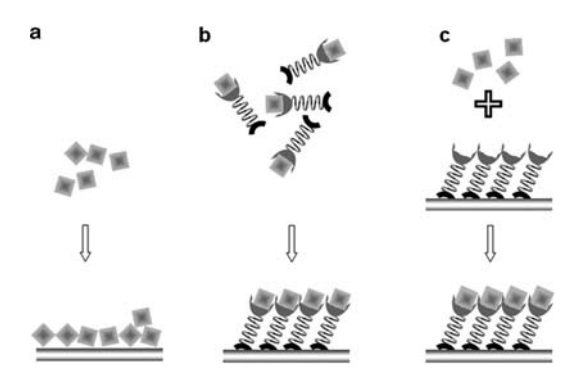


Fig. 10.9 Schematic view of three approaches for deposition of magnetic molecule (*squares*) by (a) drop casting of unfunctionalized molecules from diluted solutions; (b) self assembling of molecules pre-functionalized with suitable anchoring groups for specific surfaces; (c) functionalization of surfaces with docking groups suitable as molecule receptors

All these strategies have been adopted for the surface grafting of Mn_{12} -type SMMs. Encouraging results on the deposition of Mn_{12} clusters by scheme (a) were reported by Bucher et al. [81]. Unfortunately, the hysteresis loop observed on such samples could not be firmly attributed to adsorbed molecules due to the possible formation of multilayers. On the other hand, strategy (b) had been attempted a few years before using compound Mn_{12} -C15SAc (see Fig. 10.3), which was deposited on Au(111) as a homogeneous but disordered monolayer [82]. The third method (c) was used to covalently graft Mn_{12} derivatives on silicon surfaces prefunctionalized [83] with carboxylate groups. Attempts to use the same strategy to bind Mn_{12} complexes to gold surfaces functionalized with carboxylic groups have also been reported [84]. However, no hysteresis was observed on samples featuring a

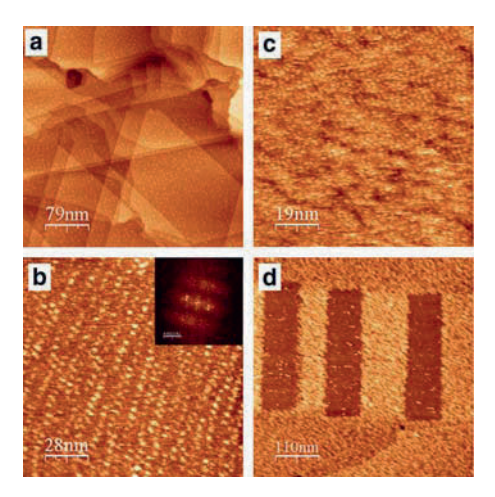


Fig. 10.10 STM topography scans of $Mn_{12}BzSMe$ on Au(111) surfaces ($V_{bias} = 0.4 \text{ V}$, $I_{tunnel} = 10 \text{ pA}$): (a) Image of a large area of the deposit obtained from THF; (b) detail of the same molecular array, with a 2D-FFT in the inset; (c) detail of a similar deposit obtained from dichloromethane; (d) image of a patterned sample where the depressions were created by removing the monolayer of $Mn_{12}BzSMe$ using a stronger tip-to-sample interaction ($V_{bias} = 0.24 \text{ V}$, $I_{tunnel} = 30 \text{ pA}$)

monolayer coverage [25]. Similar approaches have also been employed to graft Fe₄ molecules on silicon [85] as well as, more recently, on carbon nanotubes [86].

These monolayers are invariably disordered, as shown by scanning tunneling microscopy (STM) which, although unable to reveal the internal structure of the grafted molecules, has provided molecular sizes in agreement with expectation. In some cases STM has evidenced the complexity of the grafting process. For the same molecule and the same surface, deposition can give very different results depending on the solvent used to dissolve the SMM compound [87]. Figure 10.10 shows the results obtained by depositing on Au(111) a Mn₁₂ cluster with sulphide substituted carboxylates (Mn₁₂BzSMe, see Fig. 10.3). Figure 10.10a, b refers to SAMs obtained dissolving the SMM in tetrahydrofuran (THF) and show submonolayer coverage with a certain degree of order, probably induced by gold substrate reconstruction. A more dense and disordered deposit is obtained when using dichloromethane, as shown in Fig. 10.10c. In this case, the molecules appear to interact more weakly with the substrate; in fact imposing a stronger tip-to-sample interaction resulted in an almost complete removal of the monolayer (Fig. 10.10d).

X-ray photoemission spectroscopy (XPS) has an excellent sensitivity for chemical species at the surface and in some cases is able to provide information on their oxidation states. However, because of the strong overlap of both Mn_{2p} and Mn_{3p} signals with peaks from the gold substrate ($\mathrm{Au}_{4p1/2}$ and $\mathrm{Au}_{5p3/2}$, respectively), quantitative assessment of the atomic relative abundance in SAMs of Mn_{12} derivatives is severely hampered.

The key point remains, however, the characterization of the magnetic properties of these monolayers. Preliminary experiments based on traditional magnetometry proved to be extremely challenging due to the exceedingly small amount of magnetic

centers [81]. Magneto-optical techniques are more adequate and have been recently applied to Mn_{12} SAMs. Quite surprisingly, no opening of the magnetic hysteresis has been detected for the SAM of Mn_{12} clusters whose morphology is reported in Fig. 10.10a [88].

A fundamental question arises, namely whether SMM behavior is unfavorably affected by the surface environment, or the grafting process leads to changes in the chemical and electronic structure of the molecules. Only more surface-sensitive and selective techniques such us XAS – XMCD demonstrated to be able to provide such an answer, as detailed in the following section.

10.4 XAS and XMCD of SMMs

In this section, we show with some selected examples from our recent research that X-ray absorption spectroscopy is an invaluable tool for the surface scientist interested in magnetic systems. Other interesting examples are the investigation of the magnetic properties of cobalt ad-atoms on Pt terraces [20], or the detection of surface-induced ferromagnetism in Fe^{III}-octaethylporphyrin molecules deposited on metallic surfaces [22, 23], also discussed by Wende in this volume.

The key features of XAS and XMCD analysis can be summarized as follows:

- Atomic species selectivity: Unlike most magnetic characterization techniques, polarized X-ray absorption reveals element- and even oxidation-state-specific magnetic properties.
- Electronic and spin structure information: XAS spectra can be used to ascertain
 the electronic structure of the metal centers, while XMCD spectra can give precious information on spin-spin coupling. When applicable, the magneto-optical
 sum-rules yield unique and direct information on the orbital magnetic moments.
- Extreme surface sensitivity: Beam stability coupled to total electron yield (TEY) detection allow for reliable acquisition of polarized X-ray absorption spectra on monolayers of SMMs grafted to metallic surfaces.

The first XAS and XMCD measurements on molecular magnetic clusters were performed on Ni(II) and Mn(II) chromicyanides (see Fig. 10.2), for which the magnetic coupling between the central Cr(III) ion and the peripheric divalent cations could be determined [89].

However, to fully characterize the unique magnetic features of SMMs XAS and XMCD measurements must be carried out at very low temperatures and only few end-stations offer such a possibility. For our investigations we used one of the most advanced setups available, namely the TBT end-station developed by Ph. Sainctavit and J.-P. Kappler. It is equipped with a ${}^{3}\text{He}^{-4}\text{He}$ dilution refrigerator capable of reaching temperatures lower than 300 mK under photon flux; details on the TBT setup can be found in [90]. This equipment has been first used to characterize the Fe₈ SMM, allowing the observation of the XMCD signal arising from remnant magnetization [91].

10.4.1 XAS and XMCD to Investigate the Electronic Structure of Mn₁₂ Clusters

The investigation of Mn_{12} SMMs with synchrotron-based techniques has been first performed by Ghigna et al. [92] and then Moroni et al. [93] using a bulk sample of Mn_{12} ac mixed with graphite to warrant an acceptable electrical conduction. The mixed valence nature of this cluster did not allow to apply directly the sum rules to determine the magnetic and orbital contributions. A different approach has been used, which is based on spectra simulation starting from those of model compounds, such as simpler complexes comprising manganese ions in a single oxidation state. More recently also a one-electron-reduced Mn_{12} complex with formula $(PPh_4)[Mn_{12}O_{12}(O_2CPh)_{16}(H_2O)_4]$, $(PPh_4)Mn_{12}Bz$, has been characterized [25,94]. The additional electron is localized on a former Mn^{III} site and this complex can therefore be formulated as $Mn^{II}Mn^{IV}_{11}Mn^{IV}_{14}$.

It is important to recall that manganese ions in oxidation states higher than +2 are very sensitive to photo-reduction and special care must be taken to avoid sample damage. The optimization of the photon flux is therefore the first step in the characterization of molecular materials. Moreover, as small changes in the dichroic signal can be significant in SMMs, the protocol to be employed must minimize spurious signals. This requires a cycle of eight acquisitions: four of them are carried out while applying a positive external field (i.e., polarizing the spins in one direction) and the remaining ones are carried out in a negative field (spins polarized in the opposite direction). For each of the two field directions, photon helicity is varied twice. When field and photon helicity have the same sign (photon helicity is taken to be positive according to the right hand rule), the spectrum is called positive (σ^+) ; if field and photon polarization are of opposite sign, the spectrum is referred to as negative (σ^-) . This procedure holds when reversing the field is theoretically identical to changing photon helicity, that is, in the electric dipole approximation.

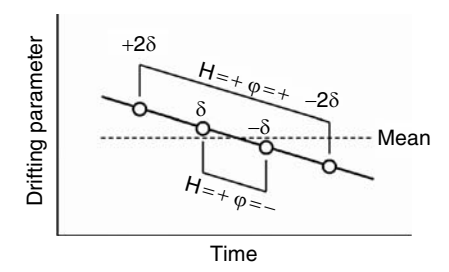
The order of such sequence (Table 10.2) is important, as it allows to compensate for any linear drift of the signal with time (e.g., a drift in energy or in the intensity of the beam), as explained in Fig. 10.11.

The above-described set of eight XAS acquisitions allows to record a XMCD spectrum without spurious effects; however, when the signal is very weak, as in

Photon helicity (φ)	Applied field (H)	Resulting spectrum
+	+	σ^+
_	+	σ^{-}
_	+	σ^{-}
+	+	σ^+
+	_	σ^{-}
_	_	σ^+
_	_	σ^+
+	_	σ^{-}

Table 10.2 A typical acquisition cycle of XMCD spectra

Fig. 10.11 Schematic picture of error canceling through the acquisition sequence shown above



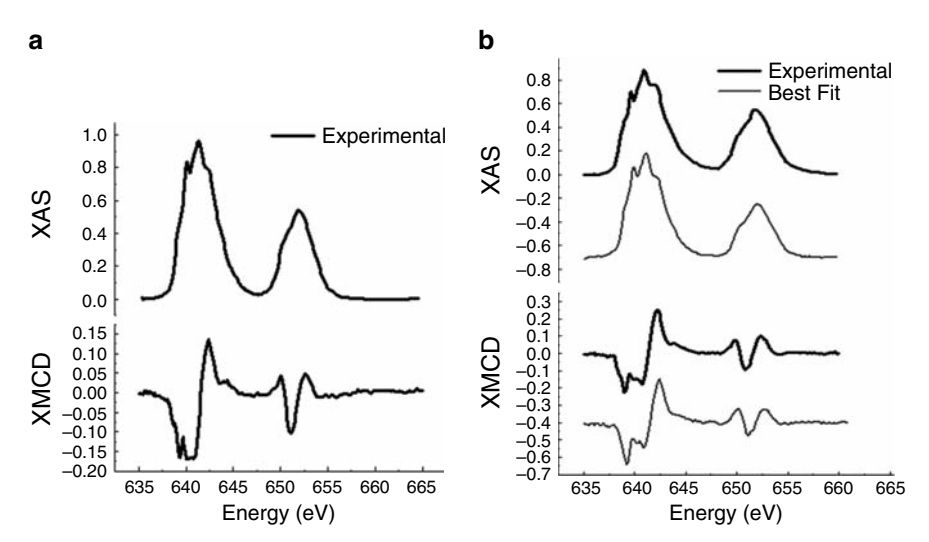


Fig. 10.12 (a) XAS-XMCD spectra of a thick film of $Mn_{12}BzSMe$ at the $L_{2,3}$ edge of manganese (H = 4T and T = 4.2 K); (b) same for the one-electron reduced species (PPh_4) $Mn_{12}Bz$, where the *grey lines* represent the calculated spectra as discussed in the text

the case of monolayers, several such datasets are required to achieve an acceptable signal-to-noise ratio.

In Fig. 10.12a, the XAS-XMCD spectra of a thick deposit of $Mn_{12}BzSMe$ are reported [25]. They are very similar to those previously reported in [93], showing that changes in the periphery of the cluster do not significantly affect the electronic properties. The XAS and XMCD spectra of a microcrystalline sample of $(PPh_4)Mn_{12}Bz$ look quite similar to those of "neutral" Mn_{12} , with a small enhancement of the dichroic signal around 639 eV, consistent with the presence of a Mn^{II} component (Fig. 10.12b).

To get more quantitative information, the experimental energy dependence of XAS spectrum intensity, I(E), can be reproduced through a linear combination of model spectra $I^{\alpha}(E)$ obtained on suitable reference compounds containing the Mn ion in the three oxidation states (α = II, III, IV) and in similar chemical environments:

$$I(E) = \Sigma_{\alpha} c^{\alpha} I^{\alpha}(E). \tag{10.14}$$

Reference spectra are normalized following the sum rules of the number of holes. The values of c^{α} give information on the relative abundance of the different valence states and percent values P_{α} can be thus extracted:

$$P_{\alpha} = 100 \frac{c^{\alpha}}{\sum_{i} c^{i}}.$$
 (10.15)

This semi-quantitative analysis of XAS data of Fig. 10.12b provided a $Mn^{II}:Mn^{IV}$ ratio (5:60:35) that is in complete agreement with expectation (8:58:33), thus confirming that the technique is able to clearly detect one-electron reduction in such a complex system.

An analogous approach can be employed to extract from the XMCD spectra, semi-quantitative information on the orientation of the local magnetic moments relative to the applied magnetic field. The energy dependence of the dichroic signal, S(E), is expressed as a linear combination of model spectra, $S^{\alpha}(E)$, at the same field and temperature values:

$$S(E) = \sum_{\alpha} c^{\alpha} \delta^{\alpha} S^{\alpha}(E), \qquad (10.16)$$

where α runs over the oxidation state numbers, c^{α} are the same coefficients resulting from the deconvolution of XAS spectra (10.14), and δ^{α} accounts for the average polarization of the local magnetic moment in the applied field (positive if parallel to the field).

To apply this type of analysis, all reference signals need to be normalized in terms of intensity to the experimental conditions used for the acquisition. In particular, the dichroic signal is assumed at the first level of approximation to scale linearly with the degree of polarization and to vary according to a simple Brillouin function with temperature and applied field.

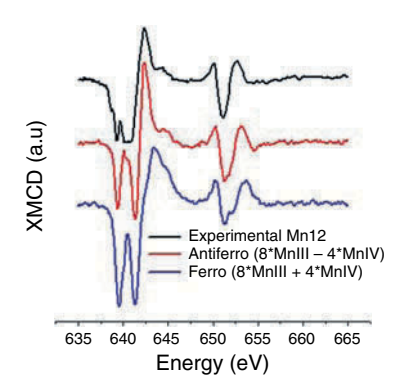
This analysis of the XMCD data provided a positive polarization for Mn^{II} in agreement with magnetic measurements, in fact the experimental spectrum is well reproduced only assuming the Mn^{II} and Mn^{III} spins parallel to each other.

To give an idea of how sensitive is XMCD to the spin structure of a high nuclearity spin cluster like Mn_{12} , we report in Fig. 10.13 the spectra of $Mn_{12}BzSMe$ calculated using (10.16) and imposing two different spin configurations: Mn^{IV} spins antiparallel or parallel to Mn^{III} ones. It is evident that in all regions of the spectrum, the agreement with experimental data is significantly better for the antiparallel alignment.

10.4.2 XAS and XMCD of Monolayers of Mn₁₂ SMMs

The extreme sensitivity of X-ray absorption spectroscopy, in particular when coupled to the surface specificity of TEY detection mode, allowed to investigate Mn_{12}

Fig. 10.13 Experimental XMCD spectrum of a thick film of Mn₁₂BzSMe (*top*) compared with the spectra calculated by convoluting spectral standards and assuming antiparallel or parallel alignment of the Mn^{III} and Mn^{IV} spins (*middle* and *bottom*, respectively)



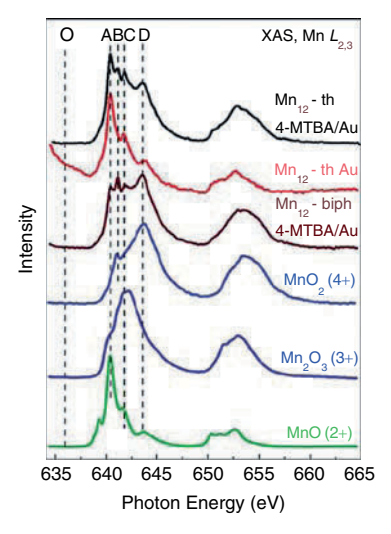


Fig. 10.14 Mn $L_{2.3}$ edge XAS spectra of different types of monolayers of Mn_{12} clusters compared to reference spectra for manganese in three different oxidation states. Mn_{12} -th is a thiophene substituted carboxylate adsorbed either on native gold or on a surface prefunctionalized with 4-mercapto-2,3,5,6-tetrafluorobenzoic acid (4-MTBA). The same gold surface is used to deposit a Mn_{12} cluster with biphenyl-carboxylate (Mn_{12} -biph). Reprinted with permission from [84] (Copyright American Physical Society)

adsorbates even if manganese ions are present in very low amounts on the gold surface (significantly less than one monolayer, considering that a large portion of the surface is occupied by organic ligands).

Voss et al. [84] employed XAS at room temperature to investigate the electronic structure of three different samples. The first two were prepared by functionalizing the Mn_{12} cluster with sulphur-containing carboxylates, according to the method schematized in Fig. 10.9b, while the third one was prepared by first depositing a layer of 4-mercapto-2,3,5,6-tetrafluorobenzoic acid (4-MTBA), and then allowing it to react with a solution of Mn_{12} via ligand exchange [95].

The recorded XAS spectra at the Mn L_{2,3} edge are displayed in Fig. 10.14 along with some reference spectra for the three different oxidations states of manganese.

It is clear from Fig. 10.14 that most of the recorded intensity for the monolayers coincides with the absorption of Mn^{II} , even if significant differences are detected between the three samples. In particular, the deposition on prefunctionalized surfaces appears to afford a weaker Mn^{II} contribution.

A more quantitative analysis has been recently performed by combining XAS and XMCD with the simulation procedure previously described [25].

In this case, two different pre-functionalized Mn_{12} clusters have been used to prepare monolayers on gold: $Mn_{12}C15/SAc$ and $Mn_{12}BzSMe$ (see Fig. 10.3 for the details of the ligand structures). They have different anchoring groups, namely a thioacetyl and a sulfide group, and also very different spacers, a long aliphatic chain and a short aromatic group, respectively. Moreover, for $Mn_{12}BzSMe$, the deposition has been performed using two different solvents, as described in Sect. 10.3.

The XAS and XMCD spectra of the three investigated samples are reported in Fig. 10.15. At a first glance, significant differences are visible between bulk phases and monolayers, as evidenced in the clearest way by inspection of dichroic spectra. The XAS spectra of prefunctionalized Mn_{12} clusters grafted on Au surface are, however, more similar to those obtained by depositing Mn_{12} on a prefunctionalized surface (see Fig. 10.14), suggesting that the deposition method of Fig. 10.9c is not necessarily better suited for SMMs.

By performing a simulation of the XAS spectra with a convolution of standard spectra according to (10.14), the percentages of the different oxidation states have been evaluated and reported [25]. Mn^{II} accounts for 20–30% of the manganese content, suggesting that the underlying redox process is not a simply one- or two-electron reduction, as observed in some Mn_{12} clusters in the bulk phase.

We noticed also that the reduction seems to involve also Mn^{IV}ions, in contrast with what was observed for the bulk phase [96,97]. Even more dramatic differences are seen in the dichroic signal. In fact, a significant reduction of the polarization is observed [25], in some cases with a complete loss of the ferrimagnetic

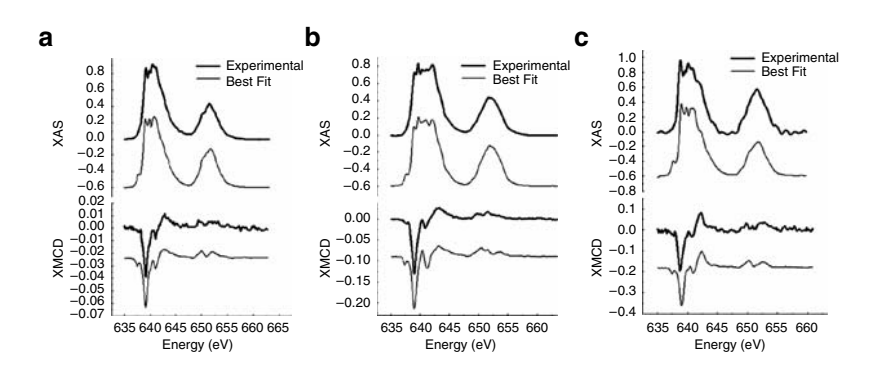


Fig. 10.15 Experimental (*bold*) and calculated XAS and XMCD spectra at the Mn $L_{2,3}$ edge for monolayers on native Au(111) of Mn₁₂C15Sac (**a**) Mn₁₂BzSMe deposited from THF (**b**), or from dichloromethane (**c**)

spin arrangement typical of Mn_{12} (see Fig. 10.3). Significant differences are also observed in the case of the same prefunctionalized cluster deposited from different solvents. In particular, the ferrimagnetic structure is partially retained when dichloromethane is employed and the molecules adsorbed on the surface can be easily removed with the STM tip, as shown in Fig. 10.10.

On the other side, the very weak magnetic polarization suggests that a complete disruption of the cluster does not occur, as the formation of monomeric units would lead to a full polarization of their magnetic moments in the employed experimental conditions of high magnetic field (40 kOe) and low temperature. This is in agreement with XPS and STM investigations that suggest surface coverage by chemical species whose size and composition are close to those of intact Mn₁₂ clusters [87]. The significant changes in the electronic and spin structure, evidenced unambiguously by XAS and XMCD, justify the absence of SMM behavior for these deposits.

10.4.3 XMCD and Magnetic Anisotropy

The conservation of a large spin in the ground state, once the molecular clusters are grafted to the surface, is not the only requirement to be fulfilled to observe SMM behavior: also the magnetic anisotropy must be preserved. XMCD probes the magnetization state of the molecule and can be used to measure the field dependence of the magnetization.

At low temperature, the effect of ZFS (see (10.5)) causes the molecules that have their easy axis parallel to magnetic field to saturate in weaker fields than a simple paramagnet, while stronger fields, indeed up to 100 kOe for Mn_{12} clusters, are necessary to align the magnetic moment along the hard axis. In the case of a random distribution of orientations of the magnetic axes, like in a polycrystalline powder specimen, in a thick deposit, or in disordered SAMs, all the orientations are present. For $|D|/k_BT << 1$, the magnetization curve of a randomly oriented sample can be reproduced by considering just the average of the magnetization curves calculated along the anisotropy axes, that is, $M(H) = \frac{1}{3}M_{||}(H) + \frac{2}{3}M_{\perp}(H)$ for a uniaxial system, but in general an integration on the solid angle must be performed [10, 30].

In Fig. 10.16a, the XAS spectra obtained with two circular polarizations and the derived dichroic signal for a bulk sample of $Mn_{12}BzSMe$ are reported [26]. The energy of 643 eV, corresponding to the maximum amplitude of the XMCD signal, has been selected to measure the field dependence up to 50 kOe and at T=0.75 K. The measured data cannot be modelized assuming that the magnetic anisotropy is that estimated from electron paramagnetic resonance [54] and typical of Mn_{12} clusters, $D/k_B=-0.7$ K (line in Fig. 10.16b), even leaving an adjustable scale factor for the XMCD signal intensity. Moreover, up-field and down-field scans coincide and hysteresis is absent even at temperatures lower than those required to observe a memory effect on bulk samples.

It is important to stress that no evidence of photo-reduction is detected in these thick films of Mn_{12} derivatives. We can also exclude that the deposition of a thick

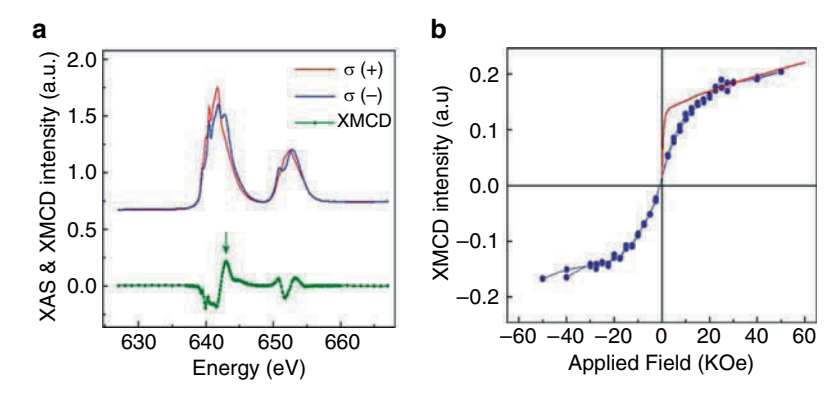
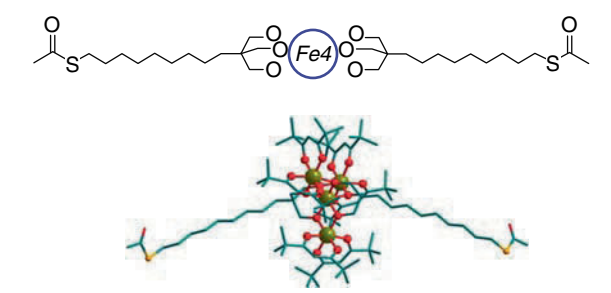


Fig. 10.16 (a) Absorption spectra (top) and dichroic signal (bottom) at the L_{2,3} edge of manganese at T=0.75 K and 40 kOe for a bulk sample of Mn₁₂BzSMe. (b) Magnetic field dependence of the XMCD signal at 643 eV, highlighted by the arrow in (a), compared to the expected magnetization curve for a bulk sample with random orientation of the crystallites ($red\ curve$). A sweeping rate of 20 Oe s⁻¹ has been employed. Original data available in [26]

Fig. 10.17 On *top*, a schematic view of the functionalization of a Fe₄ cluster with a tripodal ligand derived from 2-hydroxymethyl-1,3-propanediol, while the molecular structure as determined from X-ray diffraction is reported in the lower part



film by drop-casting affects the magnetic properties of the molecules, or gives a selective orientation of them, because a similarly prepared film investigated by standard magnetometry reveals the typical hysteresis curve of randomly oriented Mn_{12} SMMs.

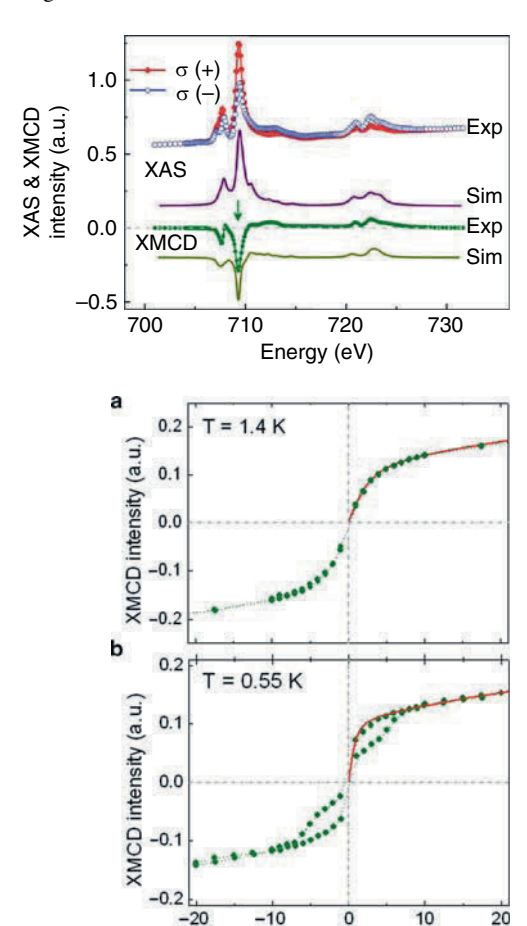
A possible explanation could be that the temperature of the sample is significantly higher (a few K) than that measured by the calibrated sensor. This hypothesis has been, however, discarded, thanks to parallel experiments on a different SMM described hereafter.

The Fe₄ cluster already mentioned in Sect. 10.2.1 has six methoxide ligands that bridge the central ion to the outer ones [34]. Methoxides can be easily replaced by two tripodal ligands, one above and one below the plane of the iron atoms [35,73]. Several tripodal ligands with different chains on the pivot carbon atom and with a functional group on the other end have been prepared to anchor Fe₄ clusters on different surfaces, i.e Si [98] and Au [99].

One of these derivatives with formula $[Fe_4(L)_2(dpm)_6]$, Fe_4C9SAc , where Hdpm is dipivaloylmethane and H_3L is the tripodal ligand schematized in the upper part of Fig. 10.17, has been extensively investigated by XAS and XMCD [26, 99].

Fig. 10.18 Fe $L_{2,3}$ edge absorption spectra (*upper*) and dichroic signal (*lower*) at T = 0.75 K and 30 kOe, along with simulated curves obtained using ligand field multiplet calculations. The *arrow* indicates the energy used to measure the field dependence reported in Fig. 10.19. Original data available in [26]

Fig. 10.19 Magnetic field dependence of the XMCD signal of a thick film of Fe₄C9SAc at 709.2 eV (multiplied by -1) at T=1.4 K (a) and T=0.55 K. (b) Each curve is compared to the expected magnetization curve for a bulk powder-like sample. A sweeping rate of 20 Oe s⁻¹ has been employed



H (kOe)

The spectra recorded on a thick film obtained by drop-casting on a gold slab are reported in Fig. 10.18. The absorption at the $L_{2,3}$ edges of iron is typical of +3 oxidation state. Interestingly, the intensity of the XMCD at high field (30 kOe) corresponds to half of the polarization expected for uncorrelated iron(III) spins. In fact, the cluster has a ferrimagnetic spin structure yielding an S=5 ground state, and the first excited states are several tens of K above in energy. As the ligand fields of the internal and external iron ions are very similar, the XMCD spectrum is much simplers than that of Mn_{12} , and the signals coming from different antiferromagnetically-coupled iron atoms partially cancel.

The field dependence of the XMCD signal at 709.2 eV, corresponding to the largest negative signal, is reported in Fig. 10.19a at $T=1.4\,\mathrm{K}$, together with the calculated magnetization assuming random orientation of molecules with S=5 and $D/k_{\rm B}=-0.63\,\mathrm{K}$. At variance with the results obtained on Mn_{12} (see figure 10.16b), the calculated data, again adjusted with an arbitrary factor for

y-scale, nicely reproduce the XMCD signal (see figure 10.19). Moreover, on decreasing the temperature, an opening of the hysteresis is observed, as discussed in detail in the next section.

The parallel investigation of the two types of SMMs allows us to exclude that the loss of SMM behavior is due to an experimental artifact. On the other side, it is evident that the behavior of Mn_{12} clusters in a thick film is different if probed with standard magnetometry or with XMCD. Recalling that the discussed XAS-XMCD spectra have all been recorded in TEY mode, it is reasonable to deduce that different portions of the sample are showing different behaviors. In fact this detection mode probes only the first few nanometer of a thick compound [100], corresponding to a couple of layers of these bulky molecules. We can therefore deduce that, in a thick film of Mn_{12} SMMs, the first few layers behave differently, as far as the magnetic anisotropy is concerned, from the remainder of the sample. This is not completely surprising. As previously discussed (see (10.6)), the magnetic anisotropy of a spin cluster depends not only on the single ion contributions and projection coefficients but also on the relative orientation of the anisotropy axes.

In Fig. 10.20a, we show the molecular structure of Mn_{12} SMMs highlighting the easy axis of $Mn^{\rm III}$ ions, which correspond to the direction of Jahn–Teller elongation of their coordination octahedra. There are two types of $Mn^{\rm III}$ sites and they form typically angles of ca. 10° and 35° with the idealized tetragonal axis, respectively. On the other hand, it is well known that the elongation axis of some of these $Mn^{\rm III}$ sites can flip in a different orientation, as shown in Fig. 10.20b. Some crystalline phases of Mn_{12} compounds have revealed to be uniquely composed by these *flipped* species [101] and show an almost halved anisotropy and a much faster relaxation. Relaxation is in fact enhanced not only by a reduction of the anisotropy barrier, but also by the breaking of the tetragonal symmetry that increases transverse anisotropy and consequently the efficiency of under barrier mechanisms. In other cases, like in the archetypal Mn_{12} ac compound, the flipped species are present only as a minority fraction, probably associated to defects in the crystal [10, 102]. We can imagine that the surface layers of the thick films present more of these defects and therefore relax faster.

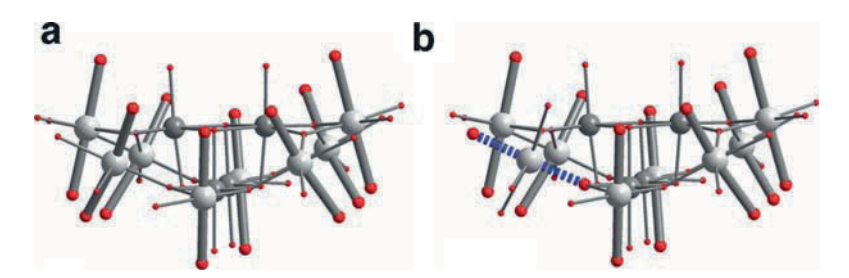


Fig. 10.20 (a) Schematic structure of the Mn_{12} cluster where the Jahn–Teller elongation axes of $Mn^{\rm III}$ ions, corresponding to the single ion easy axis of magnetization, are highlighted. (b) The elongation axis of a $Mn^{\rm III}$ ion can flip to the direction pointing towards a bridging oxygen (broken bond)

On the contrary, the magnetic anisotropy of Fe_4 cluster is related to the "helical pitch" of the molecule, that is, the dihedral angle between each FeO_2Fe "blade" and the Fe_4 plane [35,73,98]. This angle is imposed by the geometry of the rigid tripodal ligands and is probably less affected by the surface strain.

Even if this explanation remains speculative, the results reported here nicely highlight an intrinsic "lability" of the SMM behavior of Mn_{12} clusters that, associated with the redox instability induced by the grafting process, makes them unsuited for organization in nanostructures. The family of Fe₄ clusters seems more promising, despite the fact that the low blocking temperature makes them even less appealing for technological applications and complicates their characterization.

10.4.4 XMCD and the Dynamics of the Magnetization

The peculiar dynamic nature of the hysteresis of SMMs described in Sect. 10.2.3 makes the loop opening very sensitive to the field sweeping rate. The recording of the hysteresis with XMCD requires changing both field and polarization of X-rays. These operations are usually rather slow and some time-dependent features can be lost, particularly if fast relaxation occurs at the resonant fields. The investigation of the hysteretic behavior of Fe₄ has been possible thanks to the capability of the SIM beamline of the SLS synchrotron [103] to switch the polarization in a few seconds through a tune–detune operation (see the contribution of F. Nolting).

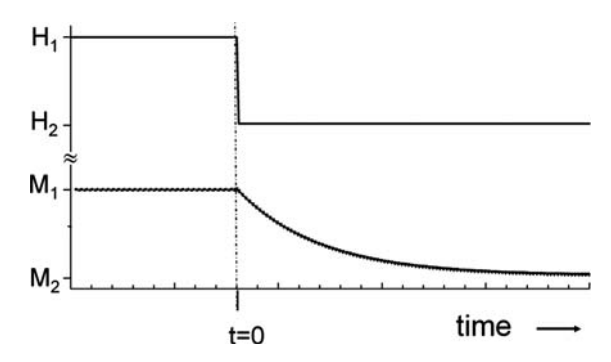
The hysteresis loop of Fig. 10.19b has been recorded by sweeping the field at $20\,\mathrm{Oe}\,\mathrm{s}^{-1}$ from one set point to the next one and then measuring at each field the XAS signal with the two polarizations at the energy of the maximum XMCD amplitude (e.g., 709.2 eV for Fe₄C9SAc). The measurement is then repeated at an energy before the edge for normalization sake. The whole hysteresis experiment requires ca. 1 h and, in order to reduce the noise, more cycles can be recorded as well (thanks to the high temperature stability of the set-up) in order to improve the signal-to-noise ratio.

Even if the combination of a dilution refrigerator with the fast switching of the polarization makes the set-up an almost unique tool to investigate SMMs, we have developed an alternative technique to probe the magnetization dynamics. It is well known that information on the relaxation time of the magnetization can be directly obtained by using an alternating field at variable frequency or by measuring in real time the evolution of the magnetization after a field change according to the scheme of Fig. 10.21.

This type of experiment is usually performed by applying a strong field to cancel the barrier and reach rapidly the equilibrium value, then changing the field and starting to measure the magnetization as a function of time. The curve is then fitted starting from a single exponential law,

$$M(t) = M_2 + (M_1 - M_2) \exp\left(-\frac{t}{\tau}\right)$$
 (10.17)

Fig. 10.21 Schematization of the procedure to measure the dynamics of the magnetization in real time. The *upper part* displays the time dependence of the applied field, while the *lower part* shows a typical magnetization measurement



where τ is the relaxation time. More complex behaviors are often encountered like a stretched exponential decay.

While M_1 is easy to detect, it is important that the experiment lasts long enough to get a precise determination of M_2 . Very often the final field is set to zero and the decay of the remnant magnetization is thus measured. Moreover, to avoid errors, the relaxation time should be much longer than the time needed to ramp the field. This instrumental parameter determines the shortest relaxation time that can be measured. A similar procedure has been employed to measure the time dependence of the dichroic signal. In this case, however, fluctuation in the photon flux could induce a parasitic signal, which fortunately resulted to be negligible, thanks to the high flux stability of SLS synchrotron [26].

In the case of Fe₄, we have decided to avoid measuring the decay of the remnant magnetization for two reasons. The first one is that Fe₄ exhibits a very efficient tunneling in zero field [35], which is also at the origin of the peculiar butterfly shape of the hysteresis loop (see Fig. 10.19b). As we cannot measure very short relaxation times, it is better to avoid this fast relaxation regime. The second reason is that the TEY detection mode has a lower signal-to-background ratio when operated in zero field.

We therefore magnetized the sample in a relatively strong field (20 kOe), then the field was quickly changed to a slightly negative value (-2.5 kOe) and the XAS measured while continuously switching the polarization. The resulting time dependence of the XMCD amplitude is reported in Fig. 10.22 [26].

The signal shows a time dependence that can be well reproduced with a monoexponential decay. Moreover, the characteristic time is strongly dependent on the temperature, being evaluated as $\tau=(285\pm10)\,\mathrm{s}$ at $T=(0.55\pm0.05)\,\mathrm{K}$, and $\tau=(87\pm5)\,\mathrm{s}$ at $T=(0.75\pm0.05)\,\mathrm{K}$. The relaxation times extracted with this procedure are in good agreement with the expected thermally activated regime and well compare with data obtained through conventional magnetometry. On the contrary, the same protocol repeated on the thick film of $\mathrm{Mn_{12}}$ molecules did not show any significant time dependence of the signal, in agreement with the absence of magnetic hysteresis (see inset in Fig. 10.22).

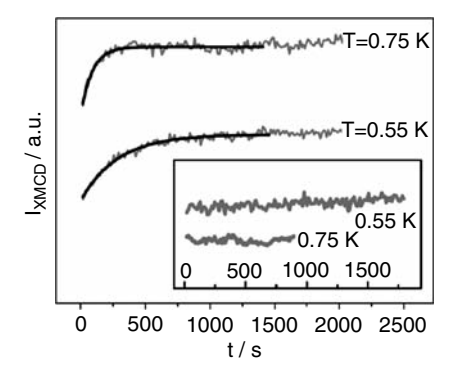


Fig. 10.22 Time dependence of the dichroic signals at the Fe $L_{2,3}$ edges measured on a thick film of Fe₄ magnetized in a strong positive magnetic field. After that, the field is rapidly ramped to a moderate negative value. *Black lines* represent the simulation with a mono-exponential decay. In the inset, the same protocol has been applied to investigate a thick film of Mn_{12}

10.5 Conclusions

In this chapter we hope to have shown to the reader that XAS and XMCD are unique tools able to address several aspects of molecular magnetism, ranging from the electronic and spin structure of polynuclear complexes to their magnetic anisotropy. The topic addressed here is the investigation of SMMs grafted to conducting surfaces, a fascinating field that hopefully may allow in the future to play with the elementary interactions between electron transport and magnetic degrees of freedom at the molecular scale. However, the characterization of complex molecules on surfaces has demonstrated to be very challenging. Thanks to the use of XAS and XMCD at sub-Kelvin temperatures, it has been possible to show that the archetypal SMMs, the Mn₁₂ family of clusters, is not suited for this type of applications because of its redox instability and also because the SMM behavior does not stand the strain typical of a surface environment. Fe₄ clusters, probably thanks to a more rigid structure induced by the tripodal ligands, are on the other side compatible with the surface environment. More recently, the approach described in this chapter has been extended to the investigation of a sub-monolayer of Fe₄ SMMs directly wired to gold. XMCD has demonstrated to have the sensitivity required to monitor the dynamics of the magnetization and has shown unambiguously that SMM behavior is compatible with the grafting to a conducting surface [99]. Despite the low blocking temperature of Fe₄ clusters, this finding represents an important result and paves the way to fundamental developments in the emerging field of molecular spintronics.

Acknowledgements We thank Prof. D. Gatteschi for stimulating this research and Prof. J. Villain for his invaluable contribution to the understanding of the dynamics of SMMs. We gratefully thank Dr. P. Imperia for assistance during XMCD measurements at BESSY. We acknowledge F. Scheurer, J.-P. Kappler, and B. Muller from the IPCMS for their help in equipment installation,

308 R. Sessoli et al.

and the staff of the X11MA-SIM BEAMLINE (SLS) for their support. In particular, we thank A. Fraile-Rodriguez, L. Joly, and F. Nolting for their excellent technical assistance. Dr. M.-A. Arrio is acknowledged for the simulation of XAS-XMCD spectra.

References

- 1. R.D.L. Carlin, Magnetochemistry (Springer, Berlin, 1986)
- R.L. Carlin, A.J. van Duyneveldt, Magnetic Properties of Transition Metal Compounds (Springer, New York, 1977)
- 3. R.D. Willet, D. Gatteschi, O. Kahn, *Magneto-Structural Correlations in Exchange Coupled Systems* (Reidel Publishing, Dordrecht, 1983)
- J.M. Manriquez, G.T. Yee, R.S. McLean, A.J. Epstein, J.S. Miller, Science 252, 1415–1417 (1991)
- 5. S. Ferlay, T. Mallah, R. Ouahes, P. Veillet, M. Verdaguer, Nature 378, 701–703 (1995)
- 6. S.M. Holmes, G.S. Girolami, J. Am. Chem. Soc. 121, 5593–5594 (1999)
- C. Train, R. Gheorghe, V. Krstic, L.M. Chamoreau, N.S. Ovanesyan, G.L.J.A. Rikken, M. Gruselle, M. Verdaguer, Nat. Mater. 7, 729–734 (2008)
- A. Caneschi, D. Gatteschi, R. Sessoli, A.-L. Barra, L.C. Brunel, M. Guillot, J. Am. Chem. Soc. 113, 5873–5874 (1991)
- R. Sessoli, H.L. Tsai, A.R. Schake, S. Wang, J.B. Vincent, K. Folting, D. Gatteschi, G. Christou, D.N. Hendrickson, J. Am. Chem. Soc. 115, 1804–1816 (1993)
- D. Gatteschi, R. Sessoli, J. Villain, Molecular Nanomagnets (Oxford University Press, Oxford, 2006)
- 11. D. Gatteschi, R. Sessoli, Angew. Chem. Int. Ed. 42, 268–297 (2003)
- 12. S. Sanvito, Nat. Mater. 6, 803–804 (2007)
- A. Cornia, A.C. Fabretti, L. Zobbi, A. Caneschi, D. Gatteschi, M. Mannini, R. Sessoli, Struct. & Bond. 122, 133–161 (2006)
- M.A. Arrio, P. Sainctavit, C. Cartier dit Moulin, C. Brouder, F.M.F. De Groot, T. Mallah, M. Verdaguer, Physica B-Cond. Mat. 209, 775–776 (1995)
- 15. K. Baberschke, Phys. Scr. **T115**, 49–53 (2005)
- G. Champion, N. Lalioti, V. Tangoulis, M.A. Arrio, P. Sainctavit, F. Villain, A. Caneschi,
 D. Gatteschi, C. Giorgetti et al., J. Am. Chem. Soc. 125, 8371–8376 (2003)
- S. Khanra, K. Kuepper, T. Weyhermuller, M. Prinz, M. Raekers, S. Voget, A.V. Postnikov, F.M.F. De Groot, S.J. George et al., Inorg. Chem. 47, 4605–4617 (2008)
- M.P. De Jong, C. Tengstedt, A. Kanciurzewska, E. Carlegrim, W.R. Salaneck, M. Fahlman, Phys. Rev. B 75, 064407 (2007)
- M.A. Arrio, P. Sainctavit, C. Cartier dit Moulin, C. Brouder, F.M.F. De Groot, T. Mallah, M. Verdaguer, J. Phys. Chem. 100, 4679–4684 (1996)
- D. Gambardella, H. Dallmeyer, K. Maiti, M.C. Malagoli, W. Eberhardt, K. Kern, C. Carbone, Nature 416, 301–304 (2002)
- V. Corradini, R. Biagi, U. Del Pennino, V. De Renzi, A. Gambardella, M. Affronte, C.A. Muryn, G.A. Timco, R.E.P. Winpenny, Inorg. Chem. 46, 4937–4943 (2007)
- H. Wende, M. Bernien, J. Luo, C. Sorg, N. Ponpandian, J. Kurde, J. Miguel, M. Piantek, X. Xu et al., Nat. Mater. 6, 516–520 (2007)
- M. Bernien, X. Xu, J. Miguel, M. Piantek, P. Eckhold, J. Luo, J. Kurde, W. Kuch, K. Baberschke et al., Phys. Rev. B 76, 214406 (2007)
- P. Gambardella, L. Claude, S. Rusponi, K.J. Franke, H. Brune, J. Raabe, F. Nolting, P. Bencok, A.T. Hanbicki et al., Phys. Rev. B 75, 125211 (2007)
- M. Mannini, P. Sainctavit, R. Sessoli, C. Cartier dit Moulin, F. Pineider, M.A. Arrio, A. Cornia, D. Gatteschi, Chem. Eur. J. 14, 7530–7535 (2008)
- M. Mannini, F. Pineider, Ph. Sainctavit, L. Joly, A. Fraile-Rodríguez, M.-A. Arrio, C. Cartier dit Moulin, W. Wernsdorfer, A. Cornia et al., Adv. Mater. 20 167–171 (2009)

- 27. D. Gatteschi, A. Cornia, M. Mannini, R. Sessoli, Inorg. Chem. 48, 3408–3479 (2009)
- N. Ishikawa, M. Sugita, T. Ishikawa, S. Koshihara, Y. Kaizu, J. Am. Chem. Soc. 125, 8694–8695 (2003)
- M.A. Aldamen, J.M. Clemente-Juan, E. Coronado, C. Marti-Gastaldo, A. Gaita-Arino, J. Am. Chem. Soc. 130, 8874

 –8875 (2008)
- 30. O. Kahn, Molecular Magnetism (VCH, Weinheim, 1993)
- 31. A. Bencini, D. Gatteschi, EPR of Exchange Coupled Systems (Springer, Berlin, 1990)
- 32. K.J. Kambe, Phys. Soc. Jpn. 5, 48–51 (1950)
- 33. J. Van Slageren, P. Rosa, A. Caneschi, R. Sessoli, H. Casellas, Y.V. Rakitin, L. Cianchi, F.D. Giallo, G. Spina et al., Phys. Rev. B 73, 014422 (2006)
- A.L. Barra, A. Caneschi, A. Cornia, F.F. De Biani, D. Gatteschi, C. Sangregorio, R. Sessoli, L. Sorace, J. Am. Chem. Soc. 121, 5302–5310 (1999)
- A. Cornia, A.C. Fabretti, P. Garrisi, C. Mortalo, D. Bonacchi, D. Gatteschi, R. Sessoli,
 L. Sorace, W. Wernsdorfer et al., Angew. Chem. Int. Ed. 43, 1136–1139 (2004)
- R.W. Saalfrank, A. Scheurer, I. Bernt, F.W. Heinemann, A.V. Postnikov, V. Schunemann, A.X. Trautwein, M.S. Alam, H. Rupp et al., Dalton Trans. 2865–2874 (2006)
- 37. D. Gatteschi, L. Pardi, Gazz. Chim. Ital. 123, 231–240 (1993)
- 38. C. Raghu, I.Rudra, D. Sen, S. Ramasesha, Phys. Rev. B 64, 064419 (2001)
- N. Regnault, T. Jolicoeur, R. Sessoli, D. Gatteschi, M. Verdaguer, Phys. Rev. B 66, 054409 (2002)
- 40. D. Gatteschi, L. Pardi, Mol. Cryst. Liq. Cryst. Sci. Technol. Sect. A 233, 217–230 (1993)
- 41. J.B. Goodenough, J. Phys. Chem. Solids **6**, 287–297 (1958)
- 42. J.B. Goodenough, Magnetism and the Chemical Bond (Interscience, New York, 1963)
- 43. J. Kanamori, J. Phys. Chem. Solids **10**, 87–98 (1959)
- 44. J. Kanamori, in Magnetism, ed. by G.T. Rado, H. Suhl (Academic Press, New York, 1963)
- 45. T. Mallah, C. Auberger, M. Verdaguer, P. Veillet, J. Chem. Soc. Chem. Commun. 61 (1995)
- A. Scuiller, T. Mallah, M. Verdaguer, A. Nivorozkhin, J.-L. Tholence, P. Veillet, New J. Chem. 20, 1–3 (1996)
- V. Marvaud, C. Decroix, A. Scuiller, C. Guyard-Duhayon, J. Vaissermann, F. Gonnet, M. Verdaguer, Chem. Eur. J. 9, 1677–1691 (2003)
- V. Marvaud, C. Decroix, A. Scuiller, F. Tuyeras, C. Guyard-Duhayon, J. Vaissermann, M. Marrot, F. Gonnet, M. Verdaguer, Chem. Eur. J. 9, 1692–1705 (2003)
- 49. T. Lis, Acta Crystallogr. B **36**, 2042–2046 (1980)
- A.M. Ako, I.J. Hewitt, V. Mereacre, R. Clerac, W. Wernsdorfer, C.E. Anson, A.K. Powell, Angew. Chem. Int. Ed. 45, 4926–4929 (2006)
- C.J. Milios, A. Vinslava, W. Wernsdorfer, S. Moggach, S. Parsons, S.P. Perlepes, G. Christou, E.K. Brechin, J. Am. Chem. Soc. 129, 2754–2755 (2007)
- A. Abragam, B. Bleaney, Electron Paramagnetic Resonance of Transition Ions (Dover, New York, 1986)
- 53. A. Bencini, D. Gatteschi, Transition Metal Chem. 8, 1 (1982)
- D. Gatteschi, A.L. Barra, A. Caneschi, A. Cornia, R. Sessoli, L. Sorace, Coord. Chem. Rev. 250, 1514–1529 (2006)
- A.L. Barra, A. Caneschi, D. Gatteschi, R. Sessoli, J. Magn. Magn. Mater. 177, 709–710 (1998)
- S. Hill, J.A.A.J. Perenboom, N.S. Dalal, T.T. Hathaway, T. Stalcup, J.S. Brooks, Phys. Rev. Lett. 80, 2453–2456 (1998)
- R. Caciuffo, G. Amoretti, A. Murani, R. Sessoli, A. Caneschi, D. Gatteschi, Phys. Rev. Lett. 81, 4744–4747 (1998)
- A.L. Barra, D. Gatteschi, R. Sessoli, G.L. Abbati, A. Cornia, A.C. Fabretti, M.G. Uytterhoeven, Angew. Chem., Int. Ed. Engl. 36, 2329–2331 (1997)
- D.P. Goldberg, J. Telser, J. Krzystek, A.G. Montalban, L.C. Brunel, A.G.M. Barrett, B.M. Hoffman, J. Am. Chem. Soc. 119, 8722–8723 (1997)
- 60. A. Bencini, I. Ciofini, M.G. Uytterhoeven, Inorg. Chim. Acta 274, 90-101 (1998)
- 61. M.R. Pederson, D.V. Porezag, J. Kortus, S.N. Khanna, J. Appl. Phys. 87, 5487–5489 (2000)
- 62. M.R. Pederson, N. Bernstein, J. Kortus, Phys. Rev. Lett. 89, 097202 (2002)

R. Sessoli et al.

- 63. J. Kortus, M.R. Pederson, C.S. Hellberg, S.N. Khanna, Eur. Phys. J. D 16, 177–180 (2001)
- 64. F. Neese, E.I. Solomon, Inorg. Chem. 37, 6568-6582 (1998)
- 65. L.F. Chibotaru, L. Ungur, A. Soncini, Angew. Chem. Int. Ed. 47, 4126–4129 (2008)
- K. Bernot, J. Luzon, L. Bogani, M. Etienne, A. Caneschi, C. Sangregorio, M. Shanmugam,
 R. Sessoli, D. Gatteschi, J. Am. Chem. Soc. 131, 5573–5579 (2009)
- 67. O. Waldmann, Inorg. Chem. 46, 10035–10037 (2007)
- A.L. Barra, A. Caneschi, A. Cornia, D. Gatteschi, L. Gorini, L.P. Heiniger, R. Sessoli, L. Sorace, J. Am. Chem. Soc. 129, 10754–10762 (2007)
- J. Luzon, K. Bernot, I.J. Hewitt, C.E. Anson, A.K. Powell, R. Sessoli, Phys. Rev. Lett. 100, 247205 (2008)
- 70. R. Sessoli, D. Gatteschi, A. Caneschi, M.A. Novak, Nature 365, 141-143 (1993)
- 71. J. Villain, F. Hartmann-Boutron, R. Sessoli, A. Rettori, Europhys. Lett. 27, 159–164 (1994)
- A. Caneschi, T. Ohm, C. Paulsen, D. Rovai, C. Sangregorio, R. Sessoli, J. Magn. Magn. Mater. 177, 1330–1336 (1998)
- S. Accorsi, A.L. Barra, A. Caneschi, G. Chastanet, A. Cornia, A.C. Fabretti, D. Gatteschi, C. Mortalo, E. Olivieri et al., J. Am. Chem. Soc. 128, 4742–4755 (2006)
- 74. M.A. Novak, R. Sessoli, in *Quantum Tunneling of Magnetization QTM'94*, ed. by L. Gunther, B. Barbara (Kluwer, Dordrecht, 1995), pp. 171–188
- 75. J.R. Friedman, M.P. Sarachik, J. Tejada, R. Ziolo, Phys. Rev. Lett. **76**, 3830–3833 (1996)
- L. Thomas, F. Lionti, R. Ballou, D. Gatteschi, R. Sessoli, B. Barbara, Nature 383, 145–147 (1996)
- 77. A. Fort, A. Rettori, J. Villain, D. Gatteschi, R. Sessoli, Phys. Rev. Lett. **80**, 612–615 (1998)
- 78. W. Wernsdorfer, R. Sessoli, Science **284**, 133–135 (1999)
- 79. S. Hill, R.S. Edwards, N. Aliaga-Alcalde, G. Christou, Science **302**, 1015–1018 (2003)
- 80. G.M. Whitesides, B. Grzybowski, Science 295, 2418–2421 (2002)
- 81. A. Nait Abdi, J.P. Bucher, P. Gerbier, P. Rabu, M. Drillon, Adv. Mater. 17, 1612–1616 (2005)
- A. Cornia, A.C. Fabretti, M. Pacchioni, L. Zobbi, D. Bonacchi, A. Caneschi, D. Gatteschi,
 R. Biagi, U. Del Pennino et al., Angew. Chem. Int. Ed. 42, 1645–1648 (2003)
- 83. G.G. Condorelli, A. Motta, I.L. Fragala, F. Giannazzo, V. Raineri, A. Caneschi, D. Gatteschi, Angew. Chem. Int. Ed. 43, 4081–4084 (2004)
- S. Voss, M. Fonin, U. Rudiger, M. Burgert, U. Groth, Y.S. Dedkov, Phys. Rev. B 75, 045102 (2007)
- G.G. Condorelli, A. Motta, G. Pellegrino, A. Cornia, L. Gorini, L.L. Fragala, C. Sangregorio, L. Sorace, Chem. Mater. 20, 2405–2411 (2008)
- L. Bogani, C. Danieli, E. Biavardi, N. Bendiab, A.L. Barra, E. Dalcanale, W. Wernsdorfer, A. Cornia, Angew. Chem. Int. Ed. 48, 746–750 (2009)
- 87. F. Pineider, M. Mannini, R. Sessoli, A. Caneschi, D. Barreca, L. Armelao, A. Cornia, E. Tondello, D. Gatteschi, Langmuir 23, 11836–11843 (2007)
- L. Bogani, L. Cavigli, M. Gurioli, R.L. Novak, M. Mannini, A. Caneschi, F. Pineider, R. Sessoli, M. Clemente-Leon et al., Adv. Mater. 19, 3906–3911 (2007)
- 89. M.A. Arrio, A. Scuiller, P. Sainctavit, C. Cartier dit Moulin, T. Mallah, M. Verdaguer, J. Am. Chem. Soc. 121, 6414–6420 (1999)
- Ph. Sainctavit, J.-P. Kappler, X-ray Magnetic Circular Dichroism at Low Temperature. In: Magnetism and Synchrotron Radiation. Lecture Notes in Physics. Vol. 565, (Springer, Berlin, Heidelberg, 2000), pp. 235–253
- I. Letard, P. Sainctavit, C. Cartier dit Moulin, J.P. Kappler, P. Ghigna, D. Gatteschi, B. Doddi, J. Appl. Phys. 101, 113920 (2007)
- 92. P. Ghigna, A. Campana, A. Lascialfari, A. Caneschi, D. Gatteschi, A. Tagliaferri, F. Borgatti, Phys. Rev. B **64**, 132413 (2001)
- R. Moroni, C. Cartier dit Moulin, G. Champion, M.A. Arrio, P. Sainctavit, M. Verdaguer,
 D. Gatteschi, Phys. Rev. B 68, 064407 (2003)
- R. Moroni, P. Ghigna, D. Bonacchi, A. Caneschi, D. Rovai, Inorg. Chem. Acta 361, 3887–3890 (2008)
- P. Artus, C. Boskovic, J. Yoo, W.E. Streib, L.C. Brunel, D.N. Hendrickson, G. Christou, Inorg. Chem. 40, 4199–4210 (2001)

- H.J. Eppley, H.-L. Tsai, N. de Vries, K. Folting, G. Christou, D.N. Hendrickson, J. Am. Chem. Soc. 117, 301–317 (1995)
- S.M.J. Aubin, Z. Sun, L. Pardi, J. Krzystek, K. Folting, L.-C. Brunel, A.L. Rheingold, G. Christou, D.N. Hendrickson, Inorg. Chem. 38, 5329–5340 (1999)
- A.L. Barra, F. Bianchi, A. Caneschi, A. Cornia, D. Gatteschi, L. Gorini, L. Gregoli, M. Maffini, F. Parenti, R. Sessoli, L. Sorace, A. M. Talarico, Eur. J. Inorg. Chem. 4145–4152 (2007)
- 99. M. Mannini, F. Pineider, Ph. Sainctavit, C. Danieli, E. Otero, C. Sciancalepore, A.M. Talarico, M.A. Arrio, A. Cornia, D. Gatteschi, R. Sessoli, Nat. Mater. 8, 194–197 (2009)
- 100. R. Nakajima, J. Stohr, Y.U. Idzerda, Phys. Rev. B 59, 6421-6429 (1999)
- 101. S.M.J. Aubin, Z.M. Sun, H.J. Eppley, E.M. Rumberger, I.A. Guzei, K. Folting, P.K. Gantzel, A.L. Rheingold, G. Christou et al., Inorg. Chem. 40, 2127–2146 (2001)
- 102. M. Evangelisti, J. Bartolomé, J. Magn. Magn. Mater. 221, 99-102 (2000)
- C. Quitmann, U. Flechsig, L. Patthey, T. Schmidt, G. Ingold, M. Howells, M. Janousch, R. Abela, Surf. Sci. 480, 173–179 (2001)

Chapter 11 Magnetic Structure of Actinide Metals

G. van der Laan and K.T. Moore

Abstract In comparison to 3d or 4f metals, magnetism in actinides remains poorly understood due to experimental complications and the exotic behavior of the 5f states. In particular, plutonium metal is most especially vexing. Over the last five decades, theories proposed the presence of either ordered or disordered local moments at low temperatures. However, experiments such as magnetic susceptibility, electrical resistivity, nuclear magnetic resonance, specific heat, and elastic and inelastic neutron scattering show no evidence for ordered or disordered magnetic moments in any of the six phases of plutonium. Beyond plutonium, the magnetic structure of other actinides is an active area of research, given that temperature, pressure, and chemistry can quickly alter the magnetic structure of the 5f states. For instance, curium metal has an exceedingly large spin polarization that results in a total moment of $\sim 8\mu_{\rm B}/{\rm atom}$, which influences the phase stability of the metal. Insight in the actinide ground state can be obtained from core-level X-ray absorption spectroscopy (XAS) and electron energy-loss spectroscopy (EELS). A sum rule relates the branching ratio of the core-level spectra measured by XAS or EELS to the expectation value of the angular part of the spin-orbit interaction.

11.1 Introduction

Actinide elements such as uranium and plutonium often conjure visions of radiationspawned monsters who wreak havoc on unsuspecting bystanders. While this makes for spectacular pulp fiction, it does not relay the fact that actinide materials are the cornerstone of nuclear energy and are scientifically fascinating. At present, nuclear power offers the only viable carbon-free energy production that can meet the growing demands of the world that will stress the power grid over the next several decades. Scientifically, the 5f electron states of actinide materials create a myriad of exciting physical behaviors, such as superconductivity, itinerant magnetism,

G. van der Laan (⋈)

Diamond Light Source, Chilton, Didcot, Oxfordshire OX11 0DE, UK e-mail: gerrit.vanderlaan@diamond.ac.uk

electron correlations, and heavy fermions [1]. Therefore, these heavyweights of the periodic table are relevant both technologically and scientifically, poised to play a key role in the resurgence of nuclear power for clean and robust energy, and expand our understanding of condensed-matter physics.

The actinide series consists of 14 elements and, accordingly, the 5f states can contain up to the same number of electrons. Adhering to Hund's rule of maximizing total spin, this means the f-shell accepts seven electrons with the same spin direction before taking electrons with opposite spin. Therefore, magnetism has the potential to be strong near the middle of the series. Indeed, this is observed in the rare-earth series where the middle elements such as Eu and Gd exhibit very strong magnetic moments due to spin polarization of the 4f states. The strong magnetic moments observed in the rare-earth series are a direct consequence of the 4f states being localized, that is, reduced wavefunction overlap with non- or weakly-bonding 4f electrons. The opposite is true for the light actinides, such as Th, Pa, U, Np, and α -Pu, because the 5 f states are delocalized in the metallic form. This changes in the latter part of the actinide series where the 5 f states become localized. The actinide series, therefore, does not simply adhere to Hund's rule. Rather, there is a competition between the exchange interaction that drives maximization of the total spin and the spin-orbit interaction of the i = 5/2 and 7/2 angular momentum levels of the 5f states [2–5]. This competition produces interesting magnetic behavior in the actinides when the states localize in heavier elements and when the light actinide elements bond with other elements.

In this chapter, we discuss in general terms the magnetism of the actinide elements, in particular Pu. A comparison will be d with the 3d, 4d, and 5d metal series as well as the 4f metals. Because electron localization is a requirement to obtain local magnetic moments, we pay specific attention to this in both metals and some compounds. For instance, the transitions from α - to δ -Pu and from α - to γ -Ce both exhibit a large change in volume, indicative of a transition from itinerant to localized behavior. However, unlike Ce metal that shows a magnetic moment in the large-volume γ -Ce phase with localized 4f states, both α - to δ -Pu show no evidence of a magnetic moment. Surprises like this litter the actinide series, often creating controversies that are fodder for fruitful and entertaining arguments. We will specifically discuss subjects such as the following:

- Localization of the 5f states across series
- Crystal phase transitions and comparison to Cerium
- Magnetic properties
- Consequences of angular-momentum coupling of the 5f states: LS, jj, and intermediate coupling
- Role of spin-orbit and electrostatic interactions
- Electron energy-loss spectroscopy (EELS) in a transmission electron microscope (TEM)
- N_{4.5} branching ratio
- Spin-orbit sum rule and its validity for the 5 f states of actinides
- Spin-orbit interaction per hole for Th, U, Np, Pu, Am, and Cm

- Electron population of the $f_{5/2}$ and $f_{7/2}$ levels
- Ramifications of these results for the magnetic structure of actinides.

We point the reader to other review articles, such as *Challenges in plutonium science*, Vol. I and II in the *Los Alamos Science Series* [6], particularly the article entitled *Plutonium Condensed-Matter Physics*. A *Survey of Theory and Experiment* by Boring and Smith [7], *Absence of Magnetic Moments in Plutonium* by Lashley et al. [8], *Handbook on the Physics and Chemistry of the Actinides* by Freeman and Lander [9], and *Nature of the 5f States in Actinide Metals* by Moore and van der Laan [1]. These reviews cover the electronic, magnetic, and crystal structure of the actinide materials. Here, we will focus on the magnetic structure of actinide metals and materials, incorporating the most current experimental and theoretical results.

11.2 Volume Change Across the Actinide Series

Figure 11.1 shows a plot of the metallic radii, which are directly proportional to volume of the actinide 5f metals, in comparison to those of 5d and 4f metals. The curve for the 5d transition-metal series is parabolic because in the first half of the series, each additional electron contributes to the cohesive energy of the solid resulting in a *decrease* of volume until the shell is approximately half full. In the second half of the d series there is an *increase* of volume due to filling of the antibonding

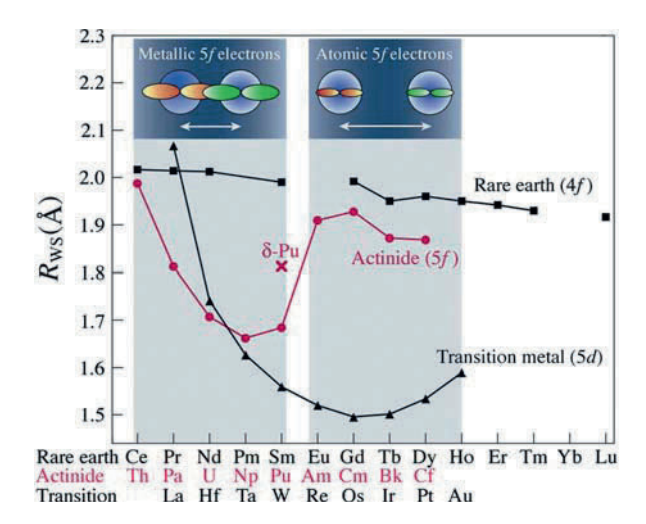


Fig. 11.1 Wigner-Seitz radius of each metal as a function of atomic number Z for the 5d, 4f, and 5f metal series (from [7]). The *upper-left* insets schematically illustrate the localized and delocalized 5f states between adjacent actinide atoms (from [10]). Note the parabolic shape of the 3d series, the almost constant values of the trivalent rare earths (for clarity the divalent Eu and Yb are omitted), and the unusual behavior of the 5f elements, with minimum volume near Pu and strong increase between Pu and Am

states. This behavior is indicative of states that are delocalized and actively bonding. The early actinides (Th to Np) exhibit a *contraction* with increasing electron count similar to the 5d series, and this in conjunction with the absence of magnetic order indicates that the 5f electrons of the early actinide elements are *itinerant* (delocalized).

In the vicinity of Pu, there is an abrupt jump in the volume and the elements Am to Cf exhibit little change in volume with increased 5f electron count. This behavior can be explained by examining the 4f rare-earth series in Fig. 11.1. Here, there is little change in metallic radii across the series because the 4f states are localized and nonbonding, leaving cohesion to the $(spd)^3$ electrons that do not change count across the series. Comparison with the 4f elements, together with the presence of ordered magnetism in Cm and elements beyond, indicate *localized* behavior of the 5f electrons.

Our discussion of the two types of bonding behaviors in the actinide series emphases the unique position of plutonium. The volume change between α -Pu and Am is $\sim 50\%$, a staggering change in volume between two neighboring elements in the periodic table considering that the only apparent change is to add one electron in the 5f shell. Indeed, unlike the lanthanide elements Eu and Yb, which are both divalent in the normally trivalent lanthanide series, there is no indication of a straightforward valence change between Pu and Am. This means that the simple addition of another 5f electron is not the pressing issue, but rather the change from itinerant to localized behavior. What we will find is that the bulk of the transition from itinerant to localized 5f states occurs within Pu itself! Compared to the ground state α -phase, the high-temperature δ -Pu phase is $\sim 25\%$ larger in volume. Thus, plutonium is the nexus between itinerant- and localized-electron behavior.

11.2.1 Photoemission Spectroscopy's Two Cents

Clear support for increased localization across actinide series is provided by 4f core and 5f valence-band photoemission of actinide metals. When examining the photoemission spectra for the elements traversing the series, the 4f photoemission of α -Th [11], α -U [11], and α -Np [12] is dominated by well-screened peaks, characteristic for itinerant behavior. Between α -Pu and δ -Pu, poorly screened peaks that are due to more localized 5f states increase in intensity compared to the well-screened peak [13]. α -Am shows almost uniquely unscreened peaks, which are characteristic for localized behavior [14]. In a similar fashion, valence-band photoemission of actinide metals shows an increase in structure from Np to Am, where growing structure indicates localization of the 5f states [12, 14–16]. The increase of structure in 4f core and 5f valence-band photoemission from Np to Am shows that the entire transition from itinerant to localized 5f states occurs over several elements; however, the α -Pu and δ -Pu spectra clearly reveal that the brunt of the change occurs within the metal's phases.

The most important insight from the previous discussion is that the 5f states in Th to Pu are slightly overlapping between neighboring actinide atoms. They

therefore occupy a very narrow energy band with very high density of states near the Fermi energy. As the number of 5f electrons populating the 5f band increases, the specific properties of the band begin to dominate the bonding properties of the metal. At plutonium, the 5f states rapidly change towards localization and this abrupt change produces a metal with more solid allotropic phases than any other element in the periodic table.

11.3 The Six Crystal Allotropes of Pu Metal

Plutonium is often described as "A physicist's dream but an engineer's night-mare" because the metal has an anomalously low melting point, a high number of allotropes, negative coefficient of thermal expansion in some phases, and the unusual preference for low-symmetry crystal structures. At ambient pressure, Pu exhibits six solid allotropic crystal structures (α , β , γ , δ , δ ', ε) between room temperature and melting, as shown in Fig. 11.2. The phase stability of Pu as a function of temperature clearly illustrates the change in volume that occurs between the low-symmetry monoclinic structure of α -Pu with 16 atoms in the unit cell and the

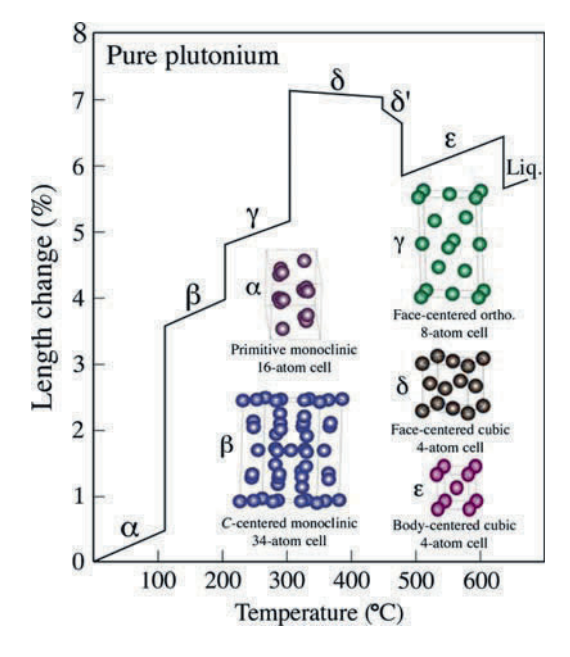


Fig. 11.2 Length change of Pu as a function of temperature, including the liquid phase. The crystal structure of all six solid allotropic phases of the metal is given in the *lower-right* side of the figure (after [17]). The structure changes from low-symmetry monoclinic (α-phase) to high-symmetry fcc (δ-phase), which occurs with exceeding large volume changes over a short temperature span. Note also the δ-phase contracts as it is heated, and plutonium contracts as it melts

high-symmetry structure of δ -Pu. Indeed, despite a cubic structure, the fcc δ -phase is perplexing, given its unusually low density and negative thermal expansion coefficient, that is, it contracts when heated. It is, however, most intriguing that the α , β , and γ phases of Pu are low symmetry monoclinic or orthorhombic structures, a geometry that is common to minerals but foreign to metals and alloys, which are usually cubic or hexagonal. An immediate question is why do the light actinides have low symmetry crystal structures if most all other metals have high symmetry atomic geometries? This is quite important, given that the high symmetry structures of most metals, such as fcc copper and aluminium, exhibit ductility by readily allowing dislocation motion through 12 slip systems. It is the ductile behavior of metals that makes them prized for many technological applications. Accordingly, the low symmetry and concomitant brittle nature of Pu and other light actinides is unwanted and we must understand its physical origins.

11.3.1 Lowering the Electronic Energy Through a Peierls-like Distortion

Protactinium, uranium, neptunium, and plutonium all exhibit low-symmetry groundstate structures rather than the high-symmetry structures usually found in metals. In the early days of actinide research, this low symmetry was attributed to directional or covalent-like bonding resulting from the angular characteristics of f electrons. However, this so-called chemist view that the pointy f-electron atomic orbitals are forming directional bonds, hence no closed-packed structure of the metals falls short of explaining the abundance of crystal structures observed of the actinide elements. Accordingly, physicists looked for a better answer and found it in the width of the band. Söderlind et al. [18] showed that as the bandwidth of a bonding state is narrowed, the crystal structure of the metal will distort through a Peierls-like distortion to a low-symmetry geometry. The original Peierls-distortion model was formulated in a one-dimensional lattice: A row of equidistant atoms can lower its total energy by forming pairs. The lower periodicity causes the degenerate energy levels to split into two bands with lower and higher energies. The electrons occupy the lower levels, so that the distortion increases the bonding and reduces the total energy. In one-dimensional systems, the distortion opens an energy gap at the Fermi level, making the system an insulator. However, in the higher dimensional systems the material remains a metal after the distortion because other Bloch states are filling the gap. This mechanism is highly effective if there are many degenerate levels near the Fermi level - that is, if the energy bands are narrow with a large density-ofstates [7]. Symmetry breaking of a crystal structure through a Peierls-like distortion due to narrow bandwidths (and concomitant high density-of-states near the Fermi level) is true for s, p, d, and f states, meaning that even aluminium can be expanded enough that a low-symmetry body-centered tetragonal structure is observed [18]. Of course for metals with s, p, and d bands actively bonding, huge theoretical tensions must be applied to narrow the bands enough to lower the crystal structure symmetry. However, the 5 f bands of Pa, U, Np, and Pu that are bonding are narrow enough to yield low symmetry structures at ambient conditions. Thus, the narrow width of the 5f band causes the low-symmetry structures of the ground state, without the need to invoke an explanation involving directional bonding.

Our discussion of Pu and energy-lowering lattice distortions means that the metal is directly on the border between itinerant and localized 5f electron behavior. The metal shows a monoclinic ground state and an fcc high-temperature phase, resulting in 5f states that are balanced between a Peierls distortion to a low symmetry structure due to stronger bonding of the f states and a high-symmetry crystal structure with strong electron correlations with weaker bonding of the f states. The fact that δ -Pu exhibits a high symmetry fcc structure even though it has active, albeit weaker, 5f electron bonding is somewhat perplexing. Surely the degree of bonding is less than in α -Pu, given that the ground-state phase is monoclinic. However, the exceedingly high electronic specific heat (Sommerfield coefficient) of 35–64 mJ K $^{-2}$ mol $^{-1}$ [19–21] tells us that there is appreciable electron weight at the Fermi level in δ -Pu, and this could only be achieved with the 5f states. To understand this apparent contradiction, we can turn our attention to a rare-earth metal that has 4f states that can be changed from bonding to nonbonding through temperature or pressure, all the while retaining its high symmetry fcc structure.

11.3.2 Comparison with Cerium

A material with similar properties as plutonium, and of comparable complexity, is cerium, the first element in the row of the lanthanides, which is known for the ambivalent character of its 4f states. It exhibits multiple crystallographic phases that are strong functions of temperature, pressure, and chemistry [22]. At ambient pressure, Ce metal exhibits four allotropic phases between absolute zero and its melting temperature at 1,071 K, namely α (fcc), β (dhcp), γ (fcc), and δ (bcc). Magnetic, nonmagnetic, and superconducting behavior is also observed. There is broad consensus that the unusual properties of Ce and its compounds originate essentially from the interplay of strong electronic correlations between the Ce 4f electrons and hybridization between 4 f - and conduction-electron states. Phenomena such as intermediate-valence, which points to noninteger occupation of the 4fshell, or heavy-fermion behavior characterized by an extremely large contribution of the electronic specific heat, are prominent observations on such systems. But perhaps one of the most intriguing phenomena is the γ - α phase transition in Ce metal [22]. It occurs under pressure at room temperature or, at ambient pressure, on cooling to low temperature. Complexity of the underlying mechanisms is reflected in the collapse of the atomic volume by $\sim 17\%$, preserving the fcc lattice symmetry, and the loss of the magnetic moment (γ -Ce is paramagnetic and α -Ce nonmagnetic). The γ - α phase boundary ends at a critical point where the two phases become indistinguishable.

The anomalous behavior of Ce at the γ - α phase transition is commonly described by mechanisms involving either a Mott transition [23] or Kondo hybridization [24, 25]. However, recent first-principle calculations provide evidence for a combination

of effects, involving strongly correlated 4 f electrons in both phases and screening as important ingredients [26–28]. The transition to the α -phase is accompanied by a sizable increase of the hybridization between 4f - and valence-electron states. It leads to a partial delocalization of the 4f states, that is, the ground state occupation number, n_f , that is almost equal to one electron in the γ -phase is reduced in the α -phase. This has been directly derived from recent measurements of resonant inelastic X-ray scattering on elemental Ce under pressure [29]. The experiments permit to conclude that the changes of the electronic structure at the phase transition mainly result from band formation of 4f electrons that concurs with reduced electron correlation and increased Kondo screening. The experiments also highlight the importance of double occupancy of the 4f states in the ground state for understanding the effects of electron correlation in this element, as stated in [27]. Considering lattice dynamics, phonon density of states of α and γ -phases in Ce_{0.9}Th_{0.1} by Manley et al. show only a very small difference in the vibrational entropy of the two phases, where most of the transition entropy can be accounted for with the crystal field and changes in the ground-state spin fluctuations [30].

In compounds, Ce shows γ - α -phase-like character depending on the 4 f-valence band hybridization strength. Interestingly, in α-like compounds, such as CeFe₂ or CeCo₅, the Ce atoms carry an ordered magnetic 4f moment [31] in contradistinction to elemental α -phase Ce metal [22]. An important concept in the theoretical description of these compounds is the hybridization between the 3d states of the transition metal and the delocalized Ce 4f states. Ce readily reacts with hydrogen. As with other light rare earth metals, it forms a cubic dihydride CeH₂ with hydrogen atoms on tetrahedrally coordinated sites (CaF₂-type structure) and dissolves, in a single phase, further hydrogen on octahedral sites up to the cubic trihydride CeH₃ (BiF₃-type structure) [32]. As the composition of the trihydride is approached, a metal-to-insulator transition occurs that is reversible. It was recognized that thin films of such rare-earth hydrides allow to rapidly switch between the contrasting optical properties of the dihydride and trihydride phases, making them technologically interesting as optical switches [33]. Model calculations of the rare earth hydrides in an ionic picture have shown the importance of electron correlations for this effect [34–36]. Strong Coulomb interactions between the electrons on hydrogen sites were shown to be responsible for opening up a gap of \sim 2 eV between the valence bands derived from rare earth-hydrogen and hydrogen-hydrogen hybridization and a set of bands predominantly of rare earth-metal d character. X-ray absorption spectra have shown that the electronic configuration of the Ce 4f states in the Ce hydrides is similar as in the γ -phase of the pure metal [37]. Below 7 K, CeH_x orders magnetically in a complex phase diagram [32, 38].

11.3.3 Stabilized δ-Plutonium

Now back to the point of why we introduced Ce. α -Ce has actively bonding f states, but the crystal structure is fcc, as observed for δ -Pu. For α -Ce, this means there is just enough f bonding to influence the physical properties such as electronic

specific heat, but not enough to reduce the crystal structure. Of course, this can easily be changed with external influences. When pressurized to about 4 GPa, the structure changes to orthorhombic Cmcm (the same as α -U), meaning the 4f states become decisive enough in bonding so as to break the cubic symmetry of the crystal. Considering δ -Pu, a similar situation is occurring where there is enough f bonding to influence the electronic specific heat, but not enough to break cubic symmetry. It is possible, there is a slight distortion from a perfect cubic symmetry in δ -Pu, but if true this would be small [39, 40]. Once δ -Pu is pressurized to about 0.1 GPa, the structure looses cubic symmetry. In a reverse manner, adding a few percent of Ga, Al, Ce, Am, or other tetravalent elements stabilizes δ -Pu at room temperature and below.

The addition of impurity atoms often destroys the coherence of the f band. Without its narrow f band actively bonding, plutonium can no longer reduce its energy by lowering its symmetry through Peierls-like distortion to the α -phase; it therefore remains in the δ -phase. Another view is that plutonium atoms relax and move toward the smaller non-f atoms, thereby reducing the f-f interactions that stabilize the α -phase. Either way, we see that addition of many different elements stabilizes δ -Pu, such as Al, Ce, Am, and, most often utilized, Ga. Indeed, we find δ -phase stabilization occurs even for defects, where it has been found that excessive plastic deformation, and, concomitantly the introduction of dislocations, stabilizes δ -Pu [41]. Once more we see how external influences, such as temperature and chemistry as well as the pressure or defects, can influence the phase stability of plutonium. What is more, we now have a way to overcome the crippling technological disadvantage of monoclinic Pu that is brittle and difficult to machine.

11.4 Revised View of the Periodic Table

Plutonium is not alone in juggling its electrons between bonding and localized states. Figure 11.3 shows a rearranged periodic table containing the d and f electron series, where the f series are placed on top and spaced slightly tighter. The localization increases going from bottom to top. Furthermore, along each series the localization increases from left to right. The elements on the white diagonal stripe form the rough dividing line between localized (local moment magnetism) and itinerant (superconductivity) long-range collective behavior. The elements on or near the transition between localized and delocalized behavior, that is, the white diagonal stripe, exhibit a large number of solid allotropic phases (see Fig. 11.3b). This is clearly illustrated in the lower part of Fig. 11.3, where the lighter shades indicate more phases, and the light band mirrors the white diagonal stripe in the rearranged periodic table above [43]. The most notable elements with numerous phases are Pu with 6, Ce with 4, Mn with 4, as well as La, U, Np, Am, and Fe, each with 3.

The elements at the diagonal white stripe in Fig. 11.3 have in common that the wave functions from different atoms are barely overlapping, and their electrons are thus bordering on being localized. These are the so-called correlated-electron

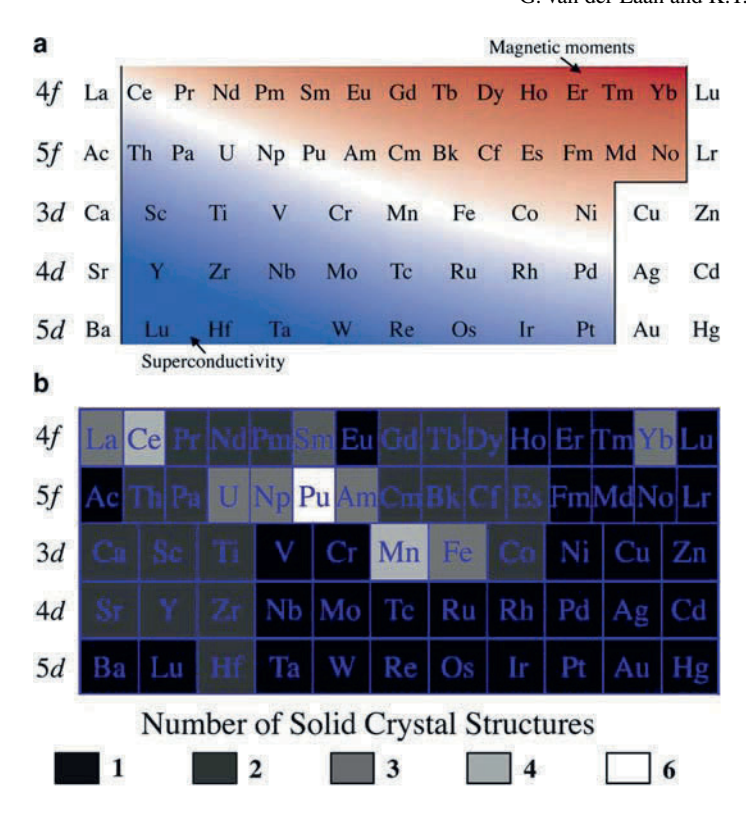


Fig. 11.3 (Color online) (a) Rearranged periodic table showing the five transition metal series, 4f, 5f, 3d, 4d, and 5d (after [42] and [7]). When cooled to the ground state, the metals in the blue area exhibit superconductivity while the metals in the red area exhibit magnetic moments. The white band running diagonally from upper left to lower right is where conduction electrons change from itinerant and pairing to localized and magnetic. Slight changes in temperature, pressure, or chemistry will move metals located on the white band to either more conductive or more magnetic behavior. (b) Version of (a) where the number of solid allotropic crystal structures for each metal is indicated by gray scale. Lighter shades indicate more phases. Notice that a band of lighter shades mirrors the white band in (a), showing that metals on or near the transition between magnetic and superconductive behavior exhibit numerous crystal phases

materials that are characterized by the presence of a narrow conduction band, giving rise to spin and charge fluctuations associated with the low-energy excitations. The exotic behaviors of these materials necessitate a description by many-electron models, such as the Kondo, Hubbard, or Anderson models. These models can be generically classed as two-electron "impurity" models, which introduce interactions between pairs of electrons, one localized on an impurity atom and one in a conduction band. The Anderson Hamiltonian contains both a repulsive Coulomb term and an electron hopping term. The former term keeps the 5f electrons localized, and the latter term leads to a partial localization of the conduction electrons [7].

11.5 Actinide Magnetism

The relation between f-electron localization and the formation of magnetic moments, as illustrated in Fig. 11.3a, leads to the following conclusions. The light actinides (Th, U, Np) are delocalized and show no magnetic ordering. Many of these metals are even superconducting at low temperatures. On the other hand, the localized heavy actinides (from Cm onwards) show magnetic ordering. Note that americium is $5f^6$ with a ground state J=0 and therefore has no magnetic ordering. Thus, magnetism – or lack thereof – of most of the actinides is clear. The situation regarding the magnetism of Pu, however, remains murky.

11.5.1 Experimental Absence of Magnetic Moments in Plutonium

Plutonium shows a large experimentally observed magnetic susceptibility, hints of heavy-fermion behavior, and an anomalous temperature dependence of the electrical resistivity. At low temperatures the resistivity increases, which is characteristic for a Kondo lattice. Judging by its small volume, the monoclinic α -phase is clearly delocalized and therefore nonmagnetic. The fcc δ -phase is more localized. So, could this phase be magnetic? In the past, ab initio electronic structure calculations that included spin and orbital polarization successfully reproduced the large volume change by localizing the 5 f electrons in δ -Pu [44–47]. One particular set of calculations by Söderlind and Sadigh [48] achieved the appropriately spaced energies and atomic volumes for five of the six allotropic phases of Pu (the high-temperature bcc ε -phase was too high in energy) as well as an equation-of-state, bulk modulus, and elastic constants that are in agreement for all the six allotropic phases. However, these calculations gave rise to a new problem, namely they concluded that Pu contained local magnetic moments. While experimental results in the early days were ambiguous, today it well established that all six phases of Pu, including δ , show no evidence of long-range magnetism.

Magnetic measurements on Pu were reviewed in 2005 by Lashley et al. [8]. To understand the large volume expansion between α - and δ -phases of plutonium, a *localization* of the 5f states is needed. With strong reasons for taking the number of 5f electrons in Pu as five, this gives a Kramer's ground state with the prediction of magnetic ordering for the δ -phase, and in some cases, even for the α -phase. The resulting moments are predicted to be large, and even though, due to their antiparallel coupling there is a partial cancelation of the spin and orbital parts, the total magnetic moments are of the order of $1-2\,\mu_{\rm B}/{\rm atom}$. This remains the case when band structure calculations take into account orbital polarization effects, in which case the absolute value of the orbital magnetic moment exceeds the value of the spin magnetic moment.

The measured magnetic susceptibilities of Pu in its various phases is shown in Fig. 11.4 [8]. This susceptibility is characteristic of metals with relatively strong

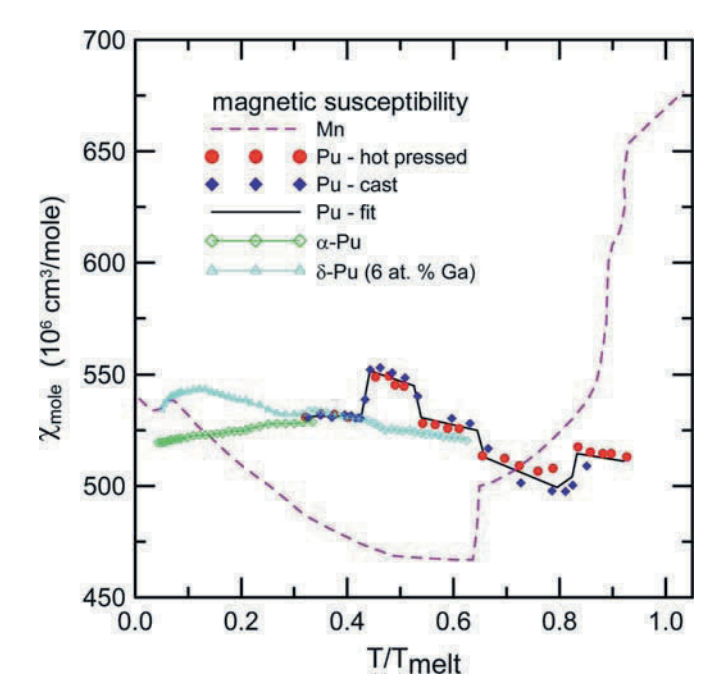


Fig. 11.4 Molar susceptibility of Mn and various forms of Pu plotted as a function of the melting point $[T_{\text{melt}}(\text{Mn}) = 1519 \, \text{K}$ and $T_{\text{melt}}(\text{Pu}) = 913 \, \text{K}]$. The susceptibility of Pu is characteristic of metals with relatively strong paramagnetism. Manganese is given for comparison. The sequence for Mn is α (complex cubic), β (complex cubic), γ (fcc), and δ (bcc). Mn orders antiferromagnetically at 95 K ($T/T_{\text{melt}} = 0.063$) in a complex tetragonal structure that is a slight distrotion of the α -phase. From [8]

paramagnetism caused by electronic band magnetism. Neither the temperature nor the magnetic field dependence of the measured susceptibilities in Pu provide evidence for disordered or ordered moments. Specific-heat measurements indicate the absence of magnetic entropy. The combination of neutron elastic and inelastic scattering data shows no convincing evidence for either long-range ordered or disordered (static or dynamic) magnetic moments. On the basis of resistivity measurements for both α - and δ -Pu, and review of other measurements, Arko et al. [49] concluded in 1972 that there was no evidence for localized moments or magnetic order. On the basis of a T^2 dependence of the resistivity near T=0, these authors suggested a model involving spin fluctuations for elemental Pu, as well as for a number of other alloys and compounds.

Review of the magnetic measurements by Lashley et al. [8] demonstrated beyond all reasonable doubt that there is no *ordered* magnetism involving the 5f electrons in Pu metal in either the α - or the δ -phases down to a base temperature of \sim 4 K. The experimental evidence presented includes magnetic susceptibility, specific heat (with an applied field of up to 14 T), nuclear magnetic resonance, and elastic and inelastic neutron scattering. Previous reports of "anomalies," seen especially in the specific heat, can in fact be ascribed to impurities or structural effects, most probably

the occurrence of martensitic transformations of some parts of the samples to the α ' phase that contains Ga. The absence of any diffuse scattering in the neutron diffraction patterns (except at high-temperature from thermal disorder) also argues against any disordered local moments. Dynamical mean-field theory (DMFT) results by Savrasov et al. [50] imply that the local moments are "washed out" over short time scales and thus may not be observable to probes such as NMR and neutron inelastic scattering, depending on the probes observational frequency window. Again, more effort to quantify these predictions for experiments on Pu would seem worthwhile [8,51].

11.5.2 Looking to Other Elements for Clues

As plutonium has no local magnetic moments, a limited comparison could perhaps be drawn with palladium, which finds itself also on the diagonal stripe in Fig. 11.3a. As bulk compound, palladium is an anomalous paramagnet on the verge of ferromagnetism [52, 53]. The free Pd atom has a $[Kr]4d^{10}$ closed-shell electronic configuration. In bulk Pd no spontaneous ferromagnetic order is observed. Although the Fermi level is located immediately above a sharp peak in the density of states, at the equilibrium volume the Stoner criterion is not satisfied. The most sensitive factors that may enhance the density of states at the Fermi level and cause the onset of ferromagnetism in Pd clusters are the electron localization associated with a reduced coordination number, the expansion of the lattice, and the change of the local symmetry [52].

One might also ask whether the conduction electrons of Pu could make it an itinerant magnet, like iron. While there is little evidence for magnetism in pure plutonium, many plutonium compounds are indeed magnetic and tend to be itinerant magnets [54]. Indeed, simply dissolving hydrogen in plutonium is enough to make the electrons localize and to turn the system ferromagnetic. Also, a comparison of the light actinides with the transition metals indicates that the light actinides should be superconductors unless they have local moments. So, the fact that plutonium is not a superconductor might indicate that plutonium is an incipient, weak itinerant magnet, and that the loss of magnetic ordering with heating plays a role in the contraction of the δ -phase.

11.6 Experimental Complications of Plutonium

Because of its toxic and radioactive nature, hands-on investigation of Pu can only be done at a small number of institutions around the world, making experimental results sparse in comparison to other materials. Furthermore, experiments on Pu suffer from the problem of self-irradiation, which heats the sample, slowly destroys the crystal structure [55, 56], grows in daughter products of the decay process, and

potentially creates local magnetic moments [57]. When a plutonium nucleus in the material undergoes α -decay, the recoiling uranium and helium nuclei knock plutonium atoms from their lattice sites. Displaced plutonium atoms come to rest at interstitial sites leaving lattice vacancies. Each displaced plutonium atom creates a Frenkel pair - consisting of a vacancy and a self-interstitial. Each decay event creates more than 2,000 Frenkel pairs. The self-heating means that in practice it is extremely difficult to achieve temperatures much below ~2 K, unless very small (<mg) samples are used, and even then there is always some doubt as to the real temperature of the sample. This, however, may be overcome by choosing the right isotope. The most common isotope is fissile ²³⁹Pu with a 24,400 year half-life, which is made in nuclear reactors: ^{238}U + neutron \rightarrow ^{239}Pu . The 239-isotope produces considerable self heating. Alternatively, ²⁴²Pu has a 376,000 year half-life, which drastically reduces heat due to self irradiation. Finally, the crème de la crème is 244 Pu with a \sim 80 million year half-life, meaning the isotope is near nonradioactive. This isotope, if separated in usable quantities (it is very rare), could open many new avenues for low-temperature experiments on Pu.

11.7 One Man's Electron Energy Loss is Another's X-Ray Absorption

While the technique of X-ray absorption spectroscopy has become routine and is the go-to measurement for physicists, actinides and their special requirements demand a different experiment: electron energy-loss spectroscopy (EELS) in a transmission electron microscope (TEM). Why is this? First, the TEM utilizes small samples, allowing one to avoid the handling of appreciable amounts of toxic and radioactive materials. The alternative XAS performed at a multi-user synchrotron radiation facility is usually less well-adapted for the delicate and secure handling of radioactive materials. Second, the technique is bulk sensitive due to the fact that the electrons traverse ~40 nm of metal, this being the appropriate thickness for quality EELS spectra of actinide materials at the primary energy used in our TEM. A few nanometers of oxide do form on the surfaces of the TEM samples, but this is insignificant in comparison to the amount of metal sampled through transmission of the electron beam. Third, actinide metals near the localized-itinerant transition exhibit numerous crystal structures that can coexist in metastable equilibrium due to the small energy difference between the phases [43]. Therefore, acquiring singlephase samples of metals at or near this transition is uncertain, making spectroscopic techniques with low spatial resolution questionable. Finally, actinide metals readily react with hydrogen and oxygen, producing many unwanted phases in the material during storage or preparation for experiments. The TEM has the spatial resolution to image and identify secondary phases [58–60], ensuring examination of only the phase(s) of interest. A field-emission-gun TEM, such as the one used in these experiments, can produce an electron probe of \sim 5 Å, meaning recording spectra from a single phase when performing experiments is easily achieved. Quantitatively measuring the reflections in electron diffraction patterns over several crystallographic

orientations proves that the correct phase is examined [61, 62]. Hence there is no need for large single crystals!

EELS spectra of the actinide metals have been collected at the Lawrence Livermore National Laboratory (LLNL) using a Phillips CM300 field-emission-gun TEM, equipped with a Gatan imaging filter [43]. The momentum transfer in EELS gives rise to multipole transitions. However, by employing a small objective aperture and using a high primary energy of the electron beam (297 kV), the low-energy transitions are electric-dipole. The similarity between high-energy EELS spectra and synchrotron-radiation-based XAS has been well established for some time, and was recently validated for f-electron systems for the case of Ce metal [63].

11.8 Theory

The behavior of the 5f electrons in the actinides is governed by the interplay of the spin-orbit and electrostatic interactions. Here, we treat the effect of these interactions on the electronic configuration in the different angular momentum coupling schemes, that is, jj-, LS-, and intermediate coupling. This will be illustrated for the example of the f^2 configuration. This two-particle state is rather straightforward as it does not require explicit use of coefficients of fractional parentage or creation and annihilation operators. It is also shown how to obtain the expectation values of the moments in each of the different coupling schemes. For further reading on these topics, we refer, for example, to the *Hitchhiker's Guide to Multiplet Calculations* [64].

11.8.1 Atomic Interactions

For n electrons moving about a point nucleus of charge, the Hamiltonian can be written in the central field approximation as

$$\mathbf{H} = \mathbf{H}_{e1} + \mathbf{H}_{so},\tag{11.1}$$

where \mathbf{H}_{el} and \mathbf{H}_{so} are the terms for the electrostatic and spin-orbit interaction, respectively. This atomic Hamiltonian can be embedded in a solid state, for example, using an Anderson impurity model [65]. Crystal field interactions are usually less prominent in the actinides, leading only to a small perturbation; therefore, we assume a spherical potential. In any case, all interactions can be separated in *angular* and *radial* parts. The angular parts depend on the angular quantum numbers of the basis states of the electronic configuration and are independent of the radial wave functions, which in the calculations are taken as empirical scaled parameters (see Sect. 11.8.3).

The basis wave functions are assumed to be an antisymmetrized product of oneelectron functions. In spherical symmetry, these basis states are eigenfunctions of the total angular momentum J and its component M_J . The states are characterized by quantum numbers αLS , where α is a suitable quantity for distinguishing between terms having the same values of the orbital and spin angular momenta, L and S.

11.8.1.1 **Electrostatic Interactions**

The nonrelativistic Hamiltonian for the electrostatic interactions of n electrons in an atom with nuclear charge Ze is

$$\mathbf{H}_{\text{el}} = -\frac{\hbar^2}{2m} \sum_{i=1}^n \nabla_i^2 - \sum_{i=1}^n \frac{Ze^2}{r_i} + \sum_{i< j}^n \frac{e^2}{r_{ij}}.$$
 (11.2)

The first term describes the kinetic energy of all electrons, and the second one gives the potential energy of all electrons in the potential of the nucleus. The third term describes the repulsive Coulomb potential of the electron-electron interaction, where the expectation value can be expressed as

$$\left\langle \alpha LS \left| \frac{e^2}{|r_1 - r_2|} \right| \alpha LS \right\rangle = \sum_k f_k F^k + \sum_k g_k G^k, \tag{11.3}$$

with angular parts f_k and g_k and radial parts F^k and G^k . The radial integrals F^k and G^k are theoretically defined by the Slater integrals [66] and experimentally treated as empirically adjustable quantities to fit the observed energy levels and their intensities. The direct integrals F^k represent the actual electrostatic interaction between the two electronic densities of electrons ℓ and ℓ' . The exchange integrals G^k arise due to the quantum mechanical principle that fermions are indistinguishable, so that the wave function is totally antisymmetric with respect to permutation of the particles. Consequently, G^k is not present for the configuration ℓ^n , where the electrons are equivalent.

The angular parts f_k and g_k can be written in terms of 3j - and 6j -symbols [67]

$$f_k(\ell,\ell') = (-1)^L [\ell,\ell'] \begin{pmatrix} \ell & k & \ell \\ 0 & 0 & 0 \end{pmatrix} \begin{pmatrix} \ell' & k & \ell' \\ 0 & 0 & 0 \end{pmatrix} \begin{cases} \ell & \ell' & L \\ \ell' & \ell & k \end{cases}, \tag{11.4}$$

$$g_k(\ell,\ell') = (-1)^S[\ell,\ell'] \begin{pmatrix} \ell & \ell' \\ 0 & 0 & 0 \end{pmatrix}^2 \begin{Bmatrix} \ell & \ell' & L \\ \ell & \ell' & k \end{Bmatrix}.$$
 (11.5)

The triangle conditions require that $f_k(\ell, \ell)$ has nonzero values for $k = 0, 2, \dots, 2\ell$, whereas $g_k(\ell, \ell')$ has nonzero values for $k = |\ell - \ell'|, |\ell - \ell' + 2| \dots, \ell + \ell'$, with $\ell \neq \ell'$. Thus the initial state f^n has the radial parameters F^0 , F^2 , F^4 , F^6 , while the final state $d^9 f^n$ has F^2 , F^4 , G^1 , G^3 , G^5 .

11.8.1.2 Spin-Orbit Interaction

Turning to the second term of (11.1), the spin–orbit interaction for the ℓ shell is given as

$$\mathbf{H}_{\text{so}} = \zeta_{\ell}(r) \sum_{i=1}^{n} \mathbf{l}_{i} \cdot \mathbf{s}_{i}, \qquad (11.6)$$

where \mathbf{l}_i and \mathbf{s}_i are the one-electron orbital and spin angular momentum operators of the ith electron of the ℓ^n configuration. $\zeta_\ell(\mathbf{r})$ gives the radial part and $\sum_i \mathbf{l}_i \cdot \mathbf{s}_i$ gives the angular part of the spin–orbit operator. For brevity, we also introduce the following notation

$$\mathbf{l} \cdot \mathbf{s} = \ell s \, w^{110} \equiv \sum_{i=1}^{n} \mathbf{l}_{i} \cdot \mathbf{s}_{i}, \tag{11.7}$$

where w^{110} is the coupled tensor for the spin-orbit interaction (see, e.g., [68, 69] for details on coupled tensors). The expectation value for a one-electron state $|\ell sj\rangle$ with $\ell \neq 0$ is

$$\langle \ell sj | \mathbf{l} \cdot \mathbf{s} | \ell sj \rangle = \frac{1}{2} \left[j(j+1) - \ell(\ell+1) - s(s+1) \right], \tag{11.8}$$

which gives a doublet $|j| = \ell \pm s$ with expectation values

$$\langle \ell s j | \mathbf{l} \cdot \mathbf{s} | \ell s j \rangle = \begin{cases} -\frac{1}{2} (\ell + 1) & \text{for } j_1 = \ell - s, \\ \frac{1}{2} \ell & \text{for } j_2 = \ell + s. \end{cases}$$
(11.9)

For the atomic many-electron state, the Hamiltonian \mathbf{H}_{so} commutates with \mathbf{J}^2 and J_z and is hence diagonal in J and independent of the magnetic quantum number M_J . However, it does not commute with \mathbf{L}^2 or \mathbf{S}^2 and can thus couple states of different LS quantum numbers. For a pure state $|\ell^n \alpha LSJ\rangle$, the expectation value is

$$\langle \ell^n \alpha LSJ | \mathbf{l} \cdot \mathbf{s} | \ell^n \alpha LSJ \rangle = \frac{1}{2} [J(J+1) - L(L+1) - S(S+1)] \frac{\zeta(\alpha LS)}{\zeta}$$
 (11.10)

where the factor $\zeta(\alpha LS)/\zeta$ is equal to n^{-1} , 0, and $-(4\ell+2-n)^{-1}$ for $n < 2\ell+1$, $n = 2\ell+1$, and $n > 2\ell+1$, respectively.

It is useful to have a general expression for $\langle \mathbf{l} \cdot \mathbf{s} \rangle$ valid for any many-electron state in intermediate coupling, including the LS- and jj-coupling limits. As the spin-orbit operator is diagonal in j, there are no cross terms between $|j_1\rangle$ and $|j_2\rangle$. Therefore, we can distribute n over n_{j_1} and n_{j_2} , which are the electron occupation numbers of $|j_1\rangle$ and $|j_2\rangle$. For the configuration ℓ^n with $n=n_{j_1}+n_{j_2}$, application of (11.8) gives the anticipated general expression

$$\langle \ell^n J | \mathbf{l} \cdot \mathbf{s} | \ell^n J \rangle = \sum_{j=j_1, j_2} \langle j | \mathbf{l} \cdot \mathbf{s} | j \rangle n_j = -\frac{1}{2} (\ell+1) n_{j_1} + \frac{1}{2} \ell n_{j_2},$$
 (11.11)

which does not depend on the values of L, S, and J.

11.8.2 LS- and jj-Coupling Schemes

The electrostatic interaction is diagonal in the LS-coupled basis, and the spin-orbit interaction is diagonal in the jj-coupled basis. Switching between the LS- and jj-coupled basis states is done using a transformation matrix containing the recoupling coefficients.

11.8.2.1 *LS* Coupling

In the *LS*-coupling scheme, which gives the eigenfunctions in the limit $\zeta_{\ell}(r) \to 0$, the particles are coupled as

$$[(\ell_a, \ell_b)L, (s_a, s_b)S]J. \tag{11.12}$$

The Russell–Saunders notation for the LSJ-coupled states is $^{2S+1}L_J$. The lowest energy term of a configuration ℓ^n , that is, the Hund's rule ground state, is that term of maximum S which has the largest value of L. In addition, according to the third Hund's rule, J = L - S (J = L + S) for less (more) than half filled shell.

11.8.2.2 jj Coupling

In the jj-coupling scheme, which gives the eigenfunctions in the limit $\{F^k, G^k\} \to 0$, the particles are coupled as

$$[(\ell_a, s_a)j_a, (\ell_b, s_b)j_b]J$$
 (11.13)

In the jj-coupled ground state, first all $j=\ell-s$ levels are filled prior to the $j=\ell+s$ levels. For equivalent electrons, that is, with equal values of j, the Pauli exclusion principle limitations on the possible values of m_j prohibit some of the J-values that would be predicted by a vector model [67]. The result is that for any two equivalent electrons ℓ^2 only the even J-values are allowed when $j_a=j_b$.

11.8.2.3 Transformation Matrix

For a given electronic configuration, we arrive in both coupling schemes at the same set of allowed values of the total angular momentum $J = |L - S|, \ldots, L + S$. This means that the Hamiltonian of (11.1) is block-diagonal in J. For each J-block, the basis states can be transformed between LS- and jj-coupling using recoupling coefficients that can be expressed in terms of 9j symbols,

$$\langle [(\ell_a, \ell_b)L, (s_a, s_b)S]J | [(\ell_a, s_a)j_a, (\ell_b, s_b)j_b]J \rangle = [L, S, j_a, j_b]^{\frac{1}{2}} \begin{cases} \ell_a \ \ell_b \ L \\ s_a \ s_b \ S \\ j_a \ j_b \ J \end{cases},$$
(11.14)

where $[x, y, ...] \equiv (2x + 1)(2y + 1)...$ These coefficients form a matrix $\mathbf{T} = \langle LS \mid jj \rangle$. For a given J-block, transformation of the wave function or operator is given by

$$|jj\rangle = \mathbf{T}|LS\rangle$$
 and $|LS\rangle = \mathbf{T}^{-1}|(jj)\rangle$,
 $\mathbf{H}^{(jj)} = \mathbf{T}\mathbf{H}^{(LS)}\mathbf{T}^{-1}$ and $\mathbf{H}^{(LS)} = \mathbf{T}^{-1}\mathbf{H}^{(jj)}\mathbf{T}$. (11.15)

11.8.2.4 LS - vs. jj -Coupled Ground State: Example for f^2

To make the angular momenta coupling more explicit, let us examine the two-electron case, f^2 . The possible LSJ states for this configuration are 1S_0 , 1D_2 , 1G_4 , 1I_6 , ${}^3P_{0,1,2}$, ${}^3F_{2,3,4}$, ${}^3H_{4,5,6}$, amounting to a total of $\sum_i (2L_i+1)(2S_i+1)=\sum_i (2J_i+1)=91M_J$ levels. For two equivalent f electrons, the Pauli principle allows the jj states $(5/2,5/2)_{0,2,4}$, $(5/2,7/2)_{1,2,3,4,5,6}$, $(7/2,7/2)_{0,2,4,6}$. This also gives a total of $\sum_i (2J_i+1)=91~M_J$ levels, which illustrates that the Hamiltonian in (11.1) is block diagonal in J.

In any coupling, including intermediate, the ground state has total angular momentum J=4. The LS-coupled Hund's rule ground state is $|{}^3H_4\rangle$ and the jj-coupled ground state is $|(5/2,5/2)_4\rangle$. Spin–orbit interaction mixes $|{}^3H_4\rangle$ with $|{}^1G_4\rangle$ and $|{}^3F_4\rangle$. The transformation matrix for

$$(|^{3}H_{4}\rangle, |^{1}G_{4}\rangle, |^{3}F_{4}\rangle) \rightarrow (|(5/2, 5/2)_{4}\rangle, |(5/2, 7/2)_{4}\rangle, |(7/2, 7/2)_{4}\rangle)$$

is obtained from (11.14) as

$$\mathbf{T} = \frac{1}{7} \begin{pmatrix} \sqrt{\frac{110}{3}} & \sqrt{11} & -\frac{2}{\sqrt{3}} \\ 4\sqrt{\frac{2}{3}} & -2\sqrt{5} & \sqrt{\frac{55}{3}} \\ -\sqrt{\frac{5}{3}} & 3\sqrt{2} & 2\sqrt{\frac{22}{3}} \end{pmatrix}.$$
 (11.16)

Note that each state is (2J + 1 = 9)-fold degenerate in the absence of a magnetic field. Using (11.15), the jj-coupled ground state can be written as a sum over LS-coupled basis states

$$|(5/2, 5/2)_4\rangle = \frac{1}{7}\sqrt{\frac{110}{3}}|^3H_4\rangle + \frac{1}{7}\sqrt{11}|^1G_4\rangle - \frac{2}{7\sqrt{3}}|^3F_4\rangle.$$
 (11.17)

The character is given as the square of the wave function coefficient, so that the jj-coupled ground state has 74.8% $|^3H_4\rangle$, 22.5% $|^1G_4\rangle$, and 2.7% $|^3F_4\rangle$. This shows that the jj-coupled ground state contains a considerable amount of low spin.

Equation (11.15) also allows us to express the LS-coupled Hund's rule ground state as a sum over jj-coupled basis states

$$|^{3}H_{4}\rangle = \frac{1}{7}\sqrt{\frac{110}{3}}|(5/2,5/2)_{4}\rangle + \frac{4}{7}\sqrt{\frac{2}{3}}|(5/2,7/2)_{4}\rangle - \frac{1}{7}\sqrt{\frac{5}{3}}|(7/2,7/2)_{4}\rangle.$$
(11.18)

Thus the jj-coupled ground-state has $74.8\% | (5/2, 5/2)_4 \rangle$, $21.8\% | (5/2, 7/2)_4 \rangle$, and $3.4\% | (7/2, 7/2)_4 \rangle$ character. As $\langle {}^3H_4 | (5/2, 5/2)_4 \rangle = 0.748$, there is $\sim 75\%$ of the total electronic state found simultaneously in $|{}^3H_4 \rangle$ and $|(5/2, 5/2)_4 \rangle$. The remaining $\sim 25\%$ is distributed over different states depending on whether the spin–orbit or Coulomb interaction prevails. As we shall see, this has important consequences for the expectation values of the moments.

11.8.3 Intermediate Coupling

To assess the importance of intermediate coupling, we show in Table 11.1 the calculated atomic Hartree-Fock (HF) values of the radial parameters of the Slater integrals for representative elements among the various transition metal series. It is seen that the HF values of the Slater integrals F^k for the different metal series are comparable in size. In practice, an empirical scaling factor is used that depends on the degree of (de)localization of the valence electrons. In localized atomic systems, the Coulomb and exchange parameters typically require a scaling to 70–80% of the HF value to account for interactions with configurations omitted in the calculation [70], but fully itinerant systems might have to be scaled down to 10–20% [71]. In line with increasing atomic number Z, the value of the spin–orbit parameter is dramatically different for each of the metal series, with the largest values found for the actinides.

While the LS-coupled Hund's rule ground state is a reasonable approximation for the rare earths, this will usually not hold for the actinides [72].

To express the wavefunctions in intermediate coupling, where $\{\zeta_\ell, F^k, G^k\} \neq 0$, we can choose either the jj- or the LS-basis states, but in both cases the Hamiltonian has off-diagonal matrix elements. The spin-orbit interaction is diagonal in jj coupling and (11.11) gives $\langle \mathbf{l} \cdot \mathbf{s} \rangle = -4, -\frac{1}{2}$, and 3 for $|(5/2, 5/2)_4\rangle$, $|(5/2, 7/2)_4\rangle$, and $|(7/2, 7/2)_4\rangle$, respectively, with radial part ζ . Transforming this diagonal Hamiltonian to the LS-coupled basis $(|^3H_4\rangle, |^1G_4\rangle, |^3F_4\rangle)$ using (11.15) and then

Table 11.1 Comparison of the radial parameters, $F^k(\ell, \ell)$, for the Coulomb interaction and the spin–orbit interaction, ζ_{ℓ} , for actinides with rare earths [70] and 3d transition metals [73]

		F^2	F^4	F^6	ζι
²⁵ Mn ²⁺	3d ⁵	8.25	5.13		0.040
$^{64}Gd^{3+}$	$4f^{7}$	11.60	7.28	5.24	0.197
⁹⁶ Cm ³⁺	$5f^{7}$	8.37	5.46	4.01	0.386

All values are in electron volt. The Slater integrals have been reduced to 80% of the atomic Hartree–Fock values

including the diagonal Coulomb interaction gives the full Hamiltonian

$$\mathbf{H}_{J=4}^{(LS)} = \begin{pmatrix} E(^{3}H) - 3\zeta - \sqrt{\frac{10}{3}}\zeta & 0\\ -\sqrt{\frac{10}{3}}\zeta & E(^{1}G) & \sqrt{\frac{11}{3}}\zeta\\ 0 & \sqrt{\frac{11}{3}} & E(^{3}F) + \frac{3}{2}\zeta \end{pmatrix},$$
(11.19)

with the energies of the Coulomb interaction obtained from (11.3) and (11.5) as

$$E(^{3}H) = F_{0} - \frac{1}{9}F^{2} - \frac{17}{363}F^{4} - \frac{25}{47157}F^{6},$$

$$E(^{1}G) = F_{0} - \frac{2}{15}F^{2} + \frac{97}{1089}F^{4} + \frac{50}{4719}F^{6},$$

$$E(^{3}F) = F_{0} - \frac{2}{45}F^{2} - \frac{1}{33}F^{4} - \frac{50}{1287}F^{6}.$$
(11.20)

As is evident from the Hamiltonian in (11.19), the spin-orbit operator can be written as

$$\mathbf{L} \cdot \mathbf{S} = L_0 S_0 + \frac{1}{2} (L_+ S_- + L_- S_+), \tag{11.21}$$

where the step-operators L_{\pm} and S_{\mp} mix LS states with $\Delta L = \pm 1$ and $\Delta S = \mp 1$.

11.8.4 Moments for f^2

From the wavefunction coefficients we can work out the expectation value of the different moments.

11.8.4.1 Spin-Orbit Expectation Value

For the LS-coupled states $|{}^3H_4\rangle$, $|{}^1G_4\rangle$, $|{}^3F_4\rangle$, we obtain from (11.19) that $\langle {\bf l}\cdot {\bf s}\rangle = -3, 0, \frac{3}{2}$, respectively. These results can be directly verified using (11.10), which is valid for pure LSJ states.

Substituting the values of the Slater integrals F^k and spin-orbit interaction ζ , and diagonalizing the Hamiltonian, we obtain the wavefunction coefficients in intermediate coupling, and from those we obtain the expectation value $\langle \mathbf{l} \cdot \mathbf{s} \rangle$. The result is shown in Table 11.2 and can be compared with the values for LS and jj-coupled states.

Alternatively, writing the wavefunction in jj-coupled states, we can use the general expression in (11.11). An arbitrary state of the ℓ^2 configuration can be written as

$$\psi(\ell^2) = c_{11}|j_1, j_1\rangle + c_{12}|j_1, j_2\rangle + c_{22}|j_2, j_2\rangle, \tag{11.22}$$

und j							
			$\langle \mathbf{l} \cdot \mathbf{s} \rangle$	$n_{5/2}$	$n_{7/2}$	$\langle L_z \rangle$	$\langle S_z \rangle$
f^2	LS	$ ^3H_4\rangle$	-3	1.71	0.29	-4.8	0.8
		$ ^1G_4 angle$	0	0.86	1.14	-4	0
		$ ^3F_4\rangle$	1.5	0.43	1.57	- 3	-1
	jj	$\left \left(\frac{5}{2},\frac{5}{2}\right)_4\right\rangle$	- 4	2	0	-4.57	0.57
		$\begin{vmatrix} \left(\frac{5}{2}, \frac{5}{2}\right)_4 \right\rangle \\ \left(\frac{5}{2}, \frac{7}{2}\right)_4 \right\rangle$	-0.5	1	1	-3.8	-0.2
		$ (\frac{7}{2},\frac{7}{2})_4\rangle$	3	0	2	-3.43	-0.57
	IC	2 2	-3.88	1.97	0.03	-4.70	0.70
f^5	LS	$ ^{6}H_{5/2}\rangle$	-3	3	2	-4.29	1.79
-	IC	, .	-7.66	4.33	0.67	-3.89	1.38
	jj		-10	5	0	-2.86	0.36

Table 11.2 Expectation values for the spin-orbit interaction and the orbital and spin magnetic moments for the LS-, jj-, and intermediate-coupled (IC) states of the atomic configurations f^2 and f^5

For IC, the Slater integrals for the actinides were reduced to 80% of the Hartree–Fock values. Also given are the occupation numbers $n_{5/2}$ and $n_{7/2}$, which are related to n and $\langle \mathbf{l} \cdot \mathbf{s} \rangle$ by (11.27) and (11.28)

where the wave-function coefficients fulfill the conditions $n_{j_1} = 2c_{11}^2 + c_{12}^2$ and $n_{j_2} = c_{12}^2 + 2c_{22}^2$. For instance, using the expression of $|^3H_4\rangle$ in (11.18) gives $n_{5/2} = 1.714$ and $n_{7/2} = 0.286$, so that with (11.11) we obtain $\langle \mathbf{l} \cdot \mathbf{s} \rangle = -2n_{j_1} + \frac{3}{2}n_{j_2} = -3$.

11.8.4.2 Orbital and Spin Magnetic Moments

To obtain the magnetic moments, we assume here that the magnetic field is infinitely small, so that J is a good quantum number. Furthermore, we take the magnetic ground state at T = 0 as $M_I = -J$.

We write $|LSJM_J\rangle$ as a sum over $|LSM_L, M_S\rangle$ using the Clebsch–Gordan coefficients

$$\langle LSM_LM_S|JM_J\rangle = (-1)^{L-S-M_J}[J]^{\frac{1}{2}} \begin{pmatrix} J & L & S \\ M_J & M_L & M_S \end{pmatrix}.$$
 (11.23)

The nonzero values for $f^2(J=4)$ are listed in Table 11.3. Only if the moments are stretched, that is, L+S=J, the $|LSJM_J\rangle$ state is a single determinant.

The expectation values of the orbital and spin magnetic moment are

$$\langle L_z \rangle \equiv \langle LSJM_J | L_z | LSJM_J \rangle = \sum_{M_L} |\langle LSM_L M_S | JM_J \rangle|^2 M_L, (11.24)$$

$$\langle S_z \rangle \equiv \langle LSJM_J | S_z | LSJM_J \rangle = \sum_{M_S} |\langle LSM_L M_S | JM_J \rangle|^2 M_S.$$
 (11.25)

Table 11.3 Values of nonzero Clebsch–Gordan coefficients $\langle LSM_LM_S|JM_J\rangle$ with $|JM_J\rangle=|4,-4\rangle$

$2S+1L_J$	$\langle LSM_LM_S JM_J\rangle$	Value
$^{3}H_{4}$	$\langle 5, 1, -5, 1 4, -4 \rangle$	$\frac{3}{\sqrt{11}}$
	$\langle 5, 1, -4, 0 4, -4 \rangle$	$-\frac{3}{\sqrt{55}}$
	$\langle 5, 1, -3, -1 4, -4 \rangle$	$\frac{1}{\sqrt{55}}$
1G_4	$\langle 4, 0, -4, 0 4, -4 \rangle$	1
$^{3}F_{4}$	$\langle 3, 1, -3, -1 4, -4 \rangle$	1

The obtained diagonal elements of $\langle L_z \rangle$ and $\langle S_z \rangle$ for the LS-coupled states are given in Table 11.2. Switching to jj-coupled basis states using (11.15) gives

$$\langle L_z \rangle^{(jj)} = \begin{pmatrix} -4.57 - 0.42 & 0 \\ -0.42 & -3.8 & 0.54 \\ 0 & 0.54 & -3.43 \end{pmatrix}, \quad \langle S_z \rangle^{(jj)} = \begin{pmatrix} 0.57 & 0.42 & 0 \\ 0.42 & -0.2 & -0.54 \\ 0 & -0.54 & -0.57 \end{pmatrix}.$$
(11.26)

Obviously, the trace of both $\langle L_z \rangle$ and $\langle S_z \rangle$ is conserved in different coupling schemes. Furthermore, the matrix $\langle L_z \rangle + \langle S_z \rangle = \langle J_z \rangle$ has diagonal elements equal to -4, while nondiagonal elements vanish.

Results for the other f^n configurations can be found in [68], which shows that the type of coupling has an important influence on the values of the moments. In Table 11.2, we reproduce the values of the moments for $f^5(J=5/2)$. If Pu would be ferro- or ferrimagnetic, then $\langle L_z \rangle$ and $\langle S_z \rangle$ could be obtained from X-ray magnetic circular dichroism (XMCD). An alternative is to measure $\langle \mathbf{l} \cdot \mathbf{s} \rangle$, which gives conclusive information about the type of angular coupling in the material. It is clear from Table 11.2 that there is a huge variation in $\langle \mathbf{l} \cdot \mathbf{s} \rangle$ across the three coupling cases. We show in Sect. 11.10 how to extract the expectation value of the spin–orbit interaction from the EELS or XAS branching ratio.

11.9 Spectral Calculations

We briefly mention how the multiplet calculations are performed. Multiplet theory [64] is ideally suited to calculate the core-level spectra for EELS or XAS at the $N_{4,5}$ and $O_{4,5}$ edges. These calculations for the transitions $5f^n \rightarrow d^9 5f^{n+1}$ are performed in the same way as for the $M_{4,5}$ and $N_{4,5}$ absorption edges of the rare earths [70], using only different radial parameters of the spin-orbit and Slater integrals (see Table 11.1). Contrary to band-structure calculations, the multiplet structure is calculated in intermediate coupling, which treats spin-orbit, Coulomb, and exchange interactions on equal footing.

First, the initial and final state wavefunctions are calculated in intermediate coupling using the atomic Hartree–Fock method with relativistic correction [67, 74]. The electric-multipole transition matrix elements are calculated from the initial state

to the final state levels of the specified configurations. At low photon energies below a few kilo electron-volt only electric-dipole transitions play a role. The electric-dipole selection rules from the ground state strongly limit the number of accessible final states, so that compared to the total manifold of final states, the allowed transitions are located within narrow energy regions [70], historically called white lines due to their appearance on photographic plates.

Examples for the $5f^0 \rightarrow d^9 5f^1$ transitions of the actinide $O_{4,5}$, $N_{4,5}$, and $M_{4,5}$ edges, corresponding to the 5d, 4d, and 3d core levels, respectively, as well as numerical results for other f^n configurations can be found in [1].

11.10 Spin-Orbit Interaction and Sum Rule Analysis

The spin-orbit sum rule relates the angular dependent part of the spin-orbit interaction to the EELS or XAS branching ratio, that is, the intensity ratio of the core d spin-orbit split j-manifolds in the $f^n \to d^9 f^{n+1}$ transition. This is discussed in detail in this section and the validity of the sum rules is discussed in the next section.

While the expectation value of the orbital and spin magnetic moments, $\langle L_z \rangle$ and $\langle S_z \rangle$, can only be measured with XMCD, the spin-orbit interaction, $\langle \mathbf{l} \cdot \mathbf{s} \rangle$, can be obtained from the branching ratio of the XAS or EELS spectra.

For the f shell, the number of electrons, n_f , and the expectation value of the angular part of the spin-orbit interaction, $\langle w^{110} \rangle$, is given by

$$n_f = n_{7/2} + n_{5/2}, (11.27)$$

$$\langle w^{110} \rangle \equiv \frac{2}{3} \langle \mathbf{l} \cdot \mathbf{s} \rangle = n_{7/2} - \frac{4}{3} n_{5/2},$$
 (11.28)

where $n_{7/2}$ and $n_{5/2}$ are the electron occupation numbers of the angular-momentum levels j = 7/2 and j = 5/2 of the f shell.

A *sum rule* [68,75–77] relates the expectation value of the angular part of the 5f spin–orbit interaction per hole to the branching ratio, B, of the core d to valence f transitions in EELS or XAS,

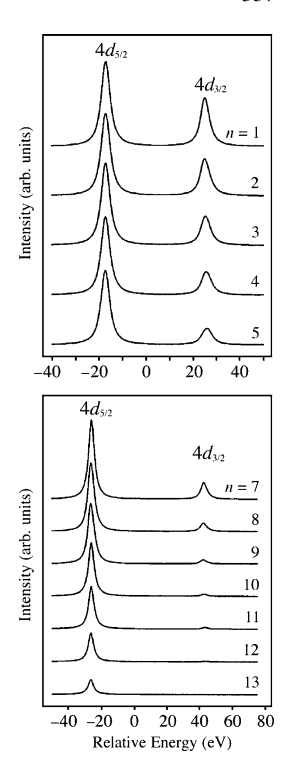
$$\frac{\langle w^{110} \rangle}{14 - n_f} - \Delta = -\frac{5}{2} \left(B - \frac{3}{5} \right), \tag{11.29}$$

where the branching ratio for the $N_{4,5}$ edge is defined as

$$B \equiv \frac{I(N_5)}{I(N_5) + I(N_4)},\tag{11.30}$$

with $I(N_5)$ and $I(N_4)$ the integrated intensities of the N_5 $(4d_{5/2} \rightarrow 5f_{5/2,7/2})$ and N_4 $(4d_{3/2} \rightarrow 5f_{5/2})$ peaks. As the expectation value of w^{110} is for the angular part of the spin-orbit interaction, it does not include the radial part, which

Fig. 11.5 Calculated electric-dipole transitions for the $N_{4.5}$ EELS or XAS spectra using many-electron atomic theory in intermediate coupling for 92 U f^1 to f^5 and 100 Fm f^7 to f^{13} . The convolution by 2 eV corresponds to the intrinsic lifetime broadening. The spectrum for f^6 (not shown) has only a $4d_{5/2}$ peak but no $4d_{3/2}$ peak. From [68]. The calculated spectra show very good agreement with the experimental $N_{4.5}$ spectra in Fig. 11.6, where $n(Th) \approx 1$, $n(U) \approx 3$, $n(Np) \approx 4$, n(Pu) ≈ 5 , $n(Am) \approx 6$, and n(Cm) ≈ 7



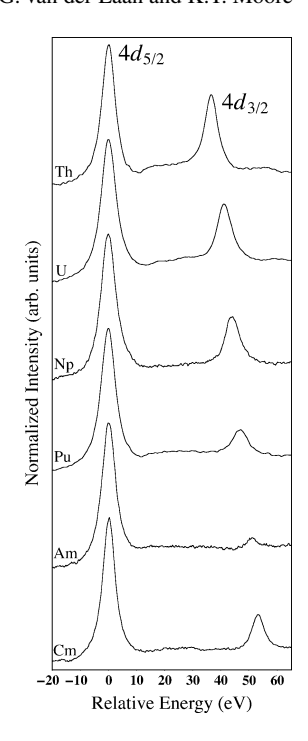
is approximately constant for given element. Therefore, the spin-orbit sum-rule analysis is complementary to, for example, optical spectroscopy, where energy level separations are measured. Thus the sum rule analysis reveals the proper angular-momentum coupling scheme in the material.

Figure 11.5 shows the calculated electric-dipole transitions $4d^{10}5f^n \rightarrow 4d^95$ f^{n+1} for the $N_{4,5}$ EELS or XAS spectra using many-electron atomic theory in intermediate coupling for 92 U $5f^1$ to f^5 and 100 Fm $5f^7$ to f^{13} [68]. The line spectra are convoluted by 2 eV, which corresponds to the intrinsic lifetime broadening. The spectrum for f^6 (not shown) contains only a N_5 peak while the N_4 peak is zero. The calculated results in Fig. 11.5 are in very good agreement with the experimental results shown in Fig. 11.6.

11.11 Validity of the Sum Rule

The sum rule in (11.29) contains a correction term Δ , which can be calculated using Cowan's relativistic Hartree–Fock code [67,74]. In the same way as the spin magnetic moment sum rule in XMCD [69], the sum rule in (11.29) is strictly valid only in the absence of core–valence electrostatic interactions, or so-called jj mixing,

Fig. 11.6 Experimental $N_{4.5}$ EELS spectra for the α -phases of Th, U, Np, Pu, Am, and Cm metal, normalized to the N_5 peak height. It is observed that the intensity of the N_4 (4 $d_{5/2}$) peak gradually decreases in intensity relative to the N_5 $(4d_{3/2})$ peak going from Th to Am, then increases again for Cm. From [4, 5]. The branching ratio of these spectra gives direct information about the expectation value of the 5fspin-orbit interaction in the actinde metal ground state



in which case the correction term Δ becomes zero [2]. In the periodic table, the different transition-metal series show a different behavior due to diverse valenceelectron interaction. For 3d transition metals, the application of the spin-orbit sum rule for the $L_{2,3}$ branching ratio is severely hampered by the large 2p-3d exchange interaction that is of similar size as the 2p spin-orbit interaction [75]. The same is true for the $M_{4,5}$ edges of the lanthanides, where the 3d-4f exchange interaction is quite strong compared to the 3d core spin-orbit interaction [70]. On the other hand, for the $L_{2,3}$ edges of 4d and 5d transition metals, associated with the deep 2p core level, the sum rule is expected to hold quite well [75]. Theoretical values obtained using relativistic atomic Hartree-Fock calculation (Cowan code) in Fig. 11.7 show that the correction factor, Δ , is proportional to the ratio of the core-valence exchange interaction and the core spin-orbit interaction, that is, $G^1(c,\ell)/\zeta_c$. Thus the condition for the sum rule is that the total angular momentum of the core hole, $j = c \pm \frac{1}{2}$, is a good quantum number, in other words, there should be no mixing of the j = 5/2 and j = 3/2 core states. This corresponds to the corevalence exchange interaction much smaller than the core spin-orbit interaction, $G^{1}(c,\ell) \ll \zeta_{c}$ [2].

Even in the worst case of the rare earth $M_{4,5}$ edges, the trend in the branching ratio can still be used to obtain the relative population of spin-orbit split states, as was demonstrated for Ce systems [78]. The situation is favorable for the $M_{4,5}$ and $N_{4,5}$ edges of the actinides, given the small exchange interactions between the 3d and 4d core levels and the 5f valence states. This means that the EELS and

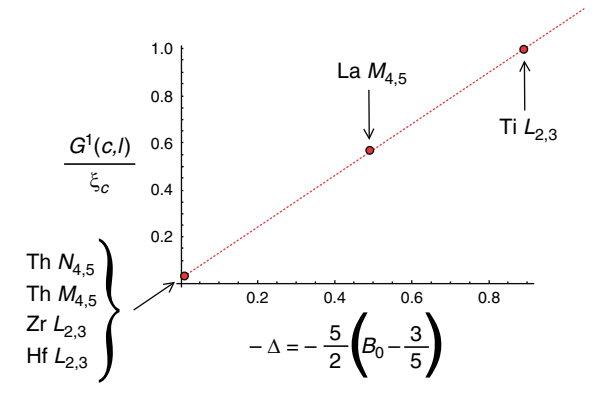


Fig. 11.7 Validity of the spin-orbit sum rule. Theoretical values obtained using relativistic atomic Hartree-Fock calculations show that the correction factor, Δ , in (11.29) is proportional to the ratio of the core-valence exchange interaction and the core spin-orbit interaction, $G^1(c, \ell)/\zeta_c$. The condition for the sum rule is that the total angular momentum of the core level, $j = c \pm \frac{1}{2}$, is a good quantum number, that is, there is no mixing of the j = 5/2 and the j = 3/2 core levels. This means the core-valence exchange interaction should be much smaller than the core spin-orbit interaction $[G^1(c, \ell)] \ll \zeta_c$. Numerical values are given in [2]

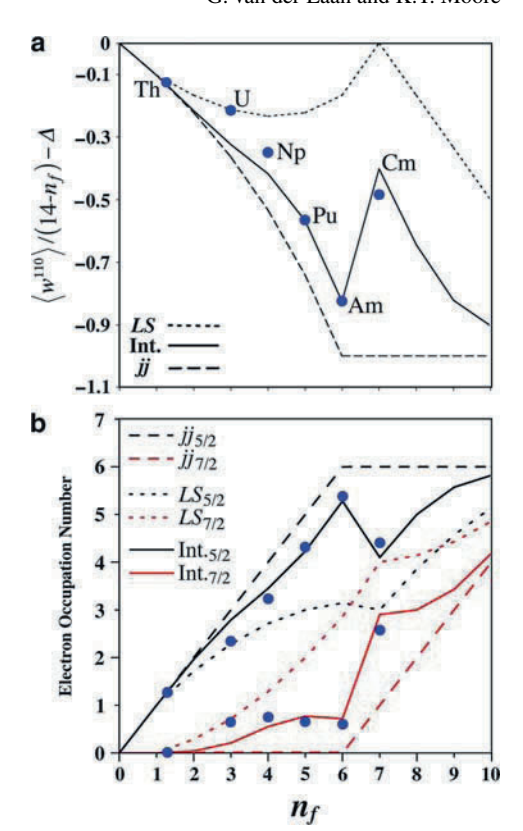
XAS branching ratios depend almost solely on the 5f spin-orbit expectation value per hole, thus affording an unambiguous probe for the 5f spin-orbit interaction in actinide materials.

11.12 Experimental Results for the $N_{4,5}$ Edges

The experimental $N_{4,5}$ ($4d \rightarrow 5f$) EELS spectra for α -phase Th, U, Np, Pu, Am, and Cm metals are displayed in Fig. 11.6. All spectra are normalized to the N_5 peak height. Noticeable is the gradually growing separation between the N_4 and N_5 peaks from Th to Cm, in pace with the increase in 4d spin—orbit splitting with atomic number. Second and more importantly, the intensity of the N_4 ($4d_{5/2}$) peak gradually decreases in intensity relative to the N_5 ($4d_{3/2}$) peak going from Th to Am, then abruptly increases for Cm [4, 5]. Applying the sum-rule analysis to the experimental branching ratio gives the values of the 5f spin—orbit interaction per hole.

To visualize the spin-orbit analysis of the EELS spectra in relation to the results of our atomic calculations, both are shown as a plot of $\langle w^{110} \rangle/(14-n_f) - \Delta$ vs. the number of 5f electrons in Fig. 11.8a. The curves for the three theoretical angular-momentum coupling schemes, LS, jj, and intermediate, as calculated using a many-electron atomic model, are plotted as a short-dashed, long-dashed, and solid line, respectively. The EELS results are indicated by the blue points. Thorium metal falls on all three curves due to the fact that it takes two electrons to tangle,

Fig. 11.8 (a) Ground-state spin-orbit interaction per hole as a function of the number of 5f electrons (n_f) . The three theoretical angular-momentum coupling schemes are shown (LS, ii, and intermediate coupling). The dots give the results of the spin-orbit sum-rule analysis using the experimental $N_{4.5}$ branching ratio of each metal in Fig. 11.6b .The spin-orbit interaction values are converted to the electron occupation numbers $n_{5/2}$ and $n_{7/2}$ of the j = 5/2 and 7/2levels in the 5f state. Shown are the three theoretical coupling schemes (curves for LS, jj, and intermediate coupling) together with the dots representing the experimental EELS results for each metal [4, 5]



and with less than one 5f electron in Th there is no difference between the coupling mechanisms. U falls directly on the LS-coupling curve, Np between the LS and intermediate curve, and Pu, Am, and Cm all fall on or near the intermediate coupling curve. The intermediate curve is strongly shifted towards the jj limit for Pu and Am, evidence of the strong preference of the 5f electrons to occupy the j=5/2 level in both metals. However, for Cm, there is a sudden and pronounced shift in the intermediate coupling curve toward the LS limit.

The values of n_f and $\langle w^{\bar{1}10} \rangle$ can be converted into the electron occupation numbers $n_{7/2}$ and $n_{5/2}$ using (11.27) and (11.28). Note that this is just a different way of presenting the same data. The experimental and theoretical results are displayed in Fig. 11.8b, where the number of electrons in the j=5/2 and j=7/2 levels as calculated in intermediate coupling using the atomic model are drawn with black and red lines, respectively. Again, the experimental EELS results are indicated with blue points. Apart from the slight deviation in the lighter actinides, U and Np, which is caused by delocalization of the 5f states and thus indicates a departure from the atomic model, the EELS results are in excellent agreement with the theoretical curves. Figure 11.8b clearly shows that for the actinide metals up to and including Am, the 5f electrons strongly prefer the $f_{5/2}$ level. However, this

changes in a striking manner at Cm, where not only does the electron occupation sharply increases for the $f_{7/2}$ level, but also *decreases* for the $f_{5/2}$ level.

The physical origin of the abrupt and striking change in the values between Am to Cm can be understood from the angular momentum coupling. In jj coupling, the electrons prefer to be in the $f_{5/2}$ level, which, however, can hold no more than six, so that the maximal energy gain in jj coupling is obtained for Am f^6 , where the $f_{5/2}$ level is full. However, for Cm f^7 at least one electron will be relegated to the $f_{7/2}$ level. The f^7 configuration has the maximal energy stabilization due to the exchange interaction, with parallel spin in the half-filled shell, which can be achieved only in LS coupling. Thus the large changes observed in the electronic and magnetic properties of the actinides at Cm are due to the transition from optimal spin-orbit stabilization for f^6 to optimal exchange stabilization for f^7 . In all cases, spin-orbit and exchange interaction compete with each other, resulting in intermediate coupling; however, increasing the f-count from 6 to 7 shows a clear and pronounced shift in the power balance in favor of the exchange interaction. The effect is in fact so strong that, compared to Am, not one but two electrons are transferred to the $f_{7/2}$ level in Cm (Fig. 11.8b) . Therefore, in Cm metal, the angular-momentum coupling in the 5f states plays a decisive role in the formation of the magnetic moment, with Hund's rule coupling being the key to producing the large spin polarization that dictates the newly found crystal structure of Cm under pressure [4, 79, 80].

11.12.1 What Our Results Mean for Pu Theory

The spin-orbit sum rule suggests an f-count near 5 for Pu, with 5.4 being a reasonable upper limit [3–5]. Further evidence for this f-count comes from Anderson impurity calculations for Pu [81] that explain photoemission results on 1–9 monolayer thin films of Pu metal [16, 82]. The 4f core-level photoemission spectra display a screened and unscreened peak, thereby acting as a ruler for the degree of localization. The results for the f-count are in agreement with the recent DMFT calculations by Shim et al. [83] and Marianetti et al. [84], as well as LDA+U calculations by Shick et al. [85], which explain the three-peak structure in 5fphotoemission and the relatively high electronic specific heat. The absence of experimentally observed magnetic moments in any of the six allotropic phases of Pu metal [8] is thought to be due to Kondo screening and a nonsingle Slater-determinant ground state in these respective models. The lack of local moments δ -Pu has also been recently explained theoretically in terms of electron coherence using dynamic mean-field theory [84]. Using DFT, a model where spin-orbit interactions and orbital polarization are strong but spin polarization is zero has been employed to yield a nonmagnetic configuration of δ-Pu [86]. This has received ancillary support by polarized neutron scattering measurements on single crystal PuCoGa₅, which shows that the orbital moment dominates the magnetization [87]. Recent magnetic susceptibility measurements have shown that local magnetic moments in the order of 0.05 $\mu_{\rm B}$ /atom form in Pu as damage accumulates due to self-irradiation [57].

11.13 Conclusions

The rare-earth metals have localized and atomic-like 4f states across the series, leading to strong magnetic moments. The 5d transition metals are itinerant and band-like, behaving as typical metals with wide bands that strongly participate in bonding. The 5f actinide metals exhibit a behavior similar to the 5d transition metals in the early actinides Th, Pa, U, and Np, but then as the 4f rare earths for the middle actinides Am, Cm, Bk, and Cf. This is directly attributed to a transition from itinerant to localized 5f states that occurs at Pu. This transition can be examined through the $N_{4,5}$ EELS spectra and the spin-orbit sum-rule analysis. The relative N_4 peak intensity reduces up to Am, then increases for Cm in EELS spectra, where the N_4 and N_5 peaks are only marginally broadened by multiplet structure. Across the actinide series, we see the light metals exhibit LS coupling while the middle metals Pu, Am, and Cm exhibit intermediate coupling. It is the transition from LS to intermediate coupling that reveals the transition from itinerant to localized 5f states. This means that the EELS $N_{4,5}$ spectra and spin-orbit sum-rule analysis can be used as a measure of the degree of itinerancy in the actinide 5f states.

The EELS spectra and spin-orbit analysis clearly support that $n_f \approx 5$ and not 6 in Pu and that it falls near intermediate coupling curve. The $5f^5$ configuration with a spin-orbit interaction that adheres to intermediate coupling near the jj limit begs the question of why Pu is not magnetic. Recent advances in band theory have begun to address this question, such as DFT with zero spin polarization but strong spin-orbit and orbital polarization [86], DMFT calculations by Shim et al. [83] and Marianetti et al. [84], and LDA+U calculations by Shick et al. [85]

Americium falls precisely on intermediate coupling curve and has the largest spin-orbit interaction of all actinide metals. The results anchor the f-count for the adjacent actinides and clearly show the metal is nonmagnetic because the $5f^6$ has a ground state J=0. Finally, the results for Cm prove that the spin-orbit sum rule works, showing that the intermediate coupling curve bends back to LS curve. The experimental results [4] show that the angular-momentum coupling mechanism dictates large spin polarization and explain the magnetic stabilization of Cm observed by Heathman et al. [79]

Acknowledgements We thank W. Felsch for his valuable contribution on the Ce comparison. Part of this work was performed under the auspices of the US Department of Energy by Lawrence Livermore National Laboratory.

References

- 1. K.T. Moore, G. van der Laan, Rev. Mod. Phys. 81, 235 (2009)
- 2. G. van der Laan et al., Phys. Rev. Lett. 93, 97401 (2004)
- 3. K.T. Moore et al., Phys. Rev. B 73, 033109 (2006)
- 4. K.T. Moore et al., Phys. Rev. Lett. 98, 236402 (2007)
- 5. K.T. Moore et al., Phys. Rev. B 76, 073105 (2007)

- 6. Challenges in Plutonium Science I and II, vol 26 (Los Alamos Science, Los Alamos, 2000)
- A.M. Boring, J.L. Smith, Challenges in Plutonium Science, vol I (Los Alamos Science, Los Alamos, 2000), p. 91
- 8. J.C. Lashley, A. Lawson, R.J. McQueeney, G.H. Lander, Phys. Rev. B 72, 054416 (2005)
- 9. A.J. Freeman, G.H. Lander (eds.), *Handbook on the Physics and Chemistry of the Actinides* (Elsevier, Amsterdam, 1984)
- 10. R.C. Albers, Nature (London) **410**, 759 (2001)
- 11. H.R. Moser, B. Delley, W.D. Schneider, Y. Baer, Phys. Rev. B 29, 2947 (1984)
- 12. J.R. Naegele, L.E. Cox, J.W. Ward, Inorg. Chem. 139, 327 (1987)
- A.J. Arko et al., in Challenges in Plutonium Science I, vol 26 (Los Alamos Science, Los Alamos, 2000), p. 168
- 14. J.R. Naegele, L. Manes, J.C. Spirlet, W. Müller, Phys. Rev. Lett. 52, 1834 (1984)
- 15. Y. Baer, J.K. Lang, Phys. Rev. B 21, 2060 (1980)
- 16. T. Gouder, L. Havela, F. Wastin, J. Rebizant, Europhys. Lett. 55, 705 (2001)
- S.S. Hecker, in Challenges in Plutonium Science II, vol 26 Los Alamos Science, Los Alamos, 2000), p. 290
- 18. P. Söderlind et al., Nature (London) **374**, 524 (1995)
- O.J. Wick, Plutonium Handbook: A Guide to the Technology (American Nuclear Society, LaGrange Park, IL, 1980)
- 20. J.C. Lashley et al., Phys. Rev. Lett. 91, 205901 (2003)
- 21. P. Javorsky et al., Phys. Rev. Lett. **96**, 156404 (2006)
- 22. D.C. Koskenmaki, J.K.A. Gschneidner, in *Handbook on the Physics and Chemistry of Rare Earths, I*, ed. by J.K.A. Gschneidner, L. Eyring (North-Holland, Amsterdam, 1978), p. 337
- 23. B. Johansson, Philos. Mag. 30, 469 (1974)
- 24. J.W. Allen, R.M. Martin, Phys. Rev. Lett. 49, 1106 (1982)
- 25. M. Lavagna, C. Lacroix, M. Cyrot, Phys. Lett. 90A, 210 (1982)
- 26. L. de' Medici, A. Georges, G. Kotliar, S. Biermann, Phys. Rev. Lett. 95, 066402 (2005)
- 27. A.K. McMahan, K. Held, R.T. Scalettar, Phys. Rev. B 67, 075108 (2003)
- 28. M. Zwölfl et al., Phys. Rev. Lett. 87, 276403 (2001)
- 29. J.-P. Rueff et al., Phys. Rev. Lett. **96**, 237403 (2006)
- 30. M.E. Manley et al., Phys. Rev. B 67, 014103 (2003)
- 31. M.S.S. Brooks, B. Johansson, in *Handbook of Magnetic Materials*, ed. by K.H.J. Buschow (North-Holland, Amsterdam, 1993)
- 32. P. Vajda, in *Handbook on the Physics and Chemistry of Rare Earths*, 20, ed. by K.A. Gschneidner, L. Eyring (Elsevier Science, Amsterdam, 1995), p. 207
- 33. J.N. Huiberts et al., Nature (London) 380, 231 (1996)
- 34. K.K. Ng, F.C. Zhang, V.I. Anisimov, T.M. Rice, Phys. Rev. Lett. 78, 1311 (1997)
- 35. K.K. Ng, F.C. Zhang, V.I. Anisimov, T.M. Rice, Phys. Rev. B 59, 5398 (1999)
- 36. R. Eder, H.F. Pen, G.A. Sawatzky, Phys. Rev. B 56, 10115 (1997)
- 37. M. Arend et al., Phys. Rev. B 59, 3707 (1999)
- 38. R.R. Arons, in *Landolt-Börnstein, New Series, Vol. III/d1*, ed. by H.P.J. Wijn (Springer, New York, 1991)
- 39. S.M. Valone, M.I. Baskes, R.L. Martin, Phys. Rev. B 73, 214209 (2006)
- 40. K.T. Moore, P. Söderlind, A.J. Schwartz, D.E. Laughlin, Phys. Rev. Lett. 96, 206402 (2006)
- 41. S.I. Gorbunov, A.G. Seleznev, Radiochemistry 43, 111 (2001)
- 42. J.L. Smith, E.A. Kmetko, J. Less-Common Met. 90, 83 (1983)
- 43. K.T. Moore et al., Phil. Mag. 84, 1039 (2004)
- 44. P. Söderlind, O. Eriksson, B. Johansson, J.M. Wills, Phys. Rev. B 50, 7291 (1994)
- 45. V.P. Antropov, M. van Schilfgaarde, B.N. Harmon, J. Magn. Magn. Mater. 144, 1355 (1995)
- 46. S.Y. Savrasov, G. Kotliar, Phys. Rev. Lett. 84, 3670 (2000)
- 47. A.L. Kutepov, S.G. Kutepova, J. Phys. Condens. Matter 15, 2607 (2003)
- 48. P. Söderlind, B. Sadigh, Phys. Rev. Lett. 92, 185702 (2004)
- 49. A.J. Arko, M.B. Brodsky, W.J. Nellis, Phys. Rev. B 5, 4564 (1972)
- 50. S.Y. Savrasov, G. Kotliar, E. Abrahams, Nature (London) **410**, 793 (2001)
- 51. R.H. Heffner et al., Phys. Rev. B **73**, 094453 (2006)

- 52. L. Vitos, B. Johansson, J. Kollar, Phys. Rev. B 62, R11957 (2000)
- 53. J.B. Staunton et al., Phys. Rev. B 62, 1075 (2000)
- 54. P. Santini, R. Lémanski, P. Erdòs, Adv. Phys. 48, 537 (1999)
- 55. A.J. Schwartz, M.A. Wall, T.G. Zocco, W.G. Wolfer, Phil. Mag. 85, 479 (2005)
- 56. K.T. Moore, C.R. Krenn, M.A. Wall, A.J. Schwartz, Metall. Mater. Trans. A 38A, 212 (2007)
- 57. S.K. McCall et al., Proc. Natl. Acad. Sci. (U.S.A.) 103, 17179 (2006)
- 58. P. Hirsch et al., Electron Microscopy of Thin Crystals, 2nd edn. (Robert E. Kreiger, FL, 1977)
- 59. L. Reimer, Transmission Electron Microscopy, 4th edn. (Springer, New York, 1997)
- B. Fultz, J.M. Howe, Transmission Electron Microscopy and Diffractometry of Materials, 2nd edn. (Springer, New York, 2001)
- 61. J.M. Zuo, J.C.H. Spence, Electron Microdiffraction (Springer, New York, 1992)
- 62. K.T. Moore, M.A. Wall, A.J. Schwartz, J. Nucl. Mat. 306, 213 (2002)
- 63. K.T. Moore et al., Phys. Rev. B 69, 193104 (2004)
- 64. G. van der Laan, Lect. Notes Phys. 697, 143 (2006)
- 65. G. van der Laan, S.S. Dhesi, E. Dudzik, Phys. Rev. B 61, 12277 (2000)
- E.U. Condon, G.H. Shortley, The Theory of Atomic Spectra (Cambridge University Press, Cambridge, 1963)
- 67. R.D. Cowan, *The Theory of Atomic Structure and Spectra* (University of California Press, Berkeley, CA, 1981)
- 68. G. van der Laan, B.T. Thole, Phys. Rev. B 53, 14458 (1996)
- 69. G. van der Laan, Phys. Rev. B 57, 112 (1998)
- 70. B.T. Thole et al., Phys. Rev. B 32, 5107 (1985)
- 71. B.T. Thole, G. van der Laan, Phys. Rev. B **50**, 11474 (1994)
- 72. F. Cricchio, F. Bultmark, L. Nordström, Phys. Rev. B 78, 100404(R) (2008)
- 73. G. van der Laan, I.W. Kirkman, J. Phys. Condens. Matter 4, 4189 (1992)
- 74. R.D. Cowan, J. Opt. Soc. Am. 58, 808 (1968)
- 75. B.T. Thole, G. van der Laan, Phys. Rev. B 38, 3158 (1988)
- 76. B.T. Thole, G. van der Laan, Phys. Rev. A 38, 1943 (1988)
- 77. G. van der Laan, B.T. Thole, Phys. Rev. Lett. **60**, 1977 (1988)
- 78. G. van der Laan et al., J. Phys. C Solid State Phys. 19, 817 (1986)
- 79. S. Heathman et al., Science **309**, 110 (2005)
- 80. P. Söderlind, K.T. Moore, Scripta Materialia 59, 1259 (2008)
- 81. G. van der Laan (unpublished)
- 82. L. Havela, T. Gouder, F. Wastin, J. Rebizant, Phys. Rev. B 65, 235118 (2002)
- 83. J.H. Shim, K. Haule, G. Kotliar, Europhys. Lett. **85**, 17007 (2009)
- 84. C.A. Marianetti, K. Haule, G. Kotliar, M.J. Fluss, Phys. Rev. Lett. 101, 056403 (2008)
- 85. A.B. Shick et al., Europhys. Lett. 77, 17003 (2007)
- 86. P. Söderlind, Phys. Rev. B 77, 085101 (2008)
- 87. A. Hiess et al., Phys. Rev. Lett. 100, 076403 (2008)

Chapter 12 Magnetic Imaging with X-rays

F. Nolting

Abstract Looking into a magnetic system with X-rays and revealing its secrets by imaging fuels a powerful and beautiful area of research. Magnetic imaging with X-rays allows us to understand and engineer the magnetic properties of thin films, heterostructures, and nanoscale magnets. In this chapter, the underlying concepts of imaging magnetic systems with X-rays are presented, and different microscope techniques are described.

12.1 Introduction

The imaging of magnetic systems is much more than just taking aesthetic pictures, which for sure is part of the beauty of this business. It reveals the microscopic details of the functionality of magnetic systems, enabling the understanding of their behaviors and engineering of their properties [1]. Besides the fascinating physics of these systems, this activity is clearly fueled by the magnetic data storage industry. There are a variety of different techniques to image the domain structure of magnetic systems [2-4], each of which has its own strengths and weaknesses. Using X-rays, a nanoscale heterostructure can be dismantled without destroying it, and one can investigate the function of the different elements (see example in Fig. 12.1 [5]). Over the last decade, magnetic imaging with X-rays has developed into a powerful tool [6, 7] and the spatial resolution has improved by almost two orders of magnitude from about 1 µm [8] down to the 10 nm level [9, 10]. In addition, the diversity of the microscopes has increased and we now have a complementary set of techniques. Up to now, magnetic imaging with X-rays is the domain of soft X-rays (below 2000 eV) as the relevant absorption edges of the 3d metals and the 4f rare earth falls into this energy range. Although magnetic dichroism can be measured in the hard X-ray range (indeed the first measurement was in the hard X-ray range [11]), the dichroism is much smaller so far preventing the use for magnetic imaging.

F. Nolting

Swiss Light Source, Paul Scherrer Institut, 5232 Villigen – PSI, Switzerland e-mail: frithjof.nolting@psi.ch

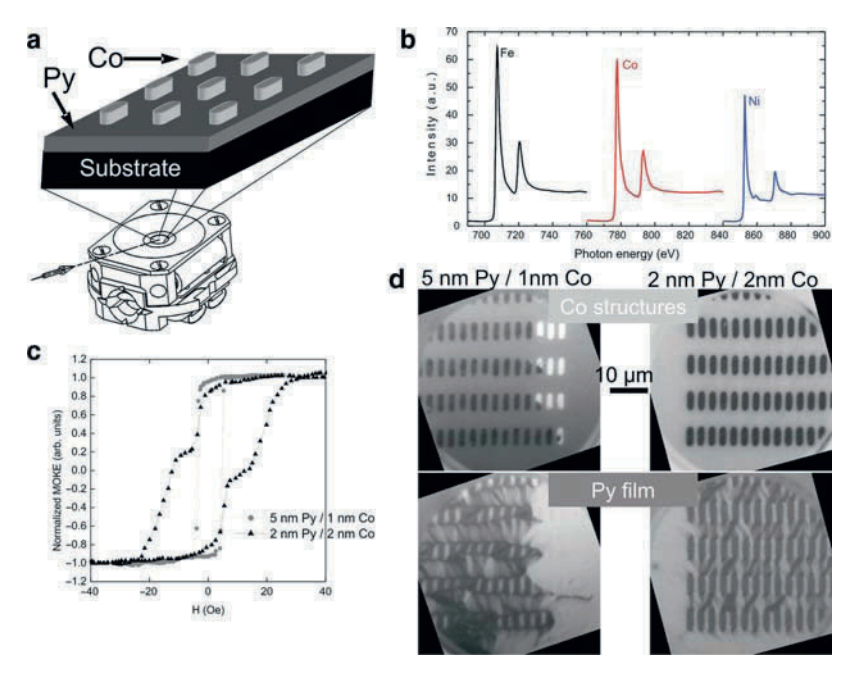


Fig. 12.1 Dismantling a magnetic heterostructure. (a) The heterostructure consists of periodic arrays of elongated $(1.7 \times 5 \,\mu\text{m}^2)$ cobalt (Co) island exchange coupled to a continuous Permalloy (Py = Ni₈₀Fe₂₀) thin film [5]. Changing the thickness from 5 nm Py/1 nm Co to 2 nm Py/2 nm Co, the hysteresis loop changes from a one-step behavior to a double-step behavior (c). Employing the elemental sensitivity of X-ray absorption spectroscopy, the magnetic domain structure in the Py film and in the Co structures can be revealed separately, as the absorption edges of Co and of Fe and Ni for the Py film are well separated (b). The obtained domain images in (d) reveals that in the 5 nm Py/1 nm Co structure, the Py below the Co structure is coupled to the rest of the Py film and the whole structures switches together, leading to the one-step hysteresis. In contrast, in the 2 nm Py/2 nm Co structure, the Py below the Co is decoupled from the rest of the Py film, which switches at a lower magnetic field than the Co/Py sandwich, leading to the double-step hysteresis. From the domain images it can be seen that the presence of Co islands results in a spatial modulation of the magnetic properties of the Py film, and domain walls are positioned at the island boundaries. Imaging the domain structure during the hysteresis loop, two reversal mechanisms could be revealed: formation of domains running between the islands (2 nm Py/2 nm Co) and coherent rotation followed by propagation of large domains (5 nm Py/1 nm Co). For the domain imaging in applied magnetic fields, the sample was mounted in a small magnet (a), which allowed applying magnetic fields up to 50 Oe while still performing domain imaging with a PEEM

The concept of absorption spectroscopy and magnetic dichroism are described in other chapters of this book (see chapter by H. Wende and C. Antoniak). The focus of this chapter is to give an introduction into the basic concept of magnetic imaging, with different types of X-ray-based instruments describing the underlying concepts of the contrast mechanism. In addition, a brief description of the different microscopes for magnetic imaging with X-rays is given: photoemission electron microscope (PEEM), transmission X-ray microscope (TXM), scanning transmission

X-ray microscope (STXM), "lensless" imaging, and combining scanning probe techniques with X-rays. It is not the aim of this chapter to give an overview of the latest results of magnetic imaging or to give a comprehensive introduction into all details of the different techniques. For recent results gained with magnetic imaging with X-rays, see, for example, the contributions from M. Kläui and C. Quitmann in this book.

12.2 Concepts of Magnetic Imaging Contrast

Most magnetic imaging techniques with X-rays are based on X-ray absorption spectroscopy (XAS) either in transmission mode, measuring the transmitted photons, or in total electron yield mode, measuring the generated photoelectrons. Other techniques employed are based on photoemission and diffraction. These variety of techniques offer a wide range of information that can be obtained. For example, going from transmission to total electron yield, the sampling depth goes from about 100 nm down to few nm, changing from probing more the bulk properties to probing surfaces and interfaces.

Common for all these techniques is that the contrast in the images originates from local variations of the X-ray absorption coefficient of the sample, which depends on the X-ray energy and polarization. How this variation of the absorption coefficient is transformed into an image contrast can be illustrated with the help of a sample containing spatially inhomogeneous distributed Fe and Co. On tuning the photon energy to the Fe absorption edge, areas with Fe will strongly absorb while Co rich areas will only weakly absorb. Measured in transmission, this would result in less transmitted photons, for example, a darker image intensity, in the Fe-rich areas compared to the Co-rich areas, which will appear brighter. If instead the total electron yield is measured, the contrast is reversed, for example, more electrons will be emitted by the Fe-rich areas, leading to a brighter image intensity. In this way, the elemental or chemical distributions in a system can be imaged.

To image magnetic domains, the polarization properties of X-ray must be employed. The contrast for imaging domains of ferromagnetic systems arises now from X-ray magnetic circular dichroism (XMCD) and for antiferromagnetic systems from X-ray magnetic linear dichroism (XMLD) [12,13]. For magnetic images, it is essential to select the corresponding photon energy, and to find the right energy, the underlying absorption spectra must be measured. Therefore, most instruments for magnetic imaging with X-rays are able to measure spectra from selected areas to optimize the imaging contrast and also to reveal its origin. In the following, the concepts of the magnetic imaging will be described. Although the examples shown are taken with PEEM, the principle behind the imaging is the same for all magnetic imaging techniques with X-rays. Of course, the technical details and quantitative analysis will vary, but a detailed description is not the aim of this chapter.

12.2.1 XMCD Image

Employing XMCD, ferromagnetic domains can be imaged by tuning the X-ray energy to the $L_{3,2}$ -edges for the 3d transition metals and to the $M_{5,4}$ -edges for the rare earths. The concept of XMCD is explained in the chapter by H. Wende and C. Antoniak. The absorption spectra for different orientations of the magnetization in a Co film with respect to the X-ray polarization vector L are shown in Fig. 12.2a. Tuning the photon energy to the L_3 peak, the domain structure can be imaged as shown in Fig. 12.2b for a 20 nm-thick square Co structure. Dividing two images taken with left and right circular polarized light at the L_3 edge leads to an image with increased magnetic contrast, which we refer to as an XMCD image as contributions to the image that do not depend on the polarization cancel out. Instead of changing the polarization, it is possible to change the energy instead, for example, dividing an image at the L_3 edge with an image at the L_2 edge. In the XMCD image, the intensity is a measure of the angle (α) between the circular X-ray polarization vector (\mathbf{L}) and the magnetic moments (\mathbf{M}) in the domains given by

$$I_{\text{XMCD}} = \mathbf{M} \cdot \mathbf{L} = \langle \mathbf{M} \rangle \cos(\alpha), \tag{12.1}$$

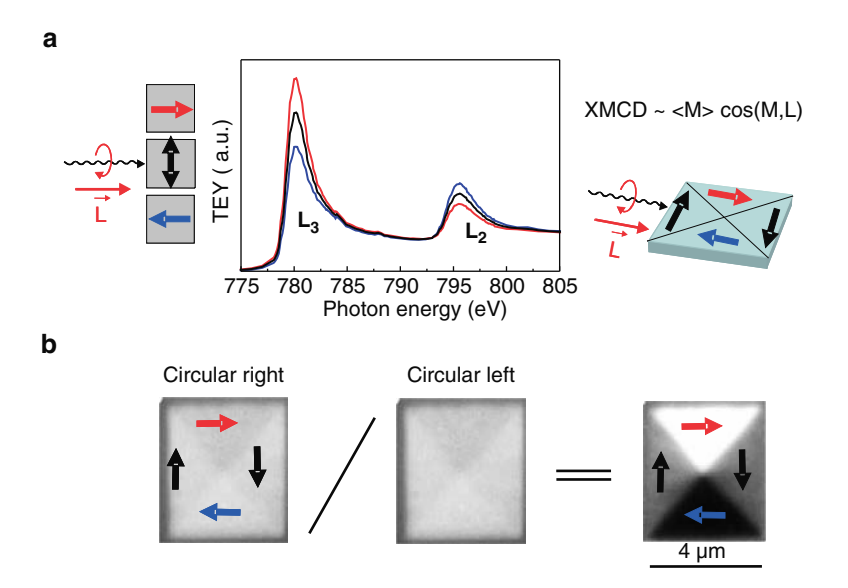


Fig. 12.2 Principle of XMCD images. (a) Spectra of the Co $L_{3,2}$ edge of a ferromagnetic Co film for different orientations of the magnetization relative to the X-ray polarization vector L are shown; parallel, perpendicular, and antiparallel. (b) Images taken at the L_3 edge with circular right and circular left are divided leading to the XMCD image. Nonmagnetic contributions cancel out as they do not depend on the X-ray polarization, and the resulting image contrast is a measure of the relative orientation of the magnetization with respect to the X-ray polarization vector, i.e., the X-ray propagation direction. Shown are images taken with a PEEM of a $4\,\mu$ m square of 20 nm thick Co showing a Landau flux closure domain structure

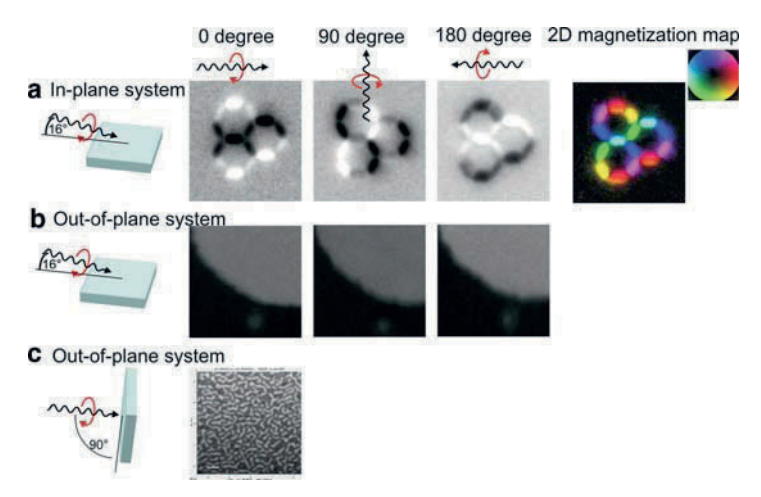


Fig. 12.3 Visualization of in- and out-of-plane domains in XMCD images. (a) In-plane system measured with grazing incident for three orientations of the X-ray direction showing how the contrast of a domain changes from *black* (0°), to *gray* (90°), and to *white* (180°). The resulting two-dimensional magnetization map with corresponding color wheel for the directions is shown on the right. Shown are XMCD images of arrays of dipolar-coupled Co islands arranged in a kagome spin ice configuration [14]. The field of view is 4 μm. (b) Out-of-plane system measured with grazing incident for three orientations of the X-ray direction showing that the contrast is independent on the X-ray direction. The XMCD images are from a 20 nm thick GdCoFe film taken at the Fe L_3 edge with a PEEM and the field of view is 20 μm. (c) Out-of-plane system measured in normal incident with a STXM. The field of view is 5 μm and the typical worm domain structure of a Co/Pt multilayer can be seen [15]

where $\langle \mathbf{M} \rangle$ is the expectation value of the magnetic moment of the probed band, for example, the *d*-band. Ferromagnetic domains with a magnetization parallel or antiparallel to the polarization vector will appear black or white in the XMCD image, while domains with a magnetization perpendicular to the polarization vector will have a gray contrast.

The direction of the magnetization in the gray domains can be revealed after a 90° rotation of the sample about the surface normal and a two-dimensional map of the magnetization can be determined from these two XMCD images, which is shown in Fig. 12.3a (example taken from [14]). For this, care has to be taken that the images have the same magnification, position, distortion, and resolution. To obtain a full three-dimensional magnetization map, a third sample angle is needed, which conveniently is 180°. Actually, any three angles will be sufficient, but at 0°, 90°, and 180°, the contrast changes are largest. Important to note is that the incidence angle of the X-rays must be taken into account. If one has grazing incident geometry, like in PEEM, mainly the in-plane component is measured, while in a normal incidence geometry, the out-of-plane component is measured. If one measures at grazing incidence, in-plane and out-of-plane domains can be distinguished by the 180° rotation

of the sample. While in-plane domains reverse their contrast (Fig. 12.3a), the out-of-plane domains will have the same contrast (Fig. 12.3b). Measuring in a normal incidence geometry, that is, 90° to the surface plane as shown in Fig. 12.3c (example taken from [15]), only the out-of-plane components are measured. While in STXM and TXM, the angle of incidence of the X-rays can be changed, it is fixed for the PEEM. The angle in PEEM is limited by the first lens geometry and is a fixed value, which varies for the different PEEMs between 16° and 30°.

It should be noted that the XMCD image as defined here (i.e., dividing one image by another) is a ratio image. A ratio image has the advantage that it is normalized to the image intensity, hence inhomogeneous sample illumination is corrected [16]. For qualitative information, such as determining the direction of the magnetization or shapes of domains, this is sufficient. However, care must be taken if quantitative information, such as spin and orbital moment [17], is required. Strictly, XMCD is defined as the difference of absorption between circular right (σ^+) and left (σ^-) polarizations and in reality one has to calculate asymmetry images

$$\frac{\sigma^+ - \sigma^-}{\sigma^+ + \sigma^-} \tag{12.2}$$

(see sum rules in the chapter by H. Wende and C. Antoniak). Also dark count rates and varying sensitivity of the imaging device must be correct by corresponding dark and sensitivity images. In practice, for images with a small XMCD contrast compared to the total image intensity, the ratio image is equivalent to the asymmetry image [16], which one can see by performing a mathematical expansion of the XMCD expression.

Another problem arises if one measures in the grazing incident geometry. Here, saturation effects will lead to a modification of the spectra [18, 19], the magnitude of which depends on the X-ray absorption coefficient. As this coefficient varies between circular right and left polarizations, the modification of the amplitude of the L_3 edge will be different for X-rays with opposite helicity. Actually, this is true not only for imaging but also for spectroscopy, which is not spatially resolved! However, often the grazing incident angle in microscopy is smaller than in spectroscopy, which increases the effect.

Even if only qualitative images are required, a healthy mistrust of the final image is good. For example, a shift of the position of the sample between the image taken with circular right and the one with circular left can lead to a black—white contrast artifact in the divided image. It is therefore important to note the contrast reversal of the individual domain in the single images taken with circular right and circular left polarization. In general, it is advisable to prove the magnetic origin of the image contrast, for example, by recording local spectra to check that there is a correct magnetic dichroism, applying magnetic fields to see if the magnetization direction changes or measure the temperature dependence to see if there is a change in the contrast as a transition temperature (Curie or Néel temperature) is approached.

12.2.2 XMLD Images

As XMCD is proportional to the net magnetization, it is not sensitive to antiferromagnetic systems where the net magnetization is zero. Therefore, a technique is needed that is not relying on the net magnetization but probes the spin axis of a sample. Using linearly polarized X-rays, this is possible employing XMLD, which probes the anisotropy of the sample that either originates from the atomic structures, for example, crystal fields or orbital bonds, or magnetism. Here I want to describe how XMLD can be employed for imaging antiferromagnetic systems. The detailed origin of XMLD is described in the chapter by H. Wende and C. Antoniak. In Fig. 12.4a, the dichroism of the Fe $L_{3,2}$ edge of a 20 nm LaFeO₃ film is shown. Actually, the spectra are recorded from individual domains that have antiferromagnetic axes perpendicular to each other [20]. As for the XMCD image, a ratio image is taken to increase the magnetic contribution and to decrease nonmagnetic contributions. As shown in Fig. 12.4b, dividing images taken at two peaks of the multiplet structure at the Fe L_3 absorption edge, that is, at L_{3a} and L_{3b} , an XMLD image is obtained. Areas with different orientations of the antiferromagnetic axis appear with different intensities in the image. As the XMLD contrast is usually weak, it is important to already see low contrast domains in the individual images with reversal of contrast at these two edges.

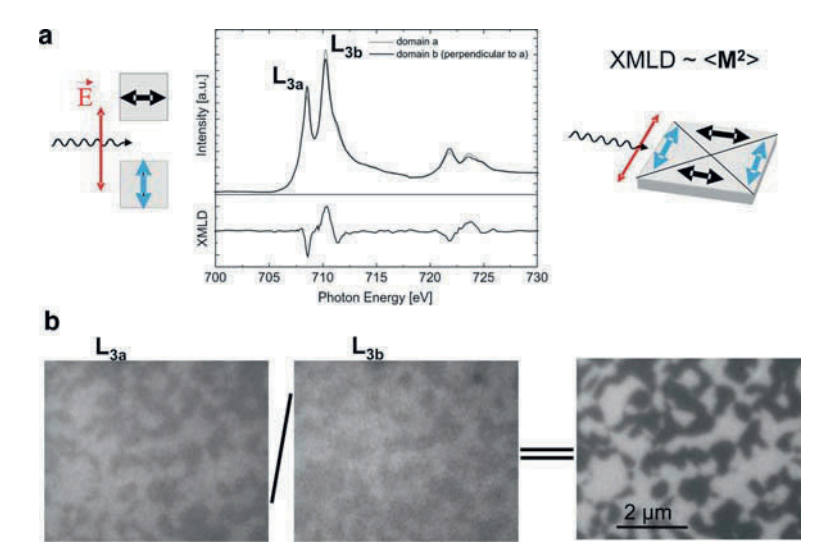


Fig. 12.4 Principle of XMLD images. (a) Fe $L_{(3,2)}$ edge spectra of an antiferromagnetic LaFeO₃ film are shown for parallel and perpendicular orientation of the polarization vector E with respect to the antiferromagnetic spin axis. The spectra are recorded from individual domains [20]. (b) Images taken at the L_{3a} and L_{3b} edge are divided resulting in the XMLD image. The polarization vector is in the plane of the sample and the antiferromagnetic domain structure of the LaFeO₃ film can be seen

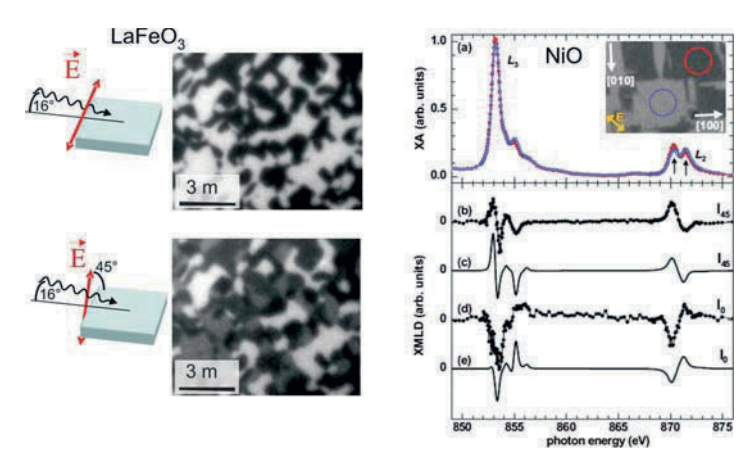


Fig. 12.5 Orientation analysis of XMLD images. (*Left*) Rotating the polarization vector, more contrast scales appear in the XMLD images of the LaFeO₃ thin film [20]. (*Right*) Using the unique fingerprint of the Ni L_3 edge [24], it is possible to determine the orientation of the spin axis of the domains in an antiferromagnetic NiO single crystal [23]. The inset shows the domain structure, and the spectra recorded from individual domains are shown in (a). The $\langle 100 \rangle$ directions of the NiO(001) plane and the orientation of the linear X-ray polarization are indicated in the inset. Comparing the obtained XMLD spectra (b) with multiplet calculations, the orientation could be determined unambiguously (reproduced from [23]). In both examples a PEEM was used for the imaging

Using linearly polarized X-rays with the polarization vector in the plane of the sample, one probes the in-plane component of the system. To be sensitive to the outof-plane component, one can rotate the polarization vector. This is demonstrated in Fig. 12.5 (left) for LaFeO₃. With the polarization vector in the plane of the sample, only two types of intensity appear (black and white), from which one could conclude that only two domain orientations exist. Rotating the polarization vector by 45° reveals actually four intensities, showing that four domain orientations are present [20]. The exact determination of the orientation of these axis turns out to be more complicated. For a long time, a rule of thumb existed, which related the ratio of the multiplet structure peaks with the orientation of the antiferromagnetic axis. This was based on the belief that XMLD is sensitive only to the relative orientation of the magnetization and the polarization vector. However, recently it was discovered that XMLD is sensitive to the relative orientation of the magnetization, the polarization vector, and the crystallographic axis [20–22]. Even the sign of the XMLD can change depending on the orientation of the crystallographic axis, which is shown in Fig. 12.5 (right) where the dichroism of a NiO single crystal is shown [23]. The domain structure of the antiferromagnetic NiO is shown in the inset and the spectra are recorded from individual domains. The XMLD signature depends on whether the polarization vector is oriented along the (110) axis (b) or along the $\langle 100 \rangle$ axis (d). The sign of the XMLD at the L_2 edge simply reverses, while at the

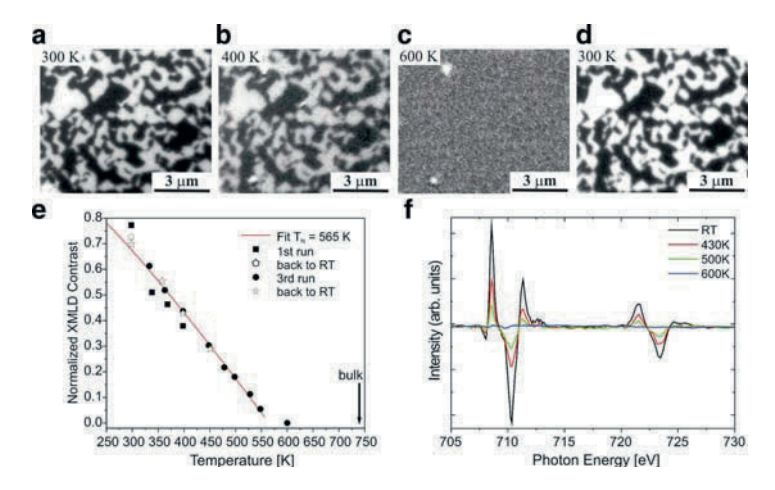


Fig. 12.6 Temperature dependence of the XMLD contrast. (a)–(c) XMLD images of a 20 nm thin LaFeO₃ film with increasing temperature [20] and (d) back to room temperature showing the same domain structure than before. (e) Detailed analysis of the contrast change in the XMLD images from which a reduced Néel temperature compared to the bulk material is obtained. (f) XMLD spectra at different temperatures

 L_3 edge a distinctly different shape of the XMLD is observed, which can be used as a fingerprint to determine the orientation of the domain [24].

For both XMCD and XMLD images, it is critical to be able to show that the observed contrast is of magnetic origin. While for ferromagnetic systems this can often be achieved by changing the magnetization direction of the domains with a magnetic field, this is rather difficult for antiferromagnetic systems, which would require extremely high fields. Instead, this check can be made by comparison with calculations such as the multiplet calculation shown in Fig. 12.5c (right) and 12.5e (right) and with temperature dependent measurements [25]. An example for a detailed temperature-dependent study of a thin film of the antiferromagnetic LaFeO₃ is shown in Fig. 12.6 [20]. In the upper row, XMLD images for different temperatures are shown. It can be seen that while the domain structure is independent of the temperature, the contrast in the images decreases with increasing temperature and disappears above 600 K, see Fig. 12.6c. In Fig. 12.6e, the quantitative image contrast is plotted together with a fit using a mean field approximation to match the $\langle M^2 \rangle$ dependence, indicating a reduced Néel temperature compared to the reported bulk value. In Fig. 12.6f, the XMLD spectra of individual domains at different temperatures are shown. The dichroism decreases without changing its signature, further supporting that the reduction of $\langle M^2 \rangle$ is the reason for the decreasing dichroism and not changes of the orientation of the antiferromagnetic axis or crystal field effects.

12.2.3 Polarization Control

For magnetic imaging with X-rays, it is essential to control the polarization. The time it takes to switch the polarization should be short to minimize possible drifts between the two images. If possible, this time should be comparable to or faster than the time it needs to take an image, which is often in the range of several seconds. The basics of producing polarized X-rays is described in the chapter by D. Cocco. Here I want to point out some nonstandard ways to switch the polarization from circular left to circular right with either an undulator or a bending magnet as source.

The first concept is based on having two apple type undulators shown in Fig. 12.7a. For imaging, a simple solution is to use the fact that the photon energy generated from an undulator has a specific, finite width in the range of a few electron-volt as shown in Fig. 12.7a right. The energy emitted from an undulator depends on the strength of the magnetic field, which in turn depends on the gap between the upper and lower row of magnets. Usually, the monochromator is set to the same energy as the center of the energy distribution of the undulator (tuned). Detuning the undulator [26] by moving now the gap by a few millimeters will shift

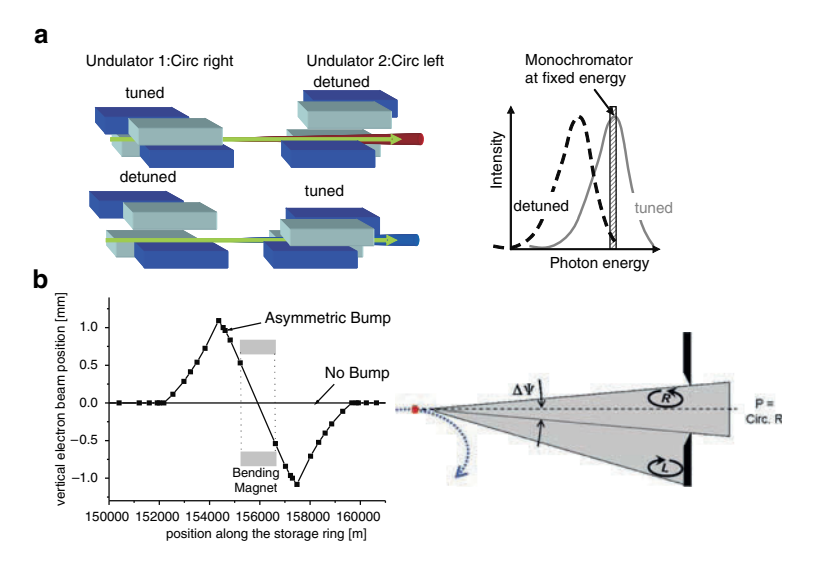


Fig. 12.7 Nonstandard ways for polarization switching. (a) The photon energy generated from an undulator has a specific, finite width in the range of a few electron-volt, which must be tuned to the energy of the monochromator to get photons on the sample. If the energy of the undulator is detuned and does not match the energy of the monochromator, no photons will hit the sample. With two undulators, it is now possible to switch between them by having one tuned and the other detuned as only photons from the tuned undulator will hit the sample, while the photons from the detuned undulator will not pass the monochromator. If now the first undulator is set to circular right polarization and the second to circular left polarization, one can switch the polarization within a few seconds. (b) The polarization from a bending magnet can be changed by tilting the synchrotron. This can be realized by an asymmetric bump of the electron beam in the bending magnet, and now the circular polarized fraction of the produced X-rays is passing the aperture

the center of the emitted photon energy away from the energy of the monochromator, such that nearly no intensity passes the monochromator. Setting one undulator to circular left polarization and the other to circular right polarization, one can switch rapidly between these two undulators having one "tuned" to the energy of the monochromator and the other "detuned" (see Fig. 12.7a left). The switching can be done in a few seconds, which for the imaging is fast enough but also slow enough so that the feedback system of the storage ring can compensate possible variations of the electron beam path. The latter is important as the polarization switching should not affect the X-ray quality at the other beamlines. This schematic in Fig. 12.7a is implemented at the SIM beamline at the SLS.

The second concept is based on a bending magnet as source with control over the electron path in the synchrotron. A bending magnet produces linearly polarized X-rays in the central plane of the synchrotron. The light is circularly polarized above and below this plane. A common way to change the polarization is to use movable apertures between the source and the end station to select the polarization. Another approach is to tilt the synchrotron, for example, to tilt the electron beam in the section of the bending magnet, with the apertures fixed [27]. The principle is sketched in Fig. 12.7b. The tilt of the electron beam is introduced by means of a vertical asymmetric bump produced by four successive dipole correctors (Fig. 12.7b left). In the example, the beam is tilted downwards and circular polarized X-rays are passing the apertures. This set-up is implemented at the PolLux beamline at the SLS and a switching time of about 1 s is achieved [15]. It should be noted that the degree of circular polarization of a bending magnet is in practice between 60 and 80%, in contrast to the undulator where 100% polarization can be reached.

12.2.4 Local Spectra

The possibility to obtain local spectra is a major advantage of magnetic imaging with X-rays as it enables the determination of the origin of the observed contrast in the images. Sometimes it enables to explain why no contrast is observed if, for example, the film is oxidized or contains the wrong elements. In addition, the combination of microscopy and spectroscopy allows studies, which would otherwise not be possible. For example, the study of the orientation of NiO domains [23] in Fig. 12.5 (right) is based on absorption spectra from individual domains. This could not have been done without spatially resolved spectroscopy as one would always average over many domains with different orientations, making it impossible to obtain the pure spectrum. Another example is the spectroscopy of individual nanocrystals [28, 29] and semiconductor dots [30]. Here the signals from individual nanocrystals can be separated in the microscope and their spectra recorded.

To obtain a local spectrum, a series of images for different photon energies is recorded and the image intensity of an area is plotted vs. the photon energy. An example is shown in Fig. 12.8. Here the spectrum of an individual Fe nanoparticle

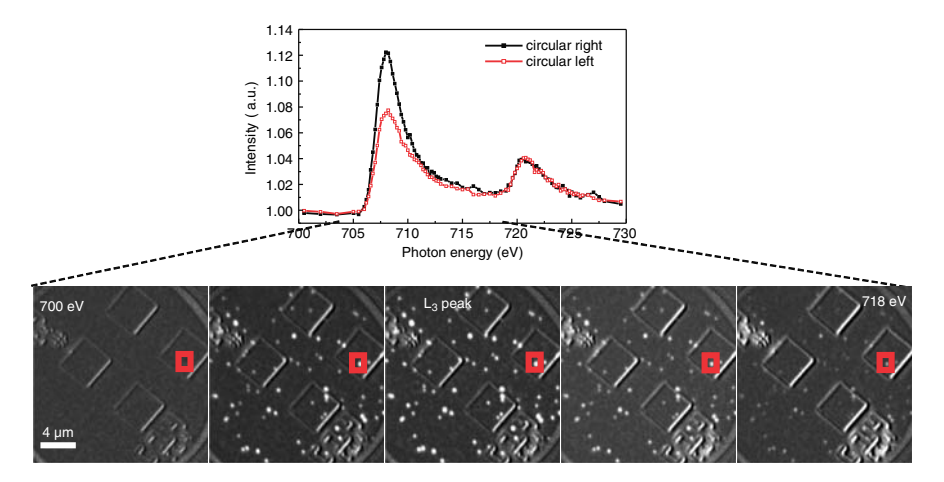


Fig. 12.8 Local spectra. Spectra of an individual 20 nm Fe nanoparticle recorded with a PEEM are shown in the upper part. These spectra were obtained from the selected area (square) of the individual images shown below the spectra taken with opposite helicity. The square structure and numbers in the images where used to identify the particles and perform measurements at the very same spot with a scanning electron microscope (SEM)

of 20 nm size is measured. The series of images is plotted at the bottom of the figure. At the pre-edge, no Fe particles are visible, but with increasing photon energy, the contrast increases at the L_3 edge. The spectra in the upper row are obtained by calculating the image intensity of a selected region, marked with a square, normalized to the area of the region, resulting in an average value of the intensity per pixel for different photon energies. The measurements were performed with circular left and right polarization with a PEEM. Although the particles are smaller than the spatial resolution, their individual spectra can be recorded as their distance is much larger than the spatial resolution.

12.2.5 Spatial Resolution

The spatial resolution is an important benchmark in microscopy, and as with many important benchmark figures, there is some freedom in the usage. Ranging from "we have seen structures that are smaller than x nm," to 10–90%, intensity change in a line scan, Rayleigh criterion, etc. These definitions are good to distinguish two spots, which is sufficient for microscopy, but they do not take into account the crosstalk between these two spots, which is important for local spectroscopy. This will be demonstrated with the help of the Rayleigh criterion, which in its simplest form takes the intensity drop between two particles as criterion [31]. In Fig. 12.9a, the intensity profile of two spots with equal intensity is plotted. To distinguish these two spots in the image, the intensity between the two spots must be 81% of that at

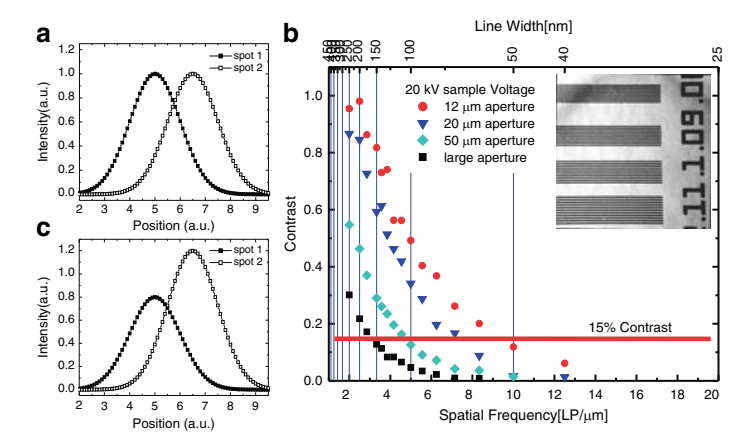


Fig. 12.9 Spatial resolution. (a) Definition of the Rayleigh criterion for two spots with the same intensity and (c) two spots with different intensity. (b) Intensity modulation for different line widths of a test sample measured with a PEEM [32]. Measurements with different aperture sizes are shown demonstrating how the spatial resolution can be improved by reducing the electron energy spread by means of an aperture [34]

the maximum on either side. However, if one wants to extract spectral information from one spot, a significant contribution from the neighboring spot will be measured as the intensity profiles of the two spots overlaps. The effect of this is illustrated in Fig. 12.9b, where the intensity modulation of a stripe pattern with varying period is plotted [32]. A contrast of unity corresponds to a full change of the intensity between the lines, for example, full intensity of the line and full intensity drop between the lines. In the example, one can see that the Rayleigh criterion results in a spatial resolution of about 50 nm for a 12 micrometer aperture. However, a full contrast change, that is, no crosstalk between the spectrum of the line and the spectrum of the area between the lines, is only achieved with a spatial resolution of 150 nm for a 12 µm aperture. Of course, this crosstalk is not important if these spots are from the same material with the same magnetization direction, but already imaging two dots with opposite magnetization will make it difficult to apply the Rayleigh criterion to define the spatial resolution. This is illustrated in Fig. 12.9c. Now, the same spots as in Fig. 12.9a have opposite magnetization and one spot has a higher intensity, while the other has a lower intensity. The intensity profile between these spots is now very different than in Fig. 12.9a and the question is how the spatial resolution would be defined. One should be careful with the given spatial resolution. The definition is only for idealized situations and therefore the value is determined in an idealized situation. Of course, it must be like this to be able to compare instruments, but the practical spatial resolution in a magnetic imaging experiment might be different.

12.3 Realization of the Magnetic Contrast with Different Microscopes

12.3.1 Photoemission Electron Microscope

In a photoemission electron microscope (PEEM), the electrons emitted from the sample on illumination with X-rays are imaged (see [34] for a recent review). A schematic diagram of a PEEM is shown in Fig. 12.10a. The low energy photoelectrons are accelerated by a strong electric field (20 kV) to maintain their local information, and these fast electrons are imaged with an electron microscope (Fig. 12.10c). The image is magnified with a set of lenses. Deflectors and stigmators are used to optimize the electron path through the microscope and to correct for image distortions. In this example, the electrons are detected with a multichannel plate and a phosphor screen and then imaged with a CCD camera. Some PEEMs are equipped with an energy filter, allowing the selection of specific electrons to be used for imaging, which can be employed to change the probing depth of the measurement. The energy distribution of the electrons leaving the sample is sketched in Fig. 12.10b. Using the Auger electrons for imaging only the first monolayers of

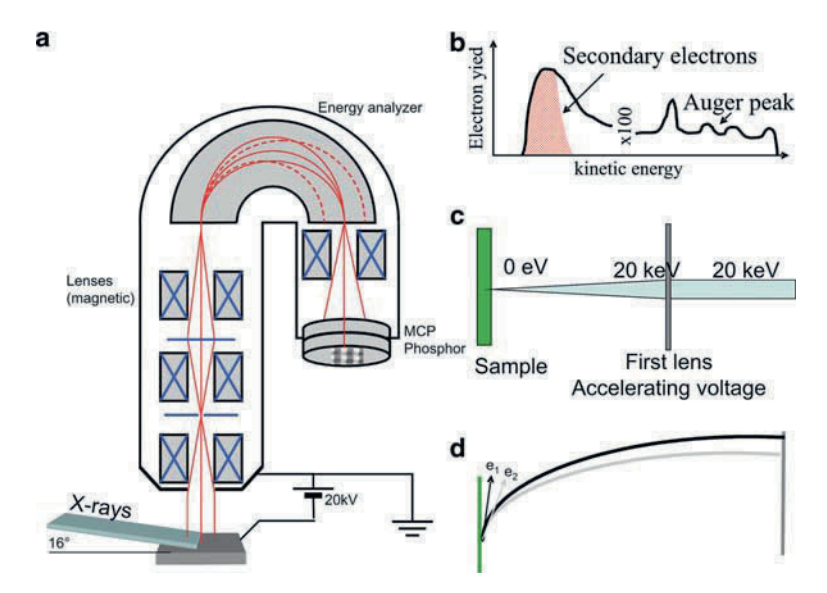


Fig. 12.10 Photoemission electron microscope (PEEM). (a) Sketch of one possible configuration of a PEEM consisting of the sample, accelerating voltage, lenses, energy filter, and detector. (b) Energy distribution of the photoelectrons emitted from the sample. (c) Accelerating of the electrons towards the microscope. As the sample and the microscope form an anode/cathode setup, it is sometimes called a cathode lens. In addition, the term immersion lens is used as the energy of the electron before and after the lens are different. (d) Trajectory of two electrons leaving the sample with different angles

the system are probed as these elastic electrons have a short escape depth. Using the secondary electrons, the probing depth is several nanometers due to the larger escape depth of these inelastic scattered electrons. As the intensity of the secondary electrons is more than 100 times larger than the intensity of the Auger electrons, it is convenient to use the secondary electrons for imaging. However, they also have a wider energy distribution, which is limiting the spatial resolution.

The contributions to the spatial resolution of the PEEM are different to those in STXM/TXM. In the PEEM, the sample is an integral part of the optical system limiting the spatial resolution. This becomes clear on having a closer look at the region between the sample and the microscope. Here the electrons are emitted from the sample with a low energy and are accelerated to about 20 keV. This acceleration is important to keep the information of the spot where the electron has been emitted and that all electron emitted from the same spot are imaged on the same spot at the CCD. This would be impossible to achieve with slow electrons. However, the emitted electrons are slow and move on a parabolic trajectory from the sample to the microscope and the exact path depends on the angle and velocity of the emitted electrons, for example, path of e_1 and e_2 in Fig. 12.10d. Hence, electrons emitted from the very same spot will not appear on the very same spot on the image (which would be the ultimate spatial resolution), but will lead to an increased spot size. The angular- and velocity-variations of the electrons leads to the spherical and angular aberration of the imaging system determining the spatial resolution. This means that a very rough surface will deteriorate the spatial resolution, and also a large energy spread of the electrons will reduce the spatial resolution. The electron energy spread can be reduced using either an aperture [33] (see also Fig. 12.9b) or an energy filter [35] at the expense of intensity. The best spatial resolution reported so far is about 20 nm [36]. New PEEMs are under construction to increase both the spatial resolution to several nanometers and the transmission of the electrons using an aberration correction mirror [37, 38].

Another consequence of the low energy of the emitted electrons is the sensitivity to magnetic fields. To measure in applied magnetic fields, a special sample holder is needed with very small stray fields. Up to now, imaging in applied fields of a few 100 Oe have been achieved [5, 39]. Unfortunately, much larger fields cannot be reached and as an alternative, measurements can be performed at remanence. Imaging in larger magnetic fields is possible only if one takes photons for imaging, which is described in the next section. A further, very important consequence of the low energy of the emitted electrons is the sensitivity to interfaces [13] and the relative freedom in choosing the sample or the substrate of the sample, that is, no transparent substrates such as SiN-membranes are needed.

12.3.2 STXM/TXM

Another approach to measure X-ray absorption is to measure in transmission, for example, to measure the X-rays transmitted through a sample with a photodetector.

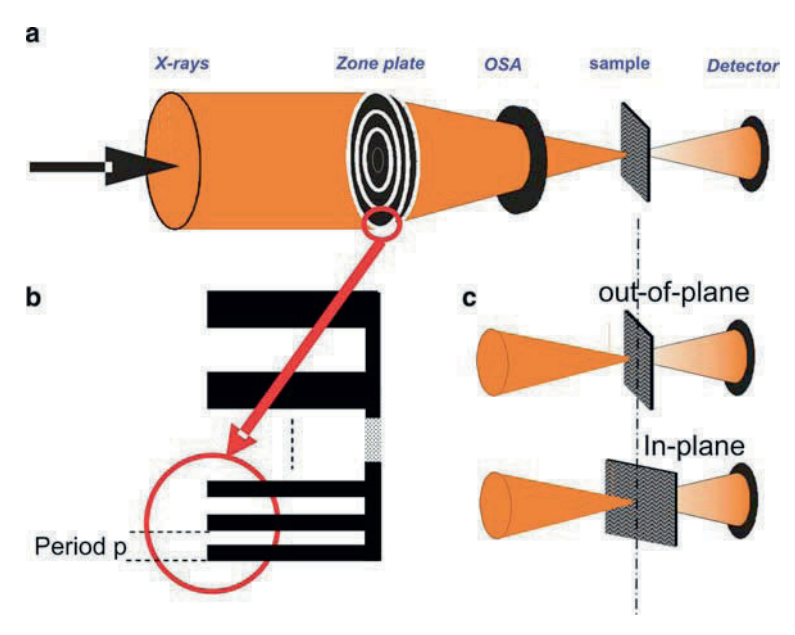


Fig. 12.11 STXM. (a) Arrangement of the Fresnel zone plate, the ordering selecting aperture, sample, and detector. (b) The Fresnel zone plate has a varying period of the lines starting with a larger period in the middle and a smaller period at the outer diameter. The outer width of the zone plate is determining the spots size. (c) Changing from out-of-plane measurement to in-plane measurement by rotating the sample

This can be done in a scanning mode, STXM [40, 41], or full field mode, TXM [42, 43]. Common to both is the use of a Fresnel zone plate (FZP), a diffractive optical element that focuses the X-ray beam.

A schematic for a STXM is shown in Fig. 12.11a. The FZP focuses the soft X-ray light to a diffraction limited spot. The focal length of the FZP depends on the photon energy. Higher diffraction orders are filtered out using an order sorting aperture (OSA), located between the FZP and the sample. The distance between OSA and the sample is typically less than 1 mm, depending on the photon energy. The sample is deposited on a semitransparent SiN-membrane or mounted on a transmission electron microscope grid. Images are formed by raster scanning the sample through the focal point while measuring the transmitted intensity using an X-ray detector. For spectroscopy, the FZP is moved along the X-ray direction to track the energy dependence of the focal length, while the sample position is kept fixed. The sample geometry can be changed from normal incidence for probing the out-of-plane component to grazing incidence for probing the in-plane component by rotating the sample as shown in Fig. 12.11c. This might sound trivial but, as the distances between the FZP, OSA, and sample are very small, down to a few 100 µm, all of the system components must be moved very precisely at the same time. The spatial resolution is given by the spot size of the focused X-rays which in turn is determined by

the outer width of the zone plate (Fig. 12.11b). New developments for the production of these zone plates lead to spatial resolutions down to about 10 nm [10].

For a full-field, transmission X-ray microscope (TXM), the set-up must be changed. Here the X-rays pass first through a condenser lens in front of the sample and than a magnifying micro-FZP behind the sample. The two-dimensional image is recorded with a CCD camera, reducing the image acquisition time. As in the STXM, the spatial resolution is determined by the outer width of the zone plate, and a spatial resolution down to 15 nm has been achieved [9].

Common for both microscopes is the possibility to apply high magnetic fields during the measurement, and magnetic fields of up to 0.7 T have been obtained. The size of the magnetic field is limited here by geometrical restrictions as the distances between the sample and FZP is very narrow. So far, STXM and TXM instruments work under moderate pressure and probe more the bulk properties of the system. Constructions of set-ups to measure in UHV conditions are underway, which will enable to perform surface science experiments. In addition, new developments with the STXM allows measurements in the total electron yield mode and transmission mode in parallel, so that one can obtain information from the surface region and from the bulk region at the same time.

12.3.3 "Lensless" Imaging

The microscopes described above are based on absorption spectroscopy, and the spatial resolution is determined by the optical system of these microscopes. Using diffraction-based imaging without lenses, the spatial resolution would not be limited by the optical system, but ultimately by the wavelength of the X-rays. Conventional diffraction requires periodic scattering objects, such as the crystal structure. This is usually not given in the case of studying magnetic domains, which have an irregular shape, and coherent X-rays must be used. Typical sources for synchrotron radiation produce incoherent X-rays, and only by selectively filtering the coherent fraction can purely coherent radiation be obtained. Using monochromatic X-rays, the longitudinal coherence is obtained and apertures can be employed to achieve transverse coherence. As the efficiency here is very small, experiments relying on coherent Xrays are possible only due to the development of very bright synchrotron sources. With coherent X-rays, the scattering from different domains within the coherence length can interfere, and from the recorded so-called speckle pattern, the domain structure can be calculated. To reconstruct the real space image from the reciprocal space pattern, the phase is needed. However, only the intensity is recorded, which is the square of the amplitude, and the phase is lost. Using phase retrieval algorithms, attempts are being made to reconstruct the image [44,45]. Another approach is based on Fourier transform holography, where a reference beam is used to allow the phase information to be recorded as intensity modulations [46].

The set-up for such an experiment is shown in Fig. 12.12. The monochromatic X-ray beam from an undulator passes through a small pinhole and is incident on

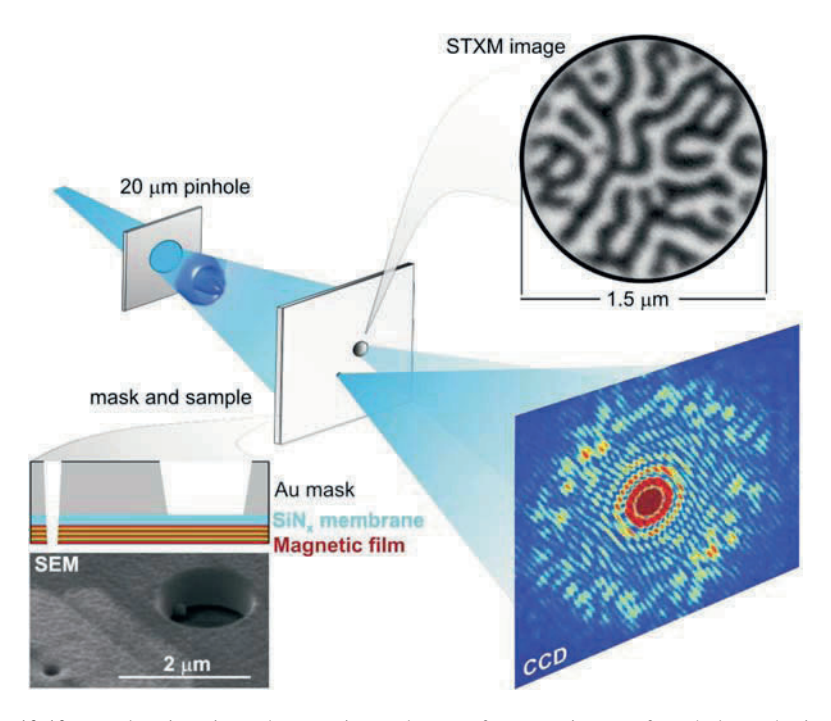


Fig. 12.12 Lensless imaging. The experimental set-up for a Fourier transform holography image using coherent X-rays is shown [46]. The special ingredient is the design of the sample set-up shown in the lower left corner. It consists of a small reference hole and the sample, which is a Co/Pt multilayer on a SiN-membrane. The worm domain structure is shown on the upper right corner (XMCD image taken with a STXM). The resulting interference of the two beams can be recorded with a CCD camera (reproduced from [46])

the sample set-up (sample and mask) which is 723 mm away. The arrangement of pinhole and sample set-up acts as a spatial filter to obtain a coherent fraction of the X-ray beam and a transverse coherence of a few micrometer is typically obtained. The sample set-up consists of two holes: one is 1.5 µm in diameter surrounding the sample to be measured and the other is the reference hole. The sample is a Co/Pt multilayer grown on a SiN-membrane and the X-ray beam is scattered by the outof-plane worm domain structure present in this multilayer. In the upper corner, an XMCD image taken with a STXM is shown. At the detector, the sample beam and the reference beam interfere, and by a Fourier transformation of the scattering intensities, the real space image is obtained. The spatial resolution is determined by the reference beam and is given by the size of the reference hole. In this experiment, the reference hole has a size of 100 nm and a spatial resolution of about 50 nm is achieved. Because of the special design of the sample set-up, this technique is limited in its use as a pure microscope. One can not scan a large sample area and also the intensity of the scattered beam of the sample must be matched to the intensity of the reference beam so that the interference pattern is not dominated by one of

the beams. Its great potential is in the "simplicity" of the set-up. The sample can be positioned in a large vacuum chamber, which allows the addition of various sample environments without any geometrical restrictions. For example, it is in principle possible to apply very large fields of a few teslas and cool the sample down to few kelvins. The other big application of this technique is for time-resolved measurements [47] and for measurements in the future with coherent X-ray free-electron laser sources.

12.3.4 Combining Scanning Probes with X-Rays

On the one hand, the spatial resolution of scanning probe microscopes, such as scanning tunneling microscopy or atomic force microscopy, is superior to that of X-ray microscopes [48]. On the other hand, the elemental and chemical sensitivity of the X-ray microscopes described above is superior to the one of the scanning probe microscopes. The obvious thing to do is to combine both techniques but, this is far from being easy. A first combination of X-ray absorption spectroscopy and scanning tunneling microscopy has been demonstrated [49–51]. In these experiments, X-rays impinge on the same side of the sample as the tip of the scanning tunneling microscope. In Fig. 12.13a, another possible set-up is shown where a conventional STXM consisting of a FZP and OSA is combined with a coaxially insulated cantilever tip behind the sample [52]. The FZP focus the X-ray beam and thus increases the emitted photoelectron density. These emitted photoelectrons are than locally collected with the cantilever tip (Fig. 12.13b). The cantilever tip can be withdrawn so that normal STXM measurements can be performed. Several developments in this direction are ongoing with the aim of spatial resolutions below 10 nm.

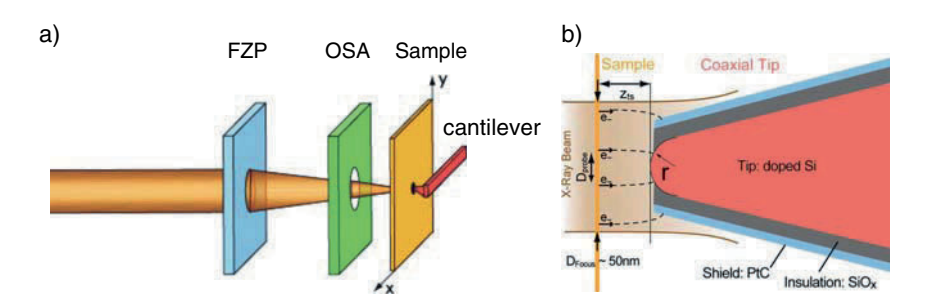


Fig. 12.13 Combining scanning probes with X-rays [52]. (a) A conventional STXM set-up is used to focus the X-rays and a scanning probe cantilever detects the photoelectrons emitted. (b) The cantilever tip has a coaxial insulating, which acts as a lens for the electrons

12.4 Summary

The last decade has seen an impressive development of the X-ray microscopes for magnetic imaging. They offer elemental and chemical sensitivity with high spatial resolution and can rely on powerful magnetic dichroism methods for imaging. A large variety of samples can be measured in different environmental conditions like magnetic fields and different temperatures (150–1,000 K). The instrument best suited for all experiments does not exist. For example, measurements in applied magnetic field are best suited for transmission measurements such as STXM/TXM. However, the samples must be grown on a thin SiN-membrane, which is not suitable for many systems such as single crystals. For these and very thin or diluted systems, the measurement of the emitted photoelectrons in PEEM is better suited. Very low temperatures of a few kelvins will be very difficult to achieve in PEEM and STXM/TXM. For this the lensless imaging approach is ideally suited, but then measurements of larger sample areas or scanning of the sample is not possible. The right technique for the experiment must be chosen, the sample carefully prepared and the complementary information from the different methods obtained. It will be interesting to see the future development of imaging magnetic systems with X-rays and to see what we have achieved when we meet at the next Mittelwihr school on Magnetism and Synchrotron Radiation.

Acknowledgements This tutorial chapter is based on many successful collaborations, which I had have over the years. In particular, the following people are acknowledged with whom I made either the shown experiments, which helped me with figures or useful discussions: L. Heyderman, A. Fraile Rodriguez, S. Czekaj, L. Joly, L. Le Guyader, E. Mengotti, A. Kleibert, C. Quitmann, J. Raabe, I. Schmid, J. Lüning, and A. Scholl.

References

- 1. J. Stöhr, H.C. Siegmann, *Magnetism*, (Springer, Berlin, 2006)
- 2. A. Hubert, R. Schäfer, *Magnetic Domains*, (Springer, Berlin, 1998)
- 3. H. Hopster, E.H.P. Oepen, *Magnetic Microscopy of Nanostructures*, Springer Series in Nanoscience and Technology, (Springer, Berlin, 2005)
- 4. W. Kuch, Magnetic Imaging, Lect. Notes Phys. 697, 275–320 (2006)
- A. Fraile Rodriguez, L.J. Heyderman, F. Nolting, A. Hoffmann, J.E. Pearson, L.M. Doeswijk, M.A.F. van den Boogaart, J. Brugger, Appl. Phys. Lett. 89, 142508 (2006)
- 6. J. Stöhr, S. Anders, T. Stammler, M.R. Scheinfein, Surf. Rev. Lett. 5, 1297 (1998)
- 7. F.U Hillebrecht, J. Phys. Condens. Matter 13, 11163 (2001)
- 8. J. Stöhr, Y. Wu, B.D. Hermsmeier, M.G. Samant, G.R. Harp, S. Koranda, D. Dunham, B.P. Tonner, Science **259**, 660 (1993)
- W. Chao, B.D. Harteneck, J. Alexander Liddle, E.H. Anderson, D.T. Attwood, Nature 435, 1210–1213 (2005)
- K. Jefimovs, J. Vila-Comamala, T. Pilvi, J. Raabe, M. Ritala, C. David, Phys. Rev. Lett. 99, 264801 (2007)
- G. Schütz, W. Wagner, W. Wilhelm, P. Kienle, R. Zeller, R. Frahm, G. Materlik, Phys. Rev. Lett. 58, 737 (1987)

- F. Nolting, A. Scholl, J. Stöhr, J.W. Seo, J. Fompeyrine, H. Siegwart, J.P. Locquet, S. Anders, J. Lüning, E.E. Fullerton, M.F. Toney, M.R. Scheinfein, H.A. Padmore, Nature 405, 767 (2000)
- H. Ohldag, T.J. Regan, J. Stöhr, A. Scholl, F. Nolting, J.Lüning, C. Stamm, S. Anders, R.L. White, Phys. Rev. Lett. 87, 247201 (2001)
- E. Mengotti, L.J. Heyderman, A.F. Rodriguez, A. Bisig, L. Le Guyader, F. Nolting, H.B. Braun, Phys. Rev. B 78, 144402 (2008)
- J. Raabe, G. Tzvetkov, U. Flechsig, M. Böge, A. Jaggi, B. Sarafimov, M.G.C Vernooij, T. Huthwelker, H. Ade, D. Kilcoyne, T. Tyliszczak, R.H Fink, C. Quitmann, Rev. Sci. Instrum. 79, 113704 (2008)
- 16. A. Scholl, H. Ohldag, F. Nolting, J. Stöhr, H.A. Padmore, Rev. Sci. Instrum. 73, 1363 (2002)
- W. Kuch, J. Gilles, F. Offi, S.S. Kang, S. Imada, S. Suga, J. Kirschner, Surf. Sci. 480, 153 (2001)
- T.J. Regan, H. Ohldag, C. Stamm, F. Nolting, J. Lüning, J. Stöhr, R.L. White, Phys. Rev. B 64, 214422 (2001)
- 19. R. Nakajima, J. Stöhr, Y.U. Idzerda, Phys. Rev. B 59, 6421 (1999)
- S. Czekaj, F. Nolting, L.J. Heyderman, P.W. Willmott, G. van der Laan, Phys. Rev B 73, 020401(R) (2006)
- 21. J. Kunes, P.M. Oppeener, Phys. Rev. B 67, 024431 (2003)
- 22. E. Arenholz, G. van der Laan, R.V. Chopdekar, Y. Suzuki, Phys. Rev. B 74, 094407 (2006)
- 23. E. Arenholz, G. van der Laan, F. Nolting, Appl. Phys. Lett. 93, 162506 (2008)
- 24. E. Arenholz, G. van der Laan, R.V. Chopdekar, Y. Suzuki, Phys. Rev. Lett. 98, 197201 (2007)
- A. Scholl, J. Stöhr, J. Lüning, J.W. Seo, J. Fompeyrine, H. Siegwart, J.P. Locquet, F. Nolting, S. Anders, E.E. Fullerton, M.R. Scheinfein, H.A. Padmore, Science 287, 1014 (2000)
- 26. M. Rowen, J.Lüning, Nucl. Instrum. Methods Phys. Res. A 467, 169-172 (2001)
- J.H. Dunn, A. Hahlin, O. Karis, D. Arvanitis, G. LeBlanc, E. Andersson, L.J. Lindgren, Am. Inst. Phys. Conf. Proc. 705, 65 (2004)
- 28. J. Rockenberger, F. Nolting, J. Lüning, J. Hu, A.P. Alivisatos, J. Chem. Phys. 116, 6322 (2002)
- A. Fraile Rodriguez, F. Nolting, J. Bansmann, A. Kleibert, L.J. Heyderman, J. Magn. Magn. Mater. 316, 426 (2007)
- S. Heun, Y. Watanabe, B. Ressel, D. Bottomley, T. Schmidt, K.C. Prince, Phys. Rev. B 63, 125 (2001)
- 31. S. Van aert, Arnold J. den Dekker, D. Van Dyck, A. Van den Bos, in *Science of Microscopy*, The Notion of Resolution, ed. by P.W. Hawkes, J.C.H. Spence (Springer, Hiedelberg, 2007)
- 32. Courtesy of A. Scholl, for details see http://xraysweb.lbl.gov/peem2/webpage/Tools.shtml
- S. Anders, H.A. Padmore, R.M. Duarte, T. Renner, T. Stammler, A. Scholl, H.R. Scheinfein, J. Stöhr, L. Seve, B. Sinkovic, Rev. Sci. Instrum. 70, 3973 (1999)
- 34. A. Locatelli, E. Bauer J. Phys. Condens. Matter **20**, 093002 (2008)
- E. Bauer, C. Koziol , G. Lilienkamp, Th. Schmidt, J. Electron Spectros. Relat. Phenom. 84, 201–209 (1997)
- Th. Schmidt, S. Heun, J. Slezak, J. Diaz, K.C. Prince, G. Lilienkamp, E. Bauer, Surf. Rev. Lett. 5, 1287 (1998)
- J. Feng, E. Forest, A.A. MacDowell, M. Marcus, H. Padmore, S. Raoux, D. Robin, A. Scholl, R. Schlueter, P. Schmid, J. Stöhr, W. Wan, D.H. Wei, Y. Wu, J. Phys. Condens. Matter 17, S1339–S1350 (2005)
- 38. Th. Schmidt, U. Groh, R. Fink, E. Umbach, O. Schaff, W. Engel, B. Richter, H. Kuhlenbeck, R. Schlögl, H.J. Freund, A.M. Bradshaw, D. Preikszas, P. Hartel, R. Spehr, H. Rose, G. Lilienkamp, E. Bauer, G. Benner, Surf. Rev. Lett. 9, 223 (2002)
- 39. Private communication F. Kronast
- 40. J. Kirz, H. Rarback, Rev. Sci. Instrum. 56, 1 (1985)
- A.L.D. Kilcoyne, T. Tyliszczak, W.F. Steele, S. Fakra, P. Hitchcock, K. Franck, E. Anderson, B. Harteneck, E.G. Rightor, G.E. Mitchell, A.P. Hitchcock, L. Yang, T. Warwick, H. Ade, J. Synchrotron Radiat. 10, 125 (2003)
- G. Denbeaux, E. Anderson, W. Chao, T. Eimüller, L. Johnson, M. Köhler, C. Larabell, M. Legros, P. Fischer, A. Pearson, G. Schütz, D. Yager, D. Attwood, Nucl. Instrum. Meth. Phys. Res. A 467, 841 (2001)

- 43. P. Fischer, T. Eimüller, G. Schütz et al., Rev. Sci. Instrum. 72(72), 2322 (2001)
- 44. D. Sayre, Acta Crystallogr. **5**, 60 (1952)
- 45. J.W. Miao, P. Charalambous, J. Kirz, D. Sayre, Nature **400**, 342–344 (1999)
- S. Eisebitt, J. Lüning, W.F. Schlotter, M. Lörgen, O. Hellwig, W. Eberhardt, J. Stöhr, Nature 432, 885 (2004)
- 47. W.F. Schlotter, R. Rick, K. Chen, A. Scherz, J. Stöhr, J. Lüning, S. Eisebitt, Ch. Günther, W. Eberhardt, O. Hellwig, I. McNulty, Appl. Phys. Lett. 89, 163112 (2006)
- 48. M. Bode, Rep. Progr. Phys. 66, 523 (2003)
- T. Eguchi, T. Okuda, T. Matsushima, A. Kataoka, A. Harasawa, K. Akiyama, T. Kinoshita,
 Y. Hasegawac, M. Kawamori, Y. Haruyama, S. Matsui, Appl. Phys. Lett. 89, 243119 (2006)
- A. Saito, J. Maruyama, K. Manabe, K. Kitamoto, K. Takahashi, K. Takami, M. Yabashi, Y. Tanaka, D. Miwa, M. Ishii, Y. Takagi, M. Akai-Kasaya, S. Shin, T. Ishikawa, Y. Kuwaharaa, M. Aonoa, J. Synchrotron. Radiat. 13, 216 (2006)
- 51. V. Rose, J.W. Freeland, K.E. Gray, S.K. Streiffer, Appl. Phys. Lett. 92, 193510 (2008)
- I. Schmid, J. Raabe, C. Quitmann, S. Vranjkovic, H.J. Hug, R.H. Fink, J. Phys. Conference Series 186, 012015 (2009)

Chapter 13

Domain Wall Spin Structures and Dynamics Probed by Synchrotron Techniques

M. Kläui

Abstract Synchrotron-based magnetic imaging techniques have proven to be powerful for the investigation of geometrically confined magnetic domain walls and their dynamics due to the interaction with fields and spin-polarized currents. The application of different high resolution imaging techniques allows one to determine the nanoscale domain wall spin structures, which are comprehensively reviewed. Different domain wall types are observed depending on the materials and the geometries resulting from the interplay of the micromagnetic energy terms. When currents are injected into the nanostructures, the interaction between the spin-polarized charge carriers and the magnetization leads to current-induced domain wall motion due to the spin transfer torque effect, which is studied by direct imaging. Domain wall motion can be induced by field pulses, and imaging with sub-nanosecond time resolution of the domain wall dynamics is presented.

13.1 Introduction

The physics of surfaces, interfaces, and nanostructures has become one of the main areas of research due to the trend in science and technology towards miniaturization of physical systems into the nanoscale. From the scientific viewpoint, such systems pose a whole new set of problems, both theoretical and experimental. Fundamentally, novel properties emerge in magnetic elements as the lateral structure dimensions become comparable to or smaller than certain characteristic length scales, such as spin diffusion length, carrier mean free path, magnetic exchange length, domain wall width, etc. The effects of the governing energy terms determine the interplay between the relevant physical length scales and the sizes of the structured materials.

But not only from a basic physics point of view have magnetic nanostructures moved into the research focus, but they have also been at the heart of a multitude of

M. Kläui

Fachbereich Physik and Zukunftskolleg, Universität Konstanz, 78457 Konstanz, Germany e-mail: Mathias.Klaeui@uni-konstanz.de

devices ranging from sensing applications to data storage. Probably the best known storage device is the magnetic disc drive [1], which was pioneered in the 1950s by IBM with the RAMAC, and since then the storage density has seen a gigantic exponential increase. While hard drives continue to excel in the high capacity market, they entail nonetheless disadvantages, which have led to other memory concepts replacing them for applications, such as lower density mobile storage. One of the key problems is the mechanical motion of the media, which poses reliability questions and can lead to catastrophic failure in the case of mechanical shock. To overcome this problem, novel storage class memory devices have been put forward. In addition to the shift register suggested by Cowburn [2, 3], S.S.P. Parkin of IBM has put forward the idea of the so-called race-track device [4,5], and both approaches are based on nanoscale magnetic wires with domains delineated by domain walls representing the bits.

These domains and domain walls occur when the geometry changes from the bulk to the nanoscale, since then the magnetic properties of ferromagnetic elements start to be governed by the element geometry and not only by the intrinsic materials properties. Such behavior and in particular the magnetization configurations and reversal in small magnetic elements have been reviewed in detail for instance in [6, 7]. Such a strong dependence on the geometry allows one then to tailor the magnetization configuration and spin switching by appropriately engineering the geometry. The magnetization configuration that constitutes the lowest energy state in a small magnetic structure can for instance be set to a multidomain state with domain walls, as the dipolar interaction (stray field) leads to the magnetization being parallel to the element edges. This results in a very reproducible and controllable spatially inhomogeneous magnetization distribution (domain configuration) [6].

Domain walls, which constitute the boundary between domains, have been intensively researched in the past, though with a focus on the domain wall types that occur in the bulk or in continuous films. The most prominent examples are the Bloch and the Néel wall types, which occur in continuous thin films [8–10]. A thorough overview of such domain walls is given in [7]. While previously relatively low resolution imaging has been used to image the wall position, the advent of synchrotron-based techniques has opened up the possibility to image the actual domain wall spin structure on the nanoscale. In addition to imaging the relaxed spin structure, the inherent time-structure of the synchrotron radiation pulses can be used to image the magnetization and in particular domain wall dynamics on the picoseconds timescale.

In this chapter, the imaging of domain walls and related spin structures is reviewed with a view to study field- and current-induced wall dynamics. After a brief introduction to the techniques employed, the actual wall spin structures are discussed and their dependence on the geometry is explained. Then the wall dynamics due to applied fields and injected currents is presented, allowing one to draw conclusions about the underlying physical interaction mechanisms. This chapter gives a broad overview of investigations that have become possible with advanced synchrotron imaging, but for further in-depth information, the reader is referred to the more specialized literature, which is referenced.

13.2 Techniques

For all these investigations, high quality magnetic nanostructures have to be fabricated. The prevailing geometries to study head-to-head domain walls are straight and zigzag wires, U-shaped, L-shaped, and half-ring elements, as well as full rings. Ring elements have proven to be a useful geometry for the investigation of domain walls as due to the high element symmetry, walls can be easily created and positioned by applying an external uniform magnetic field [11, 12]. Ferromagnetic rings can be in the flux closure vortex state or in the onion state, where they exhibit 180° head-to-head and tail-to-tail domain walls [11, 13]. To make sure that the domain walls exhibit the same behavior in straight parts of the structure as in the curved parts, the radius of curvature should be much larger than the width, as otherwise the wall can be pinned by the variation in the geometry [14].

To make the structures, a range of fabrication methods is available and details as well as reviews can be found in [13, 15–17]. In particular, for techniques based on X-ray transmission, the structures have to be defined on membranes, which entails certain complications as discussed in [16].

To study domain walls and their dynamics, different methods are employed. Direct imaging of spin structures can be carried out using scanning probe techniques (magnetic force microscopy (MFM), spin-polarized scanning tunneling microscopy, Scanning hall microscopy, etc.), magneto-optical techniques (MOKE), electron microscopy, and in particular synchrotron-based microscopy techniques. Introductory overviews can be found in [6, 7] and more detailed descriptions of the techniques can be found in various articles in [18]. The techniques used most extensively for the measurements in this review are X-ray magnetic circular dichroism photoemission electron microscopy (XMCD-PEEM) [19, 20], transmission X-ray microscopy (TXM) [21], and scanning transmission X-ray microscopy [22]. Some of these techniques are described in more detail in this book in the Chaps. 12, 14, etc.

13.3 Domain Wall Types and Wall Phase Diagrams

13.3.1 Theory of Head-to-Head Domain Wall Spin Structures

To understand theoretically the domain wall types and their spin structures, we need to briefly consider the energy terms that lead to the wall formation. The wall spin structure is a result of the energy minimization (to be more precise, the minimization of the appropriate thermodynamic potential, which is usually the Landau Free Energy (though often entropy effects are neglected and only the internal energy is considered) [6, 23]). Without any externally applied fields and as we neglect anisotropies, the two important energy terms are the exchange energy, which is at the heart of ferromagnetism, and the stray field energy due to the dipolar interaction of the spins. Qualitatively, this means that if the exchange dominates, the wall

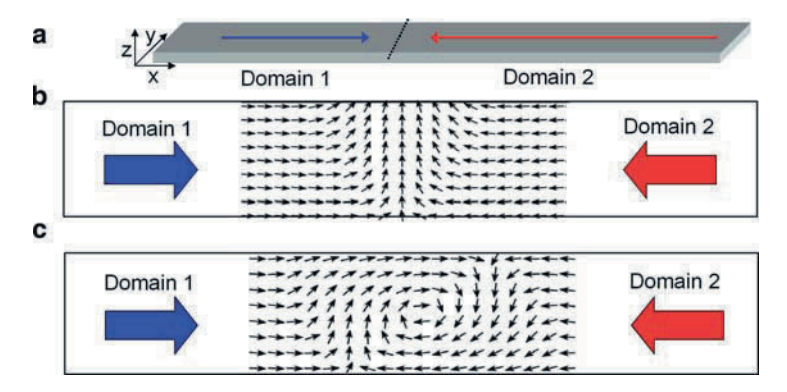


Fig. 13.1 (a) Schematic of a magnetic wire with two domains pointing in opposite directions (*light red and dark blue arrows*) and a domain wall (*dotted line*) separating the domains. The length of the wire is along the x-direction, the width W along the y-direction, and the thickness t along the z-direction. Top view (x-y plane) of the spin structure of a transverse head-to-head domain wall (**b**) and a vortex head-to-head domain wall (**c**)

should be very wide, so that there is only a small angle between adjacent spins, resulting in a small exchange energy. If the stray field energy dominates, the spins try to stay parallel to the structure edge as much as possible, yielding a narrower wall. To go beyond such qualitative considerations, numerical calculations are necessary to ascertain the spin structures that constitute local energy minima (stable wall structures). For the case of domain walls in wires, such micromagnetic simulations [24–26] were carried out by McMichael and Donahue in 1997 [27]. Two wall spin structures were predicted to occur: transverse walls (TW, see Fig. 13.1b) and vortex walls (VW, see Fig. 13.1c). In the case of the transverse wall, the spins rotate in the plane of the structure. To reduce the energy further, the shape of the wall is asymmetric along the y-axis, yielding a V-shaped wall Fig. 13.1(b). The vortex wall exhibits a very different spin structure. Here the spins curl around the vortex core, where the magnetization is pointing out of the plane (Fig. 13.1c) [28–30].

The energies of the two wall types vary with geometry and material and can be calculated from the simulations. More instructive though is an analytical calculation of the energies of the two wall types as a function of geometry, as carried out by McMichael and Donahue [27]. They assumed that as a first approximation, the difference in stray field energies between the two wall types is effectively the stray field of the transverse component in the TW, which is less present in the VW. They calculate this stray field energy difference to be

$$\Delta E_{\text{strayfield}} \approx -\frac{1}{8} \mu_0 M_{\text{s}}^2 t^2 W, \tag{13.1}$$

with M_s the saturation magnetization, t the thickness, and W the width of the structure [27]. For the difference in exchange energies, they assume that it is given by the

vortex in the VW, which yields

$$\Delta E_{\rm ex} = \approx 2\pi t A \ln \frac{r_{\rm max}}{r_{\rm min}},\tag{13.2}$$

with A the exchange constant, t the thickness, r_{max} the outer radius of the vortex, which is assumed to be half the strip width, and r_{min} the inner radius of the vortex, which is given by the vortex core radius δ . From this we can now deduce a "phase diagram" where the energetically favorable wall type is determined as a function of the geometry (width, thickness). In particular, to obtain the phase boundary, which delineates the region where one wall is favored or the other, the sum of the energy differences is set to zero (both wall types have the same energy). Neglecting the weak logarithmic dependence, this yields $Wt \approx const$, with the constant depending on the material. This means that in a width vs. thickness diagram the phase boundary is a hyperbola.

These calculations were later refined by Nakatani and Thiaville [31] and they found, in addition to symmetric transverse walls, tilted transverse walls that constitute the energy minimum in a small range of geometries, and such tilted transverse walls were actually observed experimentally [32].

These micromagnetic simulations were carried out in the 0 K limit, but the influence of thermal excitations on the wall spin structure has also been investigated theoretically. Such simulations are difficult, because a small cell size (ideally an atomistic lattice) is necessary to reproduce a realistic spin wave spectrum. So only few results have been made available, and analytical calculations as well as simulations on small systems have yielded a transition to a linear wall close to the Curie temperature [33, 34].

13.3.2 Experimental Determination of Head-to-Head Domain Wall Spin Structures

13.3.2.1 Spin Structures in Ni₈₀Fe₂₀ (Permalloy)

Here the main properties of head-to-head domain walls are presented, while a more extensive discussion can be found in [14]. To study the domain wall types experimentally [35,36], arrays of 5×5 polycrystalline Co and Permalloy (Ni $_{80}$ Fe $_{20}$) rings with different thicknesses and widths were fabricated as described in [17, 37]. For the investigation of the phase diagram, the edge-to-edge spacing between adjacent rings was more than twice the diameter to prevent dipolar interactions, which might otherwise influence the domain wall type (see [14, 38] for a study of interacting domain walls). To determine the spin structure of the domain walls as a function of ring geometry, the samples were first saturated with an external field, and then after the field is reduced to zero, the resulting domain wall spin structure is imaged using XMCD-PEEM [19].

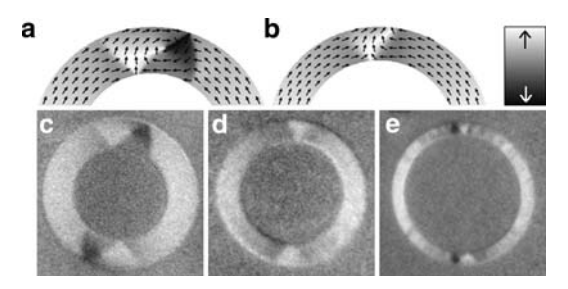


Fig. 13.2 Spin structure of (a) a vortex and (b) a transverse wall simulated using OOMMF. PEEM images of (c) 30 nm thick and 530 nm wide (outer diameter $D=2.7\,\mu\text{m}$), (d) 10 nm thick and 260 nm wide ($D=1.64\,\mu\text{m}$), and (e) 3 nm thick and 730 nm wide ($D=10\,\mu\text{m}$) Permalloy rings in the onion state. The *gray scale* indicates the direction of magnetic contrast (from [36])

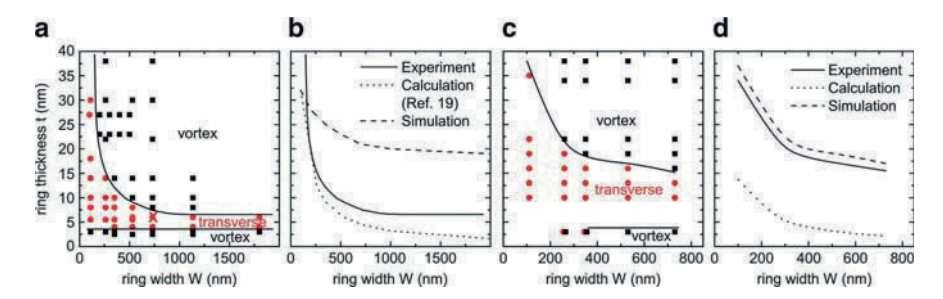


Fig. 13.3 Experimental phase diagrams for head-to-head domain walls in (a) Permalloy and (c) Co rings at room temperature. *Black squares* indicate vortex walls and *red discs* transverse walls. The phase boundaries are shown as *solid lines*. (b, d) Comparison of the upper experimental phase boundary (*solid lines*) with results from calculations (*dotted lines*) and micromagnetic simulations (*dashed lines*). Partly from [35, 36]

In Fig. 13.2, we present PEEM images of (c) a thick and wide Permalloy ring, (d) a thin and narrow ring, and (e) an ultrathin ring measured at room temperature. The contrast of the images is explained in (a) and (b). The domain wall type was systematically determined from PEEM images for more than 50 combinations of ring thickness and width for both Permalloy and Co, and the quantitative phase diagrams shown in Fig. 13.3a,c were extracted (a similar phase diagram was also obtained in [39]). The phase diagrams exhibit two phase boundaries indicated by solid lines between vortex walls (thick and wide rings, squares), transverse walls (thin and narrow rings, discs), and again vortex walls for ultrathin rings.

We discuss first the upper boundary shown in Fig. 13.3a,c. This phase boundary was investigated theoretically by McMichael and Donahue as described earlier [27]. The theoretical phase boundary (dotted lines) is shifted to lower thickness and smaller width compared to the experimental boundary (solid lines in Fig. 13.3b,d). This discrepancy can be understood by taking into account the following: The

calculations [27] compare total energies and therefore determine the wall type with the absolute minimum energy as being favorable. In the experiment, the wall type was investigated after saturation of the ring in a magnetic field and relaxing the field to zero. During relaxation, first a transverse wall is formed reversibly [40]. For the formation of a vortex wall, an energy barrier has to be overcome to nucleate the vortex core, which leads to a hysteretic behavior of the wall formation. So the observed spin structure does not necessarily constitute the absolute minimum energy, but transverse walls can be observed for combinations of thickness and width, where they constitute local energy minima even if the vortex wall has a lower energy for this geometry. Next we have simulated the experiment by calculating the domain wall spin structure after reducing an externally applied field stepwise using the OOMMF code [41] (for Permalloy: $M_s = 800 \times 10^3 \,\mathrm{A}\,\mathrm{m}^{-1}$, $A = 1.3 \times 10^{-11} \,\mathrm{J}\,\mathrm{m}^{-1}$; for Co: $M_s = 1,424 \times 10^3 \,\mathrm{A}\,\mathrm{m}^{-1}$, $A = 3.3 \times 10^{-11} \,\mathrm{J}\,\mathrm{m}^{-1}$; for both: damping constant $\alpha = 0.01$, cell size 2–5 nm). The simulated boundary (dashed line) is shifted to higher thickness and larger width compared to the experiment. This can be attributed to the fact that thermal excitations help to overcome the energy barrier between transverse and vortex walls in case of the room temperature experiment, while they are not taken into account in the T=0 simulation. Thus we can expect that for temperatures above room temperature, the upper experimental phase boundary is shifted to lower thickness and approaches the theoretical phase boundary. In other words, transverse walls formed at room temperature change to vortex walls with rising temperature.

In addition to studying domain wall spin structures in Permalloy and Co, we have also used XMCD-PEEM to image domain walls in amorphous CoFeB [42]. Here we find that due to the reduced saturation magnetization, transverse walls prevail for all the geometries studied (up to 1,500 nm width and 20 nm thickness) [42].

Transverse and vortex walls have also been imaged using TXM [43], and vortex cores have been imaged by STXM [44,45] and electron holography [29] in 3D metal structures with similar geometries to those we discussed here.

13.3.3 Further Head-to-Head Domain Wall Types

The description in the context of the phase diagrams presented here is limited to a certain geometry regime and to soft materials with no or low magnetocrystalline anisotropy. In structures with material-specific anisotropies and in elements that are significantly wider than $\approx 1 \, \mu \, m$, we observe more complicated domain wall spin structures such as distorted transverse walls, and these are discussed in detail in [14, 46, 47].

13.3.3.1 Complex Wall Types in Permalloy

In general, in wider structures, the influence of shape anisotropy is reduced and thus more complicated spin structures can constitute local energy minima and become observable. To classify these wall types, the notion explained in Fig. 13.4 was

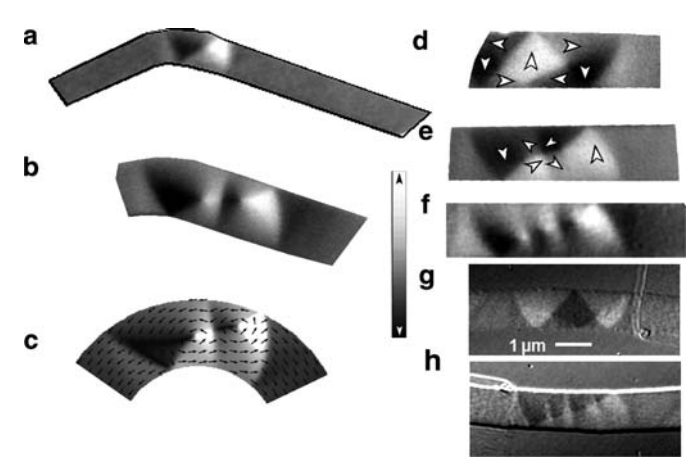


Fig. 13.4 Further domain wall types in a 1 μm wide and 28 nm thick Permalloy wire. The magnetization direction is given by the *gray scale bar*: (a) Single vortex wall (VW type) located next to a kink in the wire; (b) Double vortex wall with two parallel vortices and an antivortex in between (2P type); (c) Micromagnetic simulation of such a 2P wall visualizing the spin structure; (d) Double vortex wall with two antiparallel vortices (2AP type); (e) Extended vortex wall; (f) Triple vortex wall with three parallel vortices and 2 antivortices (3P). In (g) and (h), TXM images of domain walls in 960 nm wide and 80 nm thick permalloy wires are shown. The spin structure of the 2P type in (g) agrees well with the PEEM image in (d), while (h) shows a more complicated wall type. ((a–f) from [49], (g, h) courtesy of G. Meier taken at the XM-1 microscope at the Advanced Light Source in Berkeley)

suggested [48, 49] and will be used here. Apart from the simple single vortex wall (Fig. 13.4a), more complicated wall spin structures including vortices with the same sense of rotation (parallel P) or opposite sense of rotation (antiparallel AP) are found (Figs. 13.4b–f). One of the reasons that such spin structures are stable in very thick structures is the magnetic stray field that is present for single transverse or vortex walls due to magnetic (pseudo-) charges at the edge of the structure as discussed in detail in [48]. Observation of the double vortex wall with antiparallel vortices (2AP) was also reported using MFM [50] and transmission electron microscopy techniques [51]. In Fig. 13.4g, a TXM image of a 2AP wall is shown, and comparison with the XMCD-PEEM image in (d) shows nice agreement (the wall exhibits inverted contrast to that in (d)) [43]. To show that even more complicated spin structures can be stable in thick wires, we present in (h) a domain wall spin structure with an even higher number of (anti-) vortices.

13.3.3.2 Domain Wall Spin Structures in Fe₃O₄ (Magnetite)

The performance of devices based on current-induced domain wall dynamics depends on the spin polarization of the current. This means that it can be enhanced using ferromagnetic materials exhibiting a high degree of spin polarization. Of particular interest are so-called half-metallic ferromagnets, compounds that are metallic

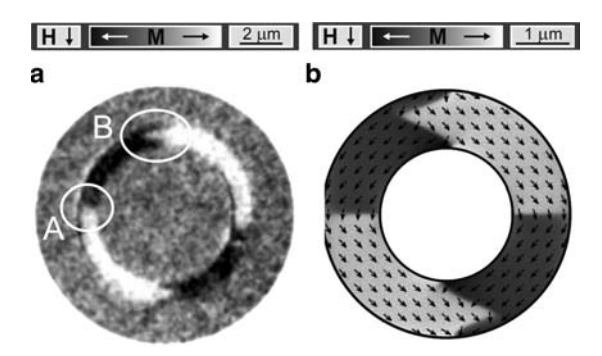


Fig. 13.5 (a) High resolution XMCD-PEEM image of a Fe₃O₄ ring ($D=10\,\mu\text{m}$, nominal width $W=1135\,\text{nm}$) at zero-field. 90° DWs are visible in the image (marked with A). A tail-to-tail zigzag DW (marked with B) as well as a head-to-head zigzag DW at the opposite side of the ring are also present. Black and white contrasts correspond to the magnetization pointing to the left and right, respectively. (b) Simulated magnetization orientation obtained from the micromagnetic calculation for the Fe₃O₄ ring ($D=5\,\mu\text{m}$, $W=1135\,\text{nm}$) in the remanent state after saturation (from [54])

for one spin component while insulating for the other spin component, thus leading to 100% spin polarization at the Fermi energy. In this context, magnetite is a promising material combining a high Curie temperature $T_{\rm C}$ = 851 K with a high spin polarization of up to -80% at room temperature [52].

Another key difference between the soft magnetic permalloy and the magnetite is the fact that magnetite exhibits an intrinsic cubic magnetocrystalline anisotropy [53, 54], while permalloy has no significant magnetocrystalline anisotropy. Furthermore, previously polycrystalline permalloy has been used where all magnetocrystalline anisotropies are averaged out anyway.

After lithographically defining various ring and wire structures in magnetite films (the details of the fabrication process are given in [54]), the spin structure is imaged using XMCD-PEEM. The image in Fig. 13.5 shows that (a) a Fe₃O₄ ring structure ($D = 10 \,\mu\text{m}$, nominal width $W = 1135 \,\text{nm}$) initially magnetized along one of the magnetocrystalline hard axes (the [001] direction) is compared with a simulated magnetization configuration obtained from micromagnetic calculations (b). The black (white) contrast in the XMCD-PEEM image (Fig. 13.5a) reflects the horizontal component of the in-plane magnetization direction pointing to the left (right). The main difference to the magnetization configurations of polycrystalline 3d metal rings is that here the in-plane magnetization deviates from the direction given by the shape of the structure. Instead of following the ring perimeter, the magnetization is divided into four domains. Within each of the domains, the magnetization points along one of the in-plane magnetocrystalline easy axes. In the neighboring segments of the ring, the magnetization vectors are perpendicular to each other, causing two 90° DWs at the right and the left side of the ring (marked with A). The configuration resembles the onion state magnetic configuration observed in 3d metal rings [14].

In this state, the Fe₃O₄ ring structure contains characteristic head-to-head and tail-to-tail DWs, indicated by the change from black to white (and vice versa) at the top and bottom of the ring (the position of the tail-to-tail DW at the top is marked with B). In contrast to the transverse or vortex DWs observed in permalloy, the head-to-head (tail-to-tail) DWs in Fe₃O₄ exhibit a zigzag shape (see, e.g., the tail-to-tail DW marked with B). To understand the remanent magnetic states observed in Fe₃O₄ rings, micromagnetic simulations of the equilibrium state at remanence are performed as shown in (b). The gray scale for the magnetization directions is chosen to be identical with the XMCD-PEEM image contrast in (a). The micromagnetic simulation reproduces the four domain structure measured by XMCD-PEEM extremely well, exhibiting two 90° DWs and two zigzag DWs. The four domain structure is a consequence of the strong fourfold in-plane magnetocrystalline anisotropy of Fe₃O₄(100) films. The magnetocrystalline anisotropy favors alignment of the magnetization along the easy axes, that is, along the in-plane <011> crystallographic directions (diagonal directions in the figure). The formation of the observed zigzag DW structure in epitaxial Fe₃O₄ rings is the result of the energetic compromise between the fourfold magnetocrystalline anisotropy, the exchange, and dipolar coupling. In a ring structure, two neighboring domains meet at 90° due to the strong magnetocrystalline anisotropy and the separating DW develops a characteristic zigzag shape to reduce the magnetic charge density compared to a straight wall, which would have a larger magnetic charge concentration. Thus increasing the zigzag angle, the magnetic charge density decreases at the expense of the wall surface.

13.4 Domain Wall Dynamics

So far we have looked at static domain walls, thus the next step is to look at the dynamics of walls. Two kinds of dynamics will be studied: (1) wall displacements, whereby the wall propagates a distance much larger than its lateral extent, and (2) small scale oscillations of domain walls, where the wall is deflected slightly from its equilibrium and then relaxes back. Both types of dynamics can be excited using magnetic fields or spin-polarized currents.

As this is a very active field of research with many open questions, we only give a brief overview of the field and discuss rather qualitatively the behavior of the wall velocity for a 1D model system and show examples where imaging at synchrotron sources was used. For further information and a more quantitative and detailed discussion for more realistic wall spin structures, the reader is advised to consult the specialized literature that we refer to.

In general, the magnetization dynamics is governed by the Landau–Lifshitz Gilbert equation augmented by spin torque terms [8,55]:

$$\frac{\partial \mathbf{m}(t)}{\partial t} = -\gamma_0 \mathbf{m} \times \mathbf{H}_{\text{eff}} + \alpha \mathbf{m} \times \frac{\partial \mathbf{m}(t)}{\partial t} - \underbrace{(\mathbf{u} \cdot \nabla) \mathbf{m}}_{\text{adiabatic}} + \underbrace{\beta \mathbf{m} \times [(\mathbf{u} \cdot \nabla) \mathbf{m}]}_{\text{non-adiabatic}}, \quad (13.3)$$

with \mathbf{H}_{eff} the effective field, γ_0 the gyromagnetic ratio, α the damping constant, and the effective velocity \mathbf{u} given by $\mathbf{u} = \frac{gP\mu_{\text{B}}}{2eM_{\text{c}}}\mathbf{j}$ (P is the spin polarization, the electron charge e, the saturation magnetization \dot{M}_{s} , the current density j, and the g-factor) [56]. The non-adiabaticity parameter is in one theory [57] given by $\beta = (\lambda_{\text{ex}}/\lambda_{\text{sf}})^2$ (ratio of the exchange length and the spin-flip length), but the theory of the non-adiabaticity is still hotly debated.

The first two terms account for precession and damping, whereas the third term is the adiabatic spin torque term due to the injected current, and the fourth term is called the non-adiabatic spin torque term (even though it can originate from spin relaxation as well as from non-adiabatic transport). As we limit ourselves here to a brief overview, the reader is referred to reviews and more specialized literature [24, 25, 56–58] for an in-depth discussion of the effects of these terms.

13.4.1 Field-induced Domain Wall Propagation

When a field is applied to a system, this tilts the energy potential and so a domain wall will move to a new energetically favorable wall position. If the field is sufficiently high to overcome the local wall pinning, the wall will move to this new equilibrium position. In a smooth wire with no pinning sites, this means that even very small fields move the domain wall. The actual field-induced propagation process was studied in an analytical model by Walker and Schryer [59] for 180° walls with an easy axis. They found that walls should move with a velocity $\mathbf{v} = (\gamma \Delta / \alpha) \cdot \mathbf{H}$, with γ the gyromagnetic ratio, Δ the wall width, and α the damping constant. As the field is increased, the wall deforms (the details depending on the wall type) and at a critical field \mathbf{H}_{Walker} , the so-called Walker breakdown occurs, where the wall spin structure transforms periodically [59]. A very thorough theoretical micromagnetic investigation of the behavior of realistic transverse and vortex head-to-head domain wall spin structures under applied fields was carried out recently [60]. In general, an increase in the velocity up to a Walker field is observed. For higher fields, depending on the geometry and field, different transformations including vortices and antivortices were found to occur, which are described in detail in [60]. Theoretically, the influence of roughness on wall propagation was also investigated and rough wires were found to suppress the vortex nucleation [61].

Experimentally, the field-induced wall motion of head-to-head domain walls was studied by a number of groups using various techniques from magneto-resistive measurements [62, 63] to magneto-optical microscopy [64]. Their experimental results agree well with the theoretical predictions and they can even detect the periodic transformations that set in above the Walker breakdown [63].

13.4.2 Current-induced Domain Wall Propagation

The influence of a current on a domain wall was investigated theoretically some time ago [66], but only recently controlled propagation of single domain walls has

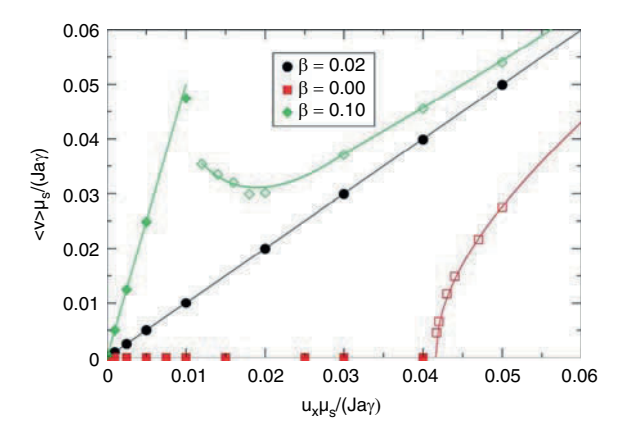


Fig. 13.6 Simulation of the wall velocity as a function of the injected current density j (details of the simulation and the units used, see [65]). The damping constant is $\alpha = 0.02$ and three different values of the non-adiabaticity parameter β are used: $\beta = 0$ (red empty squares), $\beta = 0.02 = \alpha$ (black discs), and $\beta = 0.1$ (light green diamonds). The filled symbols correspond to motion with no domain wall transformation (below the Walker breakdown), while the open symbols signify motion including wall transformations (from [65])

become possible [14, 43, 67–74]. The displacement is due to the transfer of angular momentum (adiabatic spin torque) and linear momentum (spin torque due to non-adiabatic transport and spin relaxation) from the conduction electrons to the domain wall, thus leading to current-induced domain wall motion in the direction of the electron flow [56, 57, 75].

The theoretically expected velocity as a function of current density is depicted in Fig. 13.6 [65]. The behavior depends on the parameter β , which accounts for the torque arising from non-adiabatic transport and spin relaxation that probably dominates for wide domain wall in Permalloy (for details see [56, 57, 65]). For the purely adiabatic case ($\beta=0$, red squares), a high critical current density j_c is observed as predicted by Thiaville [56] and Zhang [57], and the velocity follows a $\sqrt{(j^2-j_c^2)}$ behavior [75] and approaches an effective velocity for large current densities as detailed in [14, 56]. If non-adiabatic transport or spin relaxation exist (non-adiabaticity parameter $\beta\neq 0$), the critical current density is reduced to zero for an ideal wire and the velocity increases at first linearly with current density. For the case that the non-adiabaticity parameter is equal to the damping constant ($\beta=\alpha$, black discs), the velocity increases always linearly and the wall is not deformed. For $\beta\neq 0$ and $\beta\neq \alpha$ (green diamonds), the velocity scales with $\frac{\beta}{\alpha}$ up to a peak at the Walker current density. Above this, wall transformations set in (open symbols in Fig. 13.6) [74].

An example of experimentally observed domain wall displacements is shown in Fig. 13.7. We see in Fig. 13.7a that a vortex head-to-head domain wall and Fig. 13.7b a transverse head-to-head domain wall is displaced by a current pulse with a high current density of $10^{12} \, \mathrm{A \, m^{-2}}$ in the electron flow direction. Dynamic measurements of the velocity have been carried out by Hayashi et al. for the case

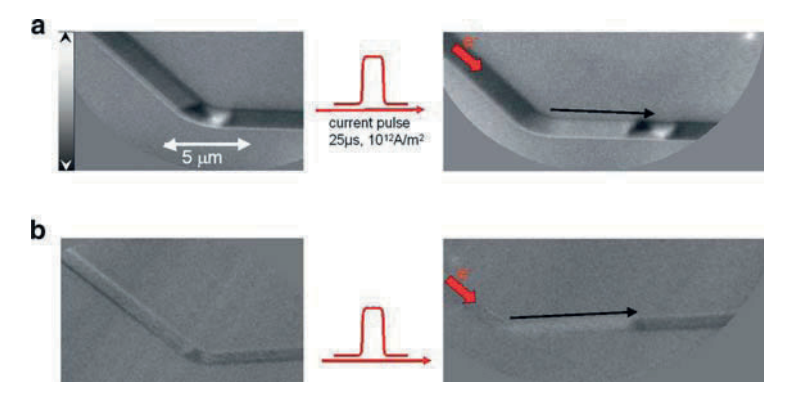


Fig. 13.7 (a) Photoemission electron microscopy images of the displacement of a vortex wall by current injection in a 28 nm thick, 1 μ m wide permalloy wire. The *gray scale bar* shows the magnetic contrast direction for all the images. (b) shows the displacement of a transverse wall in a 7 nm thick and 500 nm wide wire. In both cases, the wall spin structure stays the same after the displacement

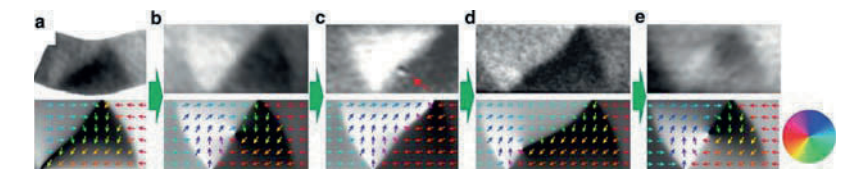


Fig. 13.8 A sequence of XMCD images of current-induced DW transformations. The *bottom* row shows results from a corresponding simulation. (a) Initial TW (vertical contrast). (b) A 25 μ s pulse transforms the TW to a VW. (c) A TW with opposite magnetization is formed after a second pulse. The dark spot close to the DW results from a channel plate defect. (d) The next pulse creates an off-center VW. This intermediate state is direct evidence for the transformation mechanism (from [74])

of a domain wall which is dynamically generated. Here, high velocities exceeding $100 \,\mathrm{m\,s^{-1}}$ have been reported [73]. Starting with a domain wall at rest, slower velocities have been observed for pure current-induced wall motion as seen in Fig. 13.7 [67,69].

As the current density is increased, wall transformations are theoretically predicted above the Walker critical current density if $\beta \neq \alpha$. To observe such transformations, we use a geometry close to the phase boundary where both transverse and vortex walls are stable (1500 nm wide, 8 nm thick) [14, 74]. After generating a transverse domain wall with a field, we switch the field off and we inject 25 μ s long current pulses with a current density of $1 \times 10^{12}~{\rm A~m^{-2}}$. The magnetization is imaged after each injection. In Fig. 13.8, a sequence of images of a DW after consecutive injections is presented. The top row shows the recorded experimental images and the bottom row shows results from a corresponding micromagnetic simulation.

The initial transverse wall in Fig. 13.8a has a dark triangular contrast, indicating that the spins are pointing downwards, as shown in the corresponding simulation.

After the first current pulse, the initial transverse wall is displaced in the direction of the electron flow and transformed to a clockwise vortex wall, Fig. 13.8b. A subsequent pulse injection brings back a transverse wall (Fig. 13.8c) but now with transverse spins pointing upwards corresponding to a white contrast. A next pulse is expected to result again in a vortex wall. However, we observe an intermediate state (Fig. 13.8d), which occurs further on when the vortex wall is on the way transforming back to the original transverse wall (Fig. 13.8a): the vortex core is pushed from the center position towards the bottom edge of the wire and we see it halfway. Normally this state should immediately relax back into a vortex wall, but probably a small material defect stabilizes this off-center vortex wall. This intermediate state is direct evidence for the transformation mechanism suggested by theory if $\beta \neq \alpha$, namely the perpendicular motion and eventual annihilation of the vortex core.

13.4.3 Field- and Current-induced Domain Wall Excitations

So far we have not actually done any real dynamic imaging, as the wall propagation was simply studied by imaging the wall before and after the pulse. This is due to the fact that dynamic measurements at the synchrotron can only be carried out in a pump-probe approach. A pump-probe measurement requires a repeatable measurement though, where the original situation is restored before every pump excitation. For the domain wall motion, this is obviously not the case as the wall after the pulse has been displaced and is thus in a different position. To make use of the time structure of the synchrotron and carry out real dynamic measurements, we need to resort to excitations combined with a restoring mechanism that resets the experiment before each pulse.

An example of an experiment that probes the real dynamics is the pulsed excitation of a pinned domain wall and other confined magnetic structures. Here a constant restoring force is provided either by a constant applied field or by the geometry that acts to keep the wall in a certain pinned position. We then apply a short field-or current-pulse excitation to deflect the wall and watch it relax into the original position.

Current-induced excitations have been difficult to study due to the impedance mismatch for current injection. The magnetic nanostructures usually have resistances far above $50\,\Omega$, which make the injection of ultra-fast current pulses difficult. Furthermore, quite often the contacts are close to the spin structure of interest, and nonhomogeneous current flow in the contact region can lead to Oersted fields, so that the excitation is due to a combination of currents and fields [76–78].

While further experiments of current-induced excitations are under way, we focus here on field-induced excitations, where the interpretation is easier and a more coherent picture of the underlying physics has been formed. Field-induced pulsed and *ac* excitations of various spin structures such as vortices have been imaged using for instance XMCD-PEEM [79, 80] and STXM [44], and here we present details of field-induced domain wall excitations.

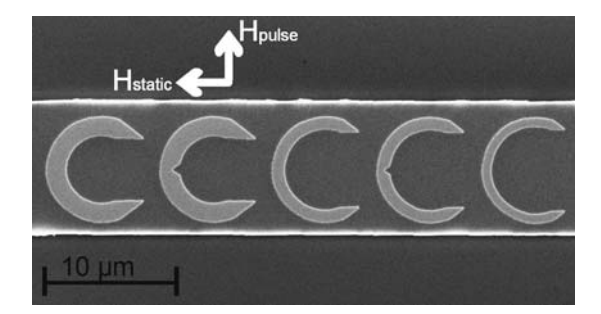


Fig. 13.9 Scanning electron microscopy (SEM) image of the 20 nm thick permalloy structures on a $10 \,\mu$ m wide coplanar waveguide. The direction of the static magnetic field and the pulsed field due to the current in the waveguide are indicated

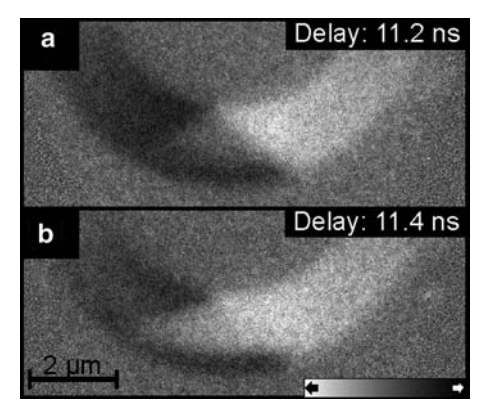


Fig. 13.10 XMCD-PEEM images of the domain wall before the pulse (a) and 200 ps later during the pulse (b). The sub-nanosecond field pulse deflects the domain wall to the left with a very high velocity of more than $1,000\,\mathrm{m\,s^{-1}}$. Note that the image is turned by 90° compared to the SEM image in Fig. 13.9

13.4.3.1 Field-induced Dynamic Wall Deflection

To investigate the domain wall dynamics, we image the wall motion of a wall during a field pulse. The geometry of interest is depicted in Fig. 13.9. A small static field $H_{\rm static}$ of 4 mT is applied to act as a restoring force that tries to keep the domain wall in the center of the structure. Then a field pulse is generated by a short current pulse in the coplanar waveguide underneath the structure. This pulsed field points perpendicularly to the static field and acts to displace the domain wall in the direction of the field. The field pulse has a very short rise time of <150 ps and reaches a maximum of around 3.5 mT. The pulse then decays on a timescale of a few hundred picoseconds.

The resulting deflection of the domain wall is shown in Fig. 13.10. In (a) the wall is in its initial position centered in the structure. As the field pulse is applied, the wall moves towards the left in the direction of the pulsed field. This is reflected

382 M. Kläui

in the increase of the white area where the spins are pointing to the left. The displacement reaches a maximum of about 150 ps after the pulse peak, which indicates that wall motion lags slightly behind the field. The velocity of the wall reaches very high values above $1,000 \, \mathrm{m \, s^{-1}}$, which bodes well for using field-induced wall displacements in applications with fast operating speeds.

We see in Fig. 13.9 that there are also structures with notches. Such structures can be used to study domain wall excitations without a static field, as the pinning is achieved due to the geometry of the notch [14,81]. Further details of such experiments can be found in [82].

13.5 Summary

We have presented an overview of the domain wall spin structures and the dynamics investigated by synchrotron-based techniques. Different techniques allow for high resolution magnetic imaging and by this the nanoscale magnetization configuration is ascertained. Making use of the time structure of the synchrotron radiation, the high frequency dynamics of a domain wall is determined and wall displacements on the picoseconds timescale are imaged.

Acknowledgements Support by the Deutsche Forschungsgemeinschaft through SFB 513, SFB 767, project KL1811, the Landesstiftung Baden-Württemberg, the EPSRC (U. K.), the Samsung Advanced Institute of Technology, and the EU through the European Regional Development Fund (Interreg III A Program), the Marie Curie Research Training Network SPINSWITCH (MRTN-CT-2006-035327) as well as the European Research Council (Starting Independent Researcher Grant ERC-2007-StG 208162) is greatly acknowledged. A large number of PhD students, postdocs, and colleagues have contributed to the various aspects of this work and all the support, help, and encouragement is gratefully acknowledged. Continuous support by the late J. A. C. Bland and U. Rüdiger was crucial to the success of the work at many stages.

References

- 1. I.R. McFadyen, E.E. Fullerton, M.J. Carey, MRS Bull. 31, 379 (2006)
- 2. R. Cowburn, D. Petit, D. Read, O. Petracic, Patent WO 2007/132174A1, 2007
- 3. D. Ilgaz, et al., Appl. Phys. Lett. 93, 132503 (2008)
- 4. S.S.P. Parkin, US patent 6,834,005 and patent application 10/984,055, 2004
- 5. S.S.P. Parkin et al., Science **320**, 190 (2008)
- M. Kläui, C.A.F. Vaz, in Handbook of Magnetism and Advanced Magnetic Materials, Vol. 2, ed. by H. Kronmüller, S.S.P. Parkin (John Wiley and Sons, Chichester, 2007)
- 7. A. Hubert, R. Schäfer, Magnetic Domains The Analysis of Magnetic Microstructures (Springer, Berlin, 1998)
- 8. L.D. Landau, E. Lifshitz, Phys. Z. Sowjetunion **8**, 153 (1935)
- L. Néel, Comptes Rendus hebdomadaires des Séances de l'Académie des Sciences 249, 533 (1955)
- 10. F. Bloch, Z. Phys. A 74, 295 (1932)
- 11. J. Rothman, et al., Phys. Rev. Lett. 86, 1098 (2001)

- 12. S.P. Li, et al., Phys. Rev. Lett. 86, 1102 (2001)
- 13. M. Kläui, C.A.F. Vaz, L. Lopez-Diaz, J.A.C. Bland, J. Phys. Cond. Matter 15, R985 (2003)
- 14. M. Kläui, J. Phys. Condens. Matter 20, 313001 (2008)
- 15. J.I. Martin, et al., J. Magn. Magn. Mater. **256**, 449 (2002)
- D. Backes, et al., Microelectron. Eng. 83, 1726 (2006)
- 17. L.J. Heyderman, et al., J. Appl. Phys. 93, 10011 (2003)
- 18. H. Kronmüller, S.S.P. Parkin, (eds.), *Handbook of Magnetism and Advanced Magnetic Materials*, Vol. 3 (John Wiley and Sons, Chichester, 2007)
- 19. J. Stöhr, et al., Science 259, 658 (1993)
- 20. J. Stöhr, S. Anders, IBM J. Res. Dev. 44, 535 (2000)
- 21. P. Fischer, Curr. Opin. Solid State Mater. Sci. 7, 173 (2003)
- 22. A.L.D. Kilcoyne, et al., J. Synchrotron Radiat. 10, 125 (2003)
- H. Kronmüller, M. Fähnle, Micromagnetism and the Microstructure of Ferromagnetic Solids, (Cambridge University Press, Cambridge, 2003)
- J. Miltat, M.J. Donahue, in *Handbook of Magnetism and Advanced Magnetic Materials*, Vol. 2, ed. by H. Kronmüller, S.S.P. Parkin (John Wiley and Sons, Chichester, 2007)
- 25. T. Schrefl, et al., in *Handbook of Magnetism and Advanced Magnetic Materials*, Vol. 2, ed. by H. Kronmüller, S.S.P. Parkin (John Wiley and Sons, Chichester, 2007)
- A. Thiaville, Y. Nakatani, in *Spin Dynamics in Confined Magnetic Structures III*, ed. by B. Hillebrands, K. Ounadjela (Springer, Berlin, 2006)
- 27. R.D. McMichael, M.J. Donahue, IEEE Trans. Magn. 33, 4167 (1997)
- 28. A. Wachowiak, et al., Science 298, 577 (2002)
- 29. F. JungiOnger, et al., Appl. Phys. Lett. 92, 112502 (2008)
- 30. E. Feldtkeller, et al., Phys. Condens. Mater. 4, 8 (1965)
- 31. Y. Nakatani, A. Thiaville, J. Miltat, J. Magn. Magn. Mater. 290-291, 750 (2005)
- 32. D. Backes, et al., Appl. Phys. Lett. 91, 112502, (2007)
- 33. N. Kazantseva, R. Wieser, U. Nowak, Phys. Rev. Lett. 94, 037206 (2005)
- 34. L.N. Bulaevskii, V.L. Ginzburg, Sov. Phys. JETP 18, 530 (1964)
- 35. M. Kläui, et al., Appl. Phys. Lett. 85, 5637 (2004)
- 36. M. Laufenberg, et al., Appl. Phys. Lett. 88, 052507 (2006)
- 37. Y.G. Yoo, et al., Appl. Phys. Lett. 82, 2470 (2003)
- 38. M. Laufenberg, et al., Appl. Phys. Lett. 88, 212510 (2006)
- 39. T.J. Bromwich, et al., J. Appl. Phys. 99, 08H304 (2006)
- 40. M. Kläui, et al., Physica B 343, 343 (2004)
- 41. The OOMMF package is available at http://math.nist.gov/oommf.
- 42. L. Heyne, et al., J. Appl. Phys. 103, 07D928 (2008)
- 43. G. Meier, et al., Phys. Rev. Lett. 98, 187202 (2007)
- 44. B. van Waeyenberge, et al., Nature 444, 461 (2006)
- 45. K.W. Chou, et al., Appl. Phys. Lett. 90, 202505 (2007)
- 46. C.A.F. Vaz, et al., Phys. Rev. B 72, 224426 (2005)
- 47. M. Kläui, et al., J. Appl. Phys. 99, 08G308 (2006)
- 48. E.M. Hempe, et al., Physica Status Solidi. A 204, 3922 (2007)
- 49. M. Kläui, et al., Appl. Phys. Lett. 88, 232507 (2006)
- 50. M.H. Park, et al., Phys. Rev. B **73**, 094424 (2006)
- 51. D. McGrouther, et al., Appl. Phys. Lett. 91, 22506 (2007)
- 52. Y.S. Dedkov, et al., Appl. Phys. Lett. 80, 4181 (2002)
- 53. M. Ziese, et al., Phys. Rev. B **02**, 134408 (2002)
- 54. C. Hartung, Diploma Thesis, Konstanz (2006)
- 55. W.F. Brown jr., Micromagnetics (Interscience Publishers, New York, 1963)
- 56. A. Thiaville, Y. Nakatani, J. Miltat, Y. Suzuki, Europhys. Lett. 69, 990 (2005)
- 57. S. Zhang, Z. Li, Phys. Rev. Lett. 93, 127204 (2004)
- 58. S.E. Barnes, S. Maekawa, in *Concepts in Spin Electronics*, ed. by S. Maekawa (Oxford University Press, Oxford, 2006)
- 59. N.L. Schryer, L.R. Walker, J. Appl. Phys. 45, 5406 (1974)
- 60. J.Y. Lee, et al., Phys. Rev. B 76, 184408 (2007)

384 M. Kläui

- 61. Y. Nakatani, A. Thiaville, J. Miltat, Nat. Mater. 2, 521 (2003)
- 62. T. Ono, et al., Science 284, 468 (1999)
- 63. M. Hayashi, et al., Nat. Phys. 3, 21 (2007)
- 64. G.S.D. Beach, et al., Nat. Mater. 4, 741 (2005)
- 65. C. Schieback, et al., Eur. Phys. J. B 59, 429 (2007)
- 66. L. Berger, J. Appl. Phys. 55, 1954 (1973)
- 67. A. Yamaguchi, et al., Phys. Rev. Lett. 92, 077205 (2004)
- 68. M. Kläui, et al., Phys. Rev. Lett. 94, 106601 (2005)
- 69. M. Kläui, et al., Phys. Rev. Lett. 95, 026601 (2005)
- 70. L. Thomas, et al., Nature 443, 197 (2006)
- 71. J. Grollier, et al., Appl. Phys. Lett. 83, 509 (2003)
- 72. C.H. Marrows, Adv. Phys. 54, 585 (2005)
- 73. M. Hayashi, et al., Phys. Rev. Lett. 98, 37204 (2007)
- 74. L. Heyne, et al., Phys. Rev. Lett. **100**, 66603 (2008)
- 75. G. Tatara, H. Kohno, Phys. Rev. Lett. 92, 086601 (2004)
- 76. A. Yamaguchi, et al., Phys. Rev. B 78, 104401 (2008)
- 77. A. Thiaville, Y. Nakatani, J. Appl. Phys. **104**, 093701 (2008)
- 78. M. Bolte, et al., Phys. Rev. Lett. **100**, 176601 (2008)
- 79. J. Raabe, et al., Phys. Rev. Lett. **94**, 217204 (2005)
- 80. K. Kuepper, et al., Phys. Rev. Lett. 99, 167202 (2007)
- 81. D. Bedau, et al., Phys. Rev. Lett. 99, 146601 (2007)
- 82. J. Rhensius, PhD thesis, Konstanz (2010)

Chapter 14 Dynamics of Mesoscopic Magnetic Objects

C. Quitmann, J. Raabe, A. Puzic, K. Kuepper, and S. Wintz

Abstract We report on the dynamic properties of mesoscopic magnetic objects. Such objects have dimensions somewhat larger than the magnetic exchange length ξ . This leads to relatively simple and stable patterns of the magnetization, which can be excited using magnetic field pulses. The subsequent dynamics can be studied using X-ray-based magnetic microscopy. We show examples of high symmetry structures where the dynamics is relatively simple and can be analyzed quantitatively in terms of amplitude, frequency, damping, and symmetry.

Intentional defects allow modifying specific modes. When using high amplitude excitations, the magnetization in such structures can be switched.

14.1 Introduction

Magnetic materials have fascinated mankind ever since their discovery many thousand years ago and have led to wide spread application ranging from compasses for navigation over generators and electro motors to modern data storage media.

Such applications have been possible only because of an ever better understanding of the fundamental properties of magnetism and because of the subsequent possibility to tailor these properties for specific applications. Until the 1950s, the interest focused on static behavior of magnetic materials. With the advent of RF-technology, the interest in dynamic aspects arose. At the same time, RF-technology enabled ferromagnetic resonance (FMR) experiments [1, 2]. Such experiments are performed on macroscopic samples having typical sizes of millimeters. Today technology requests an understanding and optimization of magnetic properties of materials on a scale of micrometers and below for applications in magnetic data storage and high frequency electronics. This has led to substantial efforts for studying magnetic properties with the highest possible spatial (Δx) and temporal (Δt) resolution [3–5]. Synchrotron-based X-ray microscopy has evolved as a technique

Swiss Light Source, Paul Scherrer Institut, 5232 Villigen-PSI, Switzerland e-mail: christoph.quitmann@psi.ch

C. Quitmann (⊠)

providing such information with up to several 10 ps temporal and about 20 nm spatial resolution.

We give an overview of the technique, describe results for simple geometrical structures, and show how the dynamics in such simple structures can be modified using intentional defects. Finally, we discuss excitations with higher amplitude, which can induce switching of the magnetization.

14.2 Macroscopic vs. Mesoscopic Magnetic Objects

14.2.1 Magnetic Interactions and Domains

The origin of ferromagnetism is the exchange interaction changing the energy of the system by an amount $\Delta E_{\rm exc}$ if the spins on atoms i and j are aligned parallel. In a localized electron model, it is given by

$$\Delta E_{\rm exc} = J_{i,j} \cdot s_i \cdot s_j. \tag{14.1}$$

This exchange energy favoring parallel spin alignment $(J_{i,j} < 0)$ and thus homogenous magnetization M of the entire sample is counteracted by the stray field energy $E_{\rm d}$

$$E_{\rm d} = -\frac{\mu_0}{2} \int_{\text{sample}} \boldsymbol{H}_{\rm d} \boldsymbol{M} \, \mathrm{d} V. \tag{14.2}$$

The stray field H_d is a consequence of the sample magnetization M and becomes large if the magnetization M points into the same direction over a significant volume V. Such a region is called a magnetic domain. Thus, it is energetically favorable to form finite sized domains with homogenous magnetization and with adjacent domains having opposite direction of the magnetization [6]. This reduces the stray field energy E_d , but increases the total energy because of the higher exchange energy E_{exc} along the interface between two domains, the domain wall. Domain configurations keeping the entire magnetic field within the sample are called flux closure structures and are often the lowest energy state of a magnetic system. The minimum distance over which the magnetization can change direction is given by the exchange length ξ , which can be estimated from measurable parameters using

$$\xi \sim \sqrt{\frac{A}{K}} \sim (1 - 10) \text{ nm.}$$
 (14.3)

Here A is the exchange constant and K is the effective magnetic anisotropy constant [6]. In soft magnetic materials like permalloy (Fe₂₀Ni₈₀), the exchange length ξ is typically of the order of a few nanometers. The exchange length determines the width of the domain walls and of the vortex core formed in flux closure structures.

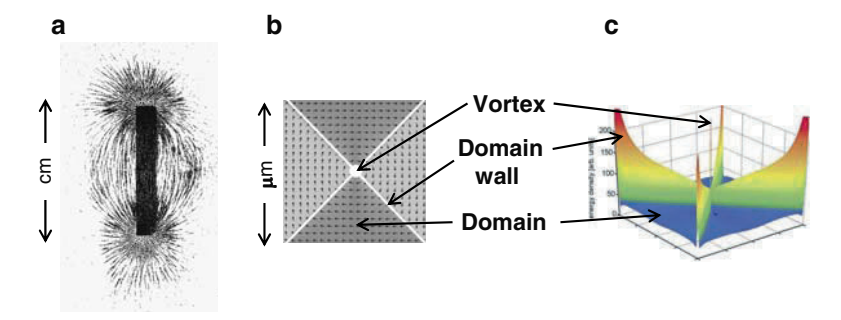


Fig. 14.1 Difference between macroscopic and mesoscopic magnetism shown by the stray field of a macroscopic bar magnet visualized using small ferromagnetic particles (**a**), the simulated magnetization in a mesoscopic soft magnetic square showing a Landau flux-closure pattern (**b**), and the energy density in the same mesoscopic square (**c**)

The formation of domains is the reason why macroscopic samples usually have saturation magnetizations far below what one would extrapolate from the atomic scale. To study the fundamental magnetization dynamics, it is essential to use samples containing a single or a few well defined domains. Otherwise, one obtains an average over many domains, which does not reveal the fundamental process and time scales of the material. Samples with a well defined number and arrangement of domains have dimensions larger than the exchange length ξ but usually not exceeding about 100 μ m and are called mesoscopic.

Figure 14.1 shows the difference between a macroscopic and a mesoscopic sample. The macroscopic sample (a) is a bar magnet with its stray field H_d made visible using fine iron particles. The stray field contains an energy $E_{\rm d}$, is dipolar, and extends to infinity. The mesoscopic sample (b) is a square with side length $a \sim \mu m$. The arrows show the orientation of the magnetization within the square as predicted by micromagnetic simulations. The magnetization lies in the plane of the square. The square contains four homogenously magnetized domains oriented at 90° to each other [6]. Together they form a so-called Landau flux-closure pattern, which has no in-plane stray field. The domains are separated by domain walls indicated by white lines. At the center of the square the domain walls intersect. Because of the finite exchange length ξ , the magnetization rotates out-of-plane forming the so-called vortex core. By this out-of-plane rotation, the system avoids having the spins on two adjacent atoms antiparallel, which would be energetically very expensive. This vortex core has a magnetization perpendicular to the plane pointing either up or down. The dimensions of the domain wall and the vortex core are both given by the exchange length $\xi \sim 10$ nm and are thus much smaller than the dimension of the square.

The energy density for the mesoscopic magnetic square is plotted in Fig. 14.1c. The domains are the lowest energy density regions of the sample. Introduction of the domain walls increases the exchange energy, resulting in a higher energy density, but this is limited to the narrow width of the domain walls, and is compensated by

the gain in stray field energy. The vortex core is the region with the highest energy density and is seen in Fig. 14.1c as a narrow spike in the center.

As even an object as simple as a square contains three sub-regions (domains, domain walls, and vortex core), it is clear that microscopy techniques are required to understand the different dynamics in such objects. In the following, we show how synchrotron-based X-ray microscopy can be used to study the dynamics of all subunits in quantitative detail.

14.2.2 Magnetic Time Scales

To perform time and spatially resolved experiments on magnetic materials, it is necessary to understand the temporal and spatial scales involved.

Figure 14.2 shows examples of the relevant time scales in magnetism. They span more than 20 orders of magnitude. For magnetic storage, a retention time of many years (10^8 s) is mandatory. Typical measurements of hysteresis loops take place on the second scale. Here domains nucleate and grow and domain walls are moved through the sample. These are quasi-static processes where the system can always be assumed to be in equilibrium. In ferromagnetic resonance experiments (FMR), the atomic spins are subject to a static magnetic field and are resonantly excited by a microwave field. The precession frequency is given by the gyromagnetic constant $\gamma = 17.6\,\mathrm{MHz}\,\mathrm{Oe}^{-1}$, resulting in typical time scales of nanoseconds. This is also

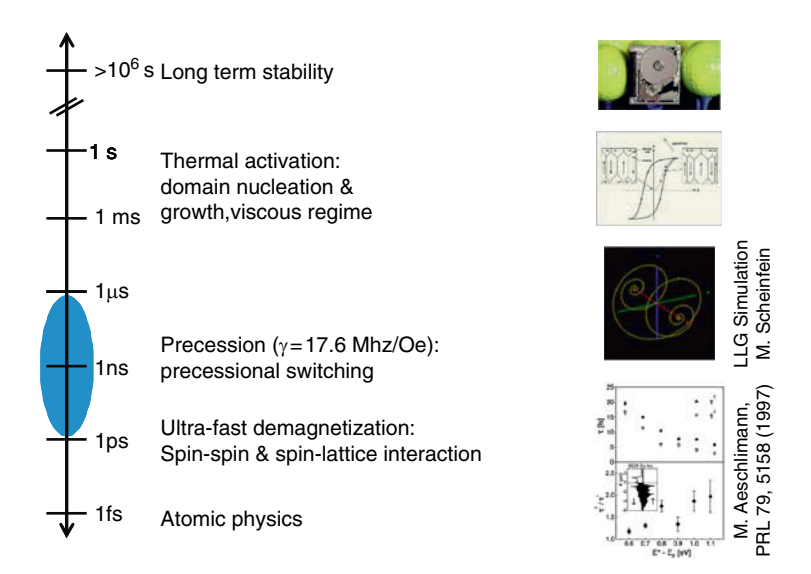


Fig. 14.2 Time scales relevant for magnetism ranging from very long times (years) required for data storage to ultra-short times (femtoseconds) relevant to processes within an atom

the regime of precessional switching [7,8], where switching of a magnetic moment from up to down is suggested to happen by first resonantly exciting its precession.

The time scale around and below 1 ps has received much attention because of the interest in ultra-fast demagnetization induced by laser pulses and the subsequent establishment of spin–spin and spin–lattice equilibrium [8, 9].

The fastest processes are those happening within the atom. Here the time scales can be estimated by the energy differences ΔE between the atomic states involved and are given by $\tau(fs) \sim 4/\Delta E(eV)$. Such processes are too fast to be coherent over many lattice sites and are mainly local intra-atomic processes.

The dynamics in mesoscopic magnetic structures happens on time scales ranging from picoseconds to many nanoseconds (marked by a blue region in Fig. 14.2). They can conveniently be studied by synchrotron radiation, which has a natural time structure of 50–100 ps. This is given by the length of the X-ray flashes that are produced by the electron bunches circulating in the storage ring [10].

14.2.3 Magnetic Length Scales

Magnetic length scales also vary by about 20 orders of magnitude (Fig. 14.3). The largest magnet in practical use is the earth with a diameter of more than $10,000 \,\mathrm{km}$. Its dipole field is used for navigation since more than $2,000 \,\mathrm{years}$. In conventional engineering, the sizes of magnets range from several meters to fractions of a millimeter. Modern hard disks store information in bits with diameters down to $100 \,\mathrm{nm}$. The exchange length ξ determines the sizes of the smallest inhomogeneous magnetic structures such as domain walls or vortex cores and is of the order of nanometers. The atoms with typical dimensions of $0.1 \,\mathrm{nm}$ are considered as the smallest building blocks in solid-state physics.

The range of mesoscopic magnetic objects with well defined and controllable magnetization pattern is between several $10\,\text{nm}$ and several $10\,\mu\text{m}$. This is conveniently covered by X-ray microscopy, which today can resolve structures down to about 15 nm [11]. In the following, we focus on structures made out of permalloy thin films of several $10\,\text{nm}$ thickness with diameters of about $1{-}20\,\mu\text{m}$. We show that their dynamics has characteristic frequencies in the range between several hundred megahertz and a few gigahertz and that damping happens on a nanosecond scale.

14.2.4 Landau-Lifshitz-Gilbert Equation

Even today, after decades of intensive research, there exists no microscopic theory consistently describing the dynamics of mesoscopic magnetic structures. Band structure methods like LSDA [12] and its many extensions have difficulties taking into account the correlation effects and therefore limit their efforts to description of

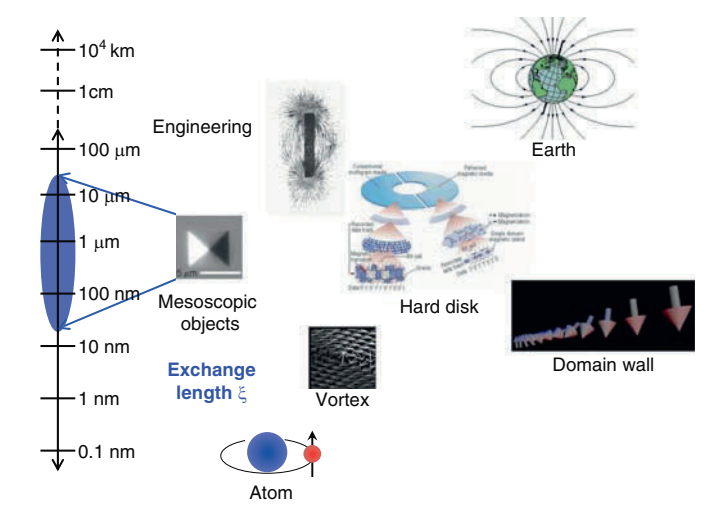


Fig. 14.3 Length scales relevant for magnetism ranging from the very large (thousands of km) as for the magnetic field of the earth to very small (Ångstrom) in the case of magnetic atoms. Mesoscopic effects appear when the sample dimensions are larger than the exchange length ξ but not much larger than typical domain sizes (\sim 1–100 μ m)

the ground-state of simple magnetic transition metals such as Fe, Co, and Ni. The models explicitly developed to take into account strong correlations like the Hubbard model and its variants, on the other hand, are numerically so demanding that it is impossible to perform calculations on the required numbers of atoms and for realistic geometries.

Thus the semi-classical equation suggested by Landau–Lifshitz in the 1930s and extended by Gilbert in 1955 [13] is still the most used equation. It relates the rate of change of the magnetization M to a torque term caused by the effective field $H_{\rm eff}$ and to a phenomenological damping term. The damping term ensures that for long times M becomes parallel to $H_{\rm eff}$.

$$\frac{\mathrm{d}\mathbf{M}}{\mathrm{d}t} = -\mathbf{M} \times \mathbf{H}_{\mathrm{eff}} + \alpha \left(\frac{\mathrm{d}\mathbf{M}}{\mathrm{d}t} \times \mathbf{M} \right). \tag{14.4}$$

The effective field is the sum of many terms containing the applied external field $H_{\rm appl}$, the saturation magnetization $M_{\rm S}$, the demagnetizing field $H_{\rm d}$, anisotropy fields $H_{\rm aniso}$, the exchange field $H_{\rm exc}$, etc. The damping is parameterized using an empirical constant, which for permalloy is typically $\alpha \sim 0.01$. The original equation has been extended by many people to take into account additional effects such as spin–torque [14]. This Landau–Lifshitz–Gilbert equation (LLG) can be applied to mesoscopic magnetic structures by calculating the magnetization M for an array of voxels (typically about $100\,{\rm nm}^3$), each treated as a macro spin. The effective field $H_{\rm eff}$ is calculated by summing up all contributions, including the sum over M from

all voxels. Time-dependent calculations are done by the use of discrete time steps of typically a few picoseconds. As soon as the magnetization in one voxel of the sample deviates from the equilibrium orientation, it influences all other voxels, thus leading to a coupling between the voxels.

Many implementations of the LLG equation exist [15–17] and are used to simulate the behavior of mesoscopic magnetic objects and to assist in the interpretation of experiments.

14.2.5 Experimental Techniques

Imaging the dynamics of mesoscopic magnetic structures requires high spatial Δx and temporal Δt resolution [18]. Two popular methods fulfilling these requirements exist. Magneto-optical Kerr effect [19] uses the rotation of linearly polarized visible light when reflected from a magnetic surface. As this rotation is proportional to the magnetization at the point r and time t of the reflection, it can be used to measure M(r,t). The polarized visible light is produced by a laser. This has the advantage of very high temporal resolution $\Delta t \sim$ fs, but the disadvantage of diffraction limited spatial resolution $\Delta x \sim \lambda/2 \sim 200$ nm.

X-ray microscopy using tunable and pulsed X-rays from a modern synchrotron is the other. Its advantage is the superior spatial resolution, which can reach $\Delta x = 15\,\mathrm{nm}$ and the ability to image separately different chemical elements and thus investigate multilayer samples. The disadvantage is the time resolution, which is given by the length of the X-ray pulses. These have typical values of $\Delta t_\mathrm{fwhm} \sim 75\,\mathrm{ps}$ at most modern synchrotrons. Details of the experimental technique are described in [10] for the work by the authors. A review of current work using photoemission electron microscopy (PEEM) is given by Locatelli et al. in [20] and by Nolting [21]. A review of time-resolved microscopy was recently compiled by Elmers et al. [22]. An alternative device to the PEEM is a scanning X-ray microscope, which is also often used in general materials and environmental science and for biology [23, 24]

All X-ray techniques for magnetic imaging make use of X-ray magnetic circular dichroism (XMCD). This is the difference in X-ray absorption $I_{\rm XAS}(r)$ depending on the relative orientation of the magnetization M(r) and the X-ray circular polarization vector P. It was first observed by Schütz et al. at the K-edge of transition metals [25]. Later it was realized that the effect is much stronger at the L-edges [26, 27]. Today it is generally assumed that the difference in the resonant absorption at the L_3 - and L_2 -edges of transition metals, when switching the helicity of the X-rays, is proportional to the magnetization, $M \sim \Delta I_{\rm XAS}(E_{2p}) = I_{\rm XAS}^+ - I_{\rm XAS}^-$. By changing the relative orientation of the circular X-ray polarization P and the magnetization M, one can measure the relative orientation $\Delta I_{\rm XAS} \sim P \cdot M$. Because the effect happens at the absorption edges of the magnetic transition metals (Fe, Co, Ni), it is element specific.

Measuring the dynamic properties on a sub-nanosecond time scale requires a stroboscopic pump-probe approach because the photon flux is by far not sufficient to create an image of reasonable quality using a single X-ray pulse. In fact, one needs to average over about 10⁹ pump-probe cycles to obtain reasonable signal-to-noise ratio. Such an experiment is thus sensitive only to repetitive dynamics, which can be averaged over a large number of cycles. All random fluctuations average out and are invisible using this technique.

The experiments shown in the following have all been performed on thin magnetic films with a typical thickness of 30 nm. They are lithographically produced on top of a coplanar wave guide (gold: width = $10 \,\mu m$, thickness = $200 \, nm$). The current in the wave guide produces a magnetic field pulse within the plane of the sample. It has an amplitude of several $10 \, Oe$ and a rise time of about $200 \, ps$.

Complementary techniques used are conventional FMR [4, 28, 29] and X-ray detected ferromagnetic resonance (X-FMR) and magnetic force microscopy. Because FMR is a resonance-based technique, it is excellently suited to measure frequencies and damping of periodic processes. While conventional FMR is not element sensitive at all, this limitation has recently been overcome by using XMCD as the detection method [30,31]. So far these FMR based techniques are not performed with spatial resolution.

Magnetic scanning probe microscopy has by far the best spatial resolution: it is done by spin-polarized scanning tunneling microscopy (SP-STM) [32] or by magnetic force microscopy (MFM) [33]. However, acquisition of a high resolution image typically requires minutes and therefore MFM not suited to study fast dynamics.

14.3 Dynamics in Simple Squares

14.3.1 Static Mesoscopic Structures

Before studying the dynamics of mesoscopic magnetic structures, we show results on their static properties. Figure 14.4 shows magnetization patterns for the equilibrium state of simple geometrical objects. The sample is an exchange coupled multilayer of Cobalt and permalloy (PY) separated by a thin nonmagnetic Ruthenium layer (PY 3 nm/Ru 0.8 nm/Co 50 nm). Shown are a circle, a square, an ellipse, and a rectangle. We first discuss the top PY layer imaged using the Fe-2p edge at an X-ray energy of 708 eV (top row). The structures show clear contrast originating from the varying orientation of the magnetization M(r) with respect to the polarization P. Regions of the sample showing high intensity (white) are aligned parallel to P while those showing low intensity (black) are antiparallel. Grey regions are at right angles to P. Theoretically they might be at 90° or 270° to P. But as the structures are known to show flux closure patterns, a unique determination of M is possible. This can be verified by rotating the sample 90° around the surface normal, as will be shown in Fig. 14.7.

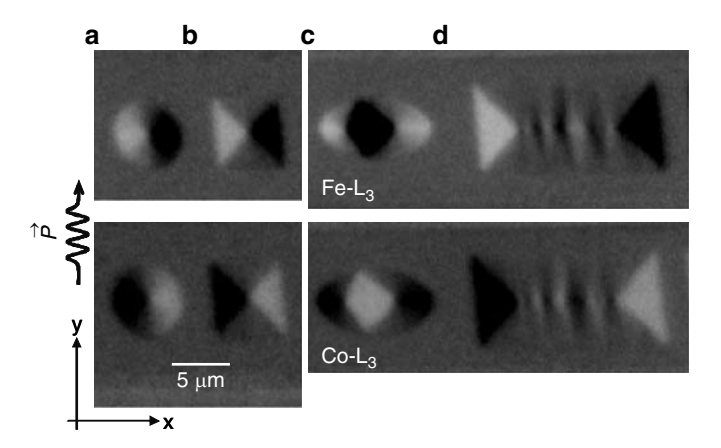


Fig. 14.4 Examples of magnetization patterns in geometrically simple magnetic objects of a magnetic trilayer *permalloy* 3 nm/Ru 0.8 nm/Co 50 nm. The circle (**a**) and square (**b**) show flux closure patterns, the ellipse (**c**) has a diamond pattern, and the rectangle (**d**) contains four cross-tie walls. Each of the domains in the top permalloy layer is antiferromagnetically coupled to its domain in the underlying Co-layer

The Landau-flux closure structures observed for the square (a) and the circle (b) are the lowest energy state and are quite stable. The experimental magnetization pattern of the square compares well to the simulated result shown in Fig. 1. One observes the four domains with magnetizations rotated by 90° relative to each other, leading to the flux closure state. The domain walls are visible as the sharp lines separating the domains. The vortex core is located at the intersection of the two domain walls. It is below the resolution of the PEEM ($\Delta x \sim 50$ nm). The circle has a magnetization continuously rotating around the perimeter (M is perpendicular to the radius vector). In the center, the circle also contains a vortex core pointing either into or out-of the plane.

The magnetization pattern of the ellipse (c) and the rectangle (d) are already more complex. The ellipse has a so-called diamond configuration. This can be thought of as consisting of two flux closure structures each containing one vortex core. They are joined by a common black domain in the center. The diamond pattern is slightly distorted (black domain shifted to the left), probably due to some material defect in the film or because of roughness along the edge caused by the lift-off process employed for the fabrication.

The rectangle shows an even more complex pattern. Again it can be thought of as having two flux-closure patterns, one on each end. In the middle, however, there are four vertical lines of alternating dark-bright contrast. They are the consequence of cross-tie domain walls [34, 35]. This is not the lowest energy configuration for a rectangle and shows that even for simple geometries the magnetization pattern can be complex. In practice, the energy differences between different magnetization patterns can be quite small, leading to many almost degenerate configurations.

Experimental results and theoretical predictions on the variation in magnetization patterns and their relative abundance agree quite well [36].

Comparing the magnetization pattern for the PY-layer (top) with the underlying Co-layer (bottom), one observes a one-to-one correlation of the magnetization patterns. For all structures, the magnetizations in the PY- and the Co-layer are antiparallel. This is a clear proof of the antiferromagnetic exchange coupling mediated by the nonmagnetic Ru layer (0.8 nm thickness) [37]. This antiferromagnetic coupling is true down to the fine details like the asymmetry of the diamond pattern in the ellipse (c) and to the number, size, and locations of the cross-tie walls in the rectangle (d).

This behavior shows that the exchange coupling is a local phenomenon occurring on a scale comparable to or smaller than the exchange length, which is about 10 nm in Permalloy. A similar local character of exchange coupling is known for antiferromagnets as well [38].

14.3.2 Pulsed Field Excitations

In this section, we analyze the dynamics of mesoscopic magnetic squares. The squares are excited by a short magnetic field pulse H_P oriented in the plane of the thin film. Ideally, the pulse is a delta function and thus excites all magnetic modes. In reality it has a finite rise time, which sets an upper limit for the frequencies that are excited.

14.3.2.1 Sequence of Dynamics

Characteristic time steps of the dynamics in a permalloy square of $a=6\,\mu\mathrm{m}$ side length are given in Fig. 14.5 for the equilibrium state and three delays up to $\Delta t=1,667\,\mathrm{ps}$ [39]. A color wheel shows the color scale used to represent the relative orientation of M(r) and P. The equilibrium state ($\Delta t=0\,\mathrm{ps}$) shows the well known Landau-flux closure state. Arrows indicate the orientation of the magnetization in the four domains, and dashed lines indicate the domain walls.

At a delay of $\Delta t = 467$ ps, the two domains oriented perpendicular to the field pulse H_P have rotated towards the y-direction. The torque exerted by H_P has caused a precession of the magnetization. This precession is essentially in the plane of the film [39]. The amplitude of this coherent precession has a maximum around $\Delta t = 500$ ps, indicating a precession frequency of about $\Delta t \sim 2$ GHz. The domains with magnetization parallel or antiparallel to the field pulse initially show little change because there is no torque acting on them [40].

At a delay of $\Delta t = 667$ ps, we observe a bulging of the domain walls. The walls that are straight lines in the equilibrium configuration are bent. This is a consequence of the precession in the domains. The deviation of M away from the equilibrium state has modified the effective field $H_{\rm eff}$ at other locations within the square, thus leading to the bending of the domain walls for example.

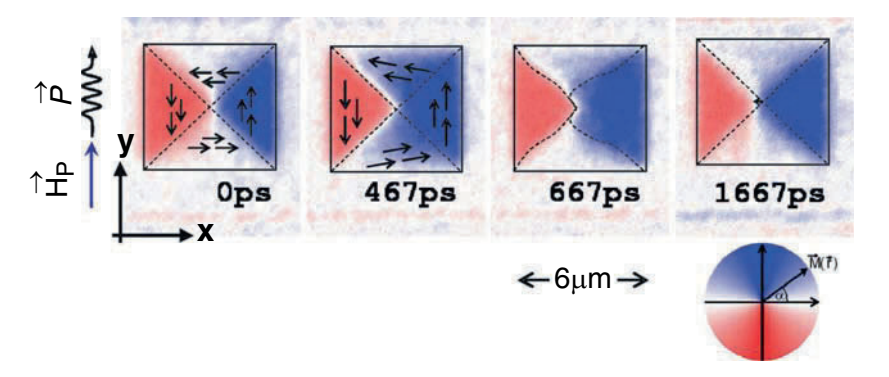


Fig. 14.5 Permalloy square shown at distinct time delays Δt after excitation by a magnetic field pulse H_P . Prior to the excitation (0 ps) it displays a Landau flux closure pattern, and after $\Delta t = 467$ ps, one observes coherent domain precession in the top and bottom domains. This is followed by domain wall bulging around 667 ps and finally by vortex motion perpendicular to H_P at 1,667 ps

For long delays, we observe a motion of the vortex core towards the left as seen for $\Delta t = 1,667$ ps. The intersection of the domain walls (dashed lines) has shifted by about 750 nm, as shown below, indicating an initial vortex core velocity of about $450 \,\mathrm{m\,s^{-1}}$.

Similar experiments on mesoscopic magnetic squares have been done by several groups. In several of these experiments, a gyrotropic spiraling motion of the vortex core has been observed [41–43]. The gyration occurs with a frequency given by $H_{\rm eff}$ and a direction given by the core orientation (up or down).

14.3.2.2 Coherent Domain Precession

We now look in more detail at the coherent precession within the domains. For this we plot the time dependence of the magnetization $M_y(\Delta t)$ averaged over a small region in the sample in Fig. 14.6 [40]. This is done for two orientations of the sample, polarization parallel to the field pulse H_P (left) and polarization perpendicular to the field pulse H_P (right). Rotating the sample like this allows measurement of both in-plane components $(M_y(\Delta t): \text{left}, M_x(\Delta t): \text{right})$. This gives maximum sensitivity to small deviations from the equilibrium orientation.

First we discuss the domains with magnetization perpendicular to the exciting field pulse. These domains experience a torque $T = M_s \times H_p(\Delta t)$ resulting in coherent precession as discussed in Fig. 14.5. Here in Fig. 14.6 (left), this coherent precession is seen as an oscillation of the magnetization M_y showing four periods over about $\Delta t = 2.5$ ns. The oscillation is identical (within experimental error) in the two areas investigated, which are indicated by circles (green and black) in the inset. As these are located on opposite sides of the symmetry line, the precessional mode is symmetric.

The situation in the domains at right angles to the field pulse is different. Not only is the amplitude lower by about a factor of four, but also regions on opposite sides

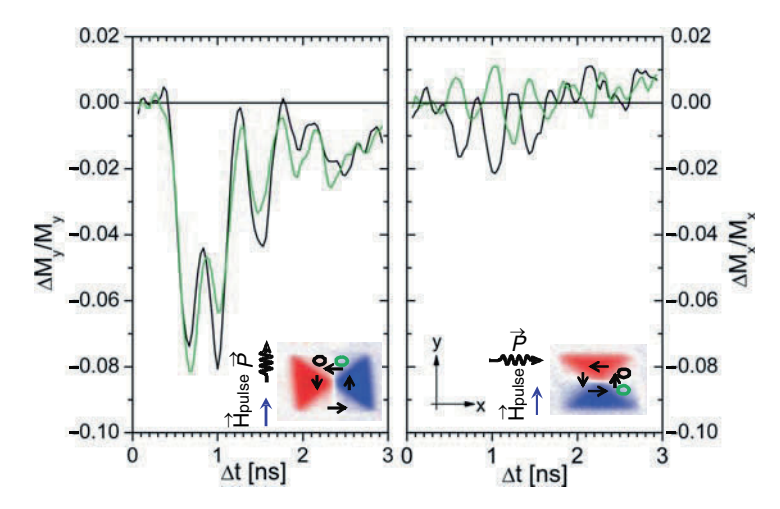


Fig. 14.6 Coherent domain mode in a square (side $a=6\,\mu\text{m}$) probed in two geometries to obtain high sensitivity to changes in the domains with magnetization perpendicular (*left*) and parallel (*right*) to the applied field pulse H_P . The inset shows the geometry used and the areas over which the magnetization was averaged to obtain its time dependence

of the symmetry line oscillate with opposite phases. Thus the precessional domain mode in these domains is antisymmetric.

Such local spectra can be fitted to damped oscillation to provide precise values of the oscillation frequency, amplitude, and damping [39]. By taking such spectra for each pixel in the image and then Fourier transforming the spectrum, it is also possible to calculate the eigen frequencies. The spatial distribution for each of the eigen frequencies is then given by the amplitude of the Fourier-components at this frequency [10, 39, 44].

To investigate the response of the vortex core following the excitation pulse, we show the results for two squares of identical size ($a=6\,\mu\mathrm{m}$) but with a different orientation (Fig. 14.7). The top row shows squares aligned parallel to the field pulse, while the middle row shows squares of the same size, but oriented at 45° relative to the field pulse. The geometry of polarization P and field pulse H_P is shown by a sketch on the left. The square tilted by 45° is seen to have only two shades of grey. The light grey results from the two domains with the magnetization oriented at 45° (left half of the square), while the dark grey results from those oriented at 135° with respect to P.

The vortex displacement is measured by comparing the intensity in four boxes surrounding the equilibrium position of the vortex core, similar to a quadrant detector. The displacement is mainly in the direction perpendicular to the field pulse. It rises rapidly reaching a maximum and then decreases very slowly back to zero. For both orientations of the square, the initial rise is completed after about $\Delta t = 1.2$ ns, but the amplitude is different. While in the square aligned to H_P the vortex core moves by ~ 750 nm, it moves by $\sim 1,420$ nm in the square rotated by 45° . This results in vortex speeds of 625 and 1,180 m s⁻¹, respectively.

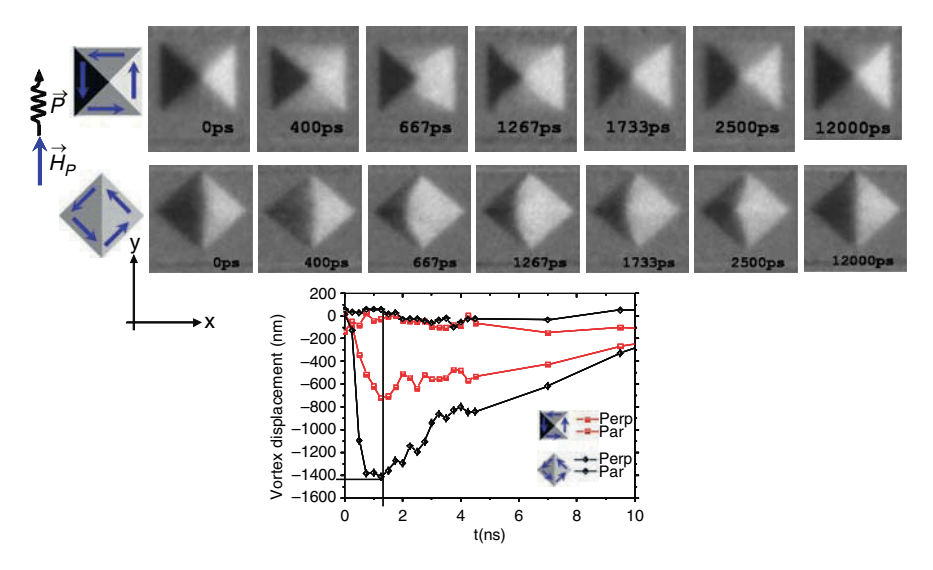


Fig. 14.7 Sequence of images of squares (side $a=6\,\mu\mathrm{m}$) showing equilibrium ($\Delta t=0$) and subsequent excited states. Note the different amplitude in the motion of the domain walls and the vortex core between squares aligned to the exciting field pulse H_P (top) and those tilted by 45° (middle). Quantitative values for the vortex motion parallel and perpendicular to the applied field pulse H_P are given in the graph (bottom)

The vortex core is moved by a larger amount and at higher speed in the tilted squares because here the field pulse exerts a torque upon the magnetization in all four domains and not only in two, as is the case for the square aligned to H_P .

After having shown how the three subcomponents of a mesoscopic magnetic square react to an exciting field pulse, we show how their response can selectively be influenced in the next chapter.

14.3.2.3 Tuning the Response of Mesoscopic Magnetic Objects using Defects

The magnetization in mesoscopic magnetic squares consists of different subcomponents with very different energy densities (see 14.1). The high energy density components like the domain wall and the vortex core are stabilized by the gain in stray field energy E_d resulting from the flux closure pattern.

As the domain wall and the vortex core have a high energy density, they can be pinned to a certain point in the mesoscopic object if this region is made non-magnetic. Focused ion beam milling (FIB) allows controlled introduction of such nonmagnetic defects into thin film samples. For this, a finely focused beam of high kinetic energy ions is directed onto the sample. By properly selecting the ion type and the kinetic energy, one can either remove the magnetic thin film creating a hole or destroy the magnetism by ion-induced defects and doping [45,46].

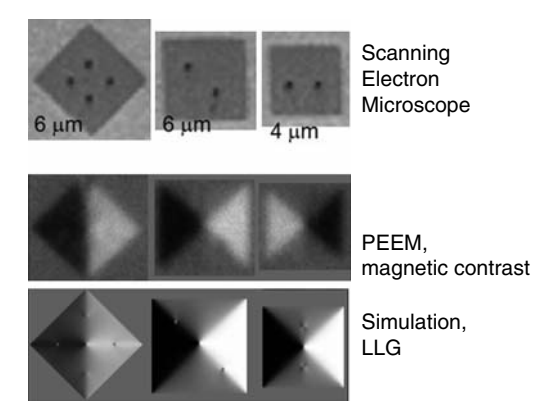


Fig. 14.8 Defects in mesoscopic magnetic squares produced using a focused ion beam (FIB). The defects are clearly visible as dark spots in the scanning electron microscope (SEM) images (*top*). The PEEM images show the magnetic domain configuration of the same squares (*middle*). Here the defects are not well visible. The micromagnetic simulations (*bottom*) show that the defects cause a change of the magnetization only in a small region, which is close to the resolution limit of the PEEM

An example of defects created using FIB is shown in Fig. 14.8. In the scanning electron microscope (top), they show up as dark spots. Shown are three squares with defects along the domain walls (left and center) or in the domains (right). These squares were imaged in the PEEM using the geometry shown schematically at the bottom. In the PEEM image the defects are not clearly visible. Their diameter is given by the region irradiated using the FIB. This needs to be comparable with the width of the vortex core or the domain wall ($\sim \xi$) to be an effective pinning site.

The micromagnetic simulations show that as expected the changes of the magnetization produced by the defects are limited to a distance a few times the size of the defects. Because the size of the defects is close to the resolution of the PEEM, they are not clearly visible in the PEEM images.

To show the effect of pinning on the dynamics, we present a sequence of images of these defect containing structures following the excitation by a field pulse H_P (Fig. 14.9). Results are shown for two squares rotated by 45° relative to the exciting field pulse H_P . One of them (configuration I) has a single defect in the center, which pins the vortex core. The other (configuration II) has two additional defects pinning domain walls.

Comparing the results shown for the defect containing squares in Fig. 14.9 with those of the defect free squares in Fig. 14.7, we observe clear differences. The defects pin the vortex core and thus hinder both the core motion and the domain wall bulging. For defect free squares, the core and the domain walls move along the -x direction (see Fig. 14.7, $\Delta t = 1,267$ ps). The small defect apparently pins the vortex for configuration I, thus also significantly reducing the bulging of the domain walls. In the difference images $M(r, \Delta t) - M(r, \Delta t = 0)$ the bulging of the walls to the -x direction is still visible (as seen by the white line in the difference images), but the amplitude is reduced significantly. Comparing configuration I and II, we see

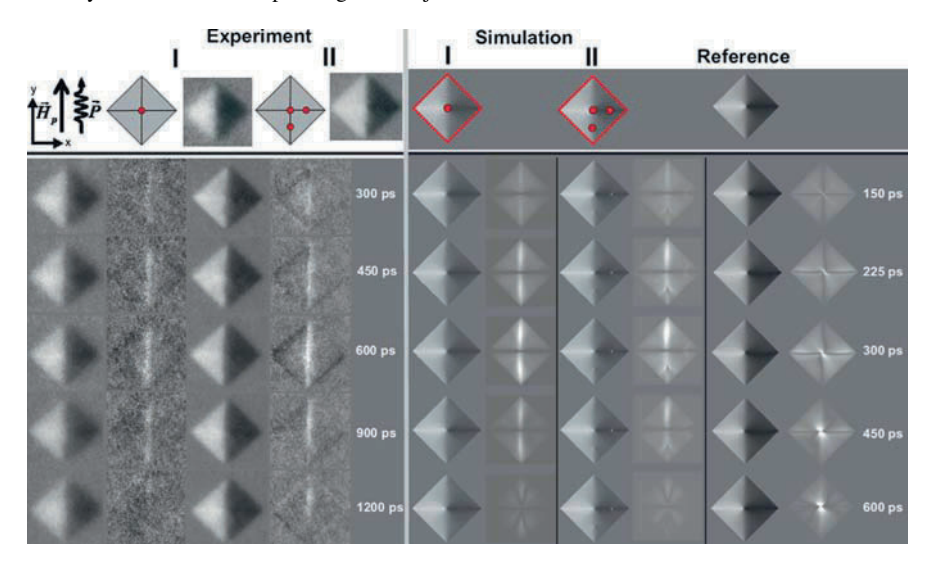


Fig. 14.9 Dynamics of two magnetic squares, containing controlled defects, following excitation by a field pulse H_P . Experiments (left) can be compared to simulations (right). To increase the visibility of small changes caused by the field pulse, we show difference images $M(r, \Delta t) - M(r, \Delta t = 0)$ adjacent to all images

that at short delays ($\Delta t \leq 600 \, \mathrm{ps}$) the domain wall moves visibly in both upper and lower half of the square. For long delays ($\Delta t \geq 900 \, \mathrm{ps}$) the wall in the upper half is still displaced, while in the lower half it has already returned to the equilibrium position. Apparently, the defects become effective only once the amplitude of the wall motion falls below a length comparable to the defect size.

The reason why the defects are more effective for the vortex core than for the domain wall is that the energy density associated with the vortex core is much higher than that associated with the domain walls (see Fig. 14.1c). The vortex core is also very narrow (diameter $\sim \xi \sim 10$ nm) and the energy gain when keeping it in the nonmagnetic defect region is very high.

Defects can thus be used to selectively influence the dynamics of the domain wall and of the vortex. Depending on the size, number, and position of such defects, the dynamic response of mesoscopic magnetic objects can be tailored. This will be shown to be useful for generating bi-stable magnetic configurations, which in principle can be used for data storage.

14.4 Vortex Dynamics and Switching

14.4.1 Current Induced Resonant Vortex Core Motion

In the following, we discuss a complementary experiment performed by Kasai et al. [47]. This experiment uses a transmission X-ray microscope (TXM) [48] and a resonant excitation by a spin-current.

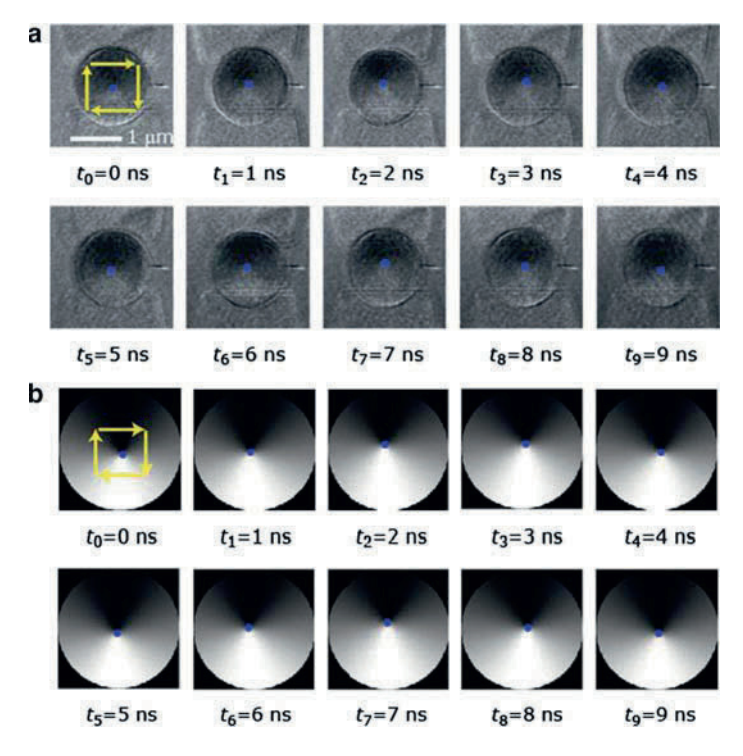


Fig. 14.10 (a) permalloy disk ($\phi = 1.5 \,\mu\text{m}$, $t = 40 \,\text{nm}$) resonantly excited by an electrical current and imaged using a transmission X-ray microscope (TXM) (from [47]). (b) Simulation of the same permalloy disk using the Landau–Lifshitz–Gilbert equation including a spin-transfer torque term. The vortex position is marked by a blue dot in both image sets and can be seen to precess around the disk center in a clock wise direction

In contrast to our PEEM experiments discussed above, the sample in a TXM experiment is at ground potential. This makes it easy to apply RF-signals to the sample and to induce dynamics. In the present experiment, the magnetic sample, a 1.5 µm diameter permalloy disk, is in electrical contact with two electrodes. In Fig. 14.10, the electrodes are visible as faint shadows on the top and the bottom of the circle. An oscillating current ($f = 220 \,\mathrm{MHz}$) is driven through the magnetic disk. Within the disk, the current becomes spin polarized because of the spin splitting of the states at the Fermi level. This current exerts a spin torque on the vortex. The torque is proportional to the spin polarization of the current. Because the frequency of the oscillating current is close to the resonance frequency of the gyrotropic rotation of the vortex core in such a disk, it excites this mode. The effect is seen in Fig. 14.10 where the vortex core (marked by a blue dot) starts at the center of the disk ($t_0 = 0$ ns), and subsequently rotates on a circular trajectory around the center. The experimental results in the upper half are well reproduced by micromagnetic simulations in the lower half. From a fit of the gyration amplitude to a harmonic oscillator, which is the solution to the LLG equation with an added spin-torque term, the authors obtain the spin polarization $P=0.67\pm0.15$ and the empirical damping constant $\alpha=(0.01\pm0.002)$.

This experiment nicely shows the complementarity between different dynamic experiments. In contrast to the PEEM experiments described above, which employed a pulsed excitation, this TXM experiment uses a resonant excitation to selectively excite one particular mode. For this it uses the torque created by a current passing through the mesoscopic magnetic disk, while in the PEEM experiments a pulsed magnetic field was used.

14.4.2 Bistable Configurations by Pinning the Vortex Core

Using the experience obtained from studies of defects in such mesoscopic magnetic objects and combining it with the result that the vortex core can be significantly displaced led us to the idea of producing objects providing two stable positions for the vortex. These are shown in Fig. 14.11. The low energy electron microscope (LEEM) image (a) shows the topography of the sample. Two disks, each containing two defects that are located off center, are well seen. The LEEM image has higher spatial resolution and contrast than the PEEM image, but does not provide any magnetic information.

In Fig. 14.11b, we show a first PEEM image. The magnetization curling around the disk center is clearly seen (clock-wise for the upper and counter-clock-wise for the lower disk).

The same disks are shown in Fig. 14.11b, c after application of about 10^7 switching pulses (at that time we were not able to isolate a single pulse from the train of magnetic field pulses). The change in black/white contrast between Fig. 14.11b and c shows that switching has taken place in both disks. The field pulse has moved the

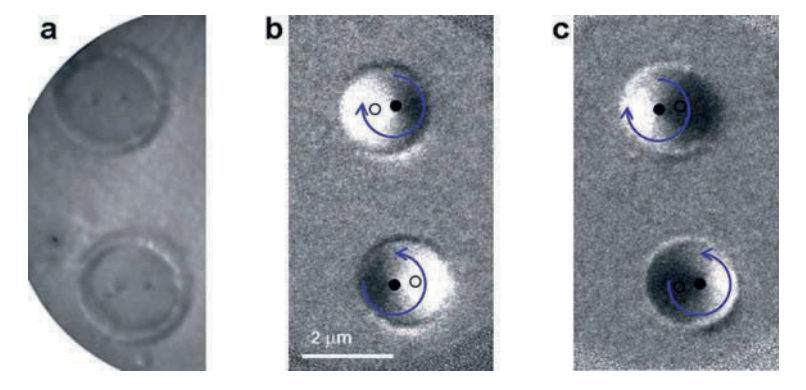


Fig. 14.11 Permalloy disks containing two defects leading to a bi-stable vortex position. LEEM image (a) showing the topography including the defects. PEEM image before (b) and after (c) applying switching pulses. The switching pulses lead to a motion of the vortex core in both disks. The chirality (*blue arrow*) of the flux closure pattern is unchanged upon the switching

vortex core from one of the two stable positions to the other. While the switching itself is easily observed, the trajectory followed by the vortex core when moving from one defect to the other could not be observed in this experiment. So far it is not clear whether this is due to a chaotic trajectory of the vortex in this highly nonlinear situation, or it is due to equal probability of the vortex following an upper and a lower trajectory, which in a stroboscopic experiment get summed up and result in zero contrast.

14.4.3 Resonant Burst Switching

The details of vortex switching have been studied in several experiments and using simulations. While in experiments, no one has observed the details of the switching so far, it can well be studied using micromagnetic simulations [49].

As an example we show results obtained by van Wayenberge et al. [50]. This experiment was performed using a scanning transmission X-ray microscope (STXM). In such an instrument, the X-ray beam is focused to a narrow diameter and the intensity of the X-rays transmitted through the semi-transparent sample is recorded as a function of position r and time (Δt). When scanning the sample in x- and y-direction, one can measure the spatial distribution of the X-ray absorption coefficient in the sample $I(r, \Delta t)$. Using XMCD, this leads to the spatially resolved magnetization $M(r, \Delta t)$. This STXM is attractive for magnetization dynamics because it makes very efficient use of the photons, as each photon absorbed contributes to the signal. As it is a scanning technique, no photons are lost in uninteresting portions of the sample. In the experiment by van Waevenberge et al., it was investigated how a vortex core could be switched from one direction $(P \uparrow \uparrow z)$ to the other $(P \downarrow \uparrow z)$ using fast and low amplitude magnetic pulses. The orientation of the vortex core was measured through the gyrotropic core motion resonantly excited by a low amplitude (0.1 mT) oscillating magnetic field. This is shown in the left part of Fig. 14.12 ($\Delta t = 0$ –12 ns). The vortex core oscillates counter clock wise revealing its orientation parallel to the z-direction. This is schematically shown in the sketch at the bottom of the figure (left) where the magnetization curls around the vortex located in the center.

At a certain moment ($\Delta t=12\,\mathrm{ns}$), an RF-burst is applied to the magnetic disk. This burst has a single cycle and an amplitude of 1.5 mT. In a static situation, fields of the order of 5 T are needed to induce switching [51, 52]. However, the situation is different when the vortex core is already excited to the low amplitude gyrotropic motion. In this case, such a relatively weak switching pulse can induce switching as evidenced by the change of the gyrotropic rotation to clockwise ($\Delta t=16-28\,\mathrm{ns}$).

This experiment shows that knowledge about the internal modes of such mesoscopic objects, such as gyrotropic precession, can be used to optimize their properties like core reversal.

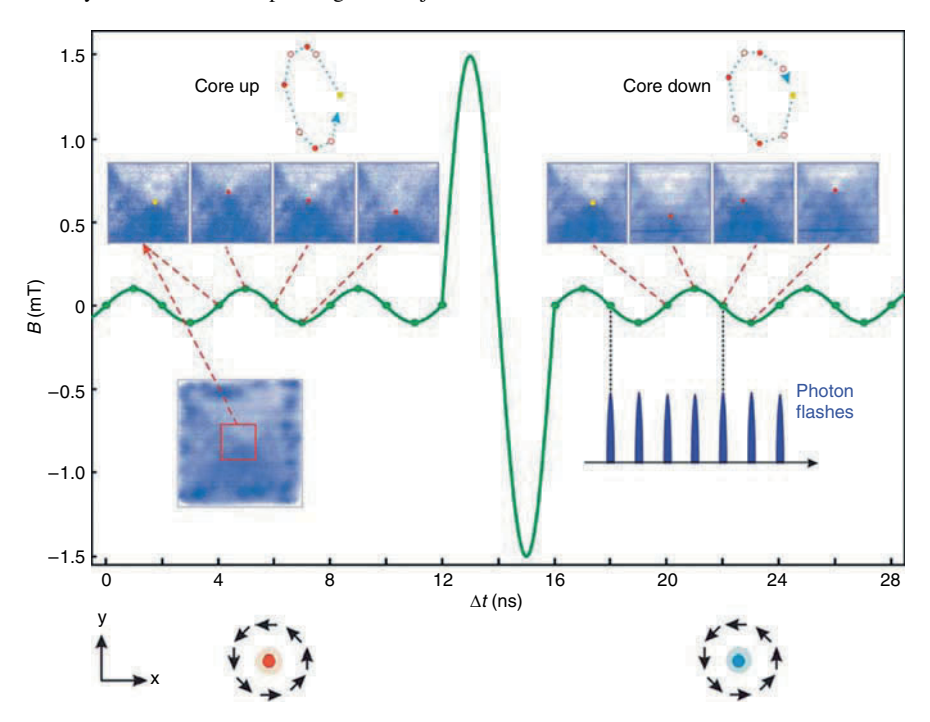


Fig. 14.12 Magnetic vortex core reversal by excitation with a short burst of an alternating field (from [50]). At the bottom, the magnetization is shown schematically before (*up*) and after (*down*) the switching. The image in the middle shows the STXM images with the vortex core gyrating counter clockwise before the switching and clockwise after the switching

14.5 Summary

Mesoscopic magnetic objects show interesting properties on a length scale of about $0.1\text{--}100\,\mu\text{m}$. Their dynamics is governed by collective modes. Pulsed field excitations excite all these modes simultaneously, thus allowing to identify and characterize the eigen-modes. Resonant excitations allow selective excitation of specific modes. Synchrotron-based X-ray microscopy has become a versatile and useful technique to study such systems as it offers not only the required spatial and temporal resolution, but also the element sensitivity.

The theoretical understanding in this field is still limited by a lack of a microscopic theory. However, the phenomenological Landau–Lifshitz–Gilbert equation successfully describes the properties of these mesoscopic objects in which true quantum effects are negligible.

Following first studies related to a basic understanding and a development of the methods, the field is now progressing toward questions related to industrial applications like increased density and optimized switching for data storage and possible applications of spin-torque.

Because of the great efforts undertaken internationally and because of the wide potential of both fundamental physics questions and industrial applications, it is likely that in the future this type of research will produce many more interesting results.

Acknowledgements It is our pleasure to thank C.H. Back, M. Buess, J. Stahl, I. Mönch, R. Mattheis, L. Bischoff, J. Fassbender, and F. Nolting who contributed to the progress of this work at various stages for data analysis, for sample preparation, and for developing the instrumentation. Part of this work was performed at the Swiss Light Source, Paul Scherrer Institute, Switzerland.

References

- 1. J.H.E. Griffiths, Nature 158, 670 (1946)
- 2. C. Kittel, Phys. Rev. 73, 155–161 (1948)
- 3. M. Farle, Rep. Prog. Phys. **61**, 755–826 (1998)
- I. Neudecker, G. Woltersdorf, B. Heinrich, T. Okuno, G. Gubbiotti, C.H. Back, J. Magn. Magn. Mater. 307, 148–156 (2006)
- M. Klàni et al., Magnetism and Synchrotron Radiation New Trends (Springer, Proceedings in Physics, Vol. 133, Berlin, 2010), ISBN: 978-3-642-04497-7
- A. Hubert, R. Schäfer, Magnetic Domains The Analysis of Magnetic Microstructures, (Springer, Berlin, 2008), ISBN: 978-3-540-64108-7
- C.H. Back, R. Allenspach, W. Weber, S.S.P. Parkin, D. Weller, E.L. Garwin, H.C. Siegmann, Science 285, 864 (1999)
- 8. M. Bauer, J. Fassbender, B. Hillebrands, R.L. Stamps, Phys. Rev. B 61, 3410 (2000)
- E. Beaurepaire, J.C. Merle, A. Daunois, J.Y. Bigot, Phys. Rev. Lett. 76, 4250–4253 (1996);
 M. Aeschlimann, PRL 79, 5158 (1997)
- 10. C. Quitmann, J. Raabe, C. Buehler, et al., Nucl. Instrum. Meth. A 588, 494-501 (2008)
- K. Jefimovs, J. Vila-Comamala, T. Pilvi, J. Raabe, M. Ritala, C. David, Phys. Rev. Lett. 99, 264801 (2007)
- 12. W. Kohn, Nobel Lecture: Rev. Mod. Phys. 71, 1253–1266 (1999)
- 13. T.L. Gilbert, IEEE Trans. Magn. 40, 3443–3449 (2004)
- J.C. Slonczewski, J. Magn. Magn. Mater. 159, L1 (1996); L. Berger, Phys. Rev. B 54, 9353 (1996)
- M.J. Donahue, D.G. Porter, OOMMF User's Guide, Version 1.0, Interagency Report NIS-TIR 6376, National Institute of Standards and Technology, (Gaithersburg, MD, 1999), http://math.nist.gov/oommf/
- 16. M. Scheinfein, LLG micromagnetic simulator (2009), http://llgmicro.home.mindspring.com.
- 17. R. Hertel, J. Appl. Phys. **90**, 5752 (2001)
- For a review see: Spin Dynamics in Confined Magnetic Structures II, Series: Topics in Applied Physics, Vol. 87, Hillebrands, Burkard; Ounadjela, Kamel (Eds.), 2003, XVI, 324 p., ISBN: 978-3-540-44084-0.
- 19. C.H. Back, D. Pescia, M. Buess, *Vortex Dynamics*, In Spin Dynamics In Confined Magnetic Structures III, Topics In Applied Physics 101 (Springer, Berlin, 2006), pp. 137–160
- 20. A. Locatelli, E. Bauer, J. Phys. Condens. Matter **20**(9), 093002 (2008)
- F. Nolting, Magnetism and Synchrotron Radiation New Trends (Springer, Proceedings in Physics, Vol. 133, Berlin, 2010), ISBN: 978-3-642-04497-7
- G. Schönhense, H.J. Elmers, S.A. Nepijko, C.M. Schneider, Adv. Imag. Electron Phys. 142, 160, (2006)
- A.L.D. Kilcoyne, T. Tyliszczak, W.F. Steele, S. Fakra, P. Hitchcock, K. Franck, E. Anderson, B. Harteneck, E.G. Rightor, G.E. Mitchell, A.P. Hitchcock, L. Yang, T. Warwick, H. Ade, J. Synchrotron Radiat. 10, 125–136 (2003)

- 24. J. Raabe, G. Tzvetkov, U. Flechsig, et al., Rev. Sci. Instrum. 79, 113704 (2008)
- G. Schütz, W. Wagner, W. Wilhelm, P. Kienle, R. Zeller, R. Frahm, G. Materlik, Phys. Rev. Lett. 58, 737 (1987)
- 26. C.T. Chen, F. Sette, Y. Ma, S. Modesti, Phys. Rev. B 42, 7262 (1990)
- F. Sette, C.T. Chen, Y. Ma, S. Modesti, N.V. Smith, X-Ray Absorption Fine Structure, ed. by S.S.Hasnain (Ellis Horwood, Chichester, UK, 1991), p. 96
- 28. K.S. Buchanan et al., Nat. Phys. 1, 172 (2005)
- 29. G.N. Kakazei, T. Mewes, P.E. Wigen, et al., J. Nanosci. Nanotechnol. 8, 2811–2826 (2008)
- J. Goulon, Magnetism and Synchrotron Radiation New Trends (Springer, Proceedings in Physics, Vol. 133, Berlin, 2010), ISBN: 978-3-642-04497-7
- G. Boero, S. Mouaziz, S. Rusponi, P. Bencok, F. Nolting, S. Stepanow, P. Gambardella, New J. Phys. 10, 013011 (2008)
- K. von Bergmann, M. Bode, A. Kubetzka, O. Pietzsch, E.Y. Vedmedenko, R. Wiesendanger, Phil. Mag. 88, 2627–2642 (2008)
- L. Abelmann, S. Porthun, M. Haasta, C. Lodder, A. Moser, M.E Best, P.J.A van Schendel, B. Stiefel, H.J. Hug, G.P. Heydon, A. Farley, S.R. Hoon, T. Pfaffelhuber, R. Proksch, K. Babcock, J. Magn. Magn. Mater. 190, 135 (1998)
- 34. E.E. Huber, D.O. Smith, J.B. Goodenough, J. Appl. Phys. 29, 294 (1958)
- K. Kuepper, M. Buess, J. Raabe, C. Quitmann, J. Fassbender, Phys. Rev. Lett. 99, 167202 (2007)
- S. Cherifi, R. Hertel, J. Kirschner, H. Wang, R. Belkhou, A. Locatelli, S. Heun, A. Pavlovska, E. Bauer, J. Appl. Phys. 98, 043901 (2005)
- 37. S.S.P. Parkin, Phys. Rev. Lett. **67**, 3598–3601 (1991)
- F. Nolting, A. Scholl, J. Stöhr, J.W. Seo, J. Fompeyrine, H. Siegwart, J.P. Locquet, S. Anders, J. Lüning, E.E. Fullerton, M.F. Toney, M.R. Scheinfein, H.A. Padmore, Nature 405, 767 (2000)
- J. Raabe, C. Quitmann, C.H. Back, F. Nolting, S. Johnson, C. Buehler, Phys. Rev. Lett. 94, 217204 (2005)
- 40. M. Buess, J. Raabe, K. Perzlmaier, C.H. Back, C. Quitmann, Phys. Rev. B 74, 100404 (2006)
- 41. S.B. Choe, Y. Acremann, A. Scholl, A. Bauer, A. Doran, J. Stöhr, H.A. Padmore, Science **304**(5669), 420–422 (2004)
- 42. A. Puzic, et al., J. Appl. Phys. 97, 10E704 (2005)
- 43. K. Kuepper, L. Bischoff, Ch. Akhmadaliev, J. Fassbender, H. Stoll, K.W. Chou, A. Puzic, K. Fauth, D. Dolgos, G. Schütz, B. Van Waeyenberge, Appl. Phys. Lett. **90**, 062506 (2007)
- 44. M. Buess, R. Hollinger, T. Haug, et al., Phys. Rev. Lett. 93, 077207 (2004)
- 45. J. Fassbender, J. McCord, JMMM 320, 579-596 (2008)
- 46. J. Fassbender, L. Bischoff, R. Mattheis, P. Fischer, J. Appl. Phys. 99, 08G301 (2006)
- S. Kasai, P. Fischer, Mi-Young Im, K. Yamada, Y. Nakatani, K. Kobayashi, H. Kohno, T. Ono, Phys. Rev. Lett. 101, 237203 (2008)
- P. Fischer, D.H. Kim, B.L. Mesler, W.Chao, E.H. Anderson, J. Magn. Magn. Mater. 310, 2689 (2007)
- 49. R. Hertel, S. Gliga, M. Fähnle, C.M. Schneider, Phys. Rev. Lett. 98, 117201 (2007)
- B. Van Waeyenberge, A. Puzic, H. Stoll, K.W. Chou, T. Tyliszczak, R. Hertel, M. Fähnle, H. Brückl, K. Rott, G. Reiss, I. Neudecker, D. Weiss, C.H. Back, G. Schütz, Nature 444, 461–464 (2006)
- 51. T. Okuno, K. Shigeto, T. Ono, K. Mibu, T. Shinjo, J. Magn. Magn. Mater. **240**, 1–6 (2002)
- 52. A. Thiaville, J. Garcia, R. Dittrich, J. Miltat, T. Schrefl, Phys. Rev. B 67, 094410 (2003)

Chapter 15

From Third- to Fourth-Generation Light **Sources: Free-Electron Lasers in the UV** and X-ray Range

M. Altarelli

Abstract Worldwide activities towards the realization of free-electron laser UV and X-ray sources to produce spatially coherent, ultra-short ~100 fs pulses with very high peak brilliance (>10²⁸-10³² photons/s/ mm²/mrad²/0.1% BW) are summarized. These sources are based on linear accelerators to overcome the limits to brilliance imposed by the ring geometry. The scientific case includes time-resolved studies of dynamics on sub-ps scales, structural studies by imaging of nonperiodic systems, and investigation of high energy-density phenomena such as nonlinear X-ray optics and the production of warm dense matter. Examples of the existing projects are presented, with emphasis on the presently operational FLASH facility at DESY, which delivers ultrashort coherent pulses at 6.5 nm wavelength. Projects in the US, in Japan, and in Europe, aiming to attain the hard X-ray region, with wavelengths of order 0.1 nm, are described. Plans to control the time and energy structure of the pulses by seeding and harmonic generation schemes are also mentioned.

15.1 Introduction

Synchrotron radiation sources have revolutionized UV and X-ray experiments in many fields of science. The driving force behind the development of light sources is the optimization of their brilliance (or spectral brightness), which is the figure of merit for many experiments. Brilliance is defined as a function of frequency given by the number of photons emitted by the source in unit time in a unit solid angle, per unit surface of the source, and in a unit bandwidth of frequencies around the given one. The units in which it is usually expressed are

photons/s/mrad²/mm²/0.1% BW,

408 M. Altarelli

where 0.1% BW denotes a bandwidth $10^{-3} \omega$ centered around the frequency ω . In the most modern synchrotron sources (the so-called third-generation light sources, such as the ESRF, Elettra, Diamond, Swiss Light Source, etc.), the average brilliance of undulator radiation reaches values up to $10^{19}-10^{20}$, in the above units (see for example [1]). Taking into account the pulsed nature of the sources, that is, the filling patterns and revolution times of storage rings, this corresponds to peak brilliance values of $\sim 10^{24}$. To achieve such values, two ingredients are essential. The first is the reduction in the phase-space volume of the circulating electrons in the two transverse directions (the horizontal and vertical directions perpendicular to the average orbit). These quantities are called horizontal (vertical) emittances and are roughly speaking a measure of the size of the electron bunch times the angular divergences of the corresponding velocity vectors projections in the horizontal (vertical) plane. Progress in accelerator physics allows reduction of the horizontal emittance to values of the order $\sim 1 \,\mu$ m mrad. It is intuitive that the properties of small dimension and high collimation of the electron beam translate into corresponding attributes of the radiated photons, and therefore in higher brilliance. The second ingredient is the extensive use of undulators as radiation sources. In undulators, the broadband radiated power of bending magnet radiation is concentrated in a spectrum of narrow lines, centered about the wavelengths

$$n\lambda = \frac{\lambda_{\rm u}}{2\gamma^2} (1 + K^2/2). \tag{15.1}$$

Here $n=1,2,3\ldots$ is the order of the harmonic, λ_u is the period of the undulator magnetic structure, γ is the electron energy of the ring, expressed in units of the electron rest energy, and K is the undulator parameter, a number of order ~ 1 given by $K=\gamma \theta$, where θ is the maximum angular deviation of the electrons from their unperturbed trajectory induced by the undulator magnetic field. Equation (15.1) identifies the wavelength of the fundamental harmonic λ as the distance by which one electron lags behind the emitted photons after traveling over the distance λ_u from the emission point.

A substantial reduction of emittance values is hardly possible in storage ring sources, because every photon emission event imparts a random recoil to the electron, and this happens many times at every turn, as each electron goes through all the bending dipoles and undulators around the ring.

Another fundamental limitation of storage rings concerns the length of the bunches, that is, the duration of the light pulses. Typically, pulse duration in storage rings is limited to some $\sim 30\,\mathrm{ps}$, and substantially shorter pulses can only be achieved at the expense of dramatic reductions of the radiated intensity. This poses a limitation to the time scales, which can be explored by time-resolved experiments with synchrotron sources: at full power they are limited to the 50 ps time scale; access to the scale of atomic motions and rearrangements (typically, sub-ps) is possible only by techniques such as "bunch slicing," which produce pulses of $\sim 100\,\mathrm{fs}$, but with intensities limited to $\sim 10^3\,\mathrm{photons}$ per pulse [2]. On the other hand, there is a high demand for ultrafast experiments capable to explore atomic

motions and configuration changes on a sub-ps time scale. The development of *fs* lasers in the infrared, the visible, and near UV has shown a variety of interesting phenomena essential for the understanding of chemical reactions, phase transitions, etc.; only shorter wavelengths, however, can resolve smaller and smaller distances, and ultimately only X-rays can provide us with atomic position information.

In the following sections, we shall review progress in the realization of UV and X-ray FEL (free-electron laser) sources, based on *linear* accelerators, which allow generation of transversely coherent ultrashort (typically $10 - 100 \, \text{fs}$) pulses, with a spectacular increase of some nine orders of magnitude in peak brilliance.

15.2 The SASE Process and Short-wavelength Free-Electron Lasers

In the undulators of a synchrotron source, electrons are forced to follow a zigzag trajectory by the device magnetic field. There is a definite phase relationship between the radiation emitted by the same electron at different points of the trajectory, and as the fields overlap (the angle θ of maximum deviation, entering the undulator parameter K of (15.1), is of order $1/\gamma$, i.e., of the aperture of the radiation cone) there is an interference, which is constructive only for the wavelengths described by (15.1). Notice, however, that under such circumstances all interference between the fields radiated by different electrons is averaged out, as no definite phase relationship occurs between them. The reason is that electrons are randomly distributed inside the bunch, with no correlation between positions of different electrons. In order to have such interference, electrons should be spatially ordered; considering for simplicity two electrons, if the longitudinal coordinate (projection on the undulator axis of the position) of the second lags behind that of the first by an integer number of wavelengths, the corresponding radiation fields will superpose in phase after the electrons have run through an integer number of undulator periods. The intensity radiated from the two electrons will be four times larger than that of one single electron. From these simple considerations, one can understand how coherence effects between different electrons can arise when the density in the bunch (integrated over the transverse direction) has a Fourier component at the wavelength of the radiation, that is, when this density shows a modulation at the radiation wavelength. The intensity of the radiation in such cases becomes proportional to the square of the number of electrons involved in the modulation.

For short wavelengths, in the *nm* range or below, controlling the electron density on that scale may appear extremely difficult. However, it turns out that, for a sufficiently low-emittance and high peak-current electron beam, in a sufficiently long undulator, the radiation does it for us. This *microbunching* phenomenon occurs because the electric field of the radiation has a small component parallel (or antiparallel) to the electron velocity (see Fig. 15.1), which tends to accelerate some electrons and decelerate those which are positioned one half radiation wavelength ahead or behind, leading to bunching on the radiation wavelength scale. Whenever

410 M. Altarelli

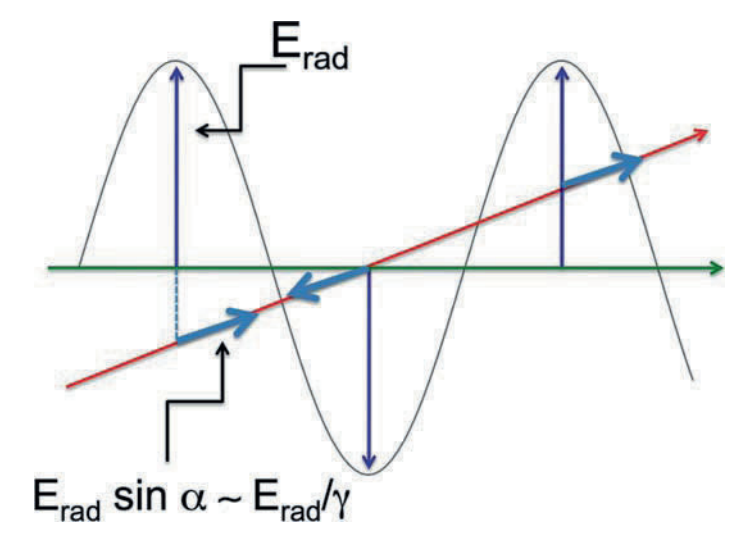


Fig. 15.1 Schematics of the microbunching process. The radiated electromagnetic wave (*black wavy line*) propagates along the undulator axis (*green line*), and the electron trajectory (*red line*) is at an angle $\alpha \sim 1/\gamma$ to this axis. Therefore, the radiation electric field $E_{\rm rad}$ has a small component (*blue arrows*) parallel or antiparallel to the electron velocity, $E_{\rm rad} \sin \alpha$, which can perform work on the electrons and therefore accelerate or decelerate them

shot-noise fluctuations in the electron bunch introduce a Fourier component of the appropriate wavelength in the electron density, the coherence effect between electrons described above increases the radiated intensity; the stronger radiation field, via the microbunching process, reinforces the density fluctuation, and so on, in a runaway process that leads to exponential amplification of the radiated intensity. The amplification proceeds until saturation, which occurs when the intense radiation and subsequent recoil effects lead to a degradation of the electron beam quality that prevents further amplification. This single-pass process, known as self-amplified spontaneous emission (SASE) was theoretically identified many years ago, long before electron beams of sufficient density and quality were technologically feasible [3–5]. It was later shown experimentally in the visible range at the LEUTL facility at Argonne National Laboratory [6], and later pushed to lower and lower wavelengths (down to 6.5 nm) at the FLASH facility at DESY, in Hamburg [7, 8]. The linear accelerator (linac) geometry is essential in allowing the low emittance and the high peak current required to trigger the SASE process. During acceleration in a linac, the normalized emittance $\varepsilon_n = \gamma \varepsilon$ is approximately constant, and this implies that the emittance decreases as the energy γ grows. So, if a sufficiently low emittance is available already at the start, that is, at the electron gun of the injector system, then transverse emittances of the order of the radiation wavelength are achievable at a sufficiently high electron energy. Furthermore, the high peak current can be achieved by compressing the bunch in one or several suitable magnetic chicanes, down to bunch lengths of order 30 µm or durations of 100 fs or less.

15.3 First Results at FLASH and the Science Case for X-Ray FELs

FLASH is a UV and soft X-ray FEL, based on the SASE principle, operating since 2005 as a user facility at DESY [9]. It is presently powered by a 1 GeV superconducting linac and produces coherent radiation pulses down to 6.5 nm wavelength, with up to $\sim\!100\,\mu\mathrm{J}$ per pulse. It has provided a unique testing ground for the investigation of the SASE process itself, as well as the first possibility to perform experiments with ultra-high peak brilliance pulses, of $\sim\!10\text{--}50\,\mathrm{fs}$ duration, with $\sim\!10^{12}$ photons per pulse. This corresponds to a peak power of Giga-watt, and it surpasses the peak brilliance of modern synchrotron sources by many orders of magnitude (see Fig. 15.2).

As it was explained in Sect. 15.2, SASE is a process starting from noise, and it contains therefore an unavoidable aspect of randomness, which makes every pulse different. In Fig. 15.3, results of a spectroscopic analysis of different pulses is shown, and the very limited pulse-to-pulse reproducibility is evident, as well as the lineshape, which is far from an ideal single gaussian or lorentzian profile [10].

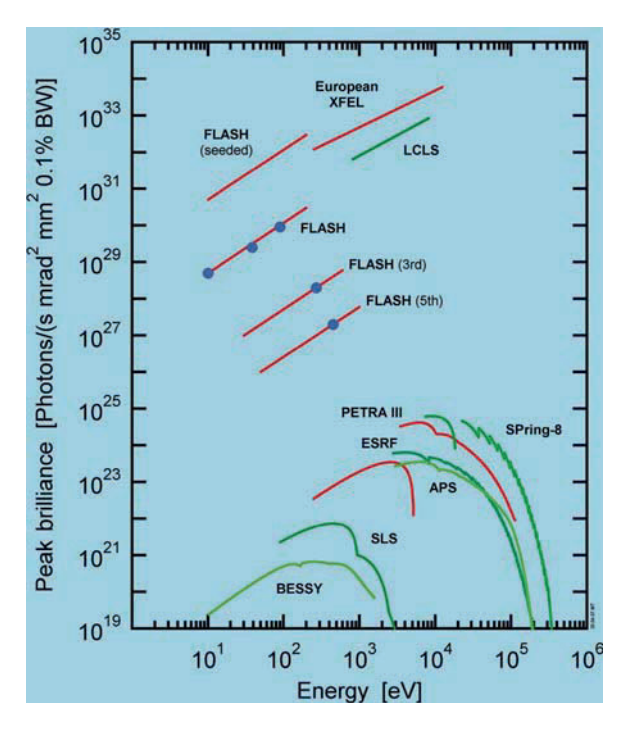


Fig. 15.2 Peak brilliance as a function of photon energy of FLASH and future FELs (the European XFEL in Hamburg, and LCLS in Stanford, see Sect. 15.4; an upgraded version of FLASH based on "seeding," see Sect. 15.5) compared with some third generation synchrotron radiation facilities. *Blue dots* denote measured values. The third and fifth harmonics of the FLASH undulator, on which lasing was observed, but not saturation, are also shown

412 M. Altarelli

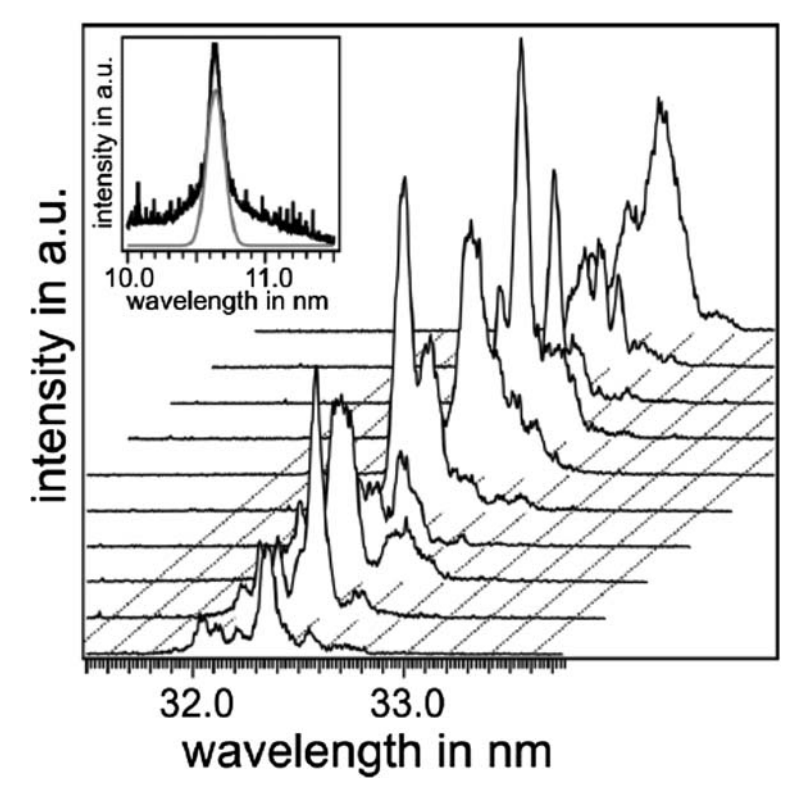


Fig. 15.3 VUV spectra for ten arbitrarily chosen FEL pulses. The main wavelength for all pulses is about 32.2 nm, with an overall width of about 0.4 nm. *Inset*, third-harmonic spectrum, centered at 10.7 nm, averaged over 2,500 pulses (after Düsterer et al.)

The revolutionary properties of FLASH have allowed many ground-breaking, completely novel experiments. Among these, one of the most celebrated is the single-pulse coherent diffraction imaging by Chapman et al. [11], in which it was demonstrated that a diffraction pattern sufficient to reconstruct an image by standard iterative algorithms could be acquired using a single FLASH pulse of 25 fs duration. As a result of the high number of photons in the pulse, photoelectric absorption deposits sufficient energy in the sample (a microstructure milled through a silicon nitride membrane) to bring it up to a temperature of 60,000 K and to destroy it completely. Nonetheless, the extremely short duration of the pulse allows collection of the relevant data before the sample is blown apart. Although the use of 32 nm radiation limits the resolution to a few tens of nanometer, which could be obtained easily by other, nondestructive, methods, the interest of this experimental breakthrough lies in the proof-of-principle of single-shot imaging of nonperiodic objects. One of the chapters of the scientific case for hard X-ray FELs is the hope to be able to image nonperiodic biological objects (from individual cells down to large macromolecules) with resolution approaching the atomic scale [12], without

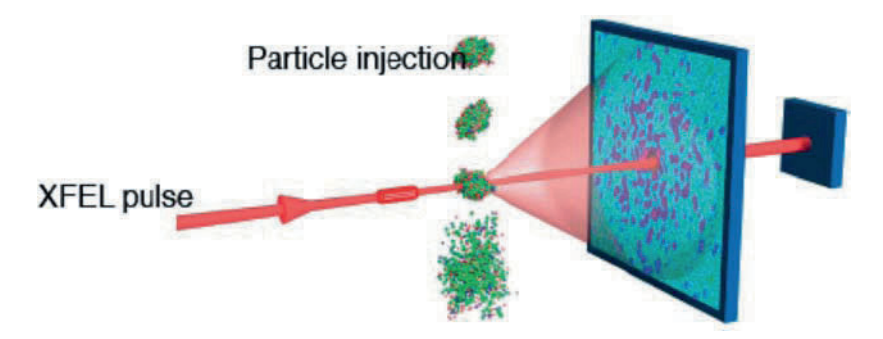


Fig. 15.4 Schematic layout of a single-particle imaging experiment, where single objects (e.g., macromolecules) are injected into the interaction region by a suitable spray device (not shown) and interact with X-ray pulses from an XFEL. The diffraction pattern is recorded by a two-dimensional detector (with a central hole to prevent damage from the direct beam). After the interaction the particle, highly ionized by the photoelectric effect, explodes

the need for crystallization – which is a major hurdle in structural biology studies (Fig. 15.4).

The possibility of acquiring valuable information in a single-pulse is not limited to imaging: very recently, a resonant magnetic scattering experiment at the Co M-edge on a Co-Pt multilayer system showed that magnetic speckles can also be collected in a single shot [13]. This pioneering results point to the possibility of ultrafast magnetization studies down to the ~ 100 fs timescale.

Another class of experiments in which the ultra-high intensity is essential is the study of extremely dilute samples. One can for instance generate and trap for a short time highly ionized atoms, such as ${\rm Fe^{23+}}$ [14]. In such a Li-like three-electron system, relativistic and QED effects are gigantic: for the $1s^22s^2S_{1/2}$ to $1s^22p_{1/2}^2P_{1/2}$ transition, radiative corrections to the transition energy are of order 1%. At FLASH the transition energy, close to 48.6 eV, was measured with unprecedented accuracy, opening up a program of investigation of QED effects extending beyond the region of perturbation theory, which could later continue with X-ray FELs with ions up to U^{89+} .

Gas phase experiments on the photoionization of neutral atoms in intense XUV fields also produced stimulating results. Sorokin et al. [15] observed that Xe gas subject to focused FLASH pulses of 13.3 nm with fluences up to $10^{16}\,\mathrm{W\,cm^{-2}}$ shows unexpected ionization states up to charge +21. From the standard theory of high-field ionization, at these fluences and frequency one should be in the multiphoton regime, and it is not yet clear whether these experimental results are reconcilable with the traditional wisdom.

To take advantage of the short pulse duration for time-resolved studies, the "pump-and-probe" experimental strategy is well known from ultrafast laser experiments: a process, for example, a chemical reaction, is triggered by a "pump" pulse; a successive "probe" pulse interrogates the system and determines a physical quantity at a later time. Repeating the experiment with different delays between the two

414 M. Altarelli

pulses, the time dependence of the physical quantity during the course of the reaction can be determined, with a resolution limited by the duration of the pulses and the accuracy in the determination of the delay. To perform such experiments with an FEL, it is therefore necessary to determine a posteriori the delay in the arrival of an FEL probe pulse with respect to another pulse [16], for example, from an optical laser, which acts as pump, because it is not possible to control the arrival time of the FEL pulses a priori with sufficient accuracy. This is because of the jitter determined by the limits in the stability of the accelerator radio frequency (RF) system and by the strong compression of the bunch length. Another strategy, also successfully pursued at FLASH, consists in extracting both pump and probe pulses from the same electron bunch. This can be done by inserting a special undulator for infrared or THz frequencies along the electron path on the way to the SASE undulator [17]; or, alternatively, by a split-and-delay device that separates each FEL pulse in two, separated by an adjustable delay; in the latter case, of course, both pulses have the same photon energy. Such a device has been realized and tested at FLASH [18], and a device for hard X-rays, based on crystal optics, has also been developed at DESY and subjected to preliminary tests at the ESRF [19].

15.4 The Quest for Hard X-Ray FELs

The remarkable results obtained at the FLASH facility have allowed considerable progress in the understanding of the SASE process itself, and demonstrated the revolutionary potential of FEL experiments for a variety of disciplines. This has provided further stimulation to projects for the realization of hard X-ray FELs. There are at present three major projects under construction worldwide, one in the USA (the Linac Coherent Light Source, LCLS, in Stanford, California [20]), one in Japan (the SCSS, SPring-8 Compact SASE Source, at SPring-8 [21]), and one in Europe (the European XFEL in Hamburg [22]), which aim at wavelengths of the order of 0.1 nm, suitable for experiments determining structural properties with atomic resolution. The main features of the three projects are summarized in Table 15.1.

The LCLS project in Stanford produced the first 0.15 nm SASE photons in April 2009. It uses the pre-existing SLAC high energy linear accelerator, or more

able 13.1 Basic parameters of the three hard A-rays FEL projects (see text)			
Project	LCLS	SCSS	European XFEL (SASE1)
Max. electron energy (GeV)	14.3	8.0	17.5
Min. photon wavelength (nm)	0.15	0.1	0.1
Photons/pulse	$\sim 10^{12}$	2×10^{11}	$\sim 10^{12}$
Peak brilliance	1.5×10^{33}	1×10^{33}	5×10^{33}
Average brilliance	4.5×10^{22}	1.5×10^{23}	1.6×10^{25}
Pulses/second	120	3,000	30,000
Date of first beam	2009	2011	2014

Table 15.1 Basic parameters of the three hard X-rays FEL projects (see text)

Brilliance are expressed in photons/s/mrad²/mm²/0.1% BW

precisely, one third of its length, to accelerate electrons and feed them into an undulator with fixed gap, 112 m long, to produce coherent X-rays with photon energies between 0.8 and 8 keV, that is, with wavelengths between 1.5 and 0.15 nm. Tuning of the photon energy occurs by tuning of the electron energy between 4.5 GeV and the maximum energy 14.3 GeV. The linear accelerator has been modified to accept the bunches produced by a RF photocathode gun and preserve the low-emittance beams required for the SASE process and also to include two stages of bunch compression. The repetition rate is 120 pulses per second. The SASE pulses are directed into two experimental halls, where a total of six instruments are foreseen to become available between 2009 and 2011:

- 1. Atomic, Molecular, and Optical Science (AMO): this instrument should continue and extend to higher photon energy the innovative experiments pioneered at FLASH on ions, atoms, and molecules.
- 2. X-ray Correlation Spectroscopy (XCS): its purpose is to use the coherence of the beams to explore dynamic fluctuations in matter, accessing unprecedented length and time scales.
- 3. X-ray Pump-Probe (XPP): the purpose of this instrument is to explore ultrafast phenomena in the physics and chemistry of solids, liquids, and soft-matter systems.
- 4. Coherent X-Ray Imaging (CXI): this instrument is devoted to the pursuit of structural studies in nonperiodic systems, especially in structural biology.
- 5. High Energy-Density Science (HED): here the idea is to use the FEL pulses to bring a target to extremely high values of temperature and then to interrogate it in order to access regions of the phase diagram not easily accessible in the laboratory (e.g., *warm dense matter* in which ordinary densities of solid materials are present at temperatures such that $k_{\rm B}T \sim 1-10\,{\rm eV}$).
- 6. Soft X-Ray Materials Science: this is a multipurpose instrument, on which different end-stations should be mounted for a variety of techniques in the soft X-ray analysis of materials, such as RIXS, fluorescence, photoemission, etc.

The Japanese SCSS project is characterized by the attempt to reduce the size and the cost of large FEL installations by daring innovations, such as the use of a thermionic cathode gun to produce very low emittance bunches, the use of C-band accelerator technology to generate very high acceleration gradients, a very high compression ratio for the bunch length (\sim 4,000) and the use of a tunable in-vacuum undulator, with a 4 mm gap in the standard operation for generation of 0.1 nm radiation with an electron energy of 8 GeV, considerably lower than in the competing projects. Validation of some of these concepts has been provided by a test facility with a 250 MeV linac, which is operating as a VUV FEL down to 49 nm wavelength. This test facility was used for some ground-breaking experiments on the "seeding" scheme based on high harmonic generation (see Sect. 15.5). The design value for the number of pulses per second is 3,000 as there are 60 RF pulses per second, each of them filled with up to 50 bunches. There are five undulators foreseen in the ultimate configuration of the facility.

416 M. Altarelli

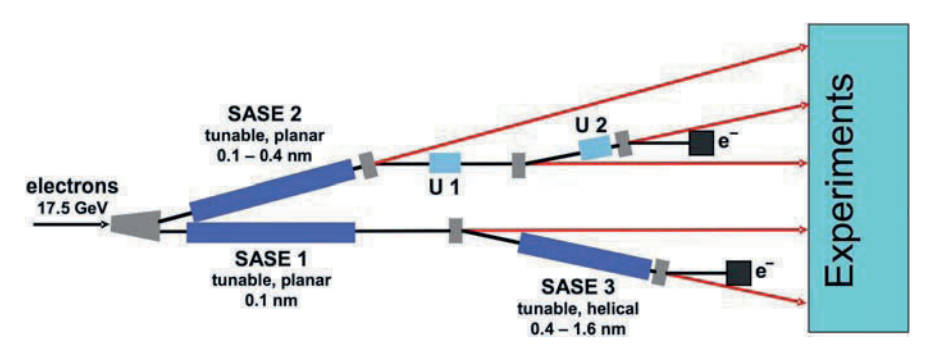


Fig. 15.5 Schematic layout of the arrangement of undulators at the European XFEL. The initial configuration of the facility does not include the spontaneous emission undulators U1 and U2, nor the helical version of SASE3, which is going to be initially built in the planar version

The European X-ray Free-Electron Laser Facility (European XFEL), which started construction in January 2009 in Hamburg, is deriving its basic technical choices from the successful FLASH experience. The photoinjector and the gun are directly derived from the corresponding FLASH components and so is the basic superconducting accelerator technology, first developed in the context of the international TESLA collaboration, coordinated by DESY. The 1.7 km long accelerator, located in an underground tunnel, can provide electrons with a 17.5 GeV energy, and feed them into two beamlines according to the scheme displayed in Fig. 15.5 [23]. The first beamline contains a hard X-ray undulator (SASE1), for 0.1 nm coherent photons, and a soft X-ray one (SASE3), which makes use of the "spent" beam resulting from saturation of SASE1 to generate soft X-rays in the 0.4–1.6 nm range (at 17.5 GeV electron energy: softer X-ray radiation is of course obtained if the electron energy is reduced). The second beamline contains a tunable hard X-ray undulator (SASE2) for the 0.1–0.4 nm range, and two tunnels downstream in which two spontaneous emission undulators, U1 and U2, can be located. In the baseline design for the initial phase of the facility, each of the three SASE undulators will feed into two instruments. The six foreseen instruments are similar in their scientific goals to the six instruments foreseen for the LCLS project.

The use of the superconducting technology allows a very wide flexibility in the operating conditions; in particular, it allows to fill each RF pulse with a very large number of electron bunches. In the European XFEL, it is foreseen to have a train of up to 3,000 bunches in each of the 10 RF pulses of 600 μ s duration. It will be possible to switch the electrons from one beamline to the other during each bunch train. The possibility to use such a large number of bunches implies considerable development work in the field of detectors, as well as in the lasers for pump-probe experiments, which should be able to follow the time structure of the XFEL pulses. The average brilliance, corresponding to this large number of X-ray pulses per unit time, could prove very important in experiments such as coherent diffraction of nonperiodic objects, illustrated in Fig. 15.4, where hits of the FEL pulses with a molecule are expected to be very rare, but a large number of them needs to be accumulated in order to achieve a satisfactory signal-to-noise ratio.

15.5 Seeded Free-Electron Lasers

As it was said in Sect. 15.2, the generation of coherent light by the SASE process is triggered by shot-noise fluctuations in the electron density. There is therefore an intrinsic random character to SASE radiation, which is reflected for example in the non-reproducibility of successive pulses, as visible in Fig. 15.3; in addition, the spectral profile of each pulse is far from an ideal, transform-limited lorentzian or gaussian shape. It would certainly be desirable for many classes of experiments to alleviate these problems of the SASE process and to obtain reproducible, spectrally pure FEL pulses. This is the motivation for the development of the "seeding" procedure. To do it in practice, one must replace the triggering by random fluctuations with a reliable and reproducible "trigger," able to impress a controllable density modulation on the electron bunch, with an amplitude larger than noise, thus making the latter irrelevant. The schemes developed so far invariably use a conventional laser as a source of reliable, reproducible, and spectrally pure pulses. Clearly, an additional advantage of such seeding schemes is the intrinsic time synchronization of the FEL pulses with the seed laser, with very important applications to pumpprobe experiments. Conventional lasers, however, are available for wavelengths in the infrared, visible, or at best near ultraviolet spectral ranges, whereas FELs, as we have seen, have demonstrated lasing in the X-ray range (down to the 0.15 nm wavelength region). To bridge this large difference in wavelength, two schemes have been proposed.

In the first one, the "seed" laser is overlapping with the electron bunch within an undulator, called "modulator," for which the resonant wavelength is that of the laser pulse (typically a Ti:saffire laser, operating at a wavelength of 800 nm, or frequencytripled at 266 nm). Here the laser pulse produces an energy modulation in the bunch, which is then led through a dispersive element (a chicane of four dipole magnets), where the energy modulation is converted to a spatial density modulation, that is, to a bunching of the electronic charge. What is important is that the bunching does not occur as a single cosine wave at the wavelength of the seed pulse, but it is also appreciable at the harmonics thereof. When the spatially modulated bunch enters now a second undulator, called "radiator," such that its resonant wavelength is one of the harmonics of the seed pulse, if the corresponding Fourier component of the bunch density modulation is large enough to trigger the exponential growth of coherent radiation, the "seeding" will be successfully transferred at a harmonic of the input pulse. This mechanism of seeding is labeled HGHG, for "High Gain Harmonic Generation." Its first demonstration in the VUV was performed in Brookhaven, where 9 ps long Ti:saffire pulses at 800 nm, with peak power in the MW region, were overlapped with the electron bunches at 177 MeV energy in a 0.8 m long modulator, and after a dispersive section, sent into a 10 m long radiator, resonant at 266 nm, that is, at the third harmonic of the seed laser pulse [24]. It was possible, under optimal condition to generate spectrally clean, reproducible coherent pulses at 266 nm wavelength, with ~100 μJ energy per pulse, exceeding the SASE output (in the absence of the seed) by orders of magnitude. It is obvious that if the radiator is tuned on the fifth or seventh harmonic of the seed laser, the output power is reduced,

418 M. Altarelli

corresponding to a decreasing harmonic contents of the density modulations induced by the seed. There are nonetheless schemes for accessing shorter and shorter wavelengths by the so-called *cascaded HGHG* set up: here the output of the radiator at a harmonic of the original seed laser is again fed into a second modulator, and then, after a dispersive section into a second radiator, resonant at an even higher-order harmonic of the original seed laser. This "cascaded" approach is supported by simulations, but how far it can really reduce the wavelength has to be proven in practice: the FERMI@Elettra project, already in an advanced state of construction in Trieste, Italy, has the ambition to use the simple HGHG scheme to reach 40 nm wavelengths, and to adopt cascaded HGHG for lasing down to 10 nm wavelength or less in a second stage [25].

A second scheme, which has been successfully tested at SPring-8 at the test VUV FEL, uses as a seed not directly a Ti:saffire laser pulse, but one of high order harmonics that the pulse generates in a gas [26]. For very intense laser pulses, it is well known that the photoionization of atoms proceeds via tunneling, the laser electric field having an intensity sufficient to bend down the steep atomic potential and to let electrons escape during one laser cycle. When the field changes direction, one half period later, the photoelectrons are accelerated back towards the parent atom, generating high harmonics in the collision (a process termed HHG for "High Harmonic Generation"). Thus, in the experiment by Lambert et al., a Ti:saffire laser focused on a xenon gas cell generates odd harmonics from the 3rd to the 21st. The fifth harmonic at 160 nm has an energy per pulse close to 1 µJ. The 50 fs pulses are spectrally selected and directed on a trajectory overlapping the 1 ps long, 150 MeV electron bunches, which are directed through two undulator sections tuned to resonate at the same 160 nm wavelength. The thus seeded emission exceeds the unseeded one by a factor of 2,600. There are good reasons to believe that seed pulses down to \sim 1 nJ can still be used as effective seeds and this opens the way to the use of higher harmonics, down to the 10 nm region.

A test facility with the HHG scheme is being implemented for FLASH, with the objective of seeding to 30 nm wavelengths and below [27]. The corresponding anticipated increase in peak brilliance is shown in Fig. 15.2.

References

- D.H. Bilderback, P. Elleaume, E. Weckert, J. Phys. B: Atom. Mol. Opt. Phys. 38, S773–S797 (1995)
- 2. R.W. Schoenlein, et al., Science 287, 2237-2240 (2000)
- 3. A.M. Kondratenko, E.L. Saldin, Sov. Phys. Dokl. 24, 986–988 (1979)
- 4. R. Bonifacio, C. Pellegrini, L.M. Narducci, Opt. Commun. 50, 373–378 (1984)
- 5. J.B. Murphy, C. Pellegrini, Nucl. Instrum. Meth. A 238, 159–167 (1985)
- 6. S.V. Milton, et al., Science 292, 2037-2041 (2001)
- 7. V. Ayvazyan, et al., Phys. Rev. Lett. 88, 104802-1-104802-4 (2002)
- 8. S. Schreiber, B. Faatz, K. Honkavaara, Proceedings of EPAC08, Genoa, Italy (2008), http://www.epac08.org/index.php?n=Main.ProceedingsDownload, pp. 133–135

- K. Honkavaara et al., Proceedings of the 14th International Conference on RF Superconductivity, Berlin 2009, available online at http://accelconf.web.cern.ch/AccelConf/srf2009/papers/mooaau01.pdf
- 10. S. Düsterer, et al., Opt. Lett. **31**, 1750–1752 (2006)
- 11. H.N. Chapman, et al., Nat. Phys. 2, 839–843 (2006)
- 12. R. Neutze, R. Wouts, D. van der Spoel, E. Weckert, J. Hajdu, Nature 406, 752-757 (2000)
- 13. C. Gutt, et al., submitted to Phys. Rev. B
- 14. S.W. Epp, et al., Phys. Rev. Lett. 98, 183001-1–183001-4 (2007)
- A.A. Sorokin, S.V. Bobashev, T. Feigl, K. Tiedtke, H. Wabnitz, M. Richter, Phys. Rev. Lett. 99, 213002-1–213002-4 (2007)
- 16. A.L. Cavalieri, et al., Phys. Rev. Lett. 94, 114801-1-114801-4 (2005)
- 17. M. Gensch, Infrared Phys. Tech. **51**, 423–425 (2008)
- 18. A. Föhlisch, W. Wurth, private communication
- W. Roseker, H. Franz, H. Schulte-Schrepping, A. Ehnes, O. Leupold, F. Zontone, A. Robert, G. Grübel, Optics. Lett. 34, 1768–1770 (2009)
- P. Emma, Proceedings of the Particle Accelerator Conference (PAC'09), Vancouver, Canada, in press
- 21. T. Shintake et al., Phys. Rev. ST-AB 12, 070701-1-070701-12 (2009) and references therein
- M. Altarelli et al., editors, "XFEL: the European X-ray Free-Electron Laser: Technical Design Report" DESY Report DESY 2006-097, July 2006. Available online at http://www.xfel.eu/documents/
- 23. M. Altarelli et al., editors, see Ref. 22, pp. 173-211
- 24. A. Doyuran et al., Phys. Rev. Spec. Top. Accel. Beams 7, 050701-1-050701-12 (2004)
- 25. G.D. Auria, et al., Conceptual Design Report of the FERMI@Elettra Project (2007), http://www.elettra.trieste.it/FERMI/index.php?n=Main.CDRdocument
- 26. G. Lambert et al., Nat. Phys. 4, 296–300 (2008)
- A. Azima et al., Proceedings of EPAC 08, Genoa, Italy http://www.epac08.org/index.php? n=Main.ProceedingsDownload/ pp. 127–129

Contributors

Altarelli, M., 409 Ansermet, JPh., 45 Antoniak, C., 147	Pineider, F., 281 Puzic, A., 387
Bombardi, A., 225 Bosak, A., 171	Quitmann, C., 387
Cocco, D., 129 Collins, S.P., 225 Cornia, A., 281	Raabe, J., 387 Rogalev, A., 171, 193 Rueff, JP., 265
Goujon, G., 193 Goulon, J., 171, 193	Sainctavit, Ph., 281 Sessoli, R., 281
Joly, Y., 79	van der Laan, G., 315
Kläui, M., 369 Kuepper, K., 387	Weber, W., 3 Wende, H., 147 Wilhelm, F., 171, 193 Wintz, S., 387
Mannini, M., 281 Moore, K. T., 315	
Nolting, F., 347	Zangrando, M., 129